Aero-Hydro-Servo-Elastic Modelling and Control of a Scaled Floating Offshore Wind Turbine on a Tension Leg Platform Including Experimental Validation



2018

MASTER THESIS FROM DEPARTMENT OF ENERGY TECHNOLOGY

AALBORG UNIVERSITET ESBJERG

DENMARK

AALBORG UNIVERSITET

Title:

Aero-Hydro-Servo-Elastic Modelling and Control of a Scaled Floating Offshore Wind Turbine on a Tension Leg Platform Including Experimental Validation

Theme:

Floating Offshore Wind Turbine
Model Development
Aerodynamics
Hydrodynamics
Tower Dynamics
Servo Dynamics
Control

Project period:

P9-P10, 2017-2018

Project group:

OES10-1

Authors:

Jesper Kirkegaard Jensen
Kasper Jessen
Kasper Laugesen
Signe Møller Mortensen

Supervisor:

Associate Professor
Mohsen Soltani

Paper total page numbers:

227

Appendix total page numbers:

104

Total page numbers:

420

Paper completed:

07-06-2018

Energy
Niels Bohrs Vej 8, 6700 Esbjerg
Telefon: 9940 9940, Fax: 9940 7710
http://www.esbjerg.aau.dk

Abstract:

As the demand for clean energy is rising, new technologies are developed. One of these new technologies is the floating offshore wind turbine (FOWT). These can be placed at locations where the sea is too deep for wind turbines with bottom fixed foundations. However by making the foundation floating, additional dynamics will be introduced into the system and thus lead to more complex systems. This calls for more precise and validated models. These models include hydrodynamics, structural dynamics, aerodynamics, servo dynamics, the coupling between these and the control system.
In this thesis two fully coupled mathematical models of the AAUE-TLP will be presented; one in the CAE tool FAST and one Simulink model developed throughout the thesis. The AAUE-TLP is a fully functional physical scaled model of a FOWT developed by the authors. Parts of some of the mathematical models will be found through simple experiments done on the AAUE-TLP, other will be purely theoretical. All models will be tested and validated through more advanced experiments on the AAUE-TLP. One control system for the generator and one control system for the pitching system will be designed and tested on the AAUE-TLP.

The thesis content is freely available, but publication (with references) must obtain permission from the authors.

Resumé 1

Dette kandidatspeciale omhandler modellering og kontroldesign af en flydende vindmølle. Flydende vindmøller vil være en klar fordel i de dele af verden, hvor der er dyb sø. Offshore vindmøller med fast fundament er kun egnede til at stå i forholdsvist lavt vand, da fundamentet skal fastgøres til havbunden. Prisen på et fast fundament øges væsentligt, når havdybden øges og derved foreværres økonomien for hele vindmøllen. De nuværende intallationsskibe har også en begrænsning for hvor store fundamenter, der kan fragtes ud og monteres på havbunden. En mulig løsning er, at de flydende fundmaneter kan trækkes ud og derved undgås anvendelsen af dyre installationsskibe. En anden mulighed er at montere selve vindmøllen i havnen eller i en tørdok, således installationsomkostningerne sænkes yderligere.
I tidligere projekter skrevet af forfatterne er der udviklet en fysisk model af en flydende vindmølle med et TLP (tension leg platform) fundament. Vindmøllen er tegnet i programmet Inventor og skaleret ift. NREL 5 MW vindmøllen og har individuel pitch regulering af vingerne. I dette speciale vil denne model blive testet vha. både bølge- og vindgenerator for at gøre belastningerne så virkelighedsnære som muligt. Der er udviklet en matematisk model af hele systemet i MATLAB Simulink, samt vha. NRELs FAST (fatique, aerodynamics, structures and turbulence) simuleringskode. Igennem hele specialet vil teorien bag modellerne blive gennemgået og de teoretiske koefficienter vil blive fundet. Herefter vil de teoretiske koefficienter, hvis det er muligt, blive valideret på den fysiske vindmølle.
Når hydrodynamikken af systemet beskrives, vil der blive brugt lineær bølgeteori. Da teorien antager, at vandoverfladen er konstant, inkluderes Wheeler udstrækning af bølgerne, hvor hastighedsprofilen kommer til at følge den faktiske bølge. Irregulære bølger beskrives ved at lægge forskellige lineære bølger sammen. Energien i bølgerne kan beskrives vha. et spektrum, hvor der i dette speciale primært anvendes JONSWAP.
Vindmøllens tårn vil blive beskrevet vha. FEM (finite element method), hvor tårnet deles op i elementer, som er afhængige af hinanden. Alle elementerne i masse-, stivheds- og dæmpningsmatricerne vil blive forklaret og de teoretiske værdier vil blive fundet. Dæmpningsmatricen bliver beskrevet ved en kombination af masse- og stivhedsmatricen. De naturlige frekvenser, samt de eksterne kræfter vil blive fundet.
Aerodynamikken vil blive beskrevet ved UBEM (unsteady blade element method) for at kunne beskrive aerodynamiske kræfter i tidsdomænet, når der sker ændringer i operationsforhold. Både rigtige vindforhold og vindforholdene fra vindgeneratoren vil blive beskrevet, og vindfeltet vil blive modelleret ud fra målinger fra vindfeltet. Her vil både blive beskrevet 1D og 3D vindfelter. Ydermere vil forskellige korrektionsmetoder, samt de dynamiske modeller for varierende operationsforhold blive implementeret i UBEM.
En matematisk model for drivtoget og generatoren, samt en simuleringsmodel for effektomformeren

vil blive udledt. Den fysiske effektomformer, der vil blive brugt i den eksperimentelle opstilling, vil være en ombygget VLT fra Danfoss. Pitchsystemet vil blive beskrevet vha. eksperimentelle modeller. Sammenkoblingen af alle undermodellerne vil blive beskrevet og udført matematisk. Tårnet vil blive koblet til TLPen og der vil blive lavet simple forsøg, der kan bruges til at tune sammenkoblingen, samt mere avancerede forsøg, hvor den matematiske model for sammenkoblingen vil blive valideret. Aerodynamikken vil blive koblet til tårnet og drivtoget, mens generatoren bliver koblet på drivtoget, og dermed opnås en samlet model for vindmøllen som skal testes så realistisk som muligt. Det vil sige, at den fysiske model vil blive testet i bølgebassinet, hvor et realistisk bølgespektrum vil blive påført TLPen og vind vil blive påført tårnet og rotoren.
For at systemet skal fungere så realistisk som muligt, skal der implementeres en kontrol. Her kan både styres på belastningen til generatoren, samt på pitchvinklen af vingerne, afhængig af hvilken vindhastighed, der påføres vindmøllen. Som kontrolmetode til generatoren anvendes FOC (field orientated control), som bliver designet ud fra rodkurve og OSM (optimum symmetric method), hvor et udvidet Kalman filter desgines og anvendes til at estimere vinklen på generatoren. Der vil blive designet to kontrolsystemer til den kollektive pitchkontrol; en med konstante PI termer og en, hvor PI termerne er varierende afhængig af pitchvinklen.

Preface 2

This master thesis project was carried out during the fall of 2017 and the spring of 2018 at the Department of Energy Technology, Aalborg University, Esbjerg.

The aim of this thesis is to gain knowledge and comprehension for different system identification and surveillance methods. This along with knowledge and comprehension for different advanced control methods. Furthermore it is desired to be able to critically judge knowledge and identify new scientific problems within the area of offshore energy systems. As skills it is sought to be able to verify the different scientific analyses and methods by advanced laboratory setups, data analysis and modelling methods, this along with being able to judge the usefulness of different scientific methods for the design of control and surveillance systems for offshore energy systems. It is furthermore sought to get competences in controlling the working and development process within the project theme, and being able to develop new solutions within control, diagnostic and surveillance of offshore energy systems. This along with being able to define and analyse scientific problems in the area of control diagnostics and surveillance of offshore energy systems, and based on that make and state the reasons for decisions made. This along with being able to set up innovative ideas within the area of control, diagnostic and surveillance of offshore energy systems, and furthermore being able to independently continue development in competences and specialisations. [1]

This thesis would not have been possible without the aid of many different people who have spent a lot of time sharing their knowledge with the authors. The authors of this thesis would like to express their sincere gratitude to our supervisor, Associate Professor Mohsen Soltani for his guidance and support throughout the thesis.
Furthermore, the authors would like to express their deepest gratitude to Ph.d fellow Kasper Jepsen, Assistant Professor Simon Pedersen and Research Assistant Jesper Liniger for valuable discussions and knowledge sharing.
Furthermore, the authors of this thesis would like to show their gratitude to engineering assistant Henry Enevoldsen for his help with experimental equipment.

Abbreviation

CAE	Computer-Aided Engineering
BC	Boundary Conditions
BEM	Boundary Element Method/Blade Element Method
BLDC	Brushless Direct Current
CW	Clock Wise
CCW	Counter Clock Wise
COB	Centre of Bouyancy
COG	Centre of Gravity
DAQ	Data Acquisition
DFT	Discrete Fourier Transform
DNS	Direct Navier Stokes
DNV	Det Norske Veritas
DOF	Degree of Freedom
EKF	Extended Kalman Filter
EMF	Electromotive Force
FAST	Fatigue, Aerodynamics, Structures, and Turbulence
FEM	Finite Element Method
FOWT	Floating offshore wind turbine
GM	Gain Margin
GPIO	General Purpose Inputs/Outputs
JONSWAP	Joint North Sea Wave Observation Project
IRF	Impulse Response Function
LES	Large Eddy Simulation
LFD	Linear Frequency Domain
LHEEA	Research Laboratory in Hydrodynamics, Energy and Atmospheric Environment
MDOF	Multiple Degree of Freedom
MMF	Magnetomotive Force
MPPT	Maximum Power Point Tracking
NREL	National Renewable Energy Laboratory
OSM	Optimum Symmetric Method
PMSG	Permanent Magnet Synchronous Generator
PM	Phase Margin/Pierson-Moscowitz
PSD	Power Spectral Density
RANS	Reynold's Average Navier Stokes
RAO	Response Amplitude Operator
SCI	Serial Communication Interface
SBEM	Steady Blade Element Method
SDOF	Single Degree of Freedom
SPWM	Sinusoidal Pulse Width Modulation
SVPWM	Space Vector Pulse Width Modulation
SWL	Still Water Line
TDD	Time Domain Dynamics
TLP	Tension Leg Platform
TSR	Tip Speed Ratio
UART	Universal Asynchronous Receiver/Transmitter

UBEM	Unsteady Blade Element Method
VSI	Voltage Source Inverter

Contents

1 Resumé **5**

2 Preface **7**

I Introduction **15**

2.1 Motivation . . . 18
2.2 Problem Definition . . . 19
2.3 State Of Art . . . 19
2.4 Previous Work . . . 22
2.5 Definitions . . . 24

3 Modelling Methods **25**

3.1 FAST . . . 25
3.2 Simulink Model . . . 28

4 AAUE-TLP **29**

4.1 Tower . . . 30
4.2 Nacelle . . . 31
4.3 Blades . . . 34
4.4 Electronics . . . 37

5 Experimental Facilities **39**

5.1 OptiTrack Camera System . . . 40
5.2 Generator Test Bench . . . 40
5.3 Wind Generator . . . 40
5.4 Wave Generator . . . 48

II Hydrodynamic Model **51**

6 Introduction **57**

7 Wave Generation **59**

7.1 Linear Wave Theory . . . 60
7.2 Irregular Wave Generation . . . 67
7.3 Spectrum . . . 69

8 Dynamical Equation of the Tension Leg Platform **73**

8.1 Hydrodynamic Coordinate System . . . 73

8.2 Time Domain Representation . . . 74
8.3 Frequency Domain Representation . . . 79

9 Hydrodynamic Coefficients 81
9.1 Numerical Software . . . 82
9.2 Inertia . . . 83
9.3 Added Mass . . . 84
9.4 Damping . . . 85
9.5 Stiffness . . . 92
9.6 Natural Frequencies . . . 96
9.7 Hydrodynamic Simulation . . . 96

10 Test and Validation 99
10.1 Elasticity of Mooring Lines . . . 99
10.2 Mooring Stiffness . . . 100
10.3 Free Decay . . . 100
10.4 Forced Harmonic Response . . . 105
10.5 Response Amplitude Operator . . . 106
10.6 Impulse Excitation of TLP . . . 110

11 Conclusion 111

III Structural Tower Model 113

12 Introduction 117

13 Finite Element Analysis 119
13.1 Governing Equation of Motion . . . 119
13.2 Model System Matrices . . . 120
13.3 Convergence Analysis . . . 128
13.4 Global Transformation . . . 129
13.5 Eigenmodes and Natural Frequencies . . . 130
13.6 Boundary Conditions . . . 132
13.7 External Loads . . . 132

14 Test and Validation 135
14.1 Young's Modulus . . . 135
14.2 Free Decay . . . 136
14.3 Impulse Excitation . . . 138
14.4 Stiffness of Tower . . . 141

15 Conclusion 143

IV Aerodynamic Model 145

16 Introduction 149

17 Wind Modelling 151

17.1 Wind Conditions . . . 151
17.2 Representation of Stationary Wind Conditions . . . 152
17.3 Wind Simulation . . . 153

18 Aerodynamic Theory **157**
18.1 Coordinate System . . . 157
18.2 Blade Element Method . . . 159
18.3 Unsteady Corrections Models . . . 163
18.4 Aerodynamic Simulation . . . 168

19 Test and Validation **171**
19.1 Wind Modelling . . . 171
19.2 Region I . . . 175
19.3 Region II . . . 176
19.4 Region III . . . 177
19.5 Impulse Excitation of Blade . . . 178

20 Conclusion **181**

V Servo and Power Electronic Models **183**

21 Introduction **187**

22 Drive Train Model **189**

23 Generator Model **191**
23.1 Power Converter Model . . . 193

24 Pitch System **197**

25 Test and Validation **201**
25.1 Drive Train . . . 201
25.2 Generator . . . 203
25.3 Power Converter Algorithm . . . 204
25.4 Region II . . . 206

26 Conclusion **209**

VI Aero-Hydro-Elastic Model **211**

27 Introduction **215**

28 Coupling of Tower and TLP **217**

29 Test and Validation **219**
29.1 Stiffness of Coupled Tower . . . 219
29.2 Damping of Coupled Tower . . . 220
29.3 Stiffness of Coupled TLP . . . 221
29.4 Free Decay of Coupled TLP and Tower . . . 223

29.5 Forced Harmonic Excitation . . . 224
29.6 Response Amplitude Operator Coupling . . . 226
29.7 Impulse Excitation of Coupled Tower . . . 228

30 Coupling of TLP, Tower and Rotor **231**
30.1 Rotor Passing Frequency . . . 232
30.2 Blade Passing Frequency . . . 232
30.3 Gyroscopic Damping . . . 233

31 Test and Validation **235**
31.1 Aerodynamics . . . 235
31.2 Aerodynamics and Hydrodynamics . . . 239
31.3 JONSWAP Spectrum and Aerodynamics . . . 243

32 Conclusion **245**

VII Control **247**

33 Intro **253**

34 Control Objective **255**
34.1 Campbell Diagram . . . 257

35 Generator Control **259**
35.1 Current Loop . . . 260
35.2 Speed Loop . . . 264

36 Collective Blade-Pitch Control **269**
36.1 Blade Pitch Control . . . 269
36.2 Blade Pitch Actuator Control Design . . . 269
36.3 Collective Blade Pitch Control Design . . . 271
36.4 Gain Schedule Blade Pitch Control . . . 274

37 Rotor Position Estimation **277**
37.1 Sensorless Position Estimation Methods . . . 277
37.2 Extended Kalman Filter Algorithm . . . 278

38 Test and Validation **283**
38.1 Generator Control Tests . . . 283
38.2 Blade Pitch Tests . . . 285
38.3 Extended Kalman Filter Tests . . . 289

39 Conclusion **297**

VIII Discussion and Conclusion **299**

40 Discussion **301**

41 Conclusion **303**

Bibliography **307**

A Appendix **315**
A.1 Wind Tunnel . . . 315
A.2 Retardation Function Estimate . . . 316
A.3 Mooring Line Test . . . 318
A.4 Wave Generator Experimental Setup . . . 319
A.5 Wave Generator Spectrum . . . 320
A.6 Calculation of Thrust Force . . . 321
A.7 Rotation in Pitch and Yaw . . . 322
A.8 Free Decay of Tower . . . 322
A.9 Drive Train Experiments . . . 323
A.10 Wind Turbine . . . 324
A.11 MATLAB Codes . . . 329
A.12 Simulink Models . . . 365
A.13 FAST Input files . . . 376
A.14 Electronics . . . 398

Part I

Introduction

Symbol	Description	Units
Δp	Pressure across screen	Pa
δ_w	Width between wires	m
ν	Kinematic viscosity	$m^2/2$
ρ	Density	kg/m^3
A_0	Free area of mesh	m^2
A_1	Area of wind screen	m^2
f_{fan}	Rotational frequency of fans	RPM
K_{pitot}	Coefficient of pitot tube	-
k	Screen coefficient	-
P_0	Ambient pressure	Pa
p	Measured pressure	Pa
p_{loss}	Pressure loss across screen	Pa
Re_{mesh}	Reynold's number for flow across mesh	-
T	Ambient temperature	°
t_{wire}	Thickness of wire	m
V_0	Wind velocity across mesh	m/s
V_1	Wind velocity before mesh	m/s
V	Wind velocity	m/s

2.1 Motivation

The need for sustainable energy is rapidly increasing and the wind energy resource is one of the largest renewable energy sources worldwide [2]. In order to reduce the cost of energy the wind turbines tend to increase in size [2]. However large wind turbines may cause visual and noise disturbances for the people living nearby, where offshore wind turbines eliminate these factors. The offshore wind characteristic is also more steady and continuous, furthermore higher energy production of an offshore wind turbine is obtained compared to an onshore of the same size. Furthermore the offshore wind profile tends to have stronger winds in the afternoon, which matches the energy demand, as it here tends to be higher [3]. Most offshore wind turbines are built with a fixed foundation penetrated into the seabed. But these are only constructed in depths up to 30-50 m for the regular monopile foundations, while the jacket foundations can be installed at seabeds up to 70 m of depth [2]. This maximum depth on beforehand limits out many potential good wind farm areas as a lot of countries, both in Europe and globally, have limited access to shallow waters, e.g. the Irish sea, see fig. 2.1.

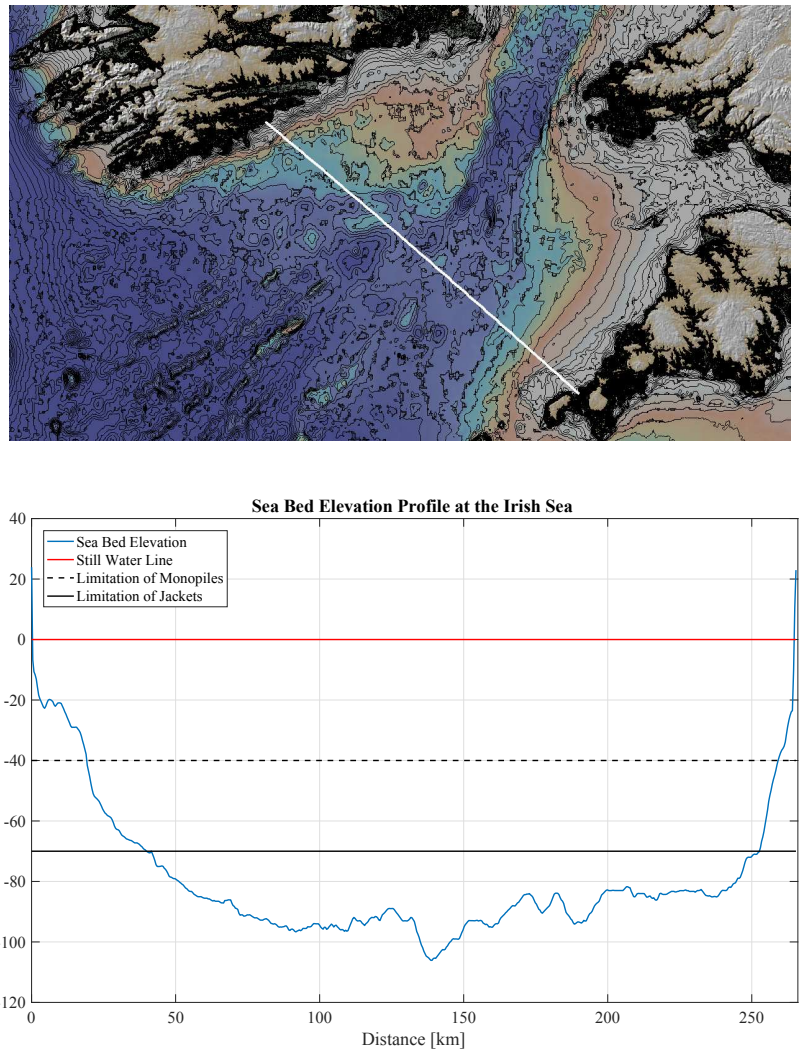

Figure 2.1: Seabed elevation at the Irish sea.

Here it can be seen that in a distance of just 20 km offshore, the depth is a limitation for offshore wind turbines with fixed foundations. As a comparison the Danish wind turbine farm Horn's Rev

lies in a range up to 44 km offshore [4]. The data were taken from the Interdisciplinary Earth Data Alliance (IEDA) [5]. The contour plot was drawn with an equidistance of 5 m while the white line indicates where the seabed elevation profile was taken from. In the seabed elevation profile, the blue line indicates the seabed, the red line indicates the still water line, while the two black lines indicate the limits of the monopiles and jackets.
For the onshore wind turbines the cost of installation and foundation is about 4-16 % [6] of the total cost of the wind turbine while for an offshore it is normally 15-25 % [6]. The operation and maintenance for offshore wind turbines are 30-35 % of the cost of electricity, while for onshore wind turbines it is only 10-15 % of the cost of electricity [7]. One of the main costs of an offshore wind turbine is the subsea structure which generally increases with increasing depth. This is due to the complexity of the structural design and the manufacturing process along with an increase in material cost [2]. Therefore new and cheaper technologies of foundations are considered, including floating foundations, in order to bring the costs down.
These floating offshore wind turbines (FOWTs) can be installed at depths of 45 m to beyond 150 m [8]. Therefore the floating foundations offer a much larger flexibility in the site location. Furthermore it is possible for FOWTs to be towed out to the wind farm site which allows easier assembly in the port. According to the International Renewable Energy Agency (IRENA) the FOWTs could be a game changer in some of the largest potential markets, such as the United States and Japan, where there are few shallow water sites suitable for offshore wind farms [9]. Furthermore IRENA states that this technology has the potential of environmental benefits compared with fixed bottoms designs due to less invasive seabed activity.

2.2 Problem Definition

FOWTs are complex systems with multiple variables, which all contribute to a highly complex dynamical behaviour. Simultaneous wind and wave loadings, which are irregular by nature, aerodynamical and hydrodynamical couplings, control of the wind turbine, electrical components and flexible structures make a sufficient scaled model a great challenge. In order for a design to be durable, accurate modelling and validation are necessary. However as the FOWTs are at an early development stage, only limited data for a few different designs exist, see section 2.3. As large scale test turbines are expensive to build and operate, most institutions tend towards small scale experiments in wave tanks and wind tunnels. However these experiments differ greatly in methodology and technique, and in many of the experiments the wind turbine itself has been simplified, whereby the associated aerodynamical effects also are simplified. Thereby do these tests not contribute to the necessary information in order to completely understand the complex coupled dynamical effects. This leads to the problem definition of this Master's thesis

Is it possible to set up the necessary mathematical coupled models for the FOWT, build a correctly 1/35 scaled physical test model with implemented control, and use it to test and validate the mathematical models?

2.3 State Of Art

Floating foundations are not a new concept as the main parts are also found in the oil and gas sector, where there has been deployed large scale commercial floating structures for decades. However the floating platforms for the wind turbines require adaptations in order to accommodate the different loading patterns and dynamic characteristics. In general four different main concepts of floating

foundations exist, these are the spar-buoy, barge, tension leg platform (TLP) and semi-submersible [9]. However different variants of these four concepts exist along with mounting of multiple turbines onto a single floating foundation.

The spar-buoy is a simple design which consist of a cylinder with a low water plane area. The spar is ballasted in such a way that the centre of gravity (COG) is below the centre of buoyancy (COB). The spar is kept in place by a catenary or taut spread mooring lines which have a low cost and are easy to install. The mooring lines are fixed to the sea bed either by a drag or suction anchor. It is advantageous in its tendency to small wave induced motions, however it is disadvantageous in its installation requirements as it is not suited for water depths below 100 m while the installation is required to be done in relatively sheltered water. The first mover in this concept was Statoil with their Hywind project [9] [10]. The Hywind project was first demonstrated with the world's first full-scale FOWT outside Karmoy in Norway in 2009 with a single wind turbine of the Siemens model SWT-2.3-82 having a capacity of 2.3 MW [11]. In 2017, six wind turbines with a capacity of 5 MW were installed 25 km north east of Aberdeen in Scotland giving a total capacity of 30 MW thereby becoming the first floating offshore wind farm that was commercialised. Other fast followers can be mentioned such as Japan Marine United (JMU), DeepWind, SeaTwirl and Windcrete. [9]

The barge platform is a floater which have a large water-plane area and a shallow draft which is often achieved by an adequate amount of ballast. The large water-plane area ensures a large hydrostatic stiffness and thereby a large righting stability. The mooring system used is often catenary mooring lines. The advantage of the barge is the simple structure and easy installation as the full system can be towed out and installed at the given wind farm. However the barge platform might give rise to large dynamics and therefore a need for complex control systems. As first movers Ideol (Floatgen) can be mentioned. Currently only pilot projects exist in France and Japan, but only one full-scale model for each has been installed. However a pilot farm with a total capacity of 24 MW is planned to be in operation at the year 2020. [12]

The TLP consists of a central column with arms connected to tensioned tendons securing the foundation through vertical mooring lines to the sea bed by suction or piled anchors. The TLP is advantageous as it is easily assembled onshore or in dry docks and then towed out to the wind farm site. Furthermore it has a tendency for low wave induced motions. However it is disadvantageous in its expensive mooring line system. Furthermore there are some uncertainties regarding the impact of possible high frequency dynamic effects on the wind turbine. The first mover in this concept is GICON who tested their first prototype in 2014/2015 in the German Baltic Sea with a 2 MW wind turbine. In 2015/2016 they tried a new prototype of a 6 MW wind turbine in the German North Sea. Of other fast followers can be mentioned Glosten Associates (PelaStar). [9]

The semi-submersible platform consists of a number of large columns linked to submerged pontoons. The columns provide the necessary hydrostatic stability while the pontoons provide an additional buoyancy. The foundation is kept in place by catenary or taut spread mooring lines attached to the sea bed by drag anchors. It is advantageous in its easy installation as it can be constructed onshore or in a dry dock and then towed out to the wind farm site. However it is disadvantageous in its tendency to high wave induced motions. Furthermore the cost of material and complex fabrication tends to be much higher than for other concepts. The

first movers in this concept is Principle Power with their WindFloat project [9]. The company has recently successfully decommissioned their WindFloat floating offshore foundation test concept featuring a Vestas V-80 2 MW [13] after completion of its project objectives. WindFloat now moves on to the next stage as the government of Portugal has approved a new project located 20 km of the coast of Northern Portugal consisting of 3 or 4 WindFloat concepts with a capacity of 25 MW connected to the national grid [13] planned to be operational in 2018. Other fast movers can be mentioned such as Fukushima Forward and Hexicon with their multi-turbine platform. [9]

Accordingly to Bloomberg New Energy Finance (BNEF) [14] the installed capacity of floating offshore wind turbines could be as much as 237 MW in the year 2020 with a capacity of 92 MW installed in Scotland alone.
[9] [15]

2.3.1 Test and Validation

In an article from 2009, researchers from Kyoto University in Japan performed a 1/22.5 scaled experiment of a 2 MW down-wind wind turbine, having a rotor diameter of 80 m and a hub height of 55 m [16]. The design of the floating platform was of the spar buoy type measuring 60 m in draft, having cross sectional areas of 12 m in the lower part, 8.4 m in the main part and 4.8 m at the upper part. The FOWT was moored by an anchor chain system. The FOWT was subjected to regular and irregular waves and its motion was examined, this together with a steady horizontal force in order to simulate a steady wind.

A small scale (1/105) of the WindFloat platform of the company Principal Power was built for experimental purposes in 2010 [17]. An actuator disc was here utilised in order to replicate the wind thrust, along with a scaled spinning mass to generate the gyroscopic forces in order to simulate a real rotor. The windFloat is a three-legged floating foundation designed to accommodate large wind turbines on one of the three columns of the hull. The experiments were mainly conducted in order to test the performance of the foundation when exposed to the 100 year wave. However also some regular wave test were conducted in order to get a baseline foundation response.
The DeepCWind Consortium, mainly led by the University of Maine, has conducted a series of experiments in a large wave basin in 2011 and then again in 2013 [18]. The experiments in 2011 was conducted on some different 1/50 scaled designs, such as a semi-submersible foundation, a TLP and the spar buoy based on the OC3 spar buoy, which is the same concept as the Hywind project [10]. The foundations were tested under a variety of conditions such as free decay, regular and irregular waves and with a wind field present. These experiments used a Froude-scaled rotor based on the NREL 5 MW blade design. However when using Froude-scaling a mismatch between the Reynold's number occurs such that a higher wind speed was needed in order to simulate the full-scale aerodynamic/hydrodynamic force balance. Due to the geometrical scaling, aerodynamic performance did not match and therefore in 2013 a new series of tests were conducted using the semi-submersible foundation with a new rotor. The rotor was designed in such a way that the performance of the full-scale 5 MW rotor was matched.
In 2011 and again in 2014 researchers from the University of Life Sciences (UMB) and the Institute for Energy Technology (IFE) tested a 1/100 scaled tension leg buoy platform and compared it to the conventional spar buoy with catenary mooring lines [19][20]. The experiments did not include a rotor or other actuators, meaning they were purely hydrodynamic.

In 2013 National Renewable Energy Centre tested a braceless semi-submersible platform called the Concrete Star Wind Floater [21]. In this experiment a controllable ducted fan was placed at the top of the tower and was used to solve the problem with the Reynold's number mismatch for the aerodynamics when using the Froude scaling. The ducted fan was capable of introducing a variable force representing the total wind thrust by the rotor. The fan thrust is controlled by the rotational speed set by a controller, which was dependent on the real time simulation of the full scale rotor in a turbulent wind field. This simulation was conducted in the program Fatigue, Aerodynamics, Structures and Turbulence (FAST) with the platform motions measured in real time in the wave tank test. Furthermore both free decay, regular and irregular wave tests were conducted both with and without the simulated aerodynamic forces.
Another approach to provide the realistic aerodynamic forces with feedback was conducted on another braceless semi-submersible platform in 2015 at MARINTEK [22]. Instead of the ducted fan approach a series of controllable tensioned wires provided the simulated force. Again FAST was used to simulate and calculate the aerodynamic forces in real time.
In 2015 an experiment was conducted for the INNWIND.eu project which tested a 1/60 scaled model of the OC4 DeepCWind semi-submersible platform [23]. The platform was redesigned in order to support a 10 MW wind turbine. The designed rotor featured high chord blades in order to match the rotor thrust, this in despise of the mismatch of the Reynold's number for the full scale. Furthermore a feedback controlled ducted fan, much alike the Concrete Star experiment, was used to simulate the thrust force. Free decay, regular and irregular waves along with extreme wave conditions were also tested. [22]

2.4 Previous Work

The authors of this project have previously written four other projects concerning FOWTs. These are 'An Approach to Build a Prototype of a Floating Wind Turbine with Maximum Power Point Tracking using Torque Control' [24], 'Hydrodynamic Modelling and Verification of a Tension Leg Platform for a Floating Offshore Wind Turbine' [25], 'Modeling and Verification of Tower Dynamics for a Scaled Floating Offshore Wind Turbine' [26] and "Wind Turbine Design, Modelling and Control of a Scaled Floating Offshore Wind Turbine" [27]. In this section short summaries of these projects are made in order to give the reader insight in the previous work and solutions.

The first project the authors wrote concerning FOWTs was on the 5th semester at bachelor level having the title 'An Approach to Build a Prototype of a Floating Wind Turbine with Maximum Power Point Tracking using Torque Control'. This project concerned two main parts: The floating foundation and the control system of the generator.
The first part concerned the design and construction of a floating spar platform, which had three pontoons attached. These pontoons could be used to regulate the pitch angle of the platform. A simple dynamic model was made for the FOWT, which was verified through various physical experiments done using the designed physical model.
The second part was to develop a dynamic model of the generator along with developing the necessary power electronics for the FOWT. The solution involved making a control system, which should be able to conduct maximum power point tracking, this was made as a field orientated control. The wind turbine used in this project was an Air Breeze wind turbine with passive stall control.

The second project the authors wrote concerning FOWTs was their bachelor thesis, having the title

'Hydrodynamic Modelling and Verification of a Tension Leg Platform for a Floating Offshore Wind Turbine'. This project concerned the development of an appropriate scaled model of a realistic FOWT. To do this Froude scaling was utilized. The scaled model design was a 1:35 scale according to the reference wind turbine, which was the National Renewable Energy Laboratory (NREL) 5 MW wind turbine [28]. The reference TLP was chosen to be a hybrid of a half-scale of the original Sea Star oil platform [29] and a TLP inspired by the GLGH design [8]. In the design process several things were analysed e.g. the fundamental frequencies of the full system, the maximum external load etc. An analytical analysis of the hydrodynamics affecting the floating platform was made, wherein different spectra for representing a real sea state were investigated. To find the hydrodynamic forces affecting the TLP Morison's equation was used. This is however a rough estimation as Morison's equation is only valid for bottom fixed structures.
A mathematical dynamic model for the TLP in all six degrees of freedom (DOFs) was made as a mass-spring-damper system, the coefficients were first found theoretically and thereafter verified in the surge direction by experiments such as free decay tests, forced tests etc.
Furthermore as the found theoretical coefficients were linearised, a Simulink model with the mathematical dynamic model for the TLP and the hydrodynamic forces was conducted such that non-linearised simulations could be conducted and verified through experiments.

The third project the authors wrote concerning FOWTs was their 1.st semester project on their master degree, having the title 'Modeling and Verification of Tower Dynamics for a Scaled Floating Offshore Wind Turbine'. This project concerned the development of an appropriate scaled model of a realistic tower of a wind turbine. The scaled model was designed in order to have the correct scaled length and mass, but also the natural frequencies of the tower should be scaled, both with and without a top mass. The tower design was developed physically and a mathematical model using the finite element method (FEM) was also developed by the authors. The developed FEM code was compared to the commercial software ANSYS. The FEM code was written in MATLAB, where the tower was considered as a mass-spring-damper system, for the analysis modal theory was utilized. The ANSYS and FEM models were verified through experiments for the physical model such as free decay tests, forced tests etc.

The fourth project the authors wrote concerning FOWTS was their 2.nd semester project on their master degree, having the title "Wind Turbine Design, Modelling and Control of a Scaled Floating Offshore Wind Turbine". This project concerned the development of the wind turbine itself. This including the blades, nacelle, rotor and electronics. The blades were designed in order to match the scaled rotor thrust force of the 5 MW NREL reference wind turbine, while the rotor was designed and constructed such that individual pitching control would be possible. The nacelle was designed and constructed such that a generator and necessary electronics would be placed inside the nacelle. The dynamic models of the generator and rotor were developed separately. The control of the two subsystems was based on two different baseline controllers, one for the generator and one for the blade pitching. The baseline controllers were only verified by simulation. In fig. 2.2 a timeline of the described projects is seen.

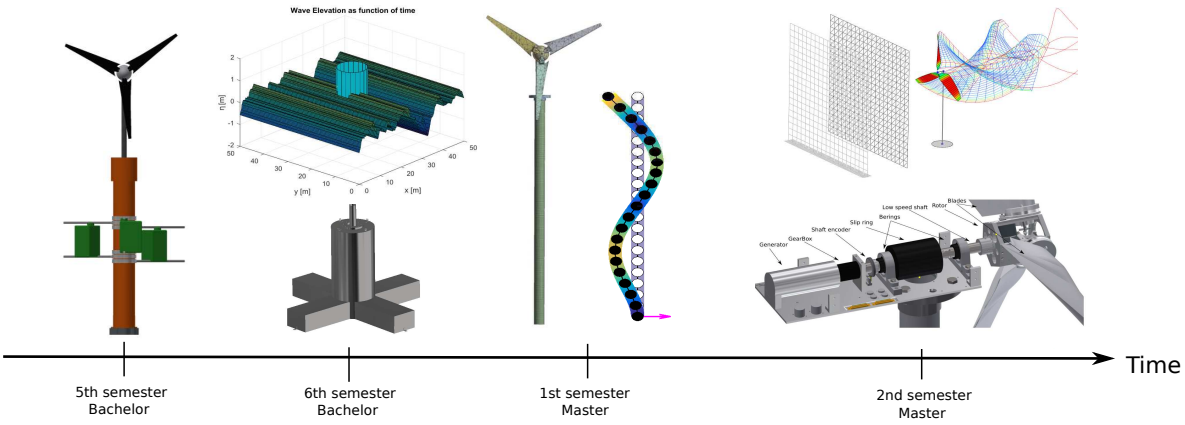

Figure 2.2: A timeline of the different projects made by the authors.

2.5 Definitions

In this section a short introduction to the definitions regarding the motion of the FOWT will be given. The global coordinate system (xyz) of the unloaded FOWT is located at the still water line (SWL), where $z = 0$, and the z-axis pointing upwards, see fig. 2.3. The primary wind and wave direction indicates the x-axis, with the x-axis pointing in the positive direction of the wave propagation. Body displacements of the TLP and tower in the x, y or z direction are denoted surge, sway or heave, while the rotation about the respective axes are denoted roll, pitch and yaw. Body displacements of the blades out of the rotor planed are denoted the flapwise direction, edgewise is the displacement of the blades in the lateral axis, while the longitudinal displacements of the blades are denoted as the spanwise direction. The rotation of the rotor about the shaft is denoted the azimuth, the rotation of the nacelle about the vertical lengthwise axis of the tower are denoted yaw, while the rotation of the blades about their lengthwise axis are denoted pitch. In fig. 2.3 a visualisation of the coordinate systems used are seen.

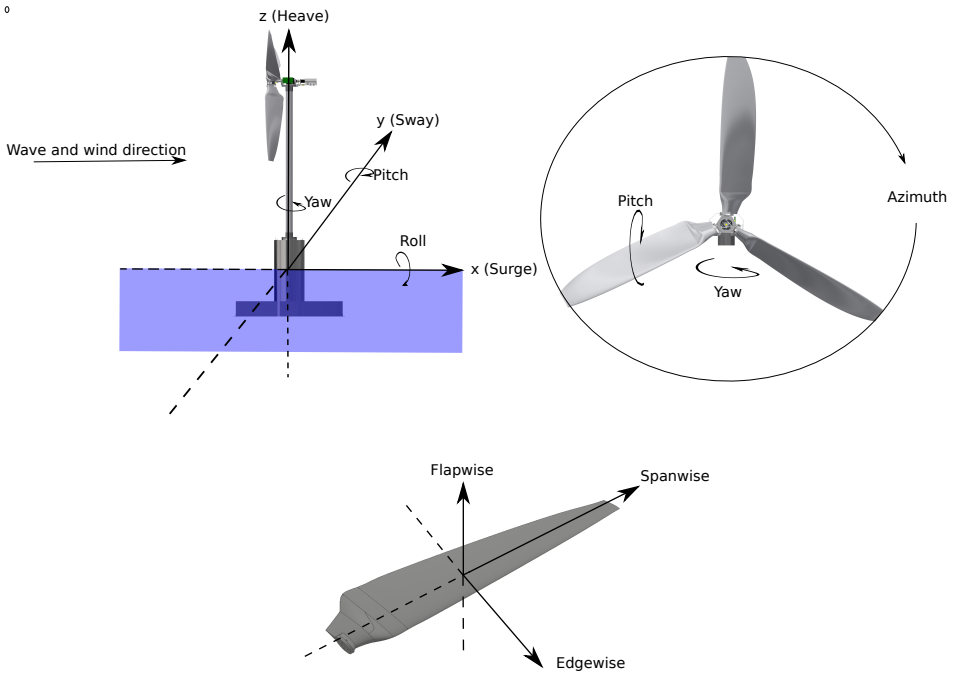

Figure 2.3: Coordinate systems used throughout the thesis.

Modelling Methods 3

A complex wind turbine multi degree of freedom (MDOF) system cannot be solved by simply analysing every subsystem individually. This is due to that each main component having a dynamical behaviour will influence the behaviour of the total system. Fully coupled models capable of capturing these effects are called aero-hydro-servoelastic and refer to the inclusion of the aerodynamics, hydrodynamics, the implementation of the control strategy forces and the structural dynamics. This thesis will develop two different models for the AAUE-TLP, one based on the aero-elastic computer-aided engineering (CAE) tool, FAST, and one based on a Simulink model developed through this thesis and previous work by the authors. In the sections below an overview of the methods used in the two different models will be presented.

3.1 FAST

FAST is a CAE tool for simulating coupled dynamic responses of wind turbines developed by NREL [30]. It combines aerodynamics, hydrodynamics, structural elastic dynamics, control and electrical systems to one coupled non-linear aero-hydro-servo-elastic simulation in time domain. FAST is capable of simulating various wind turbine configurations, including the three bladed horizontal axis, pitch regulated, upwind wind turbine, which is the type of the AAUE-TLP. The wind turbine can also be modelled with various foundation types, including floating offshore foundations. Beside the time domain simulation FAST has a linearisation tool which can create a linear state space model of the wind turbine, which can be used for control design purposes. FAST can be executed through Simulink where the control algorithm can be build within Simulink for easier implementation. FAST is based on several sub-programs which can be activated and deactivated depending on the objective of the analyse, these sub-programs will be described further below. The sub-modules used in FAST and their respective versions are seen in table 3.1. The structure of the FAST code can be seen in fig. 3.1 and the input files can be seen in appendix A.13.

Table 3.1: Sub-modules used by FAST.

Modules	Version
ElastoDyn	v1.04.00a-bjj
BeamDyn	v1.01.04
AeroDyn	v15.03.00
InflowWind	v3.03.00a
ServoDyn	v1.06.00a
HydroDyn	v2.05.01
SubDyn	v1.03.00
FEAMooring	v1.02.01

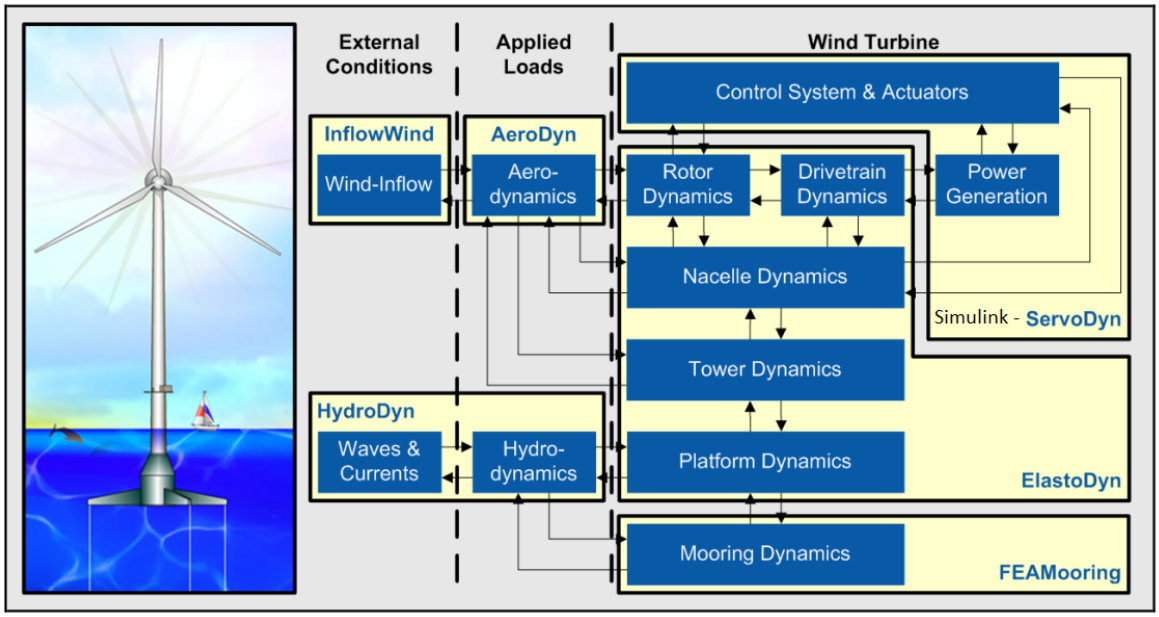

Figure 3.1: FAST code structure for AAUE-TLP. [31]

3.1.1 AeroDyn and InflowWind

AeroDyn [31] calculates the aerodynamics of a wind turbine in time domain based on the blade element method where the 3D flow around a body is approximated by local 2D flow at cross sections and the distributed pressure is approximated by lift forces, drag forces and pitching moments lumped at a node in a 2D cross section distributed along the length of each blade. The forces and moments at each node are found as distributed loads per unit length, and the total 3D aerodynamic loads are found by integrating the 2D distributed loads. AeroDyn uses correction model for the blade element method, in order to make it more precise, these are Prandtl's tip and hub loss and Glauert's correction for high induction factor. The blade element method can be calculated both as steady (SBEM) and unsteady (UBEM). SBEM describes the steady state loads and performance of the wind turbine under different operating conditions. UBEM describes the loads and performance during changing operation point and unsteady effect and is therefore a preferred choice when using the simulation model for time domain simulation, where dynamic effects are of importance.
AeroDyn includes four submodels; rotor wake/induction, blade airfoil aerodynamics, tower influence on the wind local to the blade nodes and tower drag.
When a turbulent wind field is used, the inflow wind is generated outside AeroDyn by the side program Turbsim [32] also developed by NREL.
In this thesis dynamic stall model, wake/induction model, tower influence by potential flow, tower shadow effects, tower aerodynamic loads, Prandtl tip- and hub-losses and tangential induction factor are enabled in FAST. Each blade is discretized in 20 nodes and the tower is discretized in 12 nodes. The airfoil data is found in XFOIL [33].

3.1.2 HydroDyn

HydroDyn [34] calculates the hydrodynamic loads on the floating structure in the time domain by a combination of potential flow theory and strip theory. The potential flow solution involves frequency to time domain transformation. It includes the hydrodynamic loads: linear hydrostatic restoring, added mass and damping from linear wave radiation where free surface memory effects

are included, and the incident wave excitation from first order diffraction also known as the Froude Krylov and scattering effects. The hydrodynamic coefficients required for the potential flow solution are frequency dependent and must be generated by another software which can handle frequency domain panel calculations. The HydroDyn expects an input with output format as generated from the software WAMIT [35] [36]. The authors had no licence to WAMIT so it was decided to use the free software NEMOH [37] developed by LHEEA (Research Laboratory in Hydrodynamics, Energy and Atmospheric Environment). A code was developed by the authors in MATLAB to convert NEMOH output to WAMIT output structure, this code can be seen in appendix A.14.3.
The hydrodynamic loads calculated by the strip theory can be applied on straight circular members specified by their starting and ending points called joints, cross sections, thickness and hydrodynamic coefficients. The strip theory is based on Morison's equation for the distributed fluid inertia, added mass and viscous drag components and the loads are applied as lumped loads in the joints.
The potential flow solution is suitable for large structures, while the strip theory may be preferable for small structures relative to a typical wavelength. For some substructures and sea conditions the potential theory should be augmented with the loads carried out by flow separation, found by the viscous drag component of the strip theory solution.
Both regular and irregular (stochastic) waves can be generated by HydroDyn. Either as an external generated time series or by setting the theoretical parameters for the waves.
Each time step FAST transfers the position, orientation, velocities and accelerations of the rigid structure to HydroDyn. HydroDyn then computes the hydrodynamic loads and return them back to FAST, and FAST then computes the equation of motion of the system in ElastoDyn by assuming that the platform is a rigid body with six DOFs.
This thesis applies first order wave theory and calculates the radiation memory effect by the convolution integral. A combination between the potential flow and Morison's equation has been used, as is also done in the Simulink model.

3.1.3 ServoDyn and Simulink

ServoDyn [38] models the actuators and the control of the wind turbine. In this thesis both the actuators and the control will be modelled in Simulink to apply more advanced control and to apply more detailed actuator models. The Simulink model then passes the generator torque, electric power, commanded yaw position and rate, commanded blade pitch angle and high speed shaft braking torque to ServoDyn. In this thesis, the commanded yaw position and rate are set to zero, together high speed shaft braking torque. The generator is modelled in chapter 23 and the blade pitch actuator is modelled as a first order system described in chapter 24.
The control systems will be described further in part VII.

3.1.4 ElastoDyn

ElastoDyn [30] connects all the models by calculating the equation of motion with up to 24 DOFs by combining multi body and modal dynamics. ElastoDyn takes the aerodynamic loads, hydrodynamic loads, controller commands and substructure reactions as inputs and calculates the displacements, velocities, accelerations and reaction loads. The structural dynamics of the tower is also calculated in ElastoDyn by applying modal analysis, using Bernoulli-Euler beam theory and neglecting axial and torsional DOFs.

3.1.5 FEAMooring

FEAMooring [38] calculates the mooring line restoring force at the fairlead position of the floating platform. The mooring system is modelled by finite element method using elastic rod elements. In this thesis each of the four mooring lines consists of 10 elements.

3.2 Simulink Model

A visualization of the AAUE-TLP Simulink model structure developed by the authors is seen in fig. 3.2 to visualise the different substructures and the connections between them.

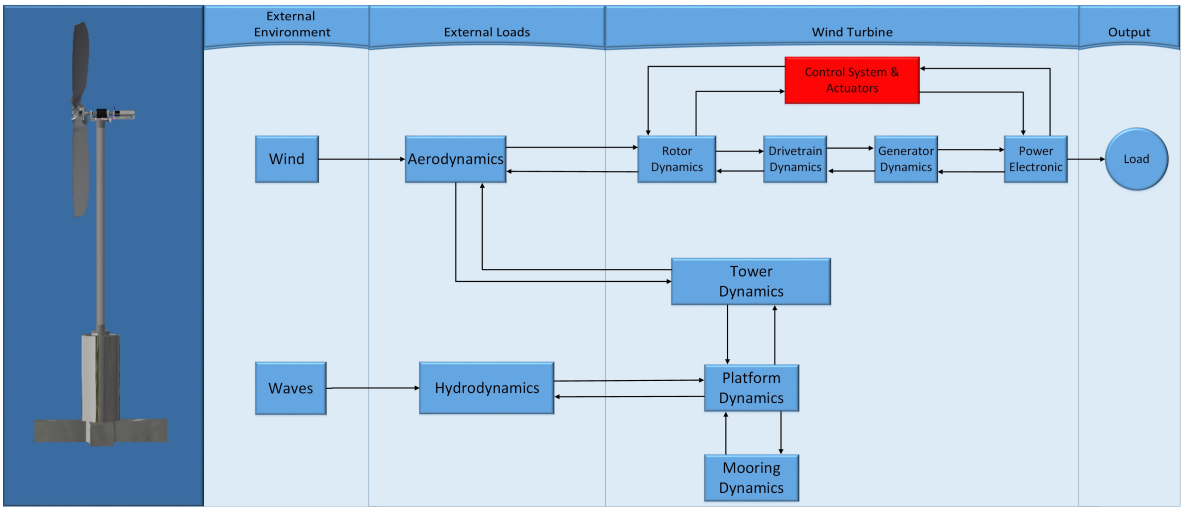

Figure 3.2: The interaction between the different subsystem.

The external environment consists of the velocity of the wind and surface elevation of the waves, the behaviour of these are found experimentally in the laboratory. The loads arising from this are modelled using linear wave theory for the hydrodynamic part, while for the aerodynamic part, UBEM is used. For modelling the wind turbine different methods have been used. For modelling the TLP the boundary element method (BEM), together with analytically descriptions of the mooring lines are used. The tower is modelled by using finite element method (FEM). These two subsystems are connected by the acceleration from the TLP to the tower, and the stiffness and damping forces from the tower to the TLP. The aerodynamic part is modelled by UBEM, this subsystem is connected to the tower through a velocity from the tower to the rotor and the thrust force from the rotor to the tower. The aerodynamic subsystem is connected to the rotor by applying a force to the rotor, while the pitch actuator system determines the angle of the blades. The rotor is connected to the drivetrain through the rotor torque while the drive train determines the mechanical rotational velocity.
The drive train is connected to the generator by the rotational velocity of the generator, and the generator feeds back the torque of the generator. Furthermore the drive train feeds the mechanical velocity to the control system, which is also fed by a,b,c currents by the generator. The control then feeds the power electronics by determining the switching pattern for the power converter necessary to generate the correct load. The power electronic is fed by the generator through a,b,c currents and voltages, while sending the load resistance back to the generator. The power electronics then feeds the load with the generated DC current.
All the different subsystems will be described further in the respective parts.

AAUE-TLP 4

The design of the AAUE-TLP was made by the authors in a previous project [25]. Many different TLP designs exist where the most significant differences are the number and geometrical properties of pontoons, thereby varying the amount of buoyancy present. The AAUE-TLP is a hybrid consisting of two different designs, namely a half scale model of a Sea Star platform and a GLGH design. The sea star platform [29] consist of three squared pontoons and approximately 60 % percent of the buoyancy comes from the main cylinder while the rest comes from the pontoons. The diameter of the main cylinder is larger than the wind turbine tower. The GLGH platform [39] consist of four cylindrical pontoons where approximately 70 % of the buoyancy comes from the pontoons. The diameter of the main cylinder is almost the same as the wind turbine tower, making it more transparent to waves, however also more sensitive to extreme conditions [8]. The scaling of the AAUE-TLP was made in order to fulfil the three similarity conditions; geometric, kinematic and dynamic. Furthermore the design was made such that a minimum of overlap between the natural frequencies of the AAUE-TLP and the wind and wave load frequencies exist. In table 4.1 the reference models and the scaled AAUE-TLP model can be seen. For continuity with previous project, [25], the Sea Star platform is refereed to as TLP3, while the GLGH platform is referred to as TLP4.

Table 4.1: The AAUE-TLP properties [8].

Scaling factor	TLP3	TLP4	1:35 scaling TLP3/TLP4	AAUE-TLP
Main cyl. diameter [m]	14	8,25	0,40/0,24	0,40
Main cyl. height [m]	32	39	0,91/1,11	1,00
Platform radius [m]	28	25	0,80/0,71	0,7
Pontoon width [m]	6,0	6,0	0,17/0,17	0,25
Pontoon height [m]	6,0	6,0	0,17/0,17	0,2
Steel mass [kg]	1.293.000	859.000	30,16/20,04	54,1
Displaced volume [m^3]	5.655	4.114	0,13/0,1	0,182

In fig. 4.1 a visualisation of the AAUE-TLP drawn in Inventor is seen.

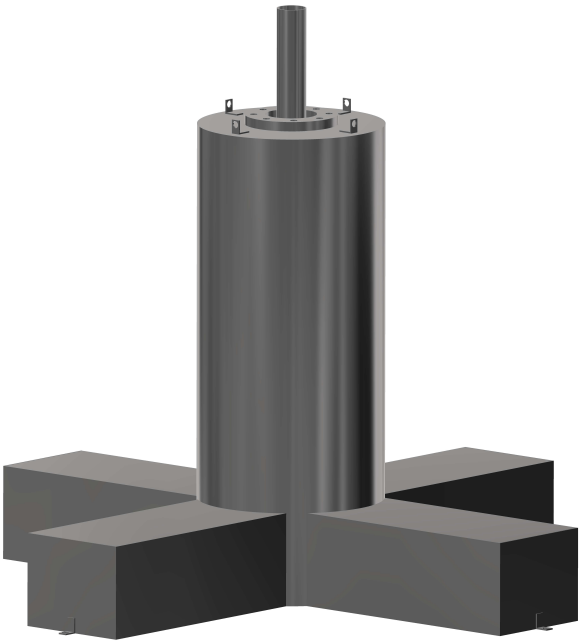

Figure 4.1: Visualisation of the AAUE-TLP.

Mooring System
Not all of the parameters of the moorings system for the two reference foundations, were available. Therefore the reference mooring system for the AAUE-TLP was in a previous project [25] chosen to be the mooring system of the MIT TLP [40]. In table 4.2 the reference mooring line properties are seen together with the scaled AAUE-TLP mooring line properties.

Table 4.2: Scaled dimensions for the mooring system of the MIT TLP [40].

Scaling factor	MIT-TLP	1:35 scaling MIT-TLP	AAUE-TLP
No. of mooring lines per spoke	2	2	1
Youngs modulus [GPa]	118.4	3.38	57.3
Diameter [m]	0.127	0.0036	0.001
Force [kN]	3.931	0.183	0.186
Unstretched length [m]	151.73	4.33	1.05
Spring stiffness [kN/m]	19,700	16.1	34.1

It is essential to note that this thesis is not a design verification nor any judgement regarding the optimal design will be given. That is the objective with the thesis is primary a validation of the simulation and control tools.

4.1 Tower

The design of the tower for the FOWT was made by the authors in a previous project [26]. The parameters of the tower should have been scaled according to the scaling laws, to get a perfect scaled model. But there are some parameters e.g. the elasticity and density of the material of the

tower which are hard to scale correctly. But also the geometrical scaling would require a special fabrication of the tower, as the tower should be conical with a varying thickness as the full-scale tower. But that was deemed to be too expensive and therefore a prefabricated cylindrical pipe was sought for.
In order to give a realistic scaled wind turbine tower, the most important properties which need to be scaled correctly were found. The priority of the correctly scaled properties were as listed below:

1 Fundamental frequency
2 Tower height
3 Tower weight
4 Tower diameter

The optimal design for the tower was found during a design process using an optimisation algorithm. The best solution was a hollow cylindrical tower made of PVC-U, for which the properties can be found in table 4.3. The tower was originally designed to operate with an Air Breeze wind turbine. But during the 8.th semester project of the authors, a new physical model of the wind turbine was designed. This wind turbine is heavier than the Air-breeze and therefore the tower has to be shorter in order to ensure proper scaling of the fundamental frequency of the tower, this is further described in 14.2.
The current tower used in this thesis has the following properties listed in table 4.3.

Table 4.3: The AAUE-TLP tower properties [41].

Scaling factor	NREL 5 MW	1:35 scaling NREL 5 MW	AAUE-TLP
Tower length [m]	77.6	2.22	1.8
Base length [m]	10	0.286	0.3
Mass [kg]	347,460	8.10	4,76
Diameter bottom [m]	6.0	0.17	0.90
Thickness bottom [mm]	27	0.77	6.7
Diameter top [m]	3.87	0.11	0.90
Thickness top [mm]	19	0.54	6.7
Young's modulus [GPa]	210	6	3.15
Shear modulus [GPa]	80.8	2.3	1,0
Material density [kg/m^3]	8500	8500	1400
Structural damping ratio [%]	1	1	1.3
1st natural frequency F-A [Hz]	0.324	1.91	1.90
1st natural frequency S-S [Hz]	0.312	1.86	1.90

4.2 Nacelle

The design of the nacelle was made by the authors in a previous project [27]. The nacelle and hub of the physical wind turbine model was designed, such that the most influential properties of a real wind turbine, concerning physical and functional issues can be scaled down or replicated. The nacelle was designed and drawn in Autodesk Inventor by the authors in previous work, only a review of the physical setup will be described in this thesis, for more detailed information and construction drawings see [27]. The nacelle and rotor was built by technical assistance from Aalborg University, Department of Energy Technology.

The first priority of scaling down the physical properties was the mass and secondary the geometry. The considered physical parameters of the reference wind turbine and the ideal down scaled parameters and physical parameters of the finished model are seen in table 4.4.

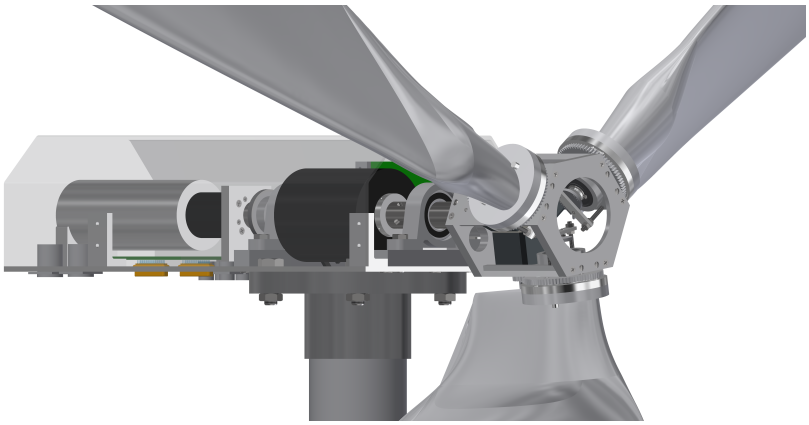

Figure 4.2: A 3D drawing of the construction of the nacelle and hub seen from the side.

Table 4.4: Nacelle parameters [41].

Scaling factor	NREL 5 MW	1:35 scaling NREL 5 MW	AAUE-TLP
Nacelle mass [kg]	240,000	5.60	10.24
Hub mass [kg]	56,780	1.32	2.02
Hub diameter [m]	3	0.086	0.13

4.2.1 Generator, Gearbox and Drive Train

In the back end of the nacelle, the generator and gear box are placed. The generator is a 200 W, 48 V, 3-phase, 4 pole brushless direct current (BLDC) motor of the series Romotion manufactured by Rotek and distributed by Compower. A 1:28.9 planetary gear is attached to the generator shaft and also fastened to the generator housing. The main shaft is held in place by two UP005 EC LDK bearing blocks. The electric signals and power are transferred from the rotating rotor to the stationary part of the nacelle through the main shaft and a slip ring. The slip ring is a TB2586-S24 from RION and can transfer 24 isolated signals, each with a rating of 5 A.

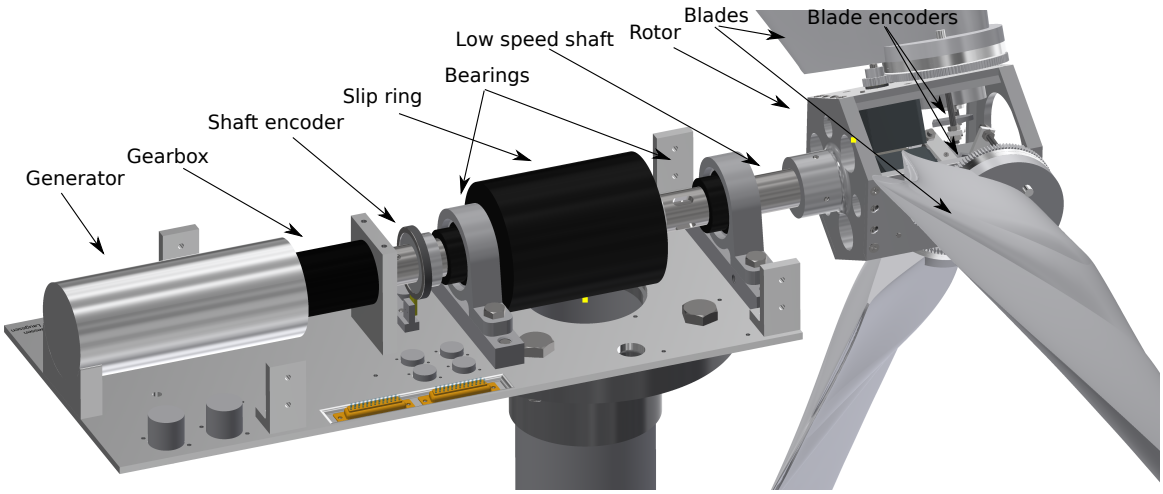

Figure 4.3: The drive train of the wind turbine.

The equivalent drive train inertia, J_{dt}, is found by adding the inertias from the blades, hub, main shaft, generator and gearbox, where the generator and gearbox inertia are mapped to the low speed reference frame by multiplying the inertia by the square of the gearing ratio. The inertia of the different components are found by Autodesk Inventor. The viscous friction and static friction were found experimentally by the authors in chapter 25 and 19 respectively.

Table 4.5: Drive train parameters w.r.t low speed shaft [41].

Scaling factor	NREL 5 MW	1:35 scaling NREL 5 MW	AAUE-TLP
Hub inertia [kg m^2]	115,926	2.2e-3	4.01e-3
Blade inertia [kg m^2]	111,776,046	2.12	0.22
Shaft inertia [kg m^2]	-	-	8.29e-5
Generator inertia [kg m^2]	5,025,500	0.1	8.4e-3
Equivalent inertia [kg m^2]	340,469,638	6.48	0.68
Gearbox ratio [-]	1:97	1:97	1:28.9
Gearbox efficiency [%]	100	100	75
Viscous friction [Nms]	6,215,000	0.7	0.43
Static friction [Nm]	-	-	0.83-1.67

The generator parameters are listed in table 4.6. The generator parameters listed with a * were found by the authors in a previous project [27].

Table 4.6: Generator parameters.

Parameter	Value
Nominal torque [Nm]	0.39
Nominal speed [RPM]	3200
Nominal current [A]	3.4
Nominal power [W]	130
Pole pairs [-]	2
Inductance* [mH]	0.505
Flux linkage* [Wb]	0.0296
Stator resistance* [Ω]	0.345

4.2.2 Pitch System

A stepper motor and a spur gearing are placed in the end of each blade for the pitch system. A gear of module 0.7 with 114 teeth is attached on the end of the blade and a gear of module 0.7 with 23 teeth is attached to the stepper motor, creating a gearing of 4.96. The stepper motor for the blade is a HS 200 1714 0150 high performance and low volume motor from the manufacturer Ametek distributed by Compower and the stepper motor drive is a G 214 from Gecko Drive. To measure the position of the blade, an AM8192B magnetic encoder from RLS is used.

Table 4.7: Pitch system parameters

Parameter	Value
Blade Gear ratio [-]	4.96
Rated Phase Current [A]	1.50
Phase Resistance [Ω]	1.25
Phase Inductance [mH]	1.80
Holding Torque [Ncm]	26
Detent Torque [Ncm]	1.26
Rotor Inertia [gcm^2]	45
Motor Mass [kg]	0.23
Maximum Voltage [V]	40
No. of leads [-]	4

4.3 Blades

The design of the blades was made by the authors in a previous project [27]. The design of the blade was done in order to scale the thrust force acting on the rotor. The scaling of steady state thrust force was chosen because the moment caused by the thrust force on the rotor and the opposing mooring reaction is of an order of magnitude higher than the sideways moment caused by the rotor torque. In an article by H. R. Martin [42] the overturning moment due to rotor torque was less than 5 % of the overturning moment caused by the rotor thrust force for typical operating conditions. This means that the thrust force will have a greater impact on the dynamics of the overall system compared to the rotor torque. Therefore a design for the blades which matched the scaled thrust force of the NREL 5 MW was aimed for. Furthermore the maximum rotational speed of 2900 RPM and thereby the maximum wind velocity generated should be taken into account. This should be done as the blades are designed for a specific range of wind velocities. The scaled rated rotor thrust force of 18.6 N, was scaled from the 5 MW NREL offshore wind turbine under rated conditions [28]. It is assumed that a thrust force of 1.2 N is present at the hub of the wind turbine, while each blade was designed to have a thrust force of 5.8 N. In addition the blades for the scaled wind turbine should also scale the mass and the length of the blades as good as possible.
It should be noted that the blades are designed to give the correct mean scaled thrust force at rated operating conditions, as it is at these conditions the peak thrust force is obtained. The blade design does therefore not take the change of field variables into account. This means that it is only the steady state thrust at rated conditions which is correctly scaled. Unsteady effects caused by e.g changing wind speeds and pitching of the blades were not taken into account in the design process.

There were different limitations for the length of the blade e.g. the size of the wind generator, see section 5.3, and also the 3D printer used for constructing the blades was only able to print objects with a height of maximum 1 m. Properties of the final blade can be seen in table 4.8.

Table 4.8: Blade parameters [28].

	NREL 5 MW	1:35 scaling	35 model
Mass [kg]	17,740	0.41	0.760
Length [m]	61.5	1.76	0.99
Max chord length [m]	4.70	0.13	0.265
Max twist [°]	13.3	13.3	60.1

The design of the blade can be visualized by the chord distribution and geometric twist of the blade, these are in fig. 4.4.

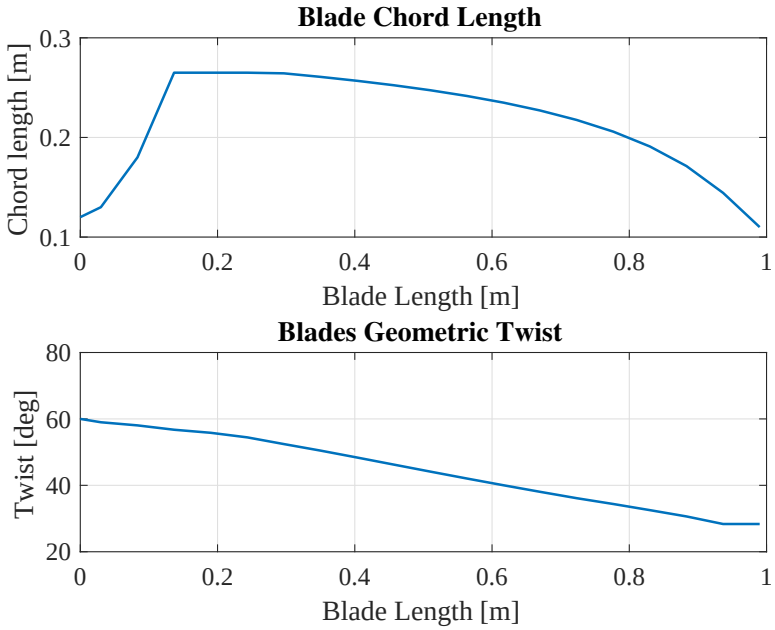

Figure 4.4: The chord length and geometric twist along the designed blade.

The blade design was drawn in Inventor, this was done by loading in 20 calculated airfoils with different chord lengths and twists. These were placed along the blade span with their respective width between them. In order to connect the 20 airfoils, the loft function in Inventor in combination with guidance rails is used. The 3D Inventor drawings are seen in fig. 4.5 and 4.6.

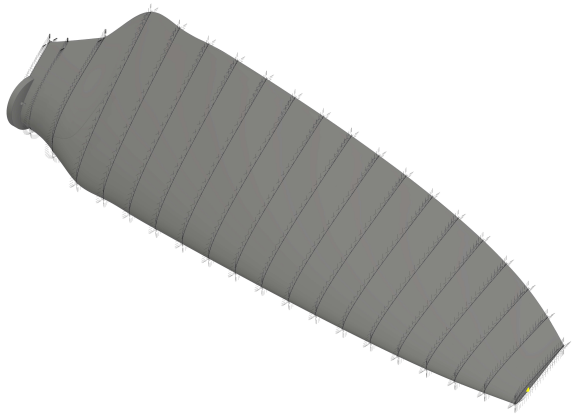

Figure 4.5: The final blade made in inventor, seen from above.

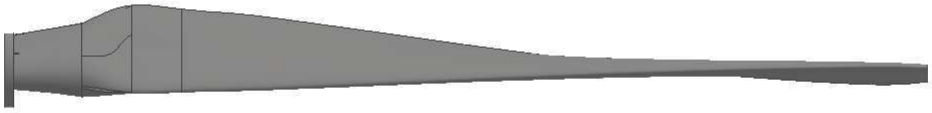

Figure 4.6: The final blade design in inventor, seen from the side.

4.3.0.1 Airfoil

Two airfoils were used for the design of the blades in this thesis. The reason for two airfoils, is that the first part of the blade is exposed to a large bending force and furthermore needs to be able to couple the blade to the pitch mechanism of the rotor. The power generated by this part is small, due to the low tangential velocity and therefore at the first part of the blade, power production properties are not important. The second part of blades is the main contributor of lift for the blade, so therefore an airfoil with a high lift and low drag is wanted.
The airfoil of the first part of the blade was chosen to be AH 93-W-300, as it is a thick airfoil, giving the blade structural strength. The airfoil has a maximum relative thickness of 30 %. The location of the maximum thickness is at 27.9 % of the chord length from the leading edge, which is preferable, as the coupling to the rotor is located at 25 % of the chord.

The second part of the blade should be designed to operate in low Reynold's number, as the magnitude of the Reynold's number over the blades will be in the order of $\mathcal{O}^3$.
The airfoil should have a slim design, this is in order to keep the weight of the blade as low as possible in order to match the scaled mass of the rotor. The power generated by the wind turbine, is sought to be as high as possible. Therefore the operation region of the blades is at a high lift to drag ratio. The airfoil chosen should also have a soft stall behaviour, this is in order to avoid abrupt changes in the lift and drag coefficients, which could lead to unwanted dynamics of the wind turbine. As the blade is going to pitch forth and back, it is wanted to have very limited or no hysteresis of the airfoil. The flow around the airfoil should be attached for a large range of angles of attack, such that the blade can be pitch regulated without stalling. Furthermore the Reynold's number over the blade is changing along the blade span, therefore the flow should also be attached for the range of Reynold's numbers considered.

The airfoil which is used, was chosen to have the following properties:

- Soft stall behaviour
- High lift to drag ratio
- Slim design
- Limited hysteresis
- Attached flow for large range of angle of attacks
- Attached flow for the operating range of Reynold's number

The airfoil series SD70xx [43] was chosen for the last part of the blade and the model SD7003 was a suitable choice, as it has a slim design and a high lift to drag ratio. The lift and drag coefficients are experimentally found in [43], for Reynold's numbers of 60,000, 100,000 and 150,000 for angles of attack in the range of -5° to 12°. The lift and drag ratios used in this thesis are found by the XFOIL analyser [44] for Reynold's numbers of 50,000, 60,000, 75,000, 100,000 and 150,000 for a large range

of angles of attacks from -20° to 80°, which is done in QBlade.

The lift and drag coefficients of the SD7003 airfoil are seen at different angles of attack and Reynold's number in fig. 4.7.

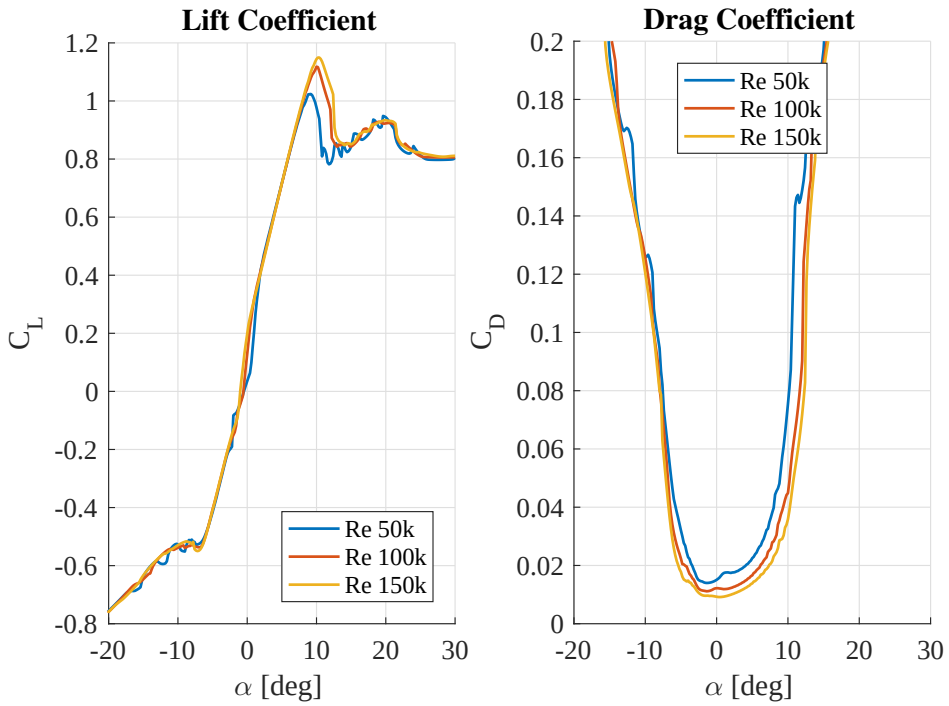

Figure 4.7: The lift and drag coefficients for the SD7003 airfoil can be seen at different angles of attack and Reynold's number.

4.4 Electronics

The control and data acquisition of the wind turbine is implemented into a dSPACE MicroLabBox which is a compact system which together with Simulink and ControlDesk make it possible to do rapid control prototyping with high computational power.
In this thesis a dSPACE is installed and connects all the sensors and actuators of the wind turbine and runs the control algorithm. This makes it possible to test the system and the control developed. The wind turbine sensors include three RLS AM8192B absolute angular magnetic encoders to measure the blade pitch angle, a RLS MR047V040B076 B00-03B miniature incremental magnetic encoder to measure the drive train position, four sets of GFLA-6-350-50-70 strain gauges placed along the tower to measure the strain along the tower, three ADXL335 3-Axis accelerometers are placed along the tower. There is a sensor board to measure the three phase currents and voltages. The sensor board was developed on a printed circuit board (PCB) by the authors of this thesis. Further two PCBs were developed for this thesis; one to use continuous filter on each input to the dSPACE and implement BNC-plugs for the analogue inputs and one to handle the strain gauge measurement. Two power supplies are used, one RS-136-8304 5V as power supply for all the sensors and a PLA600F-48 48V power supply for the stepper motor drives. The generator is controlled by a modified Danfoss VLT used as an active rectifier which is described in more detail in section 23.1. The documentation for the PCBs are seen in appendix A.14.3, A.14.4 and A.14.6 and a complete list of wires and I/O connections are seen in appendix A.14.3 and A.14.2.

Experimental Facilities 5

In this chapter an overview of the experimental equipment available to the authors will be made. The experimental equipment available is a wind generator and a wave basin. In the figure below the testing setup can be seen, including the wind generator and the wave basin.

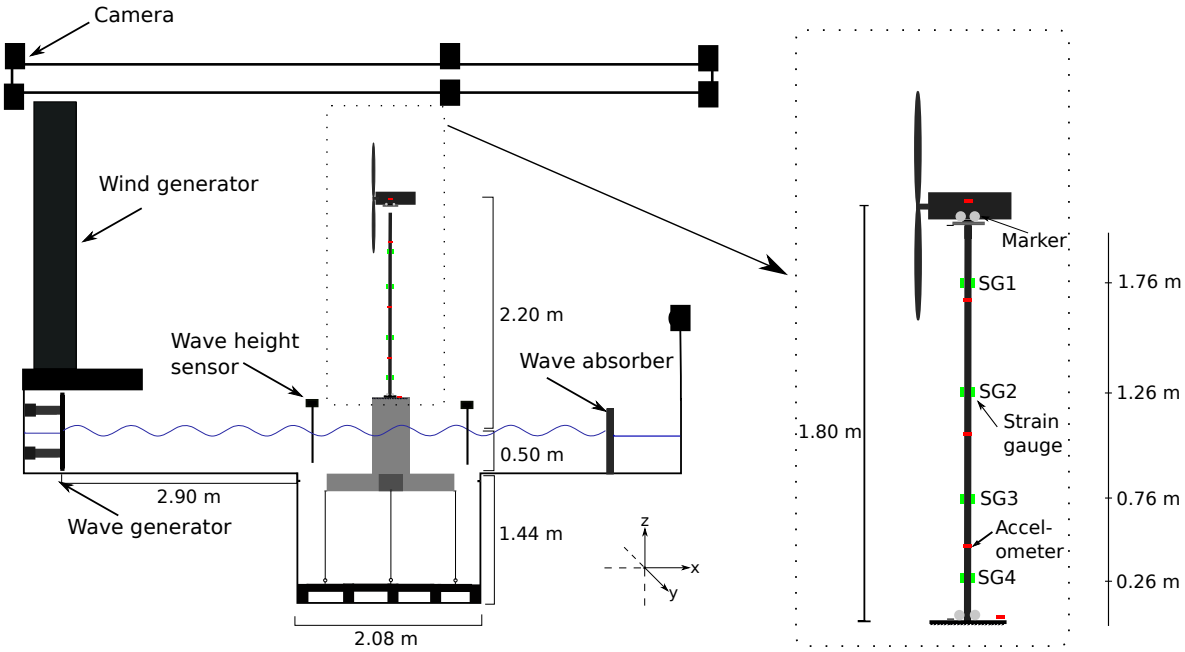

Figure 5.1: The experimental setup.

There is a pocket in the middle of the wave basin, where the TLP of the thesis is placed and anchored to the bottom of the pocket. In one end of the wave basin the wave generator of piston type is placed, this is generating the incident waves for the platform. The piston generator has a peak to peak stroke of 0.7 m and the TLP column is placed approximately 2.9 m from the piston generator when placed at its centre position. In the other end of the wave basin a passive absorber is placed, this has to absorb the waves generated by the wave generator in order to minimise reflections from the end wall. Two fixed surface elevation resistance gauges are attached at the piston generator, while five other gauges can be placed at different locations in the wave basin. The piston generator is capable of generating unidirectional regular and irregular waves with a heading of 0°. On top of the wave generator the wind generator is placed, it consists of seven fans placed in a circular pattern and provides the wind for the wind turbine. The number of fans used can be varied, and the fans can run at different RPMs, such that they generate a wind speed from 0 m/s to above 8 m/s.

Furthermore a camera system in the ceiling can measure the movement, velocity and acceleration of specific objects. Reflective markers are placed on the object and the camera can then track these markers using the infra-red spectrum. The markers are placed at different positions depending on the experiments conducted. Two other methods of monitoring the wind turbine are by the use of strain gauges and accelerometers. The strain gauges were placed in four sets with an equal distance along the tower. These were used for measuring the elongation and compression of the tower at that specific location. Five accelerometers were placed, one at the nacelle and one at the foundation and three at locations along the tower where the amount of information of each of the eigenmodes considered was good and with the possible lowest bound of the noise. This was according to the approach of min-max of the Fisher information, for a more detailed description see previous project [26].

5.1 OptiTrack Camera System

The camera system consists of nine cameras. Eight of them are mounted in a rectangular pattern in the ceiling above the wave basin and one is mounted on the railing for the wave basin. The ceiling cameras are pointing in different directions and therefore only six of them can be used for the experiments conducted in the wave basin. To track a specific object, small infrared reflective markers are placed on it. In the case of this thesis, the markers are placed on the nacelle of the wind turbine and on top of the TLP. The camera system is made by OptiTrack, which also provides the software Motive which is used for the data acquisition. In this software the individual markers are selected and a six DOFs rigid body is constructed from these, hence there will be two rigid bodies; one for the nacelle and one for the TLP.
The cameras used are Prime 13 from Optitrack, which have a frame rate between 30 FPS and 240 FPS. The cameras are calibrated such that the accuracy for each rigid body is below 1 mm, in all the experiments of this thesis.

5.2 Generator Test Bench

To perform tests on the generator setup, a stand alone test set up system has been designed. The test system can be seen in appendix A.9. The test system consist of a 24 V DC motor with a worm gear attached. The motor with gearing is capable of delivering a torque of around 6 Nm. A spider coupling couples the gear shaft with a torque sensor of the type Lorenz DR-3000 111235 having a sample rate of 2500 samples/s. At the other end of the torque sensor the generator of the thesis is attached trough a spider coupling. The torque sensor has a nominal torque ranging from 0.1 Nm to 20 Nm with an accuracy of 0.02 Nm, while the maximum speed is 20.000 RPM and with an angle resolution of 0.25°. Through a USB the torque, speed and power measurements are sent to a compatible software logging the data.

5.3 Wind Generator

The wind field generated by the wind generator without any wind speed filtering has been measured and analysed in a study done by C. Rasmussen and J. Larsen in their bachelor thesis [45]. They measured the velocity and turbulence at a distance of 2.5 m and 4 m away from the wind generator. These experiments showed that when the fans were rotating at 760 RPM, the average velocity at a distance of 2.5 m was 4.74 m/s, while the maximum velocity was 6.42 m/s and the minimum was 2.59 m/s, this indicates a high turbulence intensity. The average turbulence intensity was found to be 30.6 % at this distance.

At a distance of 4 m, the average velocity was measured to be 4.10 m/s, meaning that the velocity has dropped compared to 2.5 m of distance, as one would expect. The maximum velocity was measured to be 5.93 m/s and the minimum was 1.61 m/s. Also here the average turbulence was high, approximately 30.8 %.
Both average turbulence intensities measured were much higher than the recommend value for high turbulence intensity. According to DNV-RP-C205 [46], the recommended design turbulence intensity for offshore wind conditions where the turbulence intensity is high is 14 % at 15 m/s.
It was therefore chosen to make a filter in front of the wind generator. The filter which should be constructed, should be able to:

- Reduce the turbulence to acceptable levels according to DNV-RP-C205 in [46]
- Make the wind field more uniform
- Make the wind field as unidirectional as possible
- Develop a wind field which is at least the same size as the rotor, which is 2.12 m in diameter
- Be easily adjustable in filters
- Should be easily demounted and storable
- Should be no more then 2 m in length

The authors therefore designed a rectangular structure, which is mainly constructed from aluminium modules. The structure was developed as a rectangular casing, where the enclosure of the casing was plywood at the top and bottom, while the sides were equipped with shockproof acrylic. The structure is fastened to the wind generator in the four corners by bolts, and also fastened to the ground through four L-feet. The structure is designed to house three different filters which can be slid in and be positioned, and furthermore a honeycomb can be mounted at the outlet.

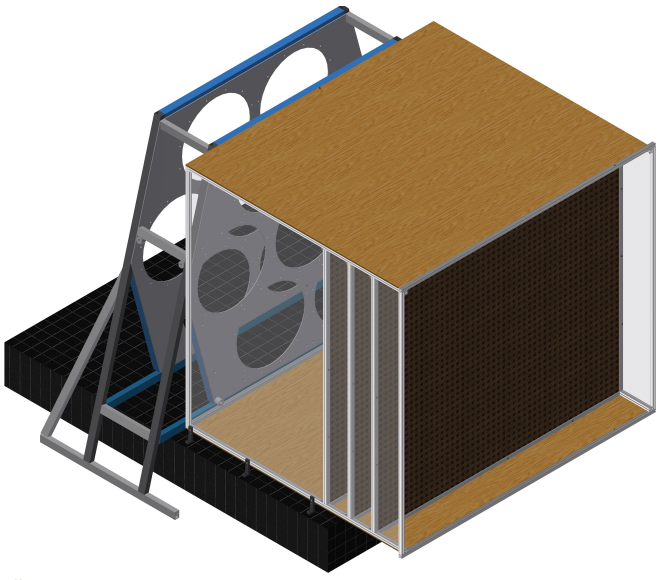

Figure 5.2: The wind generator with the filter structure, which is equipped with three meshes for filters, but no honeycomb.

5.3.1 Fans

The fans used for the wind generator is from systemair and of type AXC 640-6/12°-2-E. It is an axial fan with 6 blades in each fan. The fan have a diameter of 0.64 m and the pitch angle of the blades is 12°. The blades are directly mounted on a 4 kW 2 poled AC motor [47].

The rotational speed of the fans can be adjusted by utilizing an adjustable frequency VLT drive from Danfoss. The rotational speed of the fans can thereby be adjusted from 0 RPM to 3100 RPM. The power and pressure diagram of the fan used, are seen in fig. 5.3 below.

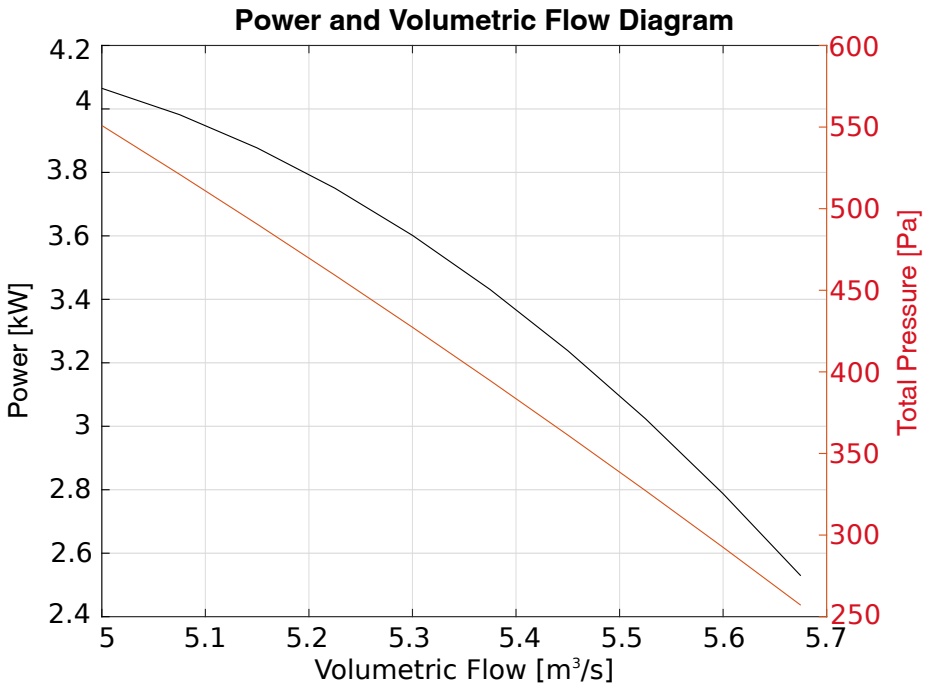

Figure 5.3: The power used by each fan and total pressure delivered by the fan AXC 640-6/12°-2-E [47].

5.3.2 Screens

Different types of screens are used in the wind tunnel to smooth out the turbulent wind. There are different suggestions on how to smoothen out the turbulent wind field. In [48] and [49] the suggestions are to have more than one screen, and that the mesh screens have different cell size, as this gives the best result. Furthermore it is common to use a honeycomb screen as the last screen before the wind is used for experiments.

In this thesis four screens will be made, three mesh screens with different cell sizes and one screen with honeycomb. Studies have shown that the honeycomb with hexagonal design have the lowest pressure loss coefficient compared to honeycomb designed with circular or square pattern [49]. The honeycomb used in this thesis has the hexagonal design, the cell size is 0.01 m, the foil thickness is 0.05 mm and the sheet thickness is 0.1 m. The thickness of the sheet should not be too short, as the wind will not have time to settle inside it, as the small scale turbulence settles into heat. But it must neither be too long, as the pressure loss increases, as the boundary layer increases, thus reducing the wind velocity.

The other three screens will consist of meshes with mesh sizes of 0.5 mm, 1.0 mm and 1.4 mm. It is recommended to have decreasing mesh sizes as the wind travels through the wind tunnel [49]. The pressure loss across the different meshes are found by using the Reynold's number for the flow crossing the mesh

$$Re_{mesh} = \frac{V_0 \delta_w}{\nu} \tag{5.1}$$

where δ_w is the width of the space between the wires, while ν is kinematic viscosity and V_0 is the velocity across the mesh found using the continuity equation

$$V_0 = \frac{A_1}{A_0} V_1 \tag{5.2}$$

where A_1 is the area of the wind screen and A_0 is the area of the free area of the mesh, while V_1 is the wind velocity before the screen. The pressure loss across the screen can then be calculated using

$$\Delta p = 0.65 \rho V_1^2 k \left(\left(1 - \frac{A_0}{A_1} \right) + \left(\frac{A_1}{A_0} - 1 \right)^2 \right) \tag{5.3}$$

given in [48], where ρ is the density of air and k is found using

$$k = \begin{cases} k = k(Re_{mesh}) & \text{for} \quad 50 < Re_{mesh} < 10^3 \\ k = 1 & \text{for} \quad 10^3 \leq Re_{mesh} \end{cases} \tag{5.4}$$

The number $k(Re_{mesh})$ is found graphically in [50] for $50 < Re_{mesh} < 10^3$. As the screens are meant to be able to move forth and back in the wind tunnel and be interchanged the rated wind speed of 7 m/s is used for calculating the pressure loss across all the screens. The different parameters for the screens, the wind speed across the screens together with the pressure loss across the screen are seen in table 5.1.

Table 5.1: Parameters for the three screens.

Screen	δ_w [mm]	t_{wire} [mm]	V_0 [m/s]	p_{loss} [Pa]
Large	1.4	0.25	9.72	3.52
Medium	1.0	0.30	12.95	19.15
Small	0.5	0.16	12.20	14.01

Here t_w is the thickness of the wire and p_{loss} is the pressure loss across the screen. As seen in fig. 5.3, the pressure loss across the screens is of minor importance compared to the total pressure of the fans.
Another important factor for getting a smooth wind field is that there has to be some distance between the screens in order for the wind field to stabilize before it enters the next screen. Therefore the wind tunnel is made as long as possible without interfering with the experimental setups.

5.3.3 Wind Filter Testing

To find the wind filter setup for this thesis, first the different combinations of the wind filters have to be investigated, here the turbulence intensity and mean wind speed are to be judged upon, by only measuring the wind speed in the centre of the wind field. Thereafter the most promising filter combination is tested further by measuring the wind speed in several points, in order to investigate if the turbulence intensity and mean speed of the wind field are uniformly distributed. For the experiments a pitot tube of the L-type from KIMO was used together with an ALMEMO 2590 data

logger. The pitot tube measures the pressure and from this pressure, the wind velocity is using a simplified Bernoulli's equation

$$V = K_{pitot}\sqrt{\frac{574.2T + 15682.77}{P_0}}\sqrt{p} \tag{5.5}$$

where V is the wind velocity, K_{pitot} is a coefficient of the pitot tube, here 1.0015 for pitot tube NPL type L is used, T is the ambient temperature, P_0 is the ambient pressure and p is the measured pressure.

5.3.3.1 Wind Filter Setup

To gain knowledge of the performance of the wind generator with different filter configurations, a series of tests of different combinations were made, in order to choose which wind filter configuration should be tested further.
The experiments were conducted by placing a pitot tube at a distance of 1.26 m away from the wind tunnel exit, which is equivalent to the distance to the rotor plane. Only a single measurement point, which was located at the centre of the wind field, was used to evaluate the performance of the different filter configuration. Measurements were taken in 60 seconds, with a sampling rate of 3.33 Hz. The wind generator fans were set to deliver 2900 RPM during all experiments.

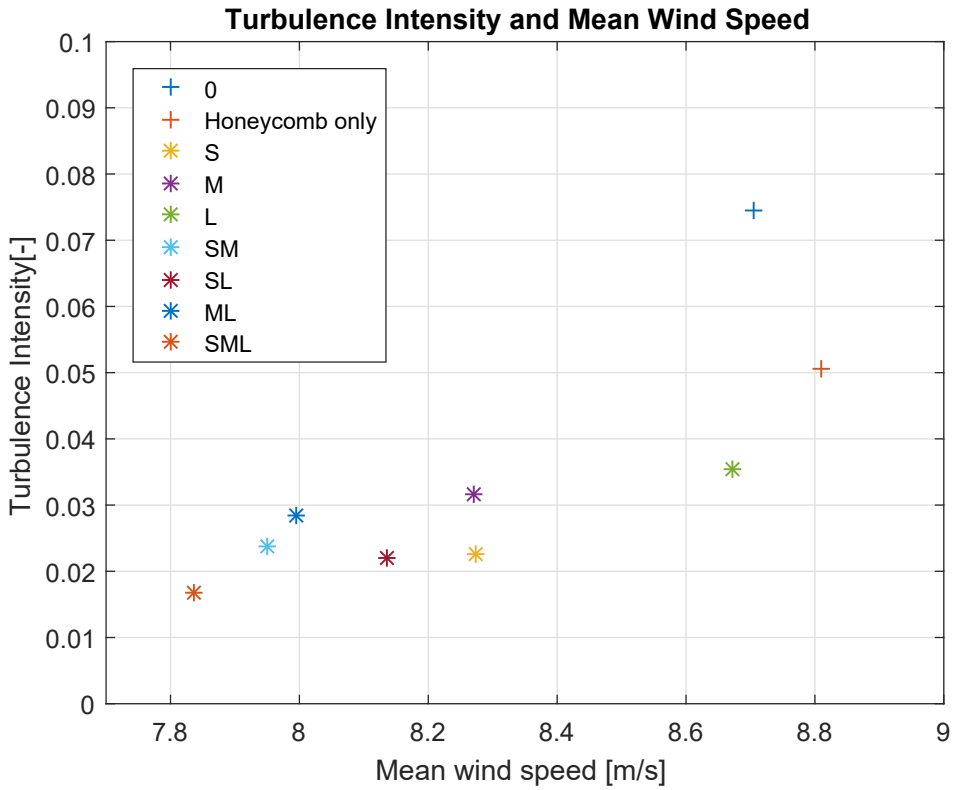

Figure 5.4: The mean wind speed and the turbulence intensity for different filter configurations of the wind tunnel. These are measured at the centre of the wind tunnel at a distance of 1.26 m away from the wind tunnel exit.

In fig. 5.4 S, M and L refer to the small, medium and large mask size of the filters, respectively. The

mask sizes of the screens can be seen in table 5.1, all the tests were done with the honeycomb placed at the outlet of the wind tunnel. The configuration 0 refers to the wind tunnel without honeycomb or filters inside.
The distances from the wind generator for the different configurations of the filters can be seen in table 5.2.

Table 5.2: The distance the screens were placed from the wind generator for the tested configurations.

Screen	Small [m]	Medium [m]	Large [m]
S	1.3	-	-
M	-	1.2	-
L	-	-	1.2
SM	1.3	1.0	-
SL	1.0	-	1.3
ML	-	1.2	0.7
SML	1.3	1.0	0.7

As a rule of thumb the settling distance of the flow after flowing through a filter is 30 mesh sizes[51]. Therefore the impact of the settling distance is not investigated further as the longest distance of 4.2 cm is fulfilled in all the tests.

As seen in fig. 5.4 the mean wind speed and turbulence intensity decrease as more filters are used. Based on these experiments the large filter (L) seems to be the most suitable, as the turbulence intensity is at an acceptable level, and the mean wind speed has not been reduced significantly. But in order to validate this wind filter setup, the wind field generated is to be investigated further, which is done in 5.3.3.2.

5.3.3.2 Wind Field Testing

These experiments were conducted by placing the pitot tube at 17 different positions at a distance of 1.26 m away from the wind tunnel exit. For the experiments, two different fan speeds were used, these were 1520 RPM and 2900 RPM. From the 17 different measurement positions the turbulence intensity and mean wind speed are analysed in order to investigate if these are uniformly distributed over the wind field. Two filter configurations were tested; one with only the filter with large masks and one with both the filter with the large masks and the filter with small masks. Both configurations were tested even though the mesh with large masks were found most suitable in the section 5.3.3.1. It was found during the experiments of this section that this mesh was not enough for distributing the wind speed uniformly across the wind field, which will be shown in this section.

In fig. 5.6 the mean wind speed and the turbulence intensity are seen, when the fans are running at 1520 RPM. The first row of figures shows the wind field when neither filters nor honeycomb are used. While the next row shows when the honeycomb and the filter with large mask size are used. And the last row shows when honeycomb and two filters with large and small mask sizes are used.

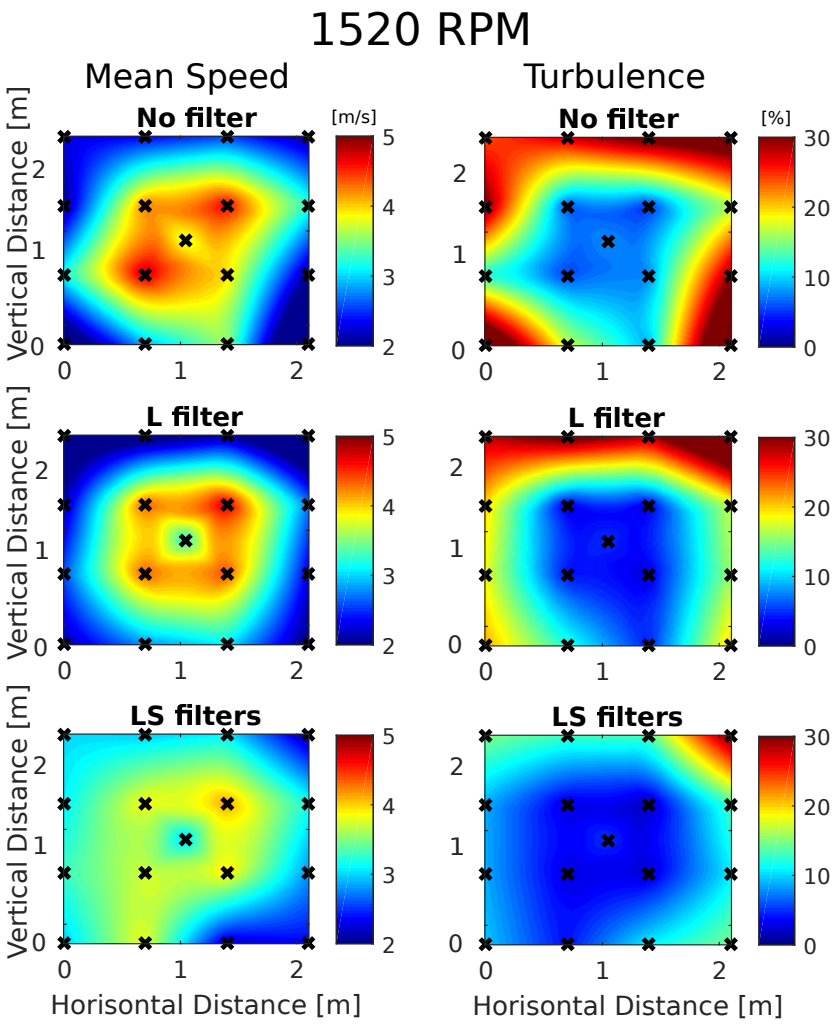

Figure 5.5: The mean wind speed and the turbulence intensity for the wind field when the fans are running at 1520 RPM.

When no honeycomb or filter are used, the mean wind speed is high in the middle but decreases towards the sides of the wind field, while the turbulence intensity increases towards the sides. As a uniformly distributed wind field is desired, this is not satisfactory. When honeycomb and the filter with large masks are used, the mean wind speed is lower in the middle, but it still decreases towards the sides, the turbulence intensity on the other hand seem to be more uniformly distributed as wanted. When two filters and the honeycomb are used, the mean wind speed is again lower, but it is much more uniformly distributed across the wind field, which has a higher priority than the wind speed. At the same time, the turbulence intensity is only higher in the corners, and as the blades of the wind turbine does not reach the corners, it is assumed unimportant.

The results from the other test with maximum rotational speed of the fan, are seen in fig. 5.6. Again it can be seen that there is the same tendency of the wind field to become more and more uniformly distributed, and again the two filters combined with the honeycomb shows the best result when looking at the turbulence intensity, while the mean wind speed is a bit low, but still uniformly distributed.

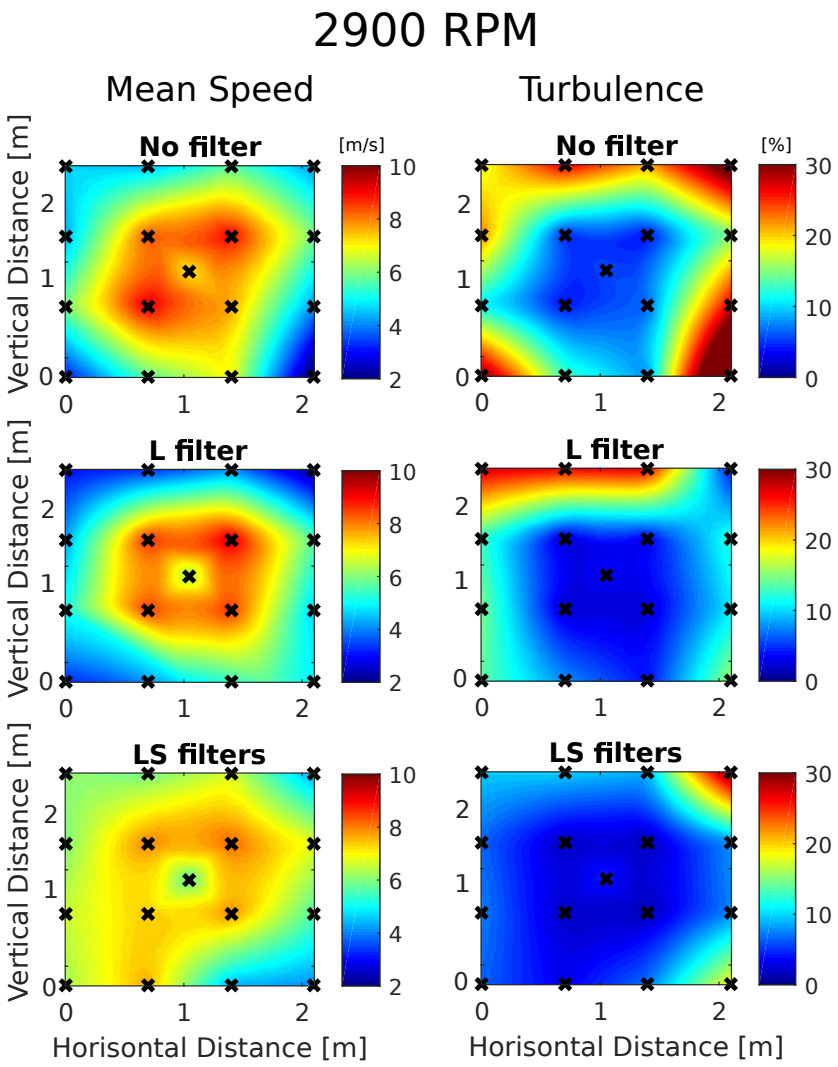

Figure 5.6: The mean wind speed and the turbulence intensity for the wind field when the fans are running at 2900 RPM.

As the uniformity of the wind field has higher priority compared to the mean wind speed, the configuration with two filters is used. The final setup of the wind tunnel us seen in appendix A.1.

5.3.3.3 Wind Speed

When the final combination of the filters are found, it is possible to determine the relationship between the wind speed and the rotational speed of the fans in the wind generator. The speed is found by using the pitot tube and the Almemo logger, measurements are taken during 30 s with a sampling time of 3.3 Hz. The wind speed is found as a mean wind speed at two points in the wind field, these two point are located 60 cm from the sides and in the vertical centre. The results are seen in fig. 5.7.

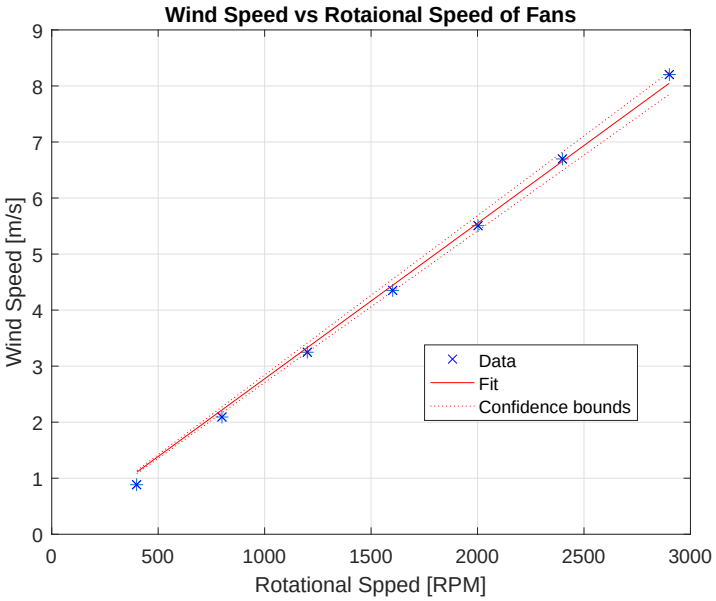

Figure 5.7: The wind velocity at different rotational speeds of the fans of the wind generator.

In the figure the blue markers are the data points, while the red dotted lines are the 95 % confidence interval for the red solid regression line.
These results give the following linear relationship

$$V = 0.00277 f_{fan} \tag{5.6}$$

where f_{fan} is the rotational speed of the fans in RPM.

5.4 Wave Generator

Waves in a laboratory can be measured in several ways e.g. by resistance electrical wave gauges, buoys or pressure transducers. However the pressure transducers give rise to some issues as the assumption of linear regular waves is needed in order to use a linear transfer function from pressure to surface elevation. In irregular cases the signal needs to be split into the different frequencies, analysed separately and then added together again. Furthermore the pressure transducers need to be located at a distance below the lowest surface elevation expected, however must not be placed too deep such that the pressure variation compared to the noise level is too low. The resistance electrical wave gauges consist of two thin rods of stainless steel in parallel. When submerged in water an electric circuit is established where the voltage drop is proportional to the level of submergence of the gauges. The calibration of the gauges is done by submerging the gauges at three known depths and a simple linear relationship between the output voltage and surface elevation is established. The resistance electrical wave gauges are used in this thesis.
It is important to notice that differences between full scale experiments and scaled experiments might occur due to different model or scale effects. The model effects can for instance be wall effects, reflection of waves due to lack of absorption at the end wall, absence of ocean currents etc. In this thesis the wall effects might have an influence on the overall response of the TLP. The pocket of the wave basin available has a limited size of 2.08 x 2.08 m and a maximum depth of 1.90 m. The scaling factor had been chosen such that the TLP would fit this pocket. When the TLP is moving

back and forth, it will move some water creating a moving pressure field. At the pocket walls the pressure field is blocked creating an opposite pressure against the TLP, which might influence the response. However as the response of the TLP is relatively small it is assumed that these wall effects are minor. Another model effect is the generated waves by the wave generator. As waves in reality are governed by the wind continuously influencing the waves, the loss of energy due to friction is of minor importance. Thereby the waves can be seen as statistically stationary and homogeneous, that is the probability distribution does not change with time nor space. This is not entirely true for the waves generated by the wave generator, as no wind is present. As a consequence the waves will start losing energy immediately after their generation. Thereby wave gauges placed different places might experience different waves, which is also seen in fig. 5.8. Sensor one, two and three are placed 20 cm from the front of the TLP in a row, with sensor two aligned with the TLP in the surge direction. Sensor four and five are placed 20 cm behind the TLP also in a row, however placed at the sides. The experimental setup can be seen in appendix A.4. The target spectrum seen in fig. 5.8, which is the spectrum the wave generator should generate, is a white noise profile with an equal energy density of 0.00005 m^2s across the frequency interval of 0.2 to 2 Hz. It can be seen that the waves deviate a lot from the target spectrum. Furthermore the energy measured by sensor two deviates much from the others, indicating a lot of reflected waves from the TLP. The other sensors look more alike, however also deviates slightly at specific frequencies. The deviations most likely occur due to loss of energy of the waves and due the reflected waves from the end wall.

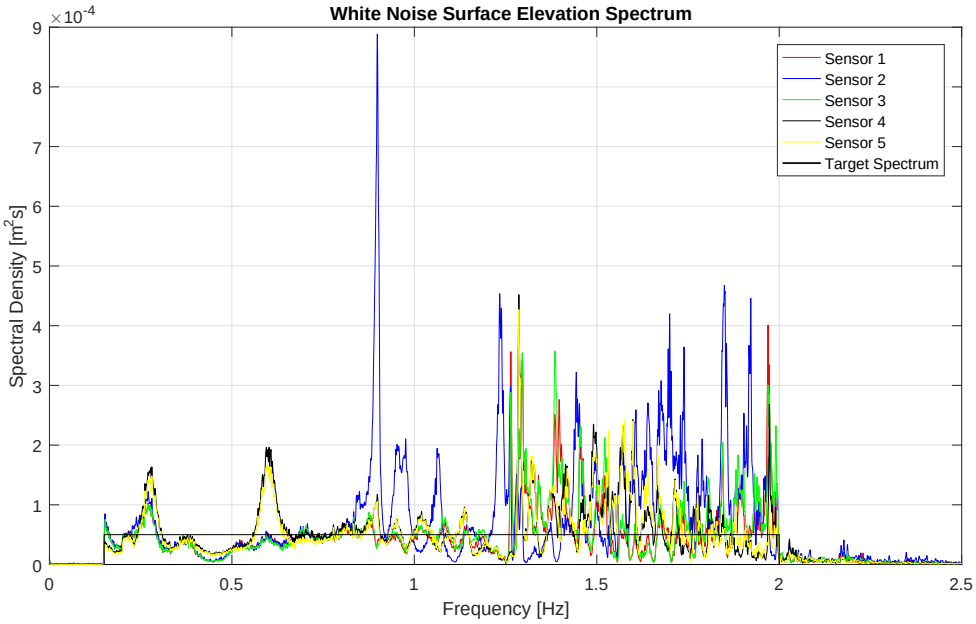

Figure 5.8: White noise surface elevation spectrum measured at five different places.

The scaled effects occur due to the similarity requirements, geometrical, kinematic and dynamic, when scaling the TLP. It is most often impossible to scale everything correctly, e.g. the gravitational acceleration and viscosity, having the consequence that it is impossible to fulfil both Froude and Reynold's number simultaneously. For a correct reproduction of the waves, which are gravity based, Froude model law is essential, however as consequence the Reynold model law cannot be fulfilled. Thereby the viscous forces might deviate between the full scale model and the scaled model. For more information regarding scaling laws and the scaling of the TLP, see previous work done by the authors [25]. As will be explained in section 7, the surface elevation of the waves will follow

a Gaussian distribution with zero mean, but only if they can be considered linear. In fig. 5.9 a Gaussian distribution and cumulative distribution of an experimental measured surface elevation are seen. It can be seen that the mean lies around zero, and the surface elevation seems normal distributed.

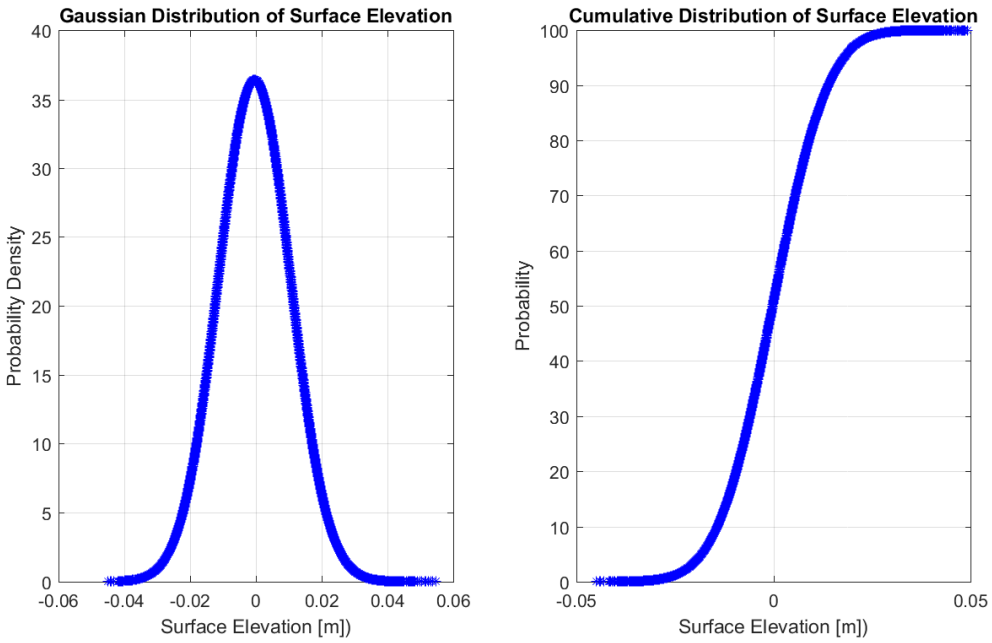

Figure 5.9: The Gaussian and cumulative distribution of the surface elevation.

As seen the surface elevation of the waves follow a Gaussian distribution. However the wave amplitudes should follow a Rayleigh distribution, but only if they can be considered linear. As seen in fig. 5.10 this is also the case. If the waves measured were non-linear, the wave amplitudes would deviate from the Rayleigh distribution.

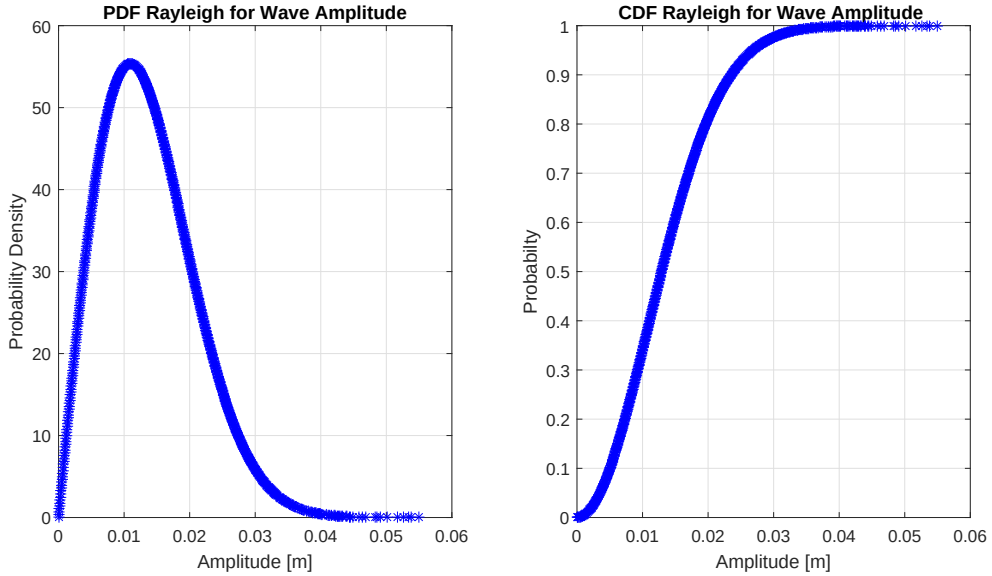

Figure 5.10: The Rayleigh and cumulative distribution of the wave amplitudes.

Part II

Hydrodynamic Model

Symbol	Description	Units
Γ	Gamma function	-
γ	Peak shape parameter	-
ε	Elongation	m/m
$\bar{\varepsilon}$	Mean energy	kg/s^2
ζ	Damping ratio	-
η	Surface elevation	m
η_a	Wave amplitude	m
$\boldsymbol{\theta}$	Vector of parameters	-
θ	Phase angle	rad
θ_j	Angular position of pontoons	rad
λ	Wave length	m
μ	State space approximation	N, Nm
$\bar{\nu}$	Narrowness of spectrum	-
$\ddot{\boldsymbol{\xi}}$	Acceleration vector	m/s^2
$\dot{\boldsymbol{\xi}}$	Velocity vector	m/s
$\boldsymbol{\xi}$	Position vector	m
ρ	Density	kg/m^3
σ	Spectral width parameter	-
	Stress	Pa
σ_{eta}	Standard deviation of surface elevation	-
ϕ	Force phase angle	rad
	Velocity potential	m^2/s
ϕ_D	Diffracted velocity potential	m^2/s
ϕ_I	Incident velocity potential	m^2/s
ϕ_R	Radiated velocity potential	m^2/s
ψ	Phase angle	rad
ω	Angular frequency	1/rad
ω_0	Natural angular frequency	rad/s
ω_d	Damped natural angular frequency	rad/s
ω_p	Angular peak frequency	1/rad
$\mathbf{A}_c$	State space matrix	-
$\mathbf{A}(\infty)$	Added mass at infinity frequency	kg, kgm^2, kgm
A	Projected area	m^2
A_γ	Normalisation factor	-
A_m	Cross section area of mooring line	m^2
A_{wp}	Water plane area	m^2
$\mathbf{B}_c$	State space matrix	-
$\mathbf{B}_{crit}$	Critical damping matrix	Ns/m, Nms
$\mathbf{B}_e$	Equivalent linear damping	Ns/m, Nms
$\mathbf{B}_{lin}$	Linear viscous damping	Ns/m, Nms
$\mathbf{B}_{pot}$	Potential damping matrix	Ns/m, Nms, Ns
$\mathbf{B}_{quad}$	Quadratic viscous damping	Ns^2/m^2, Nms^2
$\mathbf{B}_{total}$	Total linear damping matrix	Ns/m, Nms, Ns
$\mathbf{C}_c$	State space matrix	-
$\mathbf{C}_A^*$	Linear Coriolis force coefficient matrix	kgm/s, kgm^3/s, kgm^2/s
$\mathbf{C}_m^*$	Linear centripetal force coefficient matrix	kgm/s, kgm^3/s, kgm^2/s

C	Integral constant	-
C_a	Added mass coefficient	-
C_D	Drag coefficient	-
c	Phase velocity	m/s
D	Diameter of TLP	m
dz	Length of differential strip	m
E_m	Youngs modulus of mooring line	Pa
$\mathbf{F}$	Force/moment vector	N, Nm
$\mathbf{F}_{hs}$	Hydrostatic force vector	N, Nm
$\mathbf{F}_{moor}$	Static mooring force/moment vector	N, Nm
$\mathbf{F}_{rad}$	Radiation force vector	N, Nm
$\mathbf{F}_{wave}$	External wave vector	N, Nm
$\bar{\mathbf{F}}_{wave}$	Complex excitation force	N, Nm
F_T	Pretension in mooring line	N
f_n	Natural frequency	Hz
f_p	Peak frequency	Hz
g	Gravitational acceleration	m/s^2
H	Wave height	m
$H_{1/3}$	Mean height of the 1/3 highest waves observed	m
H_m	Significant wave height	m
H_{max}	Most likely wave height	m
h	Water depth	m
$\mathbf{I}$	Identity matrix	-
	Inertia matrix	kg / kgm^2
I_{AA}	Area moment of inertia of water plane area	m^4
$\mathbf{J}^*$	Transformation matrix	-
$\mathbf{K}_{hs}$	Hydrostatic stiffness matrix	N/m, Nm
$\mathbf{K}_{moor}$	Mooring line stiffness matrix	N/m, Nm, N
$\mathbf{K}_{tot}$	Total system stiffness matrix	N/m, Nm, N
k	Wave number	1/m
L_m	Length of mooring line	m
l_p	Length of pontoon	m
M_0	Zeroth moment	m^2
M_n	Spectral moments	m^2/s^n
$\mathbf{M}_{RB}$	Inertia matrix	kg, kgm^2
N_w	Number of frequencies	-
n_t	Number of mooring lines	-
p	Pressure	Pa
p_d	Dynamic pressure	Pa
p_0	Pressure at surface	Pa
$\ddot{\mathbf{q}}$	Acceleration vector	m
$\dot{\mathbf{q}}$	Velocity vector	m
$\mathbf{q}$	Position vector	m
$\mathbf{R}$	Retardation function matrix	N/m, Nm, N
Re	Reynold's number	-
S	Surface area	m^2
$S_\eta(f)$	Spectral density of surface elevation	m^2s

S_{JS}	JONSWAP spectrum	m^2s
S_{PM}	Pierson Moscowitz spectrum	m^2s
S_q	Motion response spectrum	m^2s
s	Wave steepness	-
T	Wave period	s
T_z	Zero upcrossing period	s
t	Time	s
U	Average forward speed	m/s
u	Longitudinal particle velocity	m/s
V_{sub}	Submerged volume	m^3
v	Vertical particle velocity	m/s
w	Lateral particle velocity	m/s
x_s, y_s, z_s	Distance from $\{s\}$ to $\{b\}$	m

Introduction 6

In this part the hydrodynamic theory will be described. First the generation of the waves will be outlined with the different definitions describing a wave. Then the linear wave theory and the BCs, together with the velocity profile will be outlined. Furthermore irregular waves and the spectra of these will be described. For constructing the simulation the dynamical equations of the TLP system both in time domain and frequency domain have to be found. Afterwards the hydrodynamic coefficients for the TLP are found, this includes the damping and the stiffness of the TLP, together with the natural frequencies.
At last the different parameters are found through experiments, while the analytically found coefficients are validated together with the simulation. The parameters found are the elasticity of mooring lines, the mooring stiffness, the natural frequency and damping. While the simulation is validated though free decay and forced responses.

Wave Generation 7

Various types of waves exist at the sea and they can generally be divided into groups by their respective frequency and disturbing forces generating the waves. These forces continue to influence them after generation and include the wind blowing across the sea, earthquakes, gravitational pull of the moon, etc. It should be noted that tides are commonly not considered as waves, but instead a variation in the still water line (SWL). This thesis will only consider the wind generated waves and swells which are short period waves with a period less than 40 seconds (unscaled) [52].
A sea surface influenced by a wind field can be characterized as a very irregular surface where the waves continuously arise and disappear. Smaller waves are superimposed on larger waves, and the different waves travel with different speeds and directions making real ocean waves very complex and thus they cannot be precisely predicted. In fig. 7.1 some of the most important definitions of a wave can be seen in a two-dimensional frame. The coordinate system is chosen at the SWL with positive x-axis being along the wave propagation direction and the z-axis pointing upwards, meaning that the sea bed is located at $z = -h$.

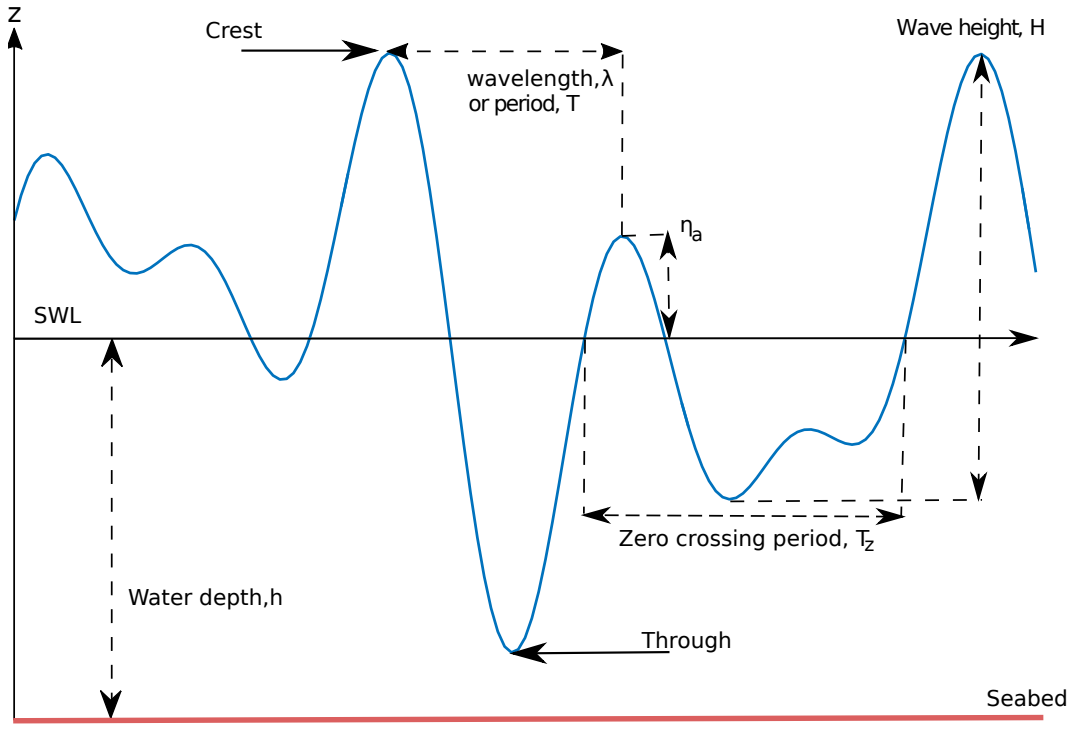

Figure 7.1: Visualisation of different parameters describing waves.

The bottom of a wave, when below the SWL, is called the wave trough while the top, when above the SWL, is called the wave crest. The wave height, H, is defined as the vertical distance between the deepest trough and the highest crest between two successive zero-upcrossings of the sea elevation process. The wave amplitude, η_a, is the distance between the SWL and the highest crest. The water surface elevation is denoted η and is a function of space and time. The wave length, λ, is a measure of the distance between two crests in space, while the period, T, is the time between two crest passages of the same vertical section. The wave number is defined as $k = \frac{2\pi}{\lambda}$, while the angular frequency is defined as $\omega = \frac{2\pi}{T}$. The wave steepness, s, is defined as the ratio between the wave height and wave length, $s = \frac{H}{\lambda}$, while the phase velocity, c, of the wave is defined as the ratio between the wave length and the wave period, $c = \frac{\lambda}{T}$. u, v and w denote longitudinal, lateral and vertical velocities of the water particle, respectively. The zero-upcrossing period, T_z, is defined as the period of time between the first time the wave elevation crosses the SWL from trough to crest and the second time it crosses the SWL from trough to crest.
As shown in section 5.4 the sea elevation, under linear conditions, follows a Gaussian probability function while the wave height follows a Rayleigh distribution which are why the waves also sometimes are called Gaussian waves,.
The wave conditions at sea can be divided into two primary classes; wind and swell seas. The wind seas exist due to local wind. But the swells have no directly relationship to the local wind area as they are waves which have travelled from where they were generated. The combination of wind and swell seas are called a sea state. Wave conditions may either be described by deterministic design wave methods or by stochastic methods. According to DNV-RP-C205 [46], structures with a significant dynamical response such as FOWTs, should be described through stochastic modelling of the sea surface and the kinematic through a time series. In the stochastic modelling the sea state is described through a wave frequency spectrum, having a given significant wave height, a representative frequency interval, a mean propagation direction and a spreading function. For the stochastic behaviour it is assumed that the sea state exist in a temporal domain and can be considered as a stationary random process such that the probability distribution parameters as the mean and variance do not change with time.
As the sea is considered to be Gaussian waves the linear wave theory, also known as Airy wave theory or Stokes' first order theory is capable of describing analytical expressions for the water particle velocity, water particle path, water particle acceleration and pressure as they are all linearly dependent on wave amplitude.
In the beginning of this chapter the linear wave theory is described. However only 2D waves with the waves travelling in the x-direction will be described, as it is not possible to experimentally generate 3D waves, due to the limit of the wave generator used in this thesis. Next the theory regarding linear irregular waves and their kinematics will be described. At last different ways of modelling the power spectrum density (PSD) of the sea states will be outlined.

7.1 Linear Wave Theory

The linear wave theory is the simplest possible case and theory. The theory is fundamental for understanding higher order theories and the analysis of irregular waves. The theory is however only valid when the wave steepness is small, that is the wavelength is much larger than the wave height (H/λ « 1) and the water is deep compared to the wave height such that H/h is small. These conditions are needed in order to secure that the waves do not brake and thus causing highly non-linear terms. In the linear theory the motion of the water particles depends on the vertical and horizontal positions and time. Furthermore in the linear theory the water particles take a circular

orbital path which is not broken, meaning that there is no exchange of momentum between the different water particles. For shallow waters, defined as $\frac{h}{\lambda} < \frac{1}{20}$, the water particles takes an elliptic pattern with the orbit progressively flattening towards the seabed, see fig. 7.2. For deep waters, defined as $\frac{\lambda}{2}$ the radius and velocity of the water particles decay exponentially and at a depth of approximately $\frac{\lambda}{2}$ the orbit dies out and the velocity is zero.

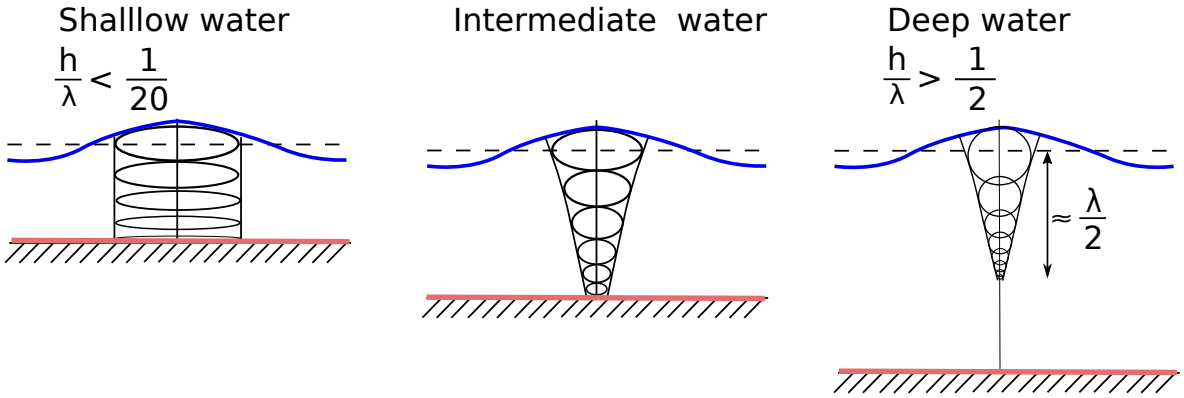

Figure 7.2: Water particle circular motions at different depths.

The angular frequency of the waves and the wave number are related, i.e shorter wavelengths also have shorter periods compared to longer wavelengths, this is known as the dispersion relation

$$kg = \omega^2 \tan(kh) \tag{7.1}$$

where g is the gravitational acceleration. The dispersion relationship can be reformulated using the definition of phase velocity as

$$c = \sqrt{\frac{g\lambda}{2\pi} \tanh\left(\frac{2\pi h}{\lambda}\right)} \tag{7.2}$$

showing that waves with different wavelengths also have different propagation velocities, that is the waves are dispersive. Using the dispersion relationship, eq. 7.1, it can be investigated whether or not the waves in the laboratory can be treated as deep, intermediate or shallow water waves. The waves generated by the JONSWAP spectrum, see section 7.3 ranges from 0.5 Hz to 2.5 Hz, whereby the wavelength ranges from 0.19 m to 4 m. In fig. 7.3 it can be seen that the waves can be treated as deep water waves indicated by the white area when the frequency is above 0.5 hz. The red horizontal lines indicate the frequency range for the waves generated by the JONSWAP spectrum. The white area indicates the deep water range, while the shaded area indicates the intermediate water.

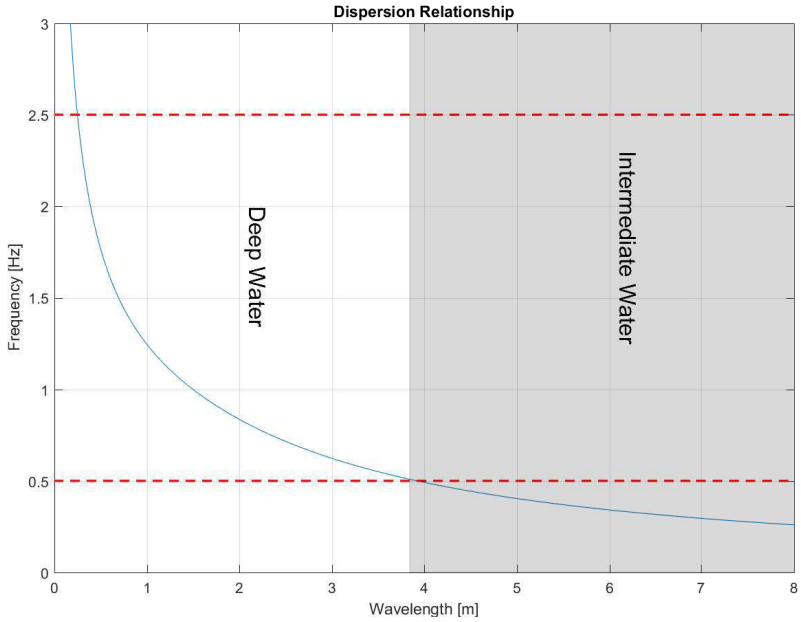

Figure 7.3: The dispersion relationship giving frequency as function of wavelength.

The governing equations describing the flow is found in the field of fluid dynamics for which the continuity equation for a flow of an incompressible fluid and thereby a constant density yields

$$\frac{\partial u}{\partial x}+\frac{\partial v}{\partial y}+\frac{\partial w}{\partial z}=0 \tag{7.3}$$

where $\mathbf{v}=[u\ v\ w]^T$ is a three dimensional velocity vector. In the case of irrotational flow the continuity equation can be expressed in terms of a velocity potential, ϕ, such that the Laplace equation is achieved

$$\nabla^2\phi=\frac{\partial^2\phi}{\partial x^2}+\frac{\partial^2\phi}{\partial y^2}+\frac{\partial^2\phi}{\partial z^2}=0 \quad \text{as} \quad \mathbf{v}=\frac{\partial\phi}{\partial \mathbf{x}} \tag{7.4}$$

Newton's second law can be applied for the water particles yielding the equation of motion expressed in the general form of Navier-Stokes' equation, which for an ideal fluid can be simplified to Euler's equation for flow

$$\rho\left(\frac{d\mathbf{v}}{dt}+\mathbf{v}\cdot\nabla\mathbf{v}\right)=-\nabla\mathbf{p}+\rho\mathbf{g} \tag{7.5}$$

where ρ denotes the density of the water, $\mathbf{p}=p(\mathbf{x},t)$ is the pressure distribution, $\mathbf{g}=[0\ 0\ -g]^T$ denotes the gravitational acceleration. The assumption of inviscid flow is an often used assumption as viscosity often only matters in a thin layer close to the structure and is therefore not necessary when describing the waves surrounding the structure. However when calculating the response of the structure it is often necessary to add these viscous effects in order to complement the potential velocities [53].
In case of irrotational flow, Euler's equation can be rewritten as the generalized Bernoulli's equation

which is an integrated form of the equation of motion

$$gz + \frac{p}{\rho} + \frac{1}{2}\left(\nabla\phi\right)^2 + \frac{\partial\phi}{\partial t} = C \tag{7.6}$$

where C is the integral constant determining the reference of the pressure. Eq. 7.4 and eq. 7.6 represent two equations with two unknowns (ϕ, p). It is possible to solve eq. 7.4 separately if only the velocity potential appears explicitly in the BCs which is usually the case. Thereafter the pressure can be found using eq. 7.6 therefore the pressure is seen as a reaction on the already determined velocity field when considering potential flows.
Appropriate BCs (on the free surface, sea bed and hull of the TLP) need to be applied. As the Laplace equation is linear, superposition holds, therefore the velocity potential can be decomposed to

$$\phi = \phi_I + \phi_D + \phi_R \tag{7.7}$$

where ϕ_I, ϕ_D and ϕ_R are the incident, diffracted and radiated wave potentials, respectively. The diffracted and radiated wave potentials occur due to the presence and displacement of the TLP, while the incident wave potential occurs due to the kinematics and dynamics of the free surface flows. For now neglecting the presence of the TLP, only the incident waves will be described, while the diffracted and radiated wave potentials will be described in more detail in chapter 8.
The free surface flow requires one BC at the bottom, two at the free surface and BCs at the lateral boundaries of the domain.

1 The bottom BC ensures there can be no flow through the bottom, that is the vertical velocity is zero at the bottom

$$\frac{\partial\phi_I}{\partial z} = 0 \quad \text{for} \quad z = -h \tag{7.8}$$

Furthermore it should be noted that due to the assumption of an ideal fluid, meaning there is no friction, a BC for the horizontal velocity is not included.

2 The kinematic BC at the free surface specifies that a water particle at the surface remains at the surface

$$\frac{\partial\phi_I}{\partial z} = \frac{d\eta}{dt} \quad \text{for} \quad z = \eta \tag{7.9}$$

As the surface elevation is a function of time and space the chain rule is applied yielding

$$\frac{\partial\phi_I}{\partial z} = \frac{\partial\eta}{\partial t} + \frac{\partial\eta}{\partial x}\frac{dx}{dt} = \frac{\partial\eta}{\partial t} + \frac{\partial\eta}{\partial x}\frac{\partial\phi_I}{\partial t} \tag{7.10}$$

3 The dynamic BC specifies that the pressure is constant at the surface, that is no wind induced pressure variation nor surface tension are included. Thereby the pressure at the surface, p_0, is only a function of time. Utilizing Bernoulli's equation, given in eq. 7.6, where the constant term is set to $C = \frac{p_o}{\rho}$ thereby implying that the equation should equal a constant pressure

$$gz + \frac{p}{\rho} + \frac{1}{2}\nabla\phi_I^2 + \frac{\partial\phi_I}{\partial t} = \frac{p_0}{\rho} \tag{7.11}$$

which can be rewritten as

$$g\eta + \frac{1}{2}\nabla\phi_I^2 + \frac{\partial\phi_I}{\partial t} = 0 \quad \text{as} \quad p = p_0 \quad \text{for} \quad z = \eta \tag{7.12}$$

4 The lateral BCs are taken care of by the assumption of the waves being periodic and progressive waves with a constant form. Thereby the variation of the surface elevation and velocity field with respect to time and space is restricted to be identical within two sections separated by an integral number of wave lengths. The requirement is mathematical expressed as

$$\eta(x,t) = \eta(x + n\lambda, t) = \eta(x, t + nT), \quad \text{for} \quad n = 1,2,3\ldots \tag{7.13}$$

which can be fulfilled if introducing a new variable $\left(\lambda\frac{t}{T} - x\right)$ where (x,t) has been combined into a single variable, such that

$$\eta\left(\lambda\frac{t}{T} - x\right) = \eta\left(\lambda\frac{(t+nT)}{T} - (x+n\lambda)\right) \tag{7.14}$$

If multiplying by 2π and dividing by the wave length the variable is expressed in dimensionless form

$$\theta = 2\pi\left(\frac{t}{T} - \frac{x}{\lambda}\right) = \omega t - kx \tag{7.15}$$

where the definition of the wave number and cyclic frequency have been utilized. Thereby the periodic conditions for $\eta(\theta)$ and $\phi(\theta)$ have been included by introducing the single variable θ.

The four BCs are summarised and visualised in fig. 7.4.

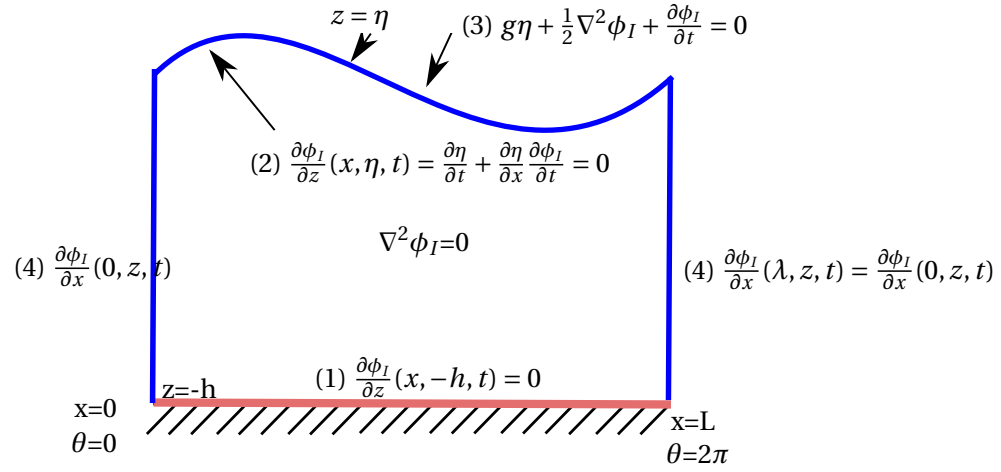

Figure 7.4: Visualisation of the BCs.

At the present state the governing equation is impossible to solve analytically as both BCs at the free surface are non-linear. Furthermore the surface elevation is one of the unknowns of the problem, however this is not included in the governing Laplace equation 7.4. Therefore a mathematical simplification is needed. By the use of the linear theory, that is assuming small amplitudes and wave steepness, the BCs can be linearised and the surface elevation can be eliminated from the

equations by the use of a Taylor series expansion from $z = 0$ instead of $z = \eta$. In [52] T. Lykke et al. showed that the error made by evaluating the velocity potential at $z = 0$ instead of $z = \eta$ is small and of second order.

5 Furthermore in [52] it is shown that the linearised surface BCs can be combined into a single BC expressed as

$$\frac{\partial \phi_I}{\partial z} + \frac{1}{g}\frac{\partial^2 \phi_I}{\partial t^2} = 0 \quad \text{for} \quad z = 0 \tag{7.16}$$

where the surface elevation has been eliminated from the BCs.

Thereby the new linearised BCs can be visualised as shown in fig. 7.5

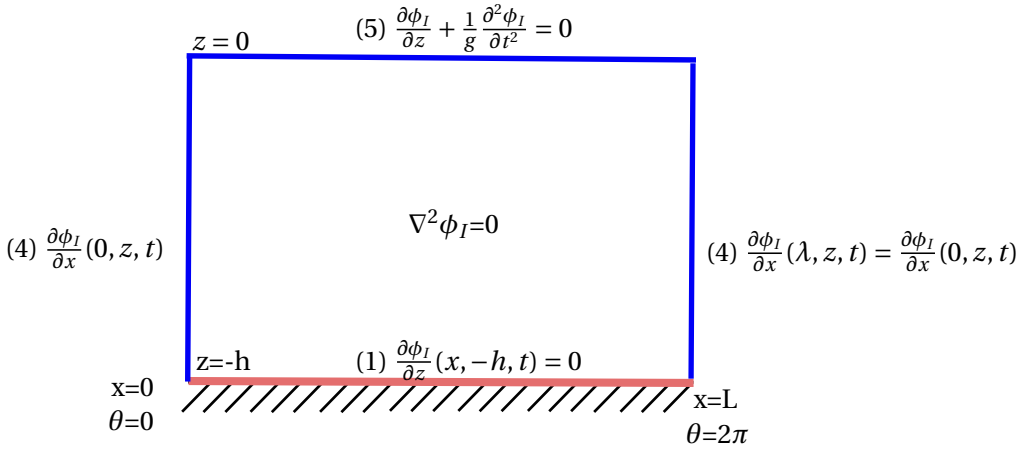

Figure 7.5: Visualisation of the linearised BCs.

The surface elevation can be written as

$$\eta = \eta_a \cos(\omega t - kx) \tag{7.17}$$

where the wave amplitude is described as $\eta_a = \frac{H}{2}$. The velocity potential satisfying the governing Laplace equation subjected to the linearised BCs is

$$\phi_I(x, z, t) = -\frac{\eta_a g}{\omega}\frac{\cosh(k(z+h))}{\cosh(kh)}\sin(\omega t - kx) \tag{7.18}$$

where the negative sign of the kx-term indicates that the wave propagates in the positive x-direction. The velocity field can be found by differentiating the velocity potential yielding

$$\begin{aligned} u(x, z, t) &= \frac{\partial \phi_I}{\partial x} = \frac{\eta_a g k}{\omega}\frac{\cosh(k(z+h))}{\cosh(kh)}\cos(\omega t - kx) \\ w(x, z, t) &= \frac{\partial \phi_I}{\partial z} = -\frac{\eta_a g k}{\omega}\frac{\sinh(k(z+h))}{\cosh(kh)}\sin(\omega t - kx) \end{aligned} \tag{7.19}$$

Likewise the acceleration field can be found by differentiating the velocity field

$$\begin{aligned}\dot{u}(x,z,t) &= -\eta_a g k \frac{\cosh(k(z+h))}{\cosh(kh)} \sin(\omega t - kx) \\ \dot{w}(x,z,t) &= -\eta_a g k \frac{\sinh(k(z+h))}{\cosh(kh)} \cos(\omega t - kx)\end{aligned} \tag{7.20}$$

Defining the dynamic pressure, p_d, which is the wave induced pressure, as the excess pressure relative to the hydrostatic pressure and the atmospheric pressure, the following equation is obtained

$$p_d = p - \rho g(-z) = p + \rho g z \tag{7.21}$$

which when inserted into the linearised Bernoulli's equation yields

$$p_d = \rho g \eta \frac{\cosh(k(z+h))}{\cosh(kh)} \quad \text{for which} \quad p_d|_{z=0} = \rho g \eta \tag{7.22}$$

Meaning that the dynamic pressure is decreasing towards the bottom and is in phase with the surface elevation. As a consequence of the linearisation of the free surface these kinematic equations are only valid for water particles up to the SWL. To allow calculation of the kinematics up to the instantaneous surface elevation different extrapolations can be used, among others the widely used Wheeler stretching or extrapolation of the wave kinematics [46]. These two methods are seen in fig. 7.6.

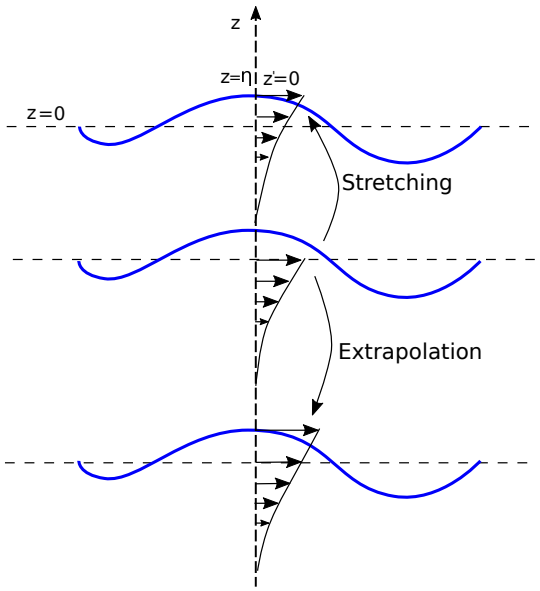

Figure 7.6: Different ways of extending the velocity profile above the still water line.

The extrapolation of the wave kinematics extrapolates the kinematics linearly from the SWL to the surface elevation. While in the Wheeler stretching method, the profiles are stretched and compressed depending on the surface elevation meaning that the point of z in the vertical direction changes with the surface elevation, as seen in eq. 7.23. Thereby Wheeler stretching takes the reduction of the particle velocity at the SWL into consideration. With the linearisation the origin was assumed to be placed at the SWL, however by applying Wheeler stretching the z-axis is stretched or

compressed such that the origin is at the instantaneous surface elevation. Thereby the evaluation coordinate is given as

$$z' = \frac{z-\eta}{1+\eta/h} \quad -h < z' < 0 \quad \text{and} \quad -h < z < \eta \tag{7.23}$$

where z' is the 'stretched' discretisation of the z-axis and z is the 'actual' discretisation of the z-axis. In fig. 7.7 a contour plot of the velocity profile with implemented Wheeler stretching generated from a regular surface elevation is shown. It can be seen that the horisontal velocity is in phase with the surface elevation, while the vertical velocity is out of phase.

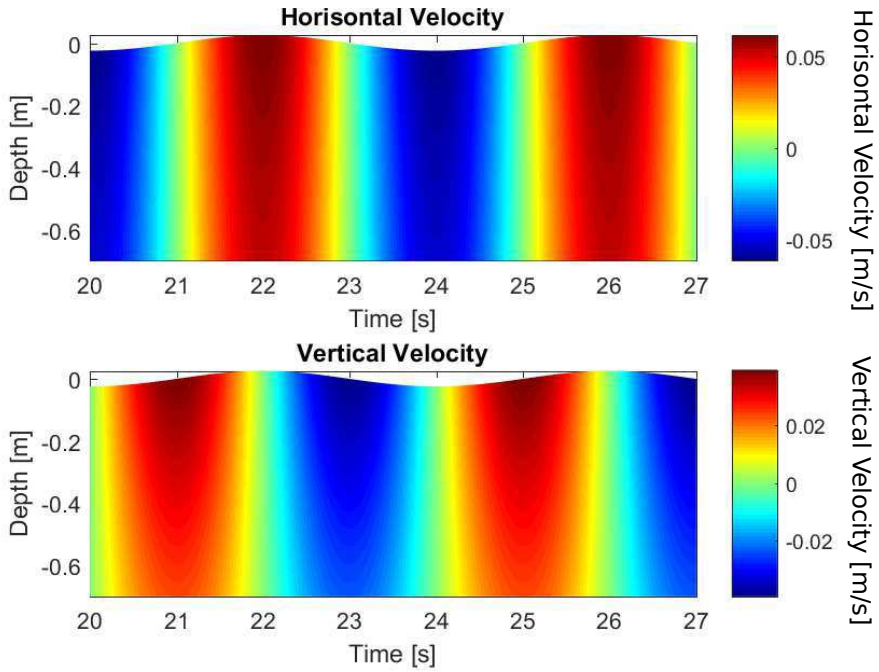

Figure 7.7: Contour plot of the horisontal and vertical velocity profile respectively. The depth is taken to 0.7 m which is the length of the submerged TLP.

[52] [54]

7.2 Irregular Wave Generation

The wave kinematics described so far are based on a purely regular sea state which is not commonly seen in a real ocean environment. Instead the waves and thereby their kinematics can be considered as a composition of infinitely many regular waves with different frequencies and amplitudes, and thereby also different energy contents, which are known as irregular waves. If considering the energy of a wave in a control volume it can be shown, as done in [54], that the mean energy $\bar{\epsilon}$ over a unit horizontal surface area S is equal to

$$\frac{\bar{\epsilon}(t)}{S} = \frac{1}{8}\rho g H^2 = \frac{1}{2}\rho g \eta_a^2 \tag{7.24}$$

while the variance of the surface elevation is given as

$$\begin{aligned}\mathrm{Var}\left(\eta(t)\right) &= E\left(\left(\eta(t)-\underbrace{\bar{\eta}(t)}_{=0}\right)^2\right) = E\left(\eta^2(t)\right) = \frac{1}{T}\int_0^T \eta^2(t)\,dt \\ &= \frac{1}{T}\int_0^T \left(\eta_a\cos(\omega t)\right)^2 dt \approx \frac{1}{2}\eta_a^2\end{aligned} \tag{7.25}$$

from which it can be seen that the difference between the energy and the surface elevation variance is approximately a factor of ρg. It has here been used that the mean surface elevation, $\bar{\eta}(t)$ is zero. Utilising that the governing equation is the Laplace equation, which is a linear second order differential equation, and that the BCs have been linearised, it is possible to apply superposition such that the irregular wave time series are composed by a series of regular waves each with their own velocity potential, surface elevation, particle velocity and dynamical pressure. That is by considering a series of regular waves it can be composed into an irregular wave by applying a Fourier series as

$$\eta(t) = \frac{1}{2}\underbrace{\eta_{A_0}}_{=0} + \sum_{n=1}^{\infty}\left(\eta_{A_n}\cos(\omega_n t - k_n x) + \eta_{B_n}\sin(\omega_n t - k_n x)\right) = \sum_{n=1}^{\infty}\eta_{a,n}\cos(\omega_n t - k_n x + \theta_n) \tag{7.26}$$

where θ_n is a phase difference between each individual regular wave, the wave number is calculated through the dispersion relationship, and it has been used that η_{A_0} is zero as $\bar{\eta}(t) = 0$ and that

$$\begin{aligned}\eta_{a,n} &= \sqrt{\eta_{A_n}^2 + \eta_{B_n}^2} \\ \theta_n &= \arctan\left(\frac{\eta_{B_n}}{\eta_{A_n}}\right)\end{aligned} \tag{7.27}$$

As for the regular waves, the linear wave theory is used to describe the wave kinematics yielding

$$\begin{aligned}u(x,z,t) &= \sum_{n=1}^{\infty}\frac{\eta_{a,n}g k_n}{\omega_n}\frac{\cosh k_n(z+h)}{\cosh(k_n h)}\cos(\omega_n t - k x_n + \theta_n) \\ w(x,z,t) &= \sum_{n=1}^{\infty}-\frac{\eta_{a,n}g k_n}{\omega_n}\frac{\sinh k_n(z+h)}{\cosh(k_n h)}\sin(\omega_n t - k x_n + \theta_n) \\ \dot{u}(x,z,t) &= \sum_{n=1}^{\infty}-\eta_{a,n}g k_n\frac{\cosh k_n(z+h)}{\cosh(k_n h)}\sin(\omega_n t - k_n x + \theta_n) \\ \dot{w}(x,z,t) &= \sum_{n=1}^{\infty}-\eta_{a,n}g k_n\frac{\sinh k_n(z+h)}{\cosh(k_n h)}\cos(\omega_n t - k_n x + \theta_n)\end{aligned} \tag{7.28}$$

In fig. 7.7 a contour plot of the velocity profile with implemented Wheeler stretching generated from an irregular surface elevation is shown.

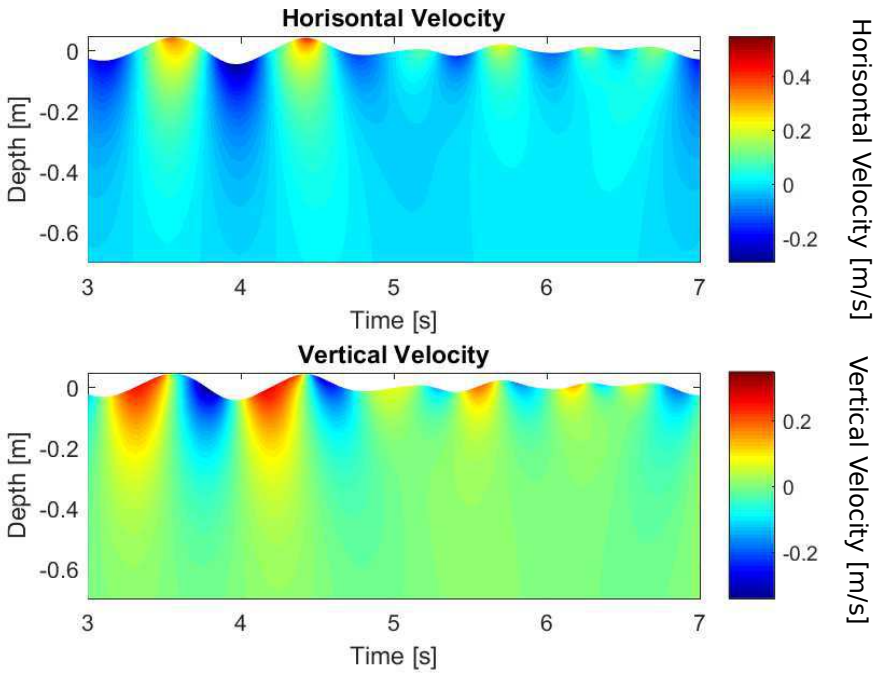

Figure 7.8: Contour plot of the horisontal and vertical velocity profile respectively. The depth is taken to 0.7 m which is the length of the submerged TLP.

The variance of each regular waves can be plotted according to their respective frequency and if normalising according to a frequency resolution Δf the surface elevation spectral density, S_η, is achieved by

$$S_\eta(f) = \frac{\frac{1}{2}\eta_a^2(f)}{\Delta f} \tag{7.29}$$

This spectrum contains no information regarding the phases, meaning that it is not possible to convert the signals from a spectrum into the original time series. However assuming uncorrelated phases and choosing the phases for each regular wave as a random number uniformly distributed between 0 and 2π gives one realisation of a time series having the target energy spectrum. Thereby the irregular wave pattern is statistically equal to the originally irregular wave pattern. [52] [54]

7.3 Spectrum

One of the most common ways to describe irregular waves is done through a spectral distribution. In this spectral distribution the irregular waves are broken down into a series of regular waves with different amplitudes, phases and frequencies. If sampled, these regular waves can be mapped into the frequency domain by a Discrete Fourier Transformation (DFT) such that the amplitudes and phases can be visualised according to the frequencies instead of a series of regular waves. The most common spectral distribution is however the PSD in which the energy content of the different regular waves are visualised according to their respective frequencies.
As mentioned the waves occur due to the wind blowing across the sea supplying energy to the waves, while the dissipation occurs due to the gravity wherefore these factors should be included when waves are described.

Many different spectra exist and the most appropriate wave spectrum depends on the geographical area at which the structure is placed. However a popular and often used spectrum for theoretical purposes is the parametrised Pierson-Moscowitz (PM) spectrum in which it is assumed that the waves have come into equilibrium with the waves after the wind has blown steadily over a large area for a long time. The parametrised spectrum is defined according to the peak frequency ω_p and the significant wave height H_{m0}

$$S_{PM}(\omega) = \frac{5}{16} H_{m0}^2 \omega_p^4 \omega^{-5} \exp\left(-\frac{5}{4}\left(\frac{\omega}{\omega_p}\right)^{-4}\right) \tag{7.30}$$

where there is a direct relation between the peak frequency and the significant wave height by

$$\omega_p = 2\pi \left(15.7\sqrt{\frac{H_{m0}}{g}}\right)^{-1} \tag{7.31}$$

The peak frequency depends on the wind speed through the following equation

$$\omega_p = \frac{0.877g}{U_{19.5}} \tag{7.32}$$

where $U_{19.5}$ is the wind speed 19.5 m above the sea surface. As the peak frequency depends on the wind speed so does the significant wave height.
The Joint North Sea Wave Observation Project (JONSWAP) spectrum $S_{JS}(\omega)$ is a modification of the PM spectrum representing a developing sea state in a fetch limited situation

$$S_{JS}(\omega) = A_\gamma S_{PM}(\omega) \gamma^{\exp\left(-\frac{1}{2}\left(\frac{\omega-\omega_p}{\sigma\omega_p}\right)^2\right)} \tag{7.33}$$

where γ is a non-dimensional peak shape parameter having an average experimental data value of 3.3 [46], A_γ is a normalisation factor, given as

$$A_\gamma = 1 - 0.287\ln(\gamma) \tag{7.34}$$

while σ is a spectral width parameter for which it follows that

$$\sigma = \begin{cases} \sigma_a & \text{for} \quad \omega \leq \omega_p \\ \sigma_b & \text{for} \quad \omega > \omega_p \end{cases} \tag{7.35}$$

having the average values of $\sigma_a = 0.07$, and $\sigma_b = 0.09$ [46]. It should be noted that for a value of $\gamma = 1$ the JONSWAP spectrum reduces to the PM spectrum. Furthermore it should be noted that a shift from the angular frequency representation to the frequency representation is done by

$$S(\omega)2\pi = S(f) \tag{7.36}$$

The spectral moments M_n of the general order n is found as

$$M_n = \int_0^\infty \omega^n S(\omega) d\omega \tag{7.37}$$

from which it can be seen that the area under the curve is equal to the zeroth moment, which again is equal to the variance of the free surface elevation. The significant wave height H_{m0} can be found from the spectral zeroth moment by

$$H_{m0} = 4\sqrt{M_0} = 4\sigma_\eta \tag{7.38}$$

where σ_η denotes the standard deviation of the surface elevation, therefore it can be seen that the significant wave height is a measure of the variability in the arbitrary wave heights. Another measure of the significant wave height is the term $H_{1/3}$ which is a measure of the mean height of the one third largest waves observed. It follows that for a narrow spectrum $H_{m0} = H_{1/3}$ while for a normal spectrum $H_{m0} = 1.08 H_{1/3}$. The narrowness of the spectrum is defined as

$$\bar{\nu} = \sqrt{\frac{M_0 M_2}{M_1^2} - 1} \tag{7.39}$$

having the physical meaning that the narrower the spectrum the more regular the wave tends to be with the limit $\bar{\nu} = 0$ representing a regular harmonic wave. On the other hand a wide spectrum represents a lot of different frequencies and therefore a more irregular sea with average of $\bar{\nu}$ between 0.2 and 0.4 [46]. In fig. 7.9 the scaled Pierson-Moscowitz and JONSWAP spectrum are seen. As reference wind speed the average wind speed at the Hywind project is used, which is 10.1 m/s [55]. This reference wind speed is then scaled according to the scaling laws. As a consequence of the scaling of the wind speed, both the peak frequency and significant wave height are scaled correctly, yielding a scaled peak frequency of 0.81 Hz and a scaled significant wave height of 0.061 m corresponding to an unscaled significant wave height of 2.13 m.

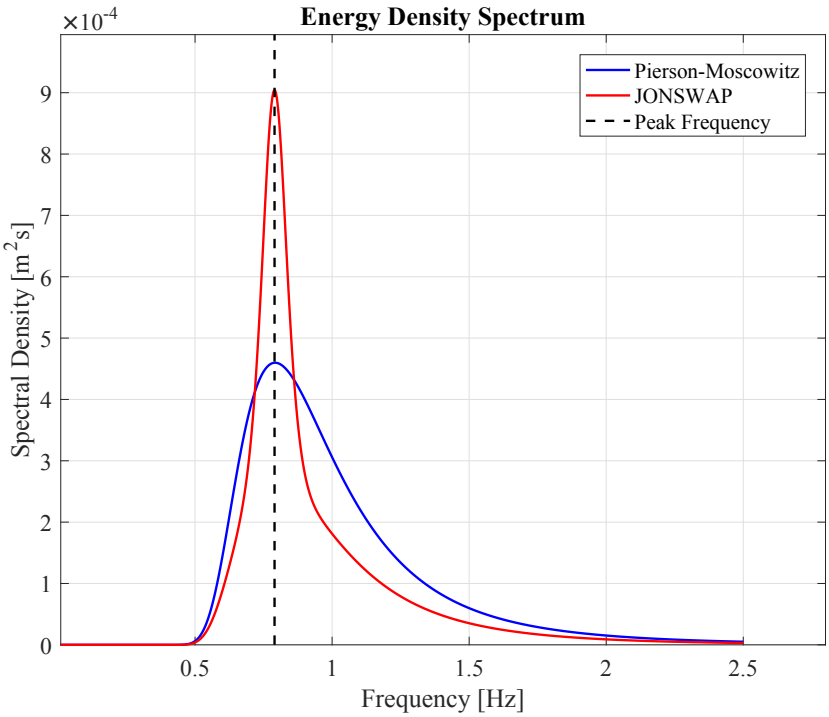

Figure 7.9: Visualisation of the scaled Pierson-Moscowitz and JONSWAP spectrum.

In reality these single peaked spectra are not always sufficient enough to describe the response of a FOWT, as swell seas has to be taken into account, as well. Swell waves tend to have long wavelengths and thereby lower frequencies resulting in a second or multiple peaks at the low frequency area of the energy density spectrum. Furthermore also different directions of propagation might occur. Other wave spectra have been proposed in order to take account of the different sea states such as the Torsethaugen spectrum, which is recommended by DNV-OS-J103 [56]. The Torsethaugen spectrum is obtained by superimposing two generalized JONSWAP functions.
However as the aim of this thesis is to validate the simulation codes, the TLP is only exposed to a single peak JONSWAP spectrum.
As mentioned in section 7 the wave heights in a fully developed sea can be approximated to follow a Rayleigh distribution described by the cumulative distribution function

$$F(H) = 1 - \exp\left(-2\left(\frac{H}{H_{m0}}\right)^2\right) \tag{7.40}$$

Applying that a typical short term sea state typically contains the order of N_w frequencies and thereby N_w different waves, the most likely maximum wave height $\tilde{H}_{max}$ can be determined from the Rayleigh distribution

$$F(H_{max}) = 1 - \frac{1}{N_w} \Rightarrow \tilde{H}_{max} = H_{m0}\sqrt{\frac{\ln(N_w)}{2}} \approx 1.86 H_{m0} \tag{7.41}$$

which is having a probability of 0.1%. Thereby the most scaled likely maximum wave height 0.11 m corresponding to an unscaled height of 3.96 m. It should be noted that wave breaking however causes the wave distribution to diverge from the Rayleigh distribution.
[54]

Dynamical Equation of the Tension Leg Platform

8

In this chapter the hydrodynamic model will be developed. Modelling the response of the FOWT subjected to operational and extreme wave loads have primary turned towards either Linear Frequency Domain (LFD) analysis or Time Domain Dynamics (TDD) or a combination of both. The LFD approach is based on linear assumptions of the waves assuming potential flow. Viscous effects are thereby either neglected or simplified to be linear. Furthermore it is assumed that the motion of the platform are small compared to the size of the platform, such that diffraction, radiation and hydrostatic effects can be superimposed. Furthermore higher order wave loads, such as ringing, are neglected. The ringing effect is a resonant response associated with transient effects. The TDD on the other hand allows for implementation of the memory effect, also known as the radiation problem, and the non-linear viscous drag forces. In this thesis the LFD analysis is used as a first hand impression of the model, while when simulating the overall response and later on the coupling with the tower the TDD approach is utilised. The non-linear effects as ringing and ocean currents will not be investigated in this thesis.

8.1 Hydrodynamic Coordinate System

One of the tasks when calculating dynamics of the TLP with interactions from waves, is the definition of the coordinate system. As seen in fig. 8.1 three different Cartesian coordinate systems are defined. One which is an earth fixed coordinate system $\{n\}$ having the coordinate system $x_n y_n z_n$ with the origin placed at o_n and the $x_n y_n$ plane placed on the SWL and with the z-axis being positive upwards. The second coordinate system is the seakeeping frame $\{s\}$ defined in a steadily translating coordinate system $x_s y_s z_s$ with the origin at o_s translating forward with the average constant speed U of the TLP, even in the trivial case of $U = 0$, where the TLP is not moving. The seakeeping frame is not fixed to the TLP but to the equilibrium state. The last coordinate system is a body-fixed frame $\{b\}$ with the coordinate system $x_b y_b z_b$ with the origin o_b placed at the centre of mass. When the TLP is in its initial position, that is in the absence of external forces, these two coordinate systems are parallel to each other with only the centre of origin to differ. On the other hand when the TLP is influenced by external forces the $\{b\}$ frame rotates around the $\{s\}$ frame. The $\{n\}$ and $\{s\}$ frame can be considered inertial, while this is not the case with the $\{b\}$ frame as it is considered as a rotating frame, which can be accelerated due to external forces.

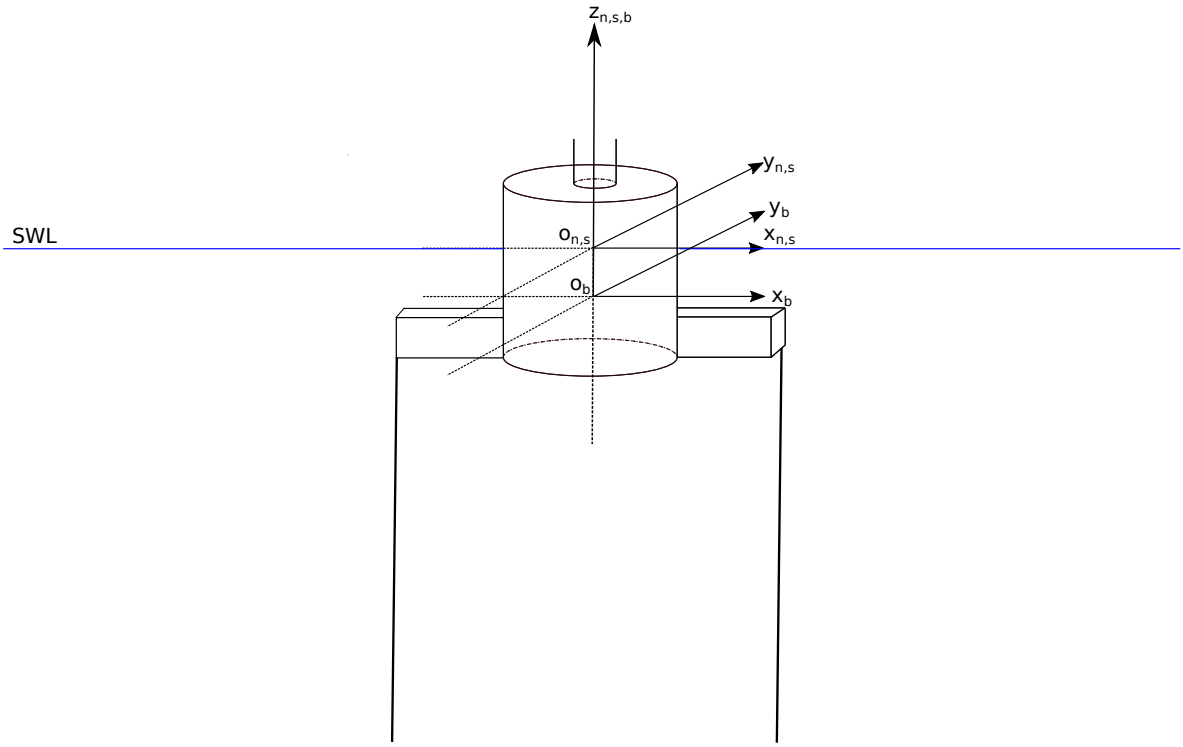

Figure 8.1: Definition of the coordinate systems for the TLP. It has here been assumed that $U = 0$, and that the seakeeping frame $\{s\}$ is placed at the earth fixed frame $\{n\}$.

[53]

8.2 Time Domain Representation

Considering the TLP as a rigid body, and for now neglecting the aerodynamical aspects, the equation of motion in the seakeeping frame $\{s\}$ can be described by Newton's second law as

$$\mathbf{M}_{RB}\ddot{\boldsymbol{\xi}} = \sum \mathbf{F} = \mathbf{F}_{rad} + \mathbf{F}_{hs} + \mathbf{F}_{moor} + \mathbf{F}_{wave} \tag{8.1}$$

where $\mathbf{M}_{RB} \in \mathbb{R}^{6x6}$ is the inertia matrix consisting of the mass of the structure and the mass moment of inertia in each of the respective DOFs, while $\ddot{\boldsymbol{\xi}} \in \mathbb{R}^6$ is the acceleration vector of the TLP in the $\{b\}$ frame relative to the $\{s\}$ frame expressed in the $\{s\}$ frame.
$\sum \mathbf{F} \in \mathbb{R}^6$ describes the forces and moments which the rigid body is influenced by. The forces can be split into the hydrodynamic radiation induced force $\mathbf{F}_{rad}$, the hydrostatic force $\mathbf{F}_{hs}$, the static mooring line force $\mathbf{F}_{moor}$ and the external wave force $\mathbf{F}_{wave}$.
The hydrodynamic radiation induced forces are the forces arising from the change in momentum of the fluid due to the movement of the structure in still water. The hydrostatic forces also known as restoring forces arise due to the interaction between gravity and buoyancy acting on the structure. The static mooring line forces arise due to the attachment of the mooring lines to the structure. The external wave forces arise from the scattering waves due to the presence of the TLP and the undisturbed pressure field, also sometimes referred to as the Froude-Krylov forces, that the incoming waves exert on the structure assuming that the TLP has no motion.
In [57] W.E. Cummins showed that the radiation induced forces in an ideal fluid can be related to a frequency independent added mass $\mathbf{A}(\infty)$ and the frequency dependent potential linear damping

$\mathbf{B}_{pot}(\omega)$ through the convolution integral of the retardation function

$$\mathbf{F}_{rad}(t) = -\mathbf{A}(\infty)\ddot{\boldsymbol{\xi}} - \int_0^t \mathbf{R}(t-\tau)\dot{\boldsymbol{\xi}}d\tau \tag{8.2}$$

Here $\dot{\boldsymbol{\xi}}$ is the velocity vector of the TLP in the $\{b\}$ frame relative to the $\{s\}$ frame expressed in the $\{s\}$ frame. $\mathbf{A}(\infty) \in \mathbb{R}^{6x6}$ is a constant positive-definite added mass matrix at an infinite frequency. The infinity added mass can be interpreted in a physical sense, explaining the instantaneous reaction of the fluid to any motion. That is as soon a movement of the fluid starts, the infinity added mass explains the inertial of the fluid to this sudden motion. It can furthermore be shown that this added mass is only a function of the geometry of the structure, meaning that it does not vary with the kinematics of the structure [58].
The second term in eq. 8.2 represents the fluid memory effect which can be interpreted as a filtered potential damping force. This effect captures the energy transfer and thereby momentum from the motion of the structure to the surrounding fluid. The convolution integral formulation is needed as a change in the fluid momentum due to the motion of the structure at a particular time instant, affects the motion of the structure at all subsequent times. $\mathbf{R}$ is a matrix of retardation functions, describing the radiation impulse response, given as

$$\mathbf{R}(t) = \frac{2}{\pi}\int_0^\infty \mathbf{B}_{pot}(\omega)\cos(\omega t)d\omega \tag{8.3}$$

which is a conversion from the frequency domain to the time domain through the Fourier transform.

Furthermore assuming that the hydrostatic forces can be modelled as a linearised restoring force and likewise that the mooring lines can be modelled as a linear spring yields

$$\begin{aligned} \mathbf{F}_{hs} &= -\mathbf{K}_{hs}\boldsymbol{\xi}(t) \\ \mathbf{F}_{moor} &= -\mathbf{K}_{moor}\boldsymbol{\xi}(t) \end{aligned} \tag{8.4}$$

where $\mathbf{K}_{hs} \in \mathbb{R}^{6x6}$ and $\mathbf{K}_{moor} \in \mathbb{R}^{6x6}$ is the hydrostatic stiffness and mooring line stiffness matrices respectively, while $\boldsymbol{\xi}$ is the displacement of the TLP in the $\{b\}$ frame relative to the $\{s\}$ frame expressed in the $\{s\}$ frame. Thereby the governing equation for the motion of the floating body in the time domain can be written as a linear vector integro-differential equation which is also known as Cummins' equation.

$$(\mathbf{M}_{RB} + \mathbf{A}(\infty))\ddot{\boldsymbol{\xi}}(t) + \int_0^t \mathbf{R}(t-\tau)\dot{\boldsymbol{\xi}}(\tau)d\tau + (\mathbf{K}_{moor} + \mathbf{K}_{hs})\boldsymbol{\xi} = \mathbf{F}_{wave}(t) \tag{8.5}$$

Using the kinematic relationships derived in [59] and assuming small angles it is possible to transform the time domain representation of Cummins' equation from the seakeeping frame $\{s\}$ to

the body frame $\{b\}$ by

$$\begin{aligned}
&\boldsymbol{\xi} = \delta\mathbf{n} \triangleq \mathbf{q} \\
&\dot{\boldsymbol{\xi}} = \delta\mathbf{v} \triangleq \dot{\mathbf{q}} + U(\mathbf{Lq} - \mathbf{e_1}) \\
&\ddot{\boldsymbol{\xi}} = \delta\dot{\mathbf{v}} \triangleq \ddot{\mathbf{q}} + U\mathbf{L}\dot{\mathbf{q}} \\
&\text{where} \\
&\mathbf{e_1} \triangleq \begin{bmatrix} 1 & 0 & \cdots & 0 \end{bmatrix}^T \text{and} \quad \mathbf{L} \triangleq \begin{bmatrix} 0 & 0 & 0 & 0 & 0 & 0 \\ 0 & 0 & 0 & 0 & 0 & 1 \\ 0 & 0 & 0 & 0 & -1 & 0 \\ 0 & 0 & 0 & 0 & 0 & 0 \\ 0 & 0 & 0 & 0 & 0 & 0 \\ 0 & 0 & 0 & 0 & 0 & 0 \end{bmatrix}
\end{aligned} \tag{8.6}$$

where $\delta\mathbf{n}$ and $\delta\mathbf{v}$ are used to indicate generalised perturbation position and velocity vectors, U indicates a forward speed of the TLP while $\mathbf{q} \in \mathbb{R}^6$ indicates the displacement vector of the TLP expressed in the body frame $\{b\}$. This representation is done in order to be consistent with the tower coordinate system. Inserting 8.6 into 8.5 yields

$$\begin{aligned}
&\big(\mathbf{M}_{RB} + \mathbf{A}(\infty)\big)\big(\ddot{\mathbf{q}}(t) + U(t)\mathbf{L}\dot{\mathbf{q}}(t)\big) + \int_0^t \mathbf{R}(t-\tau)\big(\dot{\mathbf{q}}(t) + U(t)(\mathbf{Lq}(t) - \mathbf{e_1})\big)(\tau)d\tau ... \\
&+ \big(\mathbf{K}_{moor} + \mathbf{K}_{hs}\big)\mathbf{q}(t) = \mathbf{F}_{wave}(t)
\end{aligned} \tag{8.7}$$

where the terms

$$\begin{aligned}
\mathbf{C}_A^* &= U\mathbf{A}(\infty)\mathbf{L} \\
\mathbf{C}_M^* &= U\mathbf{M}_{RB}\mathbf{L}
\end{aligned} \tag{8.8}$$

represent linear Coriolis, $\mathbf{C}_A^*$, and centripetal, $\mathbf{C}_M^*$, force coefficients due to a rotation of the $\{b\}$ frame about the frame $\{s\}$. This equation is however simplified significantly by assuming a station-keeping frame, that is $U = 0$. Furthermore the retardation function can be approximated by the state space model

$$\begin{aligned}
\dot{\mathbf{x}} &= \mathbf{A}_r\mathbf{x} + \mathbf{B}_r\mathbf{v} \\
\boldsymbol{\mu} &= \mathbf{C}_r\mathbf{x}
\end{aligned} \tag{8.9}$$

which will be explained in more detail in chapter 9.4.2. As Cummins' equation essentially is based on the potential theory, no viscous effects are present. However these viscous effects can be added directly into the equation by introducing the diagonal linear damping $\mathbf{B}_{lin,v}$ matrix $\in \mathbb{R}^{6x6}$ and the diagonal quadratic damping matrix $\mathbf{B}_{lin,v} \in \mathbb{R}^{6x6}$.

Thereby the governing equation in a $\{b\}$ frame context can be written as

$$\begin{aligned}&(\mathbf{M}_{RB}+\mathbf{A}(\infty))\,\ddot{\mathbf{q}}(t)-\int_0^z \mathbf{B}_{lin,v}\big(\mathbf{u}(t,0,0,z)-\dot{\mathbf{q}}(t,0,0,z)\big)dz-\\&\int_0^z \mathbf{B}_{quad,v}\Big(\big(\mathbf{u}(t,0,0,z)-\dot{\mathbf{q}}(t,0,0,z)\big)\Big|\mathbf{u}(t)-\dot{\mathbf{q}}(t,0,0,z)\Big|\Big)dz+\\&\boldsymbol{\mu}+(\mathbf{K}_{moor}+\mathbf{K}_{hs})\mathbf{q}(t)=\mathbf{F}_{wave}(t)\end{aligned} \tag{8.10}$$

where the relative velocity between the water particles and the TLP has been implemented in the terms regarding the viscous damping. $\mathbf{u}$ is the water particle velocity, which for simplicity only concerns the horisontal velocity when the response in surge, sway, roll, pitch and yaw are considered while when heave is considered the vertical velocity is used. An integration across the length of the TLP is here implemented as the TLP does not experience the same relative velocity across its entire length due to the water particle velocity decays exponentially as explained in section 7.1.
The energy carried by the propagating waves is introduced into the system by the wave excitation forces. These forces can be split into many different components, such as

Steady mean drift forces giving rise to an offset in the position of the TLP.

Slow frequency drift forces are predominantly oscillating with frequencies lower than the incident generated waves from the energy spectrum.

High frequency drift forces are predominantly oscillating with frequencies higher than the incident generated waves from the energy spectrum.

First order excitation forces are predominantly oscillating with the same frequencies as the incident waves generated from the energy spectrum.

This thesis will mainly focus on the first order excitation forces, which often also are the most significant regarding the dynamical response [60]. However it should be noted that both the steady mean drift force and the slow and high frequency drift forces can be very important, especially if considering the design and analysis of the mooring system [60]. For regular monochromatic waves the first order excitation force for an i DOF can be expressed as

$$F_{wave,i}=\left|\overline{F}_{wave,i}(\omega)\right|\eta_a\cos\big(\omega t+\varphi_i(\omega)\big) \tag{8.11}$$

where the terms $\overline{F}_{wave,i}(\omega)$ and $\varphi_i(\omega)$ represents a complex excitation force and a phase angle. The phase angle here represents the phase difference between the incident wave profile and the excitation force at the same reference point which is chosen as the centre of the TLP. From eq. 8.11 it can furthermore be seen that the excitation force is proportional to the wave amplitude η_a. If only considering a SDOF system the information regarding the phase angle is of no importance to the dynamics. However in MDOF systems the information regarding the phase angle is very important due to the difference in the phases between excitation forces of the different DOFs [60]. To model

the first order excitation forces for irregular waves, superposition of each N independent regular component is utilised

$$F_{wave,i}(t) = \sum_{n=1}^{N} \left| \overline{F}_{wave,i}(\omega_n) \right| \eta_{a,n} \cos\left(\omega_n t + \varphi_i(\omega_n) + \theta_n\right) \tag{8.12}$$

where the amplitudes $\eta_{a,n}$ of each frequency competent are defined from a given energy spectrum, e.g JONSWAP, while the phase angle of the surface elevation θ_n is randomly generated from a uniform distribution between 0 and 2π. N is ideally taken as $N \to \infty$, however in this thesis for practically reasons only taken to 8 Hz divided by the frequency step size, after which practically no energy is present in the energy spectrum. The step size is taken as 0.00025 Hz, whereby the signal will be repeated after approximately 70 minutes. The key advantage of writing the excitation force in this way is that it is possible to precalculate the entire force time series before simulating the TLP response, thereby speeding up the simulation itself. In fig. 8.2 a realisation of a given surface elevation and the force time series is seen.

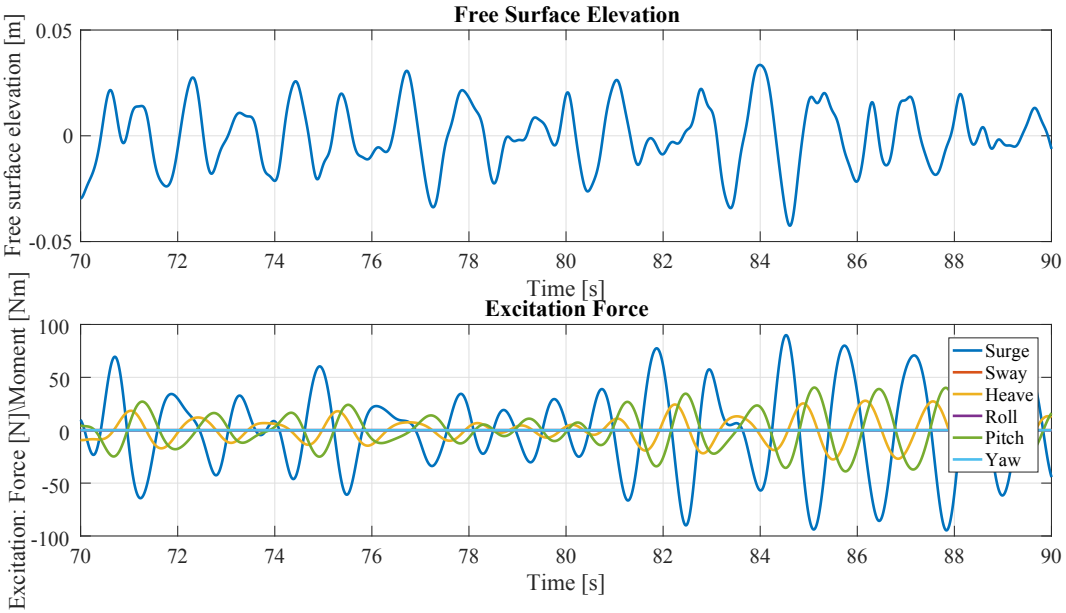

Figure 8.2: Surface elevation and resulting force time series.

The hydrodynamic coefficients $\mathbf{A}(\infty), \mathbf{A}(\omega), \mathbf{B}(\omega)$ and $\mathbf{R}(\omega)$ as well the frequency dependent excitation forces $\overline{\mathbf{F}}_{wave}(\omega)$ and phase angle $\boldsymbol{\varphi}(\omega)$ are usually computed by a hydrodynamic panel method program such as the commercial software WAMIT or as in this thesis in the free software NEMOH. The frequency dependent excitation forces are seen in fig. 8.3, while the other hydrodynamic coefficients is explained in the subsequent chapter.

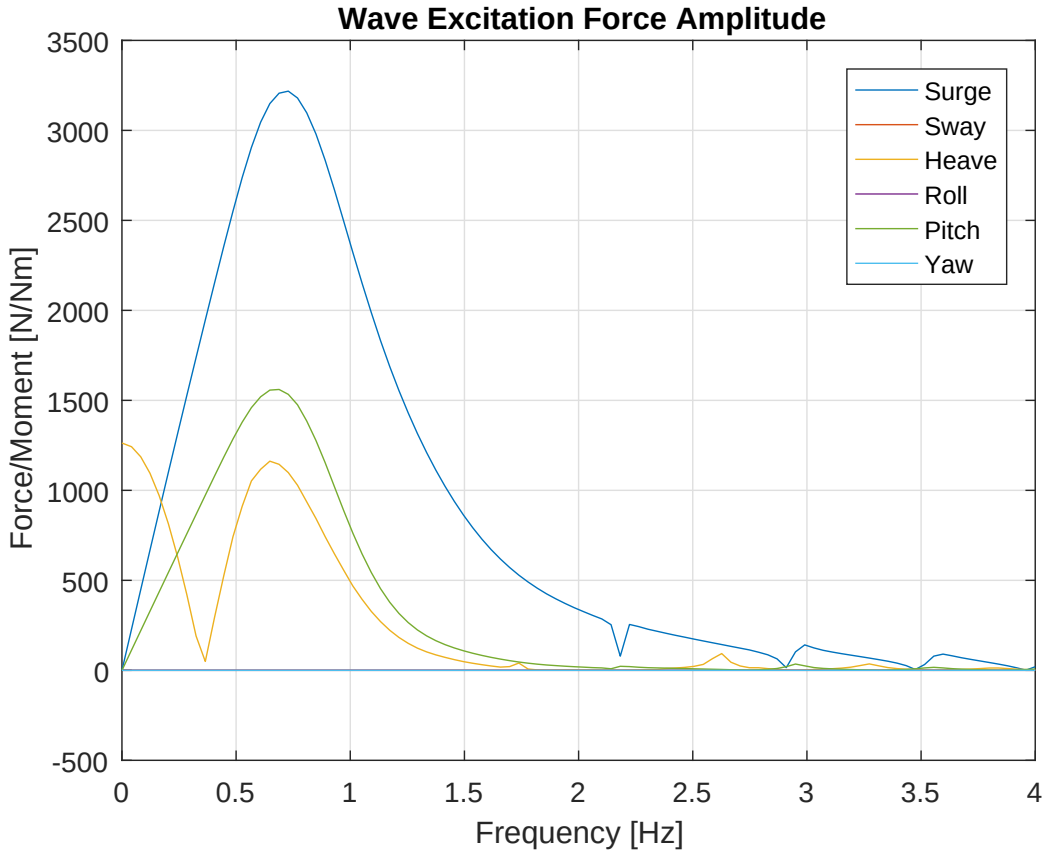

Figure 8.3: Visualisation of the hydrodynamic frequency dependent excitation forces.

[53] [54]

8.3 Frequency Domain Representation

Another way to view the dynamical equation is in the frequency domain. If the radiation forces are considered in the frequency domain they can be expressed as

$$\mathbf{F}_{rad}(j\omega) = -\mathbf{A}(\omega)\ddot{\mathbf{q}}(j\omega) - \mathbf{B}_{pot}(\omega)\dot{\mathbf{q}}(j\omega) = \omega^2\mathbf{A}(\omega)\mathbf{q}(j\omega) - j\omega\mathbf{B}_{pot}(\omega)\mathbf{q}(j\omega) \tag{8.13}$$

where the parameters $\mathbf{A}(\omega)$ and $\mathbf{B}_{pot}(\omega)$ are the frequency dependent added mass and potential damping, respectively. To account for the non-linear viscous damping a linearisation of this is needed. Denoting the total linear damping matrix as $\mathbf{B}_{total}(\omega) \in \mathbb{R}^{6\times6}$, which is the sum of the potential damping matrix and a linearisered equivalent viscous damping matrix $\mathbf{B}_{lin,eq}(\omega) \in \mathbb{R}^{6\times6}$ leads to

$$\mathbf{B}_{total}(\omega) = \mathbf{B}_{pot}(\omega) + \mathbf{B}_{lin,eq}(\omega) \tag{8.14}$$

where the linearised equivalent viscous damping matrix incorporates the linear and quadratic viscous damping in the frequency domain. This is needed to model the frequency response correctly.

Thereby the governing equation in the frequency domain is written as

$$\left(-\omega^2(\mathbf{M}_{RB}+\mathbf{A}(\omega))+j\omega\mathbf{B}_{total}(\omega)+\mathbf{K}\right)\mathbf{q}(j\omega)=\mathbf{F}_{wave}(j\omega) \tag{8.15}$$

It follows that this equation is only satisfied when the displacement **q**, derivatives of it and the excitation force are of a sinusoidal nature, that is there can be no transient motion or force. It furthermore follows that this equation only allows an oscillatory behaviour at a single frequency, however due to the linearity of the equation, it is possible to superimpose the various frequencies.

The response amplitude operator (RAO) is an expression often used to determine the likely behaviour of floating structures. The RAO is essentially a transfer function which can be used to determine the effect that a given sea state has upon the motion of the TLP. In this thesis only the absolute value of the RAO is considered as the phase between the the excitation and TLP motion is not taken into account

$$\mathbf{RAO}(\omega)=\left|\frac{\overline{\mathbf{F}}_{wave}}{-\omega^2\left(\mathbf{M}_{RB}+\mathbf{A}(\omega)\right)+j\omega\mathbf{B}_{total}(\omega)+\mathbf{K}}\right| \tag{8.16}$$

The RAO will later be compared with experiments, see section 10.5.
In [61] Ogilvie showed that the fundamental relationship between the frequency and time domain parameters of the added mass and potential damping could be expressed through the Fourier transform of the retardation function as

$$\begin{aligned}\mathbf{A}(\omega)-\mathbf{A}(\infty)&=-\lim_{t\to\infty}\frac{1}{\omega}\int_0^t\mathbf{R}(\tau)\sin(\omega\tau)d\tau\\ \mathbf{B}(\omega)&=\lim_{t\to\infty}\int_0^t\mathbf{R}(\tau)\cos(\omega\tau)d\tau\end{aligned} \tag{8.17}$$

From which it follows that the added mass tends towards the infinity added mass as the frequency tends towards infinity by the use of the Riemann-Lebesgue lemma saying that the Fourier transform of a Lebesque integral vanishes at infinity. Furthermore the conversion between the time and frequency domain retardation function is given as

$$\begin{aligned}\mathbf{R}(t)&=\frac{2}{\pi}\int_0^\infty\mathbf{B}(\omega)\cos(\omega t)d\omega\\ \mathbf{R}(j\omega)&=\int_0^\infty\mathbf{R}(t)\exp\left(-j\omega t\right)d\omega=\mathbf{B}(\omega)+j\omega(\mathbf{A}(\omega)-\mathbf{A}(\infty))\end{aligned} \tag{8.18}$$

such that the infinity added mass and the impulse response function can be found, when knowing the frequency dependent added mass and potential damping, by using Ogilvie's formula.

[53] [54]

Hydrodynamic Coefficients 9

This chapter starts by describing the method used in NEMOH to solve the potential flow problem, next a description of the development of the different hydrodynamic coefficient matrices are given. But first the transformation matrix used when transforming coefficients from $\{s\}$ to $\{b\}$ frame is described.
The natural frequency of the TLP is designed to be outside the frequency area of the waves such that only small displacements occur when influenced by the waves. Furthermore with a maximum horisontal displacement of approximately 3 cm and rotational displacement of 5° when the maximum thrust force is present, see previous work done by the authors [25], it is a fair assumption that the earth fixed, seakeaping fixed and body fixed coordinate system remain practically parallel at all times. For the hydrodynamic forces, the boundary element method (BEM) is applied to compute the frequency dependent added mass $\mathbf{A}^*(\omega)$, potential damping $\mathbf{B}^*(\omega)$ and the wave induced forces $\mathbf{F}^*_{wave}(\omega)$. These terms are all computed in the seakeeping reference frame $\{s\}$, where * denotes vectors and matrices in the $\{s\}$ frame. It is necessary to transform these matrices into the body fixed coordinate system by a transformation matrix. The transformation matrix, derived in [62], is based on the assumption that the oscillations of the $\{b\}$ frame with respect to the $\{s\}$ frame are small such that transformation matrix, $\mathbf{J}^*$, can be written as

$$\mathbf{J}^* = \begin{bmatrix} \mathbf{I}_{3x3} & \mathbf{S}^T\left(\mathbf{r}_s^b\right) \\ \mathbf{0}_{3x3} & \mathbf{I}_{3x3} \end{bmatrix} = \text{constant} \tag{9.1}$$

where $\mathbf{I}_{3x3}$ is the identity matrix, $\mathbf{0}_{3x3}$ is the zero matrix, while

$$\mathbf{S}\left(\mathbf{r}_s^b\right) = -\mathbf{S}^T\left(\mathbf{r}_s^b\right) = \begin{bmatrix} 0 & -z_s & y_s \\ z_s & 0 & -x_s \\ -y_s & x_s & 0 \end{bmatrix} \quad \text{and} \quad \mathbf{r}_g^b = \begin{bmatrix} x_s \\ y_s \\ z_s \end{bmatrix} \tag{9.2}$$

where x_s, y_s, z_s is the distance from the $\{s\}$ frame origin, o_s, to the origin of the body frame, o_b, for which it follows, due to the geometrical and mass symmetry, $x_s = y_s = 0$, while z_s is the distance from the SWL to the COG. Thereby the hydrodynamic forces, e.g. given the added mass matrix, can be transformed from the $\{s\}$ frame to the $\{b\}$ frame by the transformation

$$\mathbf{A}(\omega) = \mathbf{J}^{*T}\mathbf{A}^*(\omega)\mathbf{J}^* \tag{9.3}$$

[62]

9.1 Numerical Software

From a hydrodynamic perspective one of the challenges that a numerical model faces is the ability to incorporate arbitrary geometries. The necessity to account for the radiation and diffraction forces when these are in the same order of magnitude as the inertial forces, needs to be considered. This along with the recognition and incorporation of the frequency dependent forces in order to incorporate memory effects. Furthermore estimation of the mean and slow drift forces, current and wave-current interactions and other possible relevant phenomena such as slamming loads and vortex induced vibrations could be incorporated. Furthermore an estimation of the mooring line dynamics and their effect on the overall response should be clarified.

Wave induced loads can be determined by different numerical methods, such as BEM based on potential flow assumptions, Reynold's Average Navier Stokes (RANS) solving the transport equations for the mean flow, Large Eddy simulation (LES) solving the transport equation for resolvable eddie scales, or Direct Navier Stokes (DNS). The methods however compromise on fidelity, where DNS is the only numerical method which can resolve the problem completely, but has an impractical calculation time for most simulations. Due to the calculation time it is most common to use BEM to describe the wave induced effects, which can be done in both a linear frequency and time domain, as well as non-linear time domain. The fastest method is to calculate the BEM in the linear frequency domain in order to estimate the frequency dependent coefficients and frequency responses. One way to develop linear time-domain models is by implementing the linear frequency dependent coefficients into Cummins' equation, as explained in chapter 8.

[63]

9.1.1 Boundary Element Method

By transforming the integrals over the fluid domain to integrals over the boundaries of the fluid domain, the panel method or BEM can be applied to solve the 3D potential flow theory problem. The BEM divides the surface of the foundation and the surrounding water into discrete elements. A distribution of sources and sinks is defined for each element such that they fulfil the Laplace equation. Then the velocity potential needs to be identified by finding the strength of the distributions of the sources and sinks. Once the velocity potentials, and thus the velocities, can be found, the pressure can be computed by the use of Bernoulli's equation. By integrating the pressure over the surface of the hull of the TLP, the hydrodynamic forces are obtained. This approach is applied in different CAE tools with a suitable performance for offshore applications at zero forward speed in both frequency and time domain. NEMOH uses this approach and will be used for this thesis to compute the frequency dependent added mass, radiation damping and diffraction forces by solving the boundary value problem. However it should be noted that NEMOH is limited to compute first order wave loads. In order to define the fluid domain the TLP should be defined with respective panel sizes, however NEMOH is set to assume symmetry, so only half of the TLP is defined, as seen in fig. 9.1

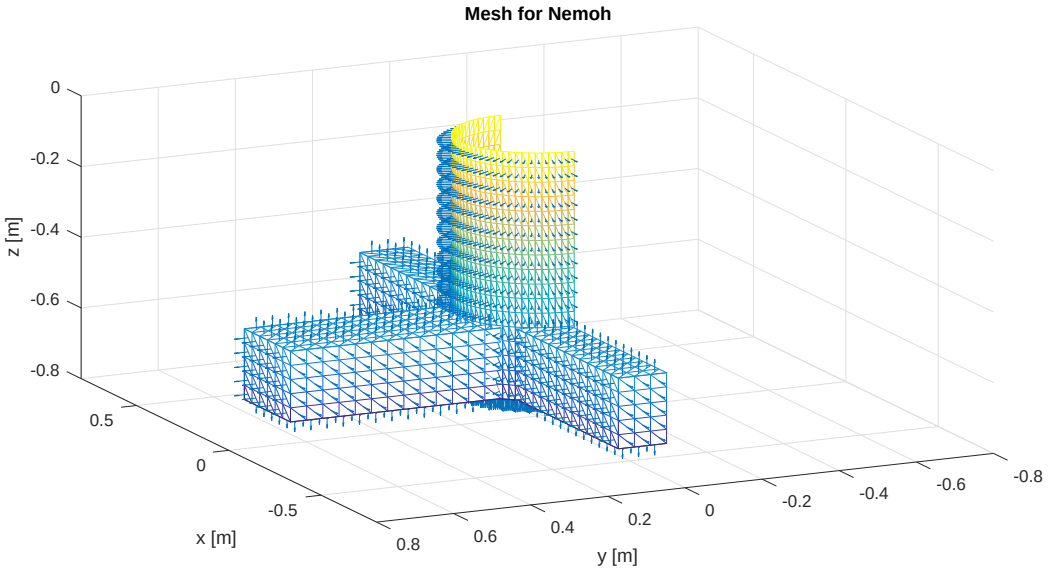

Figure 9.1: Mesh generated for NEMOH.

[64]

9.2 Inertia

The rigid body system inertia matrix with respect to the $\{b\}$ frame is written as

$$\mathbf{M}_{RB} = \begin{bmatrix} m_{tt} & 0 & 0 & 0 & 0 & 0 \\ 0 & m_{tt} & 0 & 0 & 0 & 0 \\ 0 & 0 & m_{tt} & 0 & 0 & 0 \\ 0 & 0 & 0 & I_x & -I_{xy} & -I_{xz} \\ 0 & 0 & 0 & -I_{xy} & I_y & -I_{yz} \\ 0 & 0 & 0 & -I_{xz} & -I_{yz} & I_z \end{bmatrix} \tag{9.4}$$

where m_{tt} is the total mass of the TLP and $\mathbf{I}_{3x3}$ is the mass moment of inertia matrix with respect to the COG. I_x, I_y and I_z are the mass moment of inertia around the x-axis, y-axis and z-axis, respectively, while I_{xy}, I_{xz}, I_{yz} etc. are the products of inertia about the planes xy, xz, yz and so forth. These mass moment of inertia are found by the use of Inventor.

In table 9.1 the coefficients used in the mass matrix are seen

Table 9.1: Mass properties of the TLP.

$m_{tt}[kg]$	$I_x\ [kgm^2]$	$I_y\ [kgm^2]$	$I_z\ [kgm^2]$	$I_{xy}\ [kgm^2]$	$I_{xz}\ [kgm^2]$	$I_{yz}\ [kgm^2]$
130.68	113.5	113.5	1.18	0.0011	0.025	-0.43

[53] [54]

9.3 Added Mass

The hydrodynamic added mass can be seen as a virtual mass which is added to the system because the body and the fluid cannot occupy the same space simultaneously. Therefore an accelerating or deaccelerating body will move some volume of the surrounding fluid as it moves through the space, this volume appears to be an added mass of the body. The added mass is usually significant, and in some cases even reaches the mass of the structure, and therefore it must not be omitted when analysing the dynamics of the TLP [53]. Traditionally added mass in dynamical analysis is determined according to some available analytical solutions. Such procedure for determining the added mass is well-known in the shipbuilding industry, however having the assumption of an infinite excitation frequency and simple well-known geometries. If more complex geometries and frequency dependent added mass are needed the solution tends towards the numerical methods of solving for the radiation velocity potential, ϕ_R, through Laplace equations subjected to appropriate BCs, which are the watertight condition (no flow within the structure) and the stationary condition at infinity, that is the velocity potential function vanish infinity far away from the structure [58]. The added mass can be found by considering the total total energy of the fluid around the TLP and it can be proven that the added mass only depends on the geometry of the structure and not the body velocities [58] [65].

Writing the full frequency dependent added mass matrix yields

$$\mathbf{A}(\omega) = \begin{bmatrix} A_{11}(\omega) & 0 & 0 & 0 & A_{15}(\omega) & 0 \\ 0 & A_{22}(\omega) & 0 & A_{24}(\omega) & 0 & 0 \\ 0 & 0 & A_{33}(\omega) & 0 & 0 & 0 \\ 0 & A_{42}(\omega) & 0 & A_{44}(\omega) & 0 & 0 \\ A_{51}(\omega) & 0 & 0 & 0 & A_{55}(\omega) & 0 \\ 0 & 0 & 0 & 0 & 0 & A_{66}(\omega) \end{bmatrix} \tag{9.5}$$

In fig. 9.2 the frequency dependent added mass can be seen, where the surge and sway response looks similar due to symmetry, likewise with the pitch and roll response.

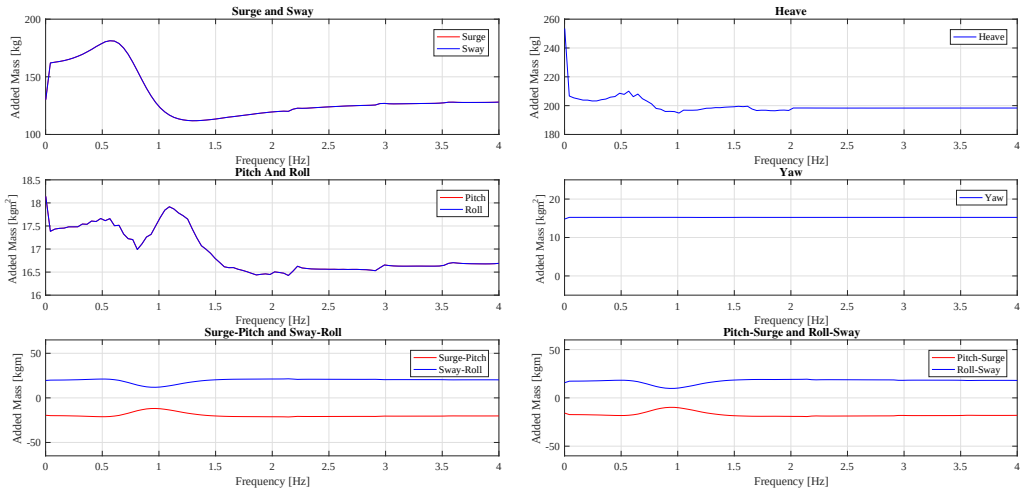

Figure 9.2: Frequency dependent added mass for the different DOFs.

By the use of Ogilvie's formula given in section 8.3, the added mass at infinity frequency and the impulse response function, which should be used in the time domain approach, can be found by

$$\mathbf{A}(\infty) = \mathbf{A}(\omega) + \lim_{t\to\infty} \frac{1}{\omega} \int_0^t \mathbf{R}(\tau)\sin(\omega\tau)d\tau$$
$$\text{where} \tag{9.6}$$
$$\mathbf{R}(t) = \frac{2}{\pi}\int_0^\infty \mathbf{B}_{pot}(\omega)\cos(\omega t)d\omega$$

where the integral time limit is taken from zero to the time where the impulse response has died out which is in order of seconds as will be explained in 9.4.1, thereby giving the following matrix

$$\mathbf{A}(\infty) = \begin{bmatrix} A_{11}(\infty) & 0 & 0 & 0 & A_{15}(\infty) & 0 \\ 0 & A_{22}(\infty) & 0 & A_{24}(\infty) & 0 & 0 \\ 0 & 0 & A_{33}(\infty) & 0 & 0 & 0 \\ 0 & A_{42}(\infty) & 0 & A_{44}(\infty) & 0 & 0 \\ A_{51}(\infty) & 0 & 0 & 0 & A_{55}(\infty) & 0 \\ 0 & 0 & 0 & 0 & 0 & A_{66}(\infty) \end{bmatrix} \tag{9.7}$$

In table 9.2 the calculated added mass at infinity frequency is seen

Table 9.2: Added mass table

$A_{11}(\infty)$ [kg]	$A_{22}(\infty)$ [kg]	$A_{33}(\infty)$ [kg]	$A_{44}(\infty)$ [kgm^2]	$A_{55}(\infty)$ [kgm^2]	$A_{66}(\infty)$ [kgm^2]
130.32	130.32	199.84	16.84	16.94	15.23
$A_{15}(\infty)$ [kgm]	$A_{24}(\infty)$ [kgm]	$A_{42}(\infty)$ [kgm]	$A_{51}(\infty)$ [kgm]		
-19.85	19.85	17.66	-17.66		

[53] [54]

9.4 Damping

The hydrodynamic damping of a floating body is often difficult to find without a hydrodynamic software, but an estimation can be achieved by looking at the most influencing damping phenomena and by using semi-empirical formulas.

Potential Damping sometimes also referred to as the radiation-induced damping which is due to the energy that the platform is using to make waves in the water while it is moving. This term is linear dependent on the frequency and is denoted by $\boldsymbol{B}_{pot}(\omega)$.

Viscous Damping is due to the drag force acting on the body, sometimes referred to as skin friction. The viscous damping can be split up in two different physical mechanisms.

Linear Viscous Damping is due to the laminar boundary layer and pressure variations, which are important when considering low frequency motions of the TLP. It is linearly frequency dependent and is denoted $\mathbf{B}_{lin}(\omega)$.

Quadratic Non-linear Damping The skin friction in the turbulent boundary layer is non-linear. This term is denoted by $\mathbf{B}_{quad}(\omega)$.

Wave Drift Damping are changes in the added resistance of the waves due to low frequency oscillating motion. The damping is derived from second order wave theory. The wave drift force will cause a drift of the body and thereby cause a mean offset of a moored TLP.

Damping Due to Vortex Shedding are vortex sheets generated due to boundary layer separation generating a wake behind the structure. This damping is therefore a consequence of form drag associated primarily with flow separation.

Lifting Force arises from two physical mechanisms.

The linear circulation of water around the TLP.
The non-linear effect also called cross flow drag, which acts as a momentum transfer from the body to the fluid

In this thesis only the potential damping and viscous damping will be incorporated in the simulation model as it is assumed these terms have the most significant impact on the response.

[53] [54]

9.4.1 Potential Damping

Likewise the added mass it can be proven that the potential damping is only dependent on the geometry of the TLP [58]. The overall frequency dependent potential damping matrix is seen in

$$\mathbf{B}_{pot}(\omega) = \begin{bmatrix} B_{11}(\omega) & 0 & 0 & 0 & B_{15}(\omega) & 0 \\ 0 & B_{22}(\omega) & 0 & B_{24}(\omega) & 0 & 0 \\ 0 & 0 & B_{33}(\omega) & 0 & 0 & 0 \\ 0 & B_{42}(\omega) & 0 & B_{44}(\omega) & 0 & 0 \\ B_{51}(\omega) & 0 & 0 & 0 & B_{55}(\omega) & 0 \\ 0 & 0 & 0 & 0 & 0 & B_{66}(\omega) \end{bmatrix} \tag{9.8}$$

The frequency dependent potential damping plots are seen in fig. 9.3. Due to symmetry surge and sway look similar, likewise with pitch and roll.

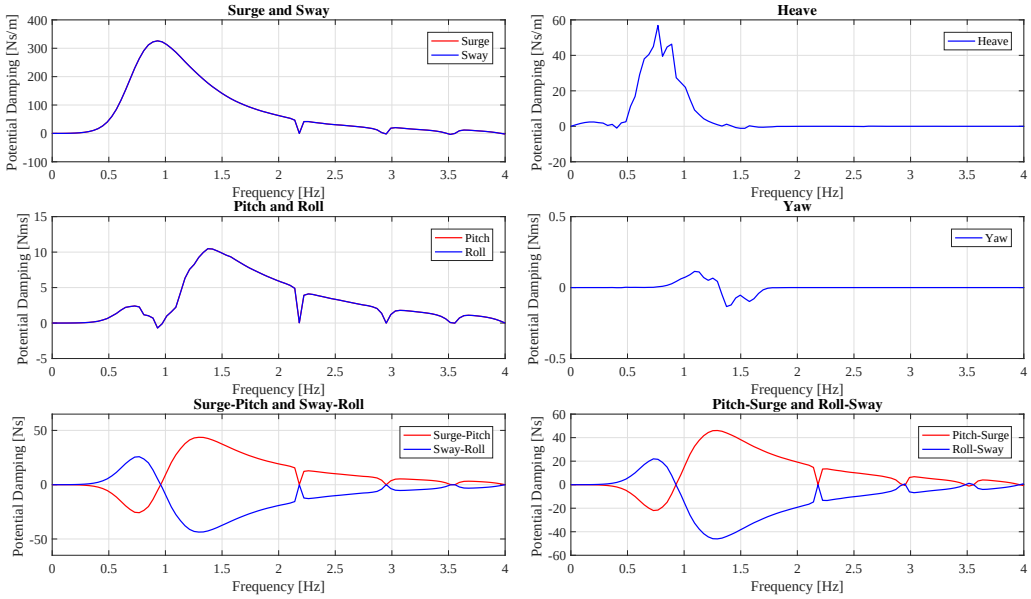

Figure 9.3: Frequency dependent potential damping for different DOFs.

The potential damping is needed to incorporate the memory effect. This effect can be incorporated in different ways e.g. either by solving the convolution integral at each time step or by replacing the convolution integral by a state space approximation making the computational calculation time shorter.

9.4.1.1 Impulse Response Function

Hydrodynamic coefficients based on hydrodynamic CAE tools for potential theory BEM are based on a non-parametric frequency response for a finite set of frequencies of interest. Therefore the retardation function is also based on a finite non-parametric model. To implement simulation models based on Cummins' equation a discrete approximation of the convolution integral is required, for which enough data of the past should be stored to evaluate the convolution at each step of the simulation.
The time domain of the impulse response function (IRF) could be written as

$$\mathbf{R}(t) = \frac{2}{\pi}\int_0^\infty \mathbf{B}_{pot}(\omega)\cos(\omega t)d\omega \tag{9.9}$$

Eq. 9.9 make use of non-parametric frequency responses for which the computational burden is large due to the need of a large memory.
One way to overcome this is truncating the integral such only a few seconds of memory t_{memory} are stored when calculating the radiation forces such as

$$\mathbf{F}_{rad}(t) = -\mathbf{A}(\infty) - \int_{t-t_{memory}}^{t} \mathbf{R}(t-\tau)\dot{\mathbf{q}}d\tau \tag{9.10}$$

The accuracy of this integral depends on the amount of time stored thus increasing the computational time. In fig. 9.4, the IRFs are seen, from which it can be seen that the signals

practically has died out in an order of seconds.

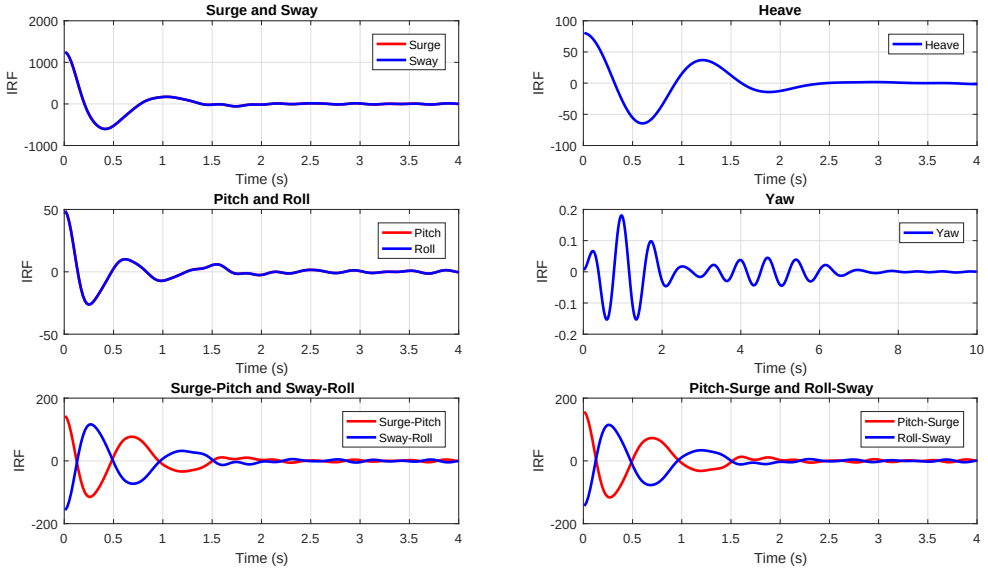

Figure 9.4: The impulse response function for different DOFs.

[53]

9.4.1.2 Convolution Replacement

As the convolution is a dynamic linear operation, it can be approximated by a linear state space model as explained by Perez and Fozzen in [66]

$$\boldsymbol{\mu} = \int_0^{\infty} \mathbf{R}(t-\tau)\dot{\boldsymbol{q}}(\tau)d\tau \Rightarrow \begin{cases} \dot{\mathbf{x}} = \mathbf{A}_c\mathbf{x} + \mathbf{B}_c\dot{\boldsymbol{q}} \\ \boldsymbol{\mu} = \mathbf{C}_c\mathbf{x} \end{cases} \tag{9.11}$$

where the matrices $\mathbf{A}_c$, $\mathbf{B}_c$ and $\mathbf{C}_c$ are time invariant and the number of components in the state vector $\mathbf{x}$ corresponds to the order of the approximated model. The advantage of this state space model is that at any time instant the values of the state $\mathbf{x}$ contains all the past information of the system, therefore it is only necessary to update the state vector of the model.

The state space can be reformulated as a rational transfer function giving

$$R_{ij}(s) = \frac{P_{ij}(s,\theta)}{Q_{ij}(s,\theta)} = \frac{b_m s^m + b_{m-1}s^{m-1} + \cdots + b_0}{s^n + q_{n-1}s^{n-1} + \cdots + q_0} \tag{9.12}$$

with the vector of parameters

$$\boldsymbol{\theta} = [b_m, \cdots, b_0, q_{n-1}, \cdots, q_0]^T \tag{9.13}$$

where the indexes i and j indicate the respective DOFs. The identification problem can be carried out either in the time domain or frequency domain. In [67] Perez and Fossen showed that the

frequency domain method in terms of accuracy and ease of implementation of the algorithms was superior. Furthermore the data from the hydrodynamic CAE tools are calculated in the frequency domain, so the frequency-domain identification is a natural approach to follow. If restricting s by only allowing it to take imaginary values, that is $s = j\omega$, the frequency response of the model is achieved. Then the parameters are determined such that this frequency response approximates the one in eq. 9.9

$$\hat{\boldsymbol{\theta}}_{ik} = \arg\min_{\boldsymbol{\theta}} \sum_{l} \omega_l \left| \mathbf{R}(j\omega_l) - \hat{\mathbf{R}}(j\omega_l, \boldsymbol{\theta}) \right|^2 \tag{9.14}$$

where ω_l are weightings that can be used to choose how important the fit is at different frequencies. This non-linear least squares problem can be solved by e.g. the Gauss-Newton algorithm.
The parametric model fitted to the retardation function should fulfil certain properties which are known beforehand by the exploration of the hydrodynamic properties of the radiation potential described by Fossen and Perez in [67]. These properties, their implications and the impact on the transfer function can be seen in table 9.3, while a more detailed explanation is found in the appendix A.2.

Table 9.3: Properties of the retardation function

Property	**Implication**	**Transfer Function**
$\lim_{\omega\to 0} \mathbf{R}(j\omega)$	There will be zeros at $s = 0$	$b_0 = 0$
$\lim_{\omega\to\infty} \mathbf{R}(j\omega)$	Strictly Proper	$\deg(Q_{ij}(\mathrm{s})) > \deg(P_{ij}(\mathrm{s}))$
$\lim_{t\to 0} \mathbf{R}(t)$	The relative degree is 1	$\deg(Q_{ij}(\mathrm{s}))$-$\deg(P_{ij}(\mathrm{s})) = 1$
$\lim_{t\to\infty} \mathbf{R}(t)$	The system is BIBO stable	$\mathrm{Re}(Q_{ij}(\mathrm{s}) = 0) < 0$
The mapping $\dot{\boldsymbol{q}} \to \boldsymbol{\mu}$ is passive	$\mathrm{diag}(\mathbf{R}(j\omega))$ is positive real	$\mathrm{Re}(\mathbf{R}(\mathrm{s})) > 0$

In fig. 9.5 the frequency response of the parametrised retardation function is seen in surge in a loglog frequency plot. These are calculated by using the MSS FDI toolbox developed by Perez and Fossen [68].

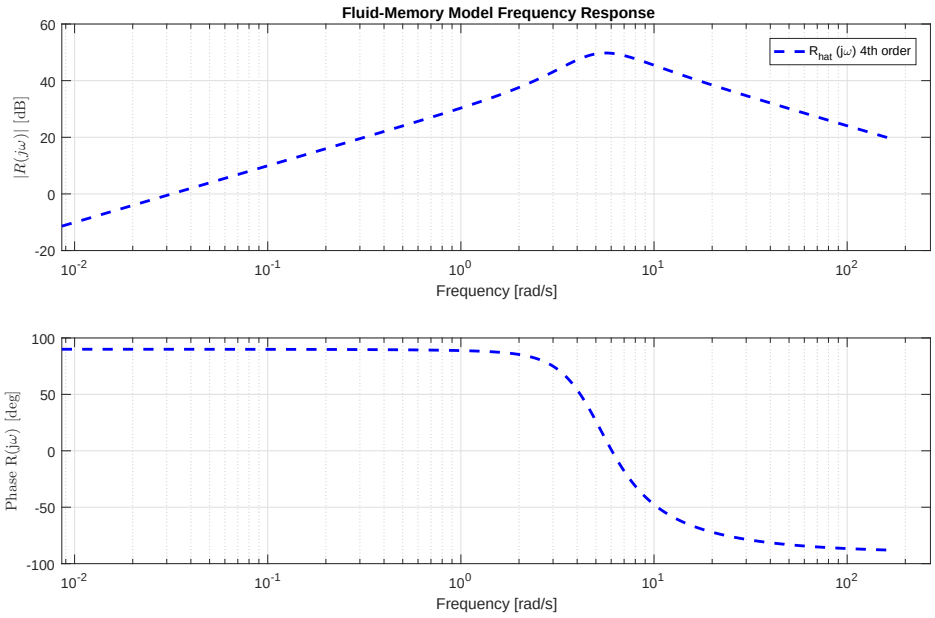

Figure 9.5: The parametrised frequency response of the retardation function in surge.

Similar responses are found for all DOFs such that a matrix of retardation transfer functions are achieved. In order to check the validity of the model the parametrised added mass and potential damping are found using eq. 9.15 and compared to the non-parametrised values of the added mass and potential damping, see fig. 9.6.

$$\begin{aligned} \mathbf{B}(\omega) &= \mathrm{Re}(\mathbf{R}(j\omega)) \\ \mathbf{A}(\omega) &= \mathrm{Im}(\omega^{-1}\mathbf{R}(j\omega)) + \mathbf{A}(\infty) \end{aligned} \tag{9.15}$$

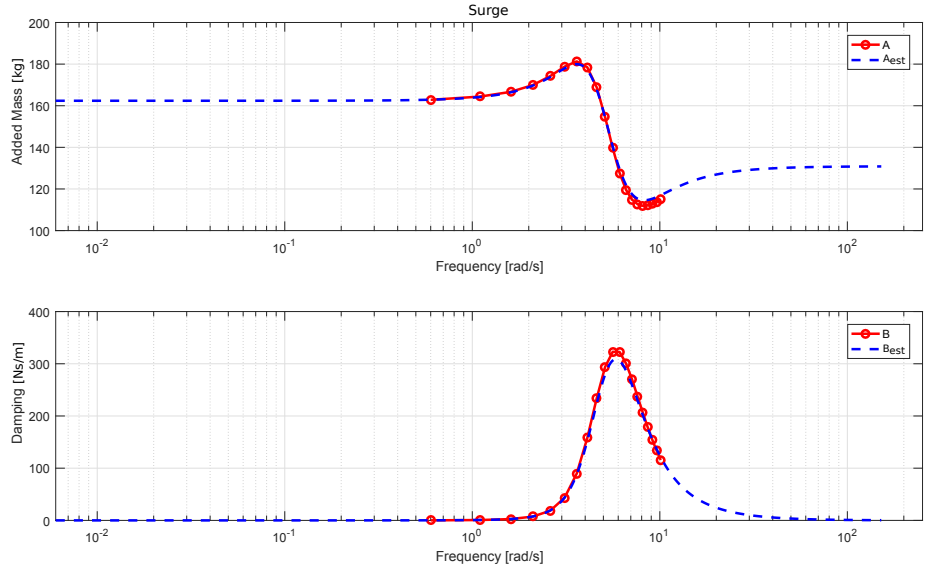

Figure 9.6: Comparison between the non-parametrised and the parametrised added mass and damping.

From here it can be seen that the fitted parametric values match the originally discrete values quite well. Another way of validating the parametrised model is to make an impulse to the state space system and compare them to fig. 9.4. This is not shown, however the impulse responses also match quite well.

9.4.2 Viscous Damping

The linear and quadratic viscous damping are primarily found experimentally, see chapter 10. However in these tests it is only possible to excite the system in surge, sway and yaw. Therefore a theoretical approach is sought to explain the viscous damping in heave, pitch and roll, while no coupled viscous damping will be implemented in this thesis. The theoretical approach will follow the same approach as FAST described in [69].
An often used, but somehow misapplied representation of the linear wave loads and non linear viscous forces are the Morison equation. In the Morison equation the TLP is split into a number of elements and in the relative form it can be expressed in the surge and sway motions as

$$\begin{aligned} dF_i(t,z) &= \frac{1}{2}C_d\rho D|\dot{u}_i(t,z)-\dot{q}_i(t,z)|(\dot{u}_i(t,z)-\dot{q}_i(t,z))dz+ \\ &(C_a+1)\rho\pi\frac{D^2}{4}\dot{u}_i(t,z)dz - C_a\rho\pi\frac{D^2}{4}\ddot{q}_i(t,z)dz \quad \text{for} \quad i=1,2 \end{aligned} \tag{9.16}$$

where the first term is the quadratic viscous drag force, which will be denoted $dF_{i,visc}$, while the two other terms include the Froude-Krylov and hydrodynamic mass forces. D is the diameter of the TLP cylinder, dz is the length of a differential strip of the TLP cylinder, C_a and C_d are normalised added mass and viscous drag coefficients. The drag coefficient, C_d, and the added mass coefficient, C_a, generally depend on Reynold's number, Keulegan-Carpenter's number and the relative roughness. It is implied that only the water particle velocity vector normal to the strip of the TLP cylinder is included. The drag coefficient is in this thesis set to 1.0 in accordance with DNV-RP-C205 [46] for cylindrical structures with Reynold's number above 10E5. Morison's equation assumes that the forces on the structure occur due to the oscillating waves, viscous effects and pressure effects. Furthermore a slender structure is assumed, implying that the diameter of the TLP column is small relative to the wave length, λ, such that the cylinder appears transparent to the waves. This implies that no wave diffraction occurs and is defined by the following condition

$$\frac{D}{\lambda} < 0.2 \tag{9.17}$$

which when comparing to the wavelength range from 0.19 to 3.9 m is a hard requirement to meet at all times in this test setup, therefore the Morison equation should be used with care. Using a similar approach as eq. 9.16 the viscous damping in roll and pitch can be defined, while the heave viscous damping is set 0 as Morison equation is only valid for bottom mounted cylinders. Thereby the Morison equation in heave, roll and pitch is written as

$$dF_{i,visc}(t,z) = \begin{cases} 0 & \text{for} \quad i=3 \\ -dF_{2,visc}(t,z)z & \text{for} \quad i=4 \\ dF_{1,visc}(t,z)z & \text{for} \quad i=5 \end{cases} \tag{9.18}$$

9.5 Stiffness

In this section the stiffness of the structure will be determined. For a TLP structure the main part of the stiffness is due to the taut mooring system, however there is also a small contribution from the hydrostatic stiffness. The combined system stiffness matrix is written as

$$\mathbf{K}_{tot} = \mathbf{C} + \mathbf{K} \tag{9.19}$$

where $\mathbf{K}_{tot}$ is a matrix for the total system stiffness. $\mathbf{C}$ is the hydrostatic stiffness matrix and $\mathbf{K}$ is the mooring system stiffness matrix, these stiffness matrices will be described in more detail below.

9.5.1 Hydrostatic Stiffness

The hydrostatic stiffness arises from the hydrostatic restoring forces, which are the forces arising when the COB of the submerged part of the structure changes due to either a translational or a rotational motion.

If considering the platform as a rigid body, assuming that the COG and COB are located at the centre line of the platform and the hydrostatic water plane moments act as torsional springs and the heave restoring is a translational spring, the elements of the hydrostatic matrix can be determined by analysing what happens if an individual displacement occurs in each DOF. The hydrostatic stiffness only depends on the water line geometry, the overall centre of buoyancy z_b and the centre of gravity z_g and only has an impact in the heave, roll and pitch directions such that

$$\begin{aligned} C_{33} &= A_{wp}\rho g \\ C_{44} &= I_{Axx}\rho g + g\left(V_{sub}\rho z_b - m_{tt} z_g\right) \\ C_{55} &= I_{Ayy}\rho g + g\left(V_{sub}\rho z_b - m_{tt} z_g\right) \end{aligned} \tag{9.20}$$

where A_{wp} is the water plane area, V_{sub} is the submerged volume of the TLP, I_{Axx} and I_{Ayy} are the second moment of area of the water plane area about the surge-axis and sway-axis, respectively. The water plane area is defined as the horizontal plane which passes through a structure on a level with the waterline, so in this case the water plane area equals the area of the cylinder. z_b is the distance from the SWL to the centre of buoyancy, while z_g is the distance from the SWL to the centre of gravity. The hydrostatic stiffness matrix is given as

$$\mathbf{C} = \begin{bmatrix} 0 & 0 & 0 & 0 & 0 & 0 \\ 0 & 0 & 0 & 0 & 0 & 0 \\ 0 & 0 & C_{33} & 0 & 0 & 0 \\ 0 & 0 & 0 & C_{44} & 0 & 0 \\ 0 & 0 & 0 & 0 & C_{55} & 0 \\ 0 & 0 & 0 & 0 & 0 & 0 \end{bmatrix} \tag{9.21}$$

In table 9.4 the coefficients used in the hydrostatic stiffness matrix are seen

Table 9.4: Hydrostatic properties of the TLP

A_{wp} $[m^2]$	I_{Axx} $[m^4]$	I_{Ayy} $[m^4]$	V_{sub} $[m^3]$	z_b $[m]$	z_g $[m]$
0.13	0.0013	0.0013	0.19	0.48	0.15

In table 9.4 it can be seen that the centre of buoyancy is placed below the centre of gravity making the system itself unstable, however the stability is achieved by the taught mooring lines. In table 9.5 the analytical calculated hydrostatic stiffness coefficients are seen.

Table 9.5: Hydrostatic stiffness coefficients table

C_{33} $[N/m]$	C_{44} $[Nm]$	C_{55} $[Nm]$
1260	730	730

9.5.2 Mooring Stiffness

The mooring line tension is an important parameter, as it is crucial to the stability of the TLP. The tension in the mooring lines arise from the excess buoyancy in the structure of the TLP. Thus the TLP is designed such that the buoyancy force is greater than the total weight of the structure. The mooring system provides stiffness which is present in all DOFs and can be found from a force/moment equilibrium, which is based on the theory of [70] and [71].

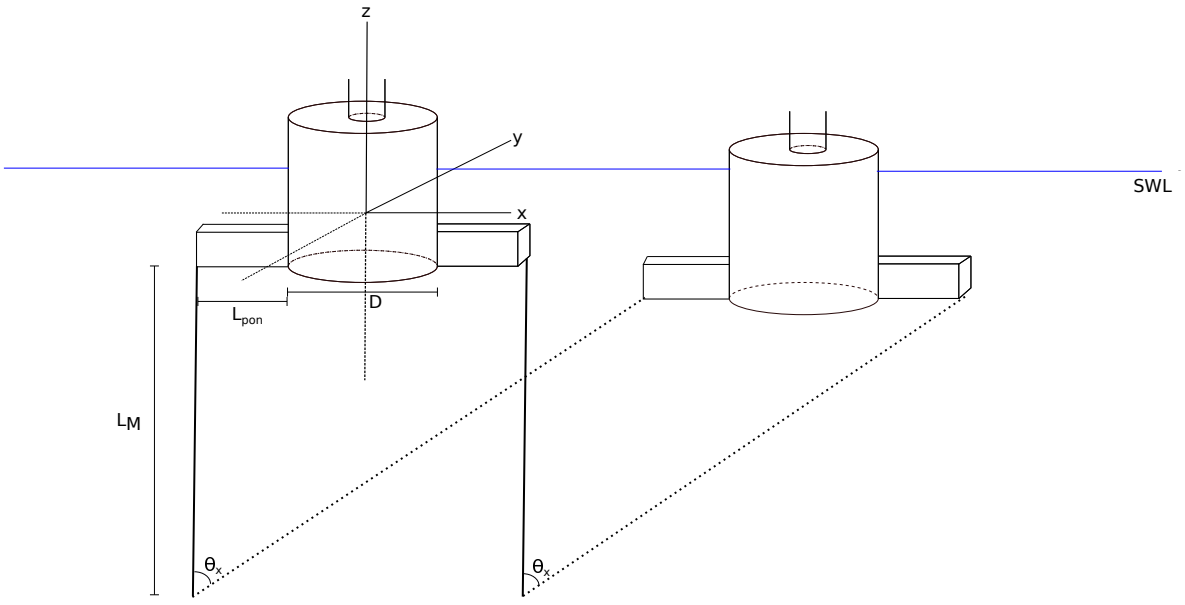

Figure 9.7: Visualisation of the TLP under influence of an arbitrary displacement in surge.

The mooring liens are well taut so no bending or slack of the lines occur. Therefore the axial motion of the mooring line can only be by a structural deformation of the mooring line. Thereby the axial stiffness of the mooring line an be described as a spring, while the horizontal and rotational directions are found considering the summation of the forces/moments when giving the TLP an

arbitrary displacement in the respective DOF. The mooring stiffness matrix is given as

$$\mathbf{K}_{moor} = \begin{bmatrix} K_{11} & 0 & 0 & 0 & K_{15} & 0 \\ 0 & K_{22} & 0 & K_{24} & 0 & 0 \\ 0 & 0 & K_{33} & 0 & 0 & 0 \\ 0 & K_{42} & 0 & K_{44} & 0 & 0 \\ K_{51} & 0 & 0 & 0 & K_{55} & 0 \\ 0 & 0 & 0 & 0 & 0 & K_{66} \end{bmatrix} \tag{9.22}$$

The first column of the mooring stiffness matrix is derived by giving the TLP an arbitrary displacement in the surge direction such that the summation of forces yields

$$K_{11} = \sum_{j=1}^{n_t} (F_T + \Delta F_T) \frac{\sin(\theta_x)}{x} \tag{9.23}$$

where n_t is the number of mooring lines, F_T is the pretension in the mooring line found by a force balance between the gravity and buoyancy, see eq. 9.24. ΔF_T corresponds to an increase in the tension in each cable for the x-displacement, while θ_x is the angle of inclination of the mooring lines with respect to the vertical positioned mooring lines, occurring when a displacement in surge is present. The force balance between gravity and buoyancy is given as

$$F_T = V_{Sub}\rho g - m_{tt} g \tag{9.24}$$

Assuming small displacements, angles and increases in tension, the non-linearity in eq. 9.23 disappears such that the stiffness can be treated as a non-varying constant.

$$K_{11} = \sum_{j=1}^{n_t} \frac{F_T}{L_M} \tag{9.25}$$

where L_M is the length of the unstretched mooring lines. It has been used that for small angles

$$\sin(\theta_x) \approx \tan(\theta_x) = \frac{x}{L_M} \Rightarrow \frac{\sin(\theta_x)}{x} \approx \frac{1}{L_M} \tag{9.26}$$

The summation of moments about the y-axis yields

$$K_{51} = -\sum_{j=1}^{n_t} (F_T + \Delta F_T) \frac{\sin(\theta_x)}{x} z_{gbot} \approx -z_{gbot} K_{11} \tag{9.27}$$

where z_{gbot} is the distance from centre of gravity to the bottom of the TLP assuming that the centre of gravity is the point of rotation.
The coefficients in the second column are found using similar considerations which due to symmetry

of the TLP are

$$\begin{aligned} K_{22} &= K_{11} \\ K_{42} &= -K_{51} \end{aligned} \tag{9.28}$$

The third column of the matrix is found giving the TLP an arbitrary displacement in the z-direction (heave) and considering the mooring lines as linear springs such that

$$K_{33} = \sum_{j=1}^{n_t} \frac{E_M A_M}{L_M} \tag{9.29}$$

where E_M is Young's modulus, found in experiment 10.1, and A_M is the cross sectional area of the mooring lines.
The coefficients in the fourth column of the mooring stiffness are found by giving the structure an arbitrary rotation θ_4 about the surge axis and summing up the moments and assuming small displacements and angles

$$\begin{aligned} K_{44} &= \cos^2(\theta_j)\left(F_T z_g \frac{\sin(\theta_4)}{\theta_4} + \frac{E_M A_M}{L_M}\left(\frac{D}{2} + l_p\right)^2 \cos(\theta_4)\right) \\ &\approx F_T z_g + \frac{E_M A_M}{L_M}\left(\frac{D}{2} + l_p\right)^2 \end{aligned} \tag{9.30}$$

where θ_j corresponds to the angular position of the pontoons, D is the diameter of the cylinder and l_p is the length of the pontoons. Furthermore due to symmetry

$$K_{24} = K_{42} \tag{9.31}$$

Similar consideration can be done for the fifth column such that

$$\begin{aligned} K_{55} &= K_{44} \\ K_{15} &= K_{51} \end{aligned} \tag{9.32}$$

At last the sixth column can be found by rotating the TLP about the z-axis such that the sum of moments about the z-axis yields and again assuming small displacements and angles

$$\begin{aligned} K_{66} &= \sum_{j=1}^{n_t} \left(\frac{F_T + \Delta F_T}{\sqrt{L_M^2 + \theta_6\left(2\left(\frac{D}{2} + l_p\right)^2\right)}}\right)\left(2\left(\frac{D}{2} + l_p\right)\right)^2 \\ &\approx \sum_{j=1}^{n_t} \frac{F_T}{L_M}\left(2\left(\frac{D}{2} + l_p\right)\right)^2 \end{aligned} \tag{9.33}$$

In table 9.6 the coefficients used in the hydrostatic stiffness matrix are seen

Table 9.6: Mooring lines properties.

L_M [m]	A_M[m^2]	E_M [GPa]	θ_j [°]	D [m]	l_p [m]
1.04	7.85e-07	63.9	90	0.4	0.5

In table 9.7 the analytical calculated mooring stiffness is seen

Table 9.7: Mooring lines stiffness.

k_{11} [N/m]	k_{22} [N/m]	k_{33} [N/m]	k_{44} [Nm]	k_{55} [Nm]	k_{66} [Nm]
550	550	182500	47350	47350	290
k_{15} [N]	k_{24} [N]	k_{42} [N]	k_{51} [N]		
-80	80	80	-80		

From which it can be seen that the TLP is stiff in heave, pitch and roll compared to surge, sway and yaw.

9.6 Natural Frequencies

The hydrodynamic coefficients can be used to give an estimate of the natural frequencies of the TLP in each DOF. The rigid body natural frequencies can be calculated by

$$f_{n,i} = \frac{1}{2\pi}\sqrt{\frac{K_{M,ii} + C_{ii}}{M_{ii} + A_{ii}(\infty)}} \tag{9.34}$$

The natural frequencies in each DOF is listed in table 9.8

Table 9.8: Natural frequencies of the TLP

f_1[Hz]	f_2 [Hz]	f_3 [Hz]	f_4 [Hz]	f_5 [Hz]	f_6 [Hz]
0.23	0.23	3.75	3.07	3.07	0.52

From which it can be seen that the natural frequencies in surge, sway and yaw are in the lower frequency end, while heave, pitch and roll are in the higher end. Furthermore it can be seen that surge and sway will lie to the left of the JONSWAP spectrum given in fig. 7.9, while heave, pitch and roll are to the right of the JONSWAP spectrum. On the other hand yaw is inside the JONSWAP spectrum. However as no wave excitation forces are present in yaw in this thesis the waves will not excite the TLP in this DOF. The natural frequencies of the TLP will be used later when plotting the Campbell diagram, see section 34.1.

9.7 Hydrodynamic Simulation

In fig. 9.8 a graphical visualisation of the hydrodynamic simulation is seen. At first the platform geometry is defined which is used to calculate the frequency dependent first order wave excitation forces, frequency dependent potential damping and frequency dependent added mass through the software NEMOH. Furthermore the platform geometry is needed in order to calculate the buoyancy of the TLP which is needed to calculate the hydrostatic stiffness and mooring line stiffness. In the

calculation of the mooring line stiffness the mooring line properties are furthermore needed. The infinity added mass in the time domain is calculated by using Ogilvie's formula, see chapter 8. The potential damping is needed in order to incorporate the memory effect which is done either through a convolution integral, see eq. 9.9, or a state space realisation, see eq. 9.11. The first order wave excitation forces are together with precalculated wave numbers, a random phase generator, and a predefined surface elevation spectrum used to generate the incident wave excitation forces in the time domain, see eq. 8.11 along with the incident wave kinematics, see eq. 7.28. The surface elevation can be generated in different ways, either by a predefined spectrum or by loading a surface elevation time series. If loading a time series, the MATLAB code calculates a spectrum and generates a new surface elevation time series, which is statistically equal to the originally one. The relative velocity between the incident wave kinematics and the TLP kinematics, which are found when solving the governing equation, see eq. 8.10 are used to calculate the linear and quadratic viscous drag damping.

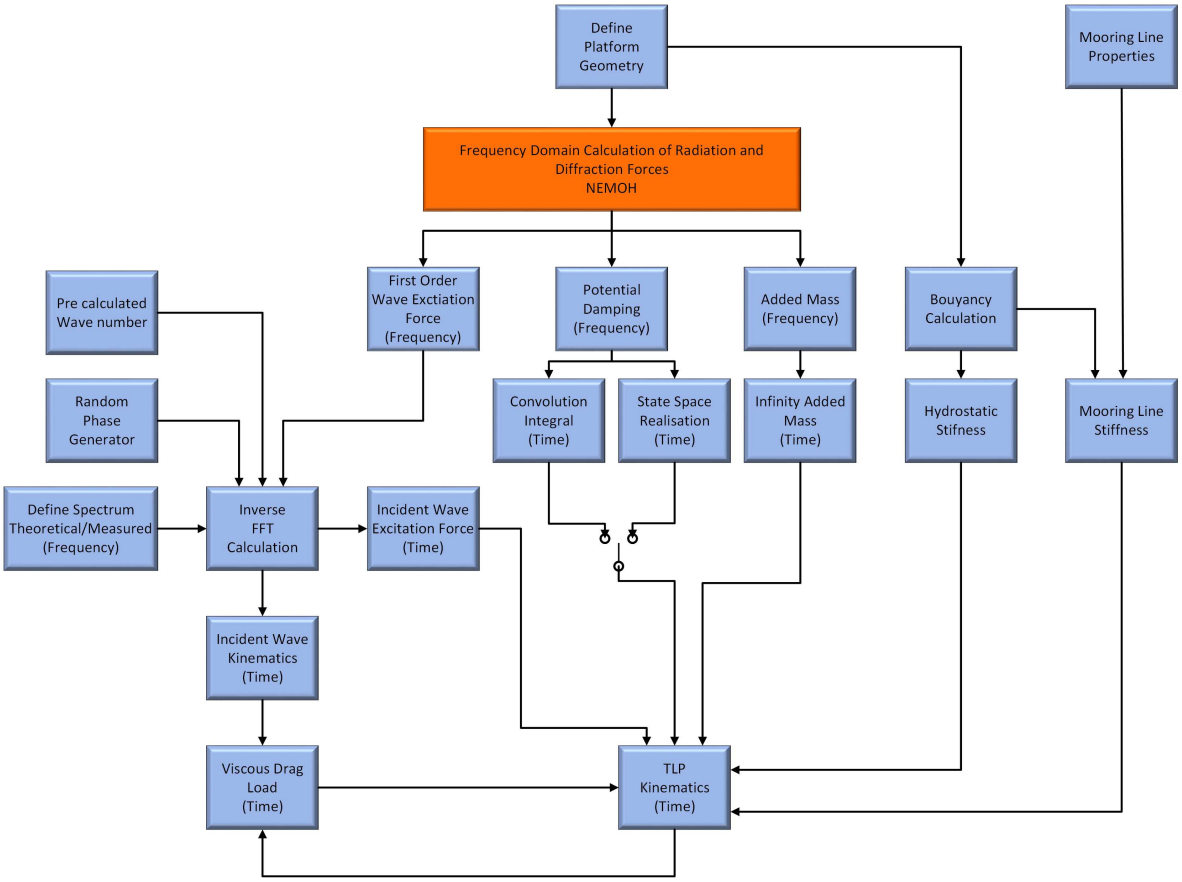

Figure 9.8: Flow diagram of the hydrodynamic simulation.

Test and Validation 10

In this chapter different tests are made in order to validate the analytically found parameters and the hydrodynamic simulation. The tests include finding the elasticity of the mooring lines by using a force calibration machine, finding the mooring stiffness by applying a force to the TLP and free decay of the TLP in order to investigate the first natural frequency and the damping. Furthermore waves are applied to the TLP for validating the hydrodynamic simulation. Both regular waves and a spectrum of irregular waves are applied and the responses are investigated.
It should be noted that a rigid mass is mounted on the TLP in all tests, this is for simulating the mass of the tower and the nacelle, but without taking the coupling into account.

10.1 Elasticity of Mooring Lines

The mooring lines were tested to find the maximum breaking load and Young's modulus. This was done using a force calibration machine where the mooring lines was attached in both ends and the machine pulls it apart while measuring the applied force and elongation, see appendix A.3. When the breaking load was reached, the mooring line broke. From this Young's modulus can be found in the linear region using

$$\sigma = E_M \varepsilon \tag{10.1}$$

where σ is the stress applied to the mooring line, E_M is Young's modulus of the mooring line and ε is the elongation of the mooring line. The test result is seen in fig. 10.1.

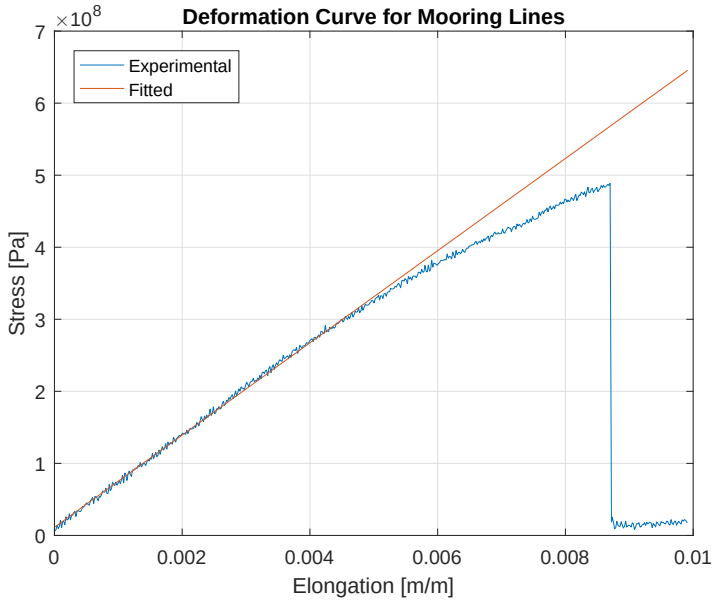

Figure 10.1: The pulling test of the mooring lines.

In the figure it is seen that the graph is linear in the beginning, which is where the red line is fitted to. Thus Young's modulus is found from the slope of the fit to be 63.9 GPa, which is 10.9 % higher than the one given in table 4.2. Furthermore the maximum breaking load was found to be 490 N.

10.2 Mooring Stiffness

A series of tests were made, where the TLP where pulled in the surge direction, while the pulling force was measured using a newtonmeter. This in order to experimentally find the mooring line stiffness in surge. The displacements of the TLP was then measured using the camera system OptiTrack. In these tests the flexibility of the tower and topmass are not taken into account, but the weight of them are. This is done using a rigid mass placed on top of the TLP, as it is only the stiffness of the TLP and mooring lines which are of interest. The measured datapoints of the tests are seen as the blue crosses in fig. 10.2.

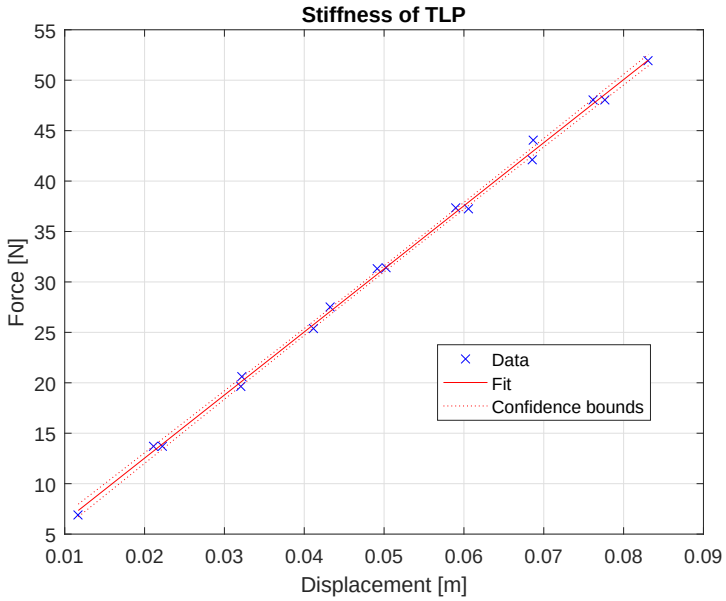

Figure 10.2: Displacement of the TLP, when force is applied.

The red line is a linear regression fitted with least squares, while the red dotted lines are the 95 % confidence interval of the regression line. The slope of the lines are the stiffness and is found to be 625.4 N/m, with a 95% confidence interval ranging from 611.0 N/m to 639.8 N/m. This estimate is approximately 13% higher than the analytically estimated stiffness, see table 9.7. Due to symmetry the mooring line stiffness in sway is assumed equal. It is not practically possible to excite the TLP in other directions, so the other DOFs are not validated.

10.3 Free Decay

As mentioned in section 9.4 the linear and quadratic damping is sought found experimentally in the surge and yaw direction as these are the only directions possible to excite well enough to give reasonable data. It is assumed that the damping in surge and sway are identical due to symmetry. To decouple the flexible tower dynamics from the TLP dynamics, the nacelle and tower are replaced with a rigid body having an equivalent mass of the replaced tower and nacelle.

10.3.1 Theory

Assuming that the TLP can be considered as a simple mass-spring-damper system neglecting the potential damping and approximating the linear and quadratic viscous damping as a linear equivalent damping term, B_e , the equation of motion of a single DOF with no external force applied can be written as

$$(M_{ii} + A_{ii}(\infty))\,\ddot{q}_i(t) + B_{e,ii}\dot{q}_i(t) + k_{total,ii}\,q_i(t) = 0 \quad \text{for} \quad i = 1,2,...6 \tag{10.2}$$

Different solutions for this differential equation exist, depending on the damping ratio of the given system. For most of the physical systems the damping is undercritical [72]. Therefore only the solution for undercritically damped systems will be considered, and thus the solution will be

$$q_i(t) = \exp(-\zeta_i\omega_{0,i}\,t)\left(q_{0,i}\cos(\omega_{d,i}\,t) + \frac{\dot{q}_{0,i} + \zeta_i\omega_{0_i}\,q_{0,i}}{\omega_{d,i}}\sin(\omega_{d,i}\,t)\right) \quad \text{for} \quad i = 1,2...6 \tag{10.3}$$

Here ζ is the damping ratio, ω_0 is the undamped natural frequency, while ω_d is the damped natural frequency . q_0 is the initial displacement of the TLP, and $\dot{q}_0$ is the initial velocity.

The damping ratio is a relationship between the equivalent damping and the critical damping B_{crit} given as

$$\zeta_i = \frac{B_{e,ii}}{B_{crit,ii}} = \frac{B_{e,ii}}{2\,(M_{ii} + A_{ii}(\infty))\,\omega_{o,i}} \tag{10.4}$$

while the damped natural frequency is defined as

$$\omega_{d,i} = \omega_{0,i}\sqrt{1-\zeta_i^2} \tag{10.5}$$

The damped natural frequency of the TLP, is the frequency of the oscillations, when the TLP is displaced and released and no other external forces are applied.
When measuring the displacement of the TLP in time, it will show that the TLP oscillates but the amplitudes of the motion decrease as time passes. An exponential fit can be applied to the top side of this graph, for which the exponential fit is given as

$$a_i(t) = \bar{A}_i\exp(-\zeta_i\omega_{0,i}\,t) \tag{10.6}$$

where $\bar{A}$ is the amplitude of the motion of the TLP and can be found as

$$\bar{A}_i = \sqrt{q_{0,i}^2 + \left(\frac{\dot{q}_{0,i} + q_{0,i}\zeta_i\omega_{0,i}}{\omega_{d,i}}\right)^2} \tag{10.7}$$

To find the damping ratio, two peak values can be compared. The peaks should fulfil the criteria $a_{m,i} > a_{m+1,i}$, thus meaning there is a positive damping in the system. The ratio between the two

amplitudes reveals the damping ratio, but first to simplify things it is possible to write the time corresponding to the latter amplitude in the following way

$$t_{n+1,i} = t_{1,i} + \frac{2n\pi}{\omega_{d,i}} \tag{10.8}$$

where n is the number of cycles between the peaks. The ratio of the displacement amplitudes can thus be found as

$$\frac{a_{1,i}}{a_{1+n,i}} = \frac{A_i \exp(-\zeta_i \omega_{0,i} t_{1,i})}{A_i \exp\left(-\zeta_i \omega_{0,i} \left(t_{1,i} + \frac{2n\pi}{\omega_{d,i}}\right)\right)} = \exp\left(\frac{2n\pi\zeta_i}{\sqrt{1-\zeta_i^2}}\right) \tag{10.9}$$

By isolating the damping ratio, an experimental way of estimating the damping ratio is found

$$\zeta_i = \frac{\ln\left(\frac{a_{n,i}}{a_{i+n,i}}\right)}{\sqrt{4\pi^2 + \ln\left(\frac{a_{n,i}}{a_{n+1,i}}\right)^2}} \tag{10.10}$$

Due to the quadratic viscous damping the damping ratio cannot be considered constant. In fact the damping ratio will increase with increasing amplitudes. If assuming small displacements it can be shown through energy considerations of the damping force, see [54], that the linear equivalent damping can be explained as

$$B_{e,(ii)} = B_{lin,(ii)} + \frac{8}{3\pi} B_{quad,(ii)} \omega_{0,i} q_i = 2(M_{ii} + A_{ii}(\infty))\omega_{0,i}\zeta_i \tag{10.11}$$

from which it can be seen that the linear damping will be the intersect of the y-axis while the quadratic damping will be the slope of the curve when plotting the equivalent damping as function of the amplitude of the TLP free decay response.

10.3.2 Results

In fig. 10.3 the experimental data of the free decay in surge and yaw are plotted along with the linear regression line and the 95% confidence intervals. The TLP response is measured with the camera system OptiTrack. The data are collected by ten individual batches in both DOFs, while the regression line is fitted by linear least squares to fit all of the data collected from the individual batches.

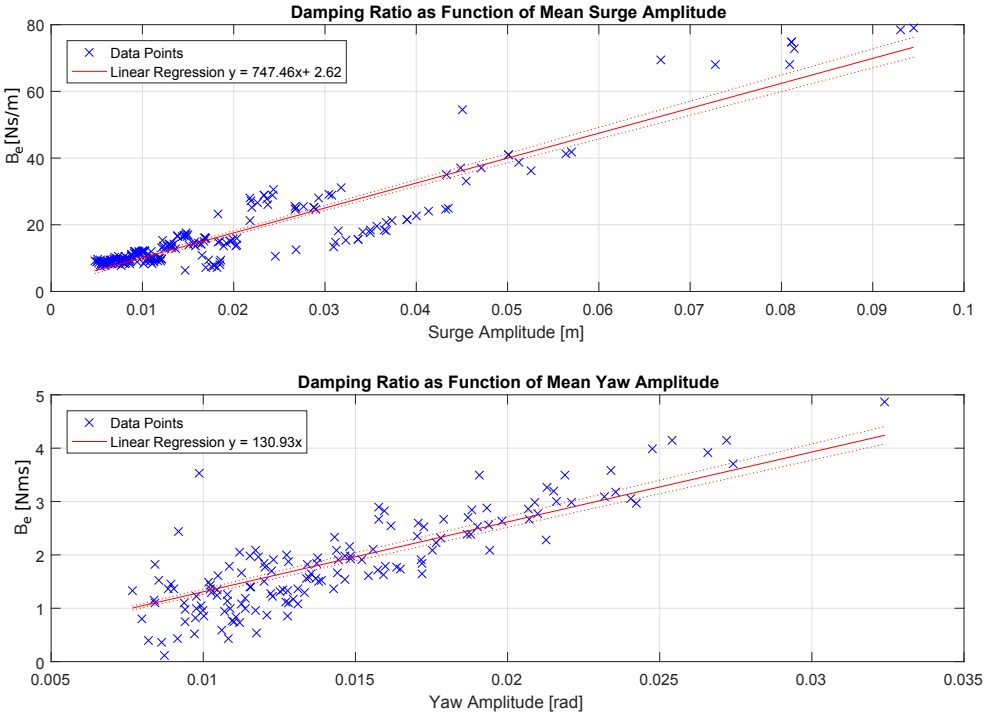

Figure 10.3: Experimental equivalent damping as function of mean amplitude.

In table 10.1 the experimental found linear and quadratic damping terms are seen along with their 95% confidence interval values

Table 10.1: Viscous linear and quadratic damping constants for surge, sway and yaw.

	Mean	Standard error	Lower limit	Upper limit
$B_{lin,11}$ [Ns/m]	2.61	0.5	1.64	3.60
$B_{lin,22}$ [Ns/m]	2.61	0.5	1.64	3.60
$B_{lin,66}$ [Nms]	0	0	0	0
$B_{quad,11}$ [Ns^2/m^2]	747.46	19.76	708.73	786.19
$B_{quad,22}$ [Ns^2/m^2]	747.46	19.76	708.73	786.19
$B_{quad,66}$ [Nms^2]	130.93	2.56	125.91	135.95

As these coefficients only are approximations they will be used as guidelines for the true values and therefore these coefficients will be used as fitting variables e.g. the quadratic damping in surge and sway is fitted to 950 Ns^2/m^2 while the linear damping is fitted to 3.60 Ns/m. This in order to get the best fit when comparing the simulated and experimental free decay, forced responses, etc. These values are not unrealistic high as they can be explained by some of the individual batches.
New tests were conducted in order to validate the Simulink and FAST models. In fig. 10.4 an experimental free decay in surge is seen indicated by the green line. It can be seen that Simulink, the red line, and FAST, the blue line, are both capable of explaining the response well.

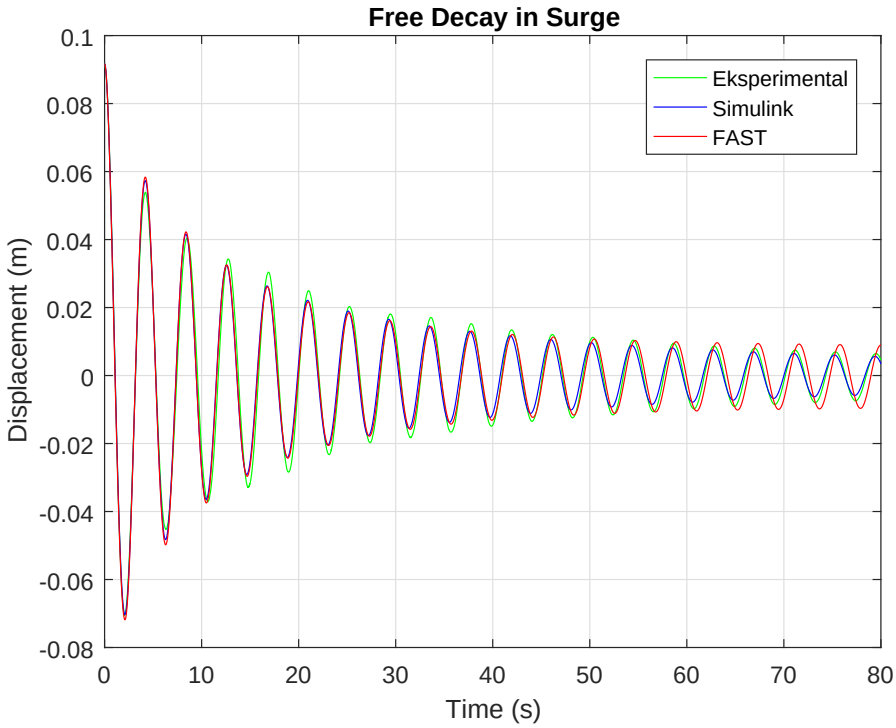

Figure 10.4: Free decay in surge.

In fig. 10.5 an experimental free decay in yaw is seen. It can be seen that Simulink and FAST are capable of explaining the response well.

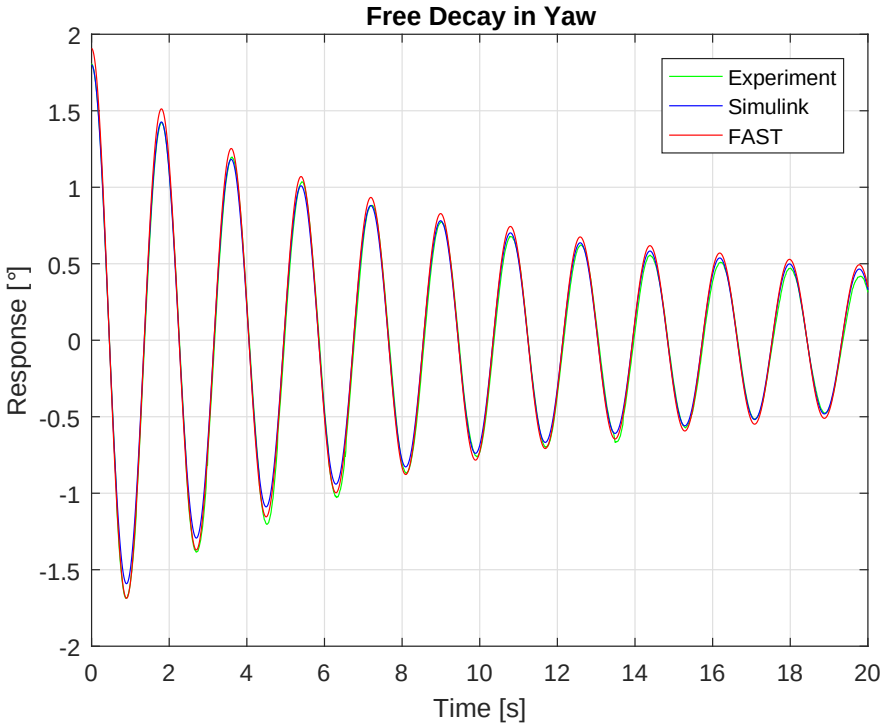

Figure 10.5: Free decay in yaw.

In the simulations the experimentally found stiffness has been used.

10.4 Forced Harmonic Response

In the forced harmonic response regular waves are applied to the TLP with a rigid mass placed on top. The response of the TLP is then measured using the camera system OptiTrack, and the waves are measured using the wave gauges. These tests are made for validating the Simulink and FAST model of the TLP.

10.4.1 Theory

The governing equation when doing forced harmonic excitation is the mass-spring-damper system with a force applied

$$(M_{ii} + A_{ii}(\infty))\,\ddot{q}_i(t) + B_{e,ii}\,\dot{q}_i(t) + K_{total,ii}\,q_i(t) = F_{wave,i}(t) \quad \text{for} \quad i = 1,2,...6 \tag{10.12}$$

where initial conditions for the system are

$$q_i(0) = q_{0,i} \quad \text{and} \quad \dot{q}_i(0) = \dot{q}_{0,i} \tag{10.13}$$

The general solution to this system contains a complimentary solution and a particular solution. The complimentary solution, $q_c(t)$, is the transient response that arises due to a change from the equilibrium or steady state which eventually dies out. The particular solution, $q_p(t)$, is the response that does not decay but continues as long as force is applied to the system, making the system oscillate with the same frequency as the force input. Thus the total solution will be

$$q(t)_i = q_{c,i}(t) + q_{p,i}(t) \tag{10.14}$$

where the complimentary solution for undercritically damped systems can be found as the same as the response for a free decay, see eq. 10.3.
As it is assumed that there is no force applied before $t = 0s$, the complimentary solution is the response caused by the initial conditions and after some time it will die out. The force applied to the TLP is a harmonic varying force which can be described using a cosine function

$$F_{wave,i}(t) = \bar{F}_{wave,i}\cos(\omega t - \phi) \tag{10.15}$$

where $\bar{F}_{wave,i}$ is the amplitude of the force and ω is the frequency at which the force is applied, ϕ is the phase between the surface elevation and the force. The partial solution can be found as

$$q_{p,i}(t) = \bar{q}_i\cos(\omega t - \psi) \tag{10.16}$$

where $\bar{q}_i$ is the amplitude of the motion and ψ is the phase between the motion and the force. From this it can be seen that the response eventually oscillates with the same frequency as the force when the transient response has died out.

10.4.2 Results

A regular wave were applied to the TLP in order to test the steady state response and compare this to the simulations. The wave height is here set to 0.005 m, while the wave frequency is 0.23 Hz, which is the highest practically possible waves to generate at this frequency without creating non linear waves. In the top of fig. 10.6 the experimental surface elevation is seen, measured four different places. Two gauges are placed in the front at the sides of the TLP, while two gauges are placed at the back at the sides of the TLP. For the simulations the wave height is set to 0.0044 m, which is average of the measured waves. In the bottom of fig. 10.6 the experimental forced response of the TLP in surge due to this surface elevation is seen together with the Simulink and FAST simulations. It can be seen that Simulink and FAST are both capable of explaining the experimental response well.

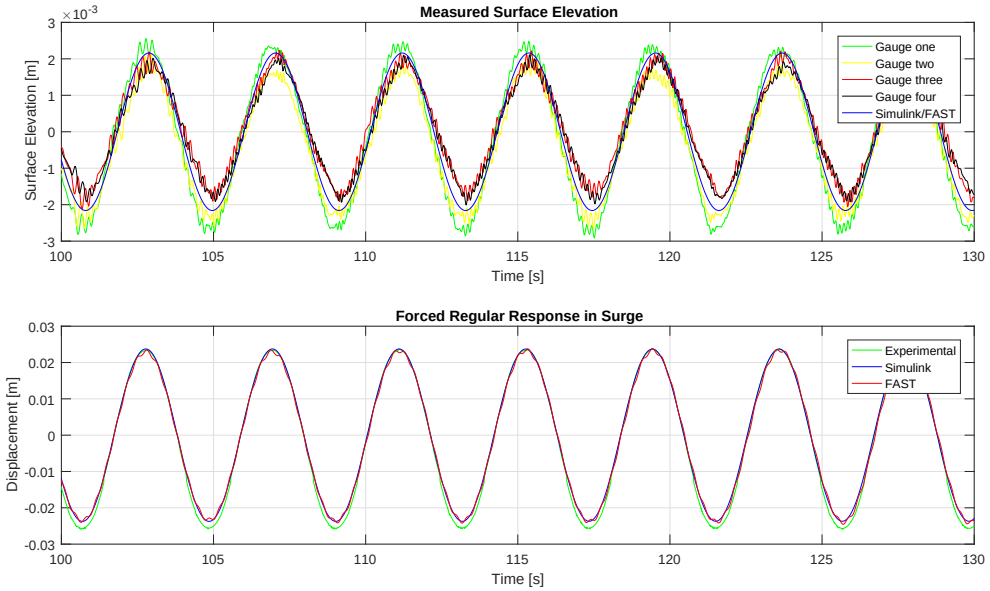

Figure 10.6: Forced response of the TLP in surge. Top figure shows the measured surface elevation, while the bottom figure shows the forced response of the TLP in surge.

The transient responses have not been compared as this would require a trigger signal between the wave generator and the data acquisition for both the waves sensors and OptiTrack, which is currently not available. Furthermore as it can be seen in the top of fig. 10.6 the four gauges measures four slightly different surface elevations, so the average of the four is only an approximation of the actual surface elevation influencing the TLP.

10.5 Response Amplitude Operator

In the tests regarding the RAO of the TLP, irregular waves are applied to the TLP with a rigid tower placed on top. The response of the TLP is measured using the camera system OptiTrack, and the waves are measured using the wave gauges. These tests are made for validating the Simulink and FAST model of the TLP.

10.5.1 Theory

The response amplitude operator (RAO) reveals useful information regarding the motion of the TLP. The RAO, which is expressed in the frequency domain, relates the steady state amplitude of the response to the amplitude of the incident waves. The RAO is based on linear wave theory along with an assumption of a linear relation between the response of the TLP and the incident waves. As a consequence the only frequencies represented in the RAO should be the same as the incoming waves. The simplest form of the RAO is derived by dividing the amplitude of the TLP motion, q_i, with the amplitude of a regular incident wave, η_a

$$RAO_i = \frac{q_i}{\eta_a} \quad \text{for} \quad i = 1 \ldots 6 \tag{10.17}$$

This regular wave however only excites the model at this single frequency, and thereby only a single point on the RAO is established. An irregular wave series on the other hand excites the TLP at a frequency band equal to the frequency band of the irregular wave series spectrum and thereby a RAO in this frequency band can be extracted. As for the irregular wave series the irregular response series can be decomposed into a sum of regular responses with infinitely many frequencies as a linear response is assumed. By using the definition of spectra given in eq. 7.29 explained in section 7.2 the spectra of the motion responses, $S_{q,i}$, and the incident waves can be described as

$$\begin{aligned} S_{q,i}(f)\Delta f &= \frac{1}{2} q_i^2(f) \\ S_\eta(f)\Delta f &= \frac{1}{2} \eta^2(f) \end{aligned} \tag{10.18}$$

dividing these two equations yields

$$\frac{S_{q,i}(f)}{S_\eta(f)} = \left(\frac{q_i(f)}{\eta_a(f)} \right)^2 = RAO^2 \tag{10.19}$$

such that it can be seen that the motion response and the wave spectrum are related through the square of the RAO or that the RAO is described through the square root of the spectra

$$RAO_i(f) = \sqrt{\frac{S_{q,i}(f)}{S_\eta(f)}} \tag{10.20}$$

10.5.2 Results

In fig. 10.7 the RAO for the TLP in the surge direction is seen. The surface elevation is measured by four different wave gauges, two gauges are placed in the front sides of the TLP, while two gauges are placed at the back sides of the TLP. The top figure shows the average measured surface elevation spectrum, indicated by the green line, and the generated surface elevation spectra for the simulations. The surface elevation spectrum used for the simulations detect the tendency of the experimental spectrum in high details. Furthermore the target spectrum, which is the spectrum input for the wave generator is seen. The target spectrum is here a JONSWAP spectrum. As it can be seen the wave generator is not quite capable of delivering the exact spectrum in the middle of the

wave tank and a large peak at the vicinity of 0.88 Hz occurs. The middle figure shows the measured response spectrum, indicated by the green line, and the response spectra generated by Simulink and FAST. The response is measured by the camera system Optitrack. The bottom figure shows the RAOs. Again the green, blue and red lines indicate the experimental, Simulink and FAST calculated RAOs, respectively. Furthermore the theoretical calculated RAO, see eq. 8.16 is indicated by the black line.

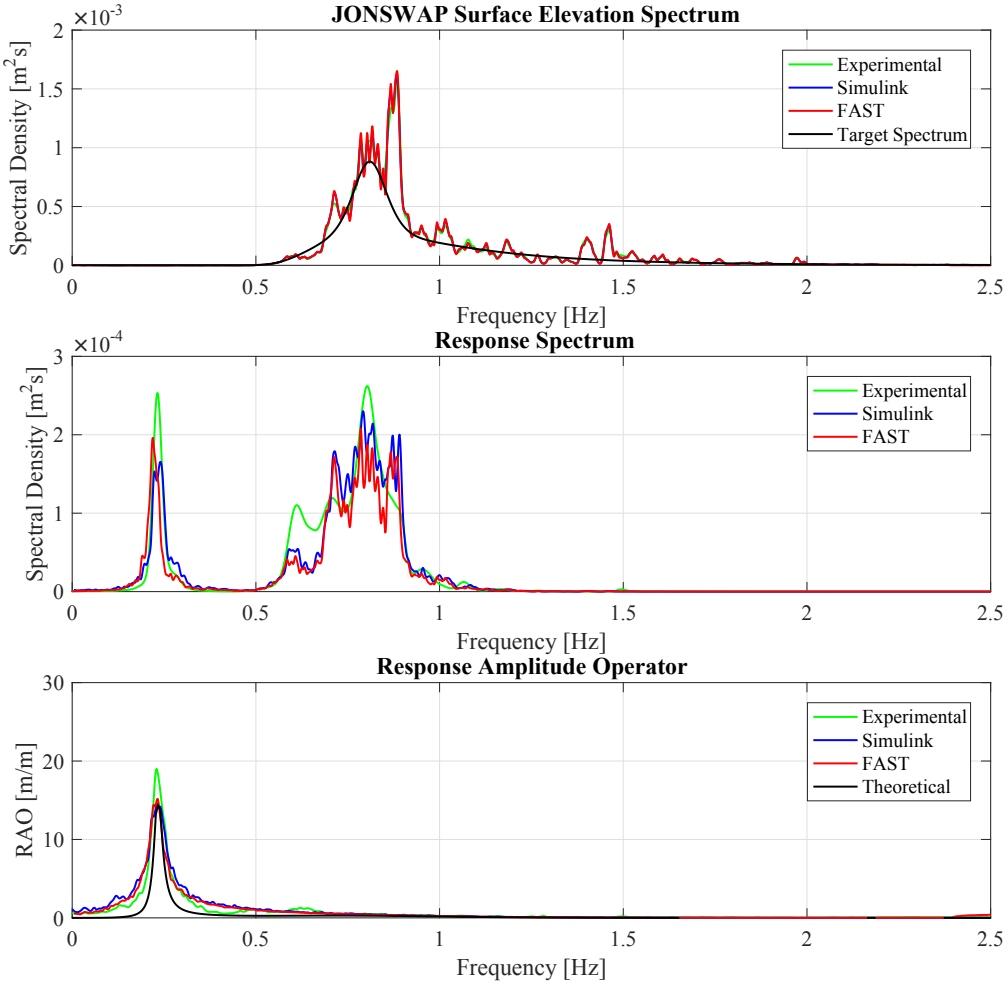

Figure 10.7: RAO of the uncoupled response of the TLP, when the TLP is influenced by a JONSWAP spectrum.

It can be seen that Simulink, FAST and the theoretical RAO are capable of explaining the experimental response spectrum and the RAO within a certain level, however they deviate slightly when estimating the amplitude. The reason for this might be due to a lot of reflected waves returning to the TLP when generating the spectrum. As the wave gauges are only capable of detecting both the incident and reflected waves, this might not give the precise impression of the actual wave hitting the TLP. Furthermore the reflected waves also hit the TLP, but it might be out of phase with the incident waves, which can give amplifications or deamplifications in the response. The natural frequency is found to be in the vicinity of 0.23 Hz which matches the analytical found frequency, see table 9.8.

In fig. 10.8 the RAO for the TLP in the surge direction is seen. This time the target spectrum is a white noise profile with an equal energy density of 0.00005 m^2s across the frequency interval of 0.2 to 2 Hz. Again the wave generator is not capable of delivering the theoretically exact spectrum

in the wave tank. However this time it is more pronounced compared to the JONSWAP spectrum profile. This inevitably gives rise to more uncertainty regarding the obtained experimental surface elevation. It can be seen the waves generated by this profile is only capable of exciting the TLP at the natural frequency of the TLP. Furthermore it can be seen that Simulink basically predicts the same RAO as before, which it should as RAO is independent of the input spectrum, however the experimental RAO deviates. This indicates that the measured surface elevation might not be the actual surface elevation impacting the TLP. In fact the reflection coefficient, which is a measure of the ratio between the complex amplitude of the reflected wave and the incident wave, varies a lot across the frequency interval ranging from 10 % to 90 % indicating a lot of reflected waves. This compared to the JONSWAP spectrum profile where the reflection coefficient varies from 10 % to 40 %. However it should be noted that a new experiment could be conducted and different reflection coefficients could be obtained. In appendix A.5 the spectrum and reflection coefficients measured at the wave generator are seen.

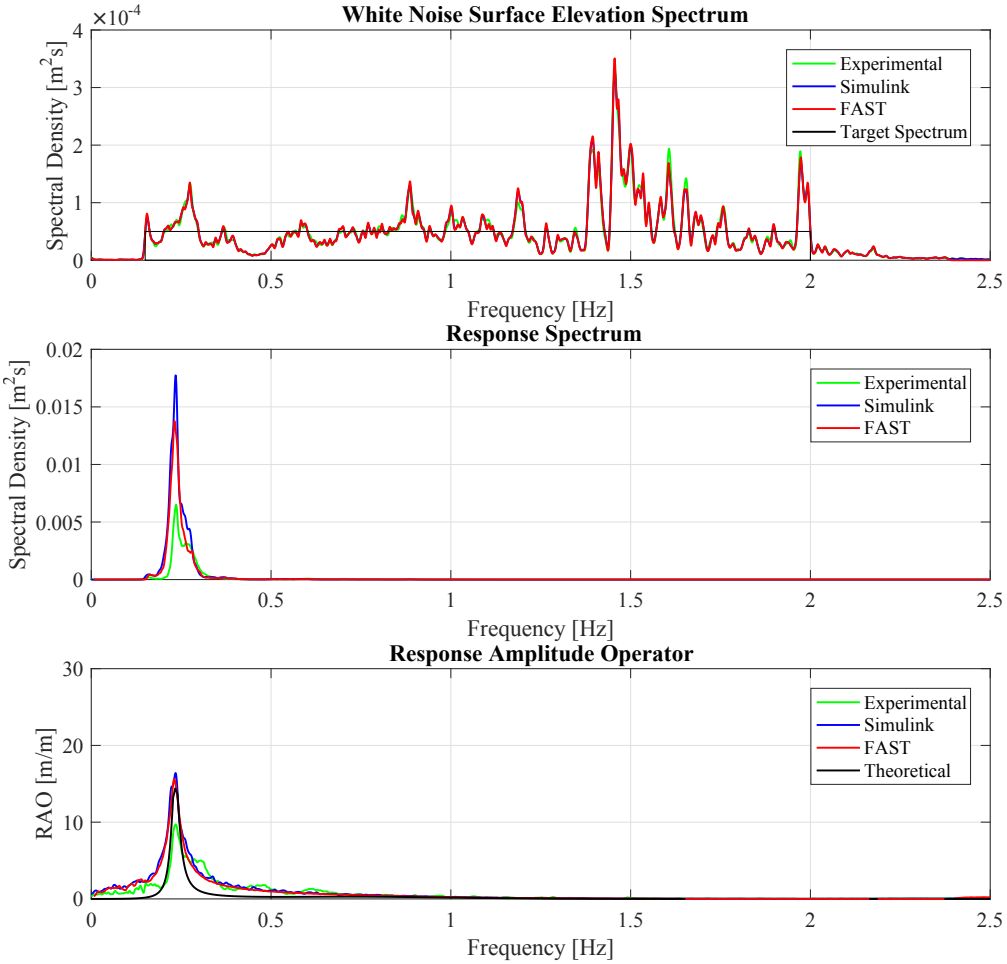

Figure 10.8: RAO of the uncoupled response of the TLP, when the TLP is influenced by a white noise spectrum.

Several tests were made, all showing the same overall behaviour.

10.6 Impulse Excitation of TLP

The theory of the impulse excitation of the tower is described in section 14.3, and the same theory will be used here. A 3-axis accelerometer of type 3D-BTA from Vernier together with LABQUEST Mini for data acquisition are used for the measurements. The sampling frequency used is 500 Hz. The accelerometer was mounted on the side of the TLP column, and the impulse excitation was also applied on the side of the TLP column.

10.6.1 Results

The accelerations in heave, surge and sway are seen in fig. 10.9

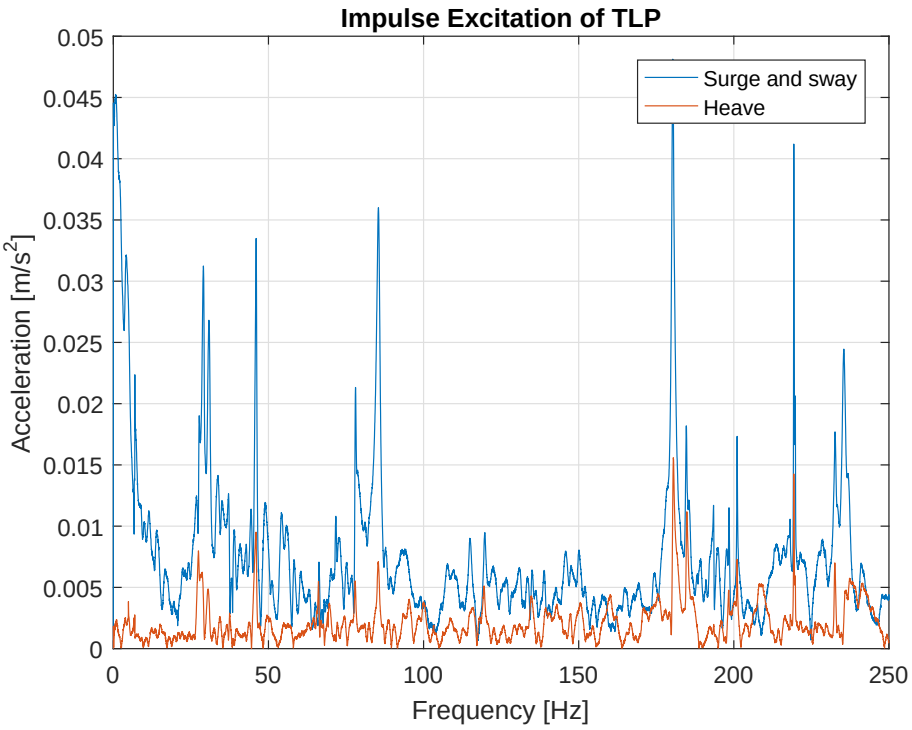

Figure 10.9: Frequency response of TLP.

The responses in surge and sway are added together, as the TLP is symmetric, and thus the response in these directions represents the same dynamics of the TLP. It can be seen that there are high peaks in the low frequency area of the plot, and according to the analytical calculations, see table 9.8, this is were the first six natural frequencies are. The next peaks are around 30 Hz and 45 Hz, and are thus not of interest, as this is beyond the frequency range of the external loads considered in this thesis.

Conclusion 11

In this part the generation of both regular and irregular waves, together with their respective spectra were described. The hydrodynamic model with implemented external wave forces, radiation forces, viscous forces, hydrostatic forces and mooring line forces was derived in six DOF. The hydrodynamic model regards the TLP as a rigid body, was explained both in the time domain and the frequency domain. The hydrodynamic coefficients including the first order wave excitation forces, the mass, the added mass, the potential damping, the linear and quadratic viscous damping, the hydrostatic and the mooring line stiffness was found. The added mass, potential damping and first order wave excitations forces were found numerically by the use of the free software NEMOH, while the mass, the linear and quadratic viscous damping, the hydrostatic stiffness and the mooring line stiffness were found analytically. NEMOH calculates the coefficients in the frequency domain, so a conversion from the frequency domain to the time domain was made. Furthermore the rigid body natural frequencies in all DOF were found, with surge and sway being 0.23 Hz, heave being 3.75 Hz, roll and pitch being 3.07 Hz and yaw being 0.52 Hz.
The last chapter deals with test and validation of the TLP. In this chapter Young's modulus of the mooring lines was found to be 63.9 GPa, which is also used in the calculations. The mooring line stiffness in the surge direction was experimentally measured to have a mean of 625.4 N/m, which is approximately 13 % higher than the analytically calculated. Free decays were made in order to experimentally find the linear and quadratic viscous damping in the surge, sway and yaw direction. The linear viscous damping in surge and sway had a mean of 2.61 Ns/m, while in yaw the mean was 0 Nms. The quadratic viscous damping in surge and sway had a mean of 747.46 Ns^2/m^2, while in yaw it was 130.93 Nms^2. Furthermore the free decays were used to compare the Simulink and FAST models with the experimentally obtained responses, where a good match was found. Forced harmonic excitation was made by exciting the TLP with regular waves. The measured experimental response of the TLP was compared to the Simulink and FAST models in the time domain with a good match. Furthermore irregular waves were applied to the TLP and the response of the TLP was compared to the Simulink and FAST models. The comparison was made in the frequency domain examining the response spectra and RAO, again a good match between the experimental obtained spectrum and the simulated spectra was found.

Part III

Structural Tower Model

Symbol	Description	Units
α	Coefficient for Rayleigh damping	-
	Coefficient for mass moment of inertia in roll and pitch	-
β	Coefficient for Rayleigh damping	-
	Coefficient for mass moment of inertia in yaw	-
γ	Weighting parameter	-
ζ	Damping ratio	-
ζ^*	Damping ratio at control frequency	-
$\mathbf{\Phi}$	Eigenmode	-
ω_0	Natural angular frequency	rad/s
ω_d	Damped natural angular frequency	rad/s
ω_i	Natural angular frequency at i DOF	rad/s
ω^*	Control angular frequency	rad/s
A_{cr}	Cross sectional area	m^2
a_n	Amplitude of nth peak	m
a_{n+1}	Amplitude of $n+1^{th}$ peak	m
$\mathbf{C}$	Global damping matrix	Ns/m
$\mathbf{C_g}$	Damping matrix in global coordinates	Ns/m
$\mathbf{c}$	Local damping matrix	Ns/m
c	Damping in SDOF system	Ns/m
d_i	Inner diameter of tower	m
d_o	Outer diameter of tower	m
E	Young's modulus	Pa
$\mathbf{e_1}, \mathbf{e_2}, \mathbf{e_3}$	Unit vectors	-
$\mathbf{F}_{ext}$	Global external force vector	N
$\mathbf{F}_{TLP}$	Force vector from TLP	N
$\mathbf{F}_{Rot}$	Force vector on rotor	N
$\mathbf{f}_{ext}$	Local external force vector	N
$\mathbf{f}_{int}$	Local internal force vector	N
f_{ext}	Local external force for SDOF system	N
G_{sh}	Shear modulus	Pa
g	Gravitational acceleration	m/s
I	Impulse	Ns
I_0	Polar moment of inertia	m^4
I_1, I_2	Mass moment of inertia in yaw	m^4
$I_{e,roll}, I_{e,pitch}$	Mass moment of inertia for half an element in roll and pitch	m^4
$I_{e,yaw}$	Mass moment of inertia for an element in yaw	m^4
I_j	Moment of inertia in j DOF	m^4
$\mathbf{K}$	Global stiffness matrix	N/m
$\mathbf{K}_g$	Stiffness matrix in global coordinates	N/m
$\mathbf{k}$	Local stiffness matrix	N/m
$\mathbf{k}_{\sigma,j}$	Initial stress stiffness vector	N/m
$\mathbf{k}_{Bend,j}$	Bending stiffness vector	N/m
k	Stiffness in SDOF system	N/m
$k_A, k_{B,i,j}, k_T$	Coefficients in stiffness matrix	N/m
L	Length of tower	m
L_e	Length of single element	m

$\mathbf{M}$	Global mass matrix	kg
$\mathbf{M}_{Con}$	Global consistent mass matrix	kg
$\mathbf{M}_g$	Mass matrix in global coordinates	kg
$\mathbf{M}_{Lum}$	Global lumped mass matrix	kg
$\mathbf{m}$	Local mass matrix	kg
$\mathbf{m}_{Con}$	Local consistent mass matrix	kg
$\mathbf{m}_{Lump}$	Local lumped mass matrix	kg
m	Mass in SDOF system	kg
$m_0, m_1, \dots m_7$	Coefficients in mass matrix	-
m_e	Mass of single element	kg
Q	Applied force	N
R_1	Inner radius of tower	m
R_2	Outer radius of tower	m
$\mathbf{T}$	Transformation matrix	-
T_{cr}	Torsional rotations of cross sections	Nm
T_m	Torsional moment	Nm
T_w	Warping torsion	Nm
t	Time	s
$\mathbf{v_1}, \mathbf{v_2}, \mathbf{v_3}$	Direction vectors	-
$\bar{\mathbf{v}}_\mathbf{2}$	Reference vector	-
w	Displacement of tower top	m
$\ddot{\mathbf{X}}$	Global acceleration vector	m/s^2
$\ddot{\mathbf{x}}$	Local acceleration vector	m/s^2
$\ddot{x}$	Acceleration in SDOF system	m/s^2
$\dot{\mathbf{X}}$	Global velocity vector	m/s
$\dot{\mathbf{x}}$	Local velocity vector	m/s
$\dot{x}$	Velocity in SDOF system	m/s
$\mathbf{X}$	Global position vector	m
$\mathbf{x}$	Local position vector	m
x	Position in SDOF system	m
(x_g, y_g, z_g)	Global coordinates	-
(x_l, y_l, z_l)	Local coordinates	-
$\ddot{\mathbf{y}}$	Acceleration of TLP	m/s^2

Introduction 12

The dynamics of the tower are modelled using FEM. This model is described further in the following chapter.
The material for the tower is PVC-U, this to get the right scaling of the elasticity, as the product of Young's modulus and the cross sectional area is scaled according to the 5 MW NREL tower, see previous work done by the authors [26].

For the tower with the new nacelle and blades, it is desired to achieve a correctly scaled first natural frequency in F-A, therefore a redesign of the tower height must be made. The first natural frequency in F-A is 0.32 Hz for the NREL 5 MW wind turbine. By 1:35 Froude scaling of this, a first natural frequency in F-A for the physical model must be designed to be 1.89 Hz. The new height of the tower is found by using the FEM code in MATLAB and validated through free decay tests with the tower fixed. Other experiments with the final tower will also be conducted, this includes free decay test, impulse excitation and deflection of the tower.

Finite Element Analysis 13

In this chapter the FEM for analysis of the dynamics of the tower is described. At first the governing equation of motion is formulated, thereafter the stiffness, mass and damping matrices are described. Then the global transformation matrix, the boundary conditions and the external loading on the tower are described.
The literature used for this chapter concerning the Finite Element Analysis (FEA) is from R. D. Cook [72].
FEM is typically applied on complex structures which are then simplified by discretising the structure into several elements. These elements are connected to each other by sharing nodes. The stiffness, mass and damping of the elements are formulated into the system matrices. In the case of a tower, it can be discretised by lumped masses in the nodes and stiffness and damping in the elements, as seen in fig. 13.1.

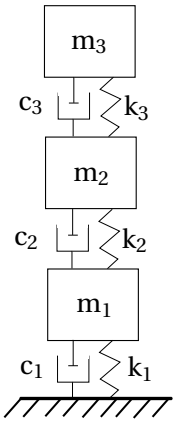

Figure 13.1: Example of the FEM discretisation.

The aim of this FEA is to describe the time-history analysis of the movement of the structure, such that the movement of the tower can be determined when influenced by the external loads described in section 13.7. For time-history analysis two methods are often preferred, these are the modal analysis or a direct integration method [72]. For this thesis the direct integration method is used, due to the simple structure of the tower.

13.1 Governing Equation of Motion

The governing equation for the structural mechanics for a 3D MDOF system, can be derived from the work balance on the system [72]. In the work balance it is assumed that the work of the external

loads applied to the system must be the same as the total work absorbed by the system. The system can absorb the work through inertial, dissipative and internal forces, for all displacements of the system, satisfying the compatibility and the essential BCs of the system. This will result in a formulation of the governing equation of motion for a single element to be

$$\mathbf{m}\ddot{\mathbf{x}}(t) + \mathbf{c}\dot{\mathbf{x}}(t) + \mathbf{f}_{int}(t) = \mathbf{f}_{ext}(t) \tag{13.1}$$

where $\mathbf{m} \in \mathbb{R}^{6\times6}$ and $\mathbf{c} \in \mathbb{R}^{6\times6}$ are the mass and damping matrices for a single element. $\ddot{\mathbf{x}} \in \mathbb{R}^6$ is the acceleration vector for a single element and $\dot{\mathbf{x}} \in \mathbb{R}^6$ is the velocity vector of a single element. The external forces are $\mathbf{f}_{ext} \in \mathbb{R}^6$ and the internal forces are $\mathbf{f}_{int} \in \mathbb{R}^6$.
As the material of the tower is considered to be linear, the loads arising from the stress in the element can be calculated as

$$\mathbf{f}_{int}(t) = \mathbf{k}\mathbf{x}(t) \tag{13.2}$$

where $\mathbf{k} \in \mathbb{R}^{6\times6}$is the stiffness of a single element and $\mathbf{x} \in \mathbb{R}^6$ is the position vector. This results in the formulation of the governing equation for a single element to be

$$\mathbf{m}\ddot{\mathbf{x}}(t) + \mathbf{c}\dot{\mathbf{x}}(t) + \mathbf{k}\mathbf{x}(t) = \mathbf{f}_{ext}(t) \tag{13.3}$$

The formulation of the governing equation for a linear system, which have multiple elements can be expressed in similar manner as eq. 13.3, but instead of local system matrices, global system matrices are utilized

$$\mathbf{M}\ddot{\mathbf{X}}(t) + \mathbf{C}\dot{\mathbf{X}}(t) + \mathbf{K}\mathbf{X}(t) = \mathbf{F}_{ext}(t) \tag{13.4}$$

where $\mathbf{M} \in \mathbb{R}^{6N\times6N}$ is the global mass matrix, where N is the number of nodes in the discretisation, in this thesis 20, see section 13.3, is chosen. $\mathbf{C} \in \mathbb{R}^{6N\times6N}$ and $\mathbf{K} \in \mathbb{R}^{6N\times6N}$ are the global damping and stiffness matrices. All the global system matrices are assembled from the local system matrices. These are further described in section 13.2. The motion of the nodes of the tower in the different DOFs are assembled in the vector $\mathbf{X}\in \mathbb{R}^{6N}$. The external forces acting on the tower are assembled into $\mathbf{F}_{ext} \in \mathbb{R}^{6N}$. The forces acting on the tower during operation could e.g. be the wind load on the rotor in the nacelle node, the wind load on the tower which is applied to all nodes along the tower and the loads induced by the acceleration of the TLP. The external loads are described in more detail in section 13.7.
The deflection of the tower is seen in the local reference frame, which is reference frame 2 as seen in fig. 18.1. This local reference frame is located on top of the TLP and is moving with it. It is therefore necessary to define the BCs with respect to the TLP.

13.2 Model System Matrices

In this section the formulation of the system matrices are described. The system has six DOFs in each node, therefore the system system matrices will be 12x12 matrices for one element in the system. It should be noted that the derivation of the system matrices are not of interest, as these can be found in several text books e.g Cook [72] etc., and is therefore deemed to be unnecessary to show here.

13.2.1 Mass Matrix

The mass matrix can be formulated in two ways; consistent or lumped, but also a combination of the two can be used. The lumped version of the mass matrix only consists of terms on the diagonal while the consistent have nonzero elements off the diagonal. Thus an advantage of using the lumped version is the computational time which is lower compared to the consistent mass matrix. But the lumped mass matrix has a tendency to underestimate the natural frequency, while the consistent mass matrix tends to overestimate it, and thus a combination of the two is often preferred according to R.D Cook [72].
The lumped mass matrix only consist of nonzero values on the diagonal. These values represent the masses at the given node, thus half of the masses of the elements connected to the node are lumped into the node. The lumped mass matrix, $\mathbf{m}_{\text{Lum}}$, for one element can thus be found as

$$\mathbf{m}_{\text{Lum}} = m_e \,\text{diag}\left[\tfrac{1}{2} \quad \tfrac{1}{2} \quad \tfrac{1}{2} \quad \beta \quad \alpha L_e^2 \quad \alpha L_e^2 \quad \tfrac{1}{2} \quad \tfrac{1}{2} \quad \tfrac{1}{2} \quad \beta \quad \alpha L_e^2 \quad \alpha L_e^2\right] \tag{13.5}$$

where m_e is the mass for a single element and α is a constant describing the mass moment of inertia of the element in the roll and pitch DOFs, while β describes the mass moment of inertia of the element in the yaw DOF. For the mass moment of inertia of the element in the roll and pitch DOF, the element can be considered as a uniform slender bar

$$I_{e,pitch} = I_{e,roll} = \frac{1}{24} m_e L_e^2 \tag{13.6}$$

where I_e is the mass moment of inertia for half the element, thus in this case $\alpha = 1/24$.
For the yaw degree of freedom the mass moment of inertia can be found as

$$I_{e,yaw} = \frac{1}{4} m_e \left(R_1^2 + R_2^2\right) \tag{13.7}$$

where R_1 and R_2 are the inner and outer radius of the tower, respectively. Thus β is given as $\beta = \frac{1}{4}\left(R_1^2 + R_2^2\right)$.
The consistent mass matrix can be derived using shape functions [72]. This means that coupling terms appear in the mass matrix for the bending DOFs. Therefore the consistent mass matrix will have values not only on the diagonal but also in the off-diagonal. The consistent mass matrix can thereby be formulated as

$$\mathbf{m}_{\text{Con}} = \frac{m_e}{420}\begin{bmatrix} m_0 & 0 & 0 & 0 & 0 & 0 & m_1 & 0 & 0 & 0 & 0 & 0 \\ & m_2 & 0 & 0 & 0 & m_3 & 0 & m_4 & 0 & 0 & 0 & -m_5 \\ & & m_2 & 0 & -m_3 & 0 & 0 & 0 & m_4 & 0 & -m_5 & 0 \\ & & & I_1 & 0 & 0 & 0 & 0 & 0 & I_2 & 0 & 0 \\ & & & & m_6 & 0 & 0 & 0 & -m_5 & 0 & -m_7 & 0 \\ & & & & & m_6 & 0 & m_5 & 0 & 0 & 0 & -m_7 \\ & & & & & & m_1 & 0 & 0 & 0 & 0 & 0 \\ & & & & & & & m_2 & 0 & 0 & 0 & -m_3 \\ & & \text{Symmetric} & & & & & & m_2 & 0 & m_3 & 0 \\ & & & & & & & & & I_1 & 0 & 0 \\ & & & & & & & & & & m_6 & 0 \\ & & & & & & & & & & & m_6 \end{bmatrix} \tag{13.8}$$

where the different components for the consistent mass matrix are given as

$$\begin{aligned} m_0 &= 140 \qquad m_1 = 70 \qquad m_2 = 256 \qquad m_3 = 22L_e \\ m_4 &= 54 \qquad m_5 = 13L_e \qquad m_6 = 4L_e^2 \qquad m_7 = 3L_e^2 \end{aligned} \tag{13.9}$$

The components for the inertia in the yaw, can in accordance to M. Paz in [73] be formulated as

$$I_1 = \frac{140I_0}{A_c r} \qquad I_2 = \frac{70I_0}{A_c r} \tag{13.10}$$

where I_0 is the polar moment of inertia of the cross sectional area, A_{cr}.
The two formulations can also be combined into a parameter varying mass matrix, which can be expressed as

$$\mathbf{M} = \mathbf{M}_{\text{Lum}}\gamma + \mathbf{M}_{\text{Con}}\left(1-\gamma\right) \tag{13.11}$$

where the weighting parameter γ is a value determining the formulation of the mass matrix, and can take a value between 0 and 1. If γ is set to 0, the mass matrix will be formulated as consistent, while if γ is set to 1 it will be lumped. For any value of γ between 0 and 1 the mass matrix is formulated as a combinational mass matrix. In this thesis a value of 0.5 is used.

For simulating the top mass of the tower, the two top elements are modelled with the mass and the mass moment of inertia found in Inventor of the nacelle.

13.2.2 Stiffness Matrix

To describe the stiffness of the system, a stiffness matrix must be formulated. The stiffness matrix for a beam in 3D, can be subdivided into three substructural elements: axial, bending and twisting. These types of deformation are visualized in fig. 13.2.

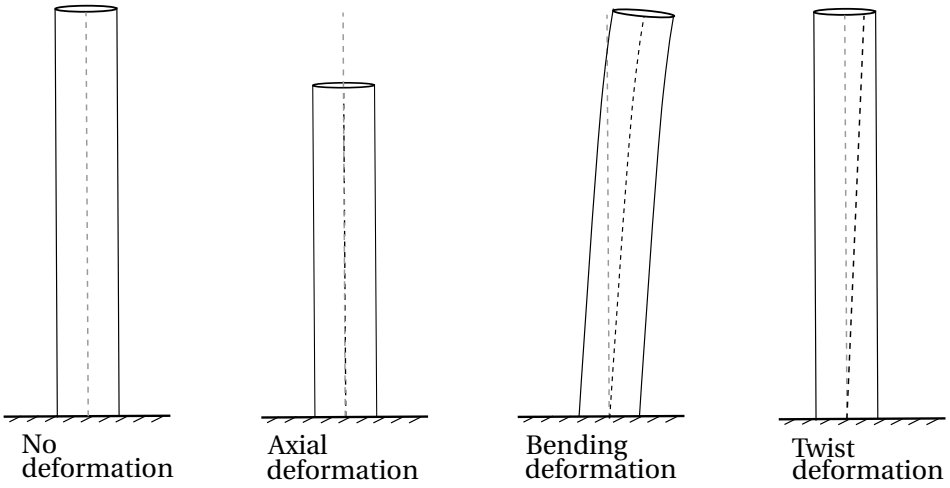

Figure 13.2: The deformation types: axial, bending and twisting on a fixed hollow cylinder, where the dotted grey line represents the non-deformed centreline, whereas the black dotted line represents the same deformed centreline.

The formulation of the stiffness matrix of a 3D beam element allows six DOFs per node; three translations and three rotations.

$$\mathbf{K} = \begin{bmatrix} k_A & 0 & 0 & 0 & 0 & 0 & -k_A & 0 & 0 & 0 & 0 & 0 \\ & k_{B1,z} & 0 & 0 & 0 & k_{B3,z} & 0 & -k_{B1,z} & 0 & 0 & 0 & k_{B3,z} \\ & & k_{B1,y} & 0 & -k_{B3,y} & 0 & 0 & 0 & -k_{B3,y} & 0 & -k_{B3,y} & 0 \\ & & & k_T & 0 & 0 & 0 & 0 & 0 & -k_T & 0 & 0 \\ & & & & k_{B2,z} & 0 & 0 & 0 & -k_{B3,y} & 0 & k_{B4,y} & 0 \\ & & & & & k_{B2,y} & 0 & -k_{B3,z} & 0 & 0 & 0 & k_{B4,z} \\ & & & & & & k_A & 0 & 0 & 0 & 0 & 0 \\ & & & & & & & k_{B1,z} & 0 & 0 & 0 & -k_{B3,z} \\ & & \text{Symmetric} & & & & & & -k_{B2,y} & 0 & k_{B3,y} & 0 \\ & & & & & & & & & k_T & 0 & 0 \\ & & & & & & & & & & k_{B2,y} & 0 \\ & & & & & & & & & & & k_{B2,z} \end{bmatrix} \tag{13.12}$$

where k_A is the axial stiffness component for the bar, $k_{Bi,j}$ is the bending and transverse stiffness for a 2D beam, and k_T is the torsional stiffness of a 3D beam. The components of the 3D stiffness matrix can be derived through different methods, such as Garlerkin, principle of virtual work, etc. The aim of the subsequent subsections is to shortly describe the components of the 3D stiffness matrix, for more detailed derivations see [72].
The two top elements for the tower are modelled as a rectangular plate with the stiffness of the nacelle, which is assumed to be aluminium.

13.2.2.1 Axial

For the axial deformation of a 3D beam element, it is assumed that the deformation is small, such that bending and twisting can be decoupled. Thereby the axial deformation of the 3D beam element can be considered as a bar element. The stiffness k_A of the bar element can be regarded as a linear spring. In the case of a wind turbine the pretension throughout the tower comes from the gravity

force of the nacelle and the tower itself. The axial stiffness can be expressed as

$$k_A = \frac{A_{cr} E}{L_e} \tag{13.13}$$

where E is Young's modulus of the material.

13.2.2.2 Bending-transverse

To describe the stiffness of a 2D beam element, the elementary beam theory is used. This theory only considers the bending deformation in the beam, and not the shear deformation. This is also known as the Euler-Bernoulli beam theory. In order to include the effect of transverse shear, the Timoshenko beam theory should be used. But the Euler-Bernoulli beam theory is often used, as it is simpler and is a good approximation as long as the ratio between the length of the beam and the thickness, i.e. the diameter in the case of a cylinder, is larger than 10 [74]. That is the beam can be considered thin relative to the length, which for the case of the tower in this thesis is true.
The bending and transverse stiffness can be described by four stiffness components, which are assembled into the bending stiffness vector $\mathbf{k}_{\text{Be,j}}$. This vector can be found as the sum of the bending stiffness vector, $\mathbf{k}_{\text{Bend,j}}$, and the initial stress stiffness vector $\mathbf{k}_{\sigma,j}$

$$\mathbf{k}_{\text{Be,j}} = \mathbf{k}_{\text{Bend,j}} + \mathbf{k}_{\sigma,j} \tag{13.14}$$

where subscript, j, represents which axis the bending occurs around. The bending stiffness vector is found as

$$\mathbf{k}_{\text{Bend,j}} = \begin{bmatrix} \frac{12EI_j}{L_e^3} \\ \frac{4EI_j}{L_e} \\ \frac{6EI_j}{L_e^2} \\ \frac{2EI_j}{L_e} \end{bmatrix} \tag{13.15}$$

Due to the initial axial force arising from the weight of the wind turbine and the tower itself, there will be a decrease in stiffness in the bending deflection. This decrease in stiffness, can be described by the initial stress stiffness vector, which can be formulated by

$$\mathbf{k}_{\sigma,\text{j}} = -\begin{bmatrix} \frac{6m_e g}{5L_e} \\ \frac{m_e g}{10} \\ \frac{2m_e g L_e}{15} \\ \frac{m_e g L_e}{30} \end{bmatrix} \tag{13.16}$$

The total stiffness for the beam in bending can be found by adding the two stiffness components

together and thus the components of this vector are

$$\begin{aligned} k_{B1,j} &= \frac{12EI_j}{L_e^3} - \frac{6m_e g}{5L_e} \\ k_{B2,j} &= \frac{4EI_j}{L_e} - \frac{2m_e g L_e}{15} \\ k_{B3,j} &= \frac{6EI_j}{L_e^2} - \frac{m_e g}{L_e} \\ k_{B4,j} &= \frac{2EI_j}{L_e} - \frac{m_e g L_e}{30} \end{aligned} \tag{13.17}$$

these can be seen in the total stiffness matrix for the 3D beam.

13.2.2.3 Twisting

When a supported beam is subjected to a torsional moment, T_m, around the longitudinal axis, generally the cross-sections along the beam will rotate around the longitudinal axis and warp. Warping describes the differential axial displacement of the cross-sections during twisting of the tower. The torsional moment applied to the supported beam is generally resisted by two torsional terms, these are torsional rotations of the cross-sections T_{cr} and the warping torsion T_w.

$$T_m = T_{cr} + T_w \tag{13.18}$$

The torsional rotation of the cross-section is caused by the uniform shear stress, which is also known as St. Vernant shear stress. This arises from the uniform rotational displacement of cross sections along the beam.
The warping torsion arises due to the resistance against warping, and causes non-uniform shear stresses. The differential warping along the beam will occur, introducing longitudinal strains. The longitudinal strains generate normal stresses, which vary along the beam.
But as the tower for this thesis has a circular cross section, it will exhibit rotational symmetry which will coincide with the shear centre. Because of this, the uniform torsion will be predominant, and thus the warping torsion can be neglected. This means the cross sections of the beam will remain plane. The torsional stiffness of the beam can be considered in the same manner as the axial deformation. This results in the torsional stiffness coefficient, k_T, to be expressed as

$$k_T = \frac{G_{sh} J_T}{L_e} \tag{13.19}$$

where G_{sh} is the shear modulus of the material of the beam and J_T is the torsion constant. The shear modulus is set to 1 GPa [75], while the torsion constant is given as

$$J_T = \frac{\pi}{32}\left(d_o^4 - d_i^4\right) \tag{13.20}$$

where d_o is the outer diameter of the tower, while d_i is the inner diameter.

13.2.3 Damping Matrix

The damping forces in vibrating structures are still not fully understood [76]. But it is known that an amount of energy is dissipated from the structure by internal damping of the beam and air resistance [77]. But in contrast to inertia and stiffness forces, it is not in general clear which state variable should be used for determining the damping force. Most often a viscous damping model is used to represent the damping. This is a linear model in which velocity is the relevant state. This was first introduced by Lord Rayleigh [78], who simplified the expression further by assuming the damping matrix to be a linear combination of the mass and stiffness matrices

$$\mathbf{C} = \alpha\mathbf{M} + \beta\mathbf{K} \tag{13.21}$$

Here α and β are coefficients determine the amount of contribution from the mass and the stiffness matrices. Rayleigh damping is often used to model damping as it is mathematical convenient, as both the mass and stiffness matrices are already known. However there is no physical reason why a general system would behave like this. The damping ratio, ζ for Rayleigh damping is found as

$$\zeta = \frac{\alpha}{2\omega_i} + \frac{\beta\omega_i}{2} \tag{13.22}$$

where ω_i is the natural frequencies of interest, and thus the two coefficients can be determined from these frequencies. From the equation it can be seen that if only mass damping is considered, that is if $\mathbf{C} = \alpha\mathbf{M}$, the damping ratio is inversely proportional to the response frequency. This is indicated by the blue line in fig. 13.3. Care should here be taken as the damping ratio at the lower frequencies is rapidly increasing with decreasing frequency. Thereby the mass damping might overdamp these lower frequencies. On the other hand it might underestimate the damping at the higher frequencies. If only considering the stiffness damping, that is if $\mathbf{C} = \beta\mathbf{K}$, it can be seen that it is linearly proportional to response frequency. This can be seen in fig. 13.3 indicated by the red line. If only stiffness damping is used then any high frequency response will be overdamped, while some of the lower frequencies might be underdamped. This damping can also be used for damping the non-physically high-frequency noise occurring when running simulations. If combining the mass and stiffness dampings, the black line in fig. 13.3 is achieved.

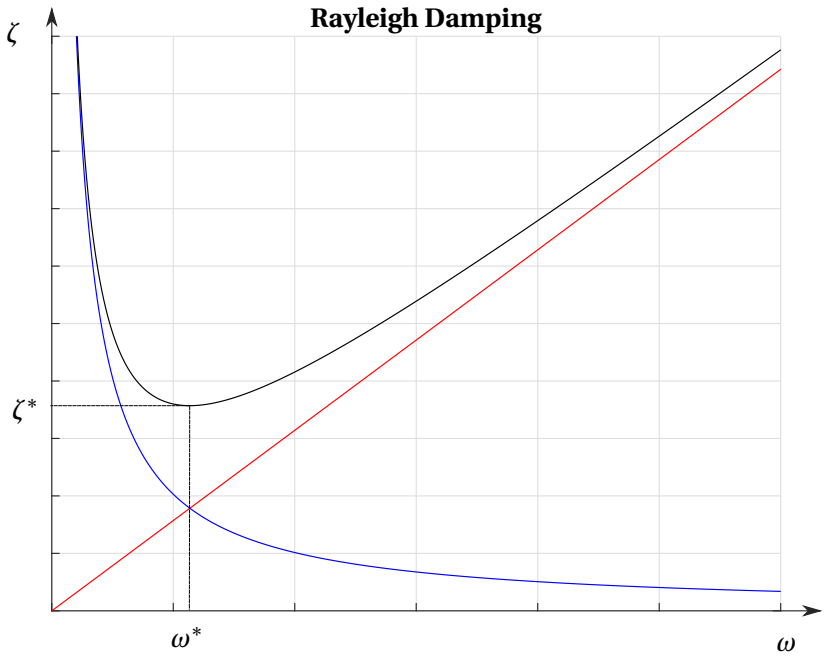

Figure 13.3: Example of Rayleigh damping.

From eq. 13.22 it can be seen that there are two unknowns for one equation. If the damping ratio is experimentally known for two different eigenmodes it is possible to assign α and β values in order to achieve the specific damping ratio at these frequencies. However it is not possible to experimentally excite and achieve the damping ratio for the tower in this thesis in higher modes than the first, and thus another approach has to be used, where only one natural frequency and the corresponding damping is known, as seen in fig. 13.3. When using this approach the two coefficients of α and β are found as

$$\alpha = \zeta^* \omega^* \quad \text{and} \quad \beta = \frac{\zeta^*}{\omega^*} \tag{13.23}$$

where ζ^* and ω^* are the damping ratio at the control frequency and the control frequency, respectively. The control frequency is usually taken as the first natural frequency. [79]

In section 14.2 the first natural frequency of the tower is found to be 1.90 Hz, while the corresponding damping ratio is found to be 1.3 %. From above equations, the α and β values are found to be 0.1544 and 0.0011, respectively. This gives a relationship between the damping ratio and the frequency as seen in the fig. 13.4.

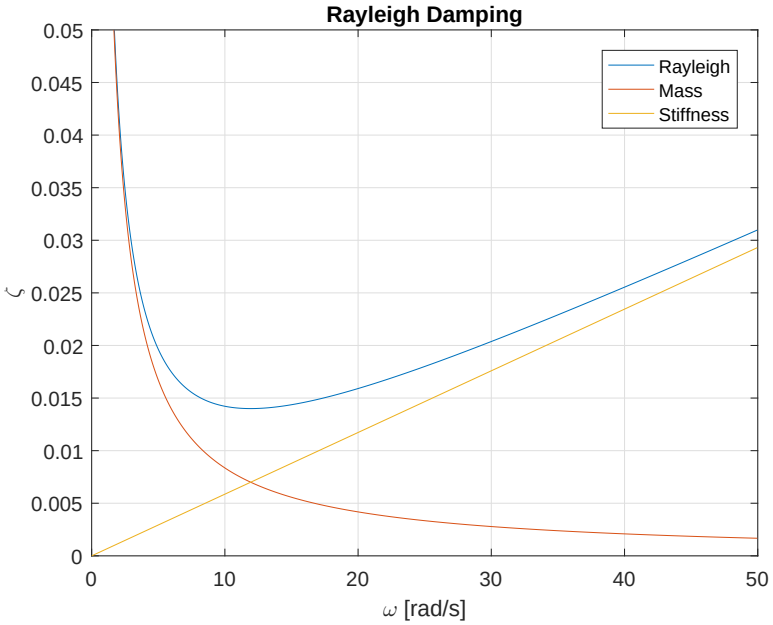

Figure 13.4: The Rayleigh damping used in this thesis.

13.3 Convergence Analysis

A convergence analysis is made in order to investigate the sufficient number of elements along the tower for the natural frequency to converge. The convergence analysis is made for the fixed tower.

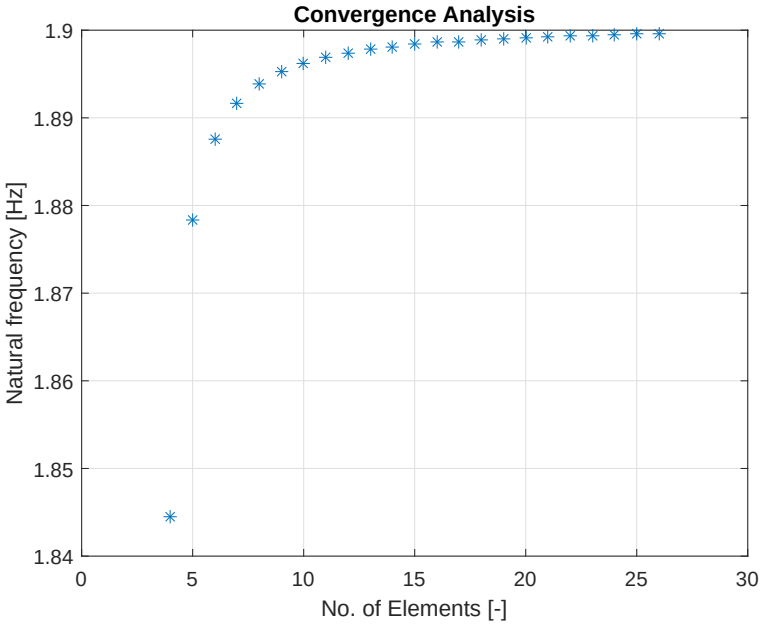

Figure 13.5: The convergence analysis made for the fixed tower.

As seen in the figure, the natural frequency starts to converge between 15 and 20 elements, and thus 20 elements are found sufficient for the model. More elements could have been used, but the computational time would have been increased with the increased number of elements.

13.4 Global Transformation

The tower is located in the global coordinate system (x_g, y_g, z_g), where the global z-axis is the longitudinal axis of the tower, for which the axial deformation occurs. A transformation is needed, as the system matrices of the 3D beam elements have been formulated in the local coordinate system (x_l, y_l, z_l). The local x-axis is the longitudinal axis, where axial deformation occurs.
The formulations of the local and global system are in order to obtain general mass, damping and stiffness matrices. The two coordinate systems are visualized in fig. 13.6.

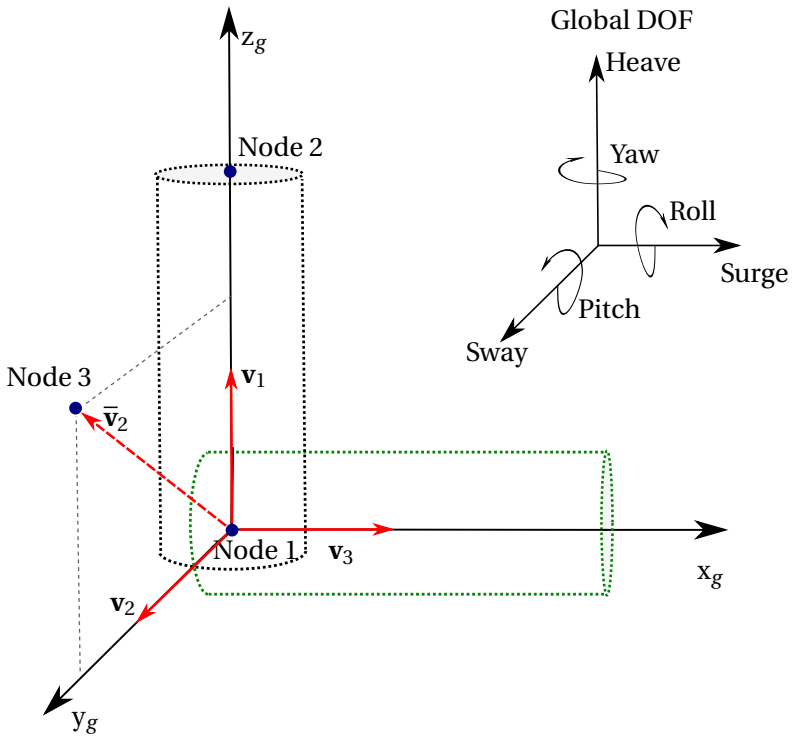

Figure 13.6: The beam element shown in global coordinates (black dotted beam) and the local formulation of the beam element in the global coordinates (green dotted beam). The unit vectors, v_1, v_2 and v_3, for the transformation matrix are shown as red lines, whereas the three nodes are indicated by blue dots.

The transformation matrix, **T**, can be found by realizing that there must exist a relationship between the global vectors and local vectors, such that

$$\begin{bmatrix} x_g \\ y_g \\ z_g \end{bmatrix} = \mathbf{T} \begin{bmatrix} x_l \\ y_l \\ z_l \end{bmatrix} \tag{13.24}$$

In fig. 13.6 there are three nodes, where node 1 and 2 define the end nodes of the beam element, while node 3 is an arbitrary node placed in the y_g, z_g-plane and is only used as a reference, as three nodes are needed in order to describe the location of an object in space.
The first direction vector, $\mathbf{v_1}$, can be found by subtracting the nodal coordinates from node 1 and

node 2

$$\mathbf{v_1} = \begin{bmatrix} x_2 - x_1 \\ y_2 - y_1 \\ z_2 - z_1 \end{bmatrix} \tag{13.25}$$

Then a reference vector must be made for the second direction vector, which is denoted $\bar{\mathbf{v}}_\mathbf{2}$. The reference vector can be found by subtracting the nodal coordinates of node 1 from node 3

$$\bar{\mathbf{v}}_\mathbf{2} = \begin{bmatrix} x_3 - x_1 \\ y_3 - y_1 \\ z_3 - z_1 \end{bmatrix} \tag{13.26}$$

The reference direction vector and the first direction vector can then be used to derive the third unit vector, as it must be orthogonal on the plane which these two vectors span

$$\mathbf{v_3} = \mathbf{v_1} \times \bar{\mathbf{v}}_\mathbf{2} \tag{13.27}$$

The second direction vector is orthogonal on the first and third unit vectors, which have just been found

$$\mathbf{v_2} = \mathbf{v_1} \times \mathbf{v_3} \tag{13.28}$$

In order to determine the unit vectors from the direction vectors, they must be divided by the length of the direction vector

$$\mathbf{e_1} = \frac{\mathbf{v_1}}{|\mathbf{v_1}|} \quad \mathbf{e_2} = \frac{\mathbf{v_2}}{|\mathbf{v_2}|} \quad \mathbf{e_3} = \frac{\mathbf{v_3}}{|\mathbf{v_3}|} \tag{13.29}$$

The three unit vectors can be assembled into the transformation matrix, which will transform the system between local and global formulation

$$\mathbf{T} = \begin{bmatrix} \mathbf{e_1} & \mathbf{e_2} & \mathbf{e_3} \end{bmatrix} \tag{13.30}$$

The transformation of the system matrices from local to the global formulation are then found as

$$\begin{aligned} \mathbf{K}_g &= \mathbf{TKT}^T \\ \mathbf{M}_g &= \mathbf{TMT}^T \\ \mathbf{C}_g &= \mathbf{TCT}^T \end{aligned} \tag{13.31}$$

13.5 Eigenmodes and Natural Frequencies

Eigenmodes are the shapes of the displacements of the tower, when the tower is excited in one of the natural frequencies of the tower. The discretisation of the tower determines the number of

eigenmodes and natural frequencies that can be represented. As the tower in this thesis is discretised into 20 elements, 120 eigenmodes and natural frequencies can be estimated, as there are six DOF in each node. The eigenmodes are the eigenvectors of the system, while the corresponding eigenvalues are the natural frequencies squared. This can be seen if investigating the eigenvalue problem

$$(\boldsymbol{K} - \omega^2 \boldsymbol{M})\boldsymbol{\Phi} = 0 \tag{13.32}$$

where $\boldsymbol{\Phi} \in \mathbb{R}^{6N \times 6N}$ are the eigenvectors of the system. To fulfill eq. 13.32, either the value in the parentheses or $\boldsymbol{\Phi}$ should be zero. When $\boldsymbol{\Phi} = \boldsymbol{0}$ it corresponds to no displacement of the tower and is thus not of interest. If the term in the parentheses should be zero, a condition of the determinant being zero should be fulfilled.
For the tower in this thesis the first ten natural frequencies are seen in table 13.1.

Table 13.1: Calculated natural frequencies of tower.

Mode no.	Direction	Natural frequency [Hz]
1	Sway/roll	1.90
2	Surge/pitch	1.90
3	Yaw	6.72
4	Sway/roll	15.87
5	Surge/pitch	17.12
6	Sway/roll	49.63
7	Surge/pitch	50.58
8	Heave	73.73
9	Yaw	89.85
10	Surge/pitch and Sway/roll	124.86

As a comparison the first natural frequency in surge/pitch for the scaled NREL 5 MW wind turbine is 1.91 Hz, which fits quite well with the natural frequency of the tower.When comparing the second natural frequency in surge/pitch the scaled natural frequency is 17.16 Hz, which also fits quite well with the calculated natural frequency of 17.12 Hz.
Eigenmode 2, 5, 7 and 8 are seen in fig. 13.7.

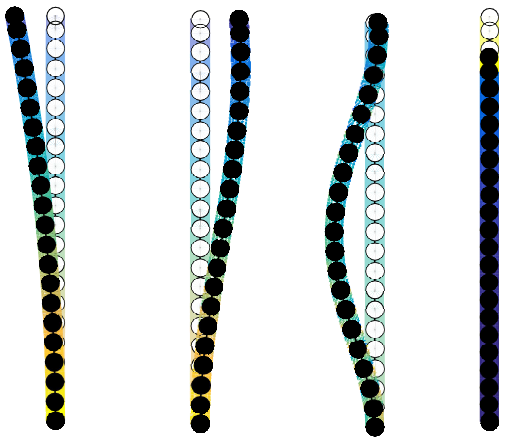

Figure 13.7: Different eigenmodes for the tower.

13.6 Boundary Conditions

In order to solve the governing equation of motion for the tower, a set of BCs for all DOFs at each node in the FEM of the tower has to be formulated.
The BCs are necessary for the FEM of the tower, as for each DOF included there are two unknowns, either the displacement or the external force. The forced displacements of the structure are called the essential BCs and the external forces acting on the structure are called the static BCs. For the FEM of the tower, the BCs imposed will consist of essential BCs for the bottom node, where the TLP is used as a support for the tower in all six DOFs. For all DOFs at the other nodes there will be a static BC. The bottom node of the tower is constrained to the TLP and will assure that the tower at all times will be fixed to the TLP, and that no relative rigid body motion can occur.

13.7 External Loads

The external loads on the tower arise due to the acceleration of the platform and wind loading on the tower and the rotor. These external loads apply to different nodes and in multiple DOFs, therefore each excitation will be further described in the subsequent sections. The total external loads considered on the tower can be described by a combination of the three force vectors

$$\mathbf{F}_{\text{Ext}} = \mathbf{F}_{\text{TLP}} + \mathbf{F}_{\text{Tow}} + \mathbf{F}_{\text{Rot}} \tag{13.33}$$

where $\mathbf{F}_{\text{TLP}} \in \mathbb{R}^{6N}$ is the force arising from the dynamics of the TLP. $\mathbf{F}_{\text{Tow}} \in \mathbb{R}^{6N}$ is the force vector describing the forces acting on the tower from the incoming wind. At last is the force vector $\mathbf{F}_{\text{Rot}} \in \mathbb{R}^{6N}$ which is the load due to the incoming wind on the rotor, transformed into a single point, acting in the middle of the rotor.

13.7.1 TLP Acceleration

The bottom node of the tower is constrained to the TLP, but as the TLP is not a stationary support, the dynamics of the TLP will influence the tower. Therefore the TLP is treated as a moving support. In order to determine the external load on the tower, the acceleration of the TLP has to be calculated, this was explained in chapter 8. The external loads from the dynamics of the TLP arise from the acceleration of the platform. As the tower is seen in a relative reference frame, only the elastic response of the tower is considered. The external load from the dynamics of the TLP can be described as

$$\mathbf{F}_{TLP}(t) = \mathbf{M}_{\text{g}} \ddot{\mathbf{y}}_{\text{TLP}}(t) \tag{13.34}$$

where $\ddot{\mathbf{y}}_{\text{TLP}}(t) \in \mathbb{R}^{6N}$ is the acceleration vector of the TLP.

13.7.2 Wind Load on Tower

The wind load on the tower is found as the drag force, where the tower is considered as a cylinder

$$\mathbf{F}_{Tow} = \frac{1}{2} \rho_{\text{air}} \mathbf{A}_e \, C_d(Re) \, \mathbf{V}^2_{\text{rel,Tow}} \tag{13.35}$$

where $\mathbf{A}_e \in \mathbb{R}^{N_t}$ is a vector of element frontal areas along the tower and $C_d(Re)$ is the drag coefficient,

which is dependent on the Reynold's number of the flow around the tower, in this thesis it is assumed to be constant at 0.5. The number of tower elements is denoted N_t
The relative velocity $\mathbf{V}_{\text{rel,Tow}} \in \mathbb{R}^{N_t}$ describes the wind flow around the tower at each element. There are several factors influencing the incoming wind on the tower. This is the dynamics of the TLP and tower, the position of the blades which create a blockage effect for the incoming wind speed and the wake behind the blades, which changes the wind speed and changes the direction and increases the turbulence.
To describe the relative wind speed, only the influence of the TLP motion in the surge direction and the wind speed are considered, as the other terms are insignificant

$$\mathbf{V}_{\text{rel,Tow}} = \mathbf{U}_0 + \mathbf{V}_{\text{TLP}} \tag{13.36}$$

where $\mathbf{U}_0 \in \mathbb{R}^{N_s}$ is the free stream velocity of the wind on the tower.

13.7.3 Wind Load on Rotor

The wind load on the rotor will be explained in section 18.2, here it will be shown how to calculate the load acting on each blade. As the positions of the blades are known, the loads along the blade can be used to calculate the moments occurring about the pitch and yaw axes of the nacelle. The force from the rotor is assumed only to be significant in the normal direction on the rotor plane, thereby the force can be calculated by

$$F_{Rot} = \sum_{1}^{NB} \sum_{1}^{NE} \mathbf{F}_{\text{NB}} \tag{13.37}$$

where F_{Rot} is the force from wind load on the rotor, $\mathbf{F}_{\text{NB}} \in \mathbb{R}^{NE}$ is the force vector describing the normal force acting along the blade in each blade element. NB is the number of blades. The sum of forces from each blade are then summed for all blades to find the total normal force acting on the rotor.
The normal force on the blades will also cause moments around the nacelle. The DOFs the moments act in are pitch and yaw as the rotor rotates around the x-axis.

$$\begin{aligned} M_{\text{Pitch}} &= \sum_{1}^{NB} \mathbf{F}_{\text{NB}} \mathbf{Br} \sin(\theta_{\text{NB}}) \\ M_{\text{Yaw}} &= \sum_{1}^{NB} \mathbf{F}_{\text{NB}} \mathbf{Br} \cos(\theta_{\text{NB}}) \end{aligned} \tag{13.38}$$

where M_{Pitch} and M_{Yaw} are the moments around pitch and yaw, respectively. $\mathbf{Br} \in \mathbb{R}^{NE}$ is the distance vector, describing the length from the rotor centre to the blade elements while θ_{NB} is the angle each blade is rotated from the y-axis. The moment in roll is due to the acceleration or deacceleration of the rotor. The roll moment can be calculated as

$$M_{\text{Roll}} = \dot{\omega_r} \sum_{1}^{NB} \mathbf{Br}\,\mathbf{mr} \tag{13.39}$$

where M_{Roll} is the moment in roll, and $\mathbf{mr} \in \mathbb{R}^{NE}$ is the mass vector for each blade.

Test and Validation 14

In this chapter the model of the tower is tested and validated. The damping, the stiffness and the natural frequencies of the tower are investigated by conducting different experiments. In this chapter only the response of the tower with the nacelle mounted is considered, meaning that the tower will be fixed on the stationary ground to decouple the motion of the tower from the TLP. This is done by using a metal coupling, see appendix A.8. This is to see the dynamics of the tower and to compare with the case where the tower is mounted on the floating platform, such that the coupling effect can be analysed.
It should be noted that the blades and rotor positions are fixed during the experiments, and no wind loads are applied.

14.1 Young's Modulus

A series of experiments were conducted to estimate Young's modulus of the tower. The camera system OptiTrack was used to capture the deflection of the tower, while different forces were applied to the top. These forces were measured using a newtonmeter. The experiments were conducted without top mass and hence the tower is 2.1 m, which is a bit higher compared to the tower with top mass. If the force and the deflection at the end of the beam are known, Young's modulus can be determined using Euler-Bernoulli's beam theory for a cantilever beam with end load

$$w = \frac{QL^3}{3IE} \tag{14.1}$$

where w is the deflection at the top of the tower, Q is the force applied to the top of the tower, L is the length of the tower, I is the area moment of inertia and E is Young's modulus.
The measurements are seen in the table together with the resulting Young's modulus.

Table 14.1: Results from experiments.

Test no.	Q [N]	w [mm]	E [GPa]
1	10.7	7.5	2.88
2	15.6	10.1	3.12
3	37.2	21.8	3.44
4	48.0	30.5	3.17

Giving a mean Young's modulus of 3.15 GPa, which will be used during the calculations and simulations of the tower.

14.2 Free Decay

When doing the free decay test, the tower is given a known initial displacement and is then released. The response is measured at the middle of the nacelle, by utilizing the camera system OptiTrack. From the free decay response it is possible to estimate the damped natural frequency and damping ratio in the first mode in F-A and S-S motion. Here the first natural frequency is calibrated for the new nacelle weight, the calibration is done by reducing the length of the tower.

14.2.1 Theory

The equation of motion for the system, when only considering a single DOF, is a mass-spring-damper system with no external force applied to the system

$$m\ddot{x}(t) + c\dot{x}(t) + kx(t) = 0 \tag{14.2}$$

As for the TLP, see chapter 10, only the solution for undercritically damped systems will be considered, and thus the solution will be

$$x(t) = \exp(-\zeta\omega_0 t)\left(x_0\cos(\omega_d t) + \frac{\dot{x_0} + \zeta\omega_0 x_0}{\omega_d}\sin(\omega_d t)\right) \tag{14.3}$$

When measuring the displacement of the tower in time, it will show that the tower oscillates but the amplitudes of the motion decrease as time passes. In the same way as for the TLP an experimental way of determining the damping ratio is found as

$$\zeta = \frac{\ln\left(\frac{a_n}{a_{n+1}}\right)}{\sqrt{4\pi^2 + \ln\left(\frac{a_n}{a_{n+1}}\right)^2}} \tag{14.4}$$

which can be used to determine the damping in the system.

14.2.2 Results

The natural frequency of the tower has to be reconsidered as the original nacelle for the tower was an Airbreeze with a mass of 8.16 kg, while the new nacelle has a mass of 12.0 kg, thus meaning that the natural frequency has changed. The natural frequency for the original 2.02 m tower is tested when the tower with nacelle is fixed on the ground, as the first natural frequency of the tower of the NREL wind turbine is determined with similar BCs. The displacement of the top is measured using the camera system OptiTrack and then displacing the top of the tower and letting the tower oscillate freely. The displacement of the top can be seen in fig. 14.1.

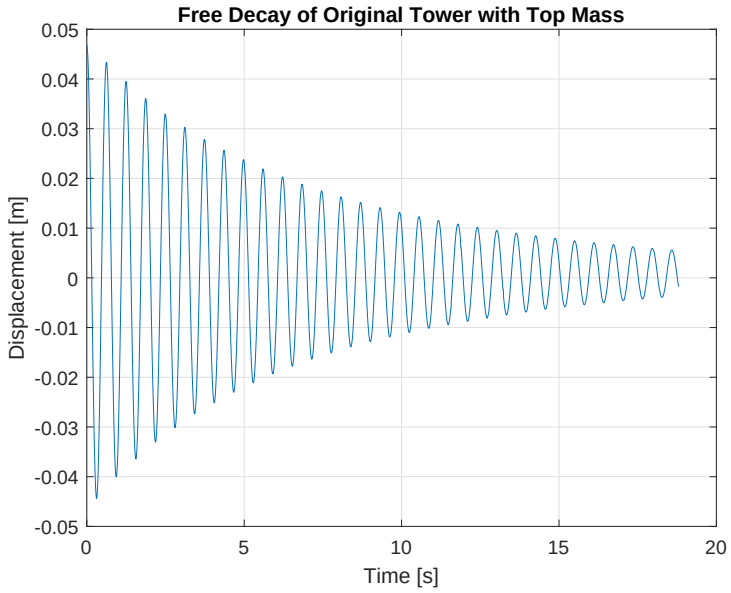

Figure 14.1: F-A free decay of original tower with top mass.

From the data the damped natural frequency can be calculated by using the period from one top to the next top and taking the inverse. From here it can be seen that the natural frequency is 1.61 Hz. If calculating the natural frequency with the FEM code the natural frequency is found to be 1.60 Hz. Since the natural frequency should be a scaled parameter from the 5 MW NREL wind turbine, the tower length has to be changed in order to re-establish this parameter. The unscaled natural frequency of the 5 MW NREL tower with top mass is 0.32 Hz [28], meaning that the natural frequency of the scaled model should be 1.89 Hz. When calculating the natural frequency using the MATLAB code of the FEM, seen in appendix A.11.6, a natural frequency of 1.90 Hz is obtained by reducing the tower height by 21.5 cm. The tower was cut by 21.5 cm and the natural frequency was again tested, and this was now found to be 1.90 Hz, while the damping ratio is found to be 1.3 %. The damping ratios found for one experiment are seen in fig. 14.2.

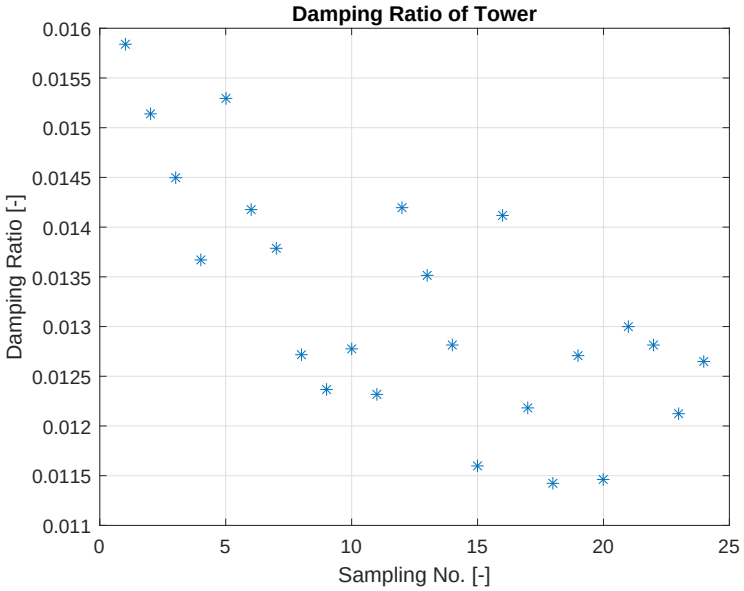

Figure 14.2: The damping ratios in F-A for one experiment.

A S-S free decay of the wind turbine was also made in order to investigate if the FEM code estimates this frequency correctly. The natural frequency was found to be 1.92 Hz in the experiments and is calculated using FEM to be 1.9 Hz.

The experimental and the F-A free decay simulated in FAST and in Simulink are all shown in fig. 14.3.

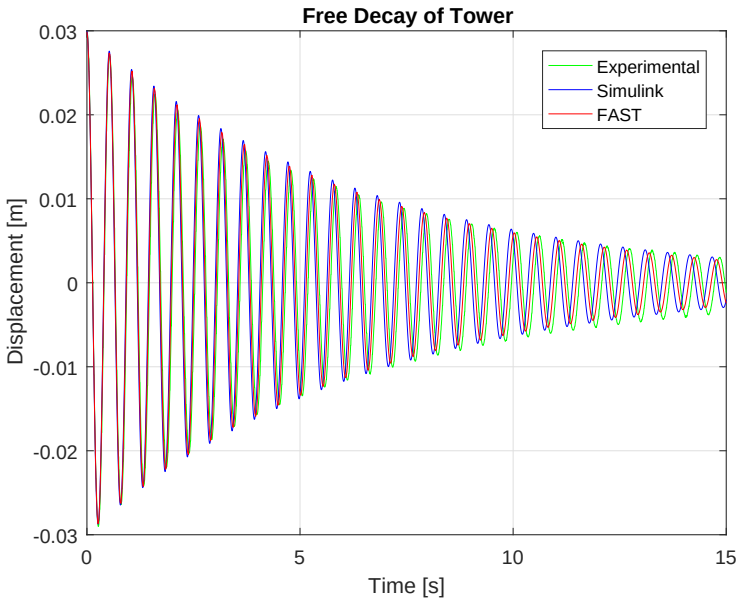

Figure 14.3: The experimental free decay in F-A together with the two simulated free decays.

As seen the simulated free decay responses fit well with the experimental response. The frequency for both simulated responses are slightly higher than the experimental, while the amplitudes fit as well as possible taking the resolution of the camera system OptiTrack into account.

14.3 Impulse Excitation

A hammer test was made in order to investigate the impulse excitation of the tower with the nacelle. When hitting the structure with an impulse excitation e.g. a hammer blow, the tower will be excited in a range of frequencies. The excitation accelerations can be measured by the accelerometer located along the tower. By doing a Fourier transformation of the measurements, it is possible to determine some of the damped natural frequencies. Here the tower is fixed on a stationary ground so the natural frequencies of the tower is not coupled with the floating foundation. The impact of the coupling is investigated further in section 29.5.

14.3.1 Theory

There are two ways to conduct a hammer test, one where a series of small impulses are applied to the structure, while the other approach is to mathematically repeat the measurement from one impulse excitation and thus consider it as a periodic signal.
In the first approach a time convolution integral is needed, as the system will remember the previous impulses before a new one is applied and this will affect the response.
In the latter approach only a single impulse is applied to the structure and the signal has to decay

completely before it is repeated mathematically, and thus a time series of impulses is created. From this time series of data it is possible to make a Fourier transform and thus possible to investigate the natural frequencies of the structure.
The definition of an impulse is to apply a force to the structure during a very short timespan, the governing equation of motion can be written as

$$m\ddot{x}(t) + c\dot{x}(t) + kx(t) = f_{\text{ext}}(t) \tag{14.5}$$

which can be rearranged in order to have the internal and external forces on the same side

$$m\ddot{x}(t) = f_{\text{ext}}(t) - c\dot{x}(t) - kx(t) \tag{14.6}$$

where the internal forces are from the damping and stiffness. By integrating both sides of eq. 14.6, from t_1 to t_2 the following equation is found

$$\int_{t_1}^{t_2} m\ddot{x}(t)\,dt = \int_{t_1}^{t_2} \left(f_{\text{ext}}(t) - c\dot{x}(t) - kx(t)\right) dt \tag{14.7}$$

By investigating the left side of the equation it is seen that a change in velocity is caused by an impulse

$$m\dot{x}(t_2) - m\dot{x}(t_1) = m\Delta\dot{x} = I \tag{14.8}$$

where I is the impulse function. Thus the impulse must be caused by the internal and external forces not being in equilibrium, leading to a change in momentum. As the time increment of the impulse is very short it can be considered that $\Delta t \to 0$, and thus t_2 can be considered as $t_2 = t_1 + \Delta t$. In this timespan there is not enough time for the structure to move, and only a change in the velocity will occur. This means that the impulse will neither relate to the damping nor the stiffness of the system, and can thus be found as

$$I = \lim_{\Delta t \to 0} \int_{t_1}^{t_2} \left(f(\tau) - c\dot{x}(\tau) - kx(\tau)\right) d\tau = \int_{t_1}^{t_2} f(\tau)\,d\tau \tag{14.9}$$

Thus it can be seen that the new velocity of the system can be found if the amplitude of the impulse is known

$$m\dot{x}(t_2) - m\dot{x}(t_1) = I \Leftrightarrow \dot{x}(t_2) = \dot{x}(t_1) + \frac{I}{m} \tag{14.10}$$

If an impact hammer with a built in force transducer is applied the damping ratio of the specific eigenmode could have been found using the half power method. But this method requires that the force is known in order to know the amplitude of the peaks in the FFT. It will therefore not be used as there is no impact hammer available to the authors. Therefore only the damped natural frequencies of the structure will be found using this method. The advantage of this method compared to a

forced harmonic excitation, is that a higher range of excitation frequencies can be applied to the structure. Furthermore the wave generator is not able to produce wave frequencies above 2 Hz, and if using the wave generator to excite the tower, it would have to be mounted on the TLP, thereby the coupled effect will be included in the response.

14.3.2 Results

The 3-axis accelerometer used is from Vernier and of type 3D-BTA. It is used together with LABQUEST Mini data acquisition board and with a sampling frequency of 400 Hz. The accelerometer was placed at three different locations along the tower and then five separate impulses were applied to the tower for each of the locations of the accelerometer. This means that different eigenmodes will be excited depending on the location of the impulse, while the location of the accelerometer determines which of the excited eigenmodes are possible to detect. The first eigenmode is easiest to detect if the accelerometer is placed in top of the tower, and the impulse is applied in top of the tower, as well. This can be seen if investigating the eigenmodes in fig. 13.7. The experimental results of these conditions are seen in fig. 14.4.

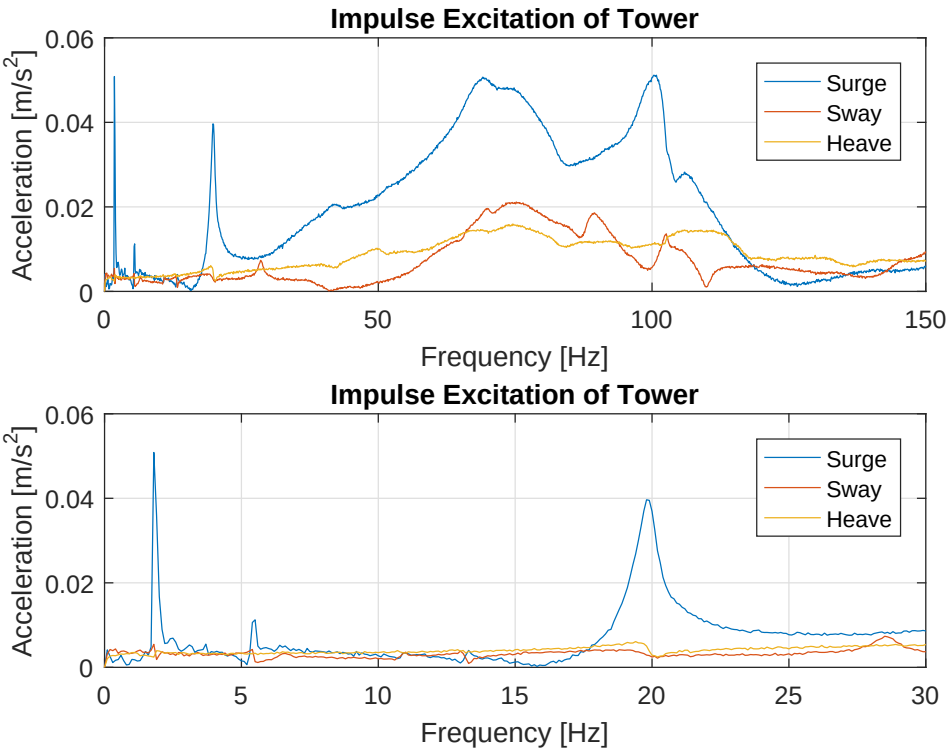

Figure 14.4: The frequencies of the tower, when impulse is applied in top of the tower.

As seen the largest response is in the surge direction, as this was the directions of the applied impulse. This also means that the eigenmodes in sway and heave are not detectable for this experiment, as they were not excited by the impulse. It can be seen there is a natural frequency at 1.80 Hz, according to table 13.1 this is around the first natural frequency of 1.90 Hz. The next peak is located at 19.8 Hz, and if investigating the calculated eigenmodes and natural frequencies, this will correspond to the second eigenmode in surge at 17.12 Hz. The next significant peaks seem to be more indistinct, and no exact natural frequencies can be determined from the rest of the response. But the first and second natural frequencies are close to the calculated frequencies.

For investigating the higher frequencies, the accelerometer is placed 0.6 m above ground, and the impulse is applied at a height of 1.2 m.

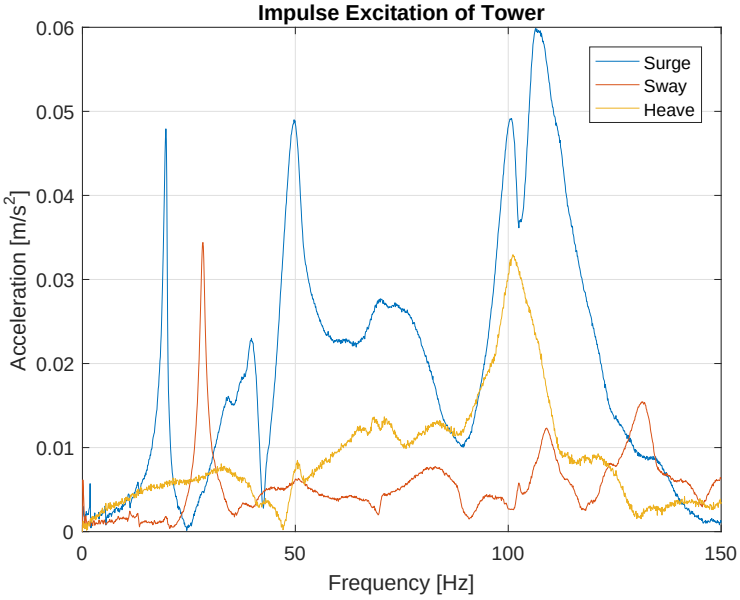

Figure 14.5: The frequencies of the tower, when impulse is applied at a height of 1.2 m.

In the fig. 14.5 it is seen that the second frequency again is found to be just beneath 20 Hz. Furthermore, it is now possible to determine the third natural frequency at 49.7 Hz which was calculated to be 50.58 Hz. The next high peaks are around and above 100 Hz, and are not very distinctive, meaning it is hard to determine a natural frequency from this. The experimentally found natural frequencies are seen in table 14.2 together with the corresponding calculated natural frequencies.

Table 14.2: Experimentally found and calculated natural frequencies.

Mode no.	Experimental frequency [Hz]	Calculated frequency [Hz]
1	1.80	1.90
5	19.8	17.12
7	49.7	50.58

14.4 Stiffness of Tower

In this experiment a linear relationship between the deflection and the force applied to the tower top in the surge direction is investigated, when the tower is fixed on ground.
This will be used to compare the stiffness when the tower is mounted on the TLP, as it is expected that the tower will become more soft, when coupled, see section 29.1. Here only the surge direction is investigated.

14.4.1 Theory

The linear relationship between the deflection of the tower and the force applied can be found using Hooke's law

$$F = kx \tag{14.11}$$

where F is the force applied by the wind, k is the stiffness of the tower and x is the displacement of the tower due to the force applied.

14.4.2 Results

The results of the tests are seen in the figure.

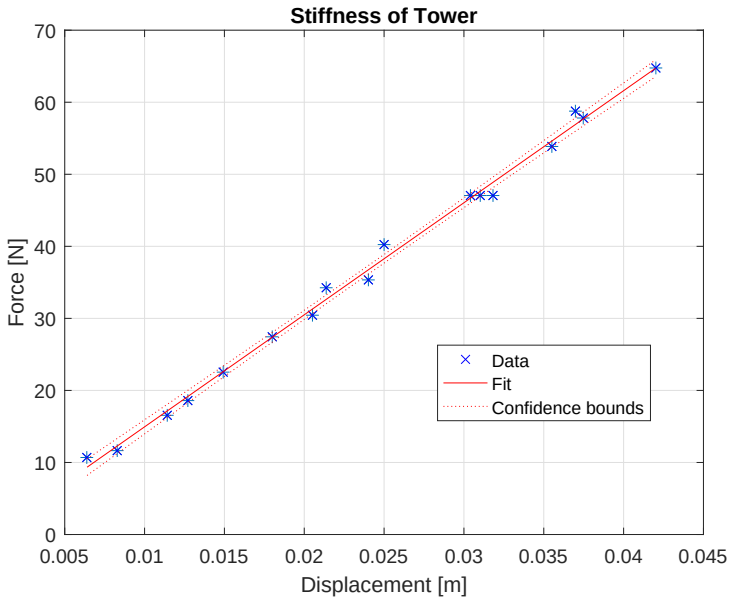

Figure 14.6: Graph showing the results of the stiffness test.

It is linear as expected, and when fitting a linear model to the data points, a stiffness of 1555.3 N/m is found. The red line is the fitted model, while the dotted lines are the 95 % confidence intervals of the fit. The confidence interval is between 1499.8 N/m and 1610.9 N/m.

Conclusion 15

In this part the structure of the FEM code for the tower with top mass was described. The mass matrix was taken as half lumped and half consistent. The damping was modelled using Rayleigh damping and the coefficients were found by the use of a free decay, where it was found that the tower has a damping ratio of 1.3 % and the damped natural frequency was found to be 1.90 Hz. A convergence analysis for the FEM model was made, and it showed that 20 elements were sufficient to model the tower. From this FEM code, the theoretical eigenmodes and natural frequencies of the tower were found. The first natural frequency in surge/pitch direction was found to be 1.90 Hz, while the second was found to be 17.12 Hz.
The chapter last chapter deals with test and validation of the tower. In this chapter Young's modulus of the tower was found to be 3.15 GPa, while the damping and damped natural frequency were found to be 1.3 % and 1.9 Hz, respectively. Furthermore the frequency response of the tower was investigated, this in order to find the higher natural frequencies, and thereby validate the code for these frequencies. The second natural frequency was found to be 19.8 Hz, while the third natural frequency was found to be 49.7 Hz, both fitted well with the calculated natural frequencies. At last the stiffness of the tower was found, this in order to investigate the difference of the stiffness when the tower is fixed to when the tower is mounted on the TLP in later parts.

Part IV

Aerodynamic Model

Symbol	Description	Units
α	Angle of attack	rad
β	Pitch angle	rad
Δt	Time step	s
θ	Blade twist angle	rad
θ_p	Centre to blade point angle	rad
θ_{rand}	Random phase angle	rad
ρ_{air}	Air density	kg/m^3
σ	Solidity	-
τ_{kf}	Flow time constant	-
τ_1,τ_2	Filter time constants for dynamic wake model	-
ϕ	Flow angle	rad
Φ_n	Phase angle	rad
ψ	Azimuthal blade angle	rad
ω_n	Phase angular frequency	rad/s
ω_r	Rotor angular frequency	rad/s
a	Axial induction factor	-
a'	Tangential induction factor	-
a_0	Fourier coefficient	-
a_c	Axial induction factor limit	-
a_n, b_n	Fourier coefficients	-
c	Chord length	m
c_d	Drag coefficient	-
c_l	Lift coefficient	-
$c_{l,inv}$	Inviscid Lift coefficient	-
$c_{l,ds}$	Fully separated lift coefficient	-
$c_{l,dyn}$	Dynamic lift coefficient	-
$c_{l,stat}$	Static lift coefficient	-
C_n	Normal force coefficient	-
C_t	Tangential force coefficient	-
Coh_{jk}	Coherence function between point j and k	-
dF_d	Sectional drag force	N
dF_l	Sectional lift force	N
dF_n	Sectional normal force	N
dF_t	Sectional Tangential force	N
dr	Blade spanwise width	m
dP_r	Sectional power	W
dp	Distance to point from tower centre	m
dT_r	Sectional torque	N/m
f	Prandtl's tip/hub coefficient	-
f_n	Phase frequency	Hz
f_{fan}	Fans rotational frequency	Hz
fs	Separation function	-
F	Prandtl's tip/hub factor	-
$\mathbf{H}_m$	Weighting matrix	-
k	Step number	-
k_{tf}	Flow time constant	-

K	Glauert's correction coefficient	-
l_{rt}	Distance between rotor and tower	m
M_{Pitch}	Pitch moment around nacelle	N/m
M_{Yaw}	Yaw moment around nacelle	N/m
n	Frequency step number	-
np	Number of points in mesh	-
nf	Number of Frequencies	-
nt	Number of time steps	-
N	Number of Frequencies	-
N_B	Blade number	-
N_s	Blade section number	-
P_r	Rotor power	W
PSD	Power spectral density function	m^2/s
PSD_x	Power spectral density at x fan frequency	m^2/s
r	Radius to from centre of hub to blade section	m
r_t	Radius of tower	m
R	Rotor radius	m
R_{hub}	Radius of hub	m
S_j	Power spectrum density at point j	m^2/s
S_k	Power spectrum density at point k	m^2/s
$\mathbf{S}_{jk}$	Cross Power spectrum density between point j and k	m^2/s
$\mathbf{S}_m$	Spectral matrix	m^2/s
t	time	s
T_r	Rotor Torque	N/m
u	Wind speed	m/s
$\bar{u}$	Mean wind speed	m/s
$\mathbf{U}_0$	Free stream wind speed matrix for all points	m/s
$\mathbf{V}$	Velocity fourier coeffcient matrix	-
$\mathbf{V}_B$	Velocity vector of blade	m/s
$\mathbf{V}_T$	Velocity vector of tower	m/s
$\mathbf{V}_{Rel}$	Relative Velocity vector for blade	m/s
$\mathbf{V}_{TLP}$	Velocity vector of TLP	m/s
V_r	Radial wind speed	m/s
V_y,V_x	Wind speed in y-direction and x-direction and	m/s
V_θ	Tangential wind speed	m/s
$\mathbf{V}_0$	Free stream wind speed vector for blade	m/s
w	Weighting function	-
$\mathbf{W}$	Induced velocity vector	m/s
$\mathbf{W}_{int}$	Intermediate induced velocity vector	m/s
$\mathbf{W}_{qs}$	Quasi-steady induced velocity vector	m/s
(x_1,y_1,z_1)	Sub-system 1 coordinates	m
(x_2,y_2,z_2)	Sub-system 2 coordinates	m
(x_3,y_3,z_3)	Sub-system 3 coordinates	m
(x_4,y_4,z_4)	Sub-system 4 coordinates	m
$\mathbf{X}_{jk}$	White noise matrix	-
$\mathbf{1}$	Vector of ones	-

16 Introduction

During operation the rotor of the wind turbine will introduce time varying loads into the system, and it is therefore necessary to model these. The loads on the rotor are dependent on the current wind speed, which is not uniform over the whole rotor area, therefore this have to be modelled. The theory of modelling the time-varying loads on the blades used, is UBEM. At last the aerodynamics of the blades are tested for different conditions in order to validate their performance and validate the UBEM model.

Wind Modelling 17

In this chapter first the wind conditions for an offshore and for the laboratory wind turbine are explained. Thereafter the representations of long term and short term wind conditions are outlined. At last the simulation of a single point wind speed and a wind field consisting of multiple points are explained.

17.1 Wind Conditions

The wind conditions for a wind turbine operating offshore compared to the wind facilities available in the laboratory are different. The wind facilities available for this thesis were explained in section 5.3. In this section the most influencing variations in the wind are described for both real wind turbines and the test facilities.

17.1.1 Real Wind Turbine Wind Conditions

Real wind turbine structures often experience a varying mean wind speed along the tower, this is called wind shear. The wind speed profile variation is dependent on the terrain conditions and atmospheric stability conditions. These conditions are at sea often idealised such that different empirical models approximate the wind speed profile. The wind speed profile can be approximated by different models, but for offshore locations DNV-RP-C205 recommends the usage of the Frøya wind speed profile, unless site-specific data indicate otherwise [46]. The wind shear will affect the wind turbine as the wind speed will vary in the vertical direction, so the blade will experience different velocities, and therefore the forces on the blade will depend on the azimuthal position of the rotor.
A wind turbine will experience wind directions changing over time, therefore the nacelle should be able to rotate in yaw, such that the rotor is aligned with the incoming wind field. If this is not done, it will cause the wake to be skewed, which will result in one side of the rotor operating partly in the wake. The misalignment of the wind inflow will cause the two sides of the rotor to have different aerodynamic performance and loads.
The mean wind speed at a single location will change over time due to the atmospheric conditions. The change of the atmospheric conditions are due to numerous sources. The modelling of the mean wind speed is often done by a Weibull distribution [46].
The mean wind speed at a location is not the instantaneous wind speed which the blades will experience, as the mean wind speed will have perturbations, which are known as turbulence. The turbulence affecting a wind turbine is due to numerous sources e.g the changing atmospheric conditions and the wind shear. The turbulent wind field will have large and small scale vortex structures, these will cause fluctuations which have different time scales. This means that the rotor will experience a time varying wind speed, which means that the aerodynamic loads will also be

time varying. The turbulence for a wind field is represented by a PSD and coherence functions. Different models exist for the PSD function and coherence functions, those recommended for offshore conditions can be seen in DNV-RP-C205 [46].
The wind turbine can also be affected by transient wind conditions, these may occur during changes of the wind speed or direction. There are different transient wind conditions, examples could be gust, squalls, extreme changes in wind direction etc. These transient wind loading conditions can introduce large aerodynamic loads on the wind turbine. The transient wind conditions can be modelled by different models, these can be seen in [80].

17.1.2 Experimental Wind Turbine Wind Conditions

The experimental model of the wind turbine will experience wind generated from the wind generator. The wind generator was described in section 5.3 and the generated wind field was analysed in section 5.3.3.2. The generated wind field is not able to generate a wind shear, but it seems to have a slightly higher mean wind speed in the centre than in the sides. The direction of the wind is always normal to the rotor plane, as the wind generator setup is not able to rotate.
The mean wind speed of the wind generator is changed manually by changing the rotational velocity of the fans on the adjustable frequency drive. The turbulence of the wind can be adjusted by changing the wind filter setup, the structure of the eddies in the wind field is not analysed. The turbulence intensities and wind speeds at different wind filter setups are seen in fig. 5.5 and 5.6. The PSD and coherence functions for the wind field are explained further in section 19.1.
The wind generator is furthermore not able to generate any transient wind conditions.

17.2 Representation of Stationary Wind Conditions

To describe the short and long term wind conditions the wind speed statistics are to be used. The short term wind conditions describe the wind speed fluctuations up to 10 minutes. The long term wind conditions refer to change in mean wind speeds and are up to 10 years or more.

17.2.1 Long Term Representation

The long term wind conditions are described by a probability distribution for the 10 minute mean wind speed, U_{10}. This probability distribution can be found from available site specific wind data. To represent the 10 minute mean wind speed, a generic distribution can be used. The most widely used is the Weibull distribution [46], which can represent the 10 minute mean wind speed at a given height above ground. In order to describe the 10 minute mean wind speed at all heights a wind speed profile can be used.
The fluctuation in the wind speed in the short term representation is known as turbulence. The turbulence is characterised by the standard deviation, σ_U, which is conditioned on the 10 minute mean wind speed. The standard deviation condition on the 10 minute mean wind speed can often be represented by a lognormal distribution.

17.2.2 Short Term Representation

In a short term wind period at an offshore location, the instantaneous wind speed can be represented as a Gaussian process, which is conditioned on the 10 minute mean wind speed and the standard deviation of it. In order to model the short term wind conditions a wind spectrum can be utilized, the most widely model used is the PSD. The PSD can be used to represent the amount of energy in the turbulence distributed over a range of frequencies.

The PSD can be found from site specific data, but often for offshore wind conditions, an empirical model spectrum can be used, unless the data of the site indicate otherwise [46]. But in order to determine the wind field in this thesis, data have to be utilized, these data can be seen in section 5.3.3.2. There exist several wind spectrum models e.g. Davenport, Frøya and Kaimall. It is therefore often required to have site specific data to determine the most appropriate spectrum [46]. In order to simulate the wind speeds at more points in space, a correlation between the wind speed points must be established. To express the spatial connectivity between two points of the wind speed, a coherence spectrum can be used. The coherence spectrum describes the correlation of the PSD of two separated points at a specific frequency. To represent the coherence spectrum, either site specific data or a model coherence spectrum must be used. Several models for coherence spectra exist such as e.g. exponential IEC, Frøya and Von Karman.

17.3 Wind Simulation

In order to simulate the time history of the wind, it is necessary to know the wind conditions. The wind conditions which will be used in this simulation will be those for the test facilities.
This section will first consider the theory for generation of a wind speed time series in a single point. This process will be expanded such that a correlated wind speed time series in multiple points can be generated. The kind of wind simulation approach is formulated by M. Hansen [81].

17.3.1 Single Point 1D Wind Simulation

The generation of a wind speed time series at a single point can be accomplished by doing an inverse DFT on the pre-described PSD function. The inverse DFT of the PSD function will result in a Fourier series, as seen in eq. 17.1, which should satisfy the used PSD function

$$u(t) = a_0 + \sum_{n=1}^{N/2} a_n \cos(\omega_n t) + b_n \sin(\omega_n t) \tag{17.1}$$

where $u(t)$ is the wind speed, and a_n and b_n are the Fourier coefficients. By rearranging of eq. 17.1 and realizing that a_0 is the mean wind speed $\bar{u}$, the equation for time varying wind speed can be found as

$$u(t) = \bar{u} + \sum_{n=1}^{N/2} \sqrt{a_n^2 + b_n^2} \cos(\omega_n t + \phi_n) \tag{17.2}$$

where ϕ_n is the phase angle at a specific frequency, ω_n. The angle, ϕ_n, is not represented in the PSD, therefore it has to be modelled by a random number drawn from a standard uniform distribution, which generates values between 0 and 2π at each time step.
By using the PSD instead of the Fourier coefficients, the obtained Fourier transform can be rewritten into a Fourier transform which matches the PSD

$$u(t) = \bar{u} + \sum_{n=1}^{N/2} \sqrt{\frac{2PSD(f_n)}{T}} \cos(\omega_n t + \phi_n) \tag{17.3}$$

$$t = k\Delta t \text{ for } k = 1, 2, .., N$$

By using this approach a 1D wind speed at a single point can be generated. To implement analytical PSD functions, a scaling has to be introduced as these PSD functions are continuous, meaning that all frequencies between 0 to ∞ are present.

But as the rotor of the wind turbine is large, a varying wind field will be present across the rotor, therefore a representative 3D wind field has to formulated.

17.3.2 Multiple Point 3D Wind Simulation

To generate the 3D wind field the method presented by Veers [82] is chosen due to its simple structure, other models such as Mann [83] is also widely used. Veers' method generates a 3D wind field from a pre-described PSD function and coherence function. The dependency between two points are to be described by a coherence function, therefore it must take the distance between the points into account, but also the energy contained in each frequency is taken into account. The reason for the frequency dependency is that the spatial variation is depending on the type of vortices present. Low frequencies are related to large-scale vortices, which cover a large volume and therefore give rise to large spatial variation. While high frequencies related to small-scale vortices cover a small volume, and therefore give rise to a small spatial variation.
The coherence function is often modelled as an exponential decay, the coherence model for the test facility was not found due to lack of experimental equipment. The coherence could have been found by measuring the wind speed simultaneous at multiple points. To describe the 3D wind field at N multiple points, a PSD at each point must be described, these PSDs are found in section 19.1.2.
The first step in generating the 3D wind field time series is to set up the points for the wind speed calculation. These are set up in a circular pattern with the same radius as the rotor. There will be 20 points on a line along the blade, and eight lines in the rotor plane will be calculated. The pattern is visualised in fig. 17.1.

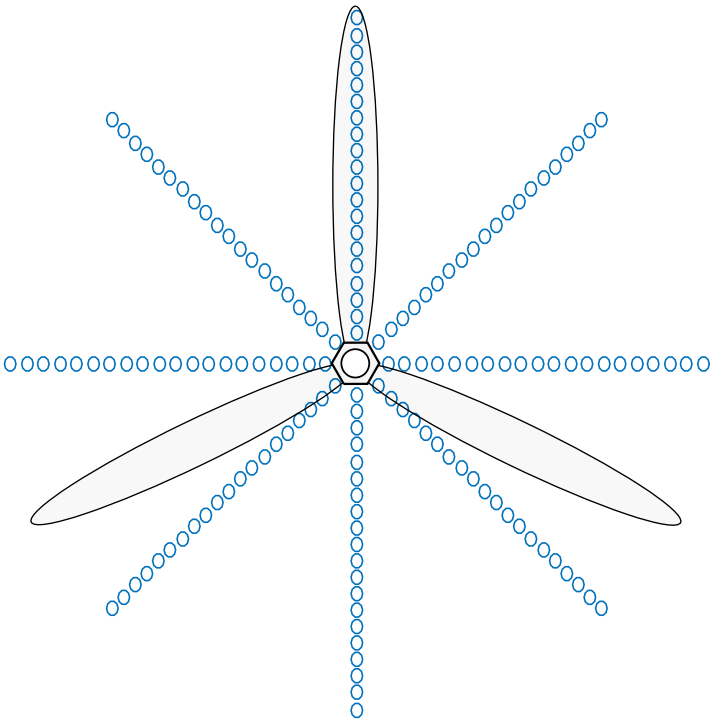

Figure 17.1: The pattern of the points for wind speed calculation.

Between the points the magnitude of the cross spectrum density must be calculated by the usage of the coherence function and the PSD for each point

$$\left|S_{jk}(f_n)\right| = Coh_{jk}(f_n)\sqrt{S_j(f_n)S_k(f_n)} \tag{17.4}$$

where $S_j(f_n)$ and $S_k(f_n)$ are the value of the PSDs at the two points j and k at a specific frequency, and Coh_{jk} is the coherence function between the two points.
There exist multiple coherence functions, a possible choice for the coherence function is given in the standard DS 472 [84] for wind turbine constructions, and will be used in this thesis. The coherence function is given as

$$Coh_{jk}(f_n) = \exp\left(-12\left(\frac{f_n L_{jk}}{\bar{u}}\right)\right) \tag{17.5}$$

where L_{jk} is the distance between the two points considered.
It can be assumed that there will be no phase difference between the points, thereby the imaginary parts of the cross spectral densities will be zero. By combining the cross spectrum densities and the PSD in a matrix, the spectral matrix $\mathbf{S}_m \in \mathbb{R}^{npxnp}$ can be obtained, where np is the number of points. The spectral matrix elements are created by

$$S_{m,jk}(f_n) = \begin{cases} S_{jk}(f_n) = S_j(f_n) & \text{for } j = k \\ S_{jk}(f_n) = |S_{jk}(f_n)| & \text{for } j \neq k \end{cases} \tag{17.6}$$

By using Cholesky decomposition on the spectral matrix, it can be factorized into a lower triangular matrix, $\mathbf{H}_m$, and its transpose

$$\mathbf{S}_m(f_n) = \mathbf{H}_m(f_n)\mathbf{H}_m(f_n)^T \tag{17.7}$$

The matrix $\mathbf{H}_m \in \mathbb{R}^{np\times np}$ is a weighting matrix for the independent unit magnitude white noise input matrix, $\mathbf{X} \in \mathbb{R}^{np\times nt}$, where nt is the number of time steps, such that the correct spectral matrix will be obtained.
The unit magnitude white noise input matrix is generated as a diagonal matrix

$$X_{jk} = \begin{cases} \exp(i\theta_{rand}) & \text{for } j = k \\ 0 & \text{for } j \neq k \end{cases} \tag{17.8}$$

where θ_{rand} is a uniformly distributed random variable, which is in the interval from 0 to 2 π.
The complex Fourier coefficients for the simulated wind speed can be found by

$$\mathbf{V}(f_n) = \mathbf{H}_m(f_n)\mathbf{X}\mathbf{1} \tag{17.9}$$

where $\mathbf{1} \in \mathbb{R}^{np\times 1}$ is a vector of ones. By taking the inverse Fourier transform of each element in $\mathbf{V}$ $\in \mathbb{R}^{np\times nt}$ the time series of wind speed at each point can be obtained.

Aerodynamic Theory 18

The theory regarding the aerodynamics of wind turbines is mainly by M. Hansen from [81]. The SBEM is adequate for estimation of the long term energy production of a wind turbine at a specific site with a known wind distribution. It is therefore not appropriate to use for estimation of transient rotor loading. But the SBEM can be modified into the UBEM, which is a better description of the unsteady flow around a wind turbine. The unsteady flow around a FOWT is caused by different factors. The factors taken into account in this thesis are the unsteady wind field with turbulence, an uneven wind field, the movement of the TLP in surge, and the translational velocity of the tower. The structural dynamics of the blade are not taken into account, as this is assumed to be small compared to the surge motion. For the UBEM some unsteady dynamic models are applied, these are a dynamic stall model, a dynamic inflow model and a tower-interference model. These are described in the subsequent sections.

18.1 Coordinate System

The coordinate system of the FOWT can be split into four separate coordinate sub-systems, these are abbreviated to as sub-systems and their directions are referred to by subscripts indexes 1 to 4. These sub-systems are visualized for the FOWT in fig. 18.1.

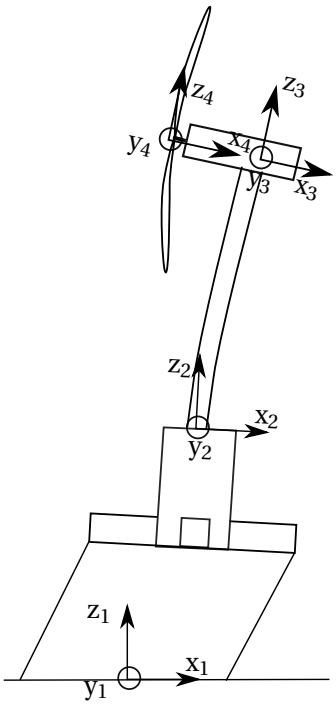

Figure 18.1: The coordinate systems for the FOWT.

The relative wind velocity a blade experiences is a combination of the free wind speed and the dynamics of the FOWT. For the evaluation of relative wind velocity, the coordinate systems of the different components must be combined through transformation matrices. The inertial coordinate system is sub-system 1, this is fixed at the bottom of the wave tank. Sub-system 2 is fixed at the top of the TLP, sub-system 3 is fixed at the tower top and sub-system 4 is placed in the hub.
The TLP motion and hydrodynamic forces will be formulated in sub-system 2. The azimuthal motion of the blades and their aerodynamic forces will be formulated in sub-system 4.
From the fixed sub-system 1 to the sub-system 2 of the platform, the rotation in pitch and the movements in heave and surge should be taken into account. From sub-system 2 to sub-system 3 of the nacelle, the tower pitch angle taken into account. From sub-system 3 to sub-system 4 the azimuthal positions of the rotor is taken into account. The transformation between the coordinate systems must be derived in order to relate one sub-system to another.

18.1.1 Aerodynamic Transformation

Due to the structural dynamics of the tower and blades and the dynamical motion of the TLP, it is not only the free stream wind velocity which has to be taken into account. In order to account for the velocities from the different sub-systems, a transformation into sub-system 4 must be done. The dynamics of each subsystem is evaluated in their own sub-system and thereafter transferred to sub-system 4. The velocities in the blade sub-system is visualized by the velocity triangle for an airfoil section of the blade in fig. 18.2.

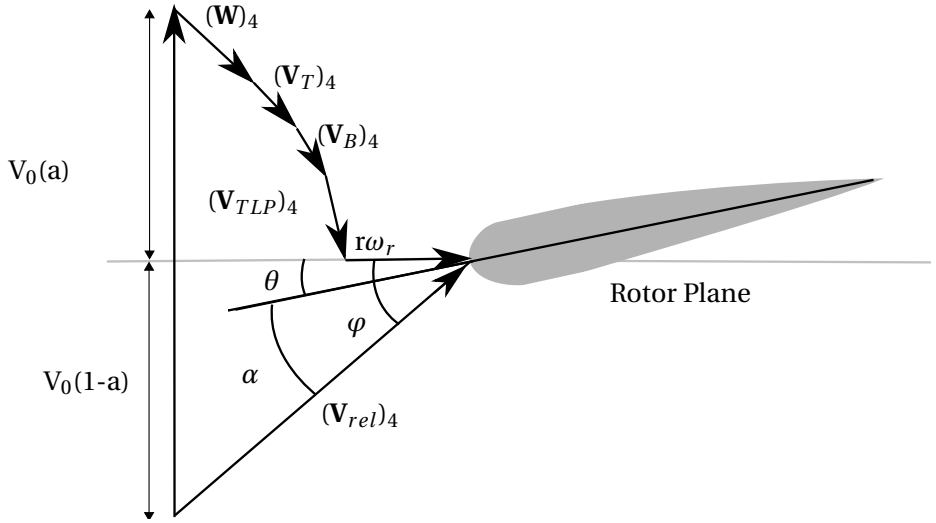

Figure 18.2: An airfoils velocity triangle for FOWT.

In this thesis the influence of the blade dynamics on the relative wind velocity experienced by the blades are not considered, as this is deemed to have a minor influence. The influence of the tower dynamics on the relative wind velocity is taken into account but only considering it to have a translational velocity. The pitch angle of the tower will have an effect by changing the rotor plane angle, and thereby changing the angle of attack (AOA) of the blades, which is not taken into account in this thesis. The influence from the dynamics of the TLP on the relative wind speed, will only be from the translational velocity in surge. The relative wind speed which the blades experience can be

described by the different components transformed into the sub-system of the hub

$$(\mathbf{V}_{rel})_4 = (\mathbf{V}_0)_4 + (\mathbf{V}_T)_4 + (\mathbf{V}_{TLP})_4 + (\mathbf{W})_4 \tag{18.1}$$

where the subscript 4 indicates that the velocity has been transformed to sub-coordinate system 4. $\mathbf{V}_0 \in \mathbb{R}^3$ is the free stream velocity, $\mathbf{V}_{rel} \in \mathbb{R}^3$ is the relative velocity which the blades experience, $\mathbf{V}_T \in \mathbb{R}^3$ is the translational velocity of the tower and $\boldsymbol{V}_{TLP} \in \mathbb{R}^3$ is the translational velocity of the TLP. $\mathbf{W} \in \mathbb{R}^3$ is the induced wind velocity the blades experience, this is often described by the axial induction factor given in eq. 18.2.

18.2 Blade Element Method

The blade element method is a combination of two theories; the 2D blade element theory and the 1D momentum theory.
In the 2D blade element theory the blade is divided into a number of sections spanwise, and it is assumed that one section does not depend on the next, meaning that the forces applied to one section cannot be felt by the other sections. The forces of each of the sections along the blade are calculated, and at last summed up along the blade in order to calculate the total force experienced by the blade.
In the 1D momentum theory the loss of momentum in the wind is caused by the work done by the wind on the blades. Using this theory the velocity of the wind flow can be calculated right before and after the plane of the rotor. The rotor plane is discretized into annular elements, for which the forces can be calculated in each annular element.
These two methods describe the same forces on the blades, and therefore these two methods can be combined in order to describe the axial and tangential induction factors. It should be noted that the force applied by the blades to the flow is constant for the whole annulus, corresponding to a wind turbine with an infinite number of blades.
The blade element theory does not hold for blades delfecting out of the rotor plane, as the theory assumes momentum balance in the plane of the rotor.
To apply the 2D aerodynamic theory, the rotation of the blades has to be taken into account, therefore the blades will generate a vortex system behind the rotor. This vortex system will have an effect on the relative wind speed which the blades experience. The vortex system induces an axial velocity component which acts opposite of the incoming wind direction, furthermore it induces a tangential velocity component which is opposite of the rotation of the rotor. The axial induction factor is found using eq. 18.2, which describes the relationship between the incoming wind speed far away and the relative wind speed the blades experience.

$$a = \frac{1}{\frac{4\sin^2(\phi)}{\sigma(r)C_n} + 1} \tag{18.2}$$

Here a is the axial induction factor, C_n is the normal force coefficient, ϕ is the flow angle, while σ is the solidity, describing the fraction the blades cover in the rotor annulus as a function of the local radius of the rotor

$$\sigma(r) = \frac{c(r)NB}{2\pi r} \tag{18.3}$$

where r is the local radius, c is the chord length and NB is the number of wind turbine blades.
The tangential induction factor, a', can be found in a similar manner as the axial induction factor

$$a' = \frac{1}{\frac{4\sin(\phi)\cos(\phi)}{\sigma(r)C_t} - 1} \tag{18.4}$$

where the C_t is the tangential force coefficient.
The normal force for each segment of the blade can be found by 2D blade element theory

$$dF_n = \frac{1}{2}\rho_{air}\frac{V_0^2(1-a)^2}{\sin^2(\phi)}c(r)C_n dr \tag{18.5}$$

where dF_n is the normal force, also known as the thrust force, applied to each segment of one blade, dr is the spanwise length of the blade segment and ρ_{air} is the density of air. The normal force coefficient for each blade segment is found using the drag and lift force. The drag and lift force can be found using 18.6 and 18.7, respectively

$$dF_d = \frac{1}{2}\rho V_{rel}^2 c(r)C_d dr \tag{18.6}$$

$$dF_l = \frac{1}{2}\rho V_{rel}^2 c(r)C_l dr \tag{18.7}$$

where F_d is the drag force, F_l is the lift force, C_d is the drag coefficient, while C_l is the lift coefficient. The drag and lift coefficients at different AOAs, for the airfoil used in this thesis can be seen in section 4.3.0.1. Four different force vectors are seen in fig. 18.3. These are the drag, lift, normal and tangential force vectors.

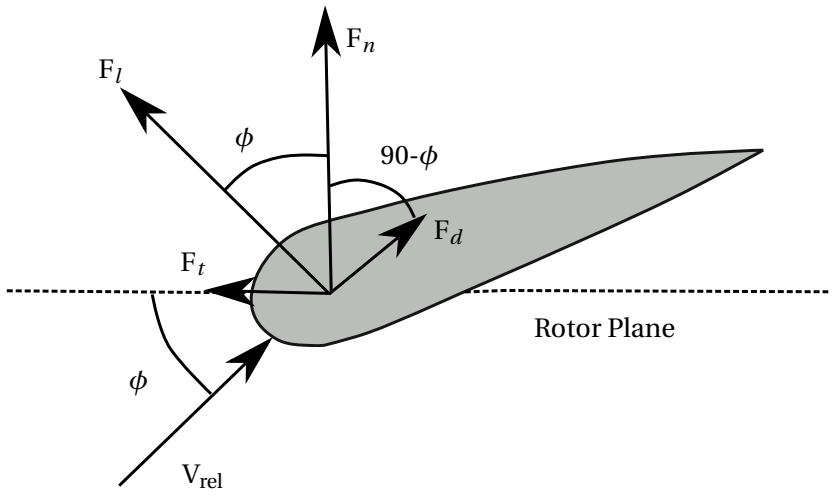

Figure 18.3: The drag, lift, tangential and normal force on a rotating airfoil section.

From the figure it can be seen that the normal and tangential forces act in these directions with respect to the rotor plane and can be found using the angle of the relative velocity and the drag and

lift forces

$$\begin{aligned} F_n &= F_l \cos(\phi) + F_d \sin(\phi) \\ F_t &= F_l \sin(\phi) - F_d \cos(\phi) \end{aligned} \tag{18.8}$$

where F_t is the tangential force.
The normal and tangential force coefficients can be found in a similar manner

$$\begin{aligned} C_n &= C_l(\alpha) \cos(\phi) + C_d(\alpha) \sin(\phi) \\ C_t &= C_l(\alpha) \sin(\phi) - C_d(\alpha) \cos(\phi) \end{aligned} \tag{18.9}$$

where α is the AOA of the blades. The lift and drag coefficients are dependent on the specific blade geometry and the AOA. These coefficients for the airfoil were explained in section 4.3.
The rotor torque is needed to calculate the power the rotor extracts, which is found by

$$P_r = \omega_r T_r \tag{18.10}$$

where P_r is the power, ω_r is the rotational speed of the rotor and T_r is the rotor torque. The torque contribution from each blade annulus at a radius, r and an annulus width of dr, can be described by 1D momentum theory

$$dT_r = 4\pi r^3 \rho_{air} V_0 \omega_r (1-a) a' dr \tag{18.11}$$

18.2.1 Correction Factors

Some of the assumptions made when using these two theories are taken care of by applying Prandtl's tip and hub loss factor to correct for the finite number of blades, generating tip and hub vortices. Also Glauert's correction for high values of the axial induction factor is used, this is used due to the breakdown of the momentum theory for high values of the axial induction factor. These are described in greater detail below.

18.2.1.1 Prandtl's Correction

Prandtl's correction is applied to account for the assumption of the blades being infinite in number. It is also called Prandtl's tip loss factor as vortices are shed from the blade tip, causing vortices in the wake of the wind turbine. The creation of vortices are most pronounced at the tip of the blade, as there is a pressure difference from the front to the back of the blade and the wind seeks the shortest way around the blade. The 2D blade theory does not take this into account as this theory does not take the finite length of the blade into account, and the 1D momentum theory assumes the rotor to be a circular disc, thus only a finite number of 3D blades are influenced by it.
The consequence of these vortices are the change of the axial, a, and tangential, a', induction

factors, which with Prandtl's correction factor changes into

$$\begin{aligned} a &= \frac{1}{\frac{4F\sin^2(\phi)}{\sigma C_n}+1} \\ a' &= \frac{1}{\frac{4F\sin(\phi)\cos(\phi)}{\sigma C_t}-1} \end{aligned} \tag{18.12}$$

where F is denoted as Prandtl's tip loss factor, which can be described by

$$\begin{aligned} F &= \frac{2}{\pi}\arccos\left(\exp(-f)\right) \\ f &= \frac{NB}{2}\frac{R-r}{r\sin(\phi)} \end{aligned} \tag{18.13}$$

where R is radius of the rotor. By using these expressions, the tip-losses can be taken into account. For the implementation of Prandtl's tip loss factor, the tip location is shifted by 1 cm in the MATLAB UBEM code, which can be found in appendix A.11.7. This is done as a singularity occurs in the expression at the tip of the blade, thereby still a small contribution for the last part of the blade is taken into account.
The hub loss is caused for similar reasons as the tip loss, namely the vortices shed from the blades near the hub of the wind turbine. The correction factor is also similar to the one used for tip losses

$$f = \frac{B}{2}\frac{r-R}{R_{hub}\sin(\phi)} \tag{18.14}$$

where R_{hub} is the radius of the hub. Again here the location of the start of the blade is shifted 1 cm in order to avoid singularity, and thereby also still take a small contribution from the first part of the blade into account. In order to correct for both tip loss and hub loss, the two corrections are multiplied into a single total loss.

18.2.1.2 Glauert's Correction

When the axial induction factor increases above approximately 0.4, the 1D momentum theory does no longer hold, as the rotor now is in the so-called turbulent wake state. This means that the flow in the far wake starts approaching the rotor again according to the momentum theory. Physically this cannot happen and in reality the flow outside the wake starts entering the wake, thus increasing the turbulence. The flow behind the rotor slows down, while the thrust force on the rotor increases.
In order to account for this change in the axial induction factor, when operating in the turbulent wake state, Glauert developed an empirical relationship between the induction factor and thrust coefficient in conjunction with the blade element theory [85] and from this, an empirical correction method was made by Wilson and Walker [86] for the thrust factor, C_T, when $a > 0.2$. The momentum method and the correction method for the thrust coefficient can be seen in the fig. 18.4.

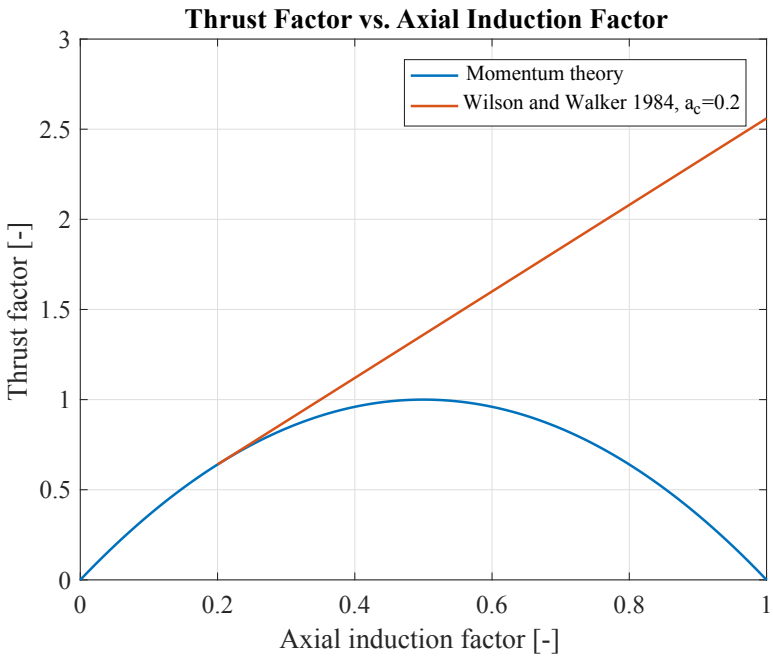

Figure 18.4: The empirical correction used for the thrust coefficient for axial induction factors above 0.2.

Glaert's correction for the axial induction factor, where tip and hub losses are included is seen below

$$a = \frac{1}{2}\left(2 + K(1-2a_c) - \sqrt{(K(1-2a_c)+2)^2 + 4\left(Ka_c^2 - 1\right)}\right) \tag{18.15}$$

$$K = \frac{4F\sin^2(\phi)}{\sigma C_n} \tag{18.16}$$

where a_c is the limit for the axial induction factor of approximately 0.2.
[86]

18.3 Unsteady Corrections Models

To describe some of the unsteady dynamics, occurring during changing operation conditions, three models are implemented. These three models are the dynamic wake model, dynamic stall model and tower shadow model, which are further described in the subsequent sections.

18.3.1 Dynamic Wake Model

During steady operation of the wind turbine, there will be a steady wake behind it. A change in operation point, by e.g. blade pitching will change the steady wake. The change between the wakes will not happen instantaneously, meaning there will be a time delay for which the wake needs to change into a new steady wake, this phenomenon is called a dynamic wake. The SBEM does not take the dynamic wake into account, and it is therefore recommended to implement a correction in order to account for the dynamic wake [87].
In this thesis the TUDK dynamic wake model from S. Øye [88] is utilized. It consists of two differential

equations: 18.17 and 18.18, acting as a filter for the induced velocities

$$\mathbf{W_{int}} + \tau_1 \frac{\mathrm{d}\mathbf{W_{int}}}{\mathrm{d}t} = \mathbf{W_{qs}} + 0.6\tau_1 \frac{\mathrm{d}\mathbf{W_{qs}}}{\mathrm{d}t} \tag{18.17}$$

$$\mathbf{W} + \tau_2 \frac{\mathrm{d}\mathbf{W}}{\mathrm{d}t} = \mathbf{W_{int}} \tag{18.18}$$

where $\mathbf{W}_{qs} \in \mathbb{R}^3$ is the quasi-steady induced velocity, which is the steady-state induced velocity occuring if the rotor does not change configuration, resulting in $\mathbf{W}_{qs} = \mathbf{W}$. $\mathbf{W}_{int} \in \mathbb{R}^3$ is an intermediate induced velocity, coupling the quasi-static induced velocity and the actual induced velocity during a change in the configuration of the wake.
The quasi-steady induced velocity can be calculated using the axial and tangential induction factors, which are calculated by usage of BEM in eq. 18.2 and eq. 18.4

$$\boldsymbol{W}_{qs} = \begin{bmatrix} aV_0 \\ (1+a')\omega_r r \\ 0 \end{bmatrix} \tag{18.19}$$

The two time constants τ_1 and τ_2 are calculated by eq. 18.20 and 18.21, which are derived from a simple vortex method, which can be seen in [88]

$$\tau_1 = \frac{1.1}{1-1.3a}\frac{R}{V_0} \tag{18.20}$$

$$\tau_2 = \tau_1\left(0.39 - 0.26\left(\frac{r}{R}\right)^2\right) \tag{18.21}$$

The dynamic filter for the induced velocity can be solved by using the assumption that the right-hand sides of eq. 18.17 and 18.18 are constants. This gives rise to the following algorithm for the dynamic wake model:

Algorithm 1 Dynamic wake algorithm

Step 1 Initialization ($k = 0$)

$$\begin{aligned} \mathbf{W}_{qs}(0) &= 0 \\ \mathbf{W}_{int}(0) &= 0 \end{aligned} \tag{18.22}$$

Step 2 Calculate the current quasi-steady induced velocity, $\mathbf{W}_{qs}(t)$, by using the axial and tangential induction factors.

Step 3 By backward difference estimate the right hand side of eq. 18.17

$$\mathbf{H(t)} = \mathbf{W}_{qs}(t) + 0.6\tau_1 \left(\frac{\mathbf{W}_{qs}(t) - \mathbf{W}_{qs}(t-\Delta t)}{\Delta t} \right) \tag{18.23}$$

Step 4 Calculate the intermediate induced velocity, $\mathbf{W}_{int}$, analytically in eq. 18.17

$$\mathbf{W}_{int}(t) = \mathbf{H(t)} + \left(\mathbf{W}_{int}(t-\Delta t) - \mathbf{W}(t) \right) \exp\left(-\frac{\Delta t}{\tau_1} \right) \tag{18.24}$$

Step 5 Calculate the actual induced velocity, $\boldsymbol{W}$, analytically in eq. 18.18

$$\mathbf{W}(t) = \mathbf{W}_{int}(t) + \left(\mathbf{W}(t-\Delta t) - \mathbf{W}_{int}(t) \right) \exp\left(-\frac{\Delta t}{\tau_2} \right) \tag{18.25}$$

By implementation of this dynamic filter for the induced velocity, the time behaviour of the loads and power can be found, when the rotor thrust is changing.

18.3.2 Dynamic Stall Model

The relative wind speed the blade experiences, can change almost constantly in the presence of gusts, blade pitching, turbulence or tower shadow, etc. But when the relative wind speed changes, a change in the AOA will follow, but this change in AOA will not affect the loads instantaneously, but rather occur with a time delay. The time delay is due to the boundary layer around the airfoil will not change instantaneously, but will take time to adapt to a change in configuration. The boundary layer around the airfoil may be attached or separated or in between.
Different models can be used to predict the performance during unsteady operations, the most common ones are Theodorsen's model for attached flow [89], Øye's model for trailing edge stall [90] and Beddos-Leishman model for attached flow and trailing edge stall[91]. It can be assumed that the most important effect for wind turbines are the trailing edge stall, when considering the dynamic airfoil data [81]. Trailing edge stall is when the flow separation will start at the trailing edge and move towards the leading edge gradually for higher AOAs. In this thesis it is therefore chosen to use the dynamic stall model made by S. Øye. This dynamic stall model considers the aerodynamic data from two extreme cases where the flow is either inviscid or fully separated and uses these to compute the lift coefficient by interpolation between the two aerodynamic data sets. The interpolation is a linear combination of the extreme cases of flow, where the linear parameter is a time dependent parameter, describing the time for the flow to change configuration. The dynamic unsteady lift coefficient can thereby be described as

$$C_{l,dyn}(\alpha, t) = f_s(t) C_{l,inv}(\alpha) + \left(1 - f_s(t)\right) C_{l,fs}(\alpha) \tag{18.26}$$

where $C_{l,dyn}$ is the dynamic unsteady lift coefficient. $C_{l,\text{fs}}$ and $C_{l,\text{inv}}$ are the lift coefficient for fully separated and inviscid flow, respectively. f_s is the separation function, which is modelled as a first order model

$$f_s(t+\Delta t) = f_s^{st} + \left(f_s(t) - f_s^{st}\right)\exp\left(-\frac{\Delta t}{\tau_f}\right) \tag{18.27}$$

where f_s^{st} is the static value of the separation function and τ_f is the time constant for the flow adaptation.
The static value of the flow separation function can be formulated from the inviscid and fully separated lift curves as follows

$$f_s^{st} = \frac{C_{l,stat} - C_{l,fs}}{C_{l,inv} - C_{l,fs}} \tag{18.28}$$

where $C_{l,stat}$ is the static airfoil lift coefficient. The time constant for the flow adaptation is in this theory assumed to be a variable of the relative wind speed and the chord length of the blade. The time constant can be approximated by

$$\tau_f = \frac{k_{\tau_f}}{V_{rel}} \tag{18.29}$$

where k_{τ_f} is a constant which usually takes the value of approximately 4. Applying the dynamic stall model for the lit coefficient, the dynamic lift coefficient will always try to chase the static lift coefficient, when the AOA is changing. The dynamic stall model is only applied for the lift coefficient of the blade, for the drag coefficient the static airfoil data is used.

18.3.3 Tower Shadow Model

As the airflow of the free stream wind cannot go through the tower, the wind field will have to bend around the tower, this effect is referred to as tower shadow. This will distort the incoming wind, the blade experiences, and the free wind stream will no longer be only in the axial direction, as a tangential velocity component will be induced.
In M. Hansen [81] the modelling of this phenomena is done by considering the tower as a blunt body, the flow around the tower can be modelled as a 2D potential flow around a cylinder. The flow around the tower is visualized in fig. 18.5. The 2D potential flow around a cylinder is described in [92].

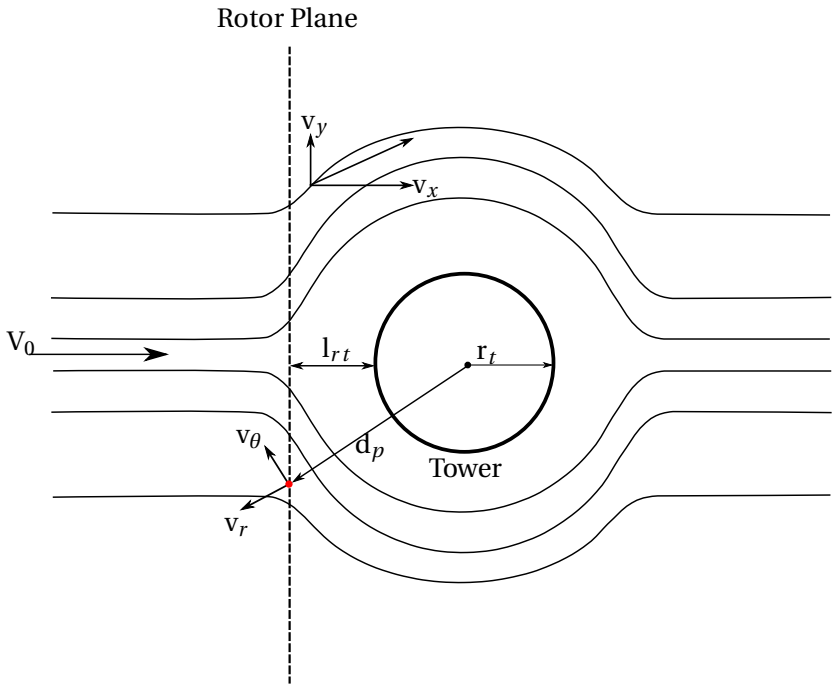

Figure 18.5: The effect of the tower on the air flow, seen in a single cross section.

Due to the blockage effect of the tower the wind velocity V_x is lower in front of the tower, while in the sides in front of the tower the wind velocity will experience a speed up due to the flow going around the tower.
The change in the free stream velocity due to the tower in sub system 2 can be expressed in polar coordinates as

$$\begin{aligned} V_{0,r} &= V_0 \left(1 - \frac{r_t^2}{d_p^2}\right) \cos(\theta_p) \\ V_{0,\theta} &= -V_0 \left(1 + \frac{r_t^2}{d_p^2}\right) \sin(\theta_p) \end{aligned} \tag{18.30}$$

where $V_{0,r}$ and V_{0,θ_p} is the radial and tangential wind velocity. r_t is the radius of the tower. d_p is the distance from the centre of the tower to the point of consideration. θ_p is the angle from the x-axis to the points of consideration.
These can be calculated in Cartesian coordinates as

$$\begin{aligned} V_{0,x} &= V_{0,r} \cos(\theta_p) - V_{0,\theta} \sin(\theta_p) \\ V_{0,y} &= -V_{0,r} \sin(\theta_p) - V_{0,\theta} \cos(\theta_p) \end{aligned} \tag{18.31}$$

where $V_{0,x}$ and $V_{0,y}$ is the wind speed in the x- and y-direction. The tower shadow effect is taken into account in the UBEM code by correcting the discrete free stream wind velocities which the blade experiences. The effect of tower shadowing can be seen on the thrust force in fig. 18.6

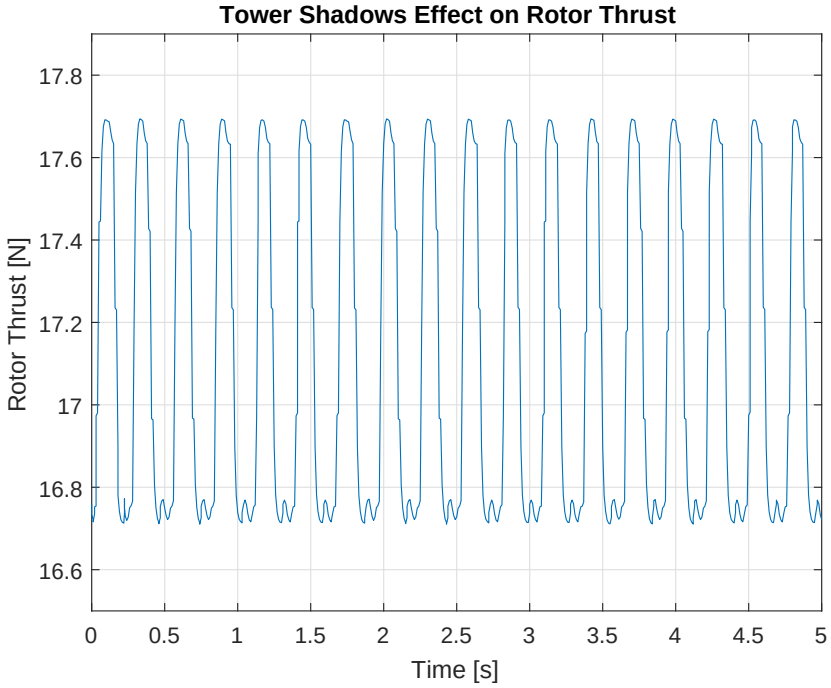

Figure 18.6: The effect of tower shadowing on the thrust force, at a uniform wind field of 7 m/s at rated rotational speed.

18.4 Aerodynamic Simulation

In fig. 18.7 a graphical visualisation of the aerodynamic simulation is seen. The first step is to generate the wind field time series. This is defined by inserting the rotational speed of the fans, and defining the mesh for the points in which the wind speed time series is desired. From this the mean wind speed in each point is calculated and the points are assigned a PSD. After the free stream calculation of the wind speed, the tower shadow model is used to correct for the free stream flow of the wind around the tower.

Thereafter the loop over each blade section N_s on each blade N_B at each time step is begun. At first the geometry of the blades is loaded, this is the chord length and geometric twist. Thereafter the azimuthal position of the rotor is found from the drive train model, such that free stream wind velocity can be assigned to each blade section. The relative wind velocity the blade section experiences is calculated by taking the rotational speed of the rotor and adding it to the translational velocity of the TLP and tower.

The flow angle is thereafter calculated, and by subtracting the pitch angle of the blade the AOA for the blade section can be found. From the AOA and the flow velocity the blade section can be assigned a lift and a drag coefficient. The assigned lift and drag coefficients found are then inserted into the dynamic stall model which then gives the instantaneous lift and drag coefficient. Thereafter Prandtl's tip and hub loss coefficients are calculated. From this the axial and tangential induction factors are calculated, if the axial induction factor exceeds 0.2 Glauert's correction must be used. There after the axial and tangential induction factors are inserted into the dynamic inflow model, from which instantaneous induced velocities over the blade section can be found. At last the normal force and torque generated by the blade section are calculated.

After calculation of the normal force and torque of each blade section, these are summed for each blade. After calculation of the normal force and torque of all blades, these are summed to provide

the thrust force and torque of the rotor. At last the pitch and yaw moments generated from each blade are calculated.

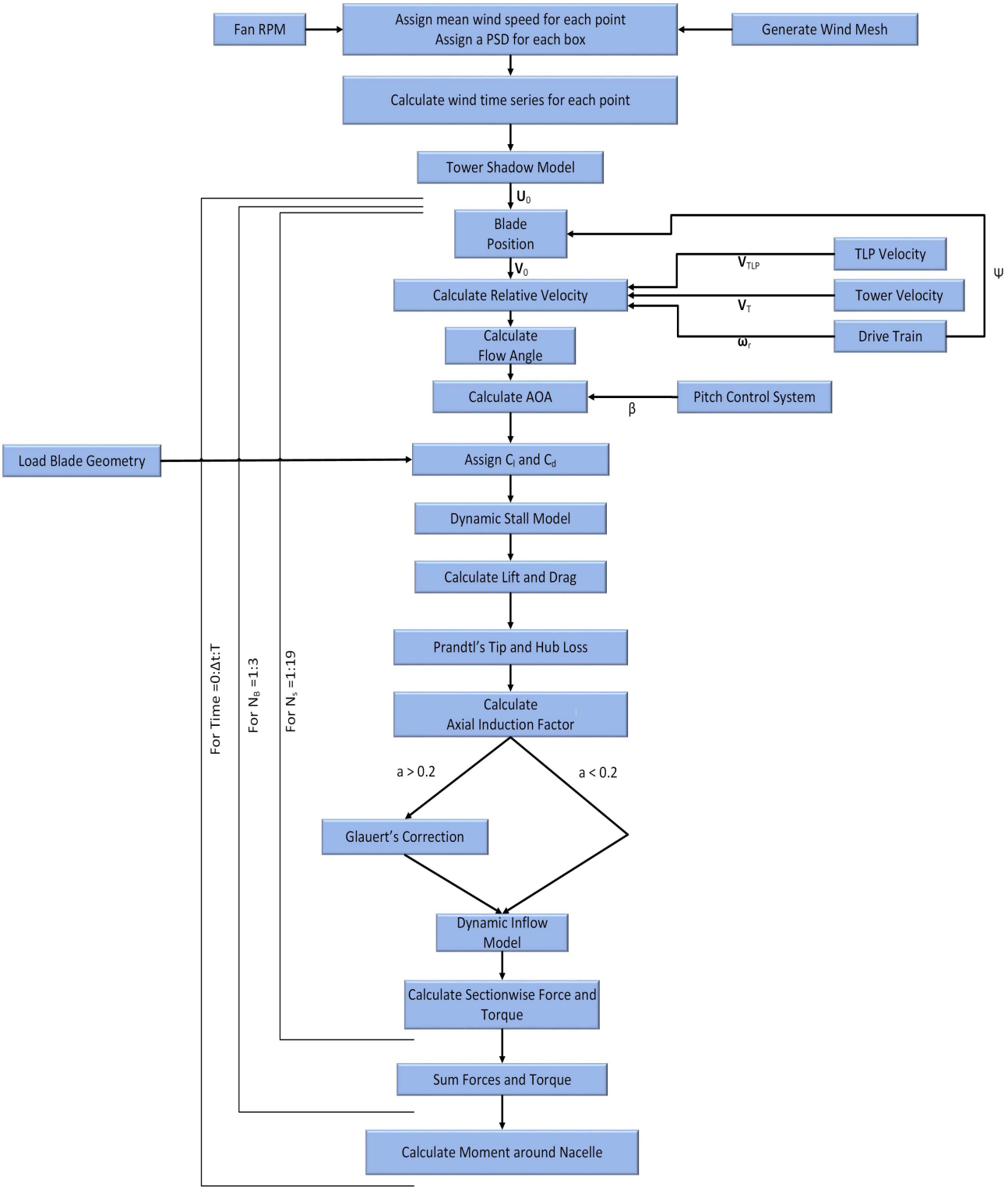

Figure 18.7: Flowdiagram for UBEM.

Test and Validation 19

In this chapter different experiments regarding the modelling of the wind generated by the wind generator and the aerodynamics of the wind turbine will be conducted. First the wind of the wind generator will be modelled by dividing the wind field into nine areas and using measurements for generating individual PSDs for these areas by using mean wind speed vectors.
Furthermore the different regions of operation for the wind turbine will be tested, this being region I for the starting torque of the wind turbine, region II for different wind speeds with fixed pitch angle and varying torque and region III for different wind speeds, but now with varying pitch angle and constant torque.
At last an impulse excitation of the blades will be conducted to find the natural frequencies of the blades.

19.1 Wind Modelling

Two experiments regarding modelling of the wind will be conducted. In the first experiment a PSD for a high and a low wind velocity is found and an interpolation function of the intermediate wind speeds are found. In the next experiment the wind field is divided into nine areas, and a PSD is generated for each of the boxes using a mean wind speed vector found through experiments.

19.1.1 Single Point Wind Modelling

In order to find the wind speed at different points, a PSD must be assigned to each point. The data available for this are from the 17 measurement points of the wind speed at two different fan speeds from the wind tunnel tested in section 5.3.3.2.
As the PSD changes with wind speed, and measurements of only two fan configurations are available at each measurement point, a weighting function between the two calculated PSDs is made. The data available is at a fan rotational speed of 1520 RPM and 2900 RPM, which approximately corresponds to a wind speed of 4 m/s and 8 m/s, respectively.
The PSD at an arbitrary wind speed in the range of the capacity of the wind generator is found as

$$PSD_x\left(f_{fan}\right) = PSD_{1520}\left(1 - w\left(f_{fan}\right)\right) + PSD_{2900}\, w\left(f_{fan}\right) \tag{19.1}$$

where PSD_x is the PSD for an arbitrary wind speed, PSD_{1520} and PSD_{2900} are the experimentally found PSDs at a fan speed of 1520 RPM and 2900 RPM, respectively. The weighting function, w, is a

linear function of the fan rotational speed, f_{fan}, which can be written as

$$w(f_{fan}) = \frac{2900 - f_{fan}}{2900 - 1520} \tag{19.2}$$

The two experimental PSD estimates of the wind speed at a fan rotational speed of 1520 RPM and 2900 RPM, and a calculated PSD estimate at a fan rotational speed of 2000 RPM are shown in fig. 19.1.

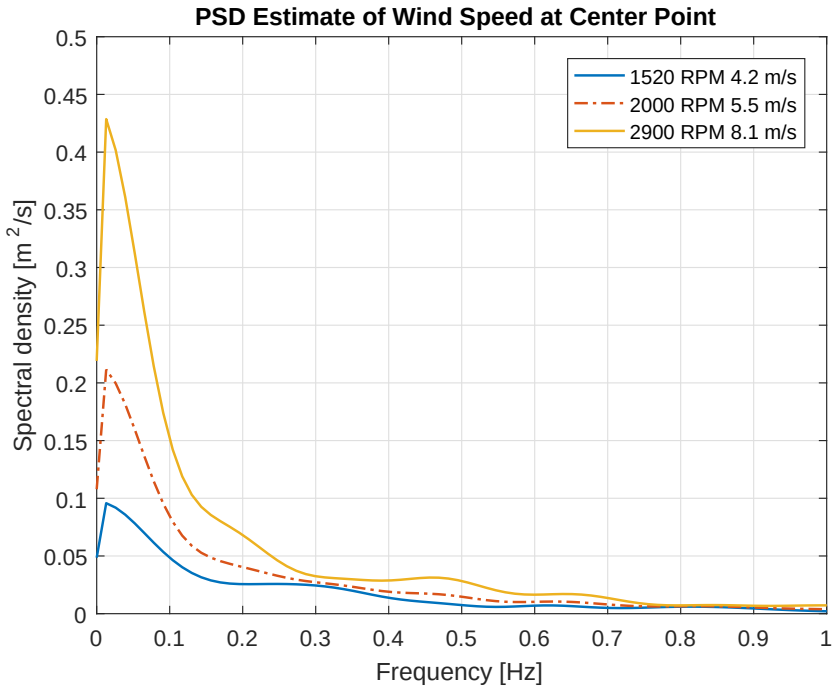

Figure 19.1: Experimental PSDs at a fan rotational speed of 1520 RPM and 2900 RPM, and a calculated PSD estimate at a fan rotational speed of 2000 RPM.

It can be seen in fig. 19.1 that the PSD estimate increases as the rotational speed of the fan increases. The energy in the wind speed fluctuations is furthermore seen to be in the low frequency region, as it can be seen that most of it is below 0.2 Hz.
TurbSim is used to create a turbulent wind field for the FAST model. As TurbSim is only able to create wind fields based on a single predefined model spectrum, it is not possible create the same spectrum and variation in mean wind speed as the experiments have shown. The PSD used in TurbSim is tuned to fit the experimental PSD measured in the centre point. The TurbSim PSD and experimental PSD at 7 m/s are seen in fig. 19.2. It can be seen that the turbulence fits well below 0.4 Hz where after TurbSim keeps decreasing while the experiment levels off.

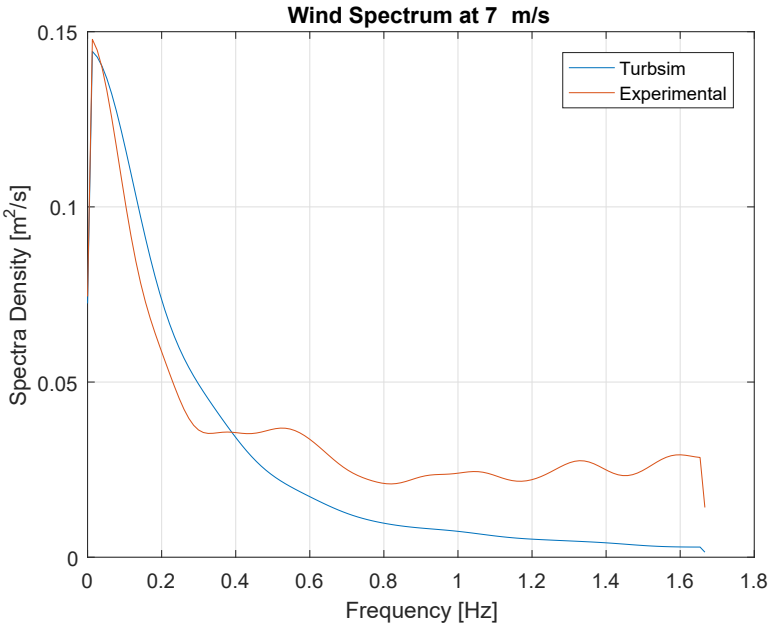

Figure 19.2: Experimental PSD and TurbSim PSD used to generate turbulent wind field for FAST.

19.1.2 Multiple Point Wind Modelling

In order to assign a PSD to all points in the simulation, the wind field is divided into nine boxes, where the PSD estimate for all wind speed simulation points in the box will be found from the data of the four measurement points enclosing the box, as illustrated in fig. 19.3
As the mean wind speed decreases towards the edge of the wind generator, eight mean wind speed Lines are constructed from the measurement data.

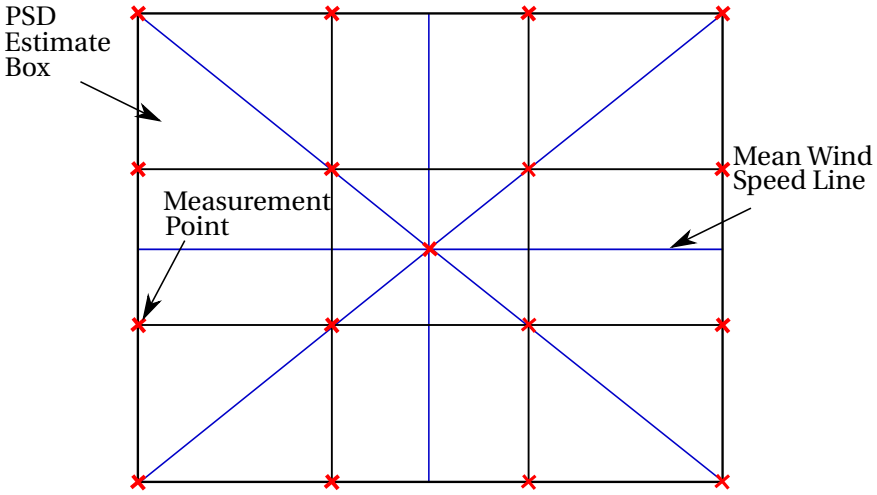

Figure 19.3: Visualization of the wind speed modelling.

The nine PSD estimates for the boxes are found by adding the single point PSD estimates enclosing the box together and dividing by the number of PSD estimates.To calculate the PSDs at all rotational speeds of the fans, a linear weighting function between the two experimental PSDs is utilized. This is the same approach as for single point PSDs, see section 19.1.1.
The mean wind speed line varies both with the rotational speed of the fans and the location of the blade. The mean wind speed at all fan rotational speeds is calculated by assuming that there is a linear correlation between the mean wind speed and the rotational speed of the fans. A linear

regression between the two measured mean wind speeds at 1520 RPM and 2900 RPM is made at all measurement points. The diagonal mean wind speed lines are found by utilizing the measurement point in which it passes through. The horizontal and vertical mean wind speed lines are found by using the mean of the two measurement points it passes through. To find the mean wind speed at all radii, a correlation between the discrete mean wind speed points and the radius must be found. By inspection of the distribution of the mean wind speed of the wind field in fig. 5.5 and 5.6, it can be seen that there is a polynomial tendency of the mean wind speed from the centre to the edge. Therefore a polynomial fit for each mean wind speed line is calculated from the measured wind speed line, normalized w.r.t. the highest mean wind speed measured in each line.

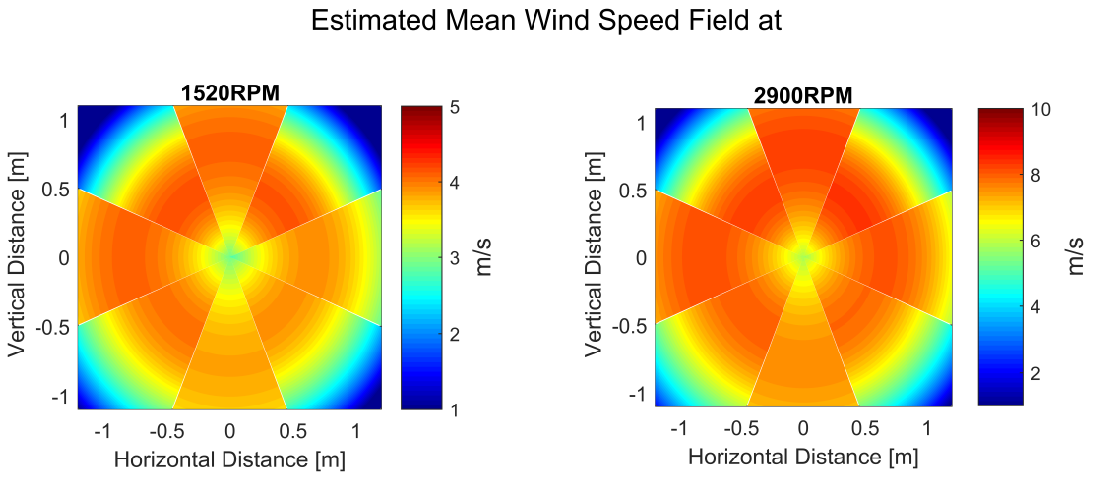

Figure 19.4: The estimated mean wind speed field used for the generation of the wind time series.

The instantaneous wind speed of the wind field at the discrete points seen in fig. 17.1, are calculated for all rotational speeds of the fan by utilizing the PSD estimates for the boxes and the mean wind speed distribution found above. Furthermore the theoretical coherence function is needed, this was described in eq. 17.5. By utilizing the above found PSD boxes and mean wind speed lines for 2500 RPM, the wind speed time series can be generated. The wind time series at four discrete points on the same line can be seen in fig. 19.5.

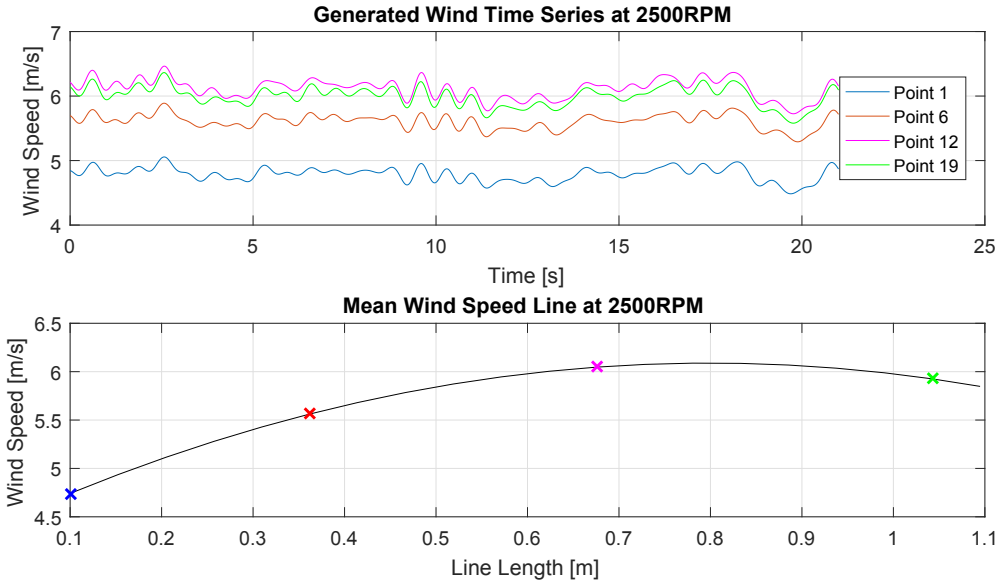

Figure 19.5: The top figure shows four generated wind time series at the discrete points 1,6,12 and 19 which are placed on the same mean wind speed line, generated at 2500 RPM. The bottom figure shows the mean wind speed mean wind speed line, where the crosses are the points along the blade to which the wind time series correspond.

19.2 Region I

In this region the wind turbine is not rotating, and the blades are feathered so the lift of the blade is as small as possible. In order for the wind turbine to start, the aerodynamic torque should be able to overcome the starting torque of the wind turbine. Eventually the wind turbine should be running at the cut in wind speed of 3 m/s, however it is found when testing region II, see section 19.3, that the wind turbine was not able to do so and so the cut in wind speed is set to 3.5 m/s instead. A way to overcome the starting torque is to pitch the blades, and thus more lift is created, and the rotor torque will become higher and overcome the starting torque, and the wind turbine will start rotating. To find this starting torque, a force transducer from PASCO is mounted on one blade, as seen in fig. 19.6. A force is applied to the force transducer, until the wind turbine starts rotating. Several tests were made with two different distances of 0.41 m and 0.12 m from the hub centre to the mounting of the force transducer.

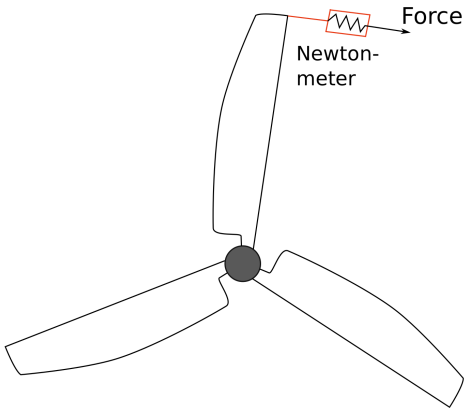

Figure 19.6: Experimental setup when measuring starting torque.

19.2.1 Results

In fig. 19.7 the results of one of the experiments are seen. The starting torque is found as the highest point on the curve as the wind turbine started rotating at this point. In the shown experiment, the starting torque is just above 1.7 Nm.

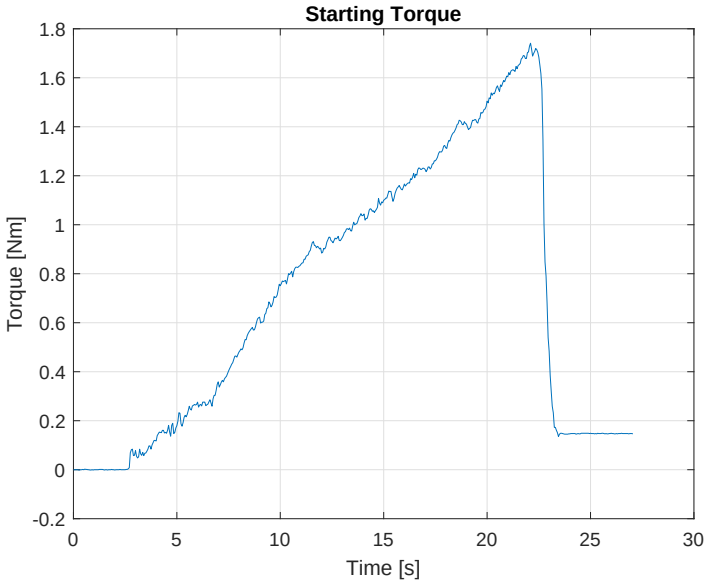

Figure 19.7: Starting torque from one experiment.

All tests showed approximately the same result and an average of 1.68 Nm was found.

19.3 Region II

In this region the wind turbine is controlled by adjusting the generator torque, while the blades are kept at a 0 ° pitch angle. In this experiment, the wind generator generates a mean wind speed from 3.5 m/s to 7 m/s and the aerodynamic power, the aerodynamic torque, the thrust force and the tip speed ratio (TSR) are measured.

19.3.1 Theory

The aerodynamic power is found by measuring the generated voltages and currents from the generator and taking the efficiency throughout the drive train into consideration, this is taken to be 60 %, see section 25.2. The aerodynamic torque is found by dividing the aerodynamic power with the rotational speed of the rotor. The thrust force is found by using the camera system OptiTrack, where the displacement of the nacelle was measured. By utilizing Hooke's law the relationship between force and displacement for this test setup is found in A.6 and is used to calculate the thrust force.

19.3.2 Results

In fig. 19.8 the experimental results are seen together with the scaled data from the NREL 5 MW wind turbine and the calculated results using both SBEM and UBEM. The SBEM MATLAB code was developed by the authors in [27] and was also used for designing the blades of the wind turbine. Furthermore the results from FAST are seen in the figure.

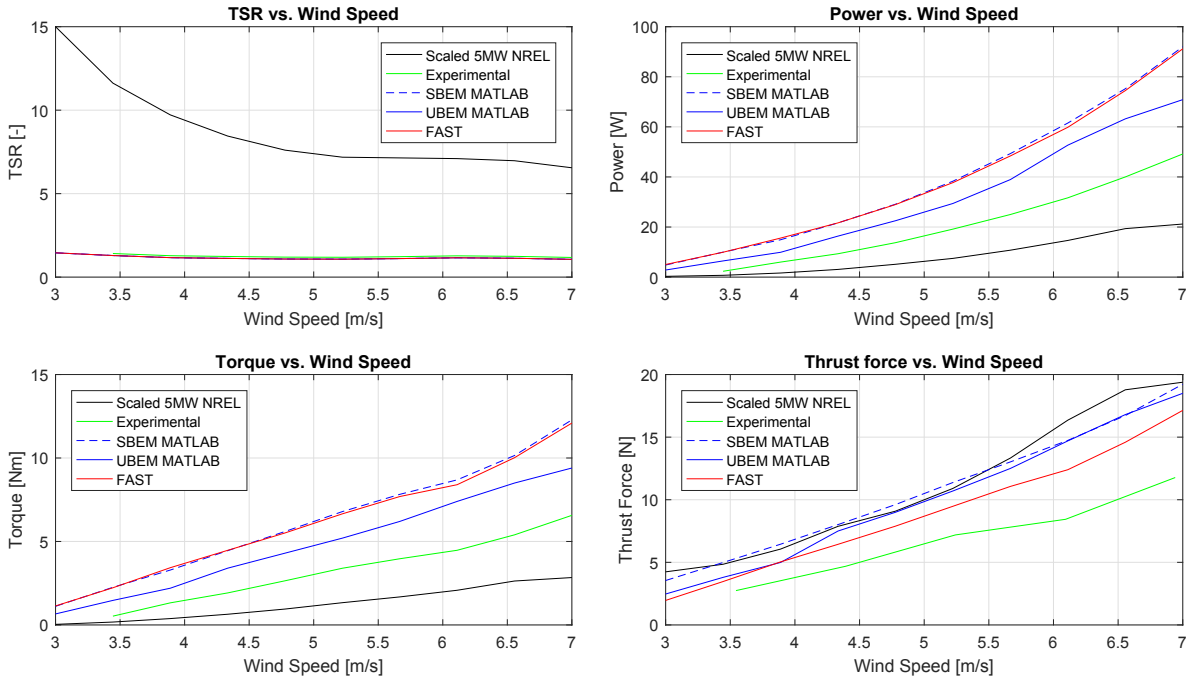

Figure 19.8: The experimental results for the rotor aerodynamics in region II, these are compared to the scaled 5 MW NREL values and the theoretical calculations from SBEM,UBEM and FAST.

It should be noted that the wind speeds used on the experiment are found using eq. 5.6 in section 5.3.3.3, relating the rotational speed of the wind generator to the wind speed.
The rotor of the wind turbine is in the experiments not placed in the centre of the wind field, therefore 0.1 m of the top rotor plane is outside the wind field. This means that the thrust and generated torque will be less in the experiments compared to the theoretical calculated. The thrust force was found to have a maximum uncertainty of ± 3.9 N, when considering the 95 % confidence interval. The reason for the large error from SBEM and FAST is mainly due to the fact that the wind field is not uniform, which the SBEM assumes. Also the comparison at different wind speeds is challenging, as only a mean wind speed at two points in the vertical centre in the wind field is used for the experiments and UBEM.

19.4 Region III

In this region the wind turbine is controlled by the pitch system, which pitches the blades and thereby changes the forces on the blades. Region III ranges from the rated wind speed of 7 m/s to the cut out wind speed of 11 m/s, however the wind generator is not able to generate a wind speed of 11 m/s, so the experimental results are only measured up to a wind speed of 8.6 m/s.

19.4.1 Theory

The collective pitch angle of the blades needed to keep the torque and thereby the rotational speed constant, depends on the wind speed. The collective pitch angle for region III has been found by usage of SBEM in previous work done by the authors [27]. The collective pitch angle for region III has also been calculated by UBEM and FAST. It should be noted that the rated torque for the different methods are different, as the rated torque is found at the rated wind speed for each method. The same procedure is done for the experiment.

19.4.2 Results

In fig. 19.9, the collective pitch angle at the different wind speeds for the scaled NREL, simulations and the experiment are seen together with the power, torque and thrust force.

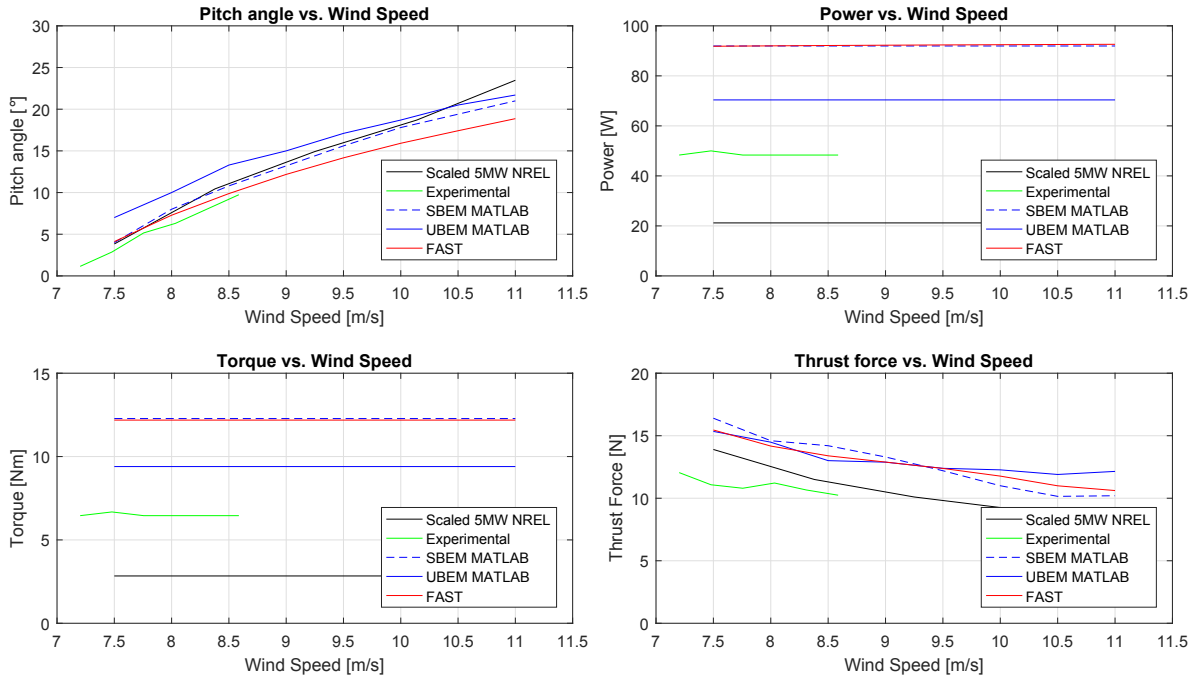

Figure 19.9: The experimental results for the rotor aerodynamics in region III, these are compared to the scaled 5 MW NREL values and the theoretical calculations from SBEM, UBEM and FAST.

As seen all the plots have the same shape. The scaled values, simulations and experiment are very similar in pitch angle and thrust force. However the thrust force found experimentally has a high standard deviation, meaning that the 95 % confidence interval is ±5.6 N, therefore it is the mean value of the thrust force which is shown. The power and torque can be seen to differ more, but as mentioned, this is because the different torques are the rated torques found in region II.

19.5 Impulse Excitation of Blade

The same theory as in section 14.3 is used for these experiments. Again the accelerometer from Vernier was used for the experiment. The accelerometer was mounted on the blade 0.49 m from the root of the blade and a sampling frequency of 400 Hz was used. Five tests were conducted, where the blade was hit a single time at different places along the blade and orthogonal to the chord. In this experiment no model of the blade is validated, as a FEM of the blade would require knowledge of the structure inside the blade. As the blade is 3D printed, the printer would have calculated the best structure inside the blade, and it has not been possible to extract this structure from the program.

19.5.1 Results

In fig. 19.10 the results from the experiment, where the blade was hit at tip are seen.

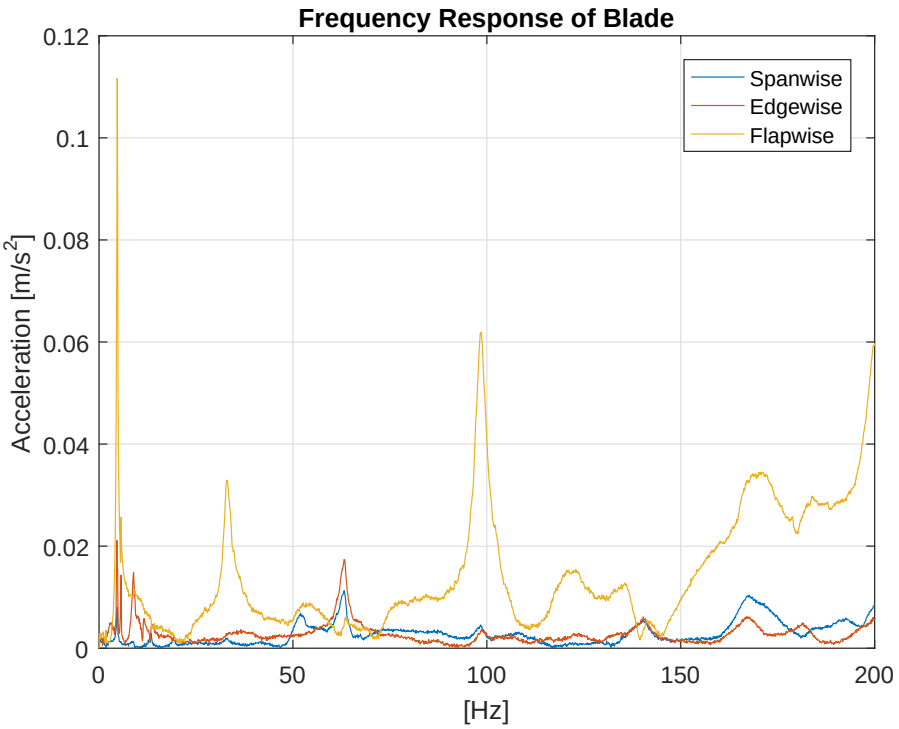

Figure 19.10: Frequency response of one of the blades.

The accelerometer measures the acceleration at three different directions, this will in the case of the blade be the spanwise direction, the edgewise direction and flapwise direction, which was also the direction at which the force was applied.

In the figure it can be seen that the frequencies out of the rotor plane are the most significant, and also the ones of most interest for this thesis, as this is the direction of the wind applied to the blades. The first natural frequency in this direction is approximately at 5 Hz, the second is at 33 Hz, while the third is at 99 Hz. The rest of the natural frequencies are assumed too far away from the range of frequencies of the excitation forces to have any influence in the overall response. The natural frequencies in the other directions are not as significant, and also of less interest compared to the flapwise direction. In order to take the frequency of the blades into consideration when designing the controller, the damped natural frequency will be inserted into the Campbell diagram, see section 34.1.

Conclusion 20

This part concerned the aerodynamics of the wind turbine. The wind conditions for a real wind turbine and the scaled model were described and compared, and it was found that there is significant difference.
It was found that a PSD and coherence function for the generated wind field is needed during investigation of short and long term wind conditions. It was decided to a use Veers' method to generate a 3D wind field from a pre-described PSD function and coherence function. The points for the wind speed generation were placed in a circular pattern.
For the aerodynamic modelling UBEM was utilized. When calculating the relative velocity it was assumed that only the tower and TLP surge motions are significant for the relative velocity the blades experience.
The torque and loads on the blades were found using UBEM, where Prandtl's and Glauert's correction method were utilized. For the unsteady correction models the dynamic wake model, dynamic stall model and tower shadow model were utilized. The method for the dynamic wake model and the dynamic stall model are both from S. Øye. The method for the tower shadow model is given by M. Hansen.
During the testing and validation of aerodynamics the wind speed was measured in 17 points. A PSD was found in a single point, at two wind speeds and a weighting function between these using the rotational speed of the wind generator was found. For the multiple point wind modelling the wind field was divided into nine boxes, and eight mean wind speed lines. It was found that the line of mean wind speed can be described by a second order polynomial. The coherence function could not be found experimentally due to lack of equipment, and therefore a theoretical one was utilized.
The testing of the aerodynamics of the wind turbine was divided into three regions. At region I the starting torque was found by pulling the blades, and the pulling force was measured by a newton meter. The mean starting torque was found to be 1.7 Nm. In the experiments for region II the power, thrust and rotational speed were measured. This experiment was then compared to the SBEM, UBEM, FAST and the scaled 5 MW NREL. The experiment was somewhat lower than the predicted from SBEM and FAST, this is due to the assumption of a uniform mean wind speed in the wind field. The UBEM takes this into account and is closer to the experimental results.
In the experiments for region III the pitch angle of the blades was changed for maintaining constant torque. Again the SBEM and FAST overpredicted the values, except in the pitch angle. UBEM is somewhat closer to the experiment, but still overpredicted, which is probably for the same reasons as explained in region II. At last an experiment with impulse excitations of the blades was made, where an accelerometer was attached to one of the blades, and impulses were applied at different locations. The measured accelerations were analysed using a FFT, showing peaks at 5 Hz, 33 Hz and 99 Hz.

Part V

Servo and Power Electronic Models

Symbol	Description	Units
ϵ	Prediction error	-
$\boldsymbol{\theta}$	Parameters to be estimated	-
$\hat{\boldsymbol{\theta}}_N^{LS}$	Least square estimation of parameter vector	-
$\boldsymbol{\lambda}_{abc}$	Flux linkage in abc frame	Wb
$\lambda_d, \lambda_q, \lambda_0$	Flux linkage in $dq0$ frame	Wb
λ_r	Rotor flux linkage	Wb
$\boldsymbol{\Phi}$	Regression vector	-
ω_e	Electrical angular velocity	rad/s
ω_m	Generator angular velocity	rad/s
ω_r	Rotor angular velocity	rad/s
$\dot{\omega}_r$	Rotor angular acceleration	rad/s^2
$a_1, ...a_{N_a}$	Output parameter to be estimated	-
$b_1, ...b_{N_b}$	Input parameter to be estimated	-
B_{dt}	Dynamic friction at low speed shaft	Nms
$c_1, ...c_{N_c}$	Moving average parameter to be estimated	-
e	White noise term	-
e_d, e_q	dq Back-EMF	V
$G_B(z)$	Discrete transfer function of blade actuator	rad s
i_{abc}	Stator current in abc frame	A
i_d, i_q, i_0	Stator current in $dq0$ frame	A
$\boldsymbol{i}_{dq0}$	Stator current in $dq0$ frame	A
J_{dt}	Equivalent drive train mass moment of inertia w.r.t the low speed shaft	kg m^2
k	Sample	-
L_d, L_q	dq generator Inductance	H
n_a	Number of poles for estimation	-
n_b	Number of zeroes plus 1 for estimation	-
N_G	High speed to low speed gear ratio	-
P_{dq0}	Power in $dq0$ frame	W
P_g	Generator power	W
$poles$	No. of generator poles	-
$\boldsymbol{R}_s$	Stator resistance	Ω
t	Time	s
T_g	Generator torque at high speed shaft	Nm
T_r	Rotor torque at low speed shaft	Nm
T_s	Sampling time	s
v_{abc}	Generator voltage in abc frame	V
V_d, V_q, V_0	Generator voltage in $dq0$ frame	V
$\boldsymbol{v}_{dq0}$	Generator voltage in $dq0$ frame	V
V_N	Least square criterion	-
u	Input for system identification	-
y	Output for system identification	-
$\hat{y}$	Output prediction	-
z	Discrete operator	-
z^{-1}	Unit delay operator	-
$\boldsymbol{Z}_N$	Experimental data set	-

Introduction 21

In this part the servo dynamics and electrical models will be described, tested and validated. First the equation of motion of the drive train is described, thereafter the generator model in the stationary reference frame and the power electronics used to control the generator. The drive train model and generator are modelled in Simulink as seen in appendix A.12.1 and A.12.1. The power converter is modelled using Simscape power system blocks in Simulink as seen in appendix A.12.1. Next the pitch system is described using system identification. In the last chapter the viscous damping is found by an ARMA model and the generator efficiency is found by experiments. The SVPWM algorithm is tested and a comparison of the drive train and generator model against experiments in region II is made.

Drive Train Model 22

The drive train transfers the rotational energy from the rotor to the generator. It consists of a low speed shaft, a gear box and a high speed shaft. The drive train is modelled by Newton's second law for rotation in a SDOF and by assuming rigid body motion

$$N_G T_g - T_r = J_{dt}\dot{\omega}_r + B_{dt}\omega_r + T_0 \tag{22.1}$$

where the DOF is the angular rotation of the low speed shaft. T_g is the generator torque on the high speed shaft, N_G is the high speed to low speed gear ratio, J_{dt} is the equivalent drive train mass moment of inertia w.r.t the low speed shaft, ω_r is the rotor velocity and $\dot{\omega}_r$ is the rotor acceleration. B_{dt} is the dynamic friction for the main shaft also known as viscous friction. T_0 is a combination of the torque contributions from the static friction, coulomb friction and the detent torque, all of them opposing the motion. The static friction is only present when the rotor is at a standstill, while coulomb friction and the detent torque are present at all times, but are constant and therefore do not represent any dynamics. The drive train parameters are shown in table 4.5. In fig. 22.1 the drive train of the wind turbine is seen. In appendix A.12.1 a simulink model of the drive train can be seen.

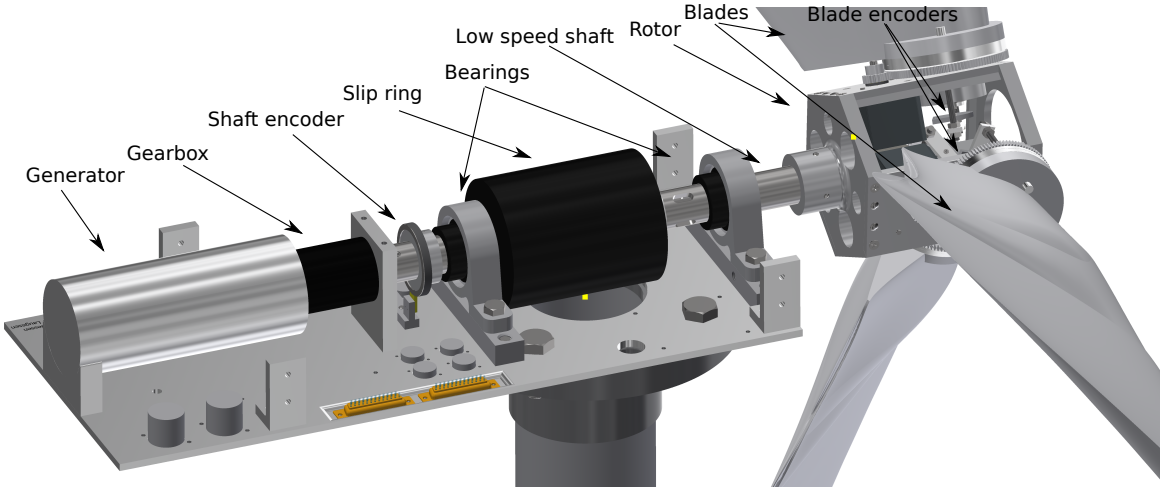

Figure 22.1: Visualization of the drive train of the wind turbine.

Generator Model 23

The generator is a BLDC motor which operates very similar to a PMSG, both are synchronous motors with permanent magnets attached to their rotors.
The three phase voltage of the generator can be written in vector form as the voltage drop across the stator windings due to the current and the time derivative of the flux linkage between the stator and the rotor

$$\mathbf{v}_{abc} = \mathbf{R}_s \boldsymbol{i}_{abc} + \frac{d}{dt}\boldsymbol{\lambda}_{abc} \tag{23.1}$$

where $\mathbf{v}_{abc}$ is the voltage, $\mathbf{R}_s$ is the stator resistance, $\mathbf{i}_{abc}$ is the current and $\boldsymbol{\lambda}_{abc}$ are the flux linkages, all described in an abc reference frame.

The three phased abc voltage equation can be transformed into the $dq0$ voltages by applying Park-Clark transformation. The Park-Clark transformation projects the rotating three phase non-linear quantities onto a reference frame rotating in synchronism with the rotor. Thereby the quantities can be seen as linear DC quantities

$$\begin{aligned} v_d &= R_s i_d + \frac{d}{dt}\lambda_d - \omega_e \lambda_q \\ v_q &= R_s i_q + \frac{d}{dt}\lambda_q + \omega_e \lambda_d \\ v_0 &= R_s i_0 + \frac{d}{dt}\lambda_0 \end{aligned} \tag{23.2}$$

where ω_e is the electrical angular velocity. v_d, v_q and v_0 are the $dq0$ voltages, respectively. i_d, i_q and i_0 is the $dq0$ currents. Under balanced conditions v_0 and i_0 are zero and they are therefore not considered further.
The instantaneous d- and q-axis synchronous flux linkage terms are given as

$$\begin{aligned} \lambda_d &= L_d i_d + \lambda_r \\ \lambda_q &= L_q i_q \end{aligned} \tag{23.3}$$

where λ_d and λ_q represent the dq flux linkages, λ_r is the rotor flux linkage and L_d and L_q represent the inductance in the $dq0$ axis reference frame. By inserting the flux linkages into the voltage

equation, the d and q voltages can be written as

$$\begin{aligned} v_d &= R_s i_d + L_d \frac{d}{dt} i_d - \omega_e L_q i_q \\ v_q &= R_s i_q + L_q \frac{d}{dt} i_q + \omega_e L_d i_d + \omega_e \lambda_r \end{aligned} \tag{23.4}$$

where the back-EMFs e_d and e_q can be written as

$$\begin{aligned} e_d &= -\omega_e \lambda_q = -\omega_e L_q i_q \\ e_q &= \omega_e \lambda_d = \omega_e L_d i_q + \omega_e \lambda_r \end{aligned} \tag{23.5}$$

The instantaneous active power in the $dq0$-axis reference frame P_{dq0} is given by the $dq0$-axis reference frame voltages $\mathbf{v}_{dq0}$ and currents $\mathbf{i}_{dq0}$ as

$$P_{dq0} = \frac{3}{2}\left(\mathbf{v}_{dq0}^T \mathbf{i}_{dq0}\right) \tag{23.6}$$

Substituting the d and q voltages into the power equation yields

$$P_{dq0} = \underbrace{\frac{3}{2}\left(R_s i_d^2 + R_s i_q^2\right)}_{\text{Power loss in conductors}} + \underbrace{\frac{3}{2}\left(L_d \frac{d}{dt}\left(\frac{i_d^2}{2}\right) + L_q \frac{d}{dt}\left(\frac{i_q^2}{2}\right)\right)}_{\text{Rate of change in magnetic field}} + \underbrace{\frac{3}{2}\left(\omega_e \lambda_d i_q - \omega_e \lambda_q i_d\right)}_{\text{Electromechanical power}} \tag{23.7}$$

where it is only the back-EMF which generates active power. Making use of eq. 23.5 the generated power can be written as

$$P_g = \frac{3}{2}\left(\mathbf{e}_{dq0}^T \mathbf{i}_{dq0}\right) = \frac{3}{2}\omega_e \left(\lambda_r i_q + \left(L_d - L_q\right) i_q i_d\right) \tag{23.8}$$

where P_g is the generated power. The generated torque T_g from the generator can then be expressed as

$$T_g = \frac{P_g}{\omega_m} = \frac{3}{2}\frac{poles}{2}\left(\underbrace{\lambda_r i_q}_{\text{Synchronous torque}} + \underbrace{(L_d - L_q) i_q i_d}_{\text{Reluctance torque}}\right) \tag{23.9}$$

where poles is the number of poles in the generator. It can be seen that the generated torque is composed of two distinct mechanisms. The first term corresponds to synchronous torque occurring between i_q and the permanent magnet, while the second term corresponds to the reluctance torque which is due to the differences in d-axis and q-axis inductances. For most non-salient PMSGs $L_d \leq L_q$, which is also shown by experiments in previous work by the authors [27]. It can be seen that if a positive i_d current is applied, the reluctance torque will have a negative impact on the generated torque from the generator. For this reason the reference for the i_d in the control should be zero to produce as much torque as possible.

In the appendix A.12.1, a Simulink model of the generator can be found. This model is both used in the overall Simulink model and as an add on to FAST. The generator parameters are shown in table 4.6 and were found by the authors in previous work [27].

23.1 Power Converter Model

The generator is controlled by an active rectifier which converts the three phase AC voltage to a DC voltage. Only the AC to DC power converter will be considered in this thesis, as this is used to control the generator torque. As modulation strategy of the power converter Space Vector Pulse Width Modulation (SVPWM) is applied.
SVPWM has been described in various literature e.g. [93], [94] and [27]. In [27] which was written by the authors, an algorithm for SVPWM was developed, which will be used in this thesis to control the switching of the converter.

23.1.1 Physical Converter

The physical converter is a modified Danfoss VLT AutomationDrive FC 301/FC 302 main supply 200-240V PK75. The Danfoss VLT is a frequency converter for motor applications, it consists of a passive rectifier on the input side, a DC bus link and a 3-phase inverter on the output side. The approach is to use the Danfoss VLT in the reverse direction by using the 3-phase inverter as an active rectifier, as they have the same topology, and disconnecting the passive rectifier. A schematic of the modification of the VLT is seen in appendix A.14.9 together with pictures of the setup. A load to consume the produced energy is placed on the DC link.

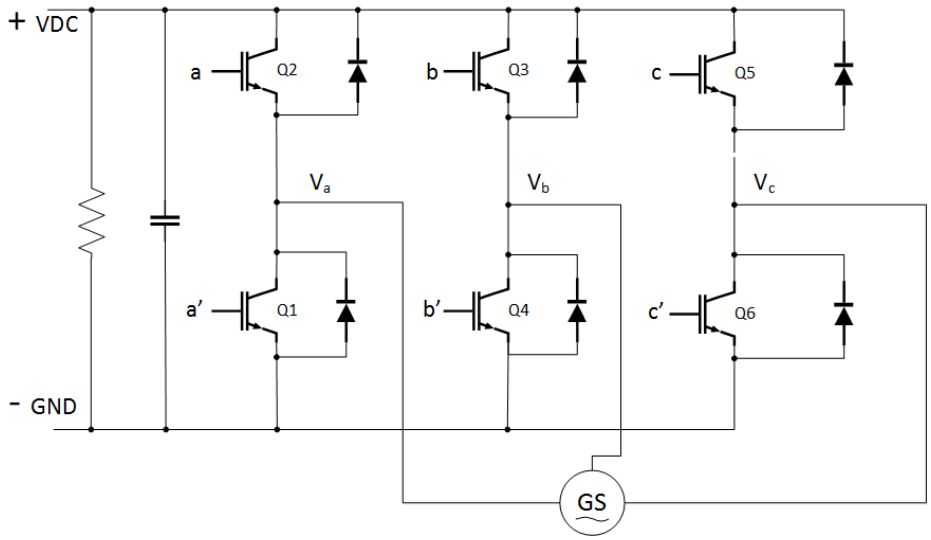

Figure 23.1: Three phased power converter.

The Danfoss VLT has a large power consumption compared to the wind turbine power production, it is therefore not possible to power up the Danfoss VLT by the wind turbine alone. The solution of this is to connect a DC power supply on the DC link on the Danfoss VLT together with the load. This means that there will be a constant power consumption, which is powered by the power supply and the wind turbine. When the wind turbine power production is low, the power supply will bring almost all the power to the system, however when the power production is high, almost all the power

will come from the wind turbine. The load on the DC link is a HS150 220R J panel mounted resistor from Arcol with a resistance of 200 Ω and the power supply is a Delta Elektronika SM660-AR-11. By a simple experiment where the DC link voltage is slowly increased until VLT start up, it was found that the Danfoss VLT has a start-up voltage of 115 V on the DC-link, which is above the voltage level of the generator. Therefore the generator voltages are transformed up through three transformers of the type RS 504-038 with a transformer ratio of 1:11.5. The transformers are mounted in a star connection as seen on the schematic, see fig. 23.2, together with the set-up.

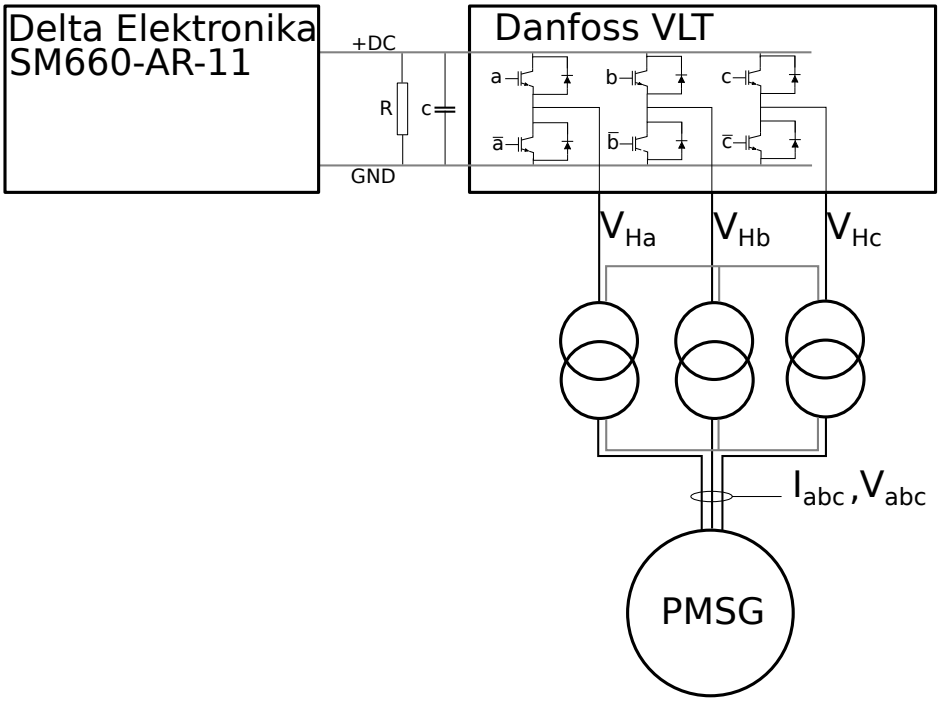

Figure 23.2: Overview of generator and converter connections.

The Danfoss VLT inverter is controlled through an interface and protection card 3 (IPC3), which replaces the original interface card and provides control over the gate drivers of the IGBTs. It furthermore protects the converter against short circuit and overcurrent at the output, DC overvoltage, overfrequency and overtemperature. A microcontroller controls the on-board cooling fan and the dead time is chosen by a DIP switch.
An optical card IPC2dSPACE allows connection of the IPC3 to the dSPACE using optical fibers. A block diagram of the connections between the dSPACE, IPC2dSPACE, IPC3 and the converter is shown in fig 23.3. The IPC3 and IPC2dSPACE were developed by the Department of Energy Technology at Aalborg University and are used in various research institutes and universities around the world.

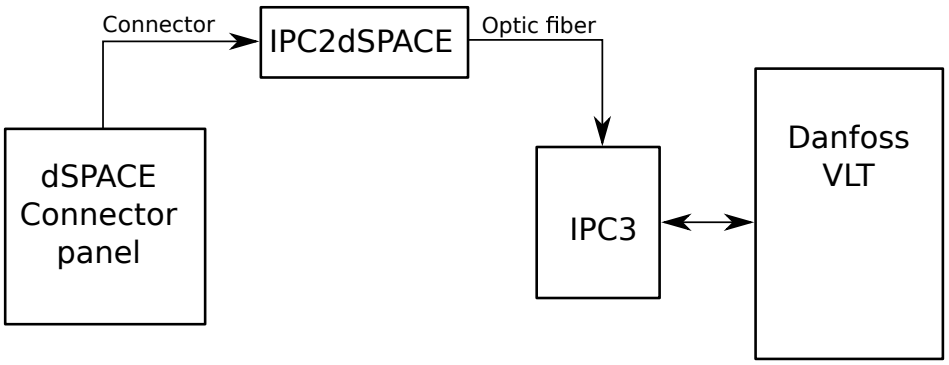

Figure 23.3: Block diagram of interface between dSPACE and Danfoss VLT.

The IPC3 interface receives five signals which are the PWM signals for each phase, UP, VP, WP, enable gate signals, EN, and reset in case of trip, RST. The IPC3 interface transmits a trip signal in case of failure and start up, the trip needs to be reset before the VLT can go into run mode.

Table 23.1: Power electronic parameters.

Parameter	Value
Transformer ratio [-]	1:11.5
Transformer efficiency [%]	87
Transformer voltage drop [%]	10
DC load resistance [Ω]	220
Dead time [μs]	4
Switching frequency [kHz]	5

Pitch System 24

The pitch system for the blades consists of a spur gearing and a stepper motor with driver. The pitch system parameters were shown in table 4.7.

In previous work by the authors [27] a computational heavy, theoretical model for the pitch system was derived and the physical parameters were found. However the dynamics of the system were found to be very fast and had a first order behaviour. The pitch system was also found to be too weak to hold the blade in a fixed position and the stepper board drive was inappropriate as it was not possible to control the holding torque, as is had an automatic idle current setting, which reduced the holding torque.
To improve the performance of the pitch system, new stepper motor drivers and blade gearings were implemented. Due to the changes in the pitch system a new model is derived, this time using a system identification approach.
The input frequency to the stepper motor drives is measured together with the output blade pitch angle. The sign of the frequency indicates the direction of the rotation of the blade, while the numerical value indicates the pulses per second send to the stepper motor drive. One data set is used to create an ARX (Auto Regression with eXtra input) model and one data set is used to validate the model.

The ARX model is described by the linear difference equation as

$$y(t) + a_1 y(t-1) + ... + a_{n_a} y(t-n_a) = b_1 u(t-1) + ... + b_{n_b} u(t-n_b) + e(t) \tag{24.1}$$

where $y(t)$ is the output at time t, n_a is the number of poles, n_b is the number of zeroes plus 1. $y(t-1)+...+y(t-n_a)$ are the previous outputs which affect the current output. $u(t-1)+...+u(t-n_b)$ are the previous inputs which affect the current output. $e(t)$ is the white noise term added to the system. The input-output parameters to be estimated are

$$\boldsymbol{\theta} = \begin{bmatrix} a_1 & a_2 & ... & a_{n_a} & b_1 & b_2 & ... & b_{n_b} \end{bmatrix}^T \tag{24.2}$$

where $\boldsymbol{\theta}$ is the parameter vector. By introducing the regression vector, $\boldsymbol{\phi}$, which can be calculated as

$$\boldsymbol{\phi}(t) = \begin{bmatrix} -y(t-1) & ... & -y(t-n_a) & u(t-1) & ... & u(t-n_b) \end{bmatrix}^T \tag{24.3}$$

the prediction output of the model, $\hat{y}$, can be written as

$$\hat{y}(t|\boldsymbol{\theta}) = \boldsymbol{\theta}^T \boldsymbol{\phi}(t) = \boldsymbol{\phi}^T(t)\boldsymbol{\theta} \tag{24.4}$$

The prediction error,ϵ, can be written as

$$\epsilon(t,\boldsymbol{\theta}) = y(t) - \hat{y}(t|\boldsymbol{\theta}) \tag{24.5}$$

using the norm $\frac{1}{2}\epsilon^2$, the least square criterion can be derived as

$$V_N(\boldsymbol{\theta}, \boldsymbol{Z}_N) = \frac{1}{N}\sum_{t=1}^{N}\frac{1}{2}\left(y(t) - \boldsymbol{\phi}^T(t)\boldsymbol{\theta}\right)^2 \tag{24.6}$$

where N is the number of data points and $\boldsymbol{Z}_N$ is the experimental data set

$$\boldsymbol{Z}_N = \begin{bmatrix} y(1) & u(1) & y(2) & u(2) & \dots & y(N) & u(N) \end{bmatrix}^T \tag{24.7}$$

By using the quadratic function for parameter vector, it is analytically possible to find the parameters, which results in the minimum of the norm of the prediction error as follows

$$\hat{\boldsymbol{\theta}}_N^{LS} = \arg\min \mathbf{V_N}(\boldsymbol{\theta}, \boldsymbol{Z_N}) = \left(\frac{1}{N}\sum_{t=1}^{N}\boldsymbol{\phi}(t)\boldsymbol{\phi}^T(t)\right)^{-1}\frac{1}{N}\sum_{t=1}^{N}\boldsymbol{\phi}(t)y(t) \tag{24.8}$$

giving the least squares estimation of the parameter vector, $\hat{\boldsymbol{\theta}}_N^{LS}$.

In previous work done by the authors, [27], it was seen that the system has first order behaviour and an ARX model with one pole and one zero is used as estimate for the system. The validation data and ARX model can be seen for each blade in fig. 24.1.

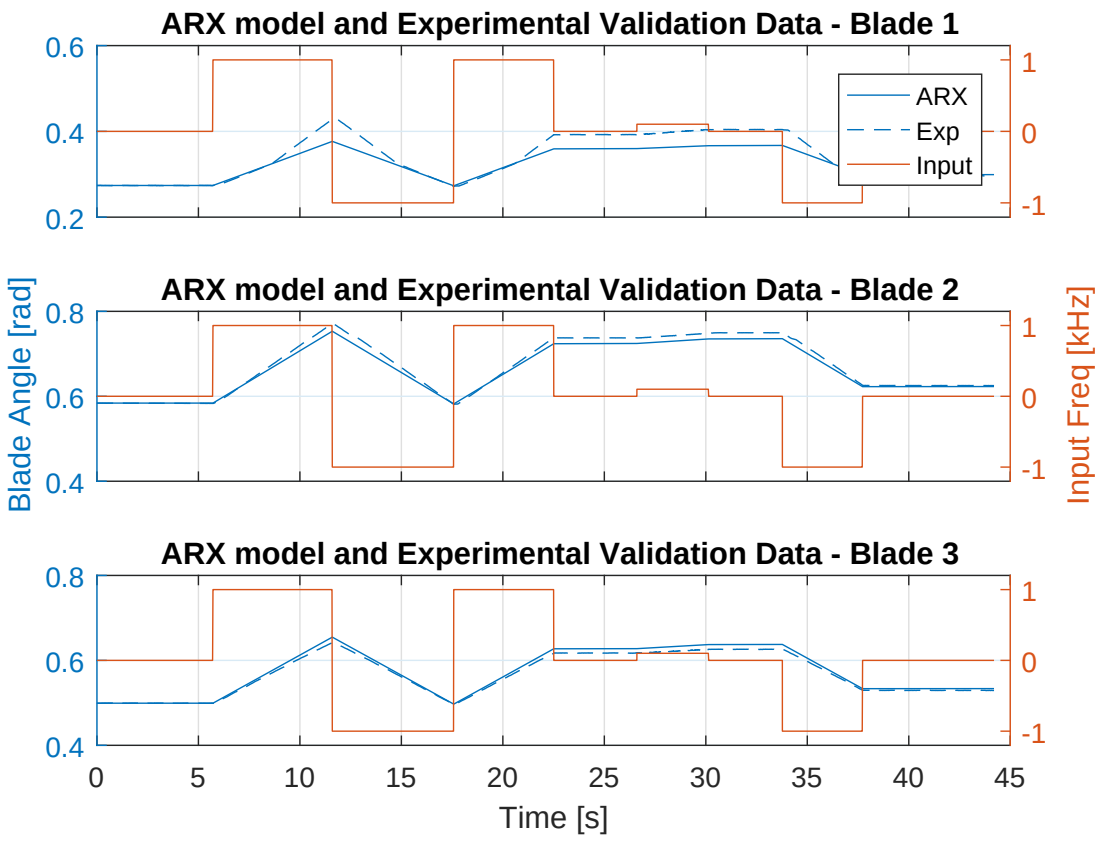

Figure 24.1: Validation input and output data and ARX model output for each blade.

The estimated model can be rewritten into a discrete transfer function using z^{-1} as unit delay operator. When the model consists of a single pole and a single zero, the discrete transfer function becomes

$$G_B(z) = \frac{b_1 z^{-1}}{1 - a_1 z^{-1}} = \frac{b_1}{z - a_1} \tag{24.9}$$

where the parameters in the ARX model, based on a sampling frequency of 5 kHz, are seen in table 24.1.

Table 24.1: Blade pitch system parameters.

Parameter	Blade 1	Blade 2	Blade 3
b_1	3.48E-9	5.74E-9	5.28E-9
a_1	1	1	1

Test and Validation 25

In this chapter the viscous friction and the generator efficiency are found experimentally. The power converter algorithm is tested experimentally and compared to the simulation. The generator and drive train model are tested in region II both experimentally and by simulation.

25.1 Drive Train

As mentioned the parameters needed to model the drive train are the rotor torque, the generator torque, the mass moment inertia of the drive train, the viscous friction and the static friction torque. The rotor torque is found by the aerodynamic models, while the generator torque is found by the generator model. The mass moment of inertia is found utilising the 3D drawing of the FOWT made in Inventor, while the static friction torque were found by experiments in section 19.2. The viscous friction is found experimentally as explained below.

25.1.1 Viscous Friction

The viscous friction of the system is found by letting the rotor deaccelerate without any rotor or generator torque and neglecting T_0, reducing the equation of motion of the drive train to

$$0 = J_{dt}\dot{\omega}_r + B_{dt}\omega_r \tag{25.1}$$

The continuous model is discretized using the backward Euler method with sampling time T_s. For sufficiently small sampling time, the following can be assumed

$$\begin{aligned} \omega_r[k] &= \omega_r(kT_s) = \omega_r(t) \\ \frac{d}{dt}\omega_r(t) &\approx \frac{\omega_r[k] - \omega_r[k-1]}{Ts} \end{aligned} \tag{25.2}$$

Thereby the discrete model of eq. 25.1 can be derived as

$$\omega_r[k] = -\frac{1}{1 + \frac{T_s}{J_{dt}}B_{dt}}\omega_r[k-1] \tag{25.3}$$

The parameters can be estimated using an autoregressive moving average (ARMA) model which is a model consisting of two parts, an autoregressive (AR) part and a moving average (MA) part. The AR model is a special case of an ARX model, described in section 24 where there is no input. The MA

part implements modelling of the error term as a linear combinations of error terms in the current and N_c number of previous time steps. The linear difference equation for the ARMA model becomes

$$y(t) + a_1 y(t-1) + ... + a_{N_a} y(t-N_a) = c_1 e(t-1) + ... + c_{N_c} e(t-N_c) + e(t) \tag{25.4}$$

which can be described by a parameter vector and a regression vector, thereby the parameters can be estimated by least squares estimation, as shown in section 24 for the ARX model.
Only a single parameter is presented in the difference equation 25.3 which gives $N_a = 1$. The MA term N_c is set to 25. The estimated parameter a_1 is a combined parameter consisting of T_s, J_{dt}, B_{dt}, since the rest of the parameters are known, the viscous friction can be isolated and calculated by

$$B_{dt} = -\frac{1 + a_1}{a_1 \frac{T_s}{J_{dt}}} \tag{25.5}$$

Five different tests were conducted and an average viscous damping of the five experiments was estimated using MA to be 0.4251 Nms, a simulation with the average viscous friction was made and compared to the experimental results as seen in the fig. 25.1.

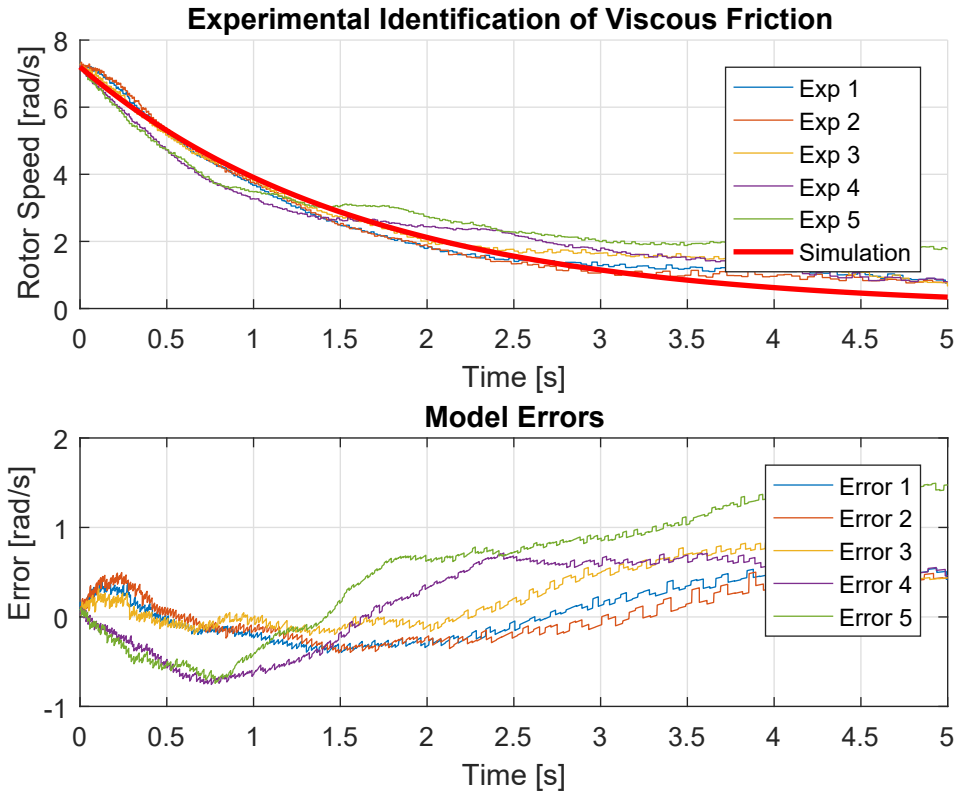

Figure 25.1: Experiment and simulation for viscous friction estimation.

It can be seen that the model predicts well until it reaches about 2 rad/s and the error starts increasing, this is however out of the operational area and it is therefore assumed satisfying.

25.2 Generator

The parameters needed to model the generator include the efficiency, the stator resistance, inductance and the peak flux linkage. The efficiency is experimentally found as explained below, while the other parameters were found in a previous project, see [27]. The resistance was found by measuring directly on the windings. The inductances were found by locking the generator such that no back emf would be produced. Thereby the voltage equation can be seen as a first order system, for which it is possible to apply sine wave voltage across a sweep of frequencies. Thereby the phase shift of the current response can be measured and the inductance can be identified. The peak flux linkage was found by rotating the PMSG with a constant speed and under no load conditions and by measuring the resulting voltage response. As the PMSG is run under no load conditions, no current will be drawn and the voltage equation can thereby be used to identify the peak flux linkage. In section 4.2 the values of these parameters are given.

25.2.1 Efficiency

To run the generator under more idealized conditions, the generator is demounted from the wind turbine and mounted on a test bench. The test bench consists of a DC-motor for running the generator and a Nordic DR-3000 torque transducer to measure the shaft torque and shaft speed. The test bench is described in section 5.2.
A series of tests were conducted with a resistive load connected to the generator in a star configuration. 15 different resistive loads were tested with 12 different rotational speeds, while the shaft torque, the generator current and voltage amplitudes and the shaft and generator power were measured.
The combined generator and gearbox efficiency can be calculated by the ratio of the generator power and the rotor power. It is investigated how the efficiency is changing by speed and torque, this change is seen in fig. 25.2.

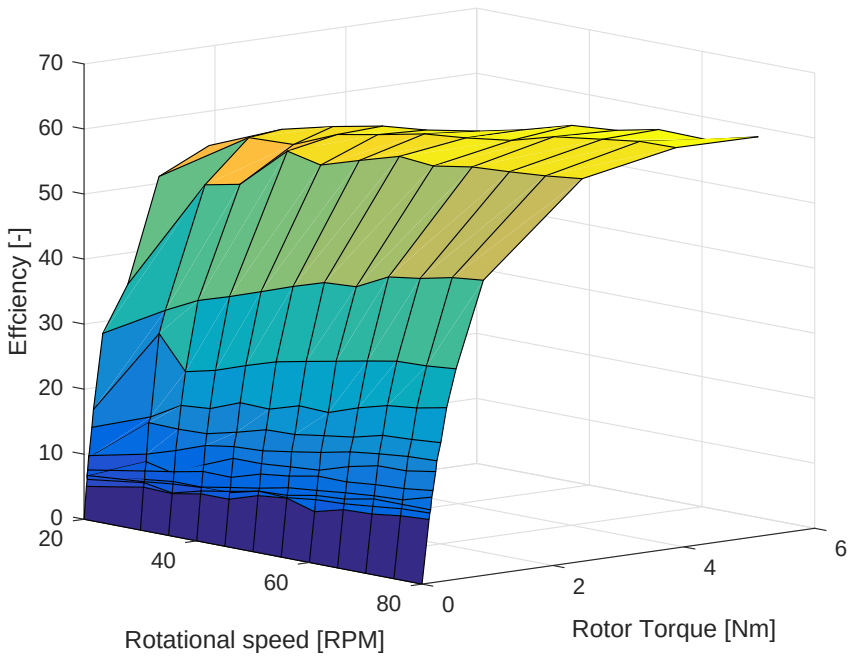

Figure 25.2: Generator efficiency, generator torque and rotational speed.

The efficiency increases with both torque and speed and levels off when the torque has reached around 2 Nm with a rotational speed of minimum 30 RPM. This is considered lower than the whole range of operation of the wind turbine, see chapter 34, so a constant efficiency of 60 % will be used for the simulations.
The test bench was not able to deliver more toque than around 6 Nm, hence it was not possible to test the generator and gearbox in the operational area. However it is expected that the efficiency will be constant throughout the rest of the operational area.

25.3 Power Converter Algorithm

In this section the algorithm for the power converter is tested. The SVPWM strategy is based on feeding modulated reference sine wave voltages to a PWM generator. Based on the reference voltages and a carrier voltage the PWM switching pattern is determined giving a high state when the carrier voltage is above the reference voltage and a low state when the carrier voltage is below the reference voltage. In fig. 25.3 experimental obtained modulated reference voltages are seen. The peak is determined by the DC bus voltage, in this case set to 200 V DC, divided by the square root of three yielding 115 V. Subtracting the voltages from each other yields the line to line voltage between the phases. The peaks of these voltages should match the DC bus voltage, which is also the case.

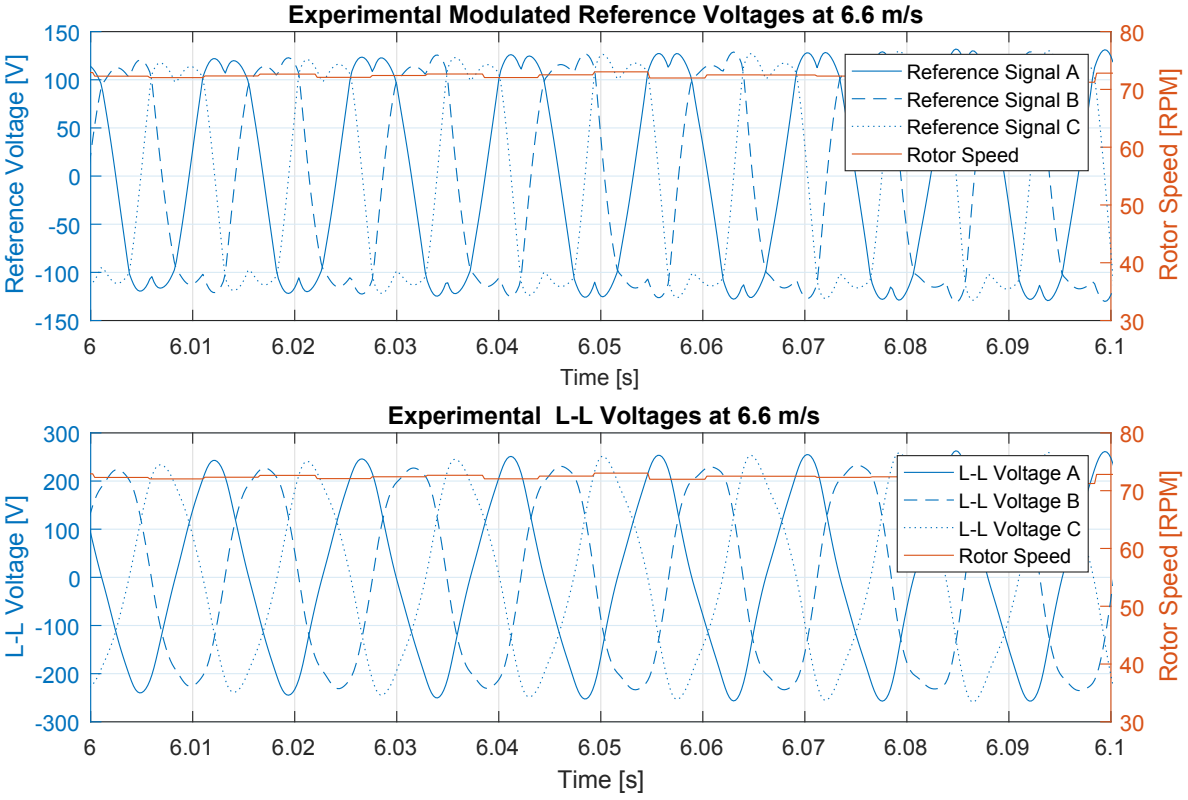

Figure 25.3: Experimental SVPWM when a 6.6 m/s wind is present running with a rotor speed of 71 RPM.

A simulation of the same case as in fig. 25.3 is shown in fig 25.4 which shows similar results.

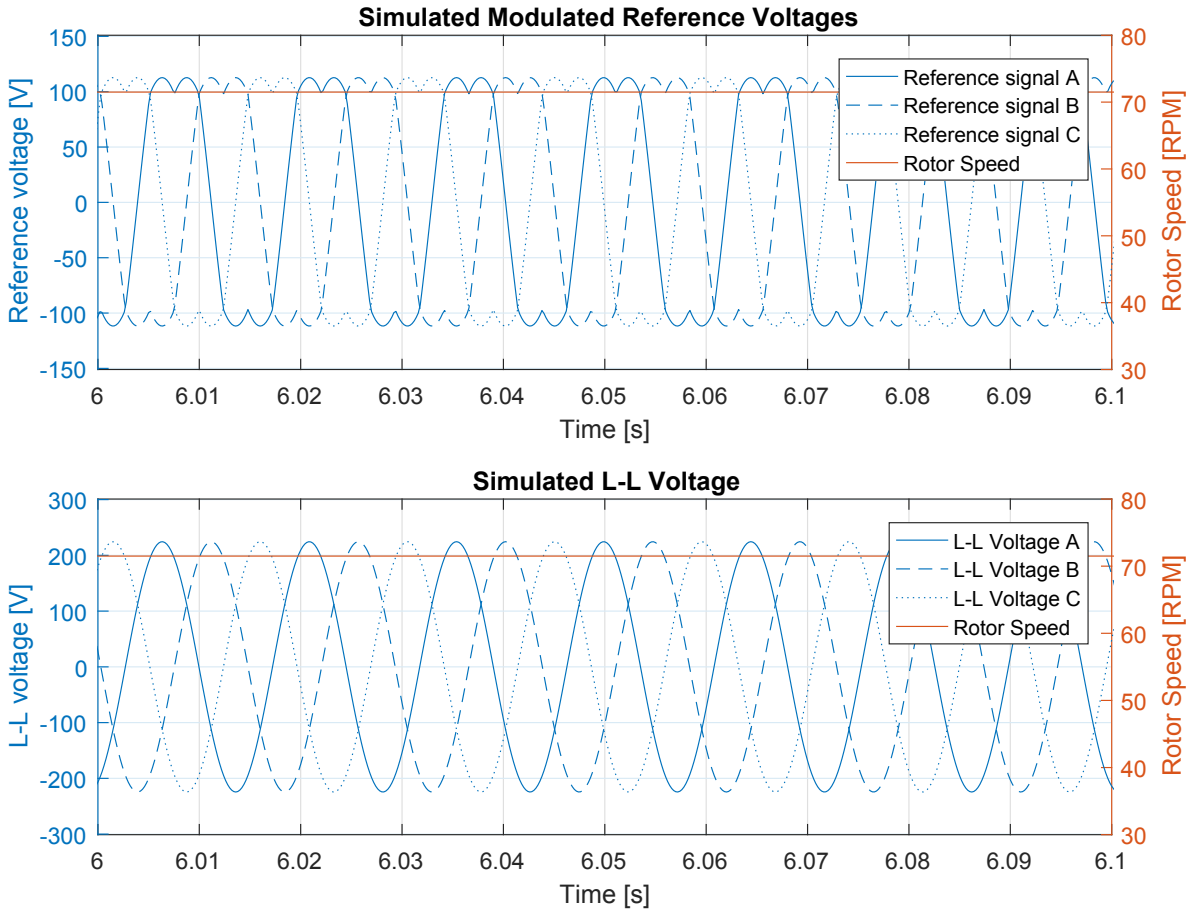

Figure 25.4: Simulated SVPWM when a 6.6 m/s wind is present running with a rotor speed of 71 RPM.

Another way to verify the algorithm is to see how the $\alpha\beta$ space vectors reference voltages track a hexagonal in the $\alpha\beta$ plane. In fig. 25.5 the trajectories of $\alpha\beta$ reference voltages are seen, normalised according to the DC bus voltage. It can be seen that the reference voltages track the sides of the hexagonal well.

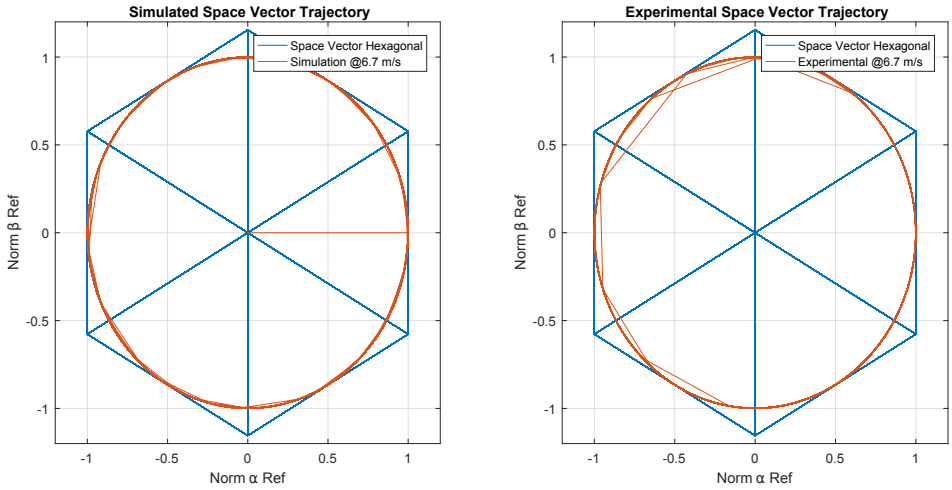

Figure 25.5: The trajectory of the space vectors $\alpha\beta$.

25.4 Region II

In Region II the wind turbine is controlled by adjusting the generator torque, while the blades are kept at a 0° pitch angle. In this experiment, the wind generator generates a mean wind speed from 3 m/s to 7 m/s and the generator power, the generator torque, rotor speed, generator *abc* and *dq0* currents and voltages are measured. The generator is controlled by the power converter where the reference rotor speed is set to the scaled reference rotor speed, explained further in part VII.

25.4.1 Theory

The generator power is found by the measured three phase *abc* voltages and currents, the generator torque acting on the rotor is found by the generator power divided by the rotor speed as in eq. 23.9 and taking the efficiency into consideration, the *dq0* currents and voltages are found using the Park-Clark transformation which uses the estimated electrical angle, described further in part VII.

25.4.2 Results

In fig. 25.6 the experimental results are seen together with the calculated results using the generator Simulink model inserted into FAST. The simulations are made using turbulent wind fields with different mean velocities in a 30 s simulation. The mean value of the results for 10 experiments is shown in the figure.

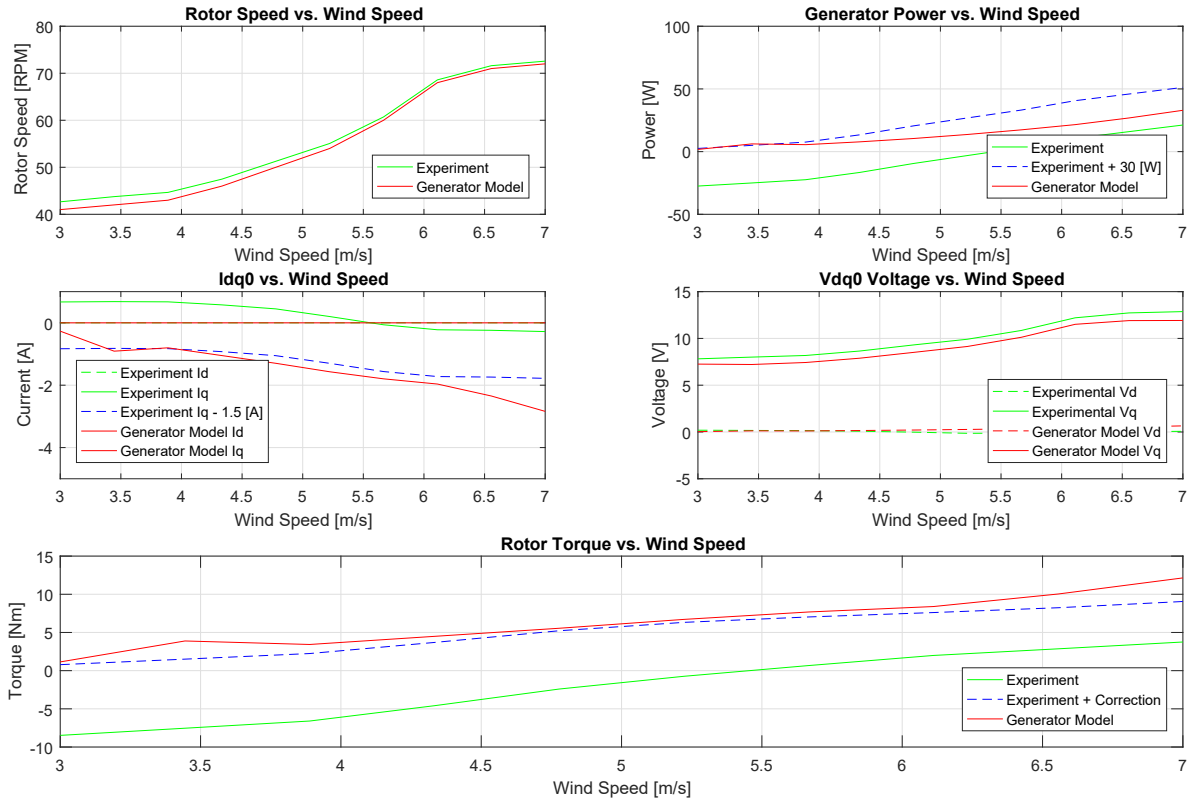

Figure 25.6: Region II simulation and experiment tests of generator.

It is seen that the experimental generator power, torque and current are offset compared to the simulated results. This is due to the fact that the power converter creates an initial load on the generator, such that it needs to run as a motor indicated by the negative sign. This is the case until 5.5 m/s where after it runs as generator. To have a better comparison between the experiments, an offset of 30 W is added to the generator power, this corrected power is also used to calculate a corrected rotor torque. The corrected power and torque are much alike the simulated. The experimental and simulated voltages fit well with a small offset, mainly because of the small offset in rotor speed. The experimental currents have the same characteristics with an offset likewise the power, the size of the current offset is around -1.5 A.

Conclusion 26

In this part the drive train model, the generator model and the power converter model were derived. Furthermore, the model of the pitch system was found using a system identification approach. The drive train was modelled as a SDOF system with rigid body motion. The model coefficients include the rotor torque, the generator torque, the drive train mass moment of inertia, the viscous damping and a combination of static friction, coulomb friction and detent torque. The rotor torque is modelled in the aerodynamic part, the generator torque is achieved from the generator model while the viscous damping and static torque are found through experiments. In the generator model the governing equation of the BLDC is given, giving a relationship between the currents, seen in a stationary reference frame, and the generated generator torque. Parameters needed to describe this relationships are the stator resistances, stator inductances and the peak flux linkage. These parameters were found experimentally in a previous project. The power converter model explained the topology of the active rectifier used in this thesis. The pitch system was found using a system identification approach using the measured input and output of the system. The found model was then validated against a new data set.
The last chapter concerns test and validation of the drive train, the generator and the algorithms used for SVPWM. The viscous friction needed to model the drive train was found through an experiment where the rotor was allowed to deaccelerate without any torque present and by assuming that the contribution from the detent torque and coulomb friction would not be present. Then by assuming that the rotor inertia was well known, the viscous friction could be found through an ARMA model. The generator parameters were found in a previous project, however the efficiency of the generator was found in this thesis. It was found that the efficiency was dependent on both the rotor torque and the rotational speed, however seems to be constant at 60% at the operational range of the generator. Next the power converter algorithm was tested experimentally to see whether or not the expected trajectories and sine wave patterns references were correctly sent to the VLT, which was the case. At last the system is tested when operating in region II indicated by a mean wind speed from 3 m/s to 7 m/s. In this test the wind turbine was controlled by adjusting the generator torque, while the blade pitch angle was kept at 0°. The steady state rotor speed, generator power, rotor torque, $dq0$ currents and voltages were measured and compared to the simulated. A good match was seen, however an offset was present in the experiments due to an initial load on the power converter.

Part VI

Aero-Hydro-Elastic Model

Symbol	Description	Units
ϕ	Azimuthal position	rad
ω_r	Rotor speed	rad/s
$\mathbf{C}_{gyro}$	Gyroscopic damping matrix	kgm^2/s
c	Damping of tower	Ns/m
$\boldsymbol{F_{gyro}}$	Gyroscopic damping force matrix	N,Nm
$F_{MI,y}$	Mass imbalance force in y-direction	N,Nm
$F_{MI,z}$	Mass imbalance force in z-direction	N,Nm
f_{TLP}	Reaction force on TLP	N
J_m	Moment of inertia of rotor	kgm^2
k	Stiffness of tower	N/m
M_g	Gyroscopic reaction moment	kgm^2/s
m	Mass of tower	kg
m_b	Mass of blade	kg
$m_{b,imb}$	Mass imbalance of blade	kg
$r_{b,cm}$	Distance from hub to mass imbalance of blades	m
$r_{r,cm}$	Distance from hub to mass imbalance of rotor	m
t	Time	s
$\ddot{x}$	Total acceleration	m/s^2
$\dot{x}$	Total velocity	m/s
x	Total displacement	m
$\dot{y}$	Velocity of TLP	m/s
y	Displacement of TLP	m
$\dot{z}$	Relative velocity	m/s
z	Relative displacement	m

Introduction 27

In this part the coupling of all previous parts will be described, tested and validated through simulations and experiments. The part is split into two sections, the first section will deal with the coupling between the tower and TLP. This coupling will be described and implemented into the mathematical model and will include the stiffness and the damping of the tower, which will be found experimentally and compared to the uncoupled model. Furthermore, the stiffness of the TLP will again be found and also compared to the uncoupled model. The changes of the mathematical model will be validated through a series of experiments. Two types of free decays will be tested, one where the TLP is given an initial displacement and one where the tower is given an initial displacement. Also forced responses will be investigated, where both regular and irregular waves will be applied to the TLP. At last an impulse excitation of the tower will be conducted for investigating the natural frequencies.

The second section of this part will deal with the coupling of the TLP, tower and rotor dynamics. Here the theories behind the coupling will be explained, and implemented into the mathematical model. Different experiments will be conducted for validating the model. These experiments include applying wind to the rotor, and investigating frequencies which have been excited and comparing it to the mathematical model. Afterwards waves will also be applied together with the wind. At last irregular waves will be applied to the TLP together with wind. In all experiments the time series and PSDs for the tower and the TLP will be investigated.

Coupling of Tower and TLP

28

Even though the TLP can be considered more or less rigid, the flexibility of the tower supporting the rotor and nacelle will affect the response of the platform. This is taken into account in the Simulink model, where the acceleration of the TLP is inserted into the tower model and the reaction forces from the tower model is inserted into the model of the TLP. In fig. 28.1 a SDOF system of this is seen.

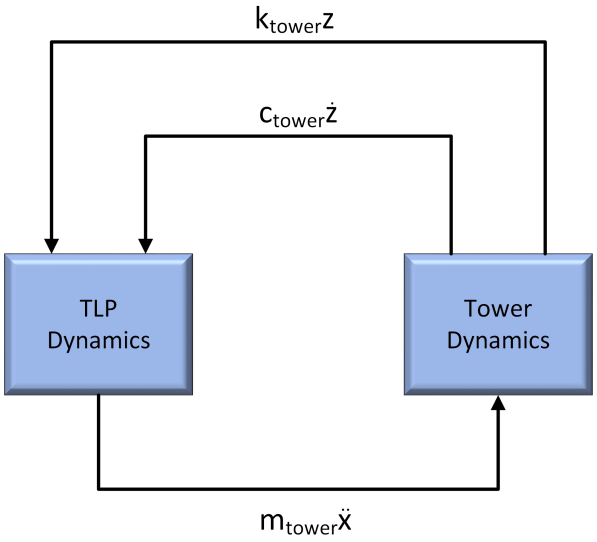

Figure 28.1: Flow diagram of TLP dynamics and tower dynamics.

The acceleration of the TLP is applied to all nodes and DOFs in the FEM model of the tower, as the TLP is considered as a moving support for the tower. While the tower is affected by the TLP, the TLP is also affected by the tower. This can be seen when considering the equations of motion regarding motions with a relative displacement. An illustration of these are seen in fig. 28.2.

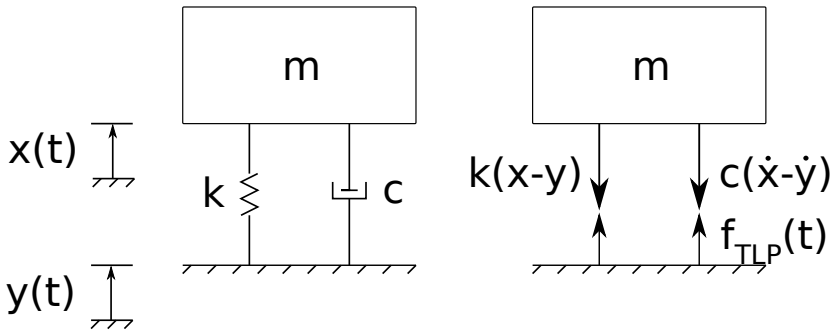

Figure 28.2: The moving support results in a relative motion and velocity.

In the figure the total displacement, $x(t)$, is the displacement caused by the moving support and the displacement of the mass, hence the relative displacement is found as

$$z(t) = x(t) - y(t) \tag{28.1}$$

where $y(t)$ is the movement of the support. As seen in fig. 28.2, the forces acting from the mass to the support is the elongation of the spring and the rate of elongation of the dashpot, thus the equation of motion of the mass can be found as

$$m\ddot{x}(t) = -k\big(x(t) - y(t)\big) - c\big(\dot{x}(t) - \dot{y}(t)\big) \tag{28.2}$$

where m is the mass of the tower and k and c are the stiffness and damping, respectively. The above equation can be rewritten with the relative displacement and velocity as

$$m\ddot{x}(t) = -kz(t) - c\dot{z}(t) \tag{28.3}$$

Hence the acceleration to the tower is supplied by the accelerating TLP, while the stiffness and damping forces are coupled to the relative motion of the tower. The tower will apply a reaction force to the TLP, f_{TLP}, because of the relative motion. This force is found as

$$f_{TLP} = kz(t) + c\dot{z}(t) \tag{28.4}$$

Here the stiffness and the damping is taken from the bottom node of the tower, as it is assumed that the coupling is rigid between the tower and the TLP.
As the coordinate system of the TLP is located in the COG of the TLP, the moments from the tower have to be transferred from the bottom node of the tower to this point.

Test and Validation 29

In this chapter the coupling between the tower and the floating platform will be investigated further. First stiffness and damping tests of the coupling when the TLP is onshore, are tested for tuning in the mathematical model of the tower. Then a stiffness test of the coupled TLP will be conducted for tuning in the mathematical model of the TLP. Thereafter free decay tests and tests with regular and irregular waves will be made, in order to validate the new mathematical models.

29.1 Stiffness of Coupled Tower

In section 14.4, the stiffness of the fixed tower was found, this in order to compare it with the stiffness for the coupled tower, and use this as a tuning parameter, when tuning the coupled model. In these tests the TLP is placed at the bottom of the wave basin without water, while the tower is mounted on top of it. This secures that the TLP will be stationary and that there will be no water interactions affecting the response of the tower. A force is applied to the topmass and the displacement is measured using the camera system OptiTrack.

29.1.1 Results

A series of tests were made and the results can be seen in fig. 29.1.

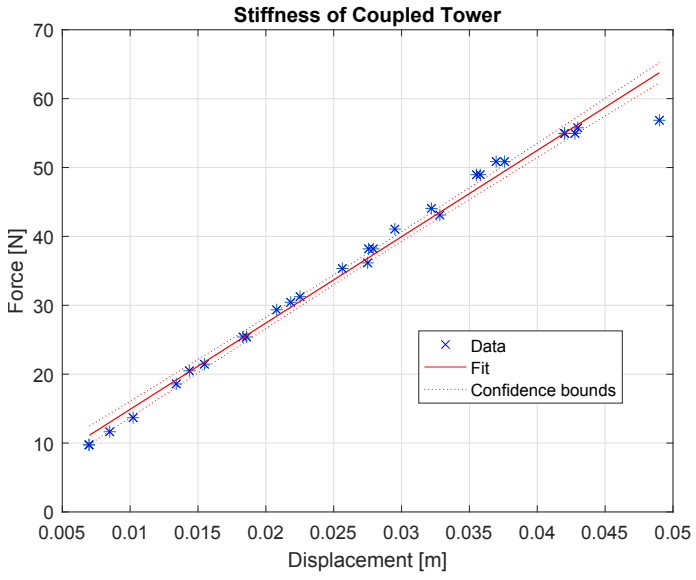

Figure 29.1: Graph showing the results of the coupled stiffness test.

The stiffness is now found to be 1253.0 N/m, meaning that the stiffness has decreased with 20 % compared to the uncoupled stiffness test in section 14.4. The 95 % confidence interval for the coupled tower stiffness is between 1195.0 N/m and 1311.1 N/m. As a comparison, the two stiffness

tests made for the uncoupled and the coupled tower are both seen in fig. 29.2.

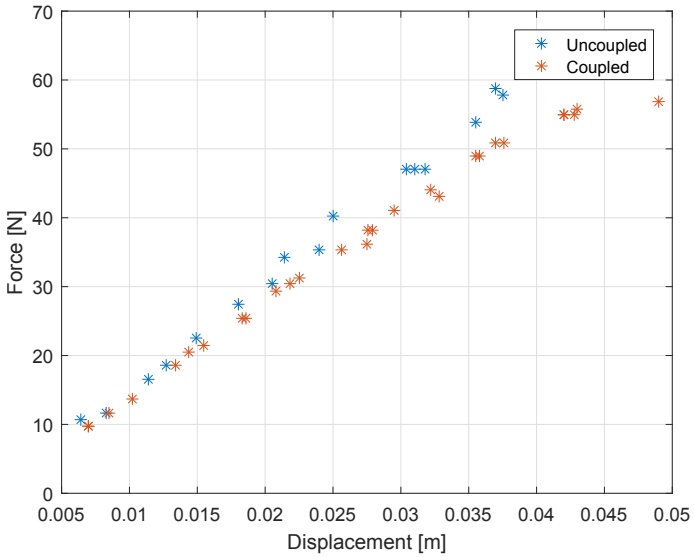

Figure 29.2: The results of the stiffness tests for both uncoupled and coupled tower.

As seen the stiffness is reduced as the support of the tower changes.

29.2 Damping of Coupled Tower

In section 14.2 the damping of the fixed tower was found. To compare it with the damping of the coupled tower, free decay tests will be made in this section and the damping will be found using the theory of logarithmic decrement. In these experiments the TLP is on the bottom of the wave basin, again to avoid the water interactions with the wave basin affecting the response.

29.2.1 Results

The damping ratio of the tower when coupled to the TLP are found during a series of experiments, the results are seen in fig. 29.3

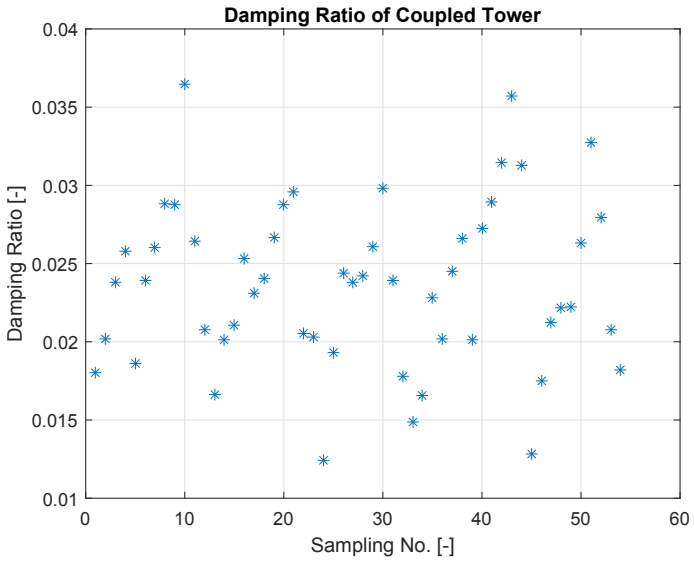

Figure 29.3: The damping ratio of the coupled tower.

As seen the damping ratio is approximately twice as high as compared to the uncoupled tower, see section 14.2, where the damping ratio was found to be 1.3 %. In fig. 29.4, the box plots for the found damping ratios for the coupled and for the uncoupled tower are seen.

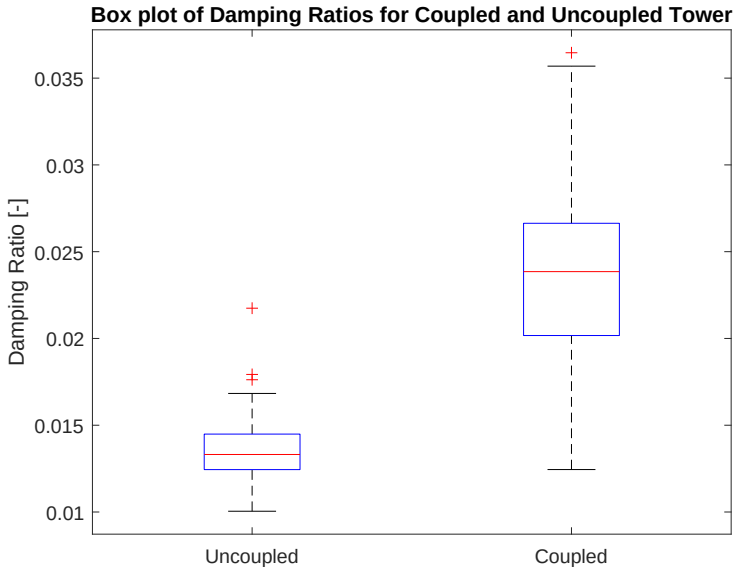

Figure 29.4: The box plots for the damping ratios of the uncoupled and coupled tower.

As seen in the box plots, it cannot be excluded, that the damping ratio are the same, as the damping ratios for the coupled tower are much more spread out compared to the damping ratios of the uncoupled tower. However a mean damping ratio of 2.5 % will be used for the simulations.

29.3 Stiffness of Coupled TLP

The mooring line stiffness of the TLP is investigated, when the tower is mounted. This is done as the tower might introduce some moments to the TLP which is not taken into account when only testing the TLP with the rigid tower mass, see section 10.2. The experiments are made by applying a known force to the TLP and measuring the displacement.

29.3.1 Results

The results of the experiments are seen in fig. 29.5

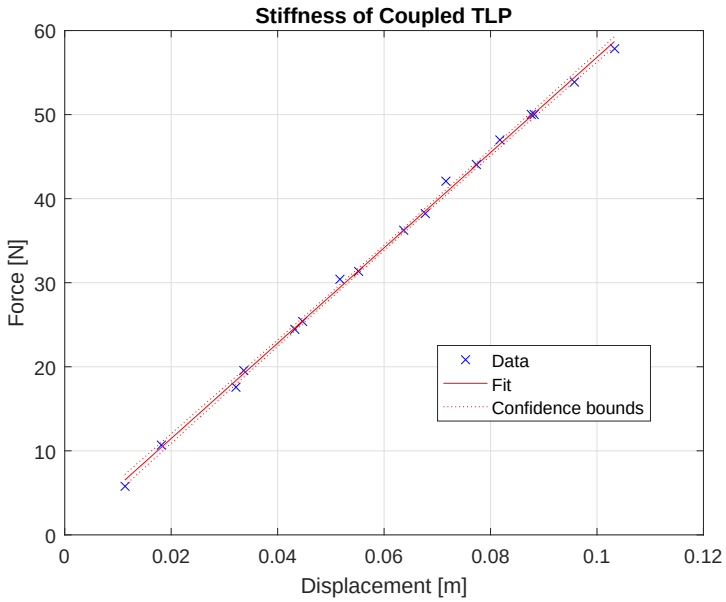

Figure 29.5: The results of the coupled stiffness test.

The new stiffness is thus found to be 567.1 N/m, and the new 95 % confidence interval ranges from 555.2 N/m to 578.9 N/m.
In fig. 29.6 also the results from the experiments done with the rigid tower mounted on the TLP are shown to see the difference.

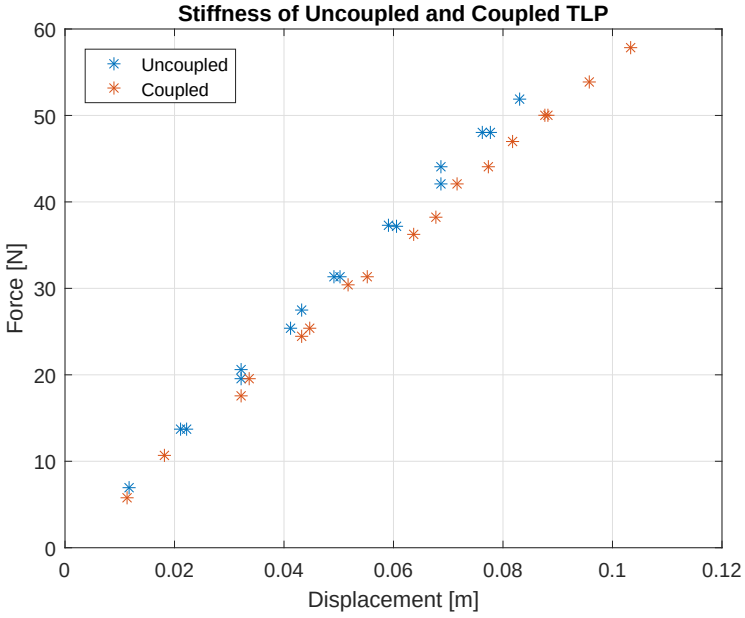

Figure 29.6: The results of the two stiffness tests.

As seen the stiffness of the coupled system is lower than the stiffness of the rigid system and has been reduced by approximately 10 % compared to the TLP with rigid tower.

29.4 Free Decay of Coupled TLP and Tower

In this section two free decays with different initial displacements will be investigated. The first free decay investigated is done by applying a force to the TLP, while the tower and nacelle is mounted on top of it. This will result in an initial displacement of the TLP but no relative initial displacement. The second type of free decay is done by applying a force to the tower top, meaning that both the tower and the TLP will have an initial displacement.
These tests are made for validating the simulations done in Simulink and FAST.

29.4.1 Free Decay of Coupled TLP

The TLP was given an initial displacement in the surge direction. The experimental response of the TLP is seen in fig. 29.7. Only the response of the TLP is investigated, as it was found that the experimental response of the tower was too small, and therefore the camera system OptiTrack could not track it properly.

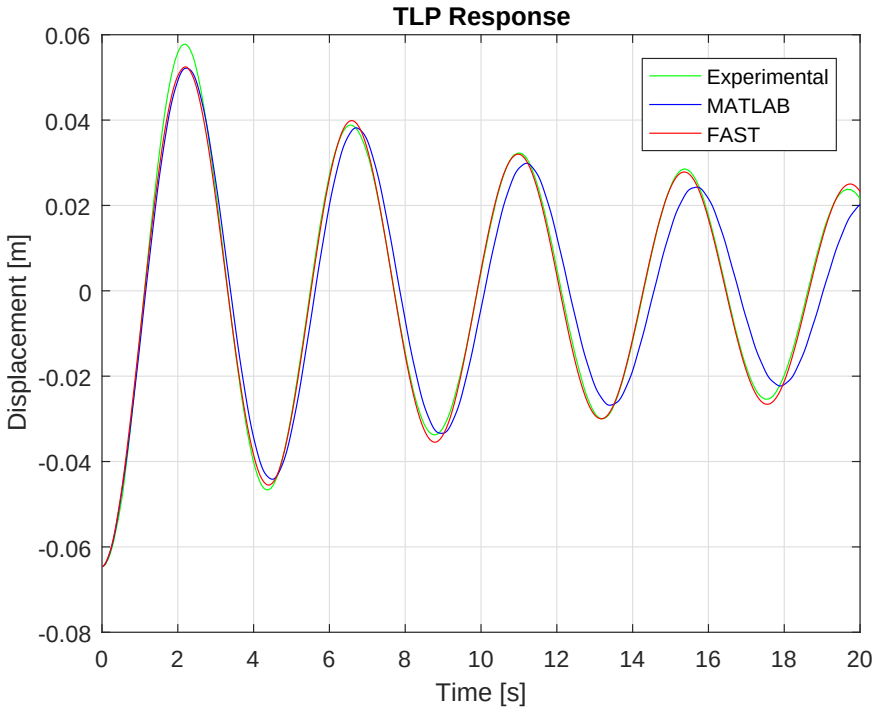

Figure 29.7: The experimental response of the coupled TLP together with the simulated responses.

As seen the simulated responses and the experimental response are much alike, both when comparing the amplitude and the frequency of the responses.

29.4.2 Free Decay of Coupled Tower

The tower was here given an initial displacement, thereby displacing the TLP, as well. This means that initial conditions in the simulations are set both for the TLP and for the tower. The experimental and simulated responses are seen in fig. 29.8.

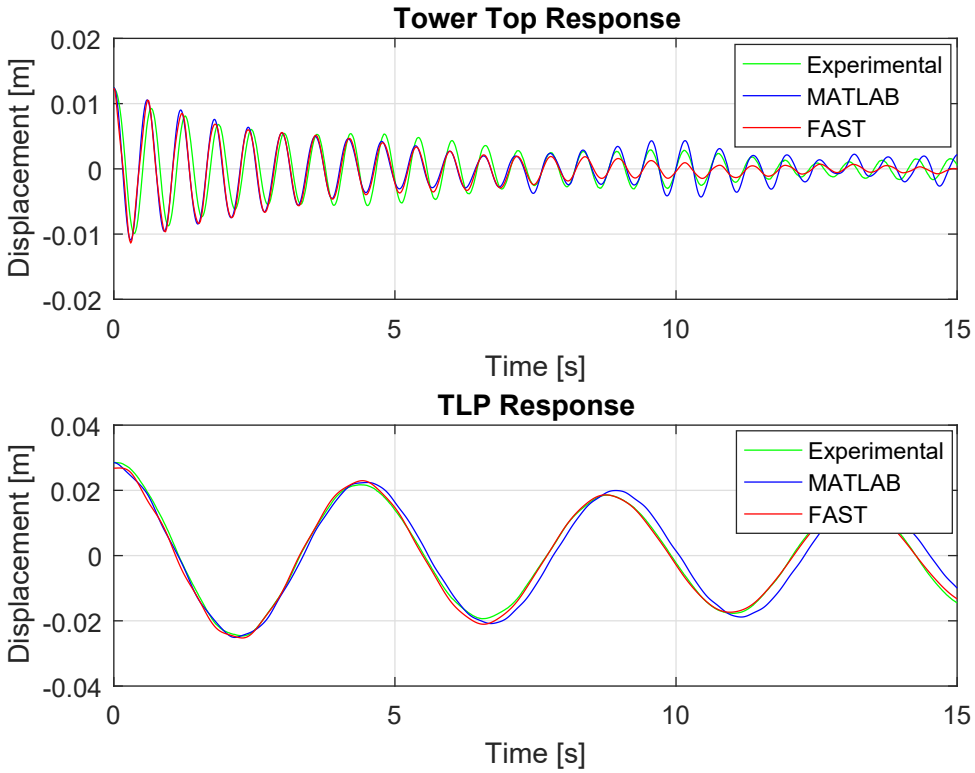

Figure 29.8: The experimental and the simulated responses for the tower and the TLP.

As seen the simulated responses and the experimental response are much alike, both when comparing the amplitude and the frequency of the responses. But after about 15 s, the experimental response is below the limit of the accuracy of OptiTrack, and the rest of the response is too uncertain to use, as only a small perturbation will make the response look completely different from experiment to experiment.

29.5 Forced Harmonic Excitation

Performing the forced harmonic response can be done by using the wave tank. This is done by applying waves to the TLP, and thus the TLP will move and act as a moving support for the tower. In this way it is possible to compare both the coupled forced response of the TLP and of the tower with the Simulink and FAST models.

29.5.1 Results

Two different tests were made. In the first test an excitation in the natural frequency of the TLP was made in order to excite the TLP and compare the steady state response. The wave height is here set to 0.005 m, while the wave frequency is 0.23 Hz. This is the highest waves possible to generate at this frequency without creating non-linear waves. In this test the tower oscillation is so small that OptiTrack is not capable of detecting the response of the tower, therefore this is not compared with the simulations. In the top of fig. 29.9 an experimental surface elevation is seen, measured at four different places. Two gauges are placed in the front sides of the TLP, while two gauges are placed at the back sides of the TLP. For the simulations the wave height is set to 0.0044 m, which seems reasonable comparing to the measured waves. In the bottom of fig. 29.9 the experimental forced response of the TLP in surge is seen. It can be seen that Simulink and FAST are capable of explaining the response well. However the Simulink simulation predicts a slightly higher amplitude.

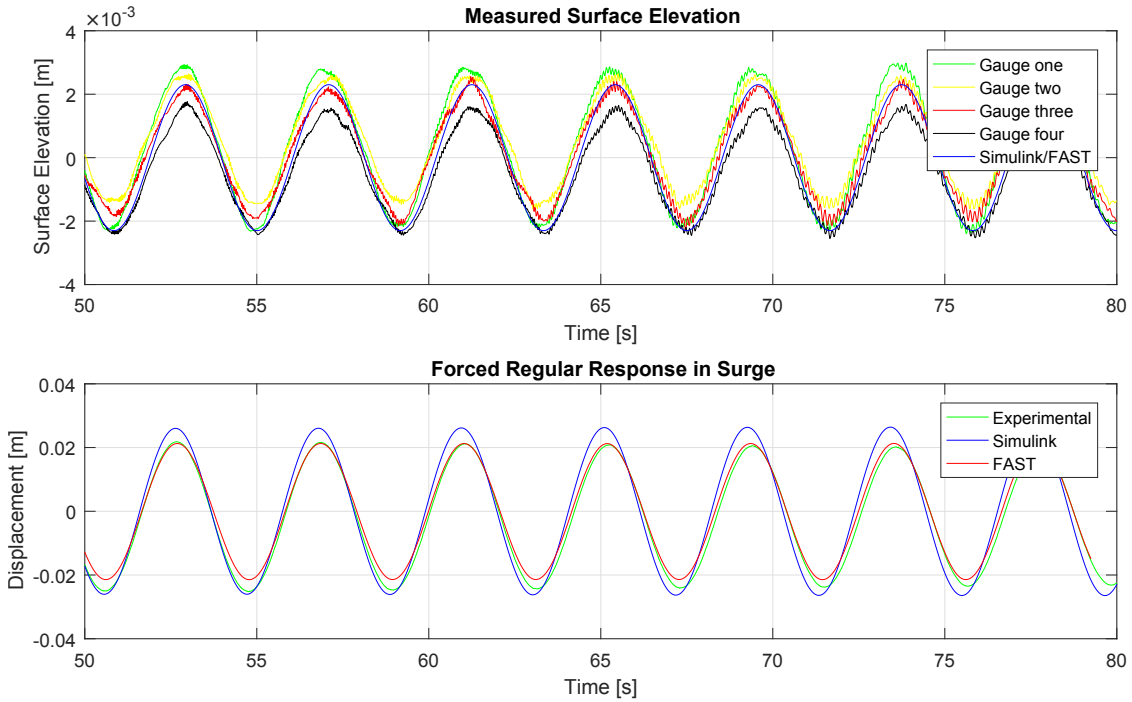

Figure 29.9: Forced response in surge with excitation in the natural frequency of the TLP.

In the second test an excitation in the natural frequency of the tower is made in order to excite the tower and compare the steady state response. The wave height is set to 0.016 m while the frequency is set to 1.72 Hz, which is also the waves used in the simulations. Again this is the highest wave possible to generate without creating non linear waves. Furthermore a large reflection coefficient will be present at this frequency. In this test OptiTrack is not capable of detecting the response of the TLP as the response is too small, therefore this is not compared with the simulations. In the top of fig. 29.10 an experimental surface elevation is seen, measured at four different places. Two gauges are placed in the front sides of the TLP, while two gauges are placed at the back sides of the TLP. It can be seen that the gauges estimate the surface elevation quite differently, which possibly is due to the large reflection occurring in the basin at this frequency. In the bottom of fig. 29.10 the experimental forced response of the tower in surge is seen. It can be seen that Simulink and FAST are capable of explaining the response well. However the simulation predicts a slightly lower amplitude. This might occur due to the large reflection coefficient at this frequency, whereby the actual waves hitting the TLP might be slightly higher.

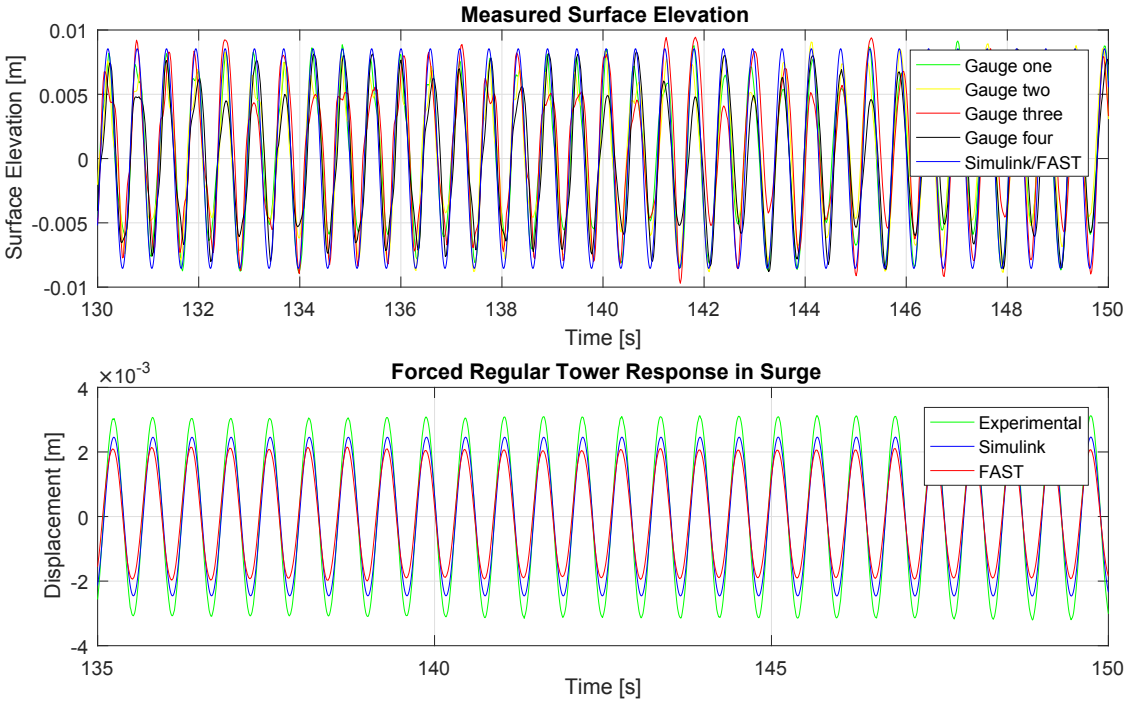

Figure 29.10: Forced response in surge with excitation in the natural frequency of the tower.

29.6 Response Amplitude Operator Coupling

In the tests regarding the coupled RAO, irregular waves are applied to the TLP with the flexible tower placed on top. The response of the TLP and tower is measured using the camera system OptiTrack, and the waves are measured using the wave gauges. These tests are made for validating the Simulink and FAST model of the coupling between the TLP and Tower.

29.6.1 Results

The TLP with the flexible tower is exposed to an irregular wave series which is generated w.r.t. a given spectrum, in this case either the JONSWAP spectrum or a white noise spectrum. The surface elevation is measured by four different wave gauges, two gauges are placed in front and to the sides of the TLP, while two gauges are placed to the sides behind the TLP. In the top left of fig. 29.11 the average measured surface elevation spectrum and the surface elevation spectrum for the simulations where Simulink and FAST use the same, are seen. The surface elevation spectrum for the simulations detect the tendency of the experimental spectrum highly detailed. Furthermore, the target spectrum, which is the spectrum input for the wave generator is seen. The target spectrum is here a JONSWAP spectrum. As it can be seen, the wave generator is not quite capable of delivering the exact spectrum in the middle of the wave tank and a large peak at the vicinity of 0.88 Hz occurs. In the top right of fig. 29.11 the measured response spectrum of the TLP is seen, along with the Simulink and FAST spectra. It can be seen that the tendency of the TLP response is captured, however the response in the natural frequency of the TLP of 0.23 Hz is underestimated. In the bottom left figure the experimental RAO of the TLP is seen together with the simulated response. Again the tendency is detected however a slightly underestimation of the amplitude is seen. The underestimations of the responses might be due to the issues with reflected waves as explained in section 10.5. In the right bottom figure the RAO between the tower and TLP is seen. Here it is seen that the simulations in Simulink and FAST underestimate the amplitude, which again might be due to the reflected waves. However the peak is at the right frequency.

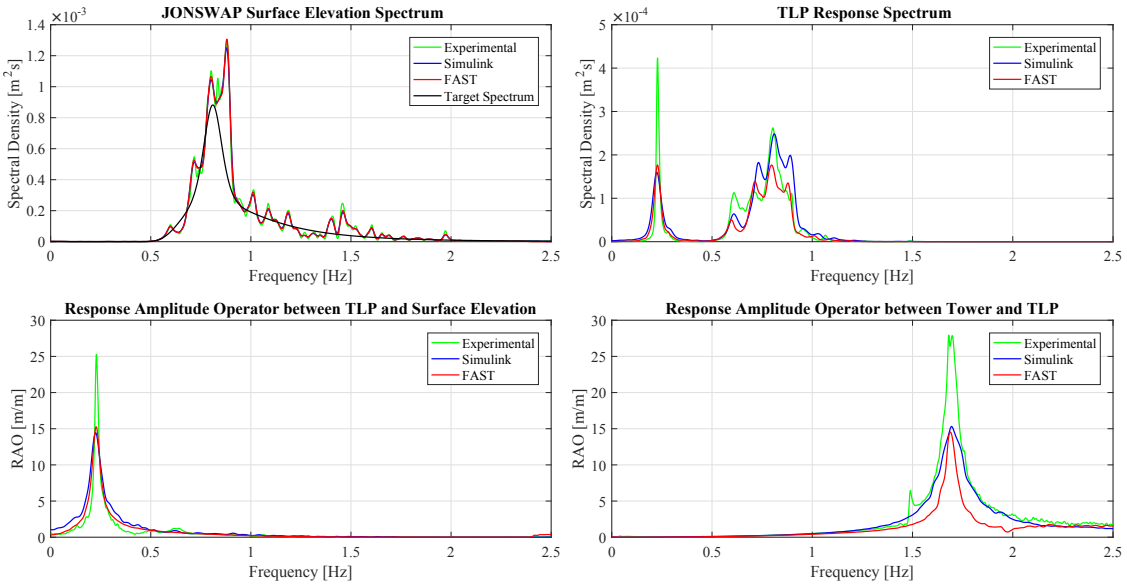

Figure 29.11: Visualisation of the experimental and simulated JONSWAP surface elevation spectrum, the TLP response spectrum, the tower response spectrum and the RAO of the TLP.

In fig. 29.12 the surface elevation is generated w.r.t a white noise spectrum with an equal energy density of 0.00005 m^2s across the frequency interval of 0.2 to 2 Hz. It can be seen the waves generated by this profile is only mainly capable of exciting the TLP in the vicinity of the natural frequency of the TLP, while the tower is excited at the natural frequency of the tower. The underestimation of the response of the tower is in this experiment much more pronounced. Again this is most likely due to the reflected waves occurring in the basin when generating the white noise spectrum. The simulated TLP response spectrum and RAO show a slightly overestimation of the responses compared to the experimental. This is opposite to the previous experiment with the JONSWAP spectrum. However as the RAO should be constant, which is also the case with the simulated responses, this is most likely due to experimental issues where the actual surface elevation influencing the TLP is not detected correctly due to the reflected waves. Several tests were made, all showing the same overall behaviour.

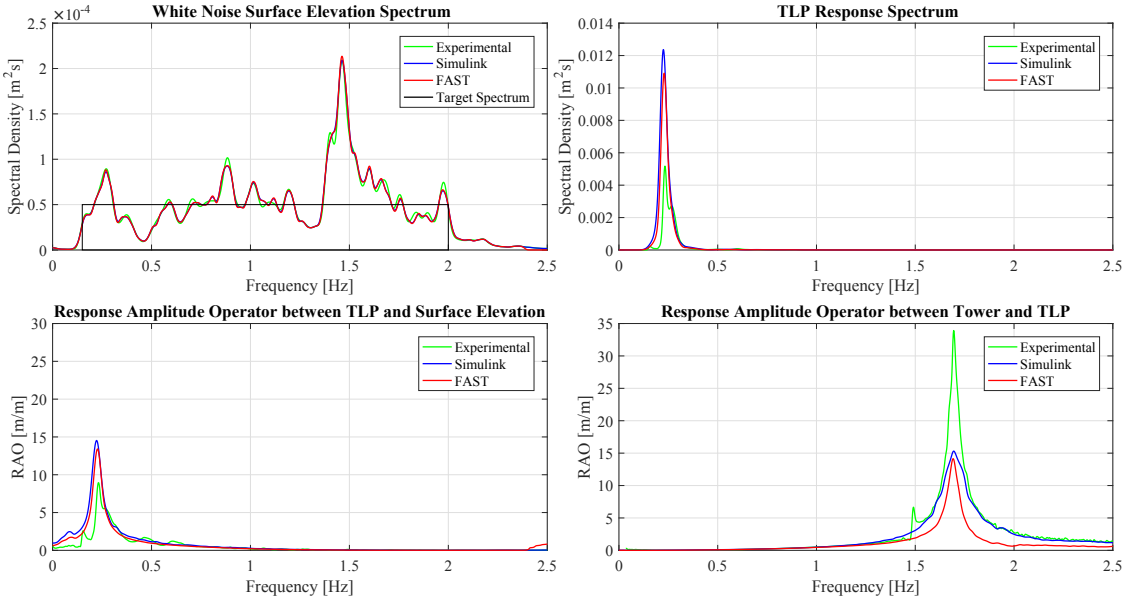

Figure 29.12: Visualisation of the experimental and simulated white noise surface elevation spectrum, the TLP response spectrum, the tower response spectrum and the RAO of the TLP.

29.7 Impulse Excitation of Coupled Tower

In this experiment the higher natural frequencies of the tower are tested. The tower is mounted on the floating TLP, and the accelerometer from Vernier is mounted on the tower. As in section 14.3, the accelerometer is mounted different places and the impulse is also applied at different locations along the tower. As the tower is coupled to the TLP, the natural frequencies have changed. The first ten natural frequencies are calculated and shown in table 29.1.

Table 29.1: Calculated natural frequencies of coupled tower.

Mode no.	Direction	Natural frequency [Hz]
1	Sway/roll	1.72
2	Surge/pitch	1.72
3	Yaw	6.09
4	Sway/roll	14.37
5	Surge/pitch	15.50
6	Sway/roll	44.94
7	Surge/pitch	45.81
8	Heave	66.77
9	Yaw	81.36
10	Surge/pitch and Sway/roll	113.06

29.7.1 Results

The frequency responses when the accelerometer is placed in the top of the tower, and when the impulse is applied in top of the tower is seen in fig. 29.13. The sampling frequency is set to 400 Hz.

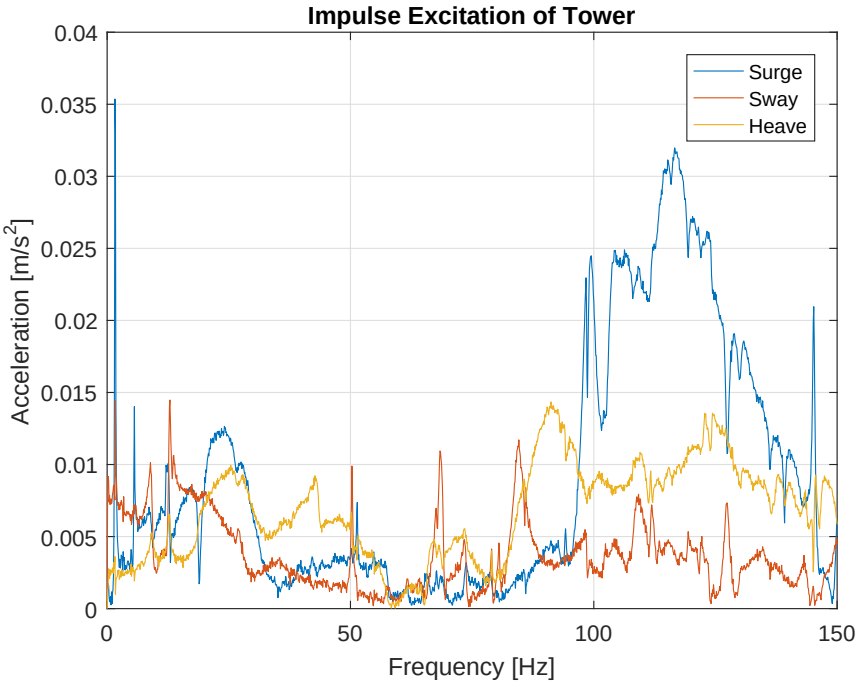

Figure 29.13: Frequency response, when accelerometer is in top of tower, and the impulse is applied in the top, as well.

In the figure it is clear that the first natural frequency is placed at 1.60 Hz. But it is hard to distinguish the different natural frequencies from each other. Also it seems that there are more response in both sway and heave than when the tower was fixed, this can either be due to that the impulse was not applied directly in the surge direction, or the coupling could have some effects on the response. Some of the higher frequencies can be found if the accelerometer is placed further down the tower, and if the impulse is applied further down. This can be seen in fig. 29.14, where the accelerometer is placed at a height of 0.6 m, and the impulse is applied at a height of 0.9 m.

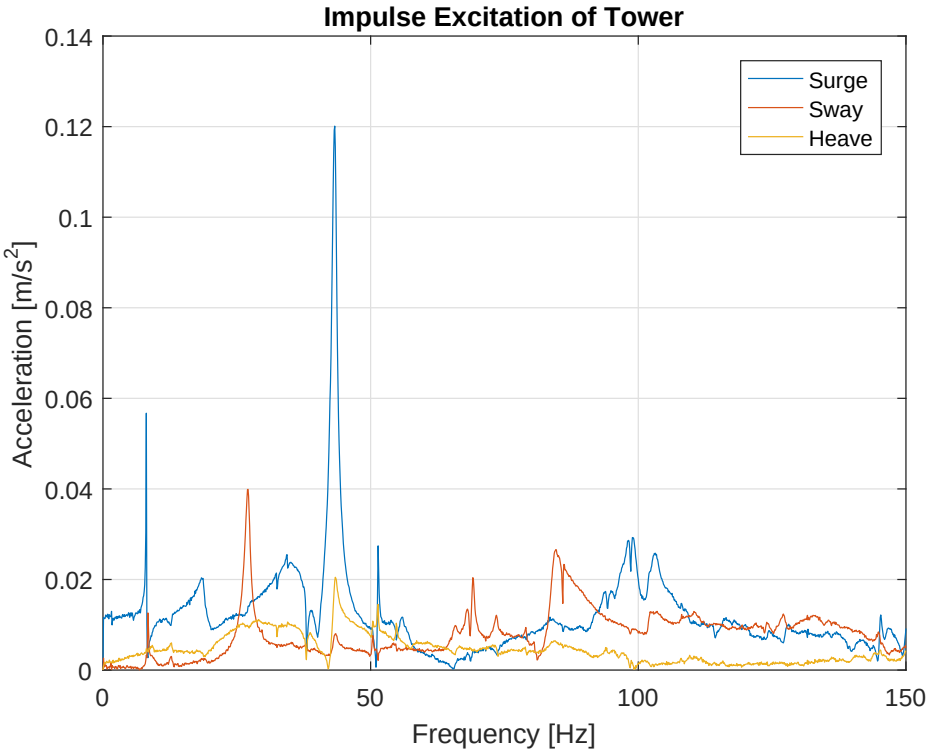

Figure 29.14: Frequency response, when accelerometer placed at a height of 0.6 m and the impulse is applied at a height of 0.9 m.

Here it is clear that there is a natural frequency at 8.10 Hz, and again one at 43.30 Hz. These would correspond to 15.50 Hz and 45.81 Hz in table 29.1. The rest of the peaks in the plot are not distinctive enough to detect higher frequencies.

Coupling of TLP, Tower and Rotor 30

When the aerodynamics are coupled to the rest of the simulation model, the drive train has to be included, as well, as this determines the rotational speed of the rotor. A flow diagram is seen in fig. 30.1

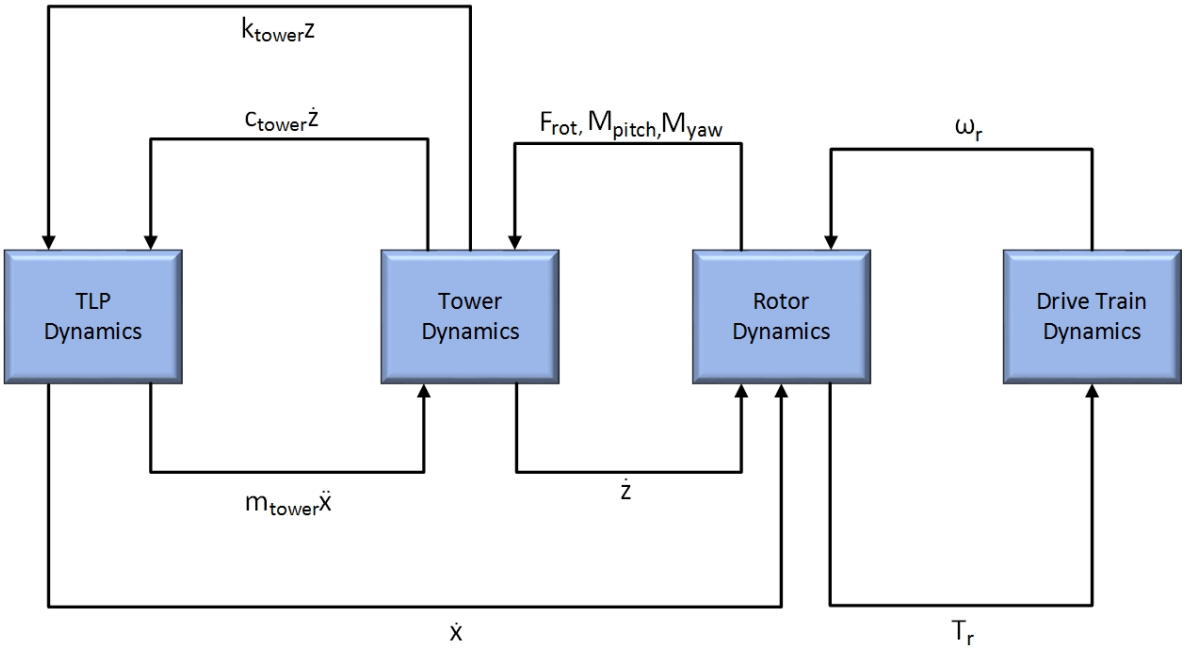

Figure 30.1: Flow diagram of the connections of the dynamic subsystems.

When the aerodynamics of the wind turbine are taken into consideration, it is coupled to the tower of the wind turbine. This is done by adding the thrust force from the rotor to the centre top node of the wind turbine tower in the surge direction. Furthermore the rotor moments in pitch and yaw are added to the respective DOFs in the centre top node.

The tower and TLP will also affect the aerodynamics as they will introduce a relative velocity, which has to be taken into account when calculating the wind velocity impacting the blades of the wind turbine. This is done by adding the velocity of the TLP and tower to the wind velocity, which is used for calculations of the aerodynamics. Also dynamics from the rotation of the rotor will have to be

included. These dynamics are arising from different sources, but are often classified according to the frequency they act in, these are the rotor passing frequency 1P, the blade passing frequency 3P and the harmonics of it. The rotation of the rotor will also introduce a gyroscopic effect, which will affect the motion in pitch and yaw. These coupled effects will be explained in greater detail below.

The rotor torque is transferred to the drive train and a reference of the rotational speed of the rotor is tracked by adjusting the rotor torque. This reference is determined by the wind speed.

30.1 Rotor Passing Frequency

The rotor passing frequency occurs due to rotor imbalances. In this thesis the rotor imbalances considered are the mass and the force imbalance of the blades. The blades of the wind turbine in this thesis are 3D-printed, but they are not completely identical, and hence a mass imbalance of the blades occurs. Therefore the centre of mass for the rotor will be slightly shifted from the geometric centre of the rotor. If only considering the centre of mass to be shifted in the rotor plane, it will cause the centre of mass to take a cyclical path in the rotor plane. A shift in the centre of mass out of the rotor plane due to mass imbalances or uneven pitching of blades can also occur, but this is not considered in this thesis. In [95] the forces arising from the mass imbalance of the rotor can be modelled by considering one blade to have a reference mass, and the two other blades to have an equal imbalance in opposite directions. The forces arising from the mass imbalance can be modelled as

$$\begin{aligned} F_{MI,y} &= 3m_b r_{r,cm}\omega_r^2 \sin(\phi) \\ F_{MI,z} &= 3m_b r_{r,cm}\omega_r^2 \cos(\phi) \end{aligned} \tag{30.1}$$

where $F_{MI,y}$ and $F_{MI,z}$ are the forces arising from the mass imbalances in the y- and z-direction, respectively. m_b is the mass of a single blade, ω_r is the rotational velocity of the rotor, while ϕ is the azimuthal position of the rotor. $r_{r,cm}$ is the radius to the centre of mass of the rotor, which can be found as

$$r_{r,cm} = \frac{\sqrt{3}}{3} r_{b,cm} \frac{m_{b,imb}}{m_b} \tag{30.2}$$

where $r_{b,cm}$ is the distance from the hub centre to centre of mass of the blades, this is guestimated to be 0.4 m. $m_{b,imb}$ is the mass imbalance of the blades, which in this thesis is guestimated to be 5% of the reference mass of 0.76 kg, giving an imbalance mass on the two other blades of ±0.038 kg. The forces from the mass imbalance of the blades are applied in the centre of top nodes of the tower.
The force imbalance of the blades can be due to fabrication errors, an offset in the blade pithing angle, etc. In this thesis the force imbalance is taken into account, by shifting the AOA of each blade, this is explained in chapter 31.

30.2 Blade Passing Frequency

When the blades pass the tower, the tower will experience a reduction in wind speed, as explained in section 18.3.3. This change in wind velocity gives rise to a change in loads on the blades, and as the blades pass three times per revolution of the rotor, this gives rise to a 3P effect and harmonics of

it. But in the experimental setup, also a reduction in the top of the wind field is present, therefore this was taken into account, too. This is explained in chapter 31.

30.3 Gyroscopic Damping

When the aerodynamics of the rotor are coupled to the tower, the gyroscopic damping effect has to be taken into account. The gyroscopic damping effect arises when an external torque is applied perpendicular to the spinning rotor. The gyroscopic damping term is present in the two rotational DOFs which are not perpendicular to the axis of the rotation of the rotor, i.e. pitch and yaw. The gyroscopic damping couples the rotation of pitch and yaw, as an inclination of the rotation plane in either pitch or yaw also will cause an inclination of the other.
The magnitude of the gyroscopic reaction moment is found as

$$M_g = \omega_r J_m \tag{30.3}$$

where M_g is the gyroscopic reaction moment and J_m is the moment of inertia of the rotor. The gyroscopic damping matrix is found to be

$$\boldsymbol{C_g} = M_g \begin{bmatrix} 0 & 0 & 0 & 0 & 0 & 0 \\ 0 & 0 & 0 & 0 & 0 & 0 \\ 0 & 0 & 0 & 0 & 0 & 0 \\ 0 & 0 & 0 & 0 & 0 & 0 \\ 0 & 0 & 0 & 0 & 0 & -1 \\ 0 & 0 & 0 & 0 & 1 & 0 \end{bmatrix} \tag{30.4}$$

where $\boldsymbol{C_g} \in \mathbb{R}^{6x6}$ is the gyroscopic damping matrix [96]. For implementing this damping, it is multiplied with the total velocity vector of the TLP and the tower and the gyroscopic damping force, $\boldsymbol{F_{gyro}}$, is found

$$\boldsymbol{F_{gyro}} = \boldsymbol{C_g}\dot{\boldsymbol{x}} \tag{30.5}$$

Test and Validation 31

In this chapter experiments regarding the coupling of the rotor dynamics, the tower dynamics and the TLP dynamics are conducted. At first experiments were conducted with only wind applied to the wind turbine, so no generated waves are present. The results from these experiments will be compared to the simulations. After this, experiments where both wind and waves were applied to the wind turbine are conducted. The results from these experiments will also be compared to the simulations. The experimental data are found using the camera system OptiTrack, where the displacement of the nacelle and the TLP are measured.
When wind is applied, the rotor will start rotating, introducing dynamics to the wind turbine. The dynamics introduced are most easily seen when investigating the PSD of the motion response of the tower and TLP, as it will introduce some excitation frequencies to the response. These frequencies are the 1P from the rotating rotor, 3P and its higher harmonics from the blades and the natural frequencies of the tower and TLP. Furthermore, when waves are applied to the TLP, the wave frequencies will also be introduced to the dynamics of the system.

31.1 Aerodynamics

In these experiments only wind is applied to the rotor while no waves are present. Three different wind velocities were tested; 6 m/s (wind generator fan speed of 2200 RPM), 7 m/s (2500 RPM) and 8.6 m/s (3100 RPM). Only the surge direction is investigated, as this is the same direction as the wind and therefore the DOF with the largest dynamical response. The pitch and yaw DOFs were also expected to have a significant dynamical response, but by investigation of the time series of these DOFs, e.g. in appendix A.7, displacement is present, but OptiTrack is not able to detect all of it and faulty measurement points are seen. This was most likely due to the fact that the cameras used to track the displacement were periodically blocked by the rotating blades. Furthermore, a bar blocked the sight for the TLP for some cameras when it moved. In fig. 31.1 the time series of the tower and TLP are seen for the three experiments conducted, together with the corresponding simulations from Simulink and FAST. The experiments were conducted for 10 minutes for each wind speed tested, while the simulations were run for 5 minutes.

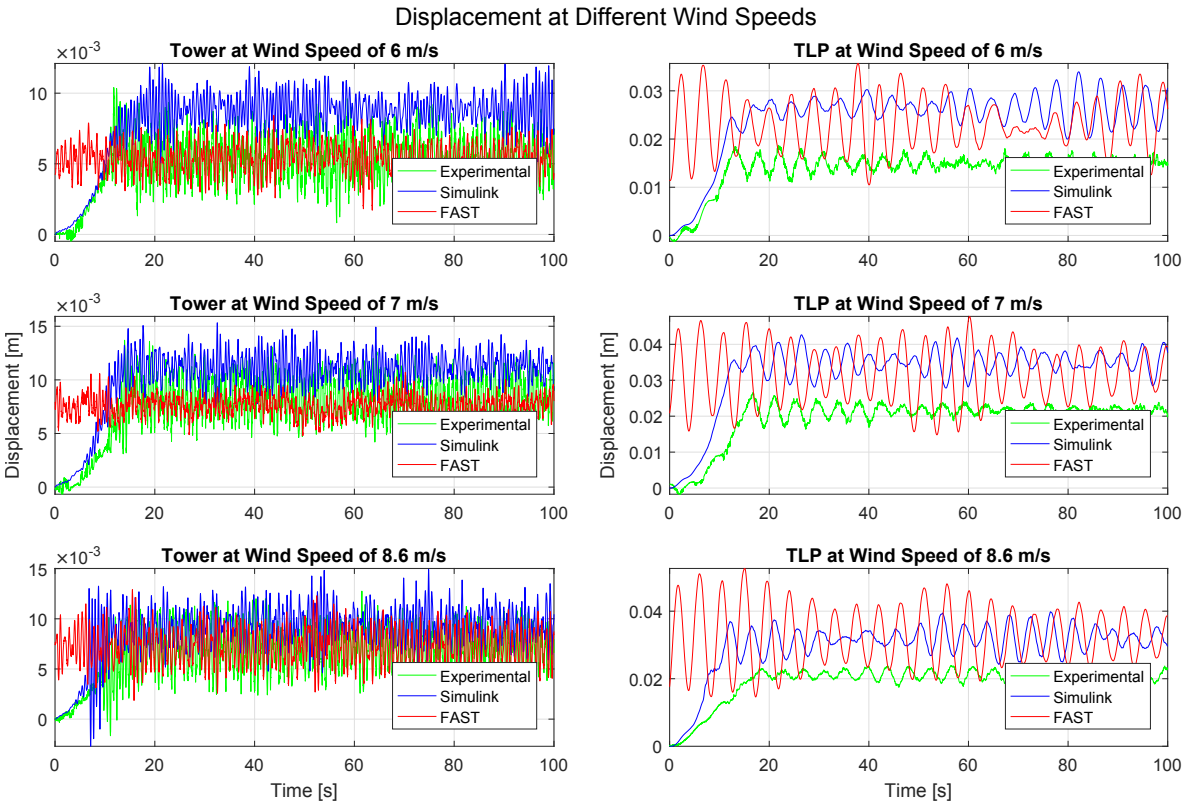

Figure 31.1: Experimental and simulated time series of tower and TLP when different wind speeds are applied.

As seen in the figure, the offset for the tower found in FAST fits well with the experimental results, while the simulations in Simulink slightly overestimates the offset. Regarding the offset of the TLP both FAST and the simulation in Simulink overestimates the mean offset, and FAST seems to overestimate the amplitudes of the oscillations.

In fig. 31.2 the PSD of the tower displacement for the three tests are seen.

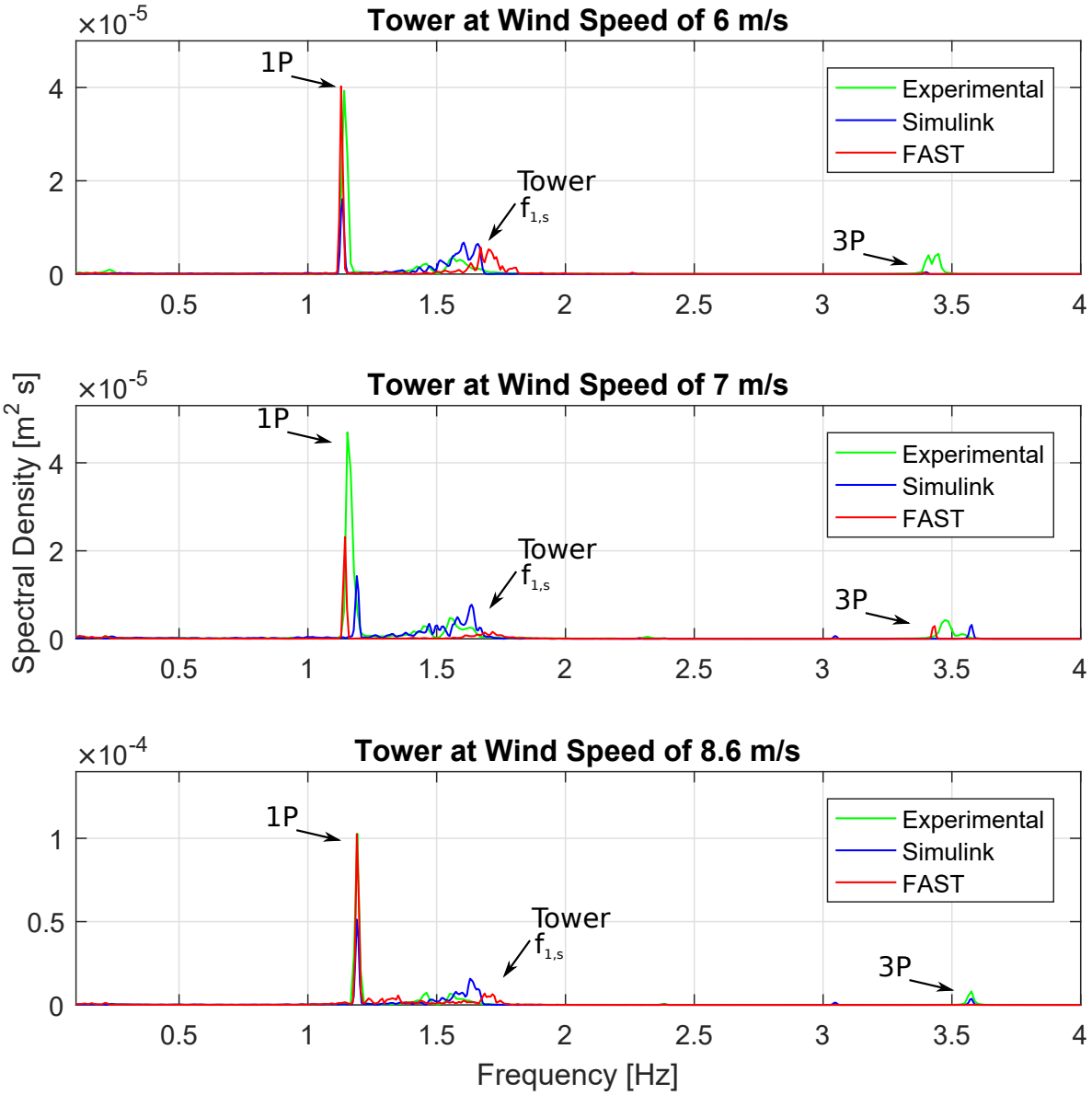

Figure 31.2: The experimental results together with the simulated results of the tower, when different wind speeds are applied to the rotor.

In the figure above two significant peaks and a more spread peak are seen. The two significant peaks are the 1P and 3P effects, while the spread peak is the first natural frequency of the tower in surge. The simulation in Simulink detects all the peaks, while FAST detects all but one 3P effect.
1P occurs for each rotor frequency, and the reason for occurring in the surge direction is the difference in blade pitch angle. The pitch angle of the physical blades are manually initialised, and hence some margin of error must be expected. Therefore the pitch angle of the blades in the simulations are pitched $\pm 5°$ in both FAST and Simulink, and thus a 1P effect in surge will occur.
The 3P effect is caused by tower shadow, the fact that the blades passes the tower, and therefore the velocity on the blades changes. The blades of this thesis have a bigger chord/length ratio compared to commercial blades, and hence they will have a bigger impact on the tower shadow as trailing edge is closer to the tower. Therefore the distance between the rotor plane and the tower was reduced in

the simulations, and a bigger 3P effect occurred. Furthermore the rotor plane of the experimental setup is not inside the wind field in the top of the plane. This will cause wind speed in this area to be different, and will hence also cause a 3P effect because of the changed aerodynamics of the blades. This reduction in wind field is incorporated in Simulink by reducing the mean wind speed vector at this point. But is has not been possible to introduce this into FAST, and therefore a smaller peak at 3P was expected.

In fig. 31.3 the PSD of the TLP displacements are seen at the tested wind speeds.

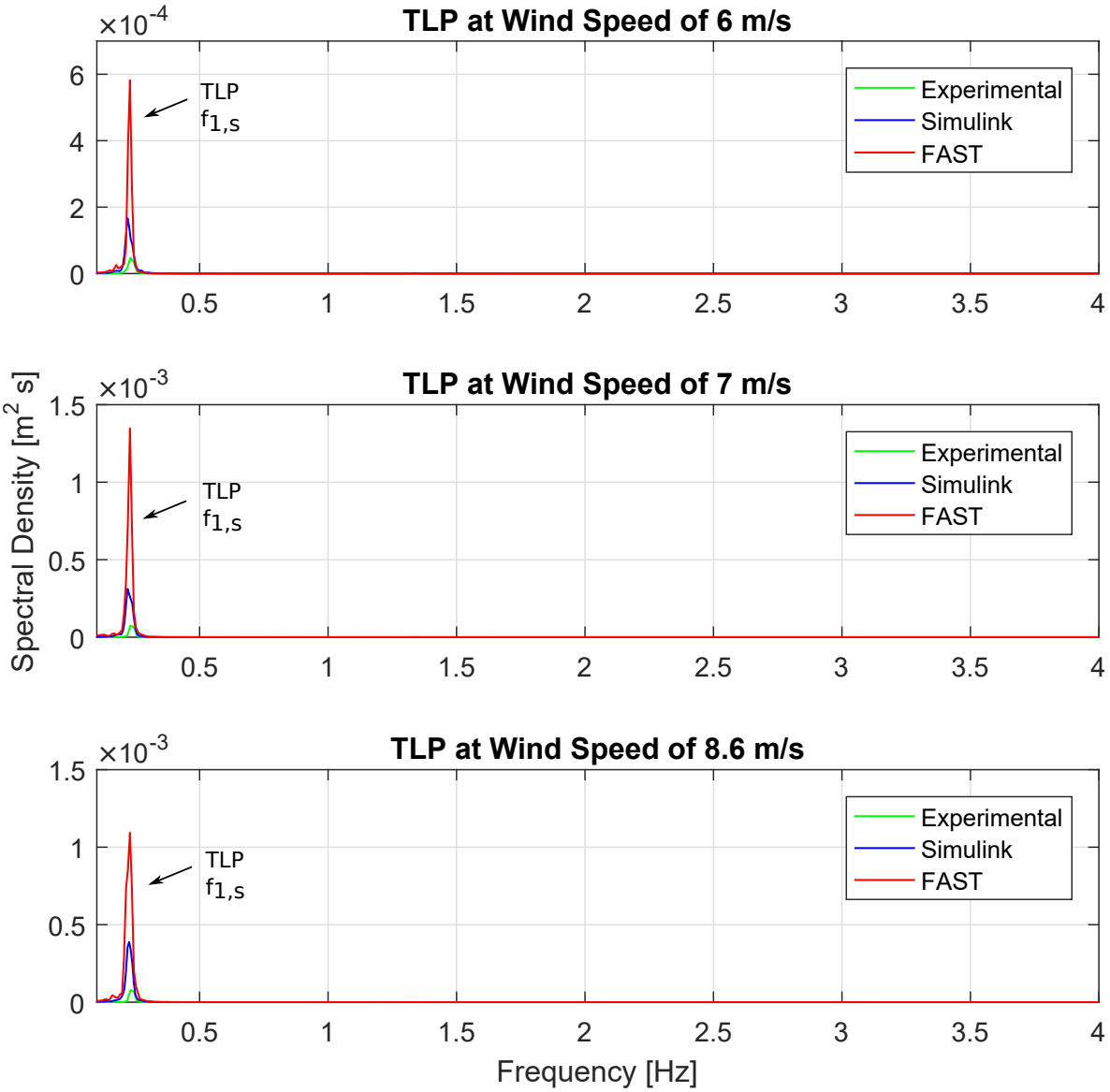

Figure 31.3: The experimental results together with the simulated results of the TLP, when different wind speeds are applied to the rotor.

In the figure only one peak appear in each PSD, this is at the natural frequency of the TLP in surge, which is denoted TLP $f_{1,s}$. The experimentally found frequency of the peak fits well with the frequency of the simulated responses, however the amplitudes differ more. The experiment shows a very small amplitude, while Simulink is a bit higher and FAST overestimates by a great amount.

This might be due to the fact that in the experiment, the wind generator ramps from 0 RPM up to the desired rotational speed, which is also done for the first 20 s in Simulink, but is not possible to do in FAST, which is also seen in fig. 31.1. Hence a forced free decay will appear which will die out very slowly. To take this into account, the data used for the PSDs was offset by 100 seconds, but still a significant amount of energy is present. This was also seen in Simulink, and hence more linear damping was implemented. The extra damping is due to the offset of the TLP caused by the wind. This extra damping is used throughout the rest of the simulations.

31.2 Aerodynamics and Hydrodynamics

A series of tests were made where both wind and waves are applied to the rotor and TLP, respectively. The wind speeds tested are 4 m/s, 7 m/s and 8.6 m/s, while the waves tested have a frequency of 0.6 Hz and 1.7 Hz, and a wave height of 0.01 m. Thus giving six tests in total. The time series of for the tower displacement for all test are seen in fig. 31.4.

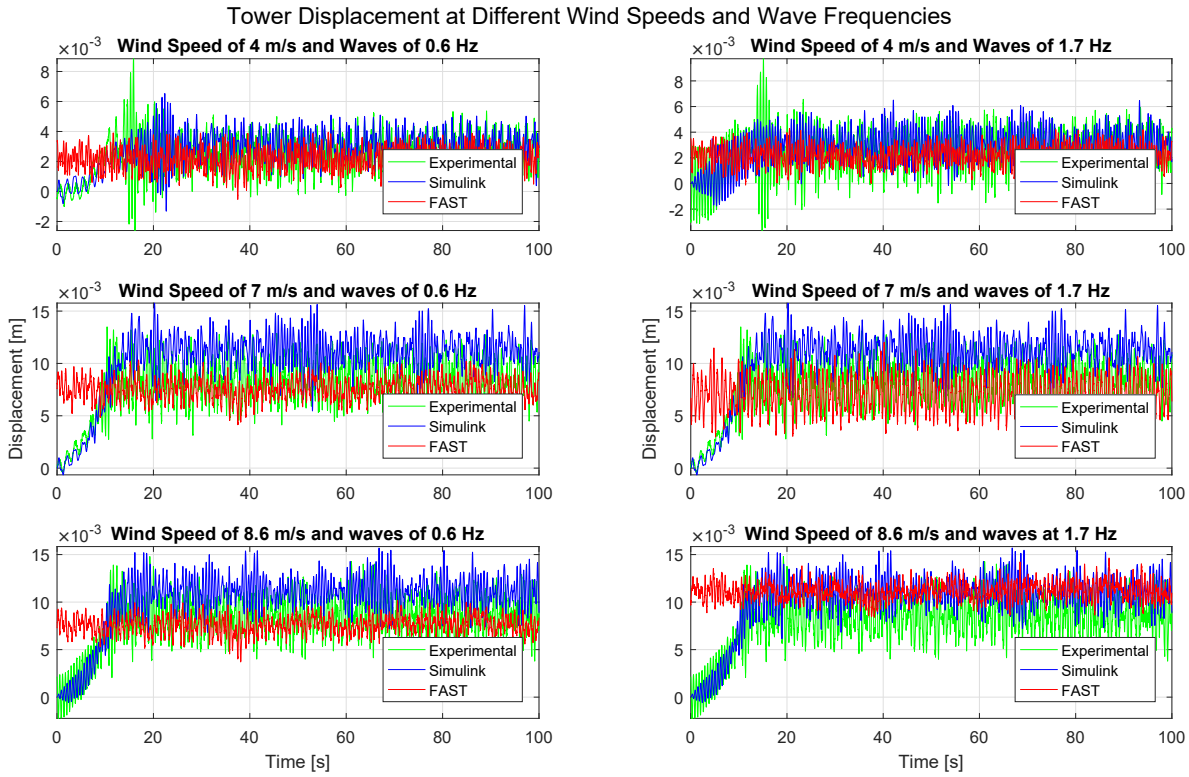

Figure 31.4: Time series of tower displacement in the different experiments.

Here it can be seen that the simulation in Simulink has a overall tendency to overestimate the mean offset, while the mean offset for the simulations done in FAST fit better with the experimental. The amplitude of the oscillations in the simulation in Simulink seems to fit well with the experimental, while FAST seems to underestimate the amplitude of the oscillatory motion.

The time series of for the TLP displacement for all test are seen in fig. 31.5.

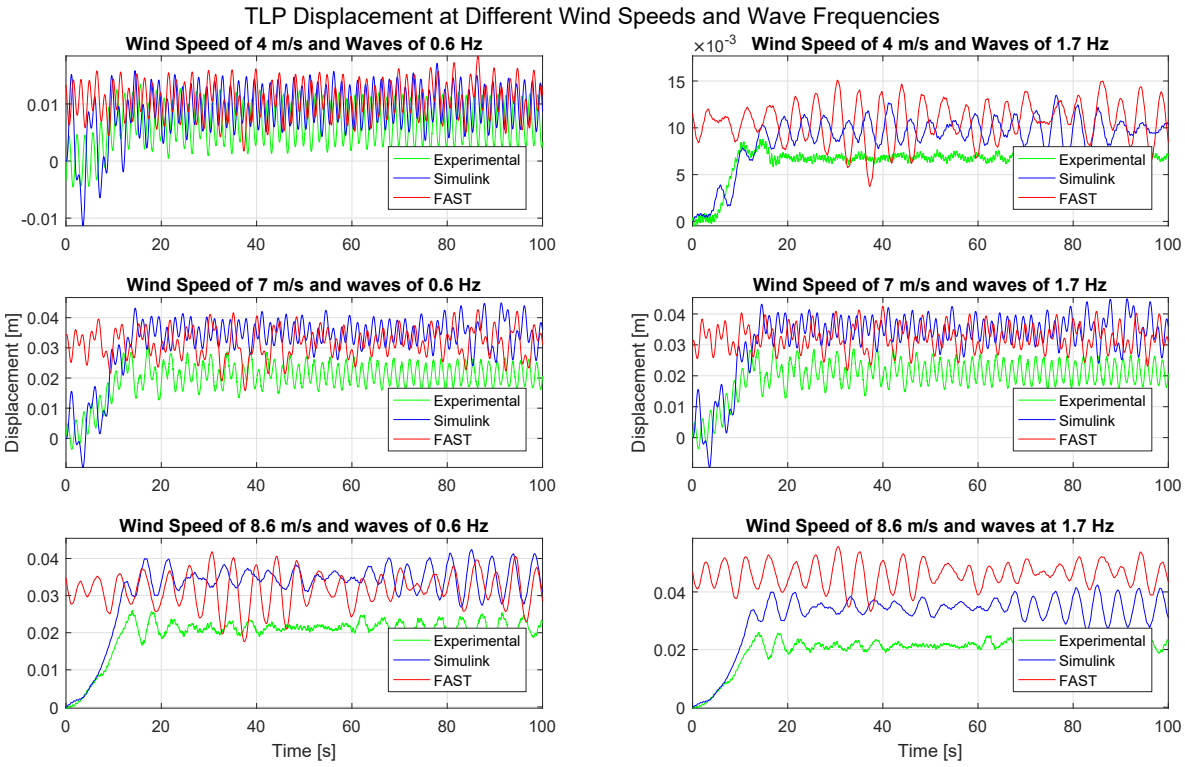

Figure 31.5: Time series of TLP displacement in the different experiments.

Here it can be seen that both the simulation done in FAST and in Simulink overestimate the mean offset, and that FAST simulations have a tendency to have bigger amplitudes in the oscillations.

In fig. 31.6, the PSDs of the tower displacements in the different tests are seen. It can be seen that the peaks at the different frequencies are found in all simulations, however the amplitudes differ. When investigating the PSDs for waves with a frequency of 0.6 Hz, it can be seen that at 0.6 Hz the amplitude is highest for the experiment, a bit lower for the simulation in Simulink and lowest for the simulation in FAST, however the amplitudes are still close to each other. The 1P and 3P effects are most significant in the experimental data, and least significant in the Simulink simulation. The first natural frequency in surge of the tower are seen as a spread peak for all the simulations and experiments.
When investigating the PSDs for waves with a wave frequency of 1.7 Hz, the same overall tendency as just described is seen. The experimental data have the most significant effect in 1P and 3P, while the Simulink simulation has the least effect in these frequencies, except for the 1P in the experiment done with a wind speed of 8.6 m/s. Here the first natural frequency of the tower in surge is again seen as a spread peak. And the wave frequency is also clear in all simulations.

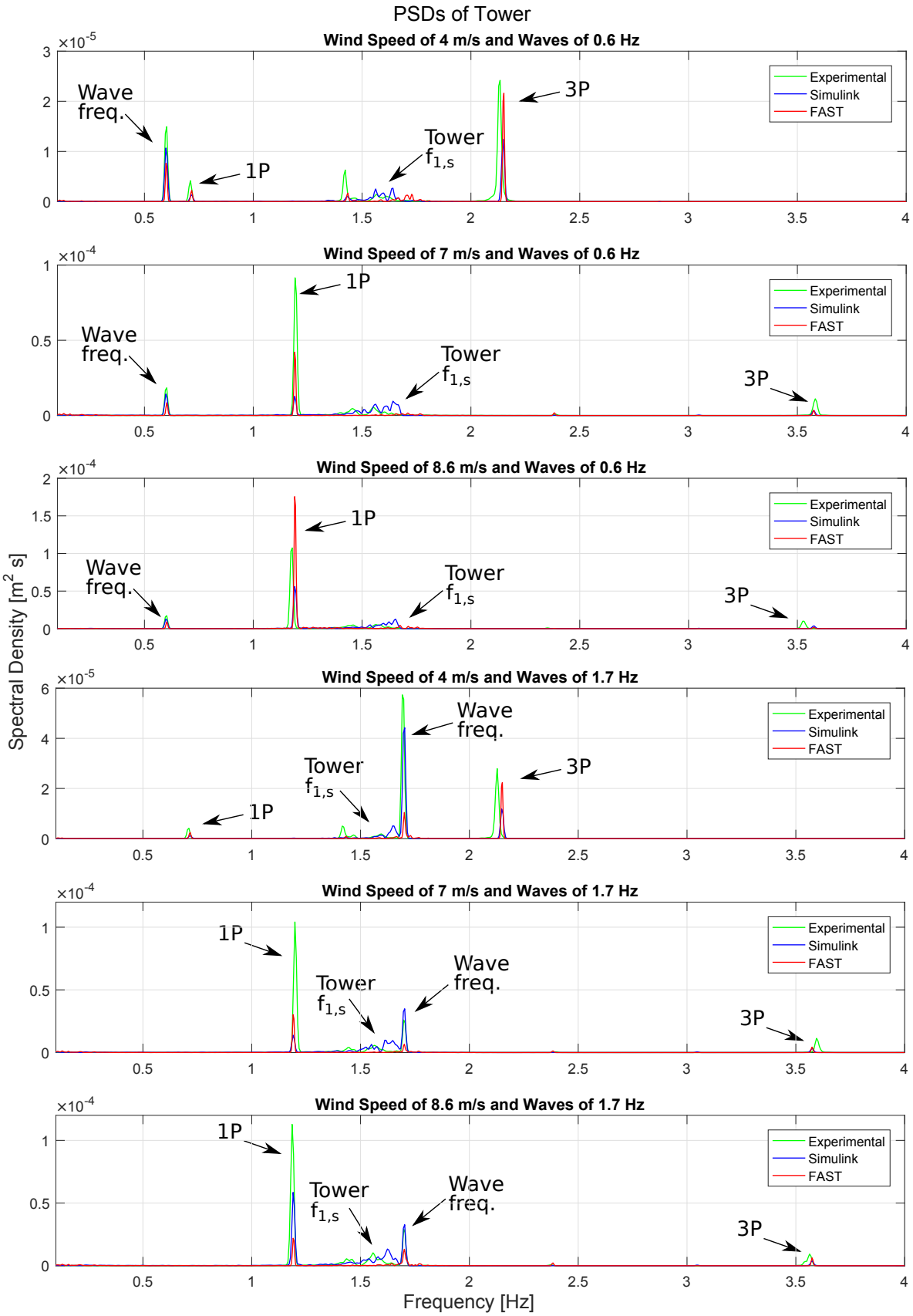

Figure 31.6: PSDs of tower displacement in the different experiments.

In fig. 31.7, the PSDs of the TLP displacements in the different tests are seen.

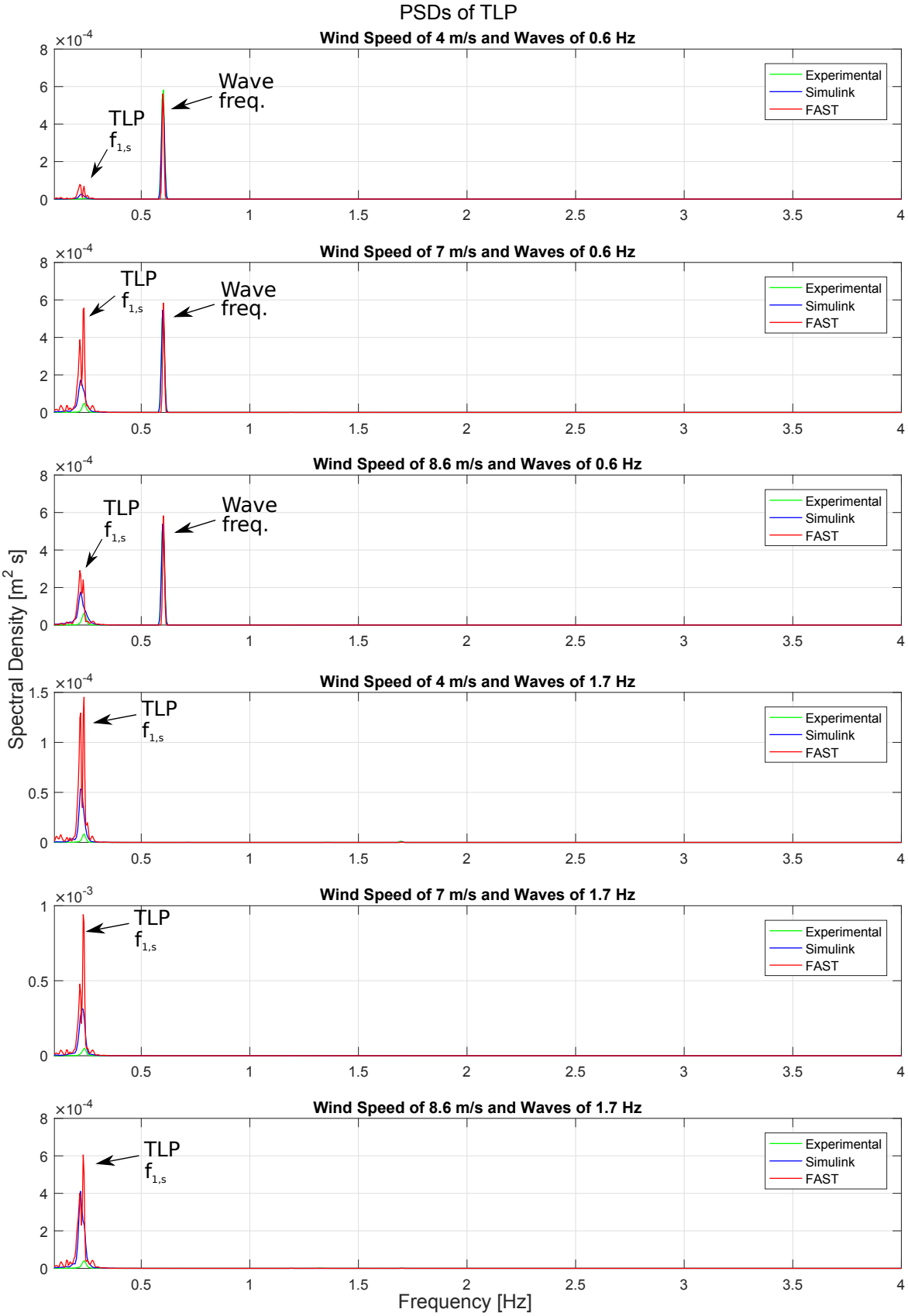

Figure 31.7: PSDs of TLP displacement in the different experiments.

Here it is seen that all peaks appear at the correct frequencies in both simulations done in FAST and Simulink. The amplitude of the first natural frequency of the TLP in surge direction are in all simulations estimated to high compared to the experimental data. However the amplitude at the frequency of the waves fit very well.

31.3 JONSWAP Spectrum and Aerodynamics

In this test wind at rated wind speed is applied to the rotor, while a JONSWAP spectrum is applied to the TLP, the parameters of the JONSWAP spectrum are the same as used in section 10.5. The experiment was conducted for 50 minutes, and the PSD of the tower and TLP are seen in fig. 31.8. Also the simulations done in Simulink and FAST are seen.

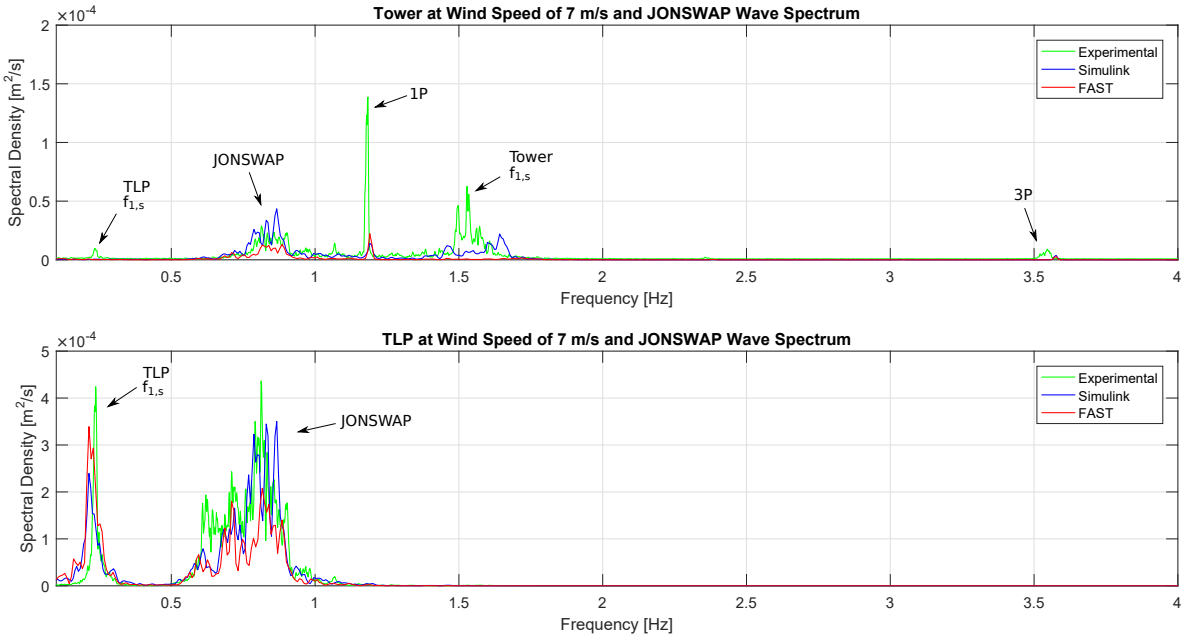

Figure 31.8: PSD of tower and TLP displacements when wind is applied together with a JONSWAP wave spectrum.

It can be seen in the top figure that 1P and the first natural frequency of the tower is excited more in the experiment compared to the simulations, and the natural frequency of the tower is not seen very clearly in FAST. Also the natural frequency of the TLP is seen in the experiment, but not in the simulations. This can be due to that the damping of the tower is overestimated below the first natural frequency of tower in surge due to Rayleigh damping and it is thus not excited in the wave frequency in the simulations. The JONSWAP spectrum in both PSDs of the tower and the TLP is seen, and both simulations show approximately the same as the experiment. The 3P effect in both simulations have the right frequency but the amplitudes are too small.

When investigating the PSD of the TLP both the natural frequency of the TLP and the JONSWAP spectrum are seen. The amplitudes of the experiment are slightly higher than the ones predicted from the simulations.

Conclusion 32

In this part the coupled mathematical model was derived, tested and validated. First the coupling of the hydrodynamics and the dynamics of the tower was investigated and implemented into the models. Thereafter the coupled model was tested. This was first done by investigating through experiments if the coupling between the tower and TLP would change the stiffness and damping of the tower. These experiments showed that the stiffness had decreased, while the damping increased, which was incorporated in the model of the tower. Afterwards the stiffness of the TLP was investigated, and it was found that this also had decreased, which also was incorporated into the model. Then free decay tests were made in order to validate the overall model, both tests done on the TLP and the tower showed to fit well with the simulations. Furthermore, forced responses were tested. Both regular and irregular waves were applied to the TLP. When applying regular waves, the experimental and simulated time series were compared, while the RAOs were compared for the irregular waves. The last experiment done for the coupling of tower and TLP was an impulse excitation, to investigate the natural frequencies of the coupled tower. It is here found that the first natural frequency of the tower was a bit lower than calculated.

The second part concerned the modelling and testing of the coupling between the TLP, tower and rotor. Again the theories behind the coupling were investigated and incorporated into the mathematical model, and this was validated through tests. First aerodynamic tests were made, where only wind was applied to the rotor and no waves were present. Both time series and PSDs of the tests were made. The mean offset is seen in the time series, where it was found that FAST predicts the mean offset of the tower best, and the simulation in Simulink predicted the TLP oscillations best. The PSDs of the TLP showed the correct frequency however the amplitudes of the simulated responses were to high compared to the experimental. The PSDs for the tower showed that FAST predicted 1P the best, but the Simulink simulation showed better performance in predicting the 3P. Different effects, e.g. pitching of the blades, were incorporated for simulating these effects.
Experiments with both wind and waves were also conducted. Again the time series of both TLP and tower were investigated and it was found that the mean offset were estimated too high in the simulations. However the PSDs for both tower and TLP were found satisfying, only the FAST simulation overpredicted the TLP responses slightly. At last the response of the TLP and tower were tested when exposed to a Jonswap spectrum together with wind at rated speed. Here almost all frequencies were detected by the simulation, except for the first natural frequency of the TLP in surge direction, which can be seen in the tower PSD. Here the simulations might have overdamped the lower frequencies of the tower, and this response is therefore not seen. The amplitudes of the PSDs were slightly underestimated by the simulations.

Part VII

Control

Symbol	Description	Units
β	Blade pitch angle	rad
β^*	Blade pitch angle reference	rad
$\beta_1, \beta_2, \beta_3$	Blade pitch angle for blade 1,2 and 3 respectively	rad
β_K	Slope of blade pitch sensitivity	W/rad^2
$\Delta\beta$	Small pertubation of blade pitch angle	rad
$\frac{\partial P}{\partial \beta}$	Pitch sensitivity	W/rad
$\frac{\partial \bar{P}}{\partial \beta}$	Mean of pitch sensitivity	W/rad
$\frac{\partial \hat{P}}{\partial \beta}$	Estimate of pitch sensitivity	W/rad
$\tau_{cur,ol}$	Current open loop time constant	s
$\tau_{cur,cl}$	Current closed loop time constant	s
θ_e	Electric angle	rad
$\dot{\phi}$	Small pertubation rotor angular velocity around rated rotor speed	rad/s^2
λ_r	Rotor flux linkage	Wb
ω_m	Generator angular velocity	rad/s
ω_m^*	Generator angular velocity reference	rad/s
ω_{BW}	Bandwidth of current loop	rad/s
ω_r	Rotor angular velocity	rad/s
$\omega_{r,0}$	Rated rotor angular velocity	rad/s
$\Delta\omega_r$	Small perturbation in rotor angular velocity around rated rotor speed	rad/s
$\Delta\dot{\omega}_r$	Small perturbation in rotor angular acceleration around rated rotor speed	rad/s^2
B_{dt}	Dynamic friction at low speed shaft	Nms
$D_{cur}(s)$	Current loop PI controller in continuous time	-
$D_{cur}(z)$	Current loop PI controller in discrete time	-
$D_{Speed}(s)$	Speed loop PI controller in continuous time	-
$e_s s$	Steady state error	-
e_{id}, e_{iq}	Current loop error in $dq0$ frame	A
e_ω	Speed loop error	rad/s
f_{pulse}	Input pulse frequency for pitch actuator 1,2 and 3 respectively	pulse/s
$G_B(z)$	Blade pitch actuator discrete transfer function	rad s
$G_{cur,ol}(s)$	Current open loop transfer function in continuous time	A/V
$G_{cur,ol}(z)$	Current open loop transfer function in discrete time	A/V
$G_{mech}(s)$	Mechanical transfer function in continuous time	rad/Nms
G_{Gen}	Generator transfer function	Nm/A
G_c	Current loop equivalent transfer function in continuous time	A/V
$G_{speed,ol}(s)$	Speed loop open loop transfer function in continuous time	rad/(V s)
$H(z)$	Current loop and controller open loop transfer function in discrete time	A/V
i_a, i_b, i_c	Stator currents in abc frame	A
i_d, i_q, i_0	Stator currents in $dq0$ frame	A
i_d^*, i_q^*	Stator current references in $dq0$ frame	A
i_x	Either d or q stator current in $dq0$ frame	A

J_{dt}	Equivalent drive train mass moment of inertia w.r.t the low speed shaft	kg m^2
$k_{P,cur}$	Proportional gain for current loop	-
$k_{I,cur}$	Integral gain for current loop	-
$k_{P,speed}$	Proportional gain for speed loop	-
k_P	Proportional gain	-
$k_{P,\beta}$	Proportional gain for collective blade pitch control	-
$K_{P,\beta}(\beta)$	Proportional gain for gain scheduling collective blade pitch control	-
$k_{I,\beta}$	Integral gain for collective blade pitch control	-
$K_{I,\beta}(\beta)$	Integral gain for gain scheduling collective blade pitch control	-
$k_{D,\beta}$	Derivative gain for collective blade pitch control	-
$k_{P,B}$	Proportional gain for blade pitch actuator	-
k_c	constant gain	-
k_{gain}	Control gain	-
k_{zero}	Placement of zero	-
L_d, L_q	dq generator Inductance	H
L_x	Equivalent generator Inductance	H
M_ϕ	Mass equivalent for collective blade pitch controlled system	-
C_ϕ	Damping equivalent for collective blade pitch controlled system	-
K_ϕ	Stiffness equivalent for collective blade pitch controlled system	-
ζ_ϕ	Damping ratio equivalent for collective blade pitch controlled system	-
$\omega_{\phi n}$	Natural frequency equivalent for collective blade pitch controlled system	-
N_G	High speed to low speed gear ratio	-
P_0	Rated power	W
P_R	Rotor power	W
$poles$	No. of generator poles	-
R_s	Stator resistance	Ω
$t_{cur,r}$	Current closed loop rise time	s
t_r	Rise time	s
t	Time	s
T_g	Generator torque at high speed shaft	Nm
T_r	Rotor torque at low speed shaft	Nm
$T_{I,speed}$	Integral time for speed loop	-
T_I	Integral time	-
v_a, v_b, v_c	Generator voltages in abc frame	V
V_α, V_β, V_0	Generator voltages in $\alpha\beta 0$ frame	V
V_α^*, V_β^*	Generator voltages reference in $\alpha\beta 0$ frame	V
V_d, V_q, V_0	Generator voltages in $dq0$ frame	V
z^{-1}	Unit delay operator	-
z_{cl}	Closed loop pole of current loop	
z	Discrete operator	-

$\mathcal{Z}$	Z-transformation	-
s	Laplace operator	-

Intro 33

In this part the control system of the AAUE-TLP will be described. First the control objective is explained together with the Campbell diagram of the system. Then the generator control is designed using FOC. Then the collective blade pitch control is designed including the blade pitch actuator control and the collective blade pitch reference control using both a constant gain and gain scheduling. Next a rotor position estimation is explained using the EKF approach. In the end is a chapter where simulations and experiments are compared for all the control schemes. The control design is inspired by the baseline control of the 5 MW reference wind turbine described in [97] and tuned to fit the AAUE-TLP.
It should be noted that the control system will differ in some sense from the reference wind turbine due to the scaling. This thesis aims to fit the scaled dynamics of the reference wind turbine, meaning that the control objective in some cases will be different.

Control Objective 34

The primary goal of a real wind turbine control scheme is to secure a maximum power output at any given wind speed. However minimizing the tower and drive train stresses are also of high importance. For this thesis the wind turbine will act as a variable speed, variable pitch wind turbine. In this scheme the wind turbine is operated at variable speed and fixed pitch below rated wind speed, and at constant speed, variable collective pitch above the rated wind speed.
The variable speed, variable pitch of a real wind turbine is generally divided into four main control regions (I, II, III and IV) with one intermediate region II 1/2. These regions are defined based on the three different wind regions, cut in, rated and cut out wind speed.

Region I Below the cut in wind speed, the wind speed is too low to overcome the inertia of the system, and even if the wind turbine would run, the generated power would not overcome the power losses in the power electronics. In this region the control should secure that the main shaft is braked, along with the blades being feathered to reduce wind loads. However at some wind speed before the cut in wind speed, the rotor could be allowed to free wheel linearly up to the cut in wind speed. This to avoid a too abrupt start up.

Region II Between cut in and rated wind speed, the wind turbine is in operation, and the power output roughly increases with the cube of the wind speed until the rated wind speed is reached. In this region the control objective is to secure optimal power conditions, which is done through a control scheme called maximum power point tracking (MPPT). The principle of MPPT is securing a constant optimum TSR in order to optimize the power coefficient. This is done by controlling the torque on the generator and thereby the rotor speed. In this region the pitch control is set to its optimal value such that a maximum of lift is present.

Region II 1/2 In this region the maximum rotor speed is reached, however the generator torque has still not reached the rated value, therefore the generator torque is capable of increasing, while keeping the rotor speed constant at its rated value.

Region III Between rated and cut out wind speed the rated power of the generator is achieved. The control objective is here to secure that the rated power is kept constant without damaging the wind turbine. In this region the blades are collectively pitched out of the wind by a greater and greater angle in order to change the AOA of the blades and thereby changing the aerodynamic forces on the blades.

Region IV If the wind speed reaches above the cut out wind speed the wind turbines are usually shut down. This could be done by feathering the blades and apply the brake such the power production stops. Other new approaches are done by pitching out the blades in such a way that power generation is reduced. This is done in order to keep the wind turbine generating power for as long as possible.

A representation of the above list of control regions are visualized in fig. 34.1.

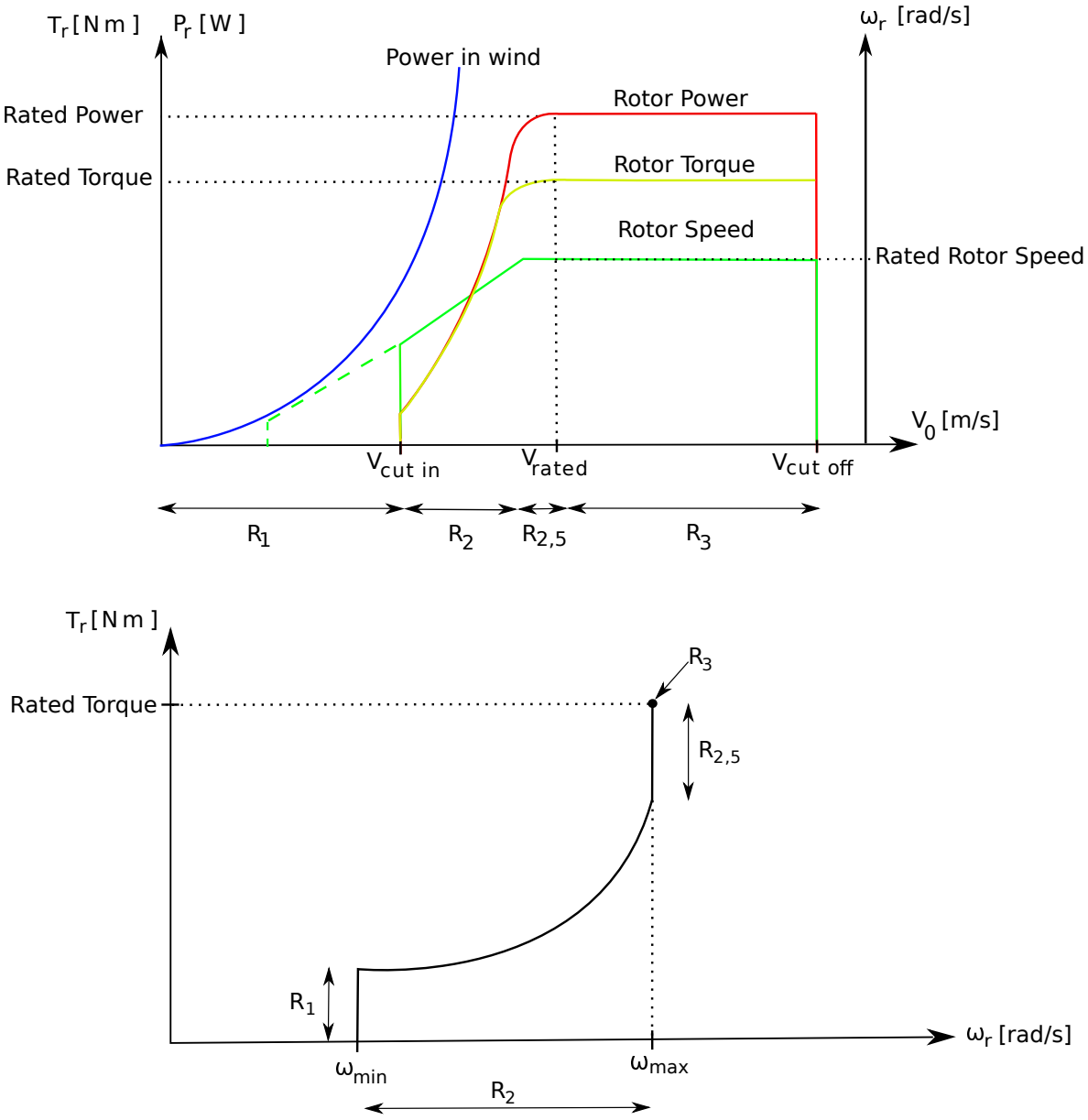

Figure 34.1: Operation conditions for a wind turbine.

The control scheme for the physical model of this thesis is similar to the general control schemes of full scale variable speed, variable pitch wind turbines. But a slight change is made, to scale the dynamics from the reference 5 MW NREL wind turbine. Again the control regions are divided into four main control regions, which will be described in further detail below.

Region I Below the cut in wind speed, the wind turbine should be at standstill.

Region I 1/2 If the rotor is at standstill at the cut in wind speed, the blades should be pitched, such that a greater rotor torque is generated in order to start up the wind turbine. When the rotor is at the cut in rotational speed, the pitch angles of the blades should be set to 0 °.

Region II Between cut in and rated wind speed, the wind turbine is in operation. The control objective is to secure that the rotor is rotating at the right scaled rotational speed at the different wind speeds. This is done by controlling the generator torque. The operation curve for rotational speed at different wind speeds can be seen in fig. 34.2.

Region III Between rated and cut out wind speed the rated power of the generator is reached. The control objective is to secure that the power is kept constant at the rated rotational speed of the wind turbine. In this region the blades are collectively pitched out of the wind to lower the rotor torque.

Region IV If the wind speed reaches above the cut out wind speed, the wind turbine should be shut down. This is to be done by feathering the blades.

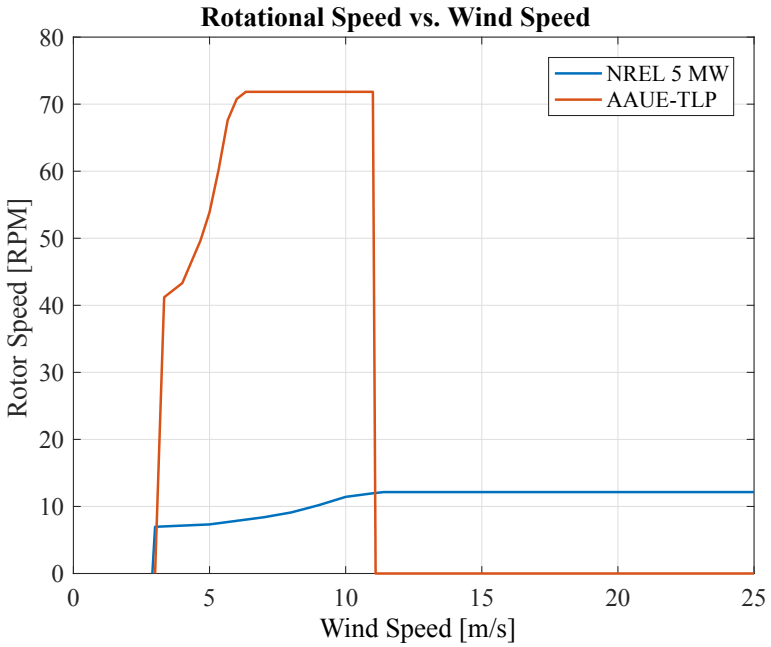

Figure 34.2: The rotational speed as function of the wind speed operating range of the 5 MW NREL wind and the AAUE-TLP.

The regions in this thesis is defined as seen in table 34.1.

Table 34.1: AAUE-TLP regions.

Region	Wind Speed Interval [m/s]	Rotor Speed [RPM]	Pitch Angle [°]
I	0-3	0	0
II	3-7	40-71.5	0
III	7-11	71.5	0-20.5
IV	>11	0	60

34.1 Campbell Diagram

In general wind turbines must be operated in such a way that excitations in the natural frequencies of the different parts are avoided. An often used visualisation is the Campbell diagram in which the

natural frequencies of the TLP, tower and blades are mapped w.r.t the rotational frequency of the rotor. In fig. 34.3 the Campbell diagram of the AAUE-TLP is seen.

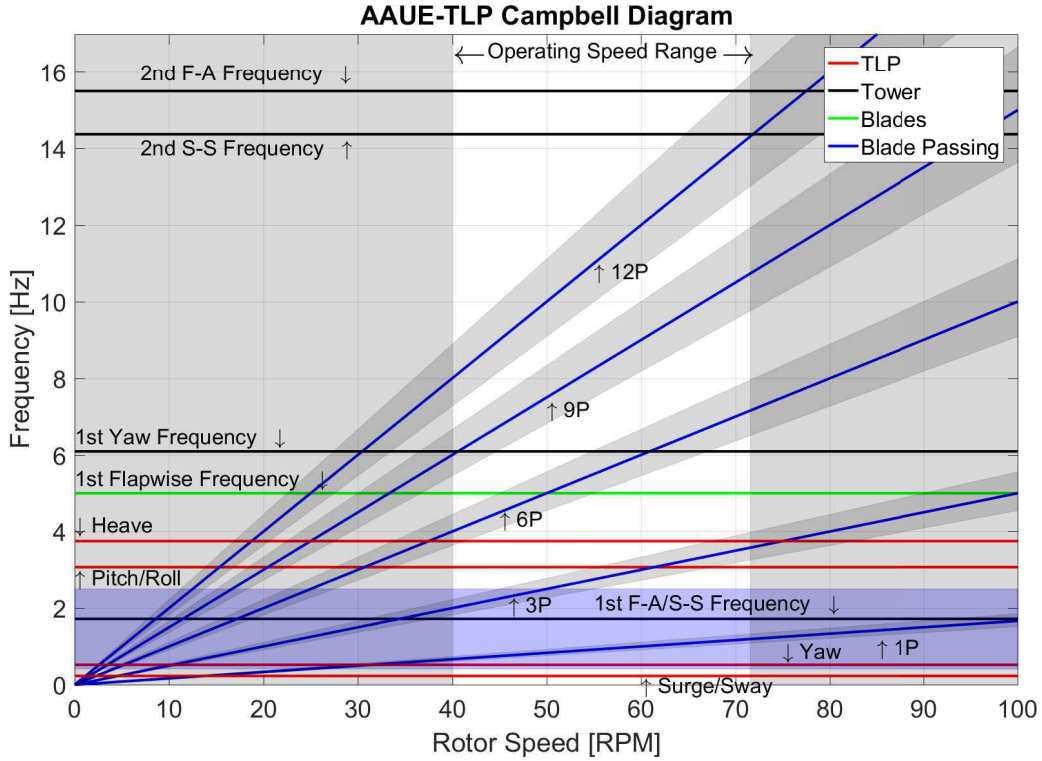

Figure 34.3: Campbell diagram of the AAUE-TLP.

The grey areas represent the rotor speed outside the allowed operational range of the AAUE-TLP, while the white area represents the operation region. The solid blue lines indicate the frequencies associated with the one per revolution (1P) associated with the rotation of the rotor and the three per revolution (3P), six per revolution (6P) and so forth associated with the blade passings. At these frequencies, rotation induced forces are expected. Recommendations from DNV is to keep the tower frequency outside ranges defined as the rotor frequency ± 10% and the blade passing frequencies ± 10%, this in order to avoid problems due to load amplifications arising from vibrations near the natural frequency [98]. The blue shaded area indicates the frequency range of the JONSWAP spectrum, as explained in section 7.3. All of the natural frequencies are assumed to be independent on the rotor speed, however it is well known that the natural frequencies of the blades are rotor speed dependent [99]. It can be seen that the tower can be seen as a soft-stiff structure, as the natural frequencies of the F-A and S-S are placed between 1P and 3P. This is also the case with the 5 MW NREL reference wind turbine [28]. As seen in the Campbell diagram the 1P effect is not influencing any vital natural frequencies within the operation range of the AAUE-TLP. The 3P effect collides with the natural frequencies of the TLP in pitch, roll and heave. However the TLP is so restrained in these DOFs that practically no motion will occur. The 6P effect might have an impact on the first flapwise natural frequency of the blades. Therefore the system might benefit from implementing some control logic to make a speed exclusion zone. Structural considerations of the blades are however out of the scope of this thesis. Likewise 6P effect might impact the natural frequency in yaw, it is however seen in appendix A.7 that practically no movement, and thereby energy, is present in yaw, whereby the impact on the tower is minimal. The same argument can be made with 9P and 12P.

Generator Control 35

The general purpose of the generator control is to control the torque on the rotor shaft such that the rotor speed tracks the reference angular speed of the rotor in region II and keeps a constant torque in region III.
The generator control is based on FOC applying the advantages of Park-Clark's transformation by only having two equivalent DC components instead of the three phase time varying stator components. Thereby the torque and flux can simply be decoupled and separately controlled. The structure of the control can be seen in fig. 35.1

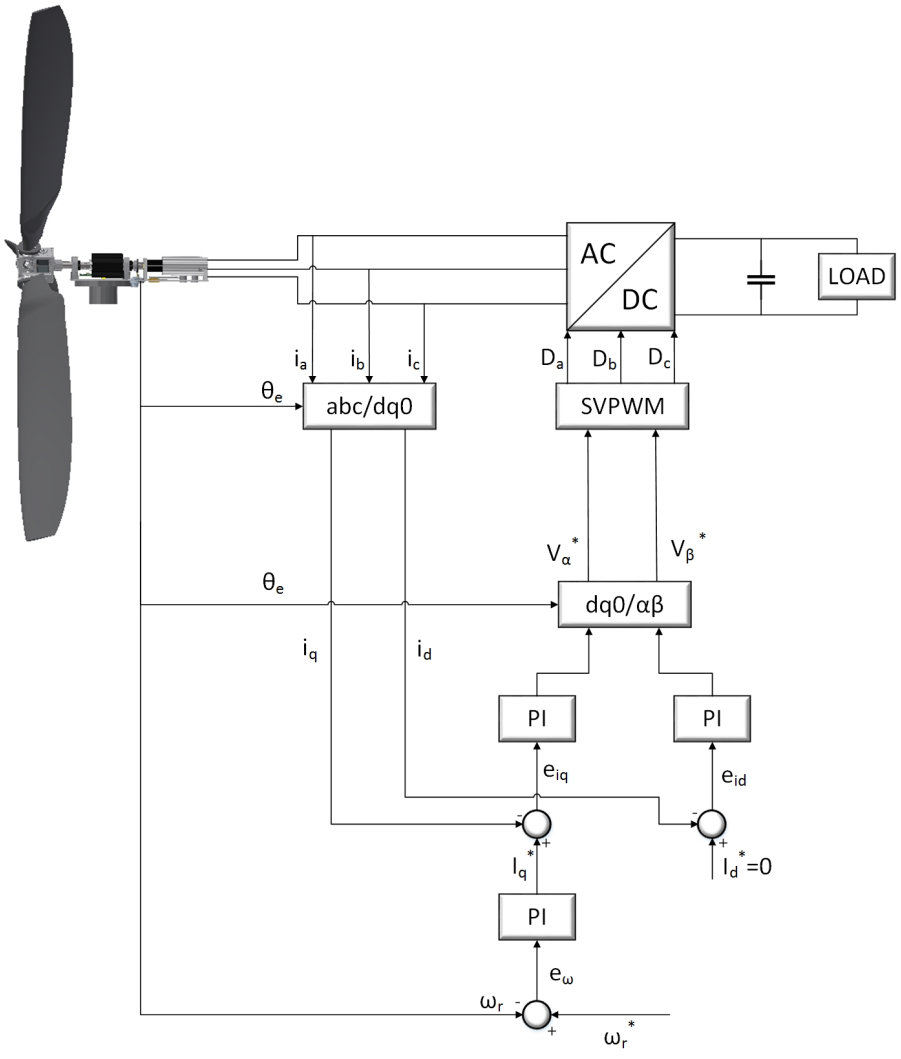

Figure 35.1: Principal sketch of implementation of FOC.

As shown in fig. 35.1 the generator control consists of three control loops; two current loops and a single speed loop. The speed loop makes the reference for the i_q current control by the error of the rotor speed, e_ω, while the reference for the i_d current loop is zero, for reasons explained in chapter 23. The two current controllers use the current errors e_{id} and e_{iq} to create a $dq0$ reference voltage which is transformed into a $\alpha\beta0$ reference voltage, V_α^* and V_β^*, using an inverse Park transformation which applies the electrical angle θ_e. These $\alpha\beta0$ reference voltages are used as reference for the SVPWM, which creates the duty cycles,D_a, D_b, D_c for the power converter. The time response of the electrical system is much faster than the aerodynamic part of the wind turbine, creating the possibility of making a cascade control structure by decoupling the electrical system and the mechanical drive train.

35.1 Current Loop

The d and q voltage equations are coupled by the currents as seen in equation 23.3 and 23.4. By seeing the coupling as a disturbance when designing the control and assuming the inductances are equal in d and q, the two voltage equations can be decoupled. Thereby two identical open loop transfer functions for voltage current relationship can be written as

$$G_{cur,ol}(s) = \frac{i_x(s)}{v_x(s)} = \frac{1}{L_x s + R_s} = \frac{1}{R_s}\frac{1}{\tau_{cur,ol}s + 1} \quad \text{where} \quad \tau_{cur,ol} = \frac{L_x}{R_s} \tag{35.1}$$

where subscript x indicates either d or q, $L_x = L_d = L_q$, R_s is the stator reductance and $\tau_{cur,ol}$ is the time constant. $G_{cur,ol}(s)$ is a first order type zero transfer function.
As the overall generator control is a cascade control, the outer loop performance is dependent on the inner loop performance. Some requirements in prioritised order are set for the current loop to secure a satisfactory performance of the generator:

- Stable at all times
- No steady state error to a step response
- Fast rise time compared to the speed loop
- No or limited overshoot

To secure that the current loop does not effect the speed loop, the rise time should be fast, which leads to a relatively high bandwidth compared to the speed loop. The closed loop rise time, $t_{cur,r}$, can be calculated by the closed loop time constant $\tau_{cur,cl}$ as

$$t_{cur,r} \approx 2.197\tau_{cur,cl} = 0.8\,\text{ms} \quad \text{where} \quad \tau_{cur,cl} = \frac{L_s}{1 + R_s} \tag{35.2}$$

which is assumed to be very fast compared to the speed loop.
In a closed loop configuration a type zero system will have a steady state error to a step input, which is also seen when applying the final value theorem on the system

$$e_{ss} = \frac{1}{1 + \lim_{s\to 0} G_{cur,ol}} \cdot 100\% = 27.8\,\% \tag{35.3}$$

By using a PI controller the system becomes a type 1 instead of type 0, and thereby the steady state

error is eliminated.
The PI current controller in continuous time $D_{cur}(s)$ can be written as

$$D_{cur}(s) = k_{P,cur} + \frac{k_{I,cur}}{s} = k_{I,cur} \frac{\frac{k_{P,cur}}{k_{I,cur}} s + 1}{s} \tag{35.4}$$

where s is the Laplace operator and $k_{P,cur}$ and $k_{I,cur}$ are the proportional and integral gain for the speed loop, respectively. The current loop is designed in the discrete time domain by utilizing the bilinear approximation also known as Tustin's method or the trapezoidal rule as emulation strategy. By the trapezoidal rule defined as

$$s = \frac{2}{T_s} \left(\frac{z-1}{z+1} \right) \tag{35.5}$$

where T_s is the sampling period and z is the discrete operator. Every occurrence of s in any $D(s)$ can be changed yielding a discrete transfer function $D(z)$.
The PI controller in the discrete domain, $D_{cur}(z)$, can thereby be written as

$$D_{cur}(z) = k_{I,cur} \frac{\frac{k_{P,cur}}{k_{I,cur}} \left(\frac{2}{T_s} \frac{z-1}{z+1} \right) + 1}{\left(\frac{2}{T_s} \frac{z-1}{z+1} \right)} \tag{35.6}$$

By algebraic manipulation the transfer function of the PI controller can be rewritten into

$$D_{cur}(z) = \underbrace{\left(k_{P,cur} - \frac{T_s k_{I,cur}}{2} \right)}_{k_{gain}} \frac{\overbrace{\left(\frac{2k_{P,cur} + T_s k_{I,cur}}{2k_{P,cur} - T_s k_{I,cur}} \right)}^{\frac{1}{k_{zero}}} z - 1}{z-1} = k_{gain} \frac{\frac{1}{k_{zero}} z - 1}{z-1} \tag{35.7}$$

where k_{gain} is an equivalent proportional gain and k_{zero} is a placement of a zero. The system transfer function $G_{cur,ol}(s)$ is mapped into the discrete time domain utilising the zero order hold (ZOH) method. The calculation delay in the dSPACE is taken into account by introducing a unit delay, such that the overall transfer function is written as

$$G_{cur,ol}(z) = z^{-1} \left(1 - z^{-1} \right) \mathcal{Z} \left[\frac{G_{cur,ol}(s)}{s} \right] \tag{35.8}$$

where $\mathcal{Z}$ is the Z-transformation. For this system the transfer function can be simplified to

$$G_{cur,ol}(z) = \frac{0.4277}{z\left(\frac{1}{k_{pole}} z - 1 \right)} = \frac{0.4277}{z\left(\frac{1}{0.8586} z - 1 \right)} \tag{35.9}$$

with a sampling time $Ts = 1/5000$ s. The PI controller and the current transfer functions are combined into a single transfer function by which the open loop system with controller can be

written as

$$H(z) = D_{cur}(z)G_{cur,ol}(z) = k_{gain}\left(\frac{\frac{1}{k_{zero}}z-1}{z-1}\right)\left(\frac{0.4277}{z\left(\frac{1}{0.8586}z-1\right)}\right) \tag{35.10}$$

The approach of the control strategy is to clamp one of the poles with the zero such that $k_{zero} = k_{pole} = 0.8586$, leaving only k_{gain} as control parameter. By varying k_{gain} in a root locus the effect can be analysed which is shown in fig. 35.2.

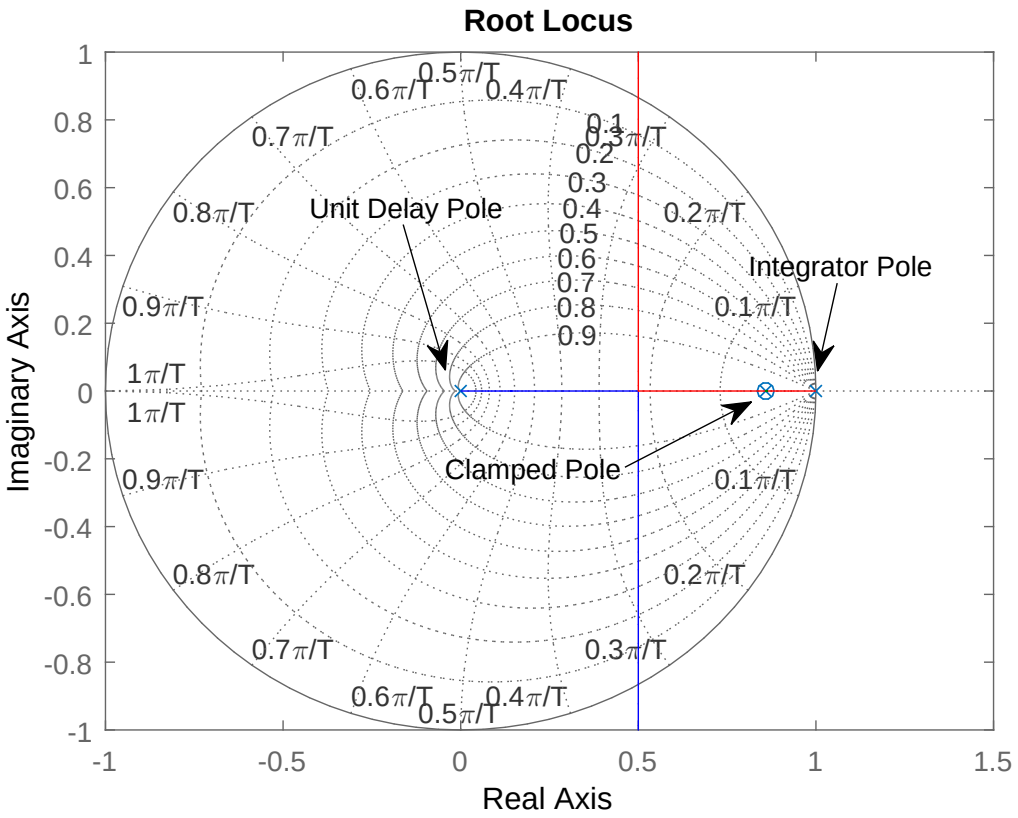

Figure 35.2: Root locus of the open loop visualising the effect of varying the gain of the closed loop system.

The system consists of three poles and one zero; the unit delay pole which is extremely fast and placed at the origin, an effectively clamped pole by one of the zeroes, the clamping is retained even when the gain is varied, the integrator pole represents the slowest dynamic behaviour and dominates the overall system response. As long the unit delay and integrator pole remains real, the system response is overdamped, and the system performance can be assumed to represent first order behaviour.

As the system can be considered as a first order system the following relationship between the bandwidth of the system, denoted ω_{BW} and the closed loop pole, denoted z_{cl}, is applicable

$$\omega_{BW} = \left|\frac{\ln z_{cl}}{T_s}\right| \tag{35.11}$$

It can be approximated that the bandwidth multiplied by the rise time is equal to 2.2 [100] and therefore rise time, t_r, for a given closed loop pole location and sampling time can be found as

$$t_r \omega_{BW} \approx 2.2 \Leftrightarrow t_r \approx \frac{2.2}{\left| \frac{\ln z_{cl}}{T_s} \right|} \tag{35.12}$$

setting the rise time to be 0.8 ms, which is fast enough to not influence the speed loop, the pole location should be approximately 0.58, which can be achieved by setting $K_{gain} = 0.60$, giving the final controller as

$$D_{cur}(z) = 0.60 \frac{\frac{1}{0.8586} z - 1}{z - 1} \tag{35.13}$$

Thereby the proportional gain and integral gain can be calculated to be $k_{P,cur} = 0.65$ and $k_{I,cur} = 494.06$, respectively. The closed loop step response with the controller is shown in fig. 35.3 with a rise time and settling time of 0.8 ms and 1.8 ms, respectively. The response has no steady state error and no overshoot and thereby fulfils the design requirements.

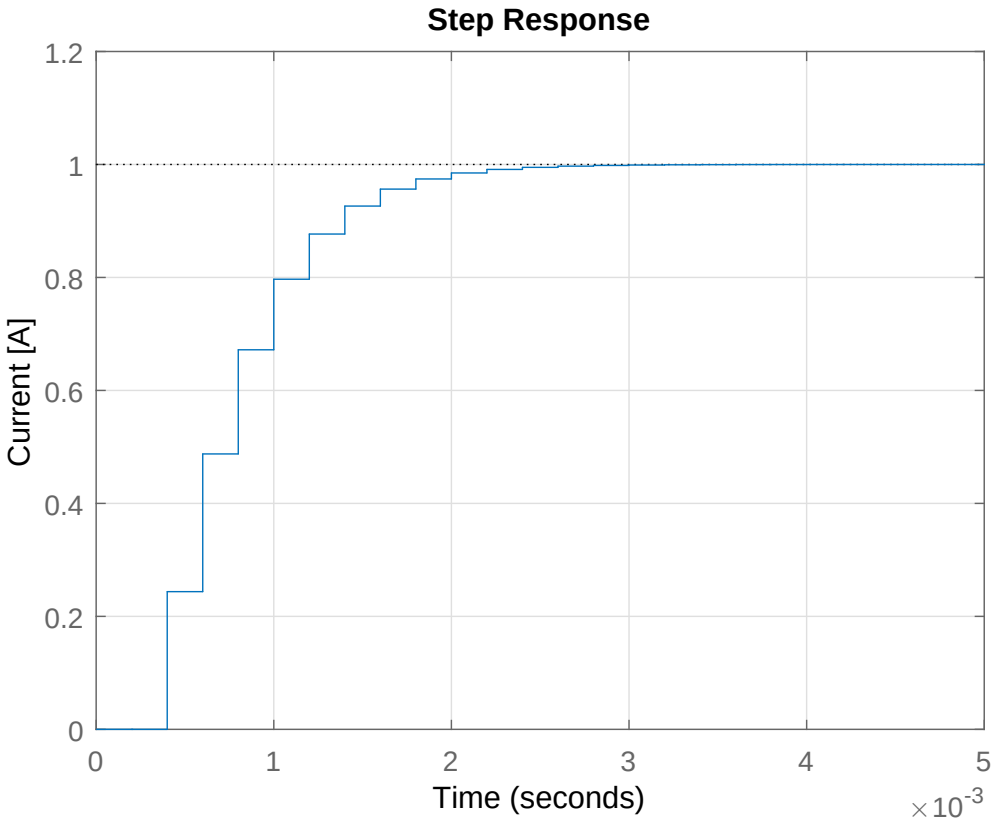

Figure 35.3: Step response of the closed loop system with the controller implemented.

Table 35.1: Current loop control parameters.

Control Gain	
$K_{P,cur}$	0.65
$K_{I,cur}$	494.06

35.2 Speed Loop

The equation of motion of the drive train, which was expressed in eq. 22.1 describes the outer speed loop.
Neglecting the static torque, as it does not represent any dynamic of the system, and using the difference between the generator torque and rotor torque as input and the mechanical angular rotor speed as the output the mechanical transfer function $G_{mech}(s)$ is achieved

$$G_{mech}(s) = \frac{\omega_r(s)}{N_G T_g(s) - T_r(s)} = \frac{1}{J_{dt}s + B_{dt}} \tag{35.14}$$

where ω_r is the rotor speed, N_G is the low to high speed gear ratio, T_g is the generator torque, T_r is the rotor torque, while J_{dt} and B_{dt} are the drive train mass moment of inertia and viscous friction, respectively. The obtained transfer function is a first order type zero system with a time constant of 4.1 s. The generator torque was expressed in eq. 23.9 and if tracking a reference $i_d^* = 0$, a constant relationship between the input current, i_q, and the output generator torque can be written as a transfer function, G_{Gen}

$$G_{Gen} = \frac{N_G T_g}{i_q} = N_G \frac{3}{2} \frac{poles}{2} \lambda_r \tag{35.15}$$

where $poles$ is the number of poles in the generator and λ_r is the flux linkage.

It was found that the inner current loop had first order behaviour and thereby the system can be approximated by a first order transfer function $G_c(s)$ as

$$G_c(s) = \frac{1}{\tau_{cur,cl}s + 1} \tag{35.16}$$

where the time constant $\tau_{cur,cl}$ is found to be 0.36 ms, which is 11000 times faster than the time constant of the drive train transfer function. By combining the drive train, the generator and the current transfer functions the closed loop step response can be found to have a large steady state error of 14%, which is unwanted. The steady state error is eliminated by implementing a PI controller having the transfer function

$$D_{speed}(s) = k_{P,speed}\left(\frac{1 + T_{I,speed}s}{T_{I,speed}s}\right) \tag{35.17}$$

where $k_{P,speed}$ is proportional gain and $T_{I,speed}$ is the integral time. The open loop speed loop has the following cascaded transfer function

$$\begin{aligned} G_{speed,ol}(s) &= D_{speed}(s)G_c(s)G_{Gen}G_{mech}(s) \\ &= k_{P,speed}\left(\frac{1 + T_{I,speed}s}{T_{I,speed}s}\right)\left(\frac{1}{\tau_{cur,cl}s + 1}\right)\left(N_G \frac{3}{2} \frac{poles}{2} \lambda_r\right)\left(\frac{1}{J_{dt}s + B_{dt}}\right) \end{aligned} \tag{35.18}$$

for which the bode plot can be seen in fig 35.4.

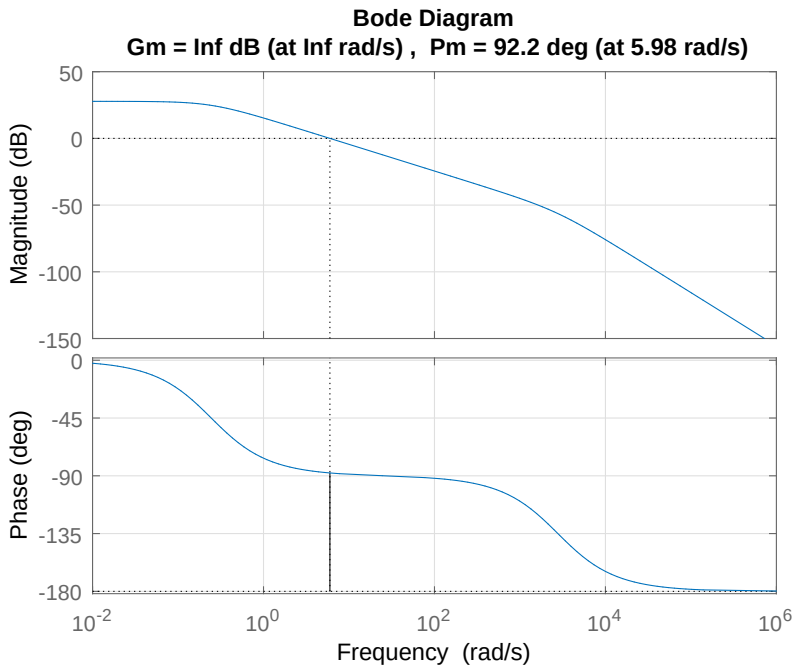

Figure 35.4: Frequency response of speed loop.

The Optimum Symmetric Method (OSM) is utilised as control strategy. The control is designed to respond well to load disturbances, which often is defined in the low frequency area. However with the compromise that a set point change can lead to large overshoot [101] [102]. The OSM maximises the phase margin and leads to symmetrical phase and magnitude characteristics around the cross over frequency. The approach of the OSM is to obtain the following form of an open loop transfer function

$$G_{OSM}(s) = \frac{k_c k_P (T_I s + 1)}{s^2 (\tau_1 T_I s + T_I)} \tag{35.19}$$

where k_c system gain constant, k_P the proportional gain, T_I the integral time and τ_1 is a time constant. This form is obtained if denoting the constant k_c as

$$k_c = N_G \frac{3}{2} \frac{poles}{2} \lambda_r \tag{35.20}$$

and for now neglecting viscous friction for control tuning, whereby eq. 35.18 can be rewritten as

$$G_{speed,ol}(s) = \frac{k_c k_{P,speed} \left(T_{I,speed} s + 1\right)}{J_{dt} s^2 \left(\tau_{cur,cl} T_{I,speed} s + T_{I,speed}\right)} \tag{35.21}$$

In equation k_c can be seen as a system gain and τ_1 the time constant of the system. The parameters of the PI control can then be obtained by The parameters of the PI control can be obtained by the system gain k_c and the time constant of the system τ_1 from equation 35.19, using the following expressions

$$\begin{aligned} k_P &= \frac{1}{a k_c \tau_1} = \omega_c \frac{1}{k_c} \\ T_I &= a^2 \tau_1 \end{aligned} \tag{35.22}$$

where the crossover frequency, ω_c, is found as

$$\omega_c = \frac{1}{a\tau_1} \tag{35.23}$$

The crossover frequency and the control tuning parameter, a, are related to the phase margin (PM) of the system by

$$PM = 2\arctan\left(\frac{a-1}{a+1}\right) \tag{35.24}$$

The frequency phase response of the speed loop will have a peak at ω_c which is symmetric around $1/T_{I,speed}$ and $1/\tau_{cur,cl}$. Comparing eq. 35.21 and 35.19 the proportional gain and integral time for the PI controller can be obtained as

$$\begin{aligned} k_{P,speed} &= \frac{J_{dt}}{ak_c\tau_{cur,cl}} \\ T_{I,speed} &= a^2\tau_{cur,cl} \end{aligned} \tag{35.25}$$

Conventional symmetrical optimum tuning sets a = 2 [102], which results in an overshoot of around 43 % and a settling time around 5.87 ms thereby still being slower than the current loop. Using eq. 35.24 the PM can be calculated to be 36.9°, which is above the recomended 30° [103].
In the bode plot in fig. 35.5 it is seen that the system shift its phase from almost -90° to almost -180°, but at the crossover frequency the phase is lifted by a significant amount to lift the PM to reach 36.9° after which it shifts back towards -180°. Thereby the symmetrical response in phase is achieved. Furthermore there is an increase in magnitude at the low frequencies compared to the original system.

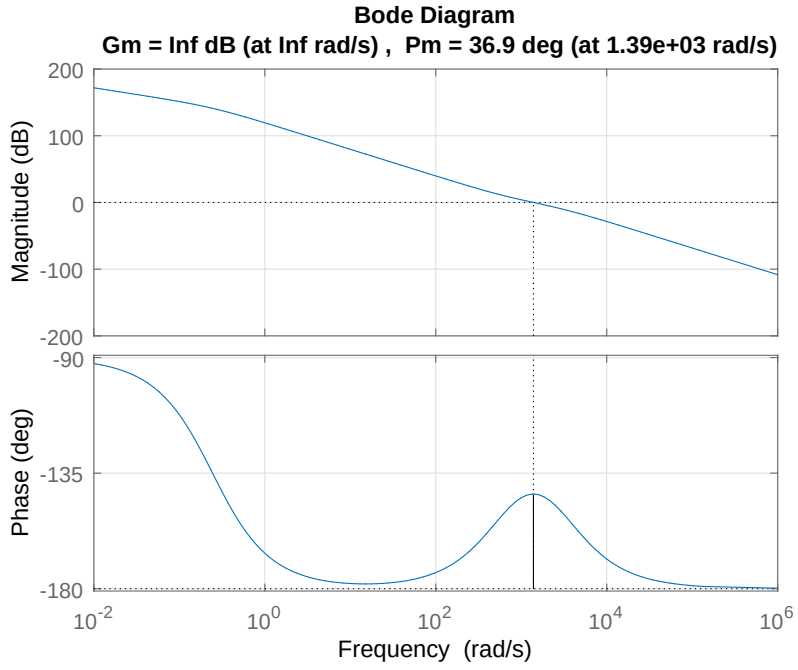

Figure 35.5: Frequency response of speed loop with controller.

By increasing a more damping can be introduced into the system, decreasing the overshoot but increasing rise and settling time. As baseline control $a = 2$ is used. In the figure below a step response of the speed loop is seen

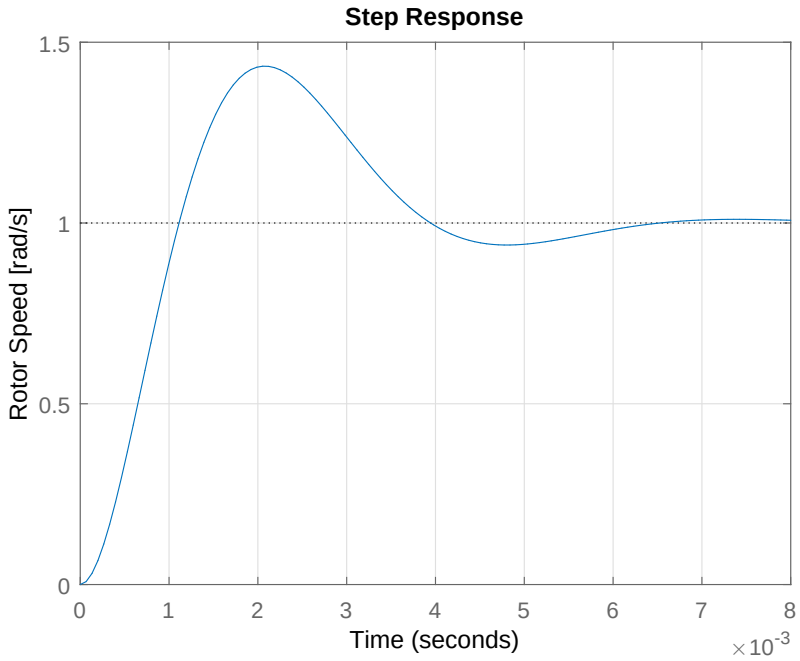

Figure 35.6: Step response of speed loop.

This is a very aggressive control and too large reference changes will demand a very large torque and thereby current reference for the generator. Therefore a limit for the current reference must be set together with an integral anti wind-up circuit to avoid instability and damaging the generator.

Table 35.2: Speed loop control parameters.

Control Gain	
$K_{P,speed}$	231.9
$K_{I,speed}$	1.610E5

Collective Blade-Pitch Control 36

The main purpose of the pitch control is to decrease the lift of the blades such that the torque does not increases as the wind speed increase above the rated wind speed. This is to keep the generator at its rated torque throughout region III.

36.1 Blade Pitch Control

This section will describe the design, simulation and test of the baseline control for the blade pitch system of the AAUE-TLP.
The blade pitch control consists of a cascade control with a fast inner actuator loop and a collective blade pitch control as seen on the block diagram in fig. 36.1.

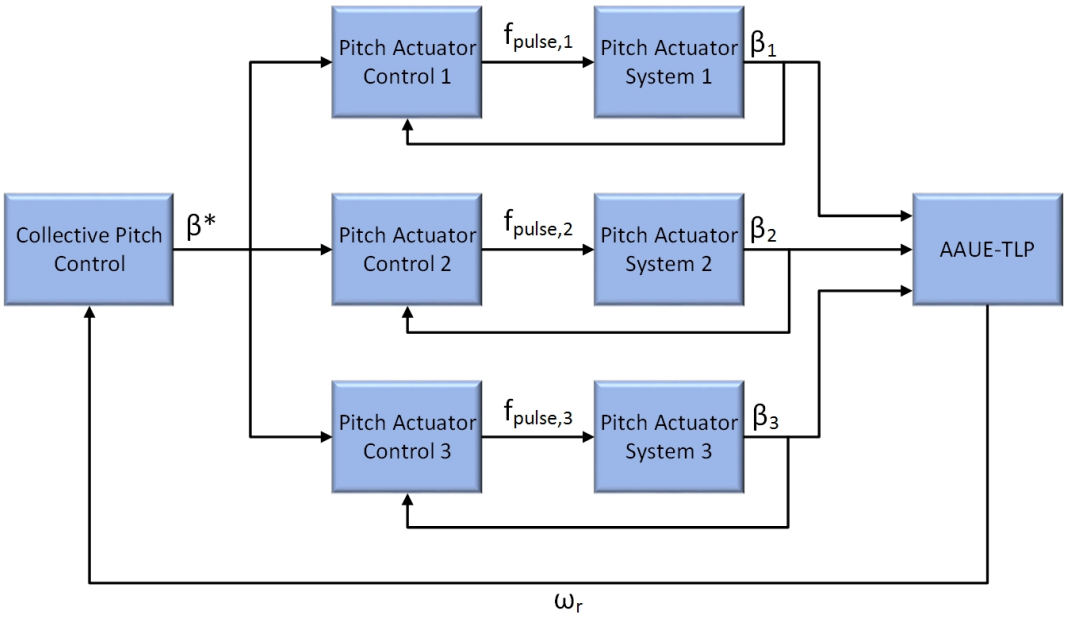

Figure 36.1: Block diagram of the baseline blade pitch control system.

36.2 Blade Pitch Actuator Control Design

A discrete transfer function describing each blade pitch actuator system, $G_B(z)$, were found in chapter 24. The systems was found to be almost similar so the same control design will be used for

all the systems and tuned for an average of the three which is

$$G_B(z) = \frac{4.83E{-}9}{z-1} \tag{36.1}$$

with a sampling time of 5 kHz.
The objective of the blade pitch actuator control is to track the reference commanded from the collective pitch control with:

- Fast rise time compared to the collective pitch loop
- No steady state error to step response
- Low settling time
- Minimum overshoot

The blade pitch rate limit of the 5 MW NREL wind turbine is ±8°/s [28], this is scaled to fit the AAUE-TLP giving 47.3°/s. The actuator system consisting of a stepper motor and a gearing which needs 705.4 steps to rotate the blade a single degree. Meaning that the limitation of the controller should be set to 33.36E3 steps per s. Furthermore a rise time of 1 s is wanted to have a faster rise time compared to the outer pitch loop.
To have a first impression of the performance of the closed loop system, a root locus is created as seen in fig 36.2. The root locus shows that there is a pole at (1,0) and when increasing the gain it will move to the left which will increase the speed of the system with a damping ratio of 1 until it reach the origin. Placing the pole in the origin with a P-control will give the theoretically best performance. It is however not possible to excite the real system with enough torque to reach this performance, therefore a lower gain is chosen.

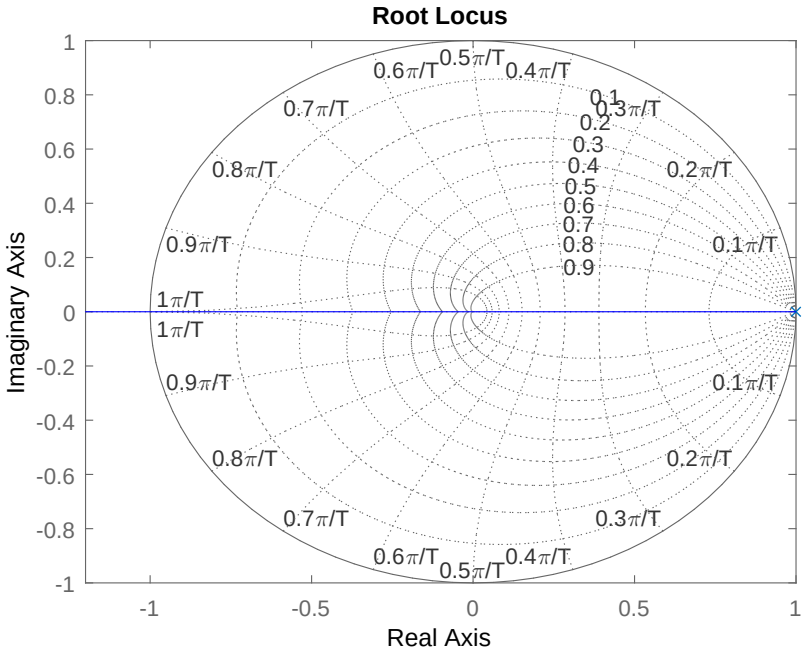

Figure 36.2: Discrete root locus of blade pitch actuator system.

The control objective of the system is achieved with a rise time of 1 s, by a P-gain of 1.61E5. The step response with control is seen in the figure below.

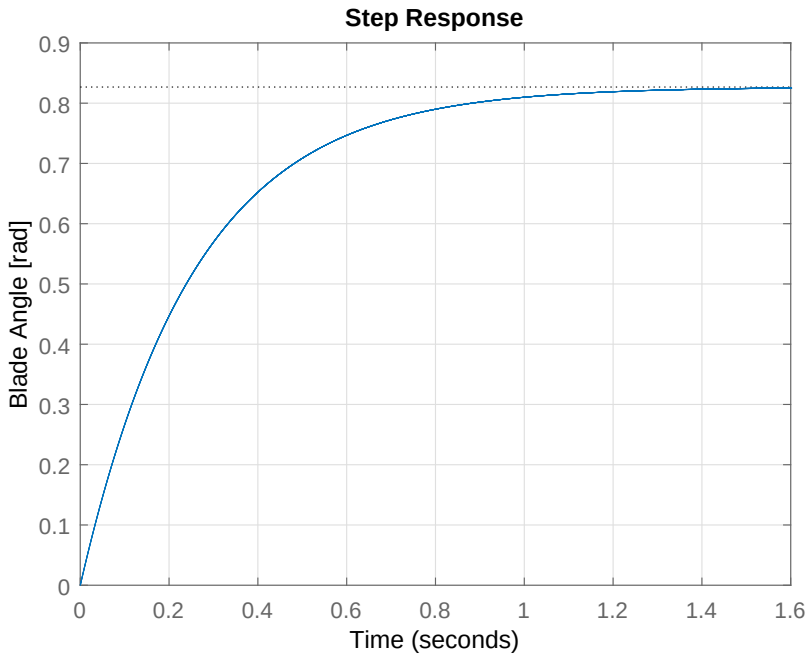

Figure 36.3: Step response of pitch actuator system with control.

Table 36.1: Blade pitch actuator control parameters.

Control Gain	
$K_{P,B}$	1.61E5

36.3 Collective Blade Pitch Control Design

The control objective of the collective blade pitch control is to create a reference for the blade pitch actuator control, which will keep a constant rotational speed for the rotor in region III. The minimum and maximum blade pitch angle of the NREL 5 MW [28] is set to 0° and 90° respectively, this will also be used as minimum and maximum for the AAUE-TLP.
The baseline control is designed by using a simple SDOF rotor model of the drivetrain, where the DOF considered is the angular rotation of the low speed shaft. The SDOF equation of motion was derived in section 22 for the drive train. To design the control eq. 22.1 was simplified by neglecting the viscous damping and static torque and considering only small perturbation in rotor acceleration $\Delta\dot{\omega}_r$ around the rated rotor speed, yielding

$$T_r - N_G T_g = J_{dt}\Delta\dot{\omega}_r \tag{36.2}$$

In region III the generator torque controller remains at constant power, which means that the generator torque is inversely proportional to the rotor speed.

$$T_g(\omega_r) = \frac{P_0}{N_G\omega_r} \tag{36.3}$$

where P_0 is the rated power.

Likewise the aerodynamic torque can be found in region III by assuming insignificant variation in torque with respect to the rotor speed

$$T_r(\beta) = \frac{P_r(\beta, \omega_{r,0})}{\omega_{r,0}} \tag{36.4}$$

where β is the collective blade pitch angle, and P_r is the rotor power.
An approximation of T_g and T_r around the equilibrium points at rated rotor speed, $\omega_{r,0}$, and P_0, respectively, can be found by utilizing a first order Taylor series expansion of eq. 36.3 and 36.4 yielding

$$\begin{aligned} T_g &\approx \frac{P_0}{N_G \omega_{r,0}} - \frac{P_0}{N_G \omega_{r,0}^2} \Delta\omega_r \\ T_r &\approx \frac{P_0}{\omega_{r,0}} + \frac{1}{\omega_{r,0}} \frac{\partial P}{\partial \beta} \Delta\beta \end{aligned} \tag{36.5}$$

where $\Delta\beta$ is a small perturbation of the blade pitch angle close to the operation point.
With a PID control, which is widely used for pitch systems of wind turbines [104], the perturbation of the blade pitch angle is related to the rotor speed perturbation by

$$\Delta\beta = K_{P,\beta} N_G \Delta\omega_r + K_{I,\beta} \int_0^t N_G \Delta\omega_r \, dt + K_{D,\beta} N_G \Delta\dot{\omega}_r \tag{36.6}$$

where $K_{P,\beta}$, $K_{I,\beta}$ and $K_{D,\beta}$ are the proportional, integral and derivative gains, respectively, for the blade pitch control. By setting $\dot{\phi} = \Delta\omega_r$, the equation becomes

$$\Delta\beta = K_{P,\beta} N_G \dot{\phi} + K_{I,\beta} N_G \phi + K_{D,\beta} N_G \ddot{\phi} \tag{36.7}$$

Inserting the Taylor approximations from eq. 36.5 and the simplified expression for the PID controller from eq. 36.7 into the equation of motion for the rotor model in eq. 36.2 yields

$$\underbrace{\left(J_{dt} + \frac{1}{\omega_{r,0}} \left(-\frac{\partial P}{\partial \beta}\right) N_G K_{D,\beta}\right)}_{M_\phi} \ddot{\phi} + \underbrace{\left(\frac{1}{\omega_{r,0}} \left(-\frac{\partial P}{\partial \beta}\right) N_G K_{P,\beta} - \frac{P_0}{\omega_{r,0}^2}\right)}_{C_\phi} \dot{\phi} + \underbrace{\left(\frac{1}{\omega_{r,0}} \left(-\frac{\partial P}{\partial \beta}\right) N_G K_{I,\beta}\right)}_{K_\phi} \phi = 0 \tag{36.8}$$

From the above summation and simplification of the PID controlled rotor speed, it can be seen that the system will be a second order system which will have a natural frequency, $\omega_{\phi n}$, and damping ratio, ζ_ϕ, expressed as

$$\begin{aligned} \omega_{\phi n} &= \sqrt{\frac{K_\phi}{M_\phi}} \\ \zeta_\phi &= \frac{C_\phi}{2\sqrt{K_\phi M_\phi}} = \frac{C_\phi}{2 M_\phi \omega_{\phi n}} \end{aligned} \tag{36.9}$$

The pitch sensitivity defined as the change in aerodynamic power to collective blade pitch angle, $\frac{\partial P}{\partial \beta}$, is negative in region III by definition. It can be seen in eq. 36.8 that a positive change of the

control gains will affect the systems as follows; the proportional term increase the damping, the integral term increase the restoring stiffness and the derivative term will increase the effective mass moment of inertia of the drivetrain. It can also be seen by eq. 36.8 that the term $-P_0/\omega_{r,0}^2$ introduce negative damping to the system, and will change when the generator torque control tries to maintain constant power. The proportional term of the blade pitch controller needs to compensate for this negative damping.

It is recommended by M. H. Hansen [104] to neglect the derivative gain, ignoring the negative damping from the generator torque controller and design for a response with a natural frequency of $\omega_{\phi n} = 0.6$ rad/s and a damping ratio of $\zeta_\phi = 0.6$ to 0.7. The natural frequency is scaled according to the scaling law giving $\omega_{\phi n} = 3.55$ rad/s. Following these recommendations leads to a direct expression for the PI control gains.

$$K_{P,\beta} = \frac{2 J_{dt} \omega_{r,0} \zeta_\phi \omega_{\phi n}}{N_G \left(-\frac{\partial P}{\partial \beta}\right)}$$
$$K_{I,\beta} = \frac{J_{dt} \omega_{r,0} \omega_{\phi n}^2}{N_G \left(-\frac{\partial P}{\partial \beta}\right)} \tag{36.10}$$

To calculate these expressions, the blade pitch sensitivity needs to be found for the AAUE-TLP, which is an aerodynamic property that depends on the wind speed, rotor speed and the blade pitch angle. In region III where the aim is to keep the rotor speed fixed at the rated rotor speed ($\omega_0 = 7.49$ rad/s), the blade pitch angle corresponding to a constant rotor power equal to the rated rotor power ($P_0 = 86$ W) can be found for each wind speed. This yields a blade pitch sensitivity for each wind speed. The blade pitch sensitivity is calculated in FAST by performing a linearisation with all DOF deactivated at rated rotor speed, a steady and uniform wind speed and a blade pitch angle corresponding to the rated power. The linearisation is done in region III from 7 to 11 m/s with an increase of 0.5 m/s to investigate the blade pitch sensitivity changes throughout region III. The linearisation at each wind speed involves perturbing the blade pitch angle and measuring the aerodynamic rotor power. The blade pitch sensitivity is then calculated by a central difference approximation and presented in table 36.2.

Table 36.2: Sensitivity of aerodynamic rotor power to blade pitch angle in region III.

Wind Speed [m/s]	Rotor Speed [rpm]	Blade Pitch Angle [deg]	$\frac{\partial P}{\partial \beta}$ [W/rad]
7.0	71.5	0.00	-249.9
7.5	71.5	4.65	-344.7
8.0	71.5	7.98	-412.7
8.5	71.5	10.81	-477.7
9.0	71.5	13.13	-539.0
9.5	71.5	15.35	-598.9
10.0	71.5	17.27	-638.1
10.5	71.5	18.99	-786.2
11.0	71.5	20.55	-895.7

In table 36.2 it is seen that the blade pitch sensitivity varies over region III, and thus a simple PI

control is not adequate, however for a baseline PI blade pitch control the blade pitch sensitivity is set to the mean value $\frac{\partial \bar{P}}{\partial \beta} = -549.2$ giving the control gains $K_{P,\beta} = 0.0016$ and $K_{I,\beta} = 0.004$.

Table 36.3: Collective blade pitch baseline control parameters.

Control Gain	
$K_{P,\beta}$	0.0016
$K_{I,\beta}$	0.004

36.4 Gain Schedule Blade Pitch Control

As mentioned in the above section about the baseline blade pitch control is a simple PI control not adequate as the blade pitch sensitivity varies with the wind speed. Inspecting the blade pitch sensitivity further shows that there is reasonable linear correlation between it and the blade pitch angle, as seen in fig. 36.4.

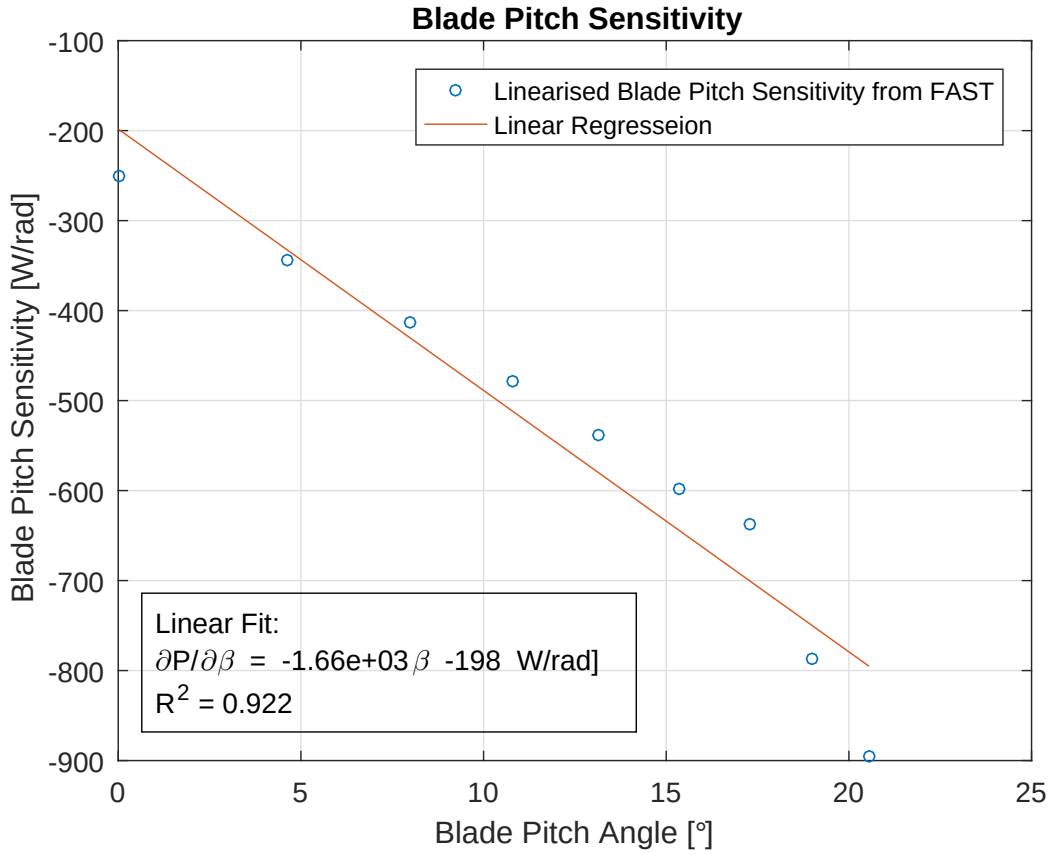

Figure 36.4: Blade pitch sensitivity with linear fit.

The linear regression for the blade pitch sensitivity can be described by the slope, β_K, and intersection point, $\frac{\partial P}{\partial \beta}\Big|_{\beta=0}$, such that the linear estimate is

$$\frac{\partial \hat{P}}{\partial \beta}(\beta) = \beta_K \beta + \frac{\partial P}{\partial \beta}\Big|_{\beta=0} \tag{36.11}$$

Inserting the linear regression into the expressions for the PI control gains from eq. 36.12 brings an expression for the control gains dependent on the pitch angle which can be used for gain scheduling

$$K_{P,\beta}(\beta) = \frac{2 J_{dt} \omega_0 \zeta_\phi \omega_{\phi n}}{N_G} \frac{1}{-\frac{\partial \hat{P}}{\partial \beta}(\beta)}$$

$$K_{I,\beta}(\beta) = \frac{J_{dt} \omega_0 \omega_{\phi n}^2}{N_G} \frac{1}{-\frac{\partial \hat{P}}{\partial \beta}(\beta)} \tag{36.12}$$

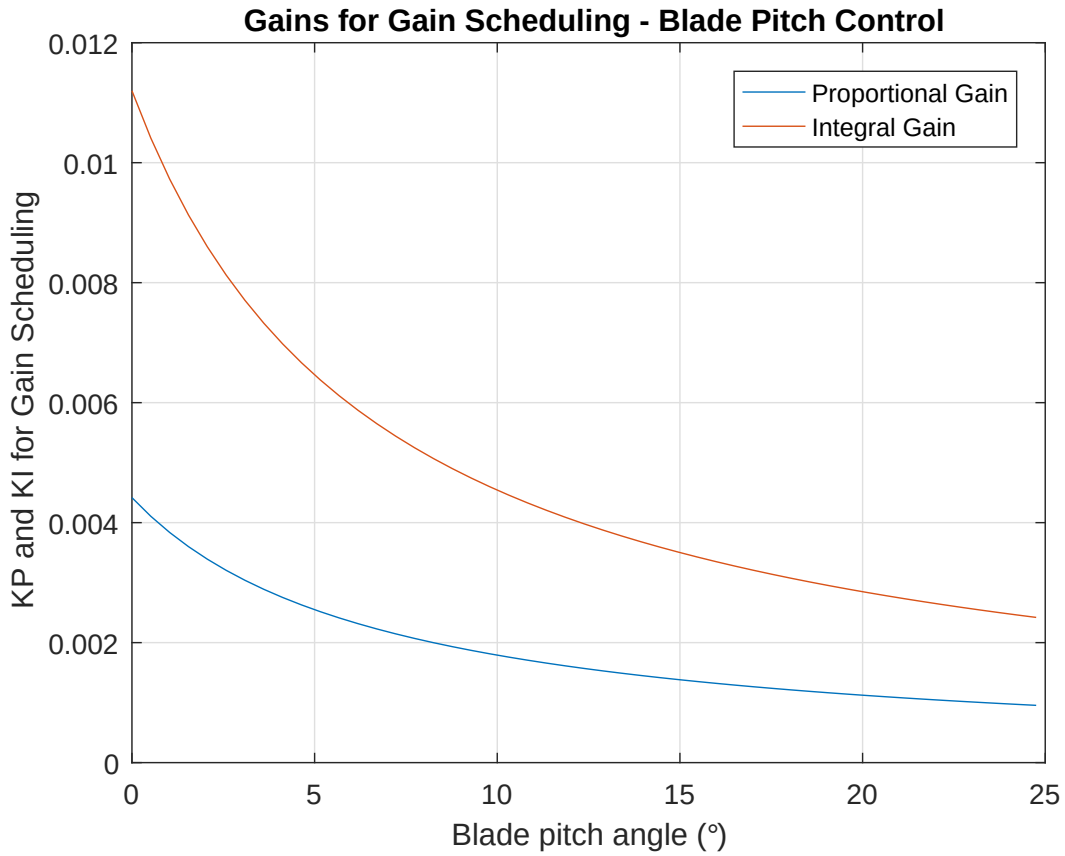

Figure 36.5: Blade pitch gain scheduling control gain vs. blade pitch angle.

When the gain scheduled blade pitch PI controller is implemented, the blade pitch angle from the previous time step is used to calculate the new control gains in the current time step.

Rotor Position Estimation 37

The control strategy of the generator is the FOC, which utilises the Park-Clark transformation of the three phase current for feedback. The Park-Clark transformation requires accurate information of the rotors electrical angle. There are different approaches in order to obtain the rotors position.

The position could be found using a mechanical encoder mounted on the generators shaft, but this is not possible for the generator of this thesis, as the generator is in an an enclosed box.
There is an mechanical encoder mounted on the low speed shaft, which could be used, but as the gearing from the low speed shaft to the generator is 1:28.9. The incremental magnetic encoder on the low speed shaft have a resolution of 0.6°, which on the high speed shaft would equal to 17°. To obtain a higher precision of the high speed shafts angle, a sensorless position estimation technique is developed.

37.1 Sensorless Position Estimation Methods

There are several methods proposed for sensorless control of PMSM [105][106][107], which also apply for the PMSG. The different methods can be divided into three main categories; fundamental excitation methods, saliency and signal injection methods and artificial intelligence methods.
The artificial intelligence methods will not be considered further, as they are out of the scope for this thesis. Instead the basic principle of operation and advantages/disadvantages of the two other categories will be described, in order to make a choice for the method used for this thesis.

37.1.1 High Frequency Signal Injection

The basic principle of high frequency signal injection for rotor position estimation is to introduce high frequency voltage or current into the stator windings and measure the output on either the voltage or current. There will be a change in the high frequency content of the measured voltage or current, as it will change with the position of the rotor due to the saliency of the rotor [108]. Therefore this method only holds for PMSGs having interior permanent magnets, and not PMSGs having surface mounted permanent magnets, which the PMSG of this thesis has. The advantage of high frequency signal injection for rotor position estimation is its robustness to parameter variation and have a good performance at standstill and low speeds. The disadvantage is that it introduces additional power losses because of the high frequency signal injection[108].

37.1.2 Fundamental Excitation

The fundamental excitation category can be split into two subcategories: Non-adaptive methods and adaptive methods.

37.1.2.1 Non-adaptive Methods

There exist several sensorless control algorithms which are based on the back EMF.
The most widely used are: Back EMF zero crossing detection and flux linkage estimation. The basic of operations and their advantages/disadvantages are shortly outlined below.
The principle of back EMF zero crossing detection method is to detect the zero crossing of the back EMF by measurements of the phase currents and voltages. Thereby an estimate of the position of the rotor can be found [109]. This method is widely used for BLDC with trapezoidal back EMF [110].
The flux linkage estimator makes use of the generator parameters and measurements of the line to line voltages and phase currents in order to estimate the flux linkages. Thereby the stator flux linkage vector can be calculated by integration of the calculated back EMF. By knowledge of the stator flux linkage vector, the position of the rotor and angular speed can be calculated [111]. Due to the integration of the flux linkage estimation, there is a prone to drift and offset [112].
The back EMF sensorless control algorithms are most suitable for high rotational speeds of the PMSG, because at low rotational speeds the induced back EMF in the stator windings is small [109] [112] [113].

37.1.2.2 Adaptive

Adaptive methods are characterised by using a mathematical model of the system and comparing the error to the real system. This error is then fed back to the model to adapt the model, such that the error is minimized. Several methods exist for this e.g the model reference adaptive estimator and observer based methods. Model reference adaptive estimator is based on a reference model and an adaptive model. The reference model is the real system and adaptive model is a mathematical model of the system. These are fed with the same input and the outputs of the two model are compared to find the error. The error is then used in an adaptive mechanism to change some parameters in the adaptive model [114]. Observer based methods are to construct a mathematical model, compare the outputs between the mathematical model and real system and feed the error back into the mathematical model, which corrects the states and minimizes the output error. The model and correction term can be modelled in different ways e.g Luenberger observer, sliding mode observer and Kalman filter.
For rotor position estimation of PMSGs the extended Kalman filter is widely used [115]. The mathematical model of the PMSG and drive train is developed in a state space formulation. The model will be given the same input as the PMSG, which is the $dq0$ stator voltages and its correction output will be the $dq0$ currents.
The disadvantage of these methods, is that they are often computational expensive, and also parameter dependent [115].
[116]

37.2 Extended Kalman Filter Algorithm

In this thesis the EKF is chosen, as this is deemed to be the most appropriate method for this thesis. The EKF is a nonlinear extension of the linear Kalman filter and is designed based on the discrete

nonlinear state space system. For the purpose of rotor position estimation, the PMSG voltage equations in 23.4 and the drive train model in eq. 22.1 are written into a discrete non-linear state space form. Starting with the continuous non-linear state space model form

$$\begin{cases} \frac{d}{dt}\boldsymbol{x} &= \boldsymbol{g}(\boldsymbol{x},\boldsymbol{u}) \\ \boldsymbol{y} &= \boldsymbol{h}(\boldsymbol{x}) \end{cases} \tag{37.1}$$

with the input vector $\boldsymbol{u} \in \mathbb{R}^3$, state vector $\boldsymbol{x} \in \mathbb{R}^4$ and output vector $\boldsymbol{y} \in \mathbb{R}^2$

$$\begin{cases} \boldsymbol{u} &= [v_d \; v_q \; T_r]^T \\ \boldsymbol{x} &= [i_d \; i_q \; \omega_R \; \theta_e]^T \\ \boldsymbol{y} &= [i_d \; i_q]^T \end{cases} \tag{37.2}$$

The non-linear continuous system model $\boldsymbol{g} \in \mathbb{R}^4$ and the output matrix $\boldsymbol{h} \in \mathbb{R}^{2\times 4}$ is written as

$$\begin{cases} \boldsymbol{g}(\boldsymbol{x},\boldsymbol{u}) = \frac{d}{dt}\boldsymbol{x} &= \begin{bmatrix} \frac{1}{L_d}\left(v_d - R_s i_d + k_1 \omega_r L_q i_q\right) \\ \frac{1}{L_q}\left(v_q - R_s i_q - k_1 \omega_r L_d i_d - k_1 \omega_r \lambda_r\right) \\ \frac{1}{J_{dt}}\left(-B\omega_r + T_r - \frac{k_1}{\eta_G}\frac{3}{2}\left(\lambda_r i_q + \left(L_d - L_q\right) i_q i_d\right)\right) \\ k_1 \omega_r \end{bmatrix} \\ \boldsymbol{h}(\boldsymbol{x}) &= \begin{bmatrix} 1 & 0 & 0 & 0 \\ 0 & 1 & 0 & 0 \end{bmatrix} \boldsymbol{x} \end{cases} \tag{37.3}$$

where $k_1 = \frac{1}{2}\left(N_G \; poles\right)$

The continuous model is dicretized by using the forward Euler method with sampling time T_s. For sufficiently small sampling time, the following can be assumed

$$\begin{aligned} \boldsymbol{x}[k] &= \boldsymbol{x}(kT_s) \approx \boldsymbol{x}(t) \\ \frac{d}{dt}\boldsymbol{x}(t) &= \frac{\boldsymbol{x}[k+1] - \boldsymbol{x}[k]}{T_s} \end{aligned} \tag{37.4}$$

Thereby the discrete non-linear model of PMSG and drive train can be derived as

$$\begin{cases} \boldsymbol{x}[k+1] &= \underbrace{\boldsymbol{x}[k] + T_s \boldsymbol{g}(\boldsymbol{x}[k],\boldsymbol{u}[k])}_{=\boldsymbol{f}(\boldsymbol{x}[k],\boldsymbol{u}[k])} + \boldsymbol{w}[k] \\ \boldsymbol{y}[k] &= \boldsymbol{h}(\boldsymbol{x}[k]) + \boldsymbol{v}[k] \\ \boldsymbol{x}[0] &= \boldsymbol{x}_0 \end{cases} \tag{37.5}$$

where $\boldsymbol{w}[k] \in \mathbb{R}^4$ and $\boldsymbol{v}[k] \in \mathbb{R}^2$ are random variables which are included in the model system uncertainties and measurement noise, respectively. The covariance of $\boldsymbol{w}[k]$ and $\boldsymbol{v}[k]$ are assumed

constant for all k such that

$$\begin{aligned} \boldsymbol{Q} &= E\left\{\boldsymbol{w}[k]\,\boldsymbol{w}[k]^T\right\} \geq 0 \\ \boldsymbol{R} &= E\left\{\boldsymbol{v}[k]\,\boldsymbol{v}[k]^T\right\} > 0 \end{aligned} \tag{37.6}$$

As the system uncertainties and measurement noise is not known beforehand, the EKF is implemented to estimate the states $\hat{\boldsymbol{x}}$ and output $\hat{\boldsymbol{y}}$ vectors. The EKF is implemented as follows

$$\begin{aligned} \hat{\boldsymbol{x}}[k+1] &= \boldsymbol{f}\left(\hat{\boldsymbol{x}}[k], \boldsymbol{u}[k]\right) - \boldsymbol{K}[k]\left(\boldsymbol{y}[k] - \hat{\boldsymbol{y}}[k]\right) \\ \hat{\boldsymbol{y}}[k] &= \boldsymbol{h}\left(\hat{\boldsymbol{x}}[k]\right) = \boldsymbol{C}\hat{\boldsymbol{x}}[k] \end{aligned} \tag{37.7}$$

where $\boldsymbol{K}[k]$ is the Kalman gain, the recursive algorithm of the EKF is listed below. The EKF achieves an optimal state estimation by minimizing the covariance of the estimation error for each time instant $k \geq 1$.

Algorithm 2 Extended Kalman Filter Algorithm

Step 1 Initialization ($k = 0$)

$$\begin{aligned} \hat{\boldsymbol{x}}[0] &= E\{\boldsymbol{x}_0\} \\ \boldsymbol{P}[0] &= E\left\{\left(\boldsymbol{x}_0 - \hat{\boldsymbol{x}}[0]\right)\left(\boldsymbol{x}_0 - \hat{\boldsymbol{x}}[0]\right)^T\right\} \\ \boldsymbol{K}[0] &= \boldsymbol{P}[0]\boldsymbol{C}^T\left(\boldsymbol{C}\boldsymbol{P}[0]\boldsymbol{C}^T + \boldsymbol{R}\right)^{-1} \end{aligned} \tag{37.8}$$

Step 2 Time update ($k \geq 1$)
(**a**) State prediction

$$\hat{\boldsymbol{x}}^-[k] = \boldsymbol{f}\left(\hat{\boldsymbol{x}}[k-1], \boldsymbol{u}^-[k-1]\right) \tag{37.9}$$

(**b**) Error covariance matrix prediction

$$\hat{\boldsymbol{P}}^-[k] = \boldsymbol{A}[k]\boldsymbol{P}[k-1]\boldsymbol{A}[k]^T + \boldsymbol{Q} \tag{37.10}$$

where

$$\boldsymbol{A}[k] = \frac{\partial}{\partial \boldsymbol{x}}\boldsymbol{f}(\boldsymbol{x}, \boldsymbol{u})\Big|_{\hat{\boldsymbol{x}}^-[k]} \tag{37.11}$$

Step 3 Compute Kalman gain ($k \geq 0$)

$$\boldsymbol{K}[k] = \boldsymbol{P}^-[k]\boldsymbol{C}^T\left(\boldsymbol{C}\boldsymbol{P}^-[k]\boldsymbol{C}^T + \boldsymbol{R}\right)^{-1} \tag{37.12}$$

Step 4 Measurement update (Correction)
(**a**) Estimation update with measurement

$$\hat{\boldsymbol{x}}[k] = \hat{\boldsymbol{x}}^-[k] + \boldsymbol{K}[k]\left(\boldsymbol{y}[k] - \boldsymbol{h}\hat{\boldsymbol{x}}[k]\right) \tag{37.13}$$

(**b**) Error covariance matrix update

$$\boldsymbol{P}[k] = \boldsymbol{P}^-[k] - \boldsymbol{K}[k]\boldsymbol{C}\boldsymbol{P}^-[k] \tag{37.14}$$

Step 5 Go back to step 2

The linearized system matrix $\boldsymbol{A}[k]$ is determined by the Jacobian matrix of the nonlinear system $\boldsymbol{f}(\boldsymbol{x},\boldsymbol{u})$

$$\boldsymbol{A}[k] = \frac{\partial}{\partial \boldsymbol{x}} \boldsymbol{f}(\boldsymbol{x},\boldsymbol{u}) = \frac{\partial}{\partial \boldsymbol{x}} \left(\boldsymbol{x}[k] + \boldsymbol{g}(\boldsymbol{x},\boldsymbol{u}) \right) = \boldsymbol{I} + \boldsymbol{J} \tag{37.15}$$

where $\boldsymbol{I} \in \Re^{4x4}$ is the identity matrix and

$$\boldsymbol{J} = \frac{\partial}{\partial \boldsymbol{x}} \boldsymbol{g}(\boldsymbol{x},\boldsymbol{u}) = \begin{bmatrix} \frac{-R_s}{L_d} & \frac{L_q k_1 \omega_r}{L_d} & \frac{k_1 L_q i_q}{L_d} & 0 \\ \frac{-k_1 \omega_r L_d}{L_q} & \frac{-R_s}{L_d} & \frac{-k_1 (L_d i_d + \lambda_r)}{L_q} & 0 \\ \frac{1}{J_{dt}} \frac{k_1}{\eta_G} \frac{3}{2} \left(L_d - L_q \right) i_q & \frac{1}{J_{dt}} \frac{k_1}{\eta_G} \frac{3}{2} \left(\left(L_d - L_q \right) i_d + \lambda_r \right) & \frac{-B}{J_{dt}} & 0 \\ 0 & 0 & k_1 & 0 \end{bmatrix} \tag{37.16}$$

where η_G is the generator and gearbox efficiency. The following values where found to be most suitable for the EKF during testing.

$$\begin{cases} \boldsymbol{Q} & = diag\{0.01, 0.01, 0.01E-3, 0.01\} \\ \boldsymbol{R} & = diag\{1, 0.001\} \\ \boldsymbol{P}[0] & = diag\{1,1,1,1\} \\ \boldsymbol{x}[0] & = (0,0,0,0)^T \end{cases} \tag{37.17}$$

The EKF is programmed in a MATLAB function block in Simulink, the MATLAB function is seen in appendix A.11.8 and the simulink model is seen in appendix A.12.1.

Test and Validation 38

In this chapter the performance of the controllers developed in this part will be tested on the experimental setup and compared to the theoretical performance.

38.1 Generator Control Tests

The performance of the generator control is tested by having a constant mean wind speed of 7 m/s on the rotor and by applying a step change form 70 to 60 RPM on the rotor speed reference. The performance of both the speed and the current loop are tested in the same experiment. The experiment is compared to the theoretical simulation of the same conditions, the simulation is conducted in Simulink and FAST.

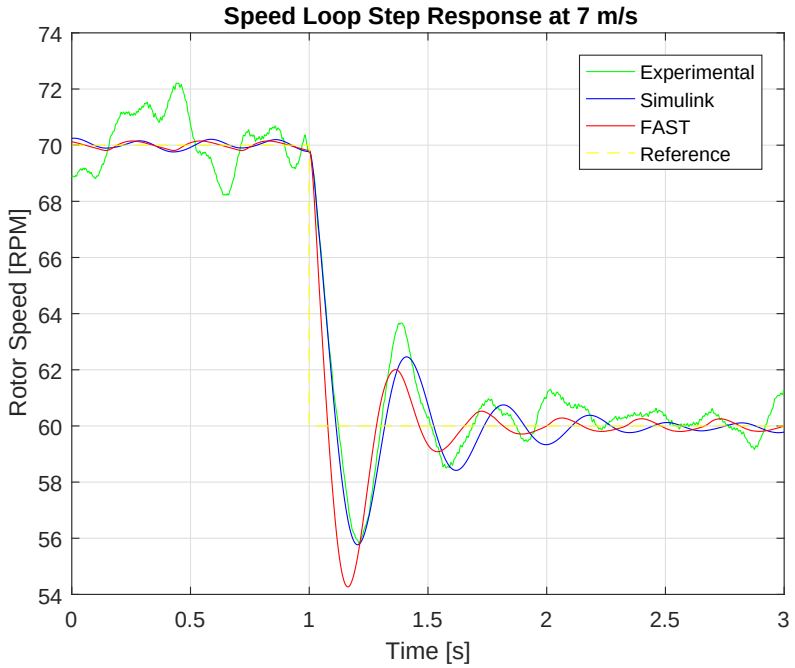

Figure 38.1: Experimental and theoretical step responses of reference speed in region II with a wind speed of 7 m/s. The experimental speed is measured by the shaft encoder.

In fig. 38.1 it is seen that the performance of the experimental and simulated speed loop are much alike. However the experimental response has more disturbance than the simulated. This is most likely due to vibrations in the drive train and rotor, along with measurement uncertainties in the encoder and turbulence in the wind, causing a variation in the wind speed.

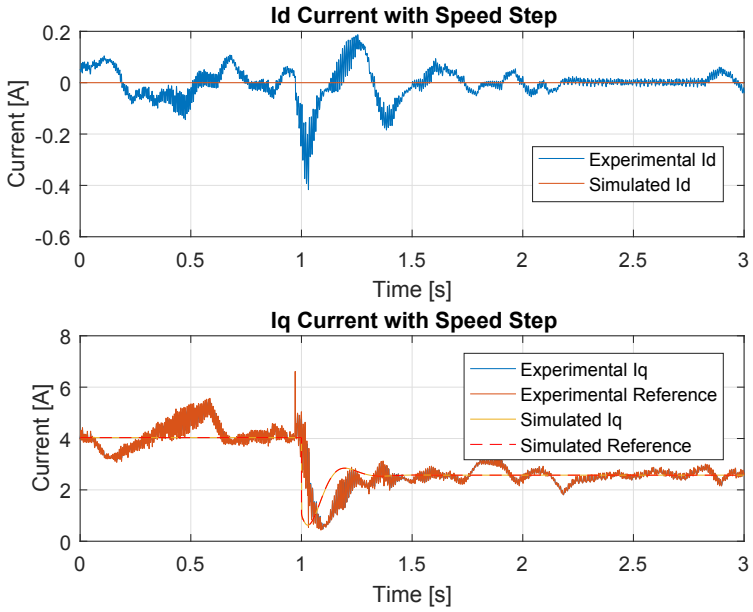

Figure 38.2: Experimental and theoretical current responses when a step response on the reference speed is made. The experimental currents are measured by the current transducers and transformed into the d and q axis currents.

In fig. 38.2 the d and q axis generator currents are shown when the step shown in fig 38.1 is applied to the speed loop. Both the experimental and FAST results are shown. The Simulink results are not shown as FAST and Simulink are based on the same model. It is seen that the simulated d-axis current tracks zero very clear however the experimental has a larger deviation. This is due to small errors in the electrical angle estimation and speed variation. The experimental q-axis current is corrected with an offset due to similar reasons as explained in section 25. The dynamic of the two signals seem similar, however the experimental is somewhat slower than the simulated.
In fig. 38.3 a zoom of fig. 38.2 is shown. It can be seen that the experimental q-current reference is oscillating, which is due to the oscillations in the speed loop. The current is however still able to track the reference well.

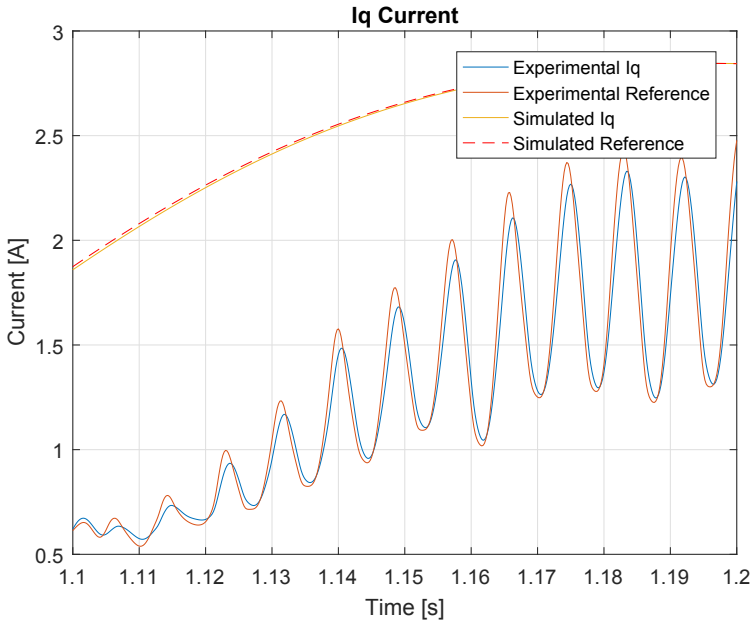

Figure 38.3: Zoom of fig. 38.2 visualising the tracking of the reference q-current.

To test the generator control across the whole region II an experiment is made with wind speed incrementally increasing from 3 m/s to 7 m/s with a step size of 0.5 m/s. The experiment is tested against both Simulink and FAST as seen in fig. 38.4.

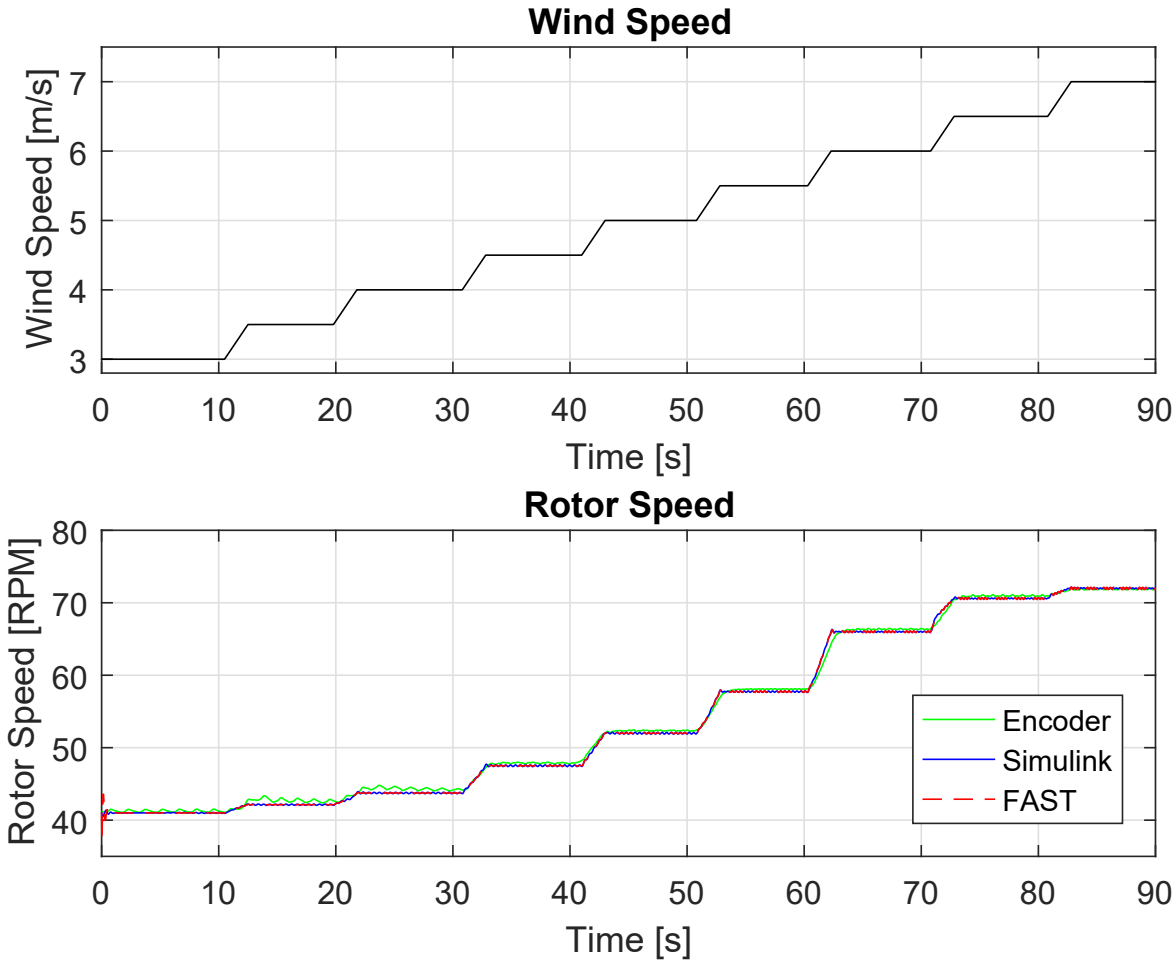

Figure 38.4: Speed response over region II.

It can be seen in fig. 38.4 that both Simulink and FAST have the same performance as the experimental.

38.2 Blade Pitch Tests

In this section the control of the blade pitch is tested. First the control for the blade pitch actuator is tested, next the control for the collective blade pitch is tested both with constant gain and with gain scheduling.

38.2.1 Blade Pitch Actuator Control Tests

The performance of the blade pitch actuator control is tested by comparing the experimental responses with the theoretical found ones. The test was done at two different wind speeds of 5.54 and 6.64 m/s, while the rotor was rotating.

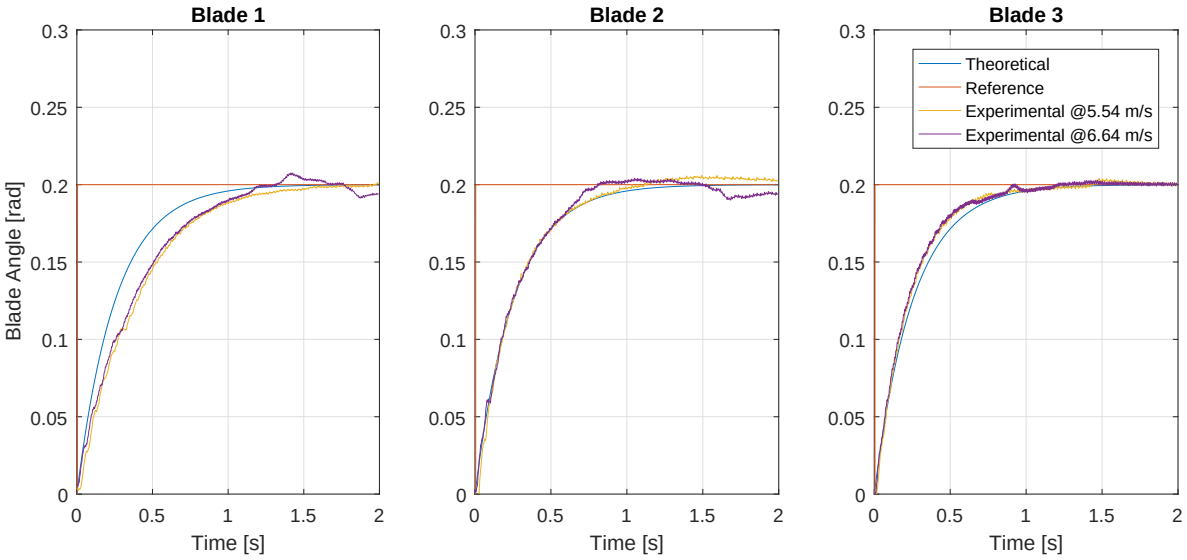

Figure 38.5: Experimental and theoretical step responses of pitch actuator system with control.

In fig. 38.5 it is seen that the theoretical and physical pitch actuator systems perform similar with only a small deviation. The response at the highest wind speed seems to have more disturbance which is due to a large load on the blades.

38.2.2 Collective Blade Pitch Control Tests

Both the constant PI and the gain schedule collective blade pitch control performances are tested. In both cases an incremental increasing wind speed is applied to the system and the experimental performance is compared to the simulated performances. Due to the limitations with a maximum wind step of approximately 8.5 m/s the increase is made within the interval of 7 m/s and 8 m/s. This limits the capability of validating the gain scheduling algorithm, as it is impossible to verify whether or not the same overall performance is met across entire region III. In fig. 38.6 the collective blade pitch control with constant gain is first tested, it can be seen that the control both experimentally and simulated is capable of tracking a constant reference of 71.5 RPM even though a step in the wind is applied. It can also be seen that the tracking is within seconds however a larger overshoot occurs in the experiment than seen in the simulations. This is seen both in the rotor speed and in the pitch angle, which is an average pitch angle of the three pitch actuators. Both Simulink and FAST predict the response within an adequate level. It can be seen that the response of FAST is more smooth than both the experimental and the Simulink response. This is due to the fact that inflow wind in FAST is modelled as steady and uniform, meaning that no turbulence is present.

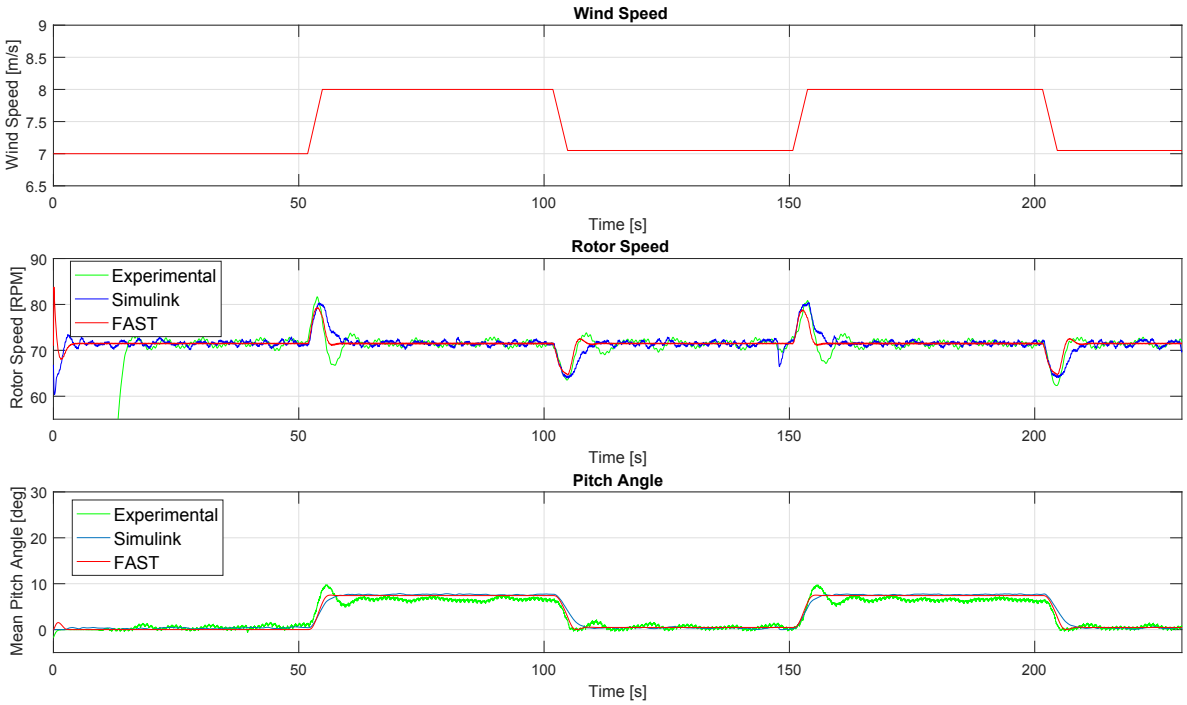

Figure 38.6: Collective blade pitch control with constant gain.

In fig. 38.7 the gain scheduling is tested. Again the control effectively tracks the reference of 71.5 RPM. Again the tracking is within seconds, this time however with a lower overshoot in both the experiment and simulations. Furthermore, it can be seen that the blade pitch actuators are less activated, whereby the pitch actuator system is run more effectively compared to the control system with constant gain.

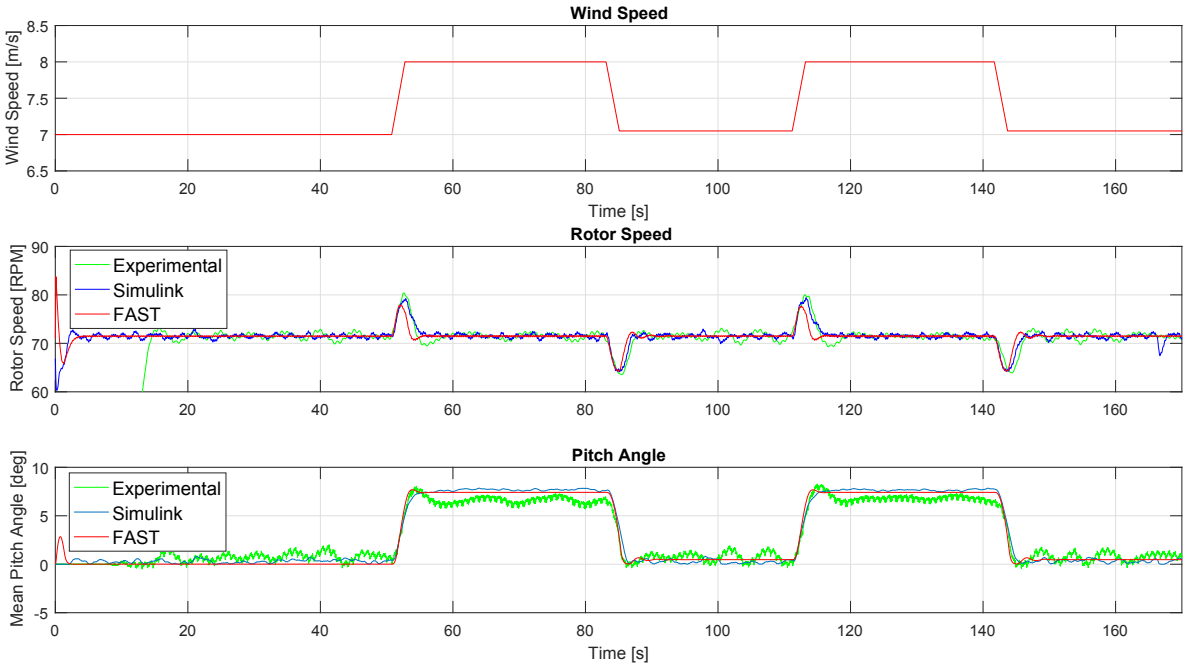

Figure 38.7: Collective blade pitch control with gain scheduling.

As it can be seen, the simulations are capable of describing the experimental response well. Therefore it is reasonable to use the simulation to check the validity of the gain scheduling method across the entire range of region III, that is increasing from 7 m/s to 11 m/s. As seen in fig. 38.8,

which shows the simulation made in Simulink, the gain scheduling is capable of keeping the same system performance across the entire region. This is not the case with the constant gain. However there is only a small difference between the constant gain and the gain schedule.

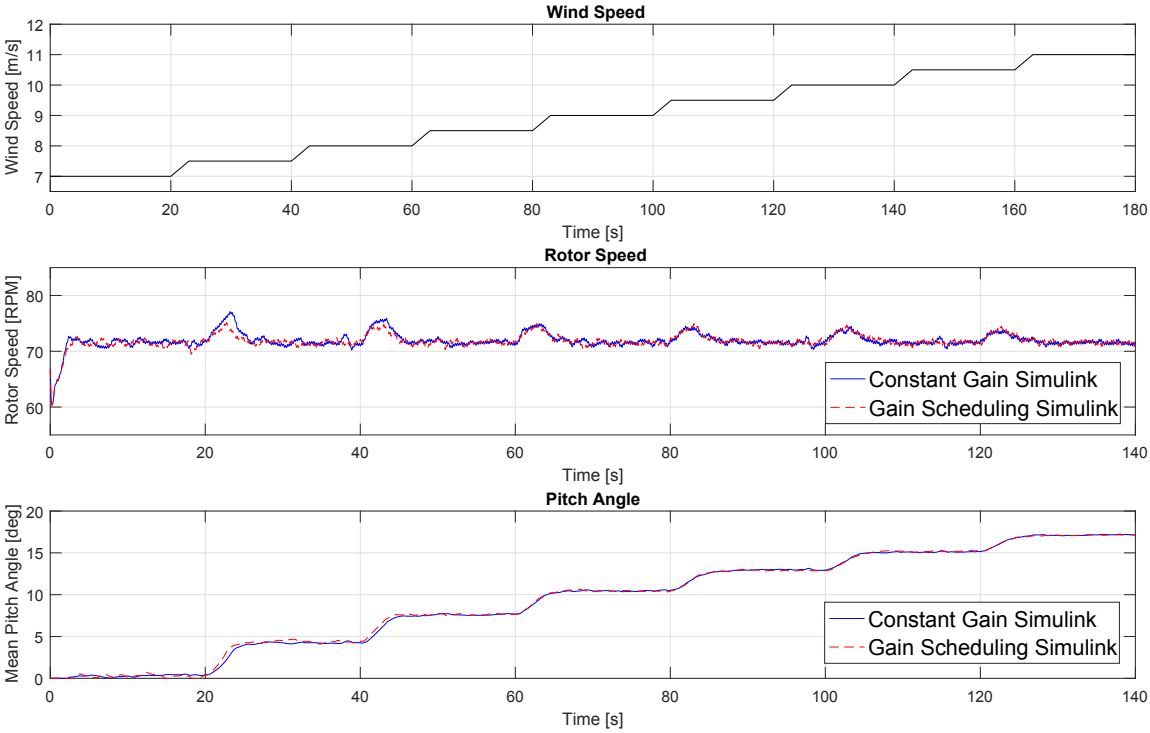

Figure 38.8: Gain scheduling vs. constant gain compared in Simulink.

Likewise the simulation was made in FAST. Again it can be seen that the gain scheduling is capable of keeping the same system performance across the entire region, which is not the case with the constant gain.

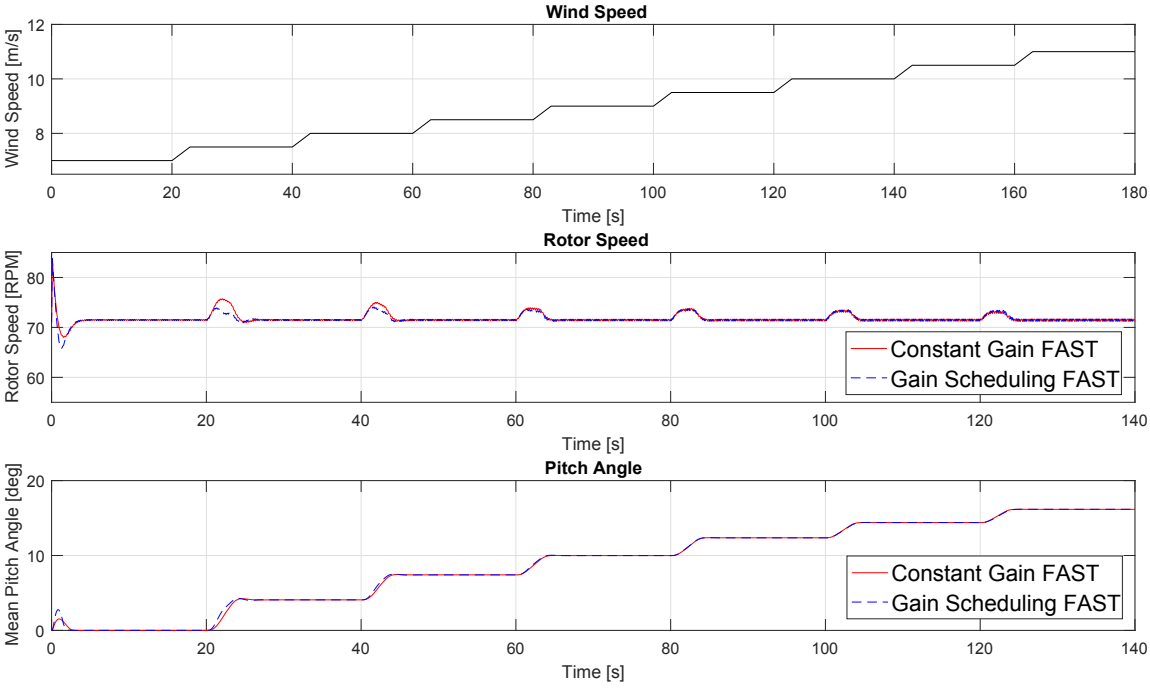

Figure 38.9: Gain scheduling vs. constant gain compared in FAST.

38.3 Extended Kalman Filter Tests

The performance of the EKF is tested against the rotor speed which is measured by the shaft encoder, as the generator angle is not measurable. First eight tests are done in region II where the steady state rotor speed is analysed. Next the performance of the EKF with a step on the rotor speed is investigated by simulation, where the performance of all estimated states can be seen. Last a test with an incremental increasing wind speed as in the experiment seen in fig. 38.4 was made. The performance of all estimated states is shown by simulation and the performance of the rotor speed is shown by experiment, too.

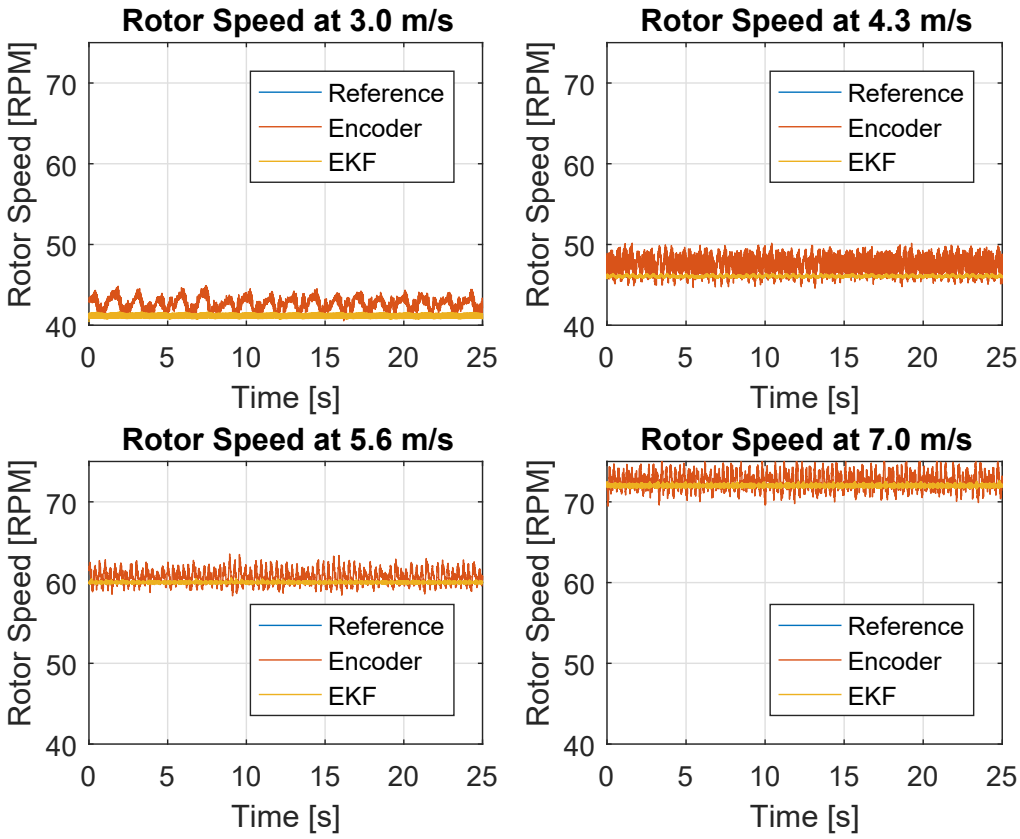

Figure 38.10: Experimental EKF estimated, encoder measured and reference in region II shown in the time domain.

In fig. 38.10 a time series of four out of eight experiments are shown. It can be seen that the EKF and the encoder have almost the same mean value, however with different variance. The encoder seems to have some disturbance which the EKF does not estimate, likewise the encoder also have larger variance than the EKF.

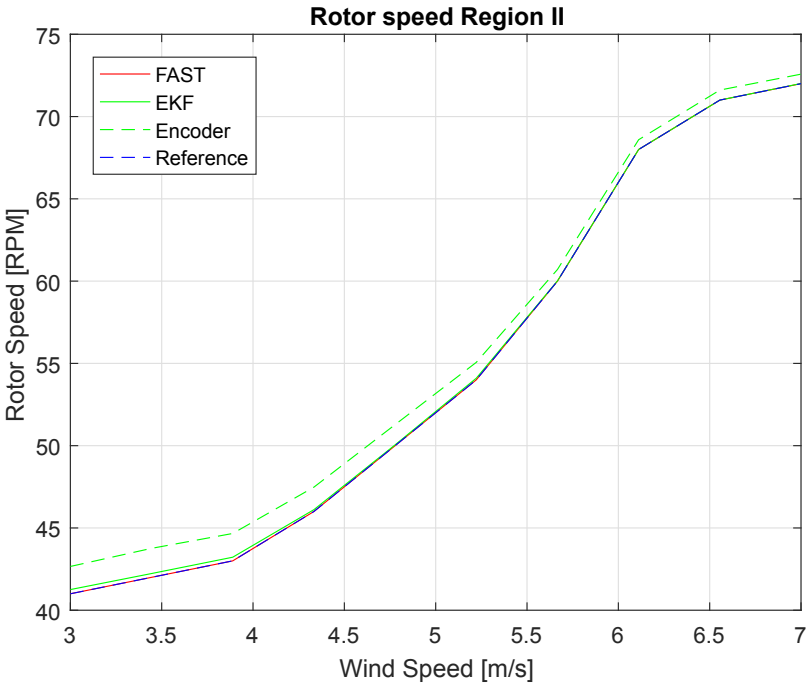

Figure 38.11: Visualisation of the mean experimental rotor speed estimated by EKF, the measured rotor speed by the encoder and the rotor speed from FAST in region II.

In fig. 38.11 the mean values of the eight test are compared from the EKF, the encoder, FAST and the reference. The encoder, FAST and the reference are similar, however the encoder has an offset which slowly decreases as the rotor speed increases. This is also expected according [117] where the error of the EKF estimate at low speed is investigated.

To test the system against dynamic changes a step response is applied on the rotor speed in region II similar to the step test in fig. 38.1. First a simulation of the test is shown in fig. 38.12, where the EKF estimated states are compared to the real simulated states. In the simulation white noise with zero mean and variance of 0.1 is added to the current input in the abc-frame before it is transformed into the $dq0$-frame. Likewise white noise with zero mean and variance of 0.5 is added to the generator torque. All initial states are set to zero.

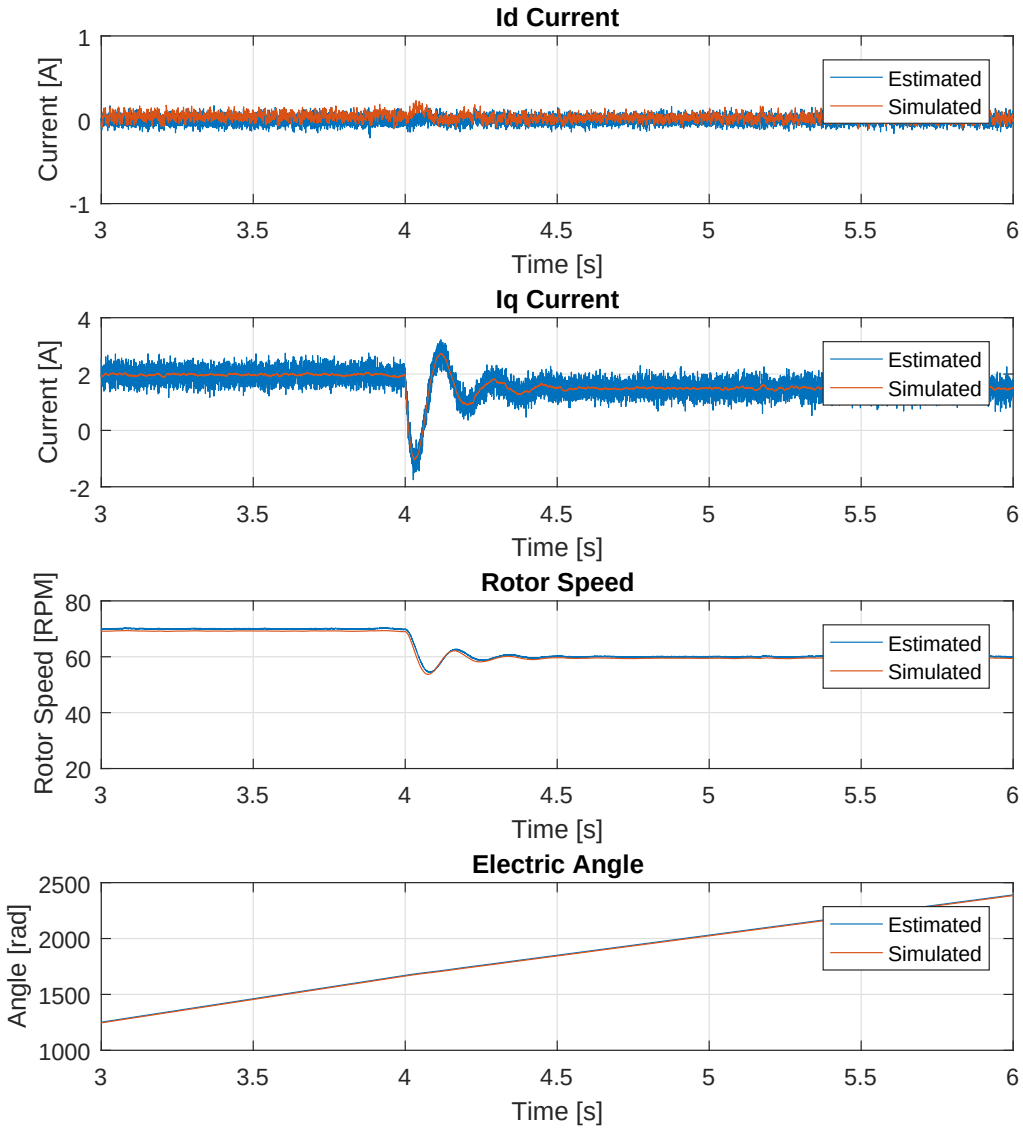

Figure 38.12: Simulates performance of the EKF when applying a step on the speed loop from 70 to 60 RPM at 7m/s.

In fig. 38.12 it is seen that the EKF estimates all states very well, in fig. 38.13 the error between the estimates and the states are seen.

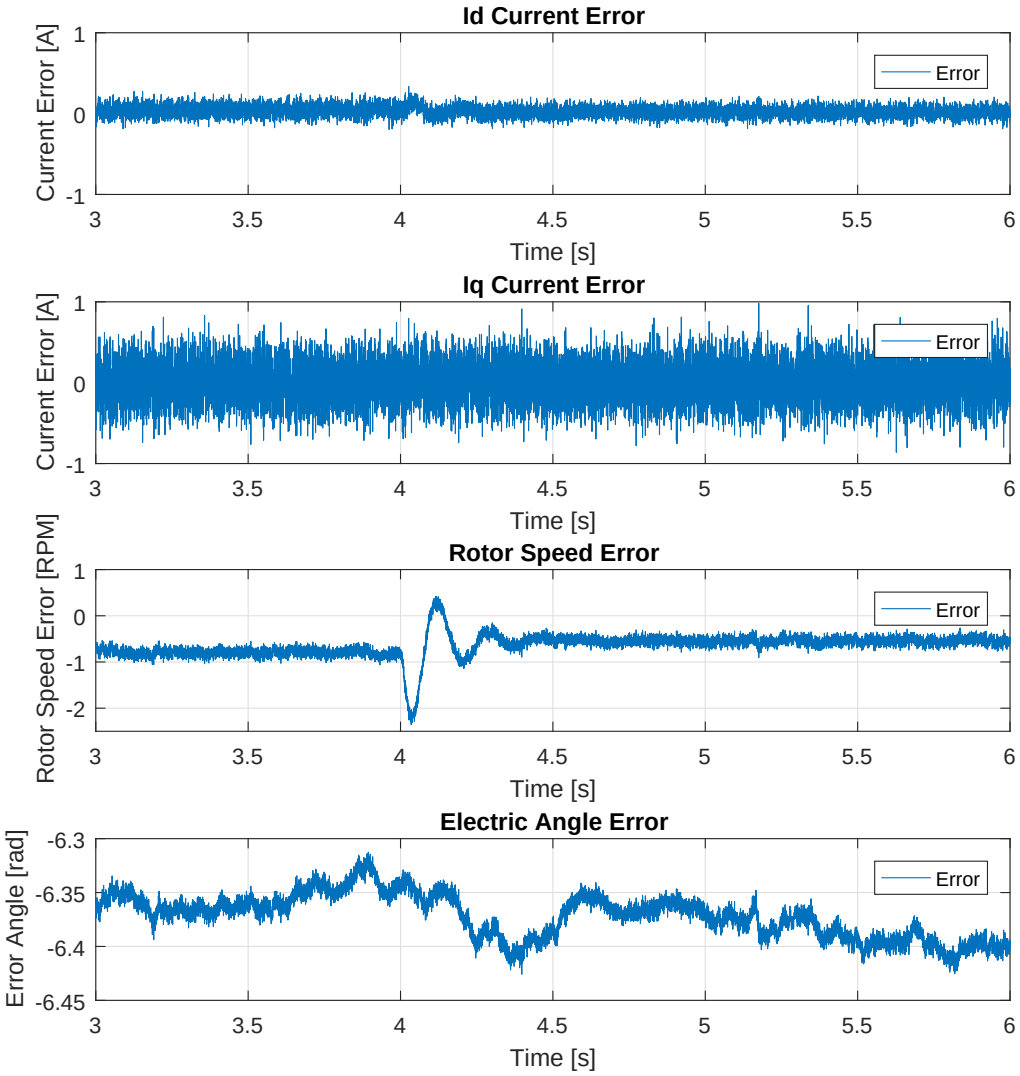

Figure 38.13: Simulated errors of the EKF when applying a step on the speed loop from 70 RPM to 60 RPM at 7 m/s.

In fig. 38.13 it seems that the errors in the two current states are pure white noise. However the rotor speed and the electrical angle state, have a mean offset. The simulation was tested with different initial state conditions and the performance of the EKF was found satisfying in all the tested situations.

In fig. 38.4 a rotor speed response was shown with an incrementally increase in wind speed. The same conditions are used to test the EKF. In fig. 38.14 the EKF estimated states are seen simulated, where it is seen that the EKF estimates all the states satisfying.

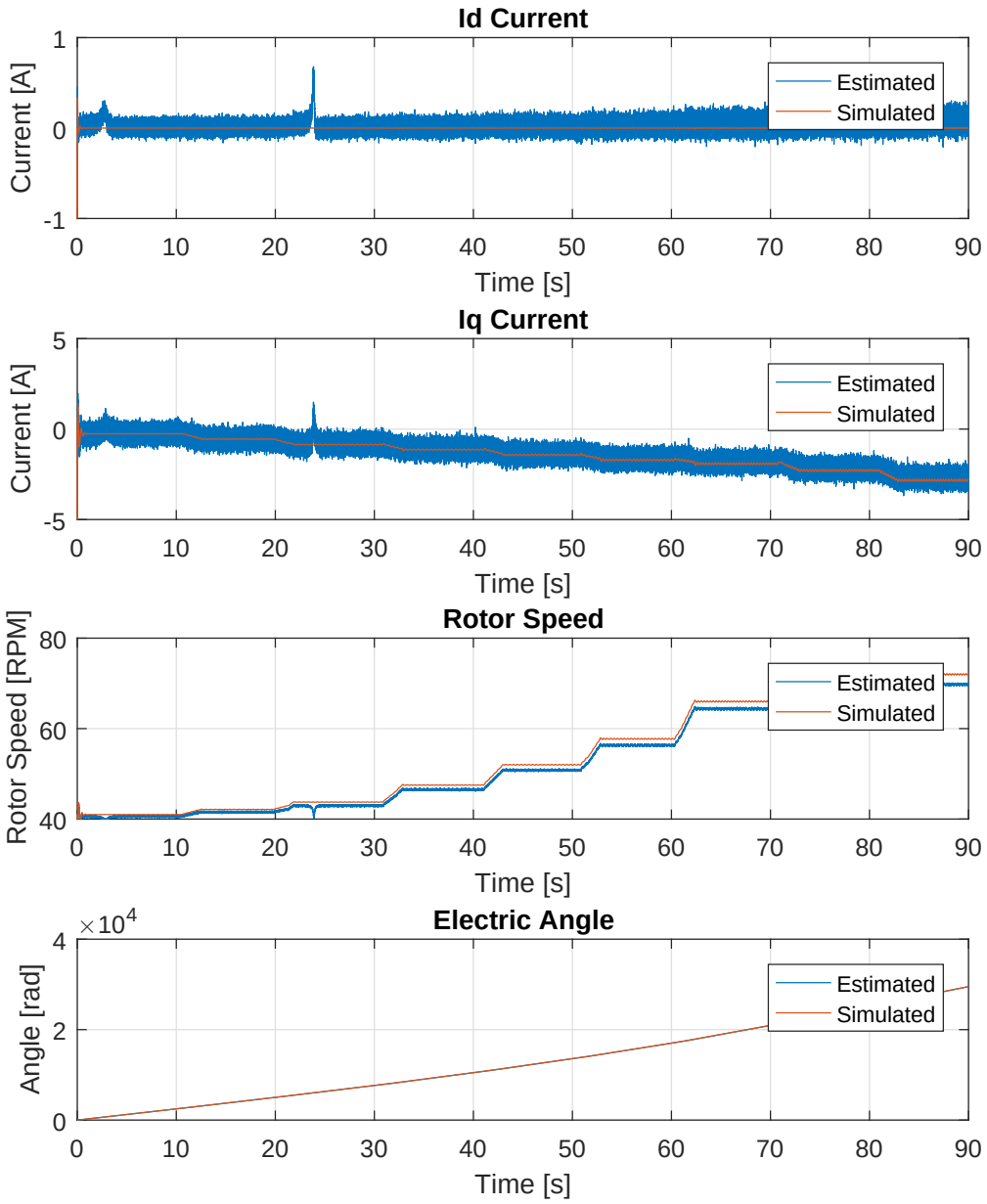

Figure 38.14: Simulates performance of the EKF when incrementally increasing in wind speed.

In fig. 38.15 it seems that the errors in the current states are almost pure white noise. However the rotor speed and electrical angle states have a drift.

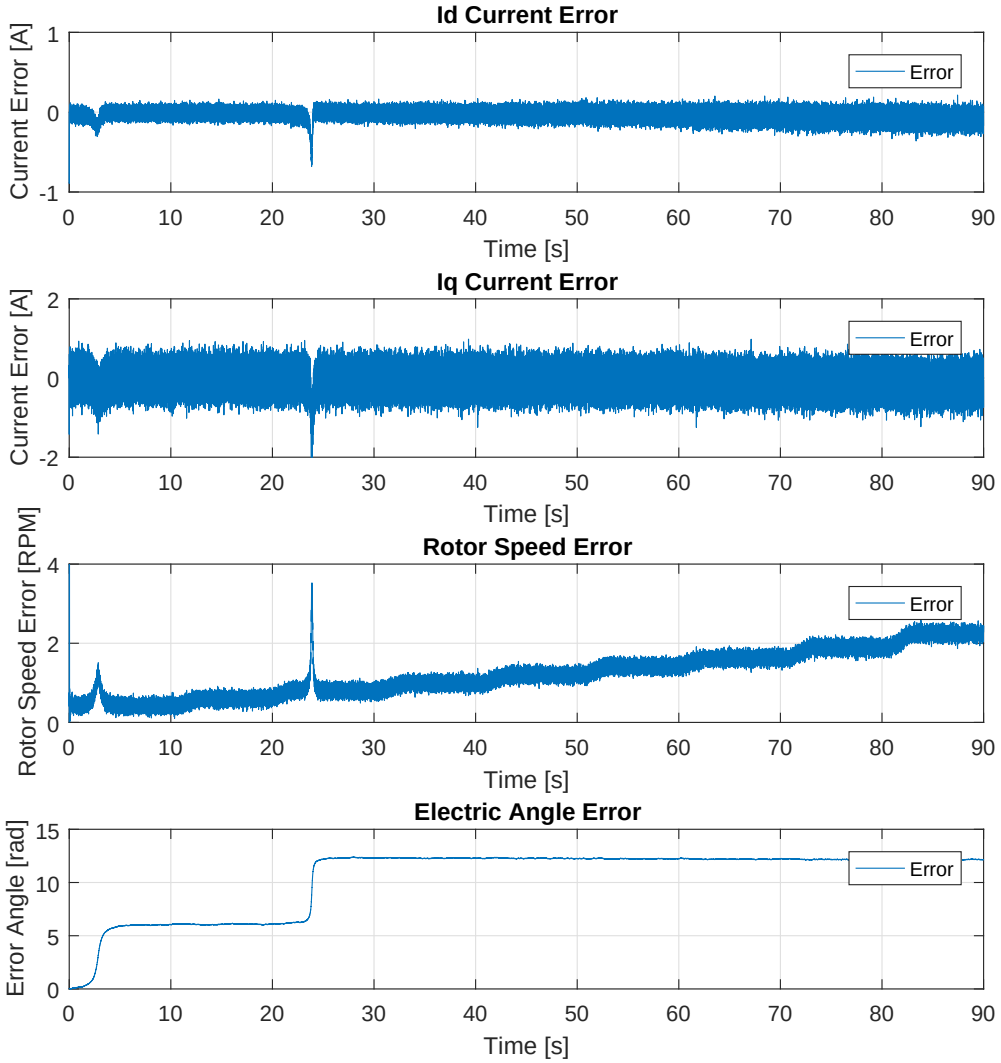

Figure 38.15: Simulated errors of the EKF when incrementally increasing in wind speed.

In fig. 38.16 the experimental rotor speed of the simulated tests in fig. 38.14 are shown. It can be seen that the EKF estimates the rotor speed well, however with a faster response than the encoder. It seems that the EKF trusts too much on the model and thereby tracks the reference faster than the actual system, however a tuning of the EKF with more trust on the measured signal was not found stable.

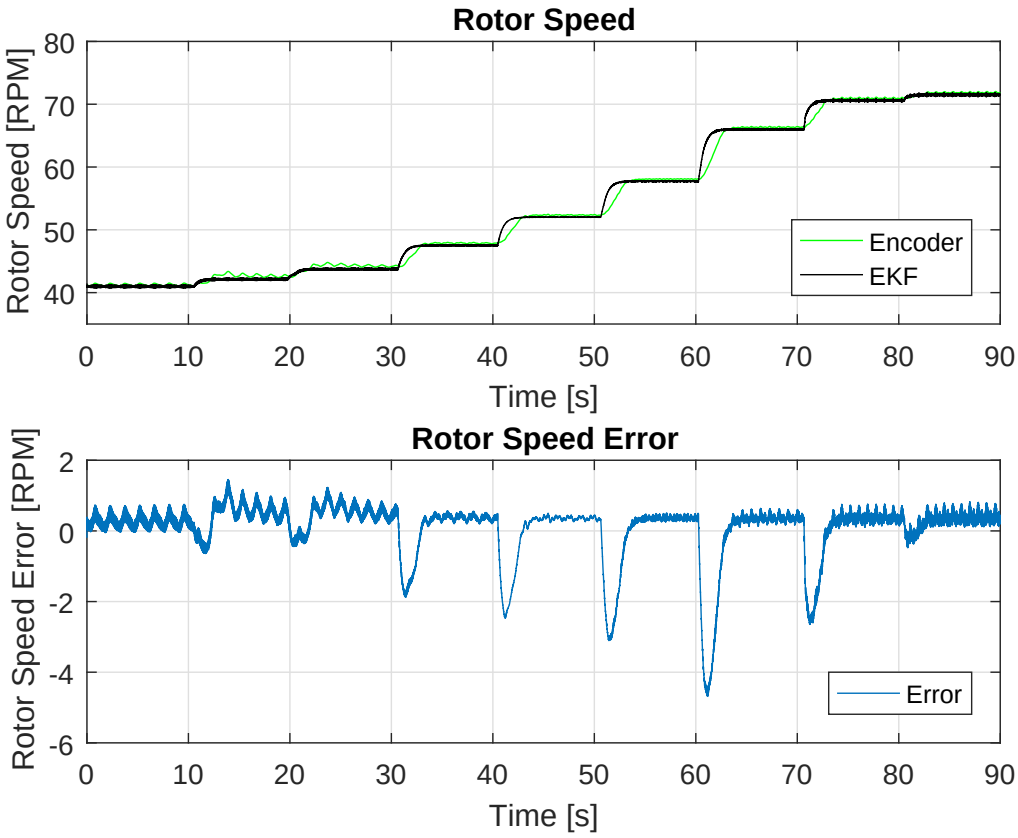

Figure 38.16: The rotor speed estimated by the EKF compared to the measured from the encoder in region II and the error between them.

Conclusion 39

In this part the control of the AAUE-TLP was explained. At first the control objectives and the different regions were explained. This together with showing the Campbell diagram of the system. Next the generator control was developed. The generator control is based on FOC applying the advantage of Park-Clarke's transformation. The generator control consists of three control loops; two inner current loops and a single outer speed loop. The current loops can be considered identical with only the reference input to differ. As the outer loop depends on the performance of the inner loop, the inner loops were designed to be stable at all times, having no steady state error regarding step responses and to have a fast rise time relative to the outer speed loop. To control the response of the inner loops a PI controller was chosen. The design was made in the discrete time domain and considering the placement of the poles compared to the stability and bandwidth of the system. The PI controller was made such the closed loop step response of the inner loop would have a rise time of 0.8 ms and a settling time of 1.8 ms, which is much faster than the outer loop. Furthermore, the response had no steady state error and no overshoot, whereby the design requirements were met.
The control of the speed loop was designed by considering the system as a cascaded transfer function consisting of the controller, the inner current loop, a static relationship between the generator torque and current and the drive train.The OSM was then utilised as control strategy, which maximises the phase margin and leads to a symmetrical phase and magnitude response around the cross over frequency. The control method leads to a large overshoot and therefore limit on the current reference together with integral anti wind-up circuit were implemented.
Next the control system for the blade pitch actuator was designed as a simple P controller. The control was implemented such that a fast rise time compared to the collective pitch loop was secured. Furthermore, it was designed such that no steady state error to a step response would be present, along with a fast settling time.
Next the collective blade pitch controller was developed. The control objective of this was to create a reference for the blade pitch actuator control, such that a constant rotational rotor speed is kept when the wind turbine is operating inside region III. The control was designed considered the dynamical equations of the drive train and approximating the generator torque and rotor torque around the equilibrium points at rated rotor speed and rated power. Considering a PID control the perturbation of the rotor speed could be related to a perturbation in the blade pitch angle. Utilising the approximations of the rotor and generator torque together with the perturbation in the pitch angle, the rotor model could be redefined yielding a second order system with a given damping ratio and natural frequency. Together with the blade pitch sensitivity and the mass moment of inertia of the drive train, the natural frequency and damping ratio defines the PI control gains. The blade pitch sensitivity is linear dependent on the blade pitch angle, whereby different gains for different blade pitching angle is necessary.

As the resolution of the generator electrical angle is 17° when using the shaft encoder, an estimation method to determine this angle is designed. This to achieve a higher precision, which is needed to run the FOC. In this thesis the extended Kalman filter algorithm is utilised.
The last chapter concerns test and validation of the implemented control, where the experimental obtained responses are compared to the simulated. At first the generator control is tested. This by applying a step on the reference rotor speed, whereby also a change in the reference currents will occur. In these tests it can be seen that the simulated responses match the experimental responses well. Furthermore, the behaviour of the systems is as expected. Next an incremental increase in the wind speed with a step size of 0.5 m/s is made. This is done to test the generator control across the entire region II. The tests showed that the simulations had the same performance as the experimental.
Next the performance of the blade pitch actuators were tested. This by applying a step in the reference pitch angle at different wind speeds, while the rotor was rotating. The theoretical and physical systems perform similar with only small deviations.
Next the collective blade pitch control is tested, this again by applying increasing wind speed. As the wind turbine is now operating in region III, the control should secure a constant rotor speed. This by pitching the blades in and out of the wind when the wind speed increases or decreases, respectively. The tests were made both with constant PI gains and with the gain scheduling approach. The results showed that the simulated responses matched the experimental responses well. Furthermore, it was seen that the gain scheduling approach used less actuator action to meet the reference tracking criteria.
At last the developed EKF algorithm is tested against the measured rotor speed. The steady state speed was analysed at different wind speeds within region II, showing that the encoder and the EKF had almost the same mean values, however with different variances. Next the mean values from EKF, the encoder and FAST from eight different test were compared to each other, showing that there was a small offset at low speed. A simulation of a step response showed the estimation performance of all the states. At last a test in region II was conducted with incremental increasing speed, where the EKF estimated rotor speed was compared to the encoder rotor speed. In this test it was seen that the EKF was a bit faster than the encoder.

Part VIII

Discussion and Conclusion

Discussion 40

This thesis concerned modelling the hydro-aero-servo-elastic coupling of a FOWT in six DOFs. Throughout the thesis different assumptions were made and different modelling aspects were left out. To give an even deeper insight of the actual behaviour of the full scaled model these assumptions and modelling aspects could be investigated further.

For the part concerning the hydrodynamics the generated waves were considered as being 2D waves, which not fully represent an actual sea state which is 3D. Furthermore, only linear waves were considered, however real waves are non-linear by nature. For further works this could be implemented in the simulation. The mooring lines were described by analytical simplifications assuming small displacements. A more detailed description could be done if FEA was considered. Furthermore, the mooring lines could be calibrated better in the physical setup, as they need to have an equal tension. For calibration and for validation of the mooring lines a force transducer on each line could be implemented. When generating waves in the wave basin it was found that many waves were reflected at the end wall. These reflected waves also have an impact on the TLP which is unwanted. For further work the reflection coefficient of the wave basin should be decreased.

For the theoretical model of the tower, the damping matrix could be investigated further. In this thesis the damping is found be using Rayleigh damping, where only one natural frequency is found. Thus the tower is only damped correctly in the natural frequency. If the damping matrix should be improved, higher natural frequencies and the corresponding damping should be investigated. This can be done by applying pulses with an impact hammer. Furthermore, to make the tower more realistic compared to real wind turbine tower, it should be conical and higher.

For the theoretical aerodynamic model constructed in Simulink, only the surge motion of the TLP and tower was taken into account and more DOFs could be implemented to affect the performance of the wind turbine, especially dynamics in yaw could be of interest. For the modelling of the wind field, a more detailed experiment regarding the wind speed measurements could be done, such that a more detailed wind field model could be constructed. For this better anemometers are needed. The wind field could be modified with more filters and better placement of these, such that a more uniform wind field could be generated. Furthermore, the blades of the wind turbine are too long for the experimental setup, therefore shorter blades could be designed and constructed. These blades should furthermore be designed such that the operational area is within the wind speed range of the wind generator and take the non uniform wind field into account. The dynamics of the blades could also be implemented in the dynamic simulation, such that a more complete model of the

wind turbine is achieved, this could be done by a FEM model.

The model of the tower, TLP, nacelle and mooring lines could be implemented in a single FEM model, such that a better coupling might be achieved. The coupling between the different elements could be investigated more, such that a better model might be achieved.

For the validation of the theoretical models, a rotational sensor on the generator and a torque sensor on the drive train shaft could be implemented. These could also be used for e.g. control of the wind turbine. In this thesis FOC and collective pitch control are implemented. The FOC could be investigated further and used for damping out torsional resonances of the drive train. While the collective pitch control could be expanded to include reduction of the fore-aft tower vibrations by using the accelerometer in top of the tower. Individual pitch control could be investigated and implemented for improving this further.

Conclusion 41

The scope of this thesis was to set up the necessary mathematical coupled models for a FOWT and simulate these. This including the hydrodynamics, the structural dynamics of the tower, the aerodynamics, the servo dynamics and the power electronics. The simulations were carried out both in a simulation model developed by the authors conducted in MATLAB and Simulink and the CAE tool FAST, thereby making it possible to compare the performance of the simulations code to code. A 1:35 scaled physical test model has been built consisting of the floating foundation, an elastic tower, three 3D printed blades, the nacelle and the necessary electrical equipment needed in order to control the system and for data acquisition. The physical test model was build to fulfil the scaling laws such that the dynamics would be comparable to a full scale model. The simulation codes could then be compared to experiments such the simulation codes could be validated.

The thesis consists of seven different parts each concerning their own topic. The first part was an introduction to FOWTs and a motivation for developing these, together with the problem definition of the thesis. Furthermore, the different modelling methods used, both in FAST and Simulink were explained. Next the properties of the scaled physical model were given and compared to full scale references. At last the experimental facilities used in the thesis were explained. As the wind field generated by the wind generator was found to be unsatisfactory a filter in front of the wind generator was designed and constructed. The primary function of the filter was to reduce the turbulence level to a more acceptable level and also make the wind field more uniform and unidirectional. The wave generator also showed some unwanted behaviour with too much reflection of the waves from the end wall. However an adjustment of this was considered to be out of the scope of this thesis.

The first part concerned the hydrodynamic model. The governing equation for irregular wave generation was explained along with describing the stochastic behaviour of a sea state. The dynamical equations of the TLP in six DOF were given. The hydrodynamic coefficients used in the dynamical equation were derived. The frequency dependent added mass, potential damping and first order wave excitation force were found by the numerical method BEM by utilising the free software NEMOH. The inertia matrix and combined stiffness matrix were found using analytical considerations. The viscous damping in surge, sway and yaw were experimentally found by free decay responses, while in heave, roll and pitch the damping was explained by the use of the Morison equation. The natural frequencies of the TLP were calculated and compared to experiments showing a good match. At last the response of the TLP when exposed to both regular and irregular waves is investigated. All the measured experimental responses were compared to Simulink and FAST both in the time domain and the frequency domain where a good match was found.

The second part concerned the structural tower model. The governing equation regarding the tower was explained and the structure of the FEM code with top mass was described. Modelling of the mass and stiffness matrix was done considering material properties of the tower, while the modelling of the damping was done using Rayleigh damping where the coefficients were found considering free decay responses. The experimental free decays were then used to compare the responses with the simulated responses. The simulated responses showed good agreement with the experimental obtained ones.

The third part concerned the aerodynamics of the wind turbine. At first the wind conditions for a real wind turbine and the scaled AAUE-TLP were described and compared. It was here found that a significant difference was present. It was decided to use Veers' method to generate a 3D wind field from a pre-described PSD function and coherence function. Regarding the aerodynamic modelling UBEM was utilised with implemented Prandtl's and Glauert's corrections, from which the rotor torque and the loads on the blades were found. Furthermore, a dynamic wake model, a dynamic stall model and a tower shadow model were described and implemented. During the testing and validations of the aerodynamics the wind speed was measured in 17 different points. A PSD was made for a single point at two different wind speeds and a weighting function between these using the rotational speed of the wind generator was found. For multiple point modelling the wind field was divided into nine boxes and eight mean speed lines and a theoretical coherence function was used. Testing of the aerodynamics was divided into three different operation regions. At region I the starting torque was found. In region II the power, thrust and rotational speed were measured and compared to SBEM, UBEM, FAST and the scaled 5 MW NREL. The experiment was somewhat lower than the predicted in SBEM and FAST, this due to the assumption of a uniform mean wind speed in the wind field. UBEM however takes this into account therefore being closer to the experimental result. In region III the pitch angle of the blades was changed to maintain a constant torque and the same properties were then measured. Again SBEM and FAST overpredict the values except the pitch angle. UBEM was again closer, but still overpredicts.

The fourth part concerned the servo dynamics and power electronics. The governing equation for the drive train was explained along with the generator model. Modelling of the drive train was done by considering it as a mass-damper system, while the generator model was derived by describing the voltage equation projected into a stationary reference frame. Utilizing the voltage equations the dynamical equation of the torque response was derived. Next the dynamical model of the pitch system was derived, this using a system identification approach from data measurements. The found model was then validated against a new data set. Next an exploration of the developed algorithms used to run the power converter were tested, showing good behaviour indicating the signals sent to the VLT were reasonable.

The fifth part concerned the coupled mathematical models for the FOWT, which was derived tested and validated. At first the coupling between the hydrodynamics and the dynamics of the tower were investigated and implemented. It was found that the coupling between the tower and the TLP would decrease the stiffness and increase the damping of the tower. Furthermore, the stiffness of the TLP was tested and it was found that this had also decreased. Therefore the tower and hydrodynamic models were corrected to match this. Free decay tests were made to validate the coupled

model. Both the response of the TLP and tower were measured and compared to the simulations conducted in Simulink and FAST showing a good fit. Next forced responses of the system were investigated, where both regular and irregular waves were applied to the TLP. When regular waves were applied the experimental and simulated time series were compared showing a good match. When performing irregular waves, the RAOs of the responses were compared, also showing a good match. However minor deviations were present. This due to large reflections of waves in the wave basin.

In the sixth part the coupling between the TLP, tower and rotor was described. At first only aerodynamic test were made, where only wind was applied to the rotor. Comparisons between the experimental and simulated time series and PSDs of the responses were made. In the time series it was found that the mean offset of the tower was best predicted by FAST, while Simulink predicts the oscillations of the TLP best. The PSD of the TLP showed the right natural frequency, however the amplitudes of the simulated were too high compared to the experimental. The PSDs for the tower showed that FAST predicts the 1P effect the best, while Simulink showed better performance in predicting the 3P effect. Furthermore tests were made with both wind and waves impacting the FOWT. Again it was found that the mean offset were estimated too high in the simulations. However the PSDs of both the tower and TLP were found satisfying with minor deviations in some of the amplitudes.

The seventh part concerned the design and implementation of the control systems. At first the control objectives for the AAUE-TLP were explained. Next the generator control which is based on FOC were developed. The FOC is based on two inner current loops and an outer speed loop. The control of the inner loops was designed in the discrete time domain by considering the placement of the poles compared to the stability and bandwidth of the system. The outer speed loop was designed by OSM which maximised the phase margin and led to a symmetrical phase and magnitude response around the cross over frequency. Next the control system for the blade pitch actuator system was designed as a simple P controller. The collective blade pitch controller was developed by using a gain scheduling approach. An EKF algorithm was implemented to estimate the electrical angle of the generator, as the resolution of the shaft encoder was too low. The implemented control was tested experimentally and compared to the simulations. At first the performance of the generator control was tested by comparing the speed and current dynamics with the simulated response under different conditions, all showing a good match. Next the performance of the pitch actuator system is tested and compared to the simulated results. Again a good match was seen. The collective pitch control is tested by applying incremental increasing wind speed and investigating whether or not the control is capable of keeping a constant reference of 71.5 RPM by increasing or decreasing the blade pitch angle. At last an EKF was developed and tested under different conditions with both simulation and experiment, showing satisfying results.

Based on the results obtained in this thesis it is concluded that it is possible to set up the necessary mathematical coupled models for a FOWT, build a correctly 1:35 scaled test model with implemented control and use it to test and validate the mathematical models.

Bibliography

[1] The Faculty of Engineering and Science. Curriculum for the master of science programme in sustainable energy engineering, 2014. URL http://www.ses.aau.dk/digitalAssets/85/85149_curriculum-for-the-master-of-science-\programme-in-sustainable-energy-engineering-2013-esbjerg.pdf.

[2] F.D. Bianchi, H. de Battista, and R.J. Mantz. *Wind Turbine Control Systems: Principles, Modelling and Gain Scheduling Design*. Advances in Industrial Control. Springer London, 2006. ISBN 9781846284939. URL https://books.google.dk/books?id=ZS8_AAAAQBAJ.

[3] Henrik Sogn Paust. Finite element modeling and structurel state estimation of a bottom fixed offshore wind turbine. , 2015.

[4] Vattenfall. Havmølleparken, 2016. URL https://corporate.vattenfall.dk/vores-vindmoller-i-danmark/horns-rev-3/om-havmolleparken/.

[5] Interdisciplinary Earth Data Alliance. Marine geoscience data system, 2016. URL http://www.marine-geo.org/index.php.

[6] The International Renewable Energy Agency. Renewable energy technologies: Cost analysis series. *Power Sector*, 1:, 2012.

[7] et. al Yoon, Jeseong. Response analysis of wind turbine support structures using fem and wind geneatin method linked to time series of measured wind speed. , 2009.

[8] Erin Elizabeth Bachynski. Design and dynamic analysis of tension leg platform wind turbines. , 2014.

[9] International Renewable Energy Agency. Floating foundations: a game changer for offshore wind power. , 2016.

[10] Statoil. Hywindâ€"the worldâ€™s leading floating offshore wind solution, 2018. URL https://www.statoil.com/en/what-we-do/hywind-where-the-wind-takes-us.html. assessed 2018-17-01.

[11] Statoil. Statoil to build the first floating wind farm: Hywind scotland, 2017. URL https://www.statoil.com/en/news/hywindscotland.html.

[12] Ideol. Ideol offshore [internet], 2018. URL http://www.ideol-offshore.com.

[13] Principel Power. Principel power - wind flat [internet], 2018. URL http://www.principlepowerinc.com/en/windfloat.

[14] Bloomberg. Race to build offshore wind farms that float on sea gathers pace, 2017. URL https://www.bloomberg.com/news/articles/2017-03-17/race-to-build-offshore-wind-farms-that-float-on-sea-gathers-pace.

[15] Van Nguyen Dinh and Biswajit Basu. On the modeling of spar-type floating offshore wind turbines. In *Key Engineering Materials*, volume 569, pages 636–643. Trans Tech Publ, 2013.

[16] Tomoaki Utsunomiya, Tomoki Sato, Hidekazu Matsukuma, and Kiyokazu Yago. Experimental validation for motion of a spar-type floating offshore wind turbine using 1/22.5 scale model. In *Proceedings of 28th International Conference on Ocean, Offshore and Arctic Engineering, Honolulu, HI, Paper No. OMAE2009-79695*, 2009.

[17] Dominique Roddier, Christian Cermelli, Alexia Aubault, and Alla Weinstein. Windfloat: A floating foundation for offshore wind turbines. *Journal of renewable and sustainable energy*, 2 (3):033104, 2010.

[18] H.R Martin. Development of a scale model wind turbine for testing of offshore floating wind turbine systems. , 2011.

[19] A Myhr. Experimental results for tension-leg-buoy offshore wind turbine platforms. *1(4):217â€“224*, 2014.

[20] A Myhr. Comparison of experimental results and computations for tension-leg-buoy offshore wind turbines. *2(1):12â€“20*, 2015.

[21] J. Azcona. Aerodynamic thrust modelling in wave tank tests of offshore floating wind turbines using a ducted fan. , 2014.

[22] Stewart. Gordon. A review and comparison of floating offshore wind turbine model experiments. , 2016.

[23] F Sandner. Model building and scaled testing of 5mw and 10mw semi-submersible floating wind turbines. , 2015.

[24] Jesper Kirkegaard Jensen, Juliane Bech Sørensen, Kasper Jessen, Kasper Laugesen, and Signe Møller Mortensen. An approach to build a prototype of a floating wind turbine with maximum power point tracking using torque control, 2015.

[25] Jesper Kirkegaard Jensen, Kasper Jessen, Kasper Laugesen, and Signe Møller Mortensen. Hydrodynamic modelling and verification of a tension leg platform for a floating offshore wind turbine, 2016.

[26] Jesper Kirkegaard Jensen, Kasper Jessen, Kasper Laugesen, and Signe Møller Mortensen. Modeling and verification of tower dynamics for a scaled floating offshore wind turbine, 2016.

[27] Jesper Kirkegaard Jensen, Kasper Jessen, Kasper Laugesen, and Signe Møller Mortensen. Wind turbine design, modelling and control of a scaled floating offshore tension leg platform, 2017.

[28] J. Jonkman S. Butterfield W. Musial and G. Scott. Definition of a 5-mw reference wind turbine for offshore system development. , page 75, 2009.

[29] Stephen E Kibbee, Steven J Leverette, Kent B Davies, Richard B Matten, et al. Morpeth seastar mini-tlp. In *Offshore Technology Conference*. Offshore Technology Conference, 1999.

[30] Jason Mark Jonkman and Marshall L Buhl Jr. Fast user's guide-updated august 2005. Technical report, National Renewable Energy Laboratory (NREL), Golden, CO., 2005.

[31] JM Jonkman, GJ Hayman, BJ Jonkman, and RR Damiani. Aerodyn v15 userâ€™s guide and theory manual. *National Renewable Energy Laboratory*, 2016.

[32] Bonnie J Jonkman. Turbsim user's guide: Version 1.50. Technical report, National Renewable Energy Lab.(NREL), Golden, CO (United States), 2009.

[33] Mark Drela. Xfoil: An analysis and design system for low reynolds number airfoils. In *Low Reynolds number aerodynamics*, pages 1–12. Springer, 1989.

[34] JM Jonkman, A Robertson, and GJ Hayman. Hydrodyn userâ€™s guide and theory manual. *National Renewable Energy Laboratory*, 2014.

[35] Chang-Ho Lee. *WAMIT theory manual*. Massachusetts Institute of Technology, Department of Ocean Engineering, 1995.

[36] Chang-Ho Lee and J Nicholas Newman. Wamit user manual. *WAMIT, Inc*, 2006.

[37] A Babarit. Nemoh, laboratory for research in hydrodynamics. *Energy, Environment, and Atmosphere, http://lheea. ec-nantes. fr/doku. php/emo/nemoh/start*, 2014.

[38] Bonnie Jonkman and Jason Jonkman. Fast v8. 15.00 a-bjj. *National Renewable Energy Laboratory*, 2016.

[39] Andrew R Henderson, Kimon Argyriadis, J Nichos, and David Langston. Offshore wind turbines on tlps-assessment of floating support structures for offshore wind farms in german waters. In *10th German wind energy conference, Bremen, Germany*, 2010.

[40] Denis Matha. Model development and loads analysis of an offshore wind turbine on a tension leg platform with a comparison to other floating turbine concepts: April 2009. *Proceedings of Offshore Technology Conference, Houston, Texas,*, 2010.

[41] J Jonkman. Definition of the floating system for phase iv of oc3. , 2010.

[42] Heather R Martin, Richard W Kimball, Anthony M Viselli, and Andrew J Goupee. Methodology for wind/wave basin testing of floating offshore wind turbines. *Journal of Offshore Mechanics and Arctic Engineering*, 136(2):020905, 2014.

[43] Donovan X Fraser Selig MS. Airfoils at low speed. , 1986.

[44] Airfoil Tools. Sd7003-085-88[internet], 2017. URL `http://airfoiltools.com/airfoil/details?airfoil=sd7003-il`.

[45] Christian Bach Rasmussen and Jesper KÃ¦r Larsen. Design of wind turbine blades for pitch control, 2016. URL `\protect\kern+.1667em\relax`.

[46] Det Norske Veritas A/S. Environmental conditions and environmental loads. , 2007.

[47] Systemair. Aksialventilatorer. Technical report, Systemair, 2012.

[48] Robert Laugesen and Anders Mandrup Hansen. Experimental study of the dynamic response of the dtu 10 mw wind turbine on a tension leg platform, 2015.

[49] Andrew Welsh. Low turbulence wind tunnel design and wind turbine wake characterization, 2013.

[50] I.E. Idelchik. *Handbook of Hydraulic Resistance*. Begell House, Inc., 2007. ISBN 978-1-56700-251-5.

[51] Jewel B Barlow, William H Rae Jr, and Alan Pope. *Low-speed Wind Tunnel Testing*. Wiley, 1999.

[52] Thomas Lykke Andersen, Peter Frigaard, and Hans F Burcharth. Lecture notes for the course in water wave mechanics, 2014.

[53] Thor I Fossen. *Handbook of marine craft hydrodynamics and motion control*. John Wiley & Sons, 2011.

[54] Odd Faltinsen. *Sea loads on ships and offshore structures*, volume 1. Cambridge university press, 1993.

[55] 4C Offshore. Hywind scotland pilot park offshore wind farm, 2018. URL `http://www.4coffshore.com/windfarms/hywind-scotland-pilot-park-united-kingdom-uk76.html`.

[56] Det Norske Veritas. Design of floating wind turbine structures. *Offshore Standard DNV-OS-J103*, 2013.

[57] WE Cummins. The impulse response function and ship motions. Technical report, David Taylor Model Basin Washington DC, 1962.

[58] Hassan Ghassemi and Ehsan Yari. The added mass coefficient computation of sphere, ellipsoid and marine propellers using boundary element method. *Polish Maritime Research*, 18(1):17–26, 2011.

[59] Tristan Perez and Thor I Fossen. Kinematic models for manoeuvring and seakeeping of marine vessels. *Modeling, Identification and Control*, 28(1):19, 2007.

[60] M. Folley. *Numerical Modelling of Wave Energy Converters: State-of-the-Art Techniques for Single Devices and Arrays*. Elsevier Science, 2016. ISBN 9780128032114. URL `https://books.google.dk/books?id=fNdwBwAAQBAJ`.

[61] T.F Ogilvie. Recent progress towards the understanding and prediction of ship motions. , 1964.

[62] Thor I Fossen and Øyvind N Smogeli. Nonlinear time-domain strip theory formulation for low-speed manoeuvering and station-keeping. *Modeling, identification and control*, 25(4): 201, 2004.

[63] Pengzhi Lin. *Numerical modeling of water waves*. CRC Press, 2014.

[64] C Berhault, V Aanesland, G Jensen, G Caprino, S Tumock, L Larsson, and V Bertram. 19th wegemt school: Numerical simulation of hydrodynamics: Ships and offshore structures. In *19th WEGEMT School: Numerical Simulation of Hydrodynamics: Ships and Offshore Structures*, 1993.

[65] A.I. Korotkin. *Added Masses of Ship Structures*. Fluid Mechanics and Its Applications. Springer Netherlands, 2008. ISBN 9781402094323. URL `https://books.google.dk/books?id=kzKTATSa5C4C`.

[66] T.I Perez. T, Fossen. Practical aspects of frequency-domain identification of dynamicmodels of marine structures from hydrodynamic data. *Ocean Engineering*, 38 (2011) 426-435, 201.

[67] T.I Perez. T, Fossen. Time-domain vs. frequency-domain identification of parametric radiation force models for marine structures at zero speed. , 2008.

[68] Tristan Perez and Thor Fossen. A matlab tool for parametric identification of radiation-force models of ships and offshore structures. *Modelling,Identification and Control*, MIC-30(1): 1-15, 2009.

[69] J Jonkman. Dynamics modelling and loads analysis of an offshore floating wind turbine dynamics modeling and loads analysis of an offshore floating wind turbine. , 2007.

[70] AK Jain. Nonlinear coupled response of offshore tension leg platforms to regular wave forces. *Ocean Engineering*, 24(7):577–592, 1997.

[71] Erin E Bachynski and Torgeir Moan. Design considerations for tension leg platform wind turbines. *Marine Structures*, 29(1):89–114, 2012.

[72] R.D. Cook. *Concepts and Applicatins of Finite Element Analysis 4Th Ed*. Wiley India Pvt. Limited, 2007. ISBN 9788126513369. URL `https://books.google.dk/books?id=QDRDKGm6xPQC`.

[73] M. Paz. *Structural Dynamics: Theory and Computation*. Springer US, 2012. ISBN 9781468499070. URL `https://books.google.dk/books?id=-oDdBwAAQBAJ`.

[74] W. Weaver, S.P. Timoshenko, and D.H. Young. *Vibration Problems in Engineering*. A Wiley-Interscience publication. John Wiley & Sons, 1990. ISBN 9780471632283. URL `https://books.google.dk/books?id=YZ7t8LgRqi0C`.

[75] Vinidex Pty. Pvc properties [internet], 2016. URL `http://www.vinidex.com.au/technical/material-properties/pvc-properties/`.

[76] S. Adhikari and J. Woodhouse. Identification of damping:part 1, viscous damping. *Journal of Sound and vibration*, 243(1), 2000.

[77] M Amouroux and Abdelhaq El Jai. *Control of Distributed Parameter Systems 1989: Selected Papers from the 5th IFAC Symposium, Perpignan, France, 26-29 June 1989*. Elsevier, 2014.

[78] J.W.S.B. Rayleigh and R.B. Lindsay. *The Theory of Sound*. Number vb. 2 in Dover Books on Physics. Dover, 1945. ISBN 9780486602936. URL `https://books.google.dk/books?id=Frvgu1wSFfUC`.

[79] Sajana Suwal. Comparative study of 1d codes for site response analyses. *International Journal of Lanslide and Environment*, 2:24–31, 11 2014.

[80] Det Norske Veritas. Design of offshore wind turbine structures. *Offshore Standard DNV-OS-J101*, 6:2004, 2004.

[81] Martin OL Hansen. *Aerodynamics of wind turbines*. Routledge, 2015.

[82] Paul S Veers. Three-dimensional wind simulation. Technical report, Sandia National Labs., Albuquerque, NM (USA), 1988.

[83] Jakob Mann. Wind field simulation. *Probabilistic engineering mechanics*, 13(4):269–282, 1998.

[84] Danish Standard. Ds 472 loads and safety of wind turbine construction, 2007.

[85] Hermann Glauert. *The analysis of experimental results in the windmill brake and vortex ring states of an airscrew*. HM Stationery Office, 1926.

[86] David A Spera. Wind turbine technology. , 1994.

[87] H Snel and JG Schepers. *Joint investigation of dynamic inflow effects and implementation of an engineering method*. Netherlands Energy Research Foundation ECN, 1995.

[88] S. oye. A simple vortex model of a turbine rotor. *Third IEA Symposium on aerodynamics of wind turbines*, 1989.

[89] Theodore Theodorsen. General theory of aerodynamic instability and the mechanism of flutter. *NACA Report 496*, pages 2–21, 1992.

[90] Stig Øye. Dynamic stall simulated as time lag of separation. *Proceedings of the 4th IEA Symposium on the aerodynamics of wind turbines*, 1991.

[91] JG Leishman and TS Beddoes. A generalised model for airfoil unsteady aerodynamic behaviour and dynamic stall using the indicial method. *Proceedings of the 42nd Annual forum of the American Helicopter Society*, pages 243–265, 1986.

[92] Emmanuel Branlard. *Wind Turbine Aerodynamics and Vorticity-Based Methods: Fundamentals and Recent Applications*, volume 7. Springer, 2017.

[93] Zhenyu Yu. Space-vector pwm with tms320c24x/f24x using hardware and software determined switching patterns. *Texas Instruments Application Report SPRA524*, 1999.

[94] Abdul Rahiman Beig, G Narayanan, and VT Ranganathan. Modified svpwm algorithm for three level vsi with synchronized and symmetrical waveforms. *IEEE Transactions on Industrial Electronics*, 54(1):486–494, 2007.

[95] HJT Kooijman, C Lindenburg, D Winkelaar, and EL van der Hooft. Aero-elastic modelling of the dowec 6 mw pre-design.

[96] Søren Christiansen, Thomas Bak, and Torben Knudsen. Damping wind and wave loads on a floating wind turbine. *Energies*, 6(8):4097–4116, 2013.

[97] Allan D Wright and LJ Fingersh. Advanced control design for wind turbines; part i: control design, implementation, and initial tests. Technical report, National Renewable Energy Laboratory (NREL), Golden, CO., 2008.

[98] Det Norske Veritas A/S and Risø. Guidelines for design of wind turbines. , 2007.

[99] PJ Murtagh, B Basu, and BM Broderick. Along-wind response of a wind turbine tower with blade coupling subjected to rotationally sampled wind loading. *Engineering structures*, 27(8): 1209–1219, 2005.

[100] G.F. Franklin, J. Powell, and A. Emami-Naeini. *Feedback Control of Dynamic Systems, Global Edition*. Pearson Education Limited, 2015. ISBN 9781292068916. URL `https://books.google.dk/books?id=ZV-pBwAAQBAJ`.

[101] O. Aydin, A. Akdag, P. Stefanutti, and N. Hugo. Optimum controller design for a multilevel ac-dc converter system. , 3(1):1660–1666, 2005.

[102] R.E. Precup S. Preitl. An extension of tuning relations after symmetrical optimum method for pi and pid controllers. , 35(1):1731–1736, 1999.

[103] Gene F Franklin, J David Powell, Abbas Emami-Naeini, and J David Powell. *Feedback control of dynamic systems*, volume 3. Addison-Wesley Reading, MA, 1994.

[104] Morten H Hansen, Anca Daniela Hansen, Torben J Larsen, Stig Øye, Poul Sørensen, and Peter Fuglsang. Control design for a pitch-regulated, variable speed wind turbine. , 2005.

[105] O Benjak and D Gerling. Review of position estimation methods for ipmsm drives without a position sensor part i: Nonadaptive methods. *Electrical Machines (ICEM), 2010 XIX International Conference on*, pages 1–6, 2010.

[106] O Benjak and D Gerling. Review of position estimation methods for ipmsm drives without a position sensor part ii: Adaptive methods. *Electrical Machines (ICEM)*, pages 40–46, 2010.

[107] O Benjak and D Gerling. Review of position estimation methods for pmsm drives without a position sensor, part iii: Methods based on saliency and signal injection. *Electrical Machines and Systems (ICEMS)*, pages 873–878, 2010.

[108] Patrick L Jansen and Robert D Lorenz. Transducerless field orientation concepts employing saturation-induced saliencies in induction machines. *IEEE Transactions on Industry Applications*, 32(6):1380–1393, 1996.

[109] RC Becerra, TM Jahns, and Mehrdad Ehsani. Four-quadrant sensorless brushless ecm drive. *Applied Power Electronics Conference and Exposition, 1991. APEC'91. Conference Proceedings, 1991., Sixth Annual*, pages 202–209, 1991.

[110] Jianwen Shao, Dennis Nolan, and Thomas Hopkins. A novel direct back emf detection for sensorless brushless dc (bldc) motor drives. *Applied Power Electronics Conference and Exposition, 2002. APEC 2002. Seventeenth Annual IEEE*, 1:33–37, 2002.

[111] Rusong Wu and Gordon R Slemon. A permanent magnet motor drive without a shaft sensor. *IEEE Transactions on Industry Applications*, 27(5):1005–1011, 1991.

[112] Tomonobu Senjyu, Tsuyoshi Shimabukuro, and Katsumi Uezato. Vector control of permanent magnet synchronous motors without position and speed sensors. *Power Electronics Specialists Conference, 1995. PESC'95 Record., 26th Annual IEEE*, 2:759–765, 1995.

[113] Song Chi, Zheng Zhang, and Longya Xu. Sliding-mode sensorless control of direct-drive pm synchronous motors for washing machine applications. *IEEE Transactions on Industry Applications*, 45(2):582–590, 2009.

[114] Yaman B Zbede, Shady M Gadoue, and David J Atkinson. Model predictive mras estimator for sensorless induction motor drives. *IEEE Transactions on Industrial Electronics*, 63(6): 3511–3521, 2016.

[115] MC Huang, AJ Moses, and F Anayi. The comparison of sensorless estimation techniques for pmsm between extended kalman filter and flux-linkage observer. *Applied Power Electronics Conference and Exposition, 2006. APEC'06. Twenty-First Annual IEEE*, pages 6–pp, 2006.

[116] Albert Qiu, Bin Wu, and Hassan Kojori. Sensorless control of permanent magnet synchronous motor using extended kalman filter. *Electrical and Computer Engineering, 2004. Canadian Conference on*, 3:1557–1562, 2004.

[117] Shan-Mao Gu, Feng-You He, and Hui Zhang. Study on extend kalman filter at low speed in sensorless pmsm drives. In *Electronic Computer Technology, 2009 International Conference on*, pages 311–316. IEEE, 2009.

Appendix A

A.1 Wind Tunnel

The final setup of the wind tunnel is seen in the figure.

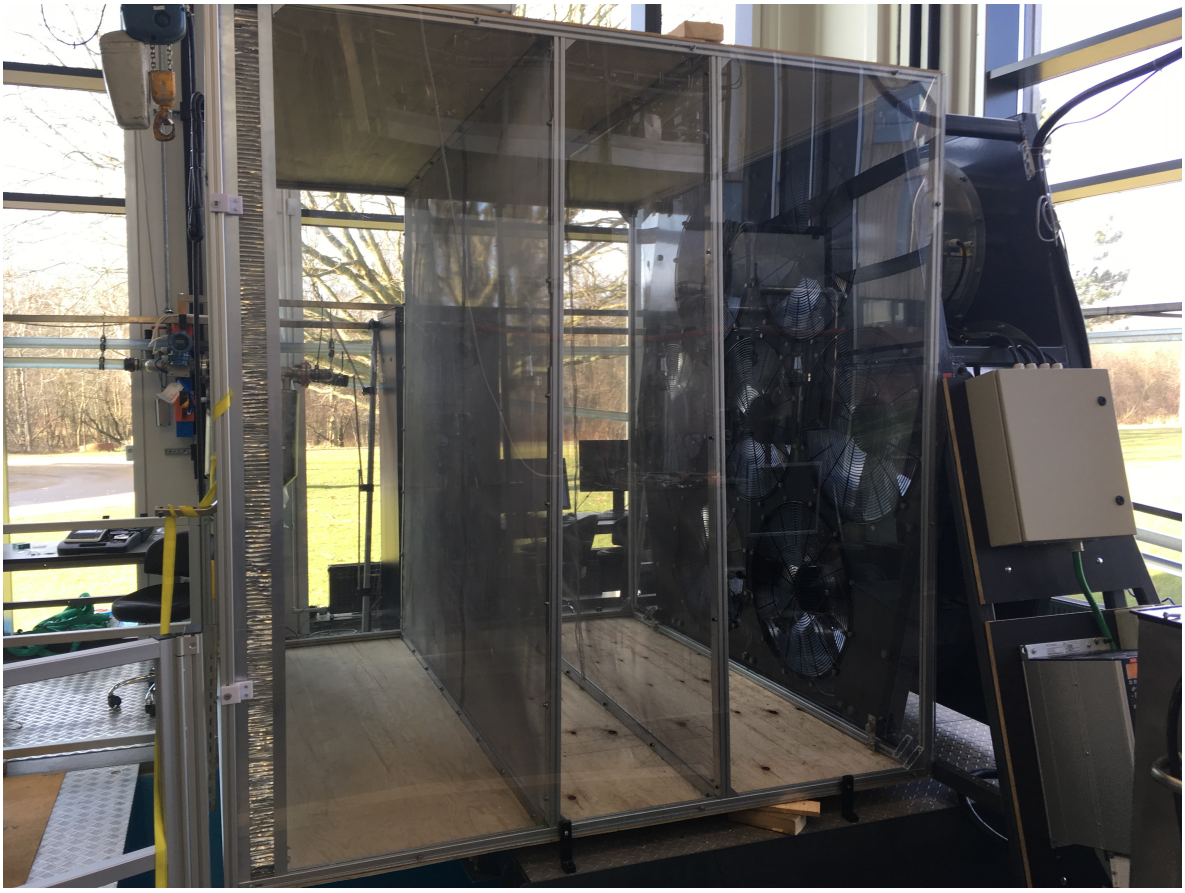

Figure A.1: Setup of wind tunnel.

A.2 Retardation Function Estimate

Rewriting the parametric model for the retardation estimate

$$\mathbf{R}(s) = \frac{P_{ij}(s)}{Q_{ij}(s)} = \frac{b_m s^m + b_{m-1} s^{m-1} + \cdots + b_0}{s^n + q_{n-1} s^{n-1} + \cdots + q_0} \tag{A.1}$$

The following properties of the convolution integral can be used to fit the retardation function formulated by Fossen and Perez in [68].

A.2.1 Low frequency limit

The low frequency asymptotic value is given as

$$\lim_{\omega \to 0} \mathbf{R}(\omega) = \lim_{\omega \to 0} \left[[\mathbf{B}(\omega) - \mathbf{B}(\infty)] + j\omega \, [\mathbf{A}(\omega) - \mathbf{A}(\infty)] \right] = 0 \tag{A.2}$$

That is at the limit where ω tends towards zero the real part will be zero as both $\mathbf{B}(0) = \mathbf{B}(\infty) = 0$. Furthermore the imaginary part tends to zero as the difference

$$\mathbf{A}(0) - \mathbf{A}(\infty) = \lim_{\omega \to 0} -\frac{1}{\omega} \int_0^\infty \mathbf{R}(t) \sin(\omega t) dt = -\int_0^\infty \mathbf{R}(t) \lim_{\omega \to 0} \frac{\sin(\omega t)}{\omega} dt = -\int_0^\infty \mathbf{R}(t) dt \tag{A.3}$$

is finite. It has here been used that $\lim_{\omega \to 0} \frac{\sin(\omega t)}{\omega} = 1$, and that the regularity condition for the exchange of the limit and integral has been fulfilled. This statement is based on the physical principal that the structure cannot radiate any waves at a zero frequency. This implies that eq. A.1 has to be zero at $s = 0$ meaning that the parameter b_0 has to be zero.

A.2.2 High Frequency limit

The high frequency limit is given as

$$\lim_{\omega \to \infty} \mathbf{R}(\omega) = 0 \Rightarrow \lim_{\omega \to \infty} \left[\mathbf{B}(\omega) + j\omega (\mathbf{A}(\omega) - \mathbf{A}(\infty)) \right] = 0 \tag{A.4}$$

The real part will be zero as $\mathbf{B}(\infty)$ has to be zero, because the excitation force tends to be zero for infinity short waves (infinity frequency) due to a pressure cancellation on the body surface. Furthermore it is clear that the difference $\mathbf{A}(\omega)$ - $\mathbf{A}(\infty)$ tends to zero when $\omega \to \infty$. The statement in eq. A.1 will only be guaranteed if the denominator grows faster than the numerator when the frequency increases, such that the retardation function drops to zero when ω tends to infinity. Thereby the degree of the denominator must be larger than the degree of the numerator, that is deg(Q(s)) > deg(P(s)) such that the transfer function is strictly proper.

A.2.3 Initial Time Value

The initial time value imposes a further constrain on the relative degree. The impulse response function of the retardation function must have an initial time value different from zero. This implies

that

$$\lim_{t\to 0}\mathbf{R}(t) = \lim_{s\to\infty} s\mathbf{R}(s) = \lim_{s\to\infty} s\frac{P(s)}{Q(s)} = \frac{b_m s^{m+1}}{s^n} \neq 0 \tag{A.5}$$

That is as s tends to infinity the values of s becomes more and more insignificant and hence the result is obtained by taking the ratio of the leading coefficients. Thereby it is clear that in order for the limit to be finite and different from zero, the relative order of the denominator and numerator must be deg(Q(s)) - deg(P(s)) = 1, that is n = m + 1.
Combined with the requirement of the first property it can be seen that the minimum order of the transfer function is at least a second order.

A.2.4 Final Time Value

The system should be stable such that the impulse response of the retardation function tends to zero when time tends to infinity. This property sets the bounded input, bounded output property of the radiation system and is given by the limit

$$\lim_{t\to\infty}\mathbf{R}(t) = \lim_{t\to\infty}\frac{2}{\pi}\int_0^\infty \mathbf{B}(\omega)\cos(\omega t)d\omega = 0 \tag{A.6}$$

Thereby the poles of the transfer function in eq. A.1 must lie on the left half complex plane.

A.2.5 Passivity of the System

This property arises from the fact that the radiation forces are dissipative, that is they can store or dissipate energy however never create it. Considering LTI systems in the frequency domain a necessary and sufficient conditions for passivity are that the real part of the transfer function is positive, that is Re($\mathbf{R}$(s)) > 0.

A.3 Mooring Line Test

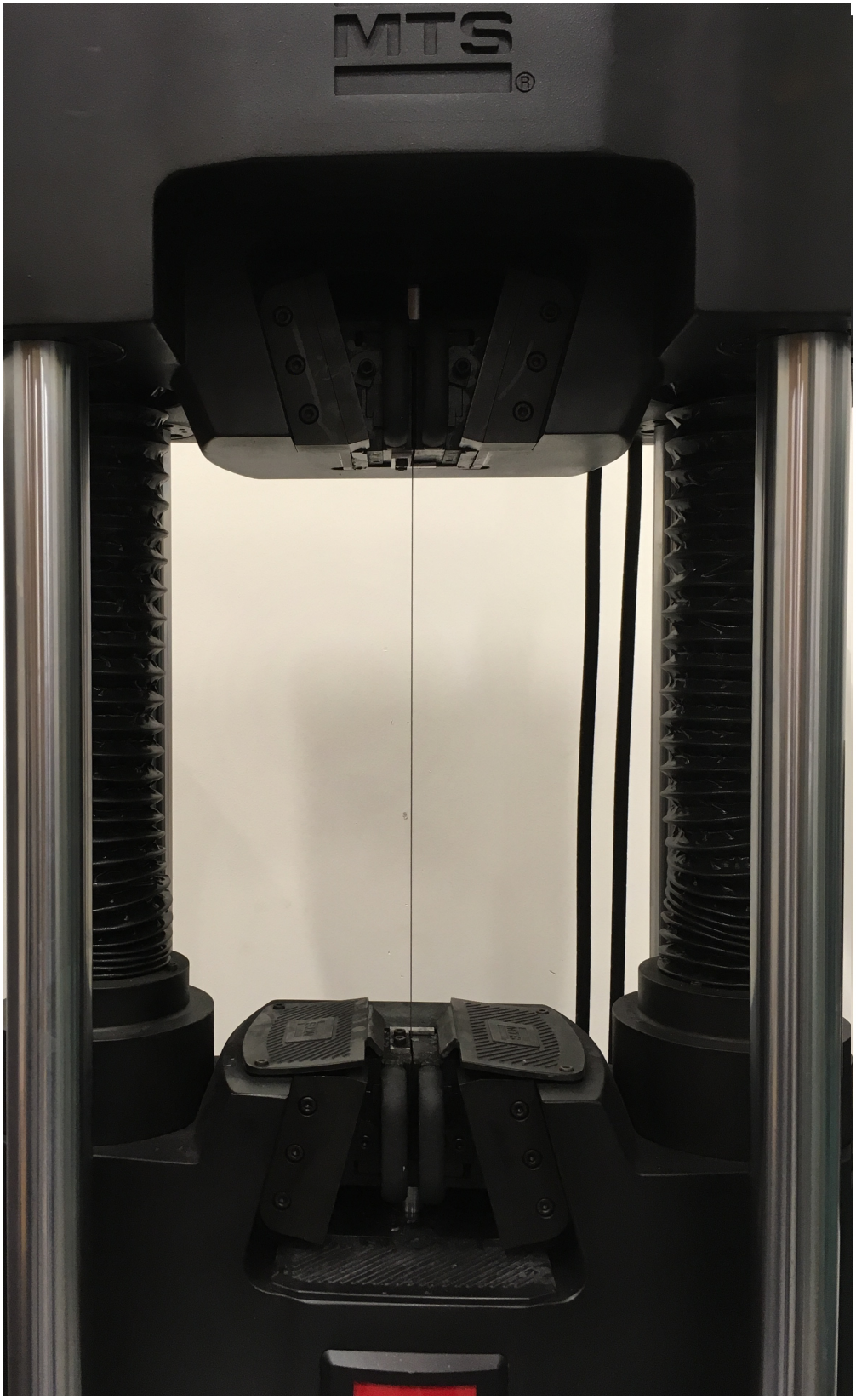

Figure A.2: Pulling test of mooring line

A.4 Wave Generator Experimental Setup

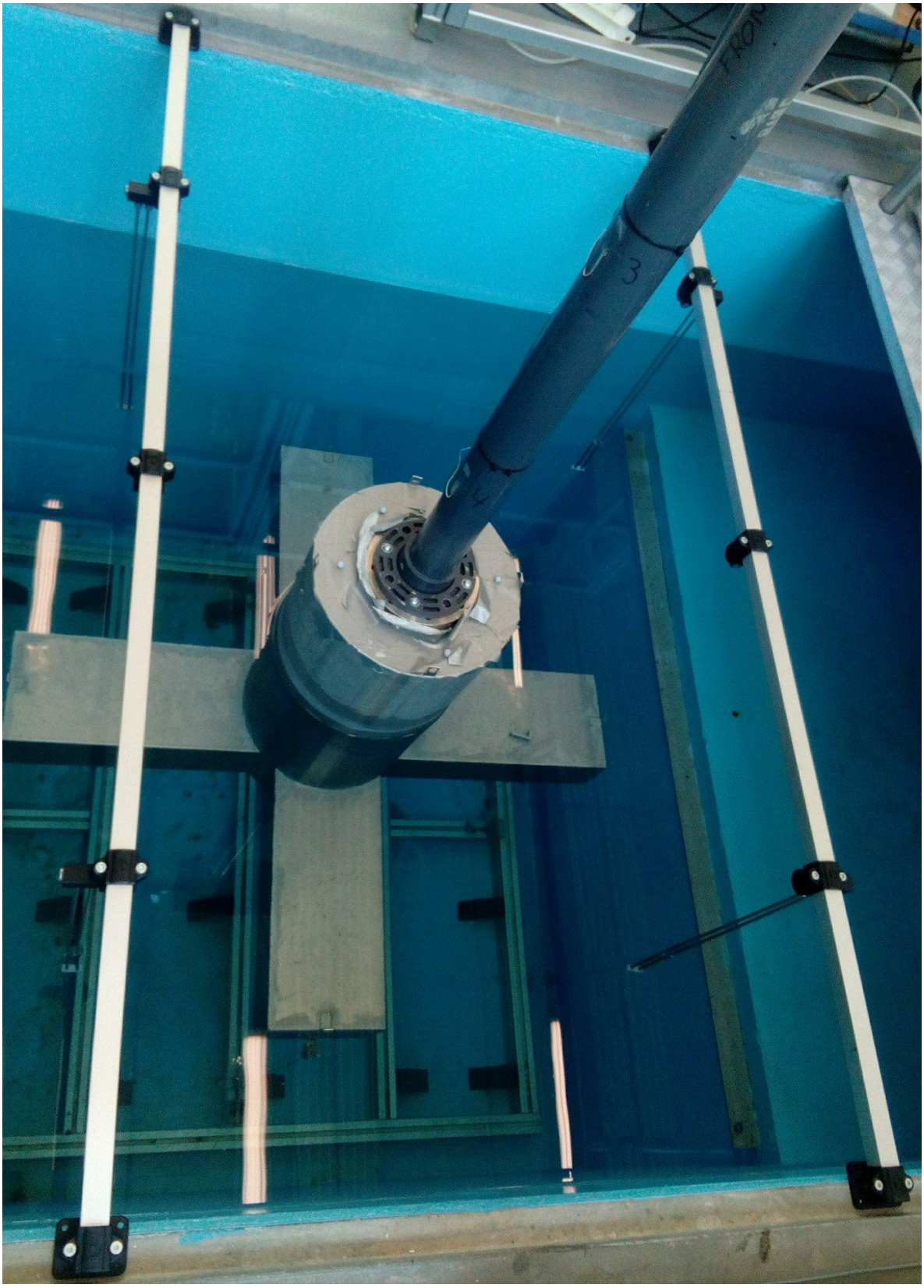

Figure A.3: Experimental setup for surface elevation measurements

A.5 Wave Generator Spectrum

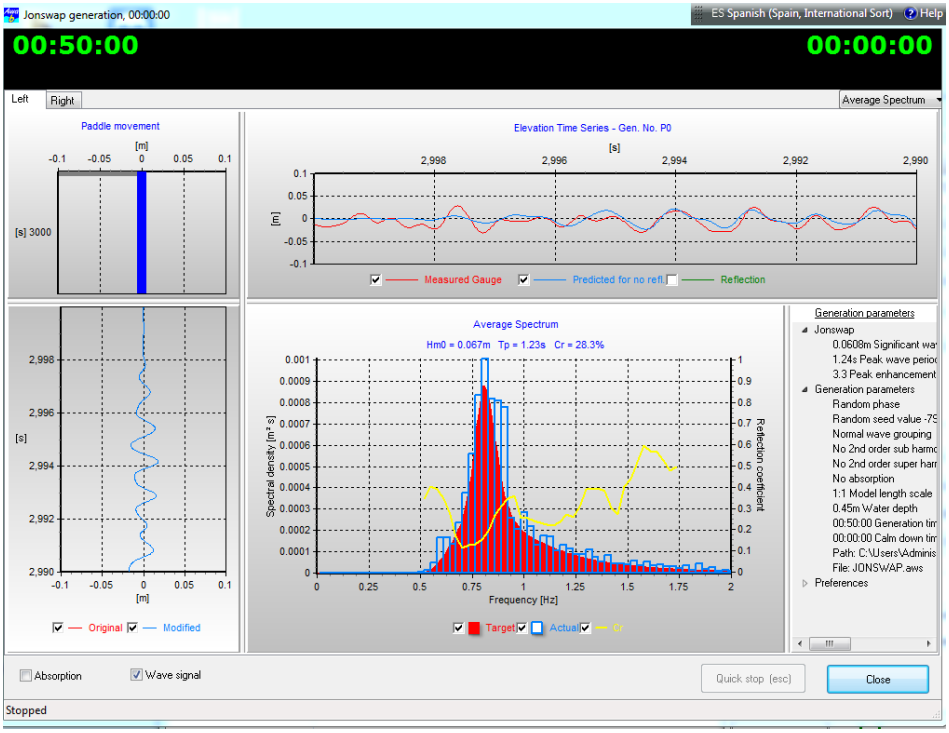

Figure A.4: JONSWAP spectrum measured by the wave generator along with the reflection coefficient.

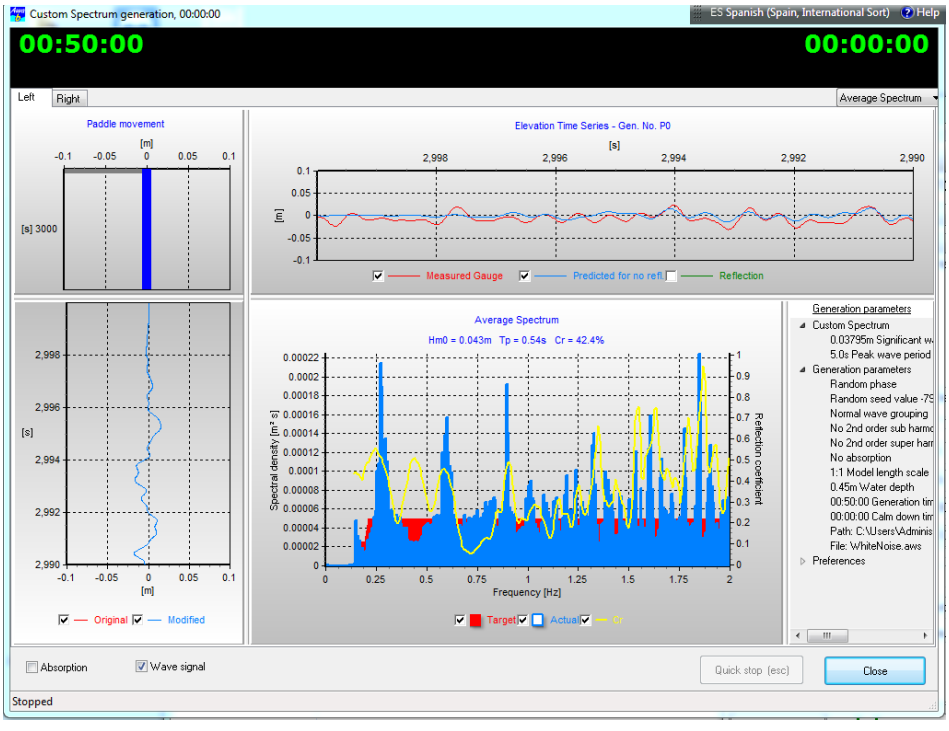

Figure A.5: White noise spectrum measured by the wave generator along with the reflection coefficient.

A.6 Calculation of Thrust Force

A series of experiments were made, where a force was applied to the nacelle and the displacement was measured using the camera system OptiTrack. The relationship between the displacement and thrust force is found by using Hooke's law. The data points and linear fit is seen in the figure.

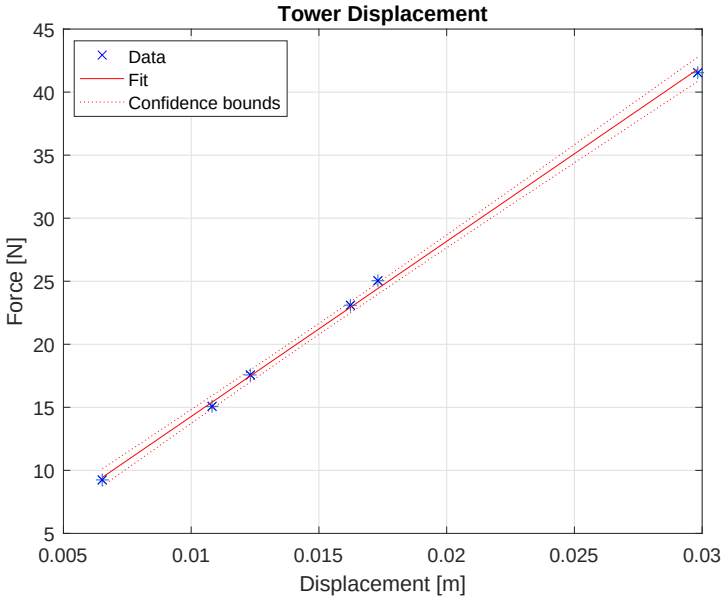

Figure A.6: Data points and linear fit with 95 % confidence bounds.

The linear fit is found to be

$$F_{thrust} = 1389 x_{Nacelle} \tag{A.7}$$

where F_{thrust} is the thrust force and $x_{Nacelle}$ is the displacement of the tower top.

A.7 Rotation in Pitch and Yaw

In the figure a time series measured by OptiTrack is seen for the rotation in pitch and yaw for the TLP and the tower. As seen the angles are too small for OptiTrack to detect correct, as especially the response of the TLP has a lot of small peaks and missed data points.

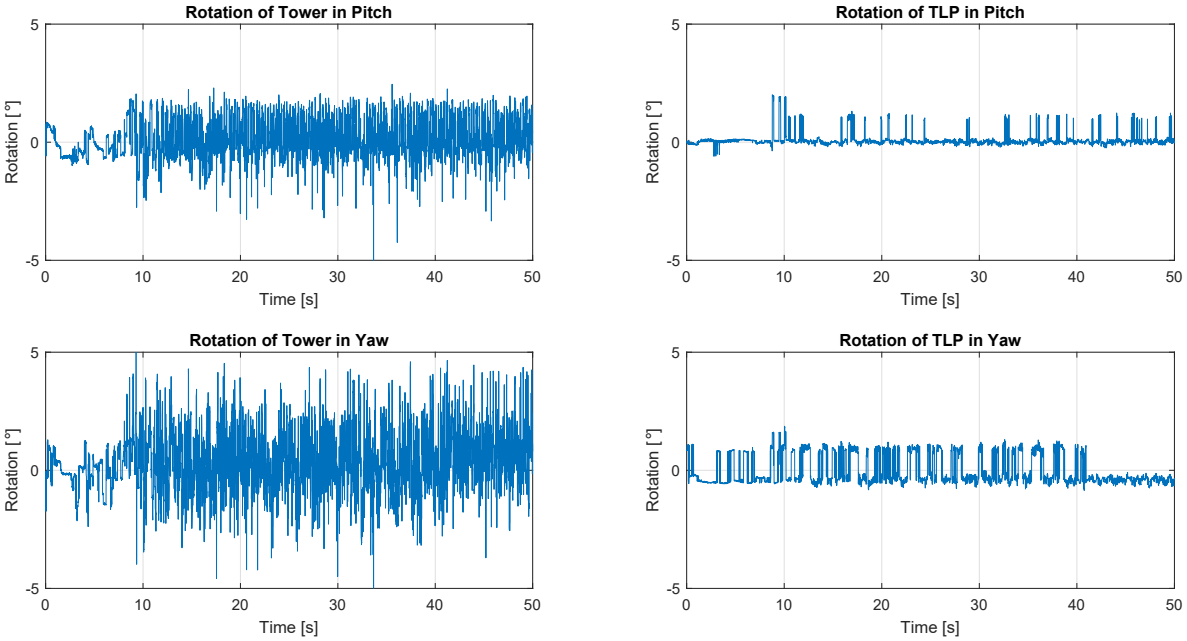

Figure A.7: Experimental rotation in pitch and yaw of the tower and TLP.

A.8 Free Decay of Tower

Free decay of tower with top mass done onshore.



Figure A.8: Setup of free decay with fixed ground.

A.9 Drive Train Experiments

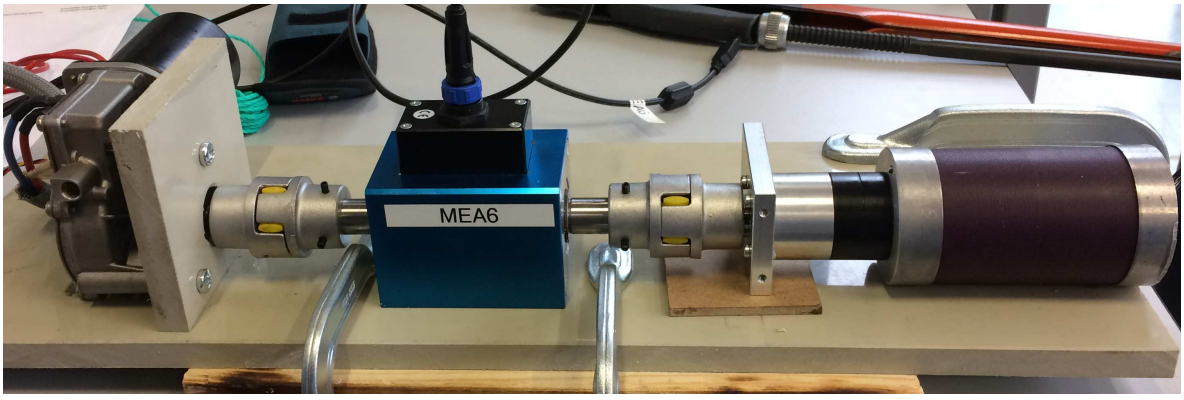

Figure A.9: Drive train test bench.

A.10 Wind Turbine

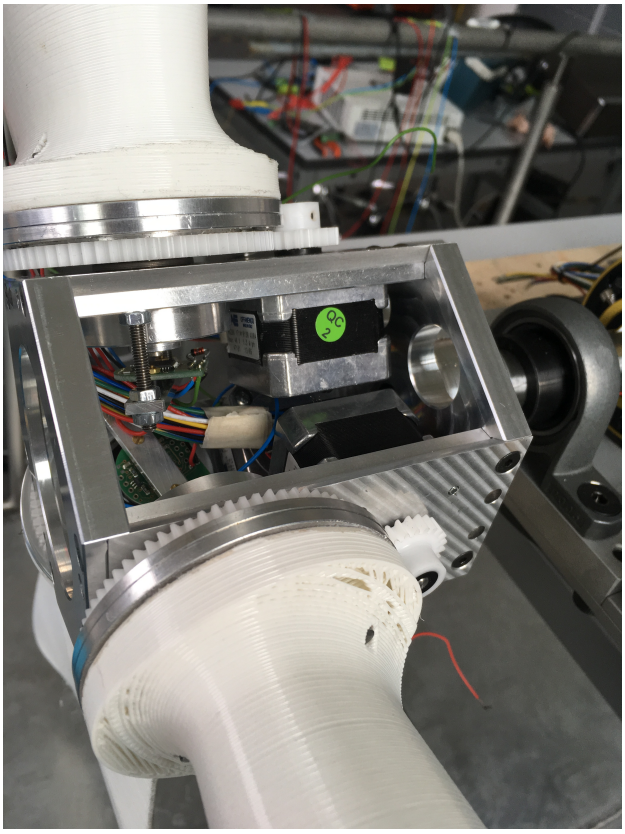

Figure A.10: Zoom on hub.

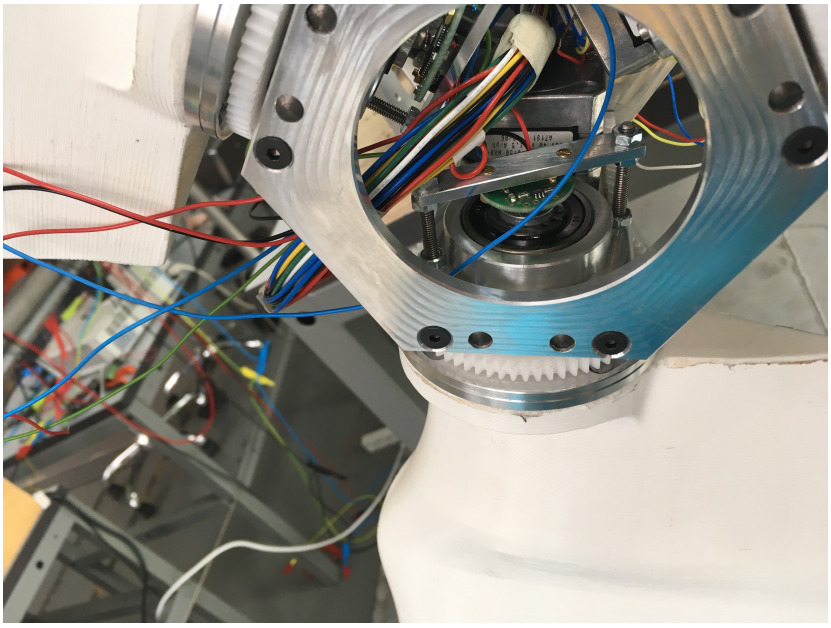

Figure A.11: Zoom on hub.

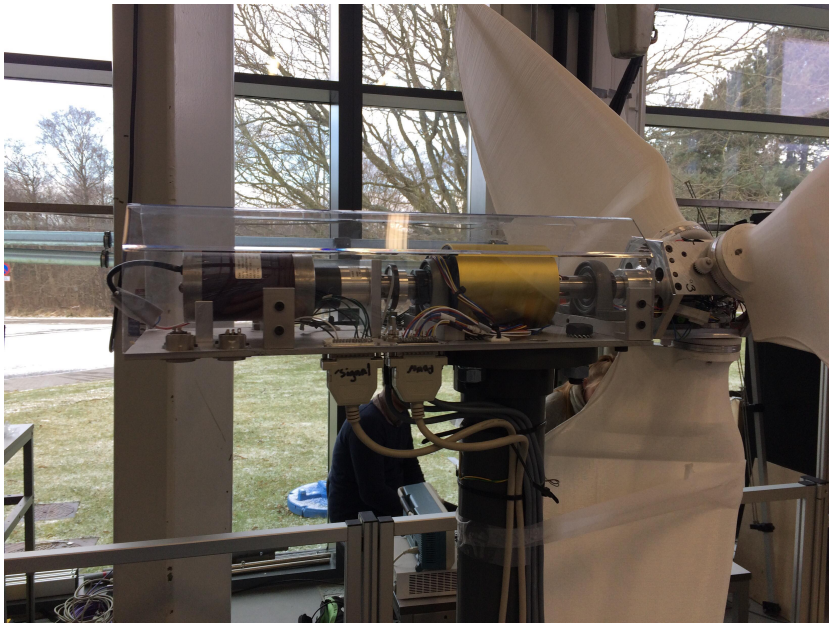

Figure A.12: Nacelle of the wind turbine.

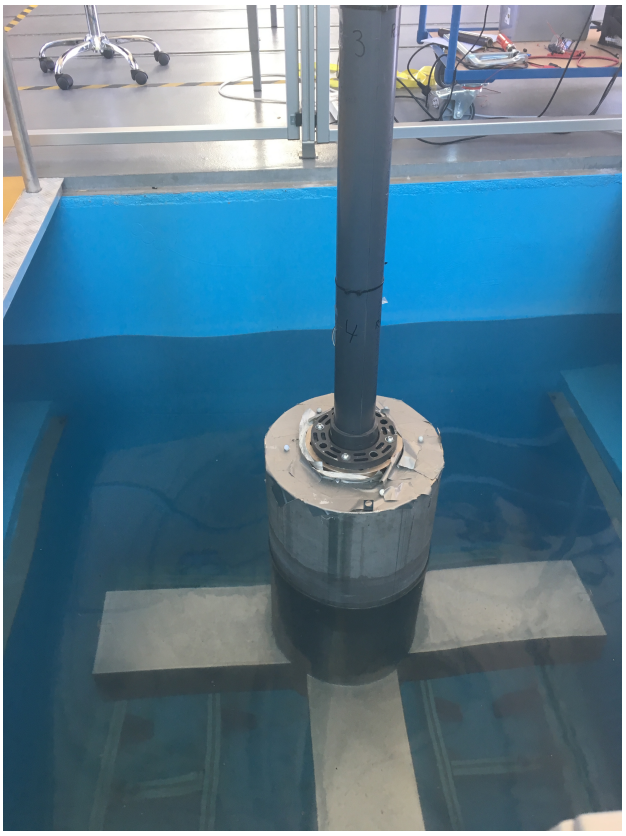

Figure A.13: TLP.



Figure A.14: Wind turbine seen from behind during experiment.



Figure A.15: Wind turbine seen from front.



Figure A.16: Wind turbine seen from side during experiment.

A.11 MATLAB Codes

A.11.1 Hydrodynamic Main Code

Contents

- Spectrum and wave generation
- Calculation of Wave kinematics and dynamics
- Plotting
- Save data for simulation


```
%-------------------------------------------------------------%
%        This program was developed by the group EN10-1
%         Aalborg Universitet Esbjerg, Energy Department
%           P9 and P10 Autumn 2017 and spring 2018
%         Jesper Jensen, Kasper Laugesen & Kasper Jessen,
%                       Signe Mortensen
%
%-------------------------------------------------------------%

% Program for calculating surface elevation, force time serie and
% statistical properties of the sea state

% Note this code expects Nemoh input in .mat structure and surface
% elevation measurements and sea state options in .log structure.  The code is calling two
% external functions "WaveElevation.m" and "SpectralProperties.m", these
% should lie in the same folder as the main script

clc, clear, close all

load('Excitation Force.mat')  % Load Excitaiton Force Named Fe
load('Frequency.mat')         % Load Frequency interval Named w

MFe = abs(Fe(:,:));           % Magnitude
PhFe = angle(Fe(:,:));        % Phase in radians
k =length(Fe);
dsa=1;                         %Direct cos addition-dsa=1 or IFFT apli.-dsa=0
ise=14;                        %Interpolated sample exp. {2^ise}
zpe=1;                         %zpe-zero padding exp. {2^ise(2^zpf-1)}(for precision incre
ment when IFFT is applied)
zp=2^ise*(2^zpe-1);            %Length of the zero padding vector
wi=(0.0:w(k)/(2^ise-1):w(k)).';

dw=wi(2)-wi(1);                %Freq step
nfreq=length(wi);
fmax=(wi(end)+dw*zp)/(2*pi);   %Freq max [Hz] or Nyquist frequency
dT=1/(2*fmax);                 %Sampling period

%%%%%%%%%%%%%%%%%%% Data Interpolation %%%%%%%%%%%%%%%%%%%%%%%%%%%%%%
% with the option 'extrap' to reach the 0 frequency by interpolation %%
MFE(:,:) = interp1(w,MFe,wi,'linear','extrap');   % Interpolation of Force Magnitude
PhFE(:,:) = interp1(w,PhFe,wi,'linear','extrap'); % Interpolation of the Force Phase

% Regenerate Excitation force in frequency domain
FEXC(:,:)=MFE(:,:).*exp(1i*(PhFE(:,:)));   % OBS this is according to a phase in radians
```

Spectrum and wave generation

```
fid = fopen('ExternalINPUT.log');  % Opens the log file determining the settings
SpcI = textscan(fid,'%f','commentstyle','%');
```

```
DSpI = textscan(fid,'%10s','delimiter','%','commentstyle','%');
fclose(fid);
se.seades=[SpcI{1}(1)]; %sea state description
se.pltspc=[SpcI{1}(2)]; %pltspc=1-0 to plot or not the spectrum
se.dirspc=[SpcI{1}(3)]; %dirspc=1-0 for dir. or nondirectional spectrum
se.frespr=[SpcI{1}(4)]; %frespr=1-0 for freq. dependent or indep. spreading

switch (SpcI{1}(1))
       case 1, se.spcdata=[SpcI{1}(5:10)];
       case 2, se.spcdata=[SpcI{1}(11:15)];
       case 3, se.spcdata=[SpcI{1}(16:17)];
       case 4, se.spcdata=[SpcI{1}(18:19)];
       case 5; se.spcdata = 0;
end

if (SpcI{1}(1)==5)  % Wave Elevation Measurements
   fields = {'h','Nfft','Nt','meth'};
   se.seam=cell2struct(DSpI{1}(10:13),fields);
end


[An teta dw  ] = WaveElevation(se, nfreq,wi,dw,dT);  % se.pltspc,se.seades,se.spcdata,se.d
irspc
```

Calculation of Wave kinematics and dynamics

```
   tramp=input('Set Force Ramp Time [s]:');                        % Set Ramp Time for for
ce time series
   fprintf('Ramp Time of %d [s] has been chosen \n' ,tramp)
   stime= [0:0.001:600]';            % Simulation Time

   ii = length(MFe(1,:));           % Degrees of freedom
   zc = -[0:0.1:1]*0.7;             % discretisation of the TLP

   h = 1.88;  % Water depth in flume
   g = 9.81;  % Gravitational Acceleration

   clear k
   load('Wavenumber.mat') % Load precalculated wavenumber, denoted as k

   tfse=zeros(1,length(stime)).' ; % Initialise surface elevation
   z = zeros(length(zc),length(stime)).';  % Initialise z
   tfsv= zeros(length(zc),length(stime)).';  % Initialise Horisontal Velocity
    tfsw= zeros(length(zc),length(stime)).';  % Initialise Vertical Velocity
   wheelerz = zeros(length(zc),length(stime)).';  % Initialise Wheeler Stretching coordina
te

   % Calculation of kinematics
   for l=2:1:nfreq
       tfse=An(l)*cos(wi(l)*stime+teta(l))+tfse;  % Surface Elevation


       for j = 1: length(zc) % Calculate velocity profile as function of depth
       z(:,j) = h*(zc(j)-tfse)./(h+tfse) ;  % Wheeler Stretching Implementation

       tfsv1(:,j) = An(l)*g*k(l)/wi(l)*cosh(k(l).*(z(:,j)+h))/(cosh(k(l)*h)).*cos(wi(l)*st
ime-k(l)*0+teta(l));  % Horisontal Velocity, Define TLP location at origo --> x=0
       %tfsv1(:,j) = An(l)*g*k(l)/wi(l)*cosh(k(l).*(zc(j)+h))/(cosh(k(l)*h)).*cos(wi(l)*st
ime-k(l)*0+teta(l));  % Horisontal Velocity Without Wheeler, Define TLP location at origo
--> x=0
```

```
      tfsw1(:,j) = -An(l)*g*k(l)/wi(l)*sinh(k(l).*(z(:,j)+h))/(cosh(k(l)*h)).*sin(wi(l)*st
ime-k(l)*0+teta(l));  % Vertical Velocity, , Define TLP location at origo --> x=0
       end

      tfsv =  tfsv1+tfsv;
      wheelerz = wheelerz + z;
      tfsw = tfsw1 + tfsw;
   end

   % Calculation of force time series
   for j=1:1:ii  % Calculate Force and Kinematic time series for each DOF
       fFexc(:,j)=MFE(:,j).*An;          % Non-normalised Magnitude
       tFexc(:,j)=zeros(1,length(stime)).';
       for l=1:1:nfreq

           tFexc(:,j)=fFexc(l,j)*cos(wi(l)*stime-teta(l)+PhFE(l,j))+tFexc(:,j);  % Excitat
ion force in time domain
       end

       % Ramp Force time series
       ind=find(stime==tramp);
       ramp=ones(1,length(stime))';  % Initialise ramp time
       ramp(1:ind)=min(0.5*(-cos(pi*stime(1:ind,1)/tramp)+1),1);
       ramp=min(stime/tramp,1);
       tFexc(:,j)=tFexc(1:end,j).*ramp;
       tfse = tfse.*ramp;
   end
```

Plotting

```
     dof=str2double([DSpI{1,1}(16:21)]);
     for d=1:1:ii
    switch (dof(d))
          case 1, a=('Surge'); case 2, a=('Sway ');
          case 3, a=('Heave'); case 4, a=('Roll ');
          case 5, a=('Pitch'); case 6, a=('Yaw  ');
        otherwise, a=([num2str(dof(d)),'DoF ']);
    end
    if d==1, LEG=a; else LEG=vertcat(LEG,a); end
end
if se.pltspc==1
    h1= subplot(2,1,1)
   plot(stime,tfse,'LineWidth',2);grid on, title 'Free Surface Elevation'
   xlim([70 90])
   ylabel('Free surface elevation [m]');  %,'FontSize',12,'FontWeight','bold'
   xlabel('Time [s]');  % ,'FontSize',8,'FontWeight','bold'
  % set(gca,'fontsize',8)
   set( findobj(gca,'type','line'), 'LineWidth',2); % linewidth of graph
   set(gca, 'Units','normalized','FontUnits','points','FontWeight','normal','FontSize',16,
'FontName','Times')
   ax=get(h1,'Position');
   ax(1)=ax(1)-0.02;
   ax(2)=ax(2)+0.02;
   ax(3)=ax(3)+0.05; %add extra length
   ax(4)=ax(4)+0.0; % add extra height
   set(h1,'Position',ax);


   h2=subplot(2,1,2)
  % figure('NumberTitle','off','Name','Excitation Force');
```

```
  % pp=[0.8 1.0 11.0 2.2];
  % set(gcf,'paperposition',pp)
  % set(gcf,'position',pp*100)
   plot(stime,tFexc(:,:),'LineWidth',2);grid on,   title 'Excitation Force'
   ylabel('Excitation: Force [N]\Moment [Nm]');   % ,'FontSize',12,'FontWeight','bold'
   xlabel('Time [s]');  % ,'FontSize',12,'FontWeight','bold'
    set( findobj(gca,'type','line'), 'LineWidth',2); % linewidth of graph
   set(gca, 'Units','normalized','FontUnits','points','FontWeight','normal','FontSize',12,
'FontName','Times')
    ax=get(h2,'Position');
    ax(1)=ax(1)-0.02;
    ax(2)=ax(2)+0.02;
    ax(3)=ax(3)+0.05; %add extra length
    ax(4)=ax(4)+0.0; % add extra height
    set(h2,'Position',ax);

   legend(LEG);set(gca,'fontsize',16)
   xlim([ 70 90])
end
```

Save data for simulation

```
  nMS = input('Enter 1 if saving data of surface elevation and force time serie is wanted:
  ');
  if nMS==1
      delete('ForceTimeSerie.mat')
       delete('Time.mat')
       delete('HorisontalVelocity.mat')
       delete('VerticalVelocity.mat')
       delete('wheelerz.mat')
       delete('SurfaceElevation.mat')

       save('ForceTimeSerie','tFexc')
       save('Time','stime')
       save('HorisontalVelocity','tfsv')
       save('VerticalVelocity','tfsw')
       save('wheelerz','wheelerz')
       save('SurfaceElevation','tfse')
  else
      fprintf('No save of data \n')
  end
```

Published with MATLAB® R2016a

A.11.2 Wave Elevation Code

Contents

- Add path to WAFO TOOLBOX
- Sea State Option 1-3 Unidirectional Waves From spectrum
- Sea State Option 4 Unidirectional Regular Waves
- Sea State Option 5 Surface Elevation Measurements


```
%-------------------------------------------------------------%
%        This program was developed by the group EN10-1
%         Aalborg Universitet Esbjerg, Energy Department
%           P9 and P10 Autumn 2017 and spring 2018
%         Jesper Jensen, Kasper Laugesen & Kasper Jessen,
%                       Signe Mortensen
%
%-------------------------------------------------------------%
% Function to calculate the surface elevation amplitude and phase %

function [An teta dw ] = WaveElevation(se,nfreq,wi,dw,dT)  % pltspc, seades, spcdata, dirs
pc
```

Add path to WAFO TOOLBOX

```
opt = 'minimum';  % Sets minimum initations
addpath(fullfile(matlabroot,'toolbox','wafo'));
initwafo(opt,1,1);
rmpath(fullfile(matlabroot,'toolbox','wafo'));
```

Sea State Option 1-3 Unidirectional Waves From spectrum

```
if se.pltspc==1 && se.seades<=3
   switch (se.seades)
          case 1, spectrum='Finite Depth JONSWAP spectrum';
          case 2, spectrum='JONSWAP Spectrum';
          case 3, spectrum='Piersom-Moskowitz Spectrum';
   end
      figure('NumberTitle','off','Name',spectrum), grid

end

switch (se.seades)
    case 1, S = tmaspec(wi,se.spcdata(1:3),se.spcdata(6),se.pltspc);   % Given in angular
frequency
    case 2, S = jonswap(wi,se.spcdata(1:3),se.pltspc);
    case 3, S = pmspec(wi,se.spcdata(1:2),se.pltspc);  % Parameterised Pierson Moscowitz s
pectrum
end
if se.dirspc==0 && (se.seades==1 || se.seades==2 || se.seades==3)
   teta=2*pi*rand([nfreq 1]);  % % Wave phase
   An=sqrt(2*S.S*dw);  % Wave Amplitude


   nMS = input('Enter 1 if spectral properties are wanted:  ');
          if nMS == 1
          [ch R chtext]=spec2char(S,[1:15],[]);
          ch = num2cell(ch);
```

```
          [chtext' ch' ]
          elseif nMS ~= 1

           fprintf('No spectral properties wanted \n')
              end
end
```

Sea State Option 4 Unidirectional Regular Waves

```
if se.seades==4    %% Regular Waves %%
   amp=se.spcdata(1)/2; S=zeros(nfreq,1);     %Cos. amplitude amp
   uu=find(wi>2*pi/se.spcdata(2)); ind=uu(1);
   S(ind)=(amp^2)/(2*dw);
   teta=zeros(1,nfreq);Ph=1;
   An=sqrt(2*S*dw);  % Wave amplitude



   if se.pltspc==1
      figure('NumberTitle','off','Name','Regular Waves');
      plot(wi,S,'o','MarkerSize',4,'MarkerFaceColor','b');
      xlabel('Frequency [rad/s]','FontSize',9);
      ylabel('S(w) [m^2 s / rad]','FontSize',9);
   end
end
```

Sea State Option 5 Surface Elevation Measurements

```
if se.seades==5
    %Import Data
   addpath('TimeData\23032018\Uncoupled')
   seadata = textread('JONSWAPSpectrum.log');
   se.data = seadata(:,1:2);
   plot(se.data(:,1),se.data(:,2),'LineWidth',2); xlim([0 1000]), title 'Raw Data of Seael
evation',ylabel 'Seaelevation [m]', xlabel 'Time [s]', grid
   nogauges = 1;
   data=seadata(1:length(seadata),1:(1+nogauges));
   fssamp = 1/(data(3,1)-data(2,1)); % sampling Frequency



    Ls=max(abs(se.data(:,2)))/std(se.data(:,2)); %Estimate of the x limits
   [g test cmax irr g2]=dat2tr(se.data,'mnonlinear','csm',0.9,'gsm',0.05,...
                       'param',[-Ls Ls 1513],'ne',7); %Gauss Transform

figure;
plot(g(:,1),g(:,2),'r',g2(:,1),g2(:,2),'k'), title 'Effect of Smoothing', grid on, legend(
'Raw Data','Smoothed Data')
        L = 30000; %1058*10;
        data=dat2gaus([se.data(:,1),se.data(:,2)],g);  %Gaussian data tranformation in ord
er to secure Gaussian data
         S=dat2spec2(se.data,L,[],[],'parzen',1/fssamp); %Using parzen Window
         Sf = ttspec(S,'f');  % Conversion from rad/s to Hz and from rad to deg if directi
onal spectrum

          if se.pltspc==1
             figure;
             specplot(S,se.pltspc), grid  % Max frequency is fs/2*2*pi according to Nyquis
```

```
t
              xlim([0 25])
              figure;
              specplot(Sf,se.pltspc), grid   % Max frequency is fs/2+dw
              xlim([0 4])
           end
              % Spectral Properties
            nMS = input('Enter 1 if spectral properties are wanted:  ');
           if nMS == 1

            fprintf('Spectral properties are \n')

            [ch chtext m mtext norm cdf_normal mu sd lc] = SpectralProperties(S,se)   ;
            Spectral_Properties = [[chtext mtext]' [ch m]'   ]

            figure;
            subplot(1,2,1)
            plot(se.data(:,2),norm,'*'), grid, title 'Gaussian Probability Density Function
', xlabel 'Wave amplitude [m]'
            subplot(1,2,2)
            plot(se.data(:,2),cdf_normal,'*'), grid, title 'Gaussian Cumulative Density Fun
ction'

            figure;
            lcplot(lc,[],mu,sd)
            grid on

             elseif nMS ~= 1
             fprintf('No spectral properties wanted \n')
           end

             S.S = interp1(S.w,S.S,wi,'spline','extrap');  % Interpolate spectrum in order
to get closer to a pure integral

            figure;
            plot(wi,S.S,'Linewidth',2), title 'Interpolated Spectral Density', xlabel 'Freq
uency [rad/s]', ylabel 'S(w) [m^2s/rad]', xlim([0 25]),grid


           m0 = trapz(wi,S.S) ;              % Zeroth moment
           dw = wi(2)-wi(1);                 % Frequency Step
           An=sqrt(2*S.S*dw);                % Wave amplitude from spectrum
           teta=2*pi*rand([length(S.S) 1]);  % Generate random phase


end
```

```
end

% Brodtkorb, P.A., Johannesson, P., Lindgren, G., Rychlik, I., Rydén, J., and Sjö, E. (200
0): WAFO - a Matlab toolbox for analysis of random waves and loads. Proceedings of the 10t
h International Offshore and Polar Engineering conference, Seattle, Vol III, pp. 343-350.
```

Published with MATLAB® R2016a

A.11.3 Spectral Properties Code

Contents

- Statistical Properties of spectrum
- PDF of data
- Crossing Spectrum


```
%-------------------------------------------------------------%
%        This program was developed by the group EN10-1
%         Aalborg Universitet Esbjerg, Energy Department
%           P9 and P10 Autumn 2017 and spring 2018
%         Jesper Jensen, Kasper Laugesen & Kasper Jessen,
%                       Signe Mortensen
%
%-------------------------------------------------------------%
         % Function to calculate spectral properties %

function  [ch chtext m mtext norm cdf_normal mu sd lc] = SpectralProperties(S,se)
```

Statistical Properties of spectrum

```
[ch R chtext]=spec2char(S,[1:15],max(se.data(1:end,1)));
ch = num2cell(ch);
[m,mtext] = spec2mom(S,1,'x',1);
m = num2cell(m);
mtext = mtext(1:end-1);
```

PDF of data

```
sigma = std(se.data(:,2));  % Standard Deviation of Data
mu = mean(se.data(:,2));    % Mean of Data (should be near zero for water waves)
norm = normpdf(se.data(:,2),mu,sigma);  % Calculate the normal/Gaussian distrubition of th
e data
pd = makedist('Normal',mu,sigma);       % Create a normal distribution object
cdf_normal = cdf(pd,se.data(:,2));
```

Crossing Spectrum

```
me = mean(se.data(:,2));  % Mean of signal
sd =std(se.data(:,2));    % Standard Deviation of signal
se.data(:,2) = se.data(:,2)-me; % mean substracted from signal
lc = dat2lc(se.data);  % Levels in first column and upcrossing of the leven in second
plotflag = 2;
lcplot(lc,plotflag,0,sd)
grid on
```

```
end
```

Published with MATLAB® R2016a

A.11.4 Nemoh Main Code

```
%-------------------------------------------------------------%
%        This program was developed by the group EN10-1
%         Aalborg Universitet Esbjerg, Energy Department
%           P9 and P10 Autumn 2017 and spring 2018
%         Jesper Jensen, Kasper Laugesen & Kasper Jessen,
%                       Signe Mortensen
%
%-------------------------------------------------------------%
% Main Program to Call NEMOH and define the structure of the TLP %

clc, clear, close all

n = 0;

if n==1
n = 3;
Radius = 5;
Draft =-10;
r = [Radius Radius 0];
z = [0 Draft Draft];
[Mass,Inertia,KHyd,XB,YB,ZB] = axiMesh(r,z,n);
M = Inertia; % Mass Matrix


else

Pon.L = .7;             % Pontoon length (from center)
Pon.B = .25/2;          % Pontoon with (half)
Pon.H = 0.2-0.7;        % pontoon height
Pon.cut = Pon.L-0.546;  % Offset for Pontoon from the cyl
cyl.r = .2;             % Cylinder Radius
cyl.h = .7;             % Cylinder hight (below water)

% Pontoon in y-axis
X(1,1,:,:) =    [Pon.B Pon.L Pon.H;        Pon.B Pon.L -.7;    -Pon.B Pon.L -.7;        -P
on.B Pon.L Pon.H]; % 1 (ende)
X(1,2,:,:) =    [Pon.B Pon.L Pon.H;        Pon.B Pon.cut Pon.H; Pon.B Pon.cut -.7;       P
on.B Pon.L -.7]; % 2 (side)
X(1,3,:,:) =    [-Pon.B Pon.L Pon.H;      -Pon.B Pon.L -.7;    -Pon.B Pon.cut -.7;      -P
on.B Pon.cut Pon.H]; % 3 (side)
X(1,4,:,:) =    [Pon.B Pon.L -.7;          Pon.B Pon.cut -.7;  -Pon.B Pon.cut -.7;      -P
on.B Pon.L -.7]; % 4 (Bund)
X(1,5,:,:) =    [Pon.B Pon.L Pon.H;       -Pon.B Pon.L Pon.H;  -Pon.B Pon.cut Pon.H;     P
on.B Pon.cut Pon.H]; % 5 (Top)

% Pontoon 1 in x-axis
X(1,6,:,:) =    [Pon.L Pon.B Pon.H;        Pon.L 0 Pon.H;     Pon.L 0 -.7;        Pon.L Po
n.B -.7]; % 6 (ende)
X(1,7,:,:) =    [Pon.L Pon.B Pon.H;        Pon.L Pon.B -.7;   Pon.cut Pon.B -.7;  Pon.cut
Pon.B Pon.H]; % 7 (side)
X(1,8,:,:) =    [Pon.cut Pon.B -.7;        Pon.L Pon.B -.7;   Pon.L 0 -.7;        Pon.cut
0 -.7];    % 8 (Bund)
X(1,9,:,:) =    [Pon.cut Pon.B Pon.H;      Pon.cut 0 Pon.H;   Pon.L 0 Pon.H;      Pon.L Po
n.B Pon.H]; % 9 (Top)

% Pontoon 2 in x-axis
X(1,10,:,:) =   [-Pon.L Pon.B Pon.H;      -Pon.L Pon.B -.7;      -Pon.L 0 -.7;        -Pon
.L 0 Pon.H]; % 6 (ende)
X(1,11,:,:) =   [-Pon.L Pon.B Pon.H;      -Pon.cut Pon.B Pon.H;  -Pon.cut Pon.B -.7;  -Pon
```

```
.L Pon.B -.7]; % 7 (side)
X(1,12,:,:) =   [-Pon.cut Pon.B -.7;      -Pon.cut 0 -.7;        -Pon.L 0 -.7;        -Pon
.L Pon.B -.7];    % 8 (Bund)
X(1,13,:,:) =   [-Pon.cut Pon.B Pon.H;    -Pon.L Pon.B Pon.H;   -Pon.L 0 Pon.H;       -Pon
.cut 0 Pon.H]; % 9 (Top)

% Cylinder in z-axis
cylinder_geometri;


nBodies=1;
n = length(X);
tX(1)=0.;
CG(1,:)=[0. 0. 0];
nfobj(1)=2000 %1000 ændrer tilbage;
[Mass,Inertia,KH,XB,YB,ZB]=Mesh(nBodies,n,X,tX,CG,nfobj);
xlabel('x')
ylabel('y')
zlabel('z')
xlim([-.8 .8])
ylim([-.8 .8])
zlim([-.8 0])

KH1(1:6,1:6) = KH(nBodies,:,:);  % Taking nBodies
KH = KH1;
Inertia1(1:6,1:6) = Inertia(nBodies,:,:);
Inertia = Inertia1
end
%save('Hydrodynamic Stiffness_nemoh','KH')  % Nemoh Made
```

Define Calculation options

```
nbfreq = 10;
w = linspace(0.01,3*2*pi,nbfreq)';
dir = 0;
depth=1.88;

[A,B,Fe] = Nemoh(w,dir,depth);
save('Frequency','w')
save('Added Mass','A')
save('Damping','B')
save('Excitation Force','Fe')
save('Total Stiffness1','K_1')
save('Total Stifness2','K_2')
```

Published with MATLAB® R2016a

A.11.5 Nemoh To Warmit Output Code

Contents

- Constants
- Convert added mass and damping *.1-fil
- Zero wave period - Added mass
- Infinite wave period - Added mass
- Convert Excitation force *.3
- Convert hydrostatic restoring


```
%-------------------------------------------------------------------%
%         This program was developed by the group EN10-1
%         Aalborg Universitet Esbjerg, Energy Department
%             P9 and P10 Autumn 2017 and Spring 2018
%         Jesper Jensen, Kasper Laugesen, Kasper Jessen &
%                      Signe Mortensen
%-------------------------------------------------------------------%
            % Convert Nemoh output to Warmit output

% note:
% Normalizes NEMOH hydrodynamic coefficients in the same manner
% that WAMIT outputs are normalized. Specifically,the linear restoring
% stiffness is normalized as, C(i,j)/(rho*g); added mass is normalized as,
% A(i,j)/rho; radiation damping is normalized as, B(i,j)/(rho*w); and,
% exciting forces are normalized as, X(i)/(rho*g).
```

Constants

```
rho         = 1025;     % Density of water
g           = 9.82;     % Gravity
[n nn nnn]  = size(A);  % size of added mass
epsilon_A   = 0.00001;  % Tolerance of added mass
epsilon_B   = 0.00001;  % Tolerance of Damping
```

Convert added mass and damping *.1-fil

```
T1          = reshape(repmat((w/(2*pi))'.^(-1),1,n*n)',n*nn*nnn,1);     % Reshaped Wave pe
riode [s]
w1          = reshape(repmat(w',1,n*n)',n*nn*nnn,1);                    % Reshaped Wave fr
equency [rad/s]
A2          = reshape(permute(A, [2 1 3]),n*nn*nnn,1)./(rho);           % Reshape Added ma
ss and normalize by rho*omega
B2          = reshape(permute(B, [2 1 3]),n*nn*nnn,1)./(rho*w1);        % Reshape Damping
and normalize by rho*omega
indexi1     = reshape(repmat(1:1:6,nn,nnn),n*nn*nnn,1);     % Create index i
indexj1     = repmat(1:1:6,1,n*nnn)';                       % Create index j

fil1        = [T1 indexi1 indexj1 A2 B2];                   % Assemble *.1 matrix

indices1    = find(abs(fil1(:,4))<epsilon_A & abs(fil1(:,5))<epsilon_B);% Find rows with A
 and B less than epsilon
fil1(indices1,:) = [];                                      % Delete rows with A and B les
s than epsilon
fil1        = fil1';                                        % Transpose fil1 to fit the wi
rte command
```

```
load('AddedMassInfinity')                                   % Load Added Mass zero period
(AinfMatrix)
```

Zero wave period - Added mass

```
T0          = -ones(n*nn,1);                                % Zero wave period
indexi0     = reshape(repmat(1:1:6,nn,1),n*nn,1);           % Create index i
indexj0     = repmat(1:1:6,1,n)';                           % Create index j
A00         = diag(diag(Ainf));                             % Zero wave period - Added mas
s
A0          = reshape(A00',n*nn,1)./rho;                    % Reshape A0
fil0        = [T0 indexi0 indexj0 A0];                      % Assemble A0

indices0    = find(abs(fil0(:,4))<epsilon_A);               % Find rows with A less than e
psilon
fil0(indices0,:) = [];                                      % Delete rows with A less than
 epsilon
fil0        = fil0';                                        % Transpose fil1 to fit the wi
rte command
```

Infinite wave period - Added mass

```
load('AddedMassZero')                                       % Load Added Mass infinity per
iod (A0Matrix)
Tinf        = zeros(n*nn,1);                                % Infinite wave period
indexiinf   = reshape(repmat(1:1:6,nn,1),n*nn,1);           % Create index i
indexjinf   = repmat(1:1:6,1,n)';                           % Create index j
Ainf        = reshape(diag(diag(A0Matrix))',n*nn,1)./rho;                % Reshape Ainf
filinf      = [Tinf indexiinf indexjinf Ainf];              % Assemble Ainf

indicesinf  = find(abs(filinf(:,4))<epsilon_A);             % Find rows with A less than e
psilon
filinf(indicesinf,:) = [];                                  % Delete rows with A less than
 epsilon
filinf      = filinf';                                      % Transpose fil1 to fit the wi
rte command

fileID = fopen('hydroDataFast\AAUTLP.1','w');               % Write *.1 file
fprintf(fileID, '%10f %8d %8d %10f\r\n',fil0);
fprintf(fileID, '%10f %8d %8d %10f\r\n',filinf);
fprintf(fileID, '%10f %8d %8d %10f %10f\r\n',fil1);
fclose(fileID);
```

Convert Excitation force *.3

```
T3          = reshape(repmat((w/(2*pi))'.^(-1),1,n)',nn*nnn,1);% Reshaped Wave periode [s]
dir         = zeros(nn*nnn,1);                              % Wave direction (hardcoded to
 zero!)
Fe2         = reshape(Fe',1,nn*nnn)'./(rho*g);              % Reshape Excitation force (co
mplex)
Fe2Real     = real(Fe2);                                    % Real value of Excitation for
ce
Fe2Im       = imag(Fe2);                                    % Imag value of Excitation for
ce
Fe2Mag      = abs(Fe2);                                     % Magnitude of Excitation forc
```

```
e
Fe2Phase    = rad2deg(angle(Fe2));                          % Phase of Excitation force
indexi3     = repmat(1:1:6,1,nnn)';                         % Create index i
fil3        = [T3 dir indexi3 Fe2Mag Fe2Phase Fe2Real Fe2Im]';% Assemble *.3 matrix

fileID      = fopen('hydroDataFast\AAUTLP.3','w');          % Write *.3 file
fprintf(fileID, '%12f %12f %8d %12f %12f %12f %12f\r\n',fil3);
fclose(fileID);
```

Convert hydrostatic restoring

```
indexihst   = reshape(repmat(1:1:6,nn,1),n*nn,1);           % Create index i
indexjhst   = repmat(1:1:6,1,n)';                           % Create index j
KHhst       = reshape(squeeze(KH),n*nn,1)./(rho*g);         % Reshape hydrostatic restorin
g
filhst      = [indexihst indexjhst KHhst]';                 % Assemble *.hst matrix

fileID      = fopen('hydroDataFast\AAUTLP.hst','w');        % Write *.hst file
fprintf(fileID, '%8d %8d %15f\r\n',filhst);
fclose(fileID);
```

Published with MATLAB® R2016a

A.11.6 FEM Code

Contents

- Input file
- FEM
- Calculating mass and stiffness matrices
- Modelling of coupling
- Adding mass moment of inertia and mass of nacelle to tower coordinates
- Damping of tower
- Reduced stiffness, damping and mass matrices
- Finding natural frequencies of tower
- Modeshapes of tower
- Initial conditions for tower


```
%-------------------------------------------------------------%
%         This program was developed by the group EN10-1
%         Aalborg Universitet Esbjerg, Energy Department
%             P9 and P10 Autumn 2017 and spring 2018
%         Jesper Jensen, Kasper Laugesen, Kasper Jessen &
%                          Signe Mortensen
%-------------------------------------------------------------%
                    % FEM code for tower dynamics
```

Input file

```
Topmass = 2;        % Without/simple/advanced topmass: 0/1/2
lumped  = .5;       % 1/0, lumped/consistent
coupled = 1;        % Coupled response: 0/1

t  = 6.7E-3;        % Thickness of tower
do = 90E-3;         % Outer diameter of tower
di = do-2*t;        % Inner diameter of tower
L  = 2.02-.215 ;    % Length of tower
E  = 3.15E9;        % Young's modulus
rho.tower = 1503;   % Density of tower (PVC-U)
Hnacelle  = .1;     % Height of nacelle

A1 = pi*((do/2)^2-(di/2)^2);    % Cross sectional area of tower
I  = pi/4*((do/2)^4-(di/2)^4);  % Area moment of inertia of tower
Ip = pi/2*((do/2)^4-(di/2)^4);  % polar moment of inertia
step = 17;                      % Step along tower
dis  = (0:1/step:1)';           % Dizcretization of the tower

    % Boundary conditions
    %     node   dof   type   value
    BC = [ 1      1      0      0
           1      2      0      0
           1      3      0      0
           1      4      0      0
           1      5      0      0
           1      6      0      0];

if Topmass == 2
        nCoord = zeros(length(dis)+3,3);     % Intializing coordinates
        nCoord(2:length(nCoord)-2,:) = [dis*0,dis*0,dis*(L)+0.05]; % Tower coordinates
```

```
    % Adding nacelle height to the discretization in two elements
    nCoord(end-1,3) = nCoord(end-2,3) + Hnacelle/2;
        nCoord(end,3)   = nCoord(end-1,3) + Hnacelle/2;

    Mnacelle = 12.2;    % Mass of the nacelle

    % Mass moments of inertia of nacelle about x-axis found by Inventor:
    Inacellex = 893616*10^(-6);
    Inacelley = 725635*10^(-6);
    Inacellez = 881912*10^(-6);

    N0 = -9.82*(Mnacelle+flip(nCoord(:,3))*rho.tower*A1); % Initial forces

elseif Topmass == 1
        nCoord = zeros(length(dis)+2,3);                % Intializing coordinates
        nCoord(2:end-1,:) = [dis*0,dis*0,dis*(L)+0.05]; % Coordinates for tower

    % Adding nacelle height to the discretization
    nCoord(end,3) = nCoord(end-1,3) + Hnacelle;

    Mnacelle = 12.2; % Mass of the nacelle

    % Mass moments of inertia of nacelle found by Inventor:
    Inacellex = 893616*10^(-6);
    Inacelley = 725635*10^(-6);
    Inacellez = 881912*10^(-6);

    N0 = -9.82*(Mnacelle+flip(nCoord(:,3))*rho.tower*A1); % Initial forces

elseif Topmass == 0
    nCoord = zeros(length(dis),3);                    % Intializing coordinates
    nCoord(1:length(nCoord),:) = [dis*0,dis*0,dis*L]; % Coordinates for tower

    N0 = -9.82*flip(nCoord(:,3))*rho.tower*A1;        % Initial forces
end

eTop = [(1:size(nCoord,1)-1)',(2:size(nCoord,1))'];   % Element topology
```

FEM

```
Nn = size(nCoord,1);  % Number of gloabal coordinates:
Ne = size(eTop,1);    % Number of global elements:
DOFPerNode = 6;       % Number of global DOFs
NDOF = Nn*DOFPerNode; % Total number of DOFs in global system

% Arranging the global DOFs into an DOFPerNode x Nn matrix:
gDOF = reshape(1:NDOF,DOFPerNode,Nn)';

One = ones(NDOF,1);
Zero = zeros(NDOF,1);
Q = [One Zero];         % Default is no external force

for n = 1:size(BC,1) % Loops for all boundary conditions
    Q(gDOF(BC(n,1),BC(n,2)),1:2) = BC(n,3:4);
end

dKnown = Q(:,1) == 0; % Displacements are known
fKnown = Q(:,1) == 1; % Forces are known
```

```
K_tower = zeros(NDOF); % Initializing global stiffness matrix
M_tower = zeros(NDOF); % Initializing global mass matrix
```

Calculating mass and stiffness matrices

```
for n = 1:Ne            % Number of elements
    ne = eTop(n,:);     % Extracting the element from global
    xe = nCoord(ne',:); % Extracting coordinates for element from global

    % Calculating local stiffens and mass matrix using function:
    [Ke, Me,Tg] = KeMeROD6DOF(xe,E,A1,rho.tower,I,N0(n),lumped,eTop,n,Nn,Topmass,Ip);

    eDOF = gDOF(eTop(n,:),:); % Determining global DOF for the element

    % Adding the stiffnes for the element to the global stiffnes matrix
    K_tower(eDOF',eDOF') = K_tower(eDOF',eDOF') + Ke;

    % Adding the mass for the element to the global stiffnes matrix
    M_tower(eDOF',eDOF') = M_tower(eDOF',eDOF') + Me;

end
```

Modelling of coupling

```
 if coupled == 1
      K_tower = K_tower*.82;
 end
```

Adding mass moment of inertia and mass of nacelle to tower coordinates

```
nsNodes = eTop(end);

if Topmass == 2
    M_tower((nsNodes)*DOFPerNode-11,(nsNodes)*DOFPerNode-11) = Mnacelle ;
    M_tower((nsNodes)*DOFPerNode-10,(nsNodes)*DOFPerNode-10) = Mnacelle ;
    M_tower((nsNodes)*DOFPerNode-9,(nsNodes)*DOFPerNode-9)   = Mnacelle ;
    M_tower((nsNodes)*DOFPerNode-8,(nsNodes)*DOFPerNode-8)   = Inacellex*1 ;
    M_tower((nsNodes)*DOFPerNode-7,(nsNodes)*DOFPerNode-7)   = Inacelley*1 ;
    M_tower((nsNodes)*DOFPerNode-6,(nsNodes)*DOFPerNode-6)   = Inacellez ;
end

if Topmass == 1
    M_tower((nsNodes)*DOFPerNode-5,(nsNodes)*DOFPerNode-5) = Mnacelle ;
    M_tower((nsNodes)*DOFPerNode-4,(nsNodes)*DOFPerNode-4) = Mnacelle ;
    M_tower((nsNodes)*DOFPerNode-3,(nsNodes)*DOFPerNode-3) = Mnacelle ;
    M_tower((nsNodes)*DOFPerNode-2,(nsNodes)*DOFPerNode-2) = Inacellex ;
    M_tower((nsNodes)*DOFPerNode-1,(nsNodes)*DOFPerNode-1) = Inacelley ;
    M_tower((nsNodes)*DOFPerNode,(nsNodes)*DOFPerNode)     = Inacellez ;
end
```

Damping of tower

```
if coupled == 0          % When not coupled to TLP
    zeta_0 = 0.013;      % Damping ratio found by free decay
    omega_0 = 1.89*2*pi; % Natural frequency found by free decay
```

```
elseif coupled == 1       % When coupled to TLP
    zeta_0 = 0.025;       % Damping ratio found by coupled free decay
    omega_0 = 1.8*2*pi;   % Natural frequency found by coupeld free decay
end

% Coefficients for Rayleigh damping
alpha = zeta_0*omega_0;
beta = zeta_0/omega_0;

C_tower = alpha*M_tower + beta*K_tower;  % Rayleigh damping
```

Reduced stiffness, damping and mass matrices

```
Mred = M_tower(fKnown,fKnown) ; % Mass matrix reduced to known forces
Cred = C_tower(fKnown,fKnown) ; % Damping matrix reduced to known forces
Kred = K_tower(fKnown,fKnown) ; % Stiffness matrix reduced to known forces
```

Finding natural frequencies of tower

```
[Sred,Dred] = eig(Kred,Mred); % Eigenvalue problem
omega0 = sqrt(diag(Dred));    % Natural frequency is eigenvalue squared
freq01 = omega0/(2*pi);       % Converting from rad/s to Hz
freq0 = sort(freq01);         % Sorting the natural frequencies
fundamentalF = freq0(2);      % Fundamental frequency in surge

fd = fundamentalF*sqrt(1-zeta_0^2); % Damped natural frequency
```

Modeshapes of tower

```
i = find(freq01 == fundamentalF);           % Finding index for fundamental frequency
modeshape = zeros(length(Sred(1:end,i)),1); % Initialising modeshape

% Normalising modeshapes:
modeshape(1:6:end) = Sred(1:6:end,i)'/(Sred(end-5,i));
modeshape(5:6:end) = Sred(5:6:end,i)'/Sred(end-1,i);
```

Initial conditions for tower

```
InitVelTow = zeros(length(modeshape),1); % Initialising intitial velocity
InitVelTow(1:6:end) = 0; % Can be changed for other surge initial velocity

InitPosTow = zeros(length(modeshape),1); % Initialising intitial posistion
% Inserting intitial positions in surge and pitch:
InitPosTow(1:6:end) = abs(modeshape(1:6:end))*(0.0124);
InitPosTow(5:6:end) = abs(modeshape(5:6:end))*(0.0083);
```

Published with MATLAB® R2016a

A.11.7 Aerodynamics MATLAB Codes

A.11.7.1 UBEM MATLAB Function

Contents

- Parameter loading
- Wind velocity on blades at their current position
- Initilize matrices
- Unsteady BEM
- 1) Calculate relative velocity
- 2) Calculate flow angle
- 3) Calculate Angle of attack
- 1P Effect by offseting the AOA of a blade
- 4) Load static Airfoil data
- 6) Calculate Lift and Drag
- 7) Prandtl
- 7) Calculate axial Induction coef.
- Dynamic Inflow model
- Save induction velocities
- Calculate forces


```
function [Cl1,T_R ,M_yaw,M_pitch,F_R,V0u,W0_last,W_qs_last , W_int_last,fs1,Alpha1] = UB
EM(NL,NPPL,RotPosi1,omega,Beta,dt,step,V_x,V_y,CL1, CD1,V0,V_ext,W0_last1,W_qs_last1, W_
int_last1,fs, DSM)
```

```
%-----------------------------------------------------------------%
%         This program was developed by the group EN10-1
%         Aalborg Universitet Esbjerg, Energy Department
%             P9 and P10 Autumn 2017 and spring 2018
%         Jesper Jensen, Kasper Laugesen, Kasper Jessen &
%                           Signe Mortensen
%-----------------------------------------------------------------%
      % UBEM Matlab-function for simulation of aerodynamics loads on rotor



% Find rotor position
RotPosi = [RotPosi1 RotPosi1+2*pi/3 RotPosi1+4/3*pi]; %  rotation vector  with three ang
ular positions

   n1  = floor(RotPosi(1)/(2*pi)); % Blade 1 rotation counter
   n2  = floor(RotPosi(2)/(2*pi)); % Blade 2 rotation counter
   n3  = floor(RotPosi(3)/(2*pi)); % Blade 3 rotation counter

   x1  = RotPosi(1) - n1 * 2*pi; % Blade 1 subtract number of rounds n1
   x2  = RotPosi(2) - n2 * 2*pi; % Blade 2 subtract number of rounds n2
   x3  = RotPosi(3) - n3 * 2*pi; % Blade 3 subtract number of rounds n3

RotPosi = [x1 x2 x3];
```

Parameter loading

[Removed]

Wind velocity on blades at their current position

```
 for NB1 = 1 : NRB                                    % For all blade
    [~,II]     = min(abs(RotV-RotPosi(NB1)));        % Find nearest windspeed region (I) f
rom different wind speed lines (RotV)
    Ux_0(:,NB1) = V_x(:,II)  ;                       % x-dir. wind speed vector for blade
in nearest region


    if RotPosi(NB1)>1.5*pi                          % Is wind direction into or against bl
ade
        sign=1; % if tagential wind is against blade
    else
        sign=-1 ; % if tagential wind is with blade
    end
    Uy_0(:,NB1) =1* sign*(abs(V_y(:,II)))  ;         % y-dir. velocity
 end
```

Initilize matrices

[Removed]

Unsteady BEM

```
for NB = 1:3                                         % For each blades

    for nn=1:BN                                      % For each section
```

1) Calculate relative velocity

```
Vrel(:,NB,nn) = [Ux_0(nn,NB) Uy_0(nn,NB) ]' + W0_last1(:,NB,nn) + [0 -omega*rv(nn)]' ; %
 Find relative velocity on blade
Vrel_norm(NB,nn) = norm(Vrel(:,NB,nn)); %  Find the magnitide of the relative velocity
```

2) Calculate flow angle

```
phi(NB,nn) = atan((Vrel(1,NB,nn))/abs(Vrel(2,NB,nn))); % From axial and tangential relat
ive velocities.
```

3) Calculate Angle of attack

```
Alpha(NB,nn) = rad2deg(phi(NB,nn) - ( Beta + Theta(nn) )) ;  % Find AOA
```

1P Effect by offseting the AOA of a blade

```
 if NB == 3 % To make offset on blade 3
    offset1 = 0; % AOA offset
    Alpha(NB,nn) = Alpha(NB,nn)-offset1;
 end
 if NB == 2 %To make offset on blade 2
    offset2 = 0; % AOA offset
    Alpha(NB,nn) = Alpha(NB,nn)-offset2;
 end
```

```
 if NB ==1 % To make offset on blade 3
    offset3 = 0; % AOA offset
    Alpha1(nn) = Alpha(NB,nn)-offset3;
 end
```

4) Load static Airfoil data

```
% AH 93-W-300 lift & drag coeffcient for different reynolds numbers
%%%%%%%%% Blade Data for first 3 sections AH-W-300 %%%%%%%%%%%%%
    if  nn < 3.3
        % AH 93-W-300 airfoil for root of wind turbine
        [~,IIc] = min(abs( (Alpha(NB,nn) - CD1(:,3)) ) ); % find AOA for static airfoil
CD data
        Cd(NB,nn) = CD1(IIc,4); % Load static airfoil CD data
        Cl(NB,nn) = CL1(IIc,4); % Load static airfoil Cl data
        %end
    end

% SD7003 lift & drag coeffcient for different reynolds numbers
%%%%%%%%% Blade Data for rest of sections SD7003 %%%%%%%%%%%%%

     if nn > 3.3 % For all other then first 3 airfois

        Recont(NB,nn) = (norm(abs(Vrel_norm(NB,nn))).*Cc(nn))./1.411E-5 ;  % Calculate R
eyn. number

                % For reynolds number of 22k
                [~,IIc2d] = min(abs( (Alpha(NB,nn) - CD1(:,1) ) ) );  % find AOA for sta
tic airfoil CD data
                Cd(NB,nn) = CD1(IIc2d,2);% Load static airfoil CD data
                Aa0 = deg2rad(-0.3); % The zero crossing for the CL coef, at which AOA
                Cl_merge = 0.35; % The merge lidt coefcient for the SD7003 airfoil
                [~,IIc2l] = min(abs( (Alpha(NB,nn) - CL1(:,1) ) ) );
                Cl(NB,nn)= CL1(IIc2l,2);

             if Recont(NB,nn) > 55E3 % Choose if Reynolds number is higher then 55k

                 [~,IIc2d] = min(abs( (Alpha(NB,nn) - CD1(:,5) ) ) ); % find AOA for sta
tic airfoil CD data
                 Cd(NB,nn) = CD1(IIc2d,6); % Load static airfoil CD data

                 % Found from inspecting data, for the dynamic stall model
                 Aa0 = deg2rad(-0.5); % The zero crossing for the CL coef, at which AOA
                 Cl_merge = 0.4; % The merge lidt coefcient for the SD7003 airfoil

                 [~,IIc2l] = min(abs( (Alpha(NB,nn) - CL1(:,5) ) ) ); % find AOA for sta
tic airfoil CL data
                 Cl1s(NB,nn)= CL1(IIc2l,6);  % Load static airfoil CL data

            end


                % [REMOVED CODE]
                % Similar for Reynold's numbers of  67 87 100 150


     end
  %5) Dynamic stall model

     if nn >3.3 % Only for SD7003 airfoil, as this is main contributor for lift
```

```
      AlphaR(NB,nn) = deg2rad(Alpha(NB,nn)); % AOA in radians

     Cl_alpha = 2*pi; % Invisid lift coef.
     Cl_inv = Cl_alpha *(AlphaR(NB,nn)-Aa0); % Invisid lift coef
     sfs = 1/2 * Cl_alpha; % seperating valvue

     a_merge = deg2rad(35); % Angle at which fully seperated and steady merge
     DAa = deg2rad(15); % region size in angle

     Aa1 = Aa0 + Cl_merge/sfs; % Dynamic AOA coefficent

     minA = min((Aa1-Aa0),DAa); % At what region is the AOA

     % Fully seperated lift coef, at different AOA
     if (AlphaR(NB,nn)) < a_merge  % AOA less then merge AOA
      Cl_fs  = Cl_merge;
     end

     if (AlphaR(NB,nn)) < (minA + Aa1)  % AOA less then set valvue
      Cl_fs = sfs*((AlphaR(NB,nn)-Aa0)) - sfs*( ( (AlphaR(NB,nn)-Aa1+minA)^2/(4*minA) )
);
     end

     if (AlphaR(NB,nn)) < (-minA + Aa1) % AOA less then set valvue
      Cl_fs = sfs*((AlphaR(NB,nn)-Aa0));
     end

     if AlphaR(NB,nn) < 0 % AOA less then zero
      Cl_fs = sfs*((AlphaR(NB,nn)+Aa0));
     end

      if AlphaR(NB,nn) < (minA + Aa1) % AOA less then set valvue
      Cl_fs = sfs*((AlphaR(NB,nn)+Aa0)) + sfs*( ( (AlphaR(NB,nn)-Aa1+minA)^2/(4*minA) ))
;
     end

     Cl1(NB,nn) = fsk(NB,nn)*Cl_inv + (1-fsk(NB,nn))*Cl_fs;   % Calculate dynamic lift c
oef. from prev. seperation func.

     fst(NB,nn) = (Cl1s(NB,nn)- Cl_fs)/(Cl_inv - Cl_fs); % Calculate steady seperation f
unction valvue

     fs1(NB,nn) = fst(NB,nn) + (fsk(NB,nn)-fst(NB,nn))*exp( - dt/( 4*Cc(nn)/Vrel_norm(NB
,nn) ) ); % Calculate sepration function value for next time step

     fssave(NB,nn) =  fs1(NB,nn); % Save for next timestep

     else  % If not SD7003 airfoil set valvues to zero

     fsk(NB,nn)    = 0;
     fst(NB,nn)    = 0;
     fst1(NB,nn)   = 0;
     fssave(NB,nn) = 0;

     end
```

6) Calculate Lift and Drag

```
   Cn(NB,nn) = Cl1(NB,nn).*cos(phi(NB,nn)) + Cd(NB,nn).*sin(phi(NB,nn)); % Thrust force
```

```
coef. using dynamic CL

   Ct(NB,nn) = Cl1(NB,nn).*sin(phi(NB,nn)) - Cd(NB,nn).*cos(phi(NB,nn)); % Torque coef.
using dynamic CL
```

7) Prandtl

```
    %  Prandl Tip loss coef.
   F1(NB,nn) = 2/pi * acos( exp( -(3/2)*(R+Rs - rv(nn))./ (rv(nn).*sin(phi(NB,nn)) ) ) )
;

    %  Prandl Hub loss coef.
   F2(NB,nn) = 2/pi * acos( exp( -(3/2)*(rv(nn) - Rs)./ (rv(nn) *sin( phi(NB,nn)) )  ) )
;

    % Combined loss factor
   F(NB,nn)  = F1(NB,nn)*F2(NB,nn);
```

7) Calculate axial Induction coef.

```
    sigma(NB,nn) = Cc(nn)*3/( 2*pi*rv(nn) ); % Correction for finite number of wings

   anew  = 1./( ((4*F(NB,nn).*sin(phi(NB,nn))).*sin(phi(NB,nn))).*(sigma(NB,nn).*Cn(NB,nn
))) + 1 ); % Calculate axial induction factor using prandl
   adnew = 1./( ((4*F(NB,nn).*cos(phi(NB,nn))).*sin(phi(NB,nn))).*(sigma(NB,nn).*Ct(NB,nn
))) - 1 ); % Calculate tangential induction factor

   % Glauert Correction
     if anew > 0.2 % limit for axial induction factor
            K(NB,nn) = abs(4*F(NB,nn)*(sin(phi(NB,nn))*sin(phi(NB,nn)))/(sigma(NB,nn)*(C
n(NB,nn)))); % Glauert correction factor
             Ac       = 0.4; %
             anew     = 0.5*( 2 + K(NB,nn) *(1-2*Ac) - sqrt( (K(NB,nn) *(1-2*Ac)+2)^2 + 4
*(K(NB,nn) *Ac^2-1) ) ); %Recalculate axial induction factor
     end

   aan(NB,nn) = anew;  % Save axial induction factor
   aadn(NB,nn)=adnew;  % Save Tangential induction factor
```

Dynamic Inflow model

Equbrilum values

```
  % Quasi-steady induced velocity in x
   W_x_qs(NB,nn) = - norm(V0B(nn,NB)) * anew;
   % Quasi-steady induced velocity in y
   W_y_qs(NB,nn) = - omega * rv(nn)  * adnew;

    % Quasi-steady induced velocity vector
   W_qs(:,NB,nn) = [ W_x_qs(NB,nn) ; W_y_qs(NB,nn)]; % Vector

   % Time constants
   Tau1 = (1.1 / ( 1 - 1.3 * aan(NB,nn) )) * ((R + Rs) / norm(Ux_0(nn,NB)));

   Tau2 = ( 0.39 -  0.26 * ( rv(nn)/(R+Rs) )^2 ) * Tau1;
```

```
    % Filters
    H    = W_qs(:,NB,nn) + 0.6 * Tau1 * (W_qs(:,NB,nn) - W_qs_last1(:,NB,nn))/dt;

    W_int(:,NB,nn)  = H + (W_int_last1(:,NB,nn) - H) * exp(-dt/Tau1);

    W0(:,NB,nn)     = W_int(:,NB,nn) + ( W0_last1(:,NB,nn) - W_int(:,NB,nn) ) * exp(-dt/T
au2);
```

Save induction velocities

```
  W_int_last(:,NB,nn) = W_int(:,NB,nn);
  W_qs_last(:,NB,nn)  =  W_qs(:,NB,nn);
  W0_last(:,NB,nn)    =   W0(:,NB,nn);
```

Calculate forces

Thrust Force per blade section

```
 dTTx(NB,nn) = 0.5*1.23*Vrel_norm(NB,nn).^2*Cc(nn).*Cn(NB,nn)*dr(nn);

     % Torque per blade section
 dTx(NB,nn)  = 0.5*1.23*Vrel_norm(NB,nn).^2*Cc(nn).*Ct(NB,nn)*dr(nn)*rv(nn);
```

```
    end % end loop per blade section

end % End loop per blade

% Forces and torques per blade
T_B = sum(dTx);  % Sum Torque for each element
F_B = sum(dTTx); % Sum Force for each element

% Forces and torques on rotor
T_R = sum(T_B);          % Torque Rotor
F_R = sum(F_B)+F_hub;    % Normal Force Rotor

% Pitching Moment
M_pitch =  sum(dTTx(1,:).*rv(2:20)*sin(RotPosi(1)) ...  % From blade 1
        + dTTx(2,:).*rv(2:20)*sin(RotPosi(2)+2*pi/3) ...% From blade 2
        + dTTx(3,:).*rv(2:20)*sin(RotPosi(3)+4*pi/3));  % From blade 3

% Yaw Moment
M_yaw   =  sum(dTTx(1,:).*rv(2:20)*cos(RotPosi(1)) ...   % From blade 1
        + dTTx(2,:).*rv(2:20)*cos(RotPosi(2)+2*pi/3) ... % From blade 2
        + dTTx(3,:).*rv(2:20)*cos(RotPosi(3)+4*pi/3));   % From blade 3

% Tower drag force
Cd_hub = 1.2; % Drag coef For blunt half circle
A_hub = pi*r_hub^2; % Area of hub
F_hub = 0.5*Cd_hub*A_hub*V0B(1,1)*mean(Ux_0(1,:)).^2; % Force on hub, mean
    % velocity of all the first points in circle
```

Published with MATLAB® R2016a

A.11.7.2 Wind Generation Code

Contents

- Wind field
- !!! INSERT RPM !!!!
- Parameters
- Init. Matrices
- Calculate Box PSDs
- Assign PSDs to boxes
- Interpolation between PSDs
- Mean velocities for all points, as a func. of fan rot. speed.
- Mean wind speed vectors
- Mean wind speed vector for radius fit
- Genertate mesh
- Calculate distance between points
- Calculate mean velocity between points


```
 %-------------------------------------------------------------%
%         This program was developed by the group EN10-1
%         Aalborg Universitet Esbjerg, Energy Department
%             P9 and P10 Autumn 2017 and spring 2018
%         Jesper Jensen, Kasper Laugesen, Kasper Jessen &
%                          Signe Mortensen
%-------------------------------------------------------------%
          % Matlab code for generating wind speed time series in points.
```

Wind field

```
16 15 14 13
12 11 10 9
8  7  6  5
4  3  2  1
```

!!! INSERT RPM !!!!

```
%%%%%%%%%%%%%%%%%%%%%%%%
       RPM =2500;  % Fans rotational speed (2x what VLT says)
%%%%%%%%%%%%%%%%%%%%%%%%

Time = 180;                               % Length of time, for the wind speeds generated
```

Parameters

```
dt = 0.01;                        % Sampling time
Nsteps=Time/dt+1;                 % Number of steps
t = linspace(0,Time,Nsteps);      % Time vector
```

Init. Matrices

[Removed]

Calculate Box PSDs

```
% Load wind speed data for all points Low/high
load('Vh') ;        % load wind data for high RPM
load('Vl') ;        % load wind data for low RPM

% Make structure organizer
V2 = struct('V1',1,'V2',2,'V3',3,'V4',4,'V5',5,'V6',6,'V7',7,'V8',8,'V9',9,'V10',10,'V11
',11,'V12',12,'V13',13,'V14',14,'V15',15,'V16',16);
fieldV2= fieldnames(V2);

% For Pwelch
Ts = 0.3;    % Sampling time
Fs = 1/Ts;   % Sampling freq.
Window = 30; % Window for Pwelch


for k=1:numel(fieldV2)                              % Low RPM PSD
   VV =  Vl.(fieldV2{k});
   [PSDl(k,:),fp(k,:)] = pwelch(VV-mean(VV),Window,[],[],Fs);
end

for k=1:numel(fieldV2)                              % High RPM PSD
   VV =  Vh.(fieldV2{k});
   PSDh(k,:) = pwelch(VV-mean(VV),Window,[],[],Fs);
end


tt=[1:3 5:7 9:11];              % Grid vector for points for boxes
```

Assign PSDs to boxes

```
for i=1:9                  % Low RPM box PSD
    k=tt(i);
    PSDl_box(i,:) =  ( PSDl(k,:) +  PSDl(k+1,:) + PSDl(k+4,:) + PSDl(k+5,:) )./4; % PSD(
1,2,5,6) ....
end

for i=1:9                   % high RPM box PSD
    k=tt(i);
    PSDh_box(i,:) =  ( PSDh(k,:) +  PSDh(k+1,:) + PSDh(k+4,:) + PSDh(k+5,:) )./4; % PSD(
1,2,5,6) ....
end
```

Interpolation between PSDs

```
if RPM < 2899
 wf = (2900-RPM)/(2900-1520);                    % Weighting function

else  % If using higher RPM then measured, then use highest PSD

 wf = 0.01; % Correct for higher wind speeds then measured
end
 if RPM < 1521 % If using lower RPM then measured, then use lowest PSD
 wf =0.99; % Correct for lower wind speeds then measured
  end
```

```
PSDx_box = PSDl_box*(wf) + PSDh_box*(1-wf) ;      % Box PSD for all fan rot. speed
```

Mean velocities for all points, as a func. of fan rot. speed.

```
for k=1:numel(fieldV2)   % Find linear fit for all point dependency on fan speed
Vls = Vl.(fieldV2{k});
Vhs = Vh.(fieldV2{k});
fit(:,k) = glmfit([1520 2900],[mean(Vls) mean(Vhs)]); % Fit linear function for RPM vs m
ean wind velocity
end

% mean at center point, found in data.
Vlmidt = 2.99; % m/s low RPM
Vhmidt = 5.64; % m/s high RPM


Vpx = fit(2,:).*RPM + fit(1,:);        % Mean wind speed for all points as func. of RPM
```

Mean wind speed vectors

```
dy = 0.73;      % Distance between points horizontally
dz = 0.70;      % Distance between points vertically

p_d  = [1 6; 4 7 ; 13 10 ; 16 11];      % Points on diag.
p_h  = [12 8 11 7;  9  5 10  6];        % Points on hori.
p_v  = [ 2 3  6 7; 14 15 10 11];        % Points on verti.

r_d  = [sqrt((dy/2 + dy)^2+(dz/2 + dz)^2 ) sqrt((dy/2)^2+(dz/2)^2) 0]; % diag radius vec
tor from center
r_h  = [dy/2+dz dy/2 0];                                                % horizontally
r_v  = [dz/2+dz dz/2 0];                                                % vetically

for k = 1:size(PSDh_box,1) - 1         % Make radius mean speed vector (start diag to po
int 1 and round the clock)

    if k == 1 || k==3 || k==5 || k==7% diag
        tt =[1 0 2 0 3 0 4];
        pfit(:,k) = polyfit([r_d r_d],[ [mean(Vl.(fieldV2{p_d(tt(k),1)})) mean(Vl.(field
V2{p_d(tt(k),2)})) Vlmidt]./max([mean(Vl.(fieldV2{p_d(tt(k),1)})) mean(Vl.(fieldV2{p_d(t
t(k),2)} ))]) ...
                                        [mean(Vh.(fieldV2{p_d(tt(k),1)})) mean(Vh.(field
V2{p_d(tt(k),2)})) Vhmidt]./max([mean(Vh.(fieldV2{p_d(tt(k),1)})) mean(Vh.(fieldV2{p_d(t
t(k),2)} ))])],2);
    % p(1) x^2 + p(2)x +p(1)
    end

 %%%%%%%%%% Vertical %%%%%%%%%%%%%

    if k == 2 || k==6    % Vertic.
         tt =[0 1 0 0 0 2];
         pfit(:,k) = polyfit([r_v r_v],[ [ ...
             (mean(Vl.(fieldV2{p_v(tt(k),1)}))+mean(Vl.(fieldV2{p_v(tt(k),2)})))/2  ...
             (mean(Vl.(fieldV2{p_v(tt(k),3)}))+mean(Vl.(fieldV2{p_v(tt(k),4)})))/2 Vlmid
t]./((mean(Vl.(fieldV2{p_v(tt(k),3)}))+mean(Vl.(fieldV2{p_v(tt(k),4)})))/2) ...
            [(mean(Vh.(fieldV2{p_v(tt(k),1)}))+mean(Vh.(fieldV2{p_v(tt(k),2)})))/2  ...
             (mean(Vh.(fieldV2{p_v(tt(k),3)}))+mean(Vh.(fieldV2{p_v(tt(k),4)})))/2 Vhmid
t]./((mean(Vh.(fieldV2{p_v(tt(k),3)}))+mean(Vh.(fieldV2{p_v(tt(k),4)})))/2) ],2) ;
```

```
    end

    %%%%%%%%%%%% Horizontally %%%%%%%%%%%%%%%%

        if k == 4 || k==8    % Hori.
         tt =[0 0 0 1 0 0 0 2];
         pfit(:,k) = polyfit([r_h r_h],[ [...
             (mean(Vl.(fieldV2{p_h(tt(k),1)}))+mean(Vl.(fieldV2{p_h(tt(k),2)})))/2  ...
             (mean(Vl.(fieldV2{p_h(tt(k),3)}))+mean(Vl.(fieldV2{p_h(tt(k),4)})))/2 Vlmid
t]./((mean(Vl.(fieldV2{p_h(tt(k),3)}))+mean(Vl.(fieldV2{p_h(tt(k),4)})))/2) ...
            [(mean(Vh.(fieldV2{p_h(tt(k),1)}))+mean(Vh.(fieldV2{p_h(tt(k),2)})))/2  ...
             (mean(Vh.(fieldV2{p_h(tt(k),3)}))+mean(Vh.(fieldV2{p_h(tt(k),4)})))/2 Vhmid
t]./((mean(Vh.(fieldV2{p_h(tt(k),3)}))+mean(Vh.(fieldV2{p_h(tt(k),4)})))/2) ],2) ;
        end
end
```

Mean wind speed vector for radius fit

```
Vgx = [Vpx(6) (Vpx(6)+Vpx(7))/2 Vpx(7) (Vpx(7)+Vpx(11))/2 Vpx(11) (Vpx(10)+Vpx(11))/2 Vp
x(10) (Vpx(10)+Vpx(6))/2];
```

Genertate mesh

```
R  = [0.1 1.1]; %Rotor begining and blade ending radius

for n=1:NL % for all lines
for rr=1:2; % For rotor begining and blade ending
    r=R(rr); % choose length

    theta=2*pi/NL*n-2*pi/NL -(pi/2-pi/4); % Angle of line
    X(rr,n) = r*cos(theta); % The start and end X cordinates of wind mesh
    Y(rr,n) = r*sin(theta); % The start and end Y cordinates of wind mesh
end
end

for ll=1:NL % Generate NPPL discrete points in between line begining and endning
PointsX(ll,:) = linspace(X(1,ll),X(2,ll),NPPL);
PointsY(ll,:) = linspace(Y(1,ll),Y(2,ll),NPPL);
end

for lll=1:NL % Collect wind mesh in a matrix
POINTS(NPPL*(lll-1)+1:NPPL*lll,:) = [ PointsX(lll,:)' PointsY(lll,:)'];
end
```

Calculate distance between points

```
nNodes = NPPL*NL;           % Number of nodes
nodes.Y = PointsX;          % Grid of Xnodes
nodes.Z = PointsY;          % Grid of Ynodes

dy = zeros(nNodes,nNodes);    % matrix distance along y
dz = zeros(nNodes,nNodes);    % matrix distance along z
meanU = zeros(nNodes,nNodes); % mean wind speed between two nodes


for kk= 1:nNodes  % for all nodes
    for mm = 1:nNodes % for all nodes
```

```
        dy(kk,mm) = abs(nodes.Y(kk)-nodes.Y(mm));  % Calculate distance between nodes in
 y directon
        dz(kk,mm)  = abs(nodes.Z(kk)-nodes.Z(mm)); % Calculate distance between nodes in
 y directon
    end
end
```

Calculate mean velocity between points

```
% Assign velocities to all points

for n=1:NL % for all lines
PVm(n,:) = Vgx(n)*(pfit(1,n).*RV.^2 + pfit(2,n).*RV + pfit(3,n)); % using mean velocity
and linear fit, assign mean velocities too all points on line

end

for kk= 1:nNodes,
    for mm = 1:nNodes,
meanU(kk,mm)  =  0.5.*(PVm(kk)+PVm(mm)); % For all nodes calc mean velocity between them
    end
end
```

```
   for jj = 1: 1:length(fp),
    % co-coherence function
    coh_u = exp( -12 * fp(jj) *0.1*sqrt(dy.^2+dz.^2)./ (meanU) );

 for kk = 1:NL*NPPL % For all nodes
 o = floor(kk/20)+1; % counter on which line is to be used

     if kk < 21*b-20 + 7  % for first points on line choose middle PSD box (9)
        Su11(jj,kk) = PSDx_box(9,jj);
     else % For other points use respective PSD box, in which the line lie.
        Su11(jj,kk) = PSDx_box(o,jj);
     end
 end
       Su=Su11(jj,:)'; % Transpose and save
end

    Suu = sqrt(Su*Su').*coh_u; % Fund spectral matrix between points

    phi = 2*pi.*rand((nNodes),1); % Make random angle vector
    phi=repmat(phi,[1,Nsteps]);   % Replicate to make it as long as the time series
    ft =fp(jj).*repmat(t,[(nNodes),1]); % The frequency vector, replicate to fit

    A=cos(2.*pi.*ft+phi); % The sinusoidal behaviour of wind signal
    [B,F]=ldl(Suu,'lower'); % LDL decom. to get lower triangular matrix
    H = B*sqrt(F); % find lower spectral matrix
    dummySpeed = dummySpeed + sqrt(2*df).*abs(H)*A; % calculate turbulent wind time seri
es for each frequency and add

   end

dummySpeedm = repmat(PVm(:),1,size(dummySpeed,2))+dummySpeed; % Take mean velocity for p
oints and add turbulent wind series.
```

A.11.7.3 Tower Shadow Model

Contents

- Free stream rotor inflow velocity
- Init. matrices
- Tower shadow
- Save velocities


```
function [step,V_x,V_y,V0,VP] = Untitled(prevstep,Vxlast, time, Rt, center, POINTS, TowP
OINTX, dTR, V_0, V_ext,ramp, PVm)
```

```
 %-------------------------------------------------------------------%
%         This program was developed by the group EN10-1
%         Aalborg Universitet Esbjerg, Energy Department
%             P9 and P10 Autumn 2017 and spring 2018
%         Jesper Jensen, Kasper Laugesen, Kasper Jessen &
%                          Signe Mortensen
%-------------------------------------------------------------------%
                    % Function for assigning the wind speed to the blades,
                    % and aplying tower shadow to the free wind field

 NPPL=20; % Number of discrete points per line, which should have a wind speed time seri
es
 NL  =16; % Number lines
```

Free stream rotor inflow velocity

```
step = floor(time+1.1); % Set step counter, in order to load in the right wind speed fro
m the generated wind field

Windfield = 3; % 1 mean wind speed (TS =1), 2 mean wind speed + TLP motion(TS =1), 3 Tur
bulent wind + TLP motion(TS =1)
TowShadow = 1; % 1 - ON / 0 - OFF

if Windfield == 1 % The mean wind speed in all points at given RPM + Veloity of tower an
d TLP
UV = (repmat(sum(PVm)/size(PVm,1),NL,1))'*ramp + V_ext ;
V0 = (repmat(sum(PVm)/size(PVm,1),NL,1))'*ramp + V_ext;
end

if Windfield == 2 % A constant wind speed of 7 in all points, used for testing code.
    UV = ones(NPPL,NL)*7*ramp + V_ext;
    V0 = ones(NPPL,NL)*7*ramp ;
end

if Windfield == 3 % Turbulent wind field witg external movement too, this is used for si
mulation
    UV = (V_0(:,:,step))*ramp + V_ext; % rotor speed free stream + movement of TLP
    V0 = UV;
end
```

Init. matrices

```
%[Removed]
```

Tower shadow

```
if TowShadow == 1 % Include tower shadow, if TowShadow = 1
```

```
for n11 = 1:NL % For all lines, This is used to see which lines there should be tower sh
adow included in.
    % Which is only lines in the lower half plane
    theta=2*pi/NL*n11-2*pi/NL; % Vector of the angle of the different lines
   if  theta <pi  % If lines are at an angle below pi set to zero
       TowCor(n11) = 0;
   else  % If lines are at an angle ablove pi set one
       TowCor(n11) = 1;
   end
   if theta == 0 % at angle equal to zero, set to one
       TowCor(n11) = 1;
   end
end


for n11 = 1:NL      %For all lines make vector with cordinates of points

TowCor1 = TowCor(n11); % Find if tower model should be used for this line

    if TowCor1==1 % Find only points to be used in tower shadow model
     POINTSTOW(NPPL*n11-(NPPL-1):NPPL*n11,:) = POINTS(NPPL*n11-(NPPL-1):NPPL*n11,:)-cent
er; % z y from origin (0,0)
    else % If not used, set points to zero
     POINTSTOW(NPPL*n11-(NPPL-1):NPPL*n11,:) = zeros(NPPL,2);
    end

end

 RP  = sqrt((POINTSTOW(:,1)).^2+(POINTSTOW(:,2)).^2); % distance from rotor center to po
ints P


 for n11 = 1:NL      %For all lines, find distance from tower to lines

     TowCor1 = TowCor(n11);% Find if tower model should be used for this line

    if TowCor1==1% Find ony points to be used in tower shadow model

     TowPOINTX(NPPL*n11-(NPPL-1):n11*NPPL,:) = POINTSTOW(NPPL*n11-(NPPL-1):NPPL*n11 , 1)
'; % Get x postion of line (length from horizontal axis)
           RTP(NPPL*n11-(NPPL-1):n11*NPPL,:) = sqrt((TowPOINTX(NPPL*n11-(NPPL-1):NPPL*n1
1 , 1).^2 + (dTR).^2)); % Use x postion and the distance betwen tower and rotor plane

    else % If not tower model should be used for this line set to zero

     RTP(NPPL*n11-(NPPL-1):n11*NPPL,:) = 0;

    end

 end

 % Tower shadow calculation of wind speed.
 for ll = 1 : NL % For all lines
     TowCor1 = TowCor(ll);  % Find if tower model should be used for this line
```

```
    if TowCor1 == 1% Tower model should be used for this line

  RTP1   = RTP(ll*NPPL-(NPPL-1):ll*NPPL) ;
  TPX1   = TowPOINTX(ll*NPPL-(NPPL-1):ll*NPPL);
  COS = (TPX1./RTP1);
  SIN = -(dTR./RTP1);

  Vr(:,ll)     =   UV(:,ll).*(1-(Rt./(RTP1)).^2).* COS;
  Vtheta(:,ll) = - UV(:,ll).*(1+(Rt./(RTP1)).^2).* SIN;

  Vx(:,ll)     =   Vr(:,ll).*COS - Vtheta(:,ll).*SIN;
  Vy(:,ll)     = - Vr(:,ll).*SIN - Vtheta(:,ll).*COS;

    else % if not tower model should be used for this line, use free stream wind veloci
ty and no tangential wind velocity


        Vx(:,ll) = UV(ll*NPPL-(NPPL-1):ll*NPPL);
        Vy(:,ll) = 0;

    end

 end
```

Save velocities

```
 if Towersha == 1 % Use tower shadow corrected wind speeds, if TowSha=1
V_x = Vx; %  Use wind speed in discrete points for axial direction with tower shadow eff
ect.
V_y = Vy; % Use wind speed in discrete points for tangential direction with tower shadow
 effect.

else % If not tower shadow model is initlized us free stream velocity
V_x = UV;   % Use wind speed in discrete points for axial direction without tower shadow
 effect.
V_y = UV*0; %Set wind speed in discrete points for tangential direction without tower sh
adow effect.
 end
```

```
end
```

Published with MATLAB® R2016a

A.11.8 Extended Kalman Filter Code

Contents

- Load Constants
- Jacobian matrix
- Step 2
- Step 3 Compute Kalman Gain
- Step 4 Measurement update


```
%-----------------------------------------------------------------%
%         This program was developed by the group EN10-1
%         Aalborg Universitet Esbjerg, Energy Department
%             P9 and P10 Autumn 2017 and spring 2018
%         Jesper Jensen, Kasper Laugesen, Kasper Jessen &
%                           Signe Mortensen
%-----------------------------------------------------------------%
          %%%%%%% Extended Kalman Filter Function %%%%%%%

function [x_est, P_est,K] = fcn(I_dq, u_prev, x_est_prev, P_est_prev,GenPar)
```

Load Constants

```
J           = GenPar(1);    % Mass moment of inertia
lambda_r    = GenPar(2);    % Rotor Flux linkage
poles       = GenPar(3);    % No. of pole pairs
Ts          = GenPar(4);    % Time Step
Rs          = GenPar(5);    % Stator Resistance
B           = GenPar(6);    % Viscous Damping
Gear        = GenPar(7);    % Gear Ratio
Ld          = GenPar(8);    % Inductance d-axis
Lq          = GenPar(9);    % Inductance q-axis
Gear_Eff    = GenPar(10);   % Gear Efficiency
Gen_Eff     = GenPar(11);   % Generator Efficiency

Eff = Gear_Eff*Gen_Eff;     % Combined Gear and Generator efficiency

C = [1 0 0 0;
     0 1 0 0];                          % Output Matrix
Q  = diag([0.01 0.01 0.01e-3 0.01]);    % State covariance matrice
R  = diag([1 0.001]);                   % Sensor/Input covariance matrice
```

Jacobian matrix

```
k1 =  1/2 * Gear * poles;   % Constant
Jacobian =  [-Rs/Ld                     Lq/Ld*k1*x_est_prev(3)                  Lq/Ld*k1*x
_est_prev(2)                    0
             -Ld/Lq*k1*x_est_prev(3)    -Rs/Lq                                  -k1*(Ld*x_
est_prev(1)+lambda_r)/Lq       0
             1/J* k1/Eff * 3/2 * (Ld-Lq)*x_est_prev(2)   1/J*k1/Eff * 3/2 *((Ld-Lq)*x_est_
prev(1)+lambda_r)     -B/J     0
             0                          0                                       k1
                                0];
A_k = eye(size(Jacobian)) + Jacobian*Ts; % Linearized System matrix
```

Step 2

State Pediction (Nonlinear equation)

```
g1 = 1/Ld*(u_prev(1)-Rs*x_est_prev(1)+k1*Lq*x_est_prev(3)*x_est_prev(2));
                              % Derivative d-axis current
g2 = 1/Lq*(u_prev(2) - Rs*x_est_prev(2) - k1*Ld*x_est_prev(3)*x_est_prev(1)  - lambda_r*k1
*x_est_prev(3));              % Derivative q-axis current
g3 = 1/J * (-B*x_est_prev(3) - u_prev(3) + k1/Eff*3/2*(lambda_r*x_est_prev(2) + (Ld-Lq)*x_
est_prev(1)*x_est_prev(2)));  % Derivative of current rotor speed
g4 = k1 * x_est_prev(3);
                              % Derivative of electric angle

% Step 2 (a) Non-linear preditcion of x
x_pred = x_est_prev + Ts*[g1 g2 g3 g4]';

% Step 2 (b) Error Covariance prediction
P_pred = A_k*P_est_prev*A_k' + Q;
```

Step 3 Compute Kalman Gain

```
y_est_pred  = C * x_pred;                                % Predicted output estimate
y_err       = I_dq - y_est_pred;                         % Output estimate error
S           = C*P_pred*C'+R;                             %
K           = (P_pred*C'/S);                             % Kalman Gain
```

Step 4 Measurement update

```
x_est       = x_pred+K*y_err;                            % Estimate states
P_est       = (eye(length(A_k)) - K * C) * P_pred;       % State covariance
```

Published with MATLAB® R2016a

A.11.9 Extended Kalman Filter Code

Contents

- Constants
- Angle Calculation
- Calculate Switch time


```
%-------------------------------------------------------------%
%         This program was developed by the group EN10-1
%         Aalborg Universitet Esbjerg, Energy Department
%             P9 and P10 Autumn 2017 and spring 2018
%         Jesper Jensen, Kasper Laugesen, Kasper Jessen &
%                          Signe Mortensen
%-------------------------------------------------------------%
                    %%%%%%% SPWM Function %%%%%%%
                % Determine the duty cycles for the IGBT's



function [Da, Db, Dc] = DutyCyleGen(Ud, Uq)
```

Constants

```
T = 5000;       % Switching frequency
```

Angle Calculation

```
B = atan2d(Uq, Ud);

% Calculation of sector and basic vector
%%%%%%%%%%%%%%%%%%%%%%%%%%%%%%%%%%%%%%%%%%%%%%
if B >= 60 && B < 120 %N == 1
    Q = 2;
    Ux = [-1/sqrt(6); 1/sqrt(2)];
    Uy = [1/sqrt(6); 1/sqrt(2)];

elseif B >= -60 && B < 0 % N == 2
    Q = 6;
    Ux = [sqrt(2)/sqrt(3); 0];
    Uy = [1/sqrt(6); -1/sqrt(2)];

elseif B >= 0 && B < 60 %N == 3
    Q = 1;
    Ux = [sqrt(2)/sqrt(3); 0];
    Uy = [1/sqrt(6); 1/sqrt(2)];

elseif B >= -180 && B < -120 %N == 4
    Q = 4;
    Ux = [-1/sqrt(6); -1/sqrt(2)];
    Uy = [-sqrt(2)/sqrt(3); 0];
elseif B >= 120 && B <= 180 %N == 5
    Q = 3;
    Ux = [-1/sqrt(6); 1/sqrt(2)];
    Uy = [-sqrt(2)/sqrt(3); 0];
elseif B >= -120 && B < -60 % N == 6
    Q = 5;
```

```
    Ux = [-1/sqrt(6); -1/sqrt(2)];
    Uy = [1/sqrt(6); -1/sqrt(2)];
else
    %set duty to 0
    Da = 0;      % If an error occur
    Db = 0;      % If an error occur
    Dc = 0;      % If an error occur
    return;

end
```

Calculate Switch time

T1 T2 and T0 Where Time = [T1; T]

```
n1 = sqrt(3)/sqrt(2);                       % Normalization of basicvector
n2 = (sqrt(1-0.5^2))/(sqrt(2));      % Normalization of Vdq

Time = T * (n1*[Ux Uy])^(-1) * n2*[Ud; Uq];
T1 = Time(1);
T2 = Time(2);
T0 = T - T1 - T2;


% Determine SVPWM waveform Pattern
%%%%%%%%%%%%%%%%%%%%%%%%%%%%%%%%%%%%

%Section 1
if Q == 1
    Da = (T1 + T2 + T0/2)/T;
    Db = (T2 + T0/2)/T;
    Dc = (T0/2)/T;

%Section 2
elseif Q == 2
    Da = (T2 + T0/2)/T;
    Db = (T1 + T2 + T0/2)/T;
    Dc = (T0/2)/T;

%Section 3
elseif Q == 3
    Da = (T0/2)/T;
    Db = (T1 + T2 + T0/2)/T;
    Dc = (T2 + T0/2)/T;

%Section 4
elseif Q == 4
    Da = (T0/2)/T;
    Db = (T2 + T0/2)/T;
    Dc = (T1 + T2 + T0/2)/T;

%Section 5
elseif Q == 5
    Da = (T2 + T0/2)/T;
    Db = (T0/2)/T;
    Dc = (T1 + T2 + T0/2)/T;

%Section 6
elseif Q == 6
```

```
    Da = (T1 + T2 + T0/2)/T;
    Db = (T0/2)/T;
    Dc = (T2 + T0/2)/T;

else
    Da = 0;      % If an error occur
    Db = 0;      % If an error occur
    Dc = 0;      % If an error occur
end
```

Published with MATLAB® R2016a

A.12 Simulink Models

A.12.1 Overall Simulink Model

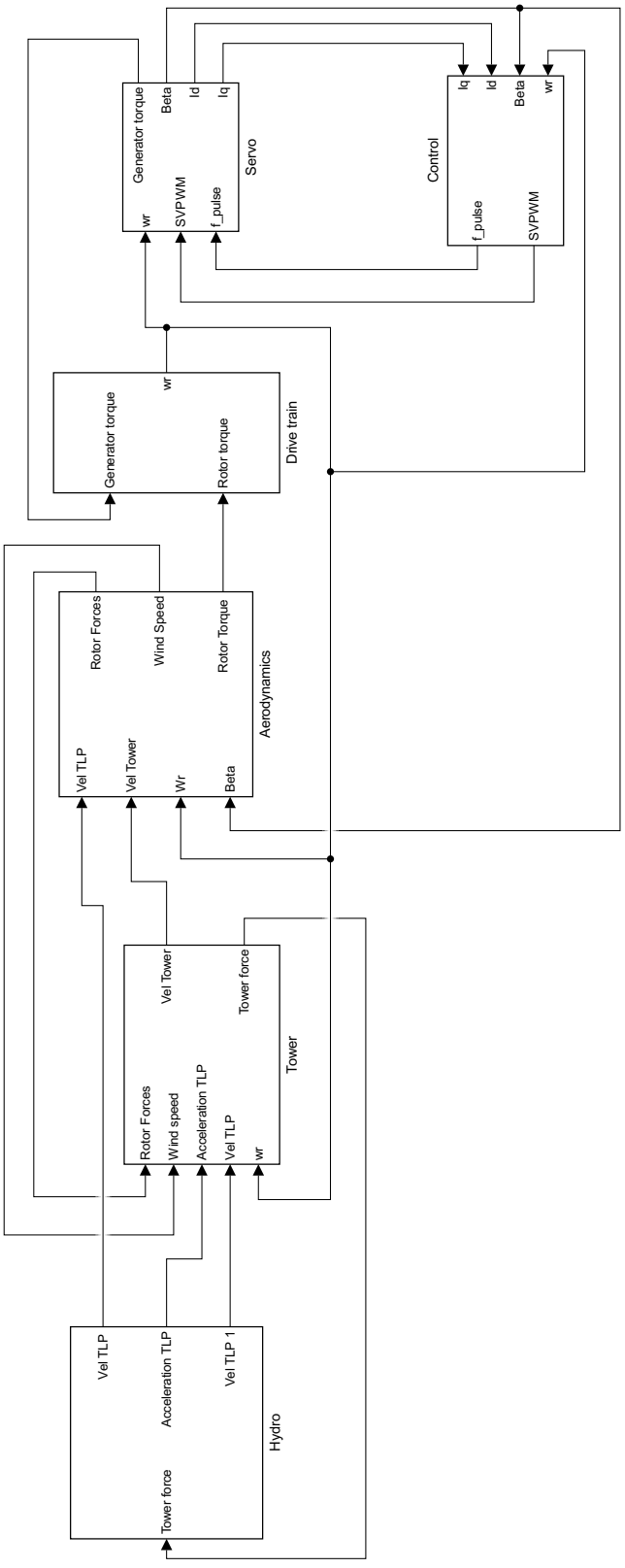

A.12.2 Hydrodynamic Simulink Model

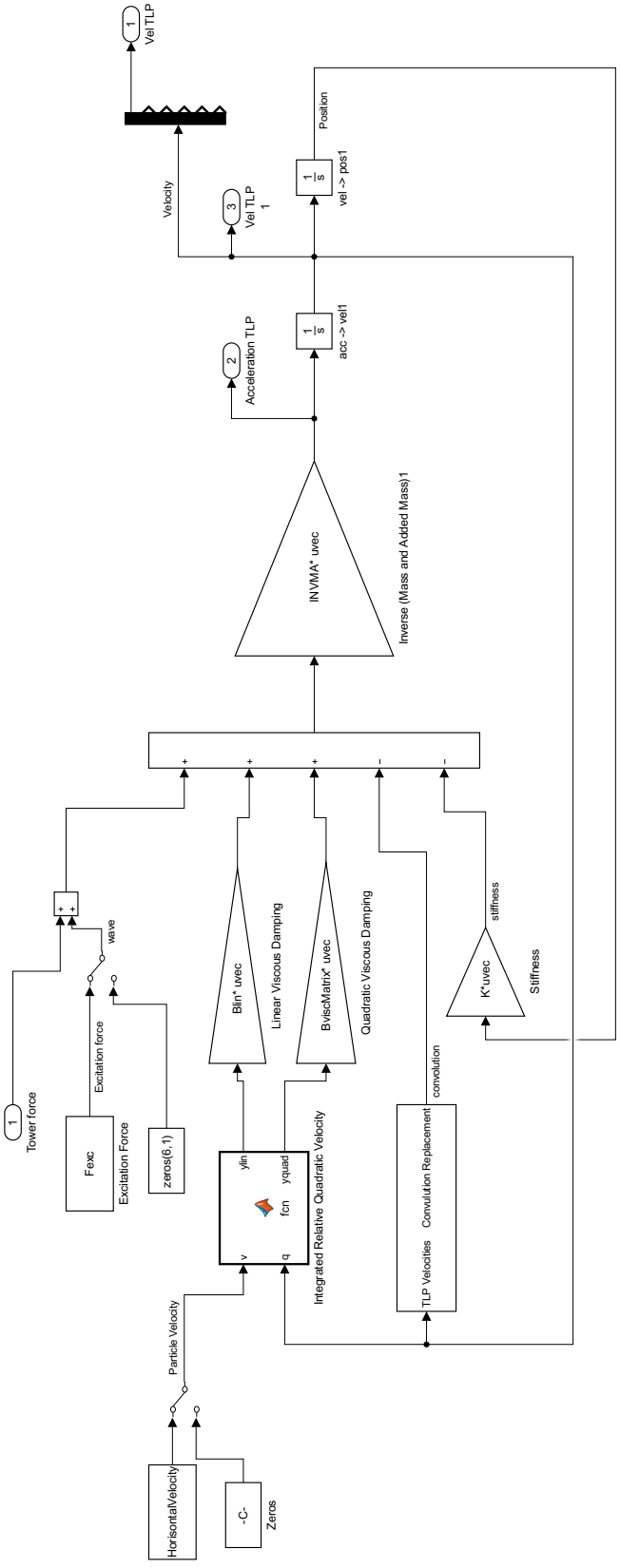

A.12.3 Tower Simulink Model

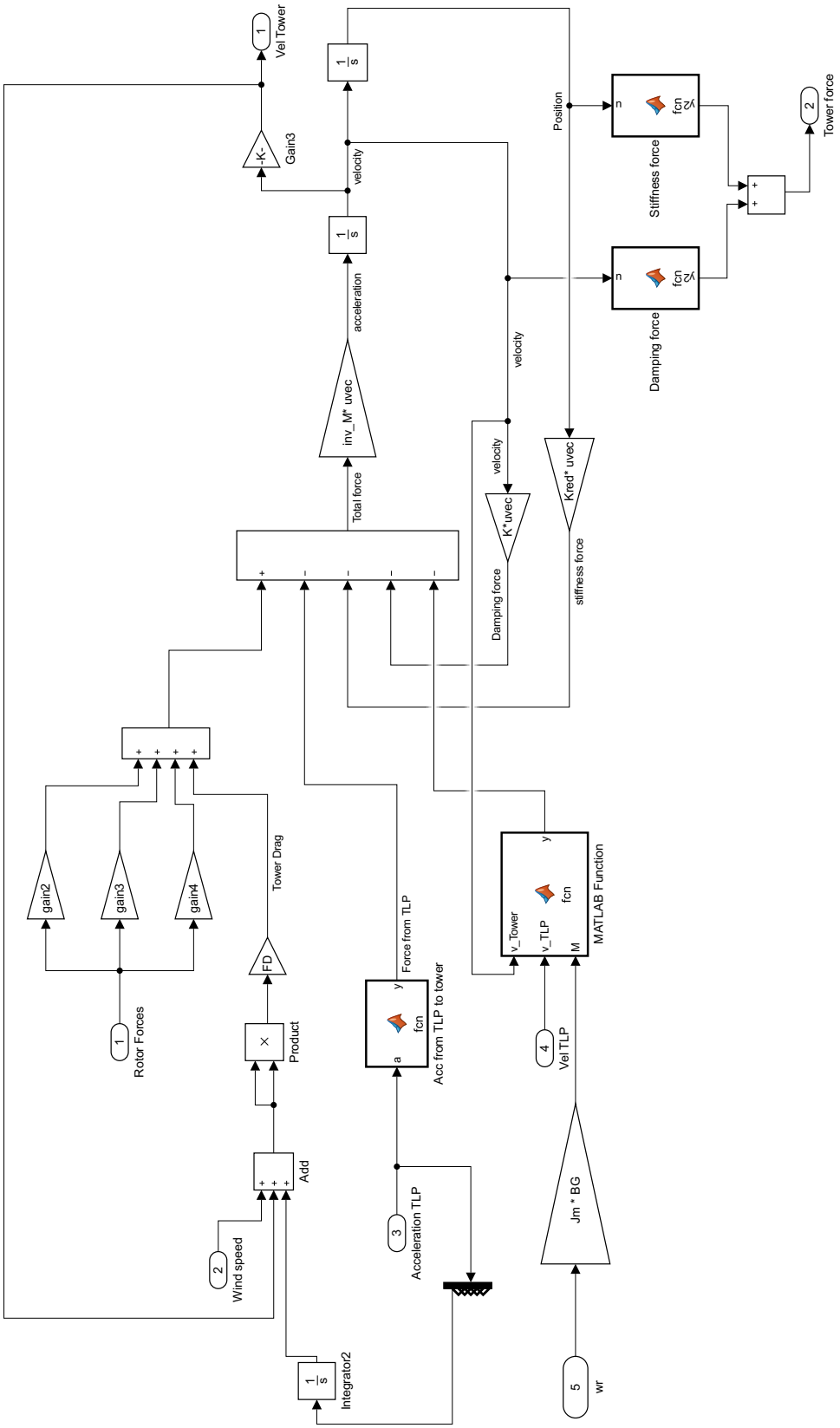

A.12.4 Aerodynamic Simulink Model

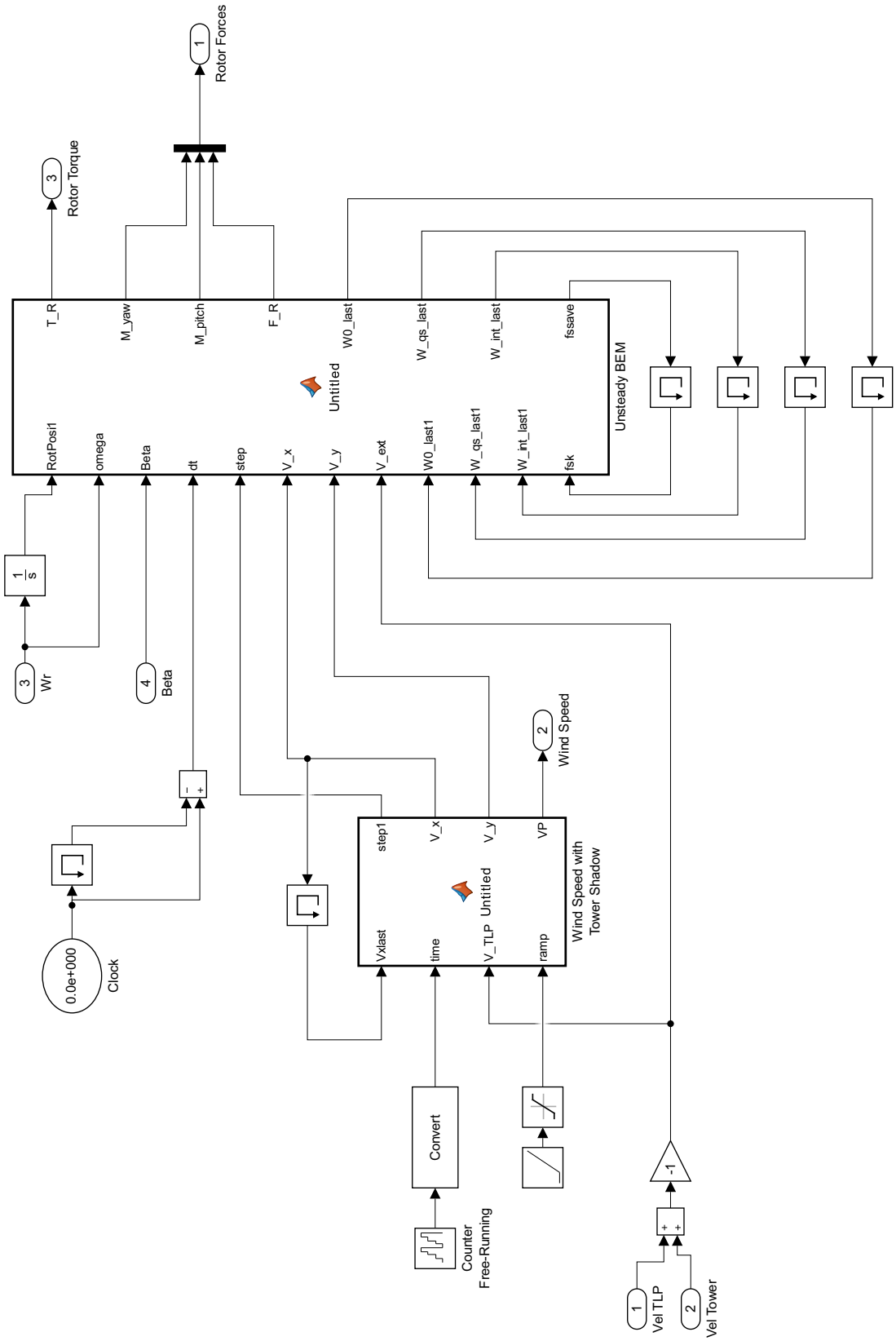

A.12.5 Drive Train Simulink Model

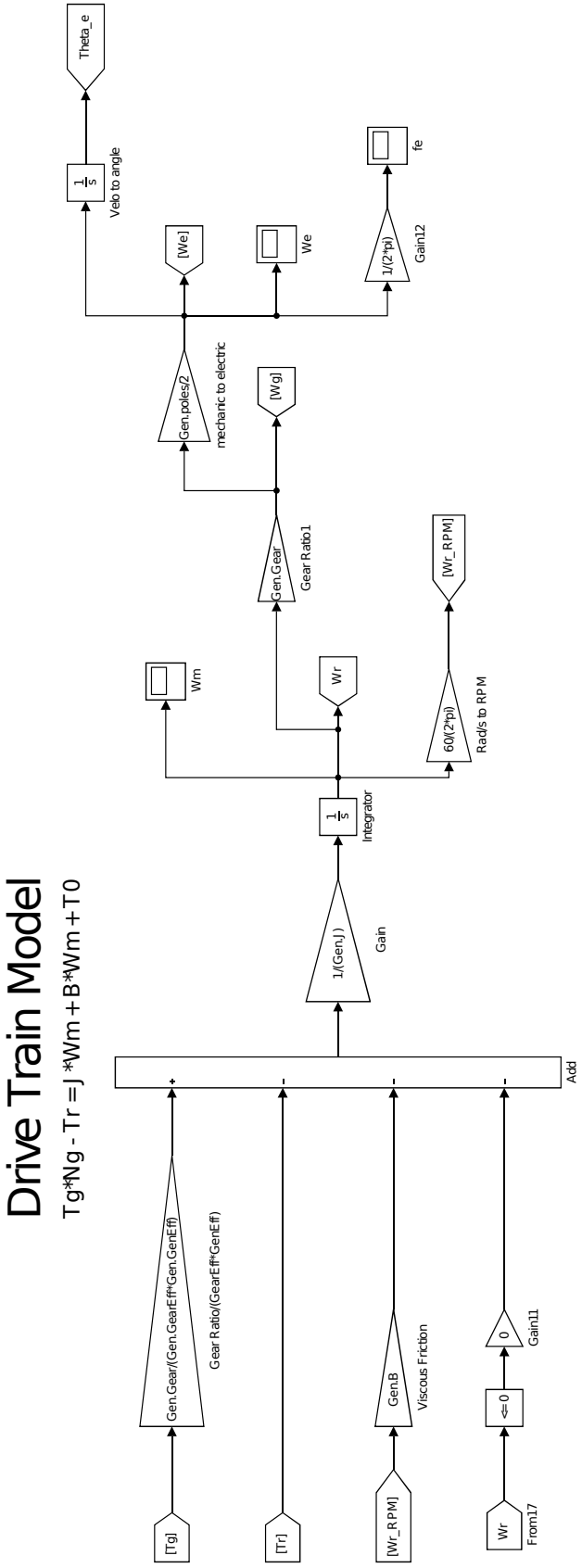

A.12.6 Generator Simulink Model

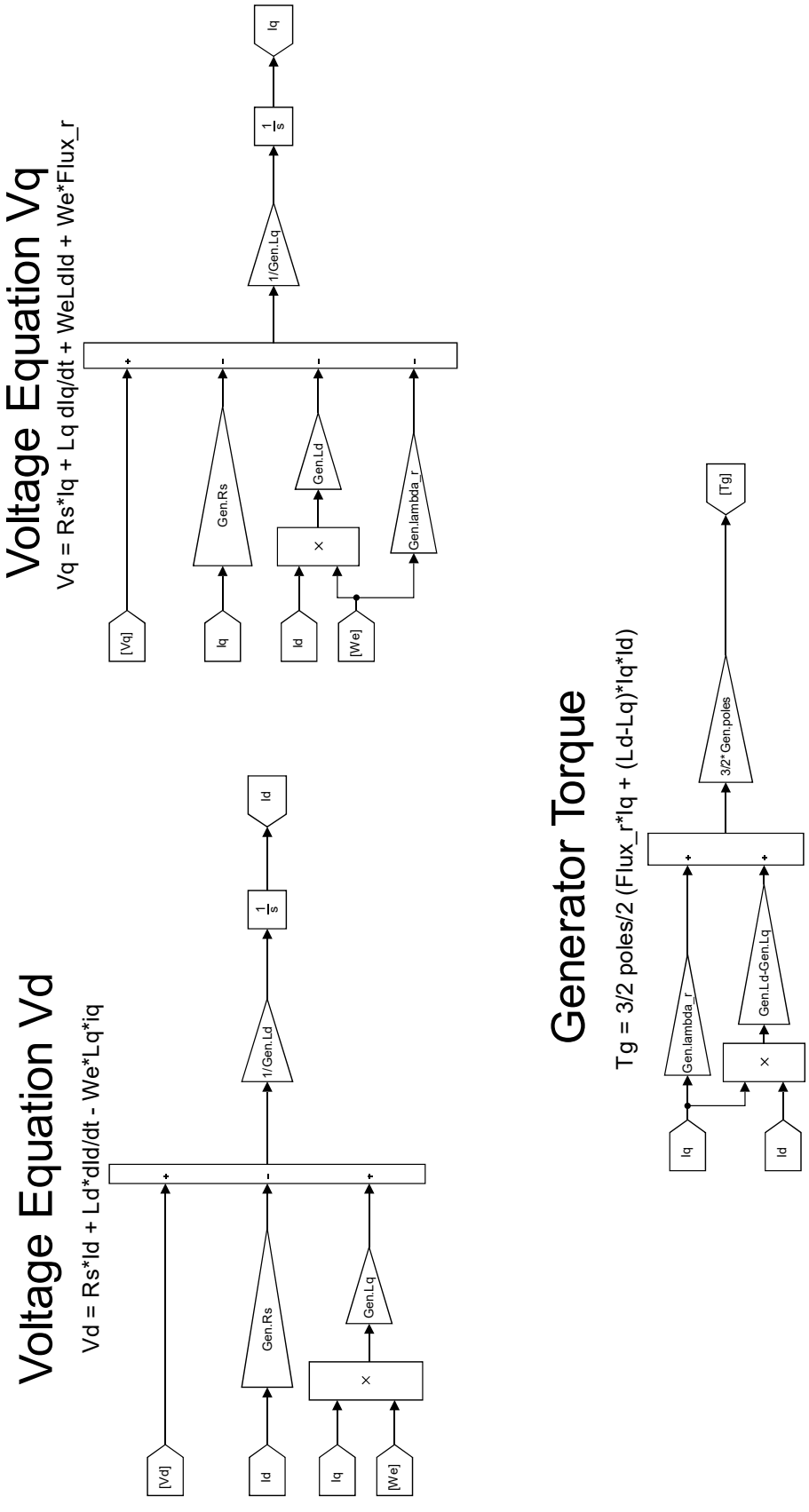

A.12.7 Field Oriented Control Simulink Model

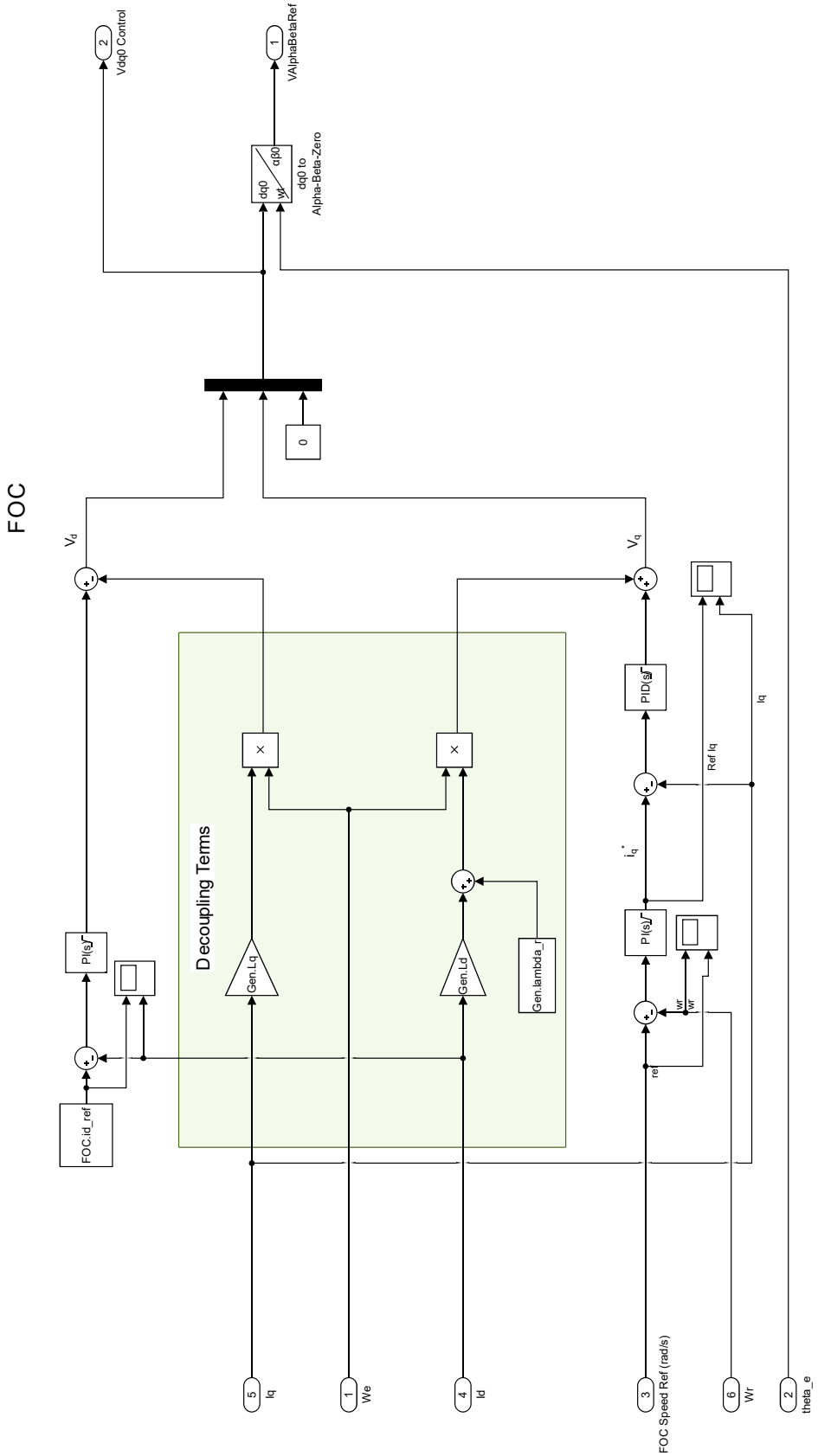

A.12.8 Power Converter Simulink Model

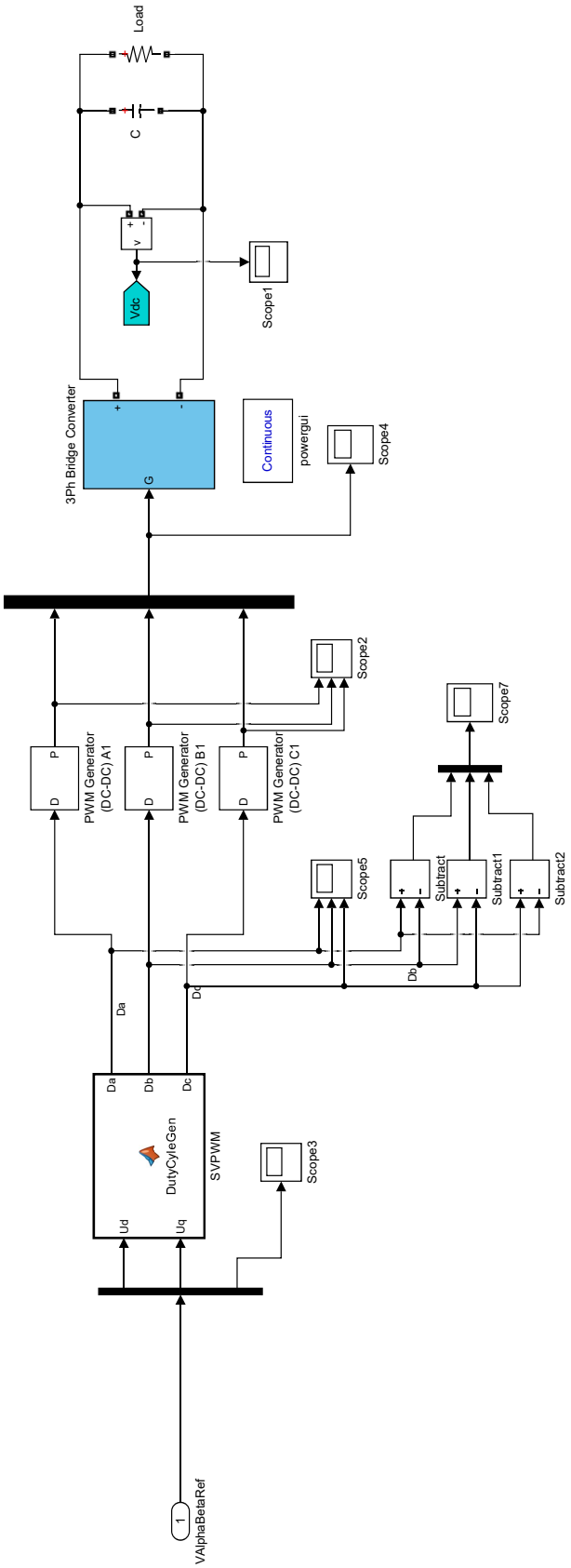

A.12.9 Extended Kalman Filter Simulink Model

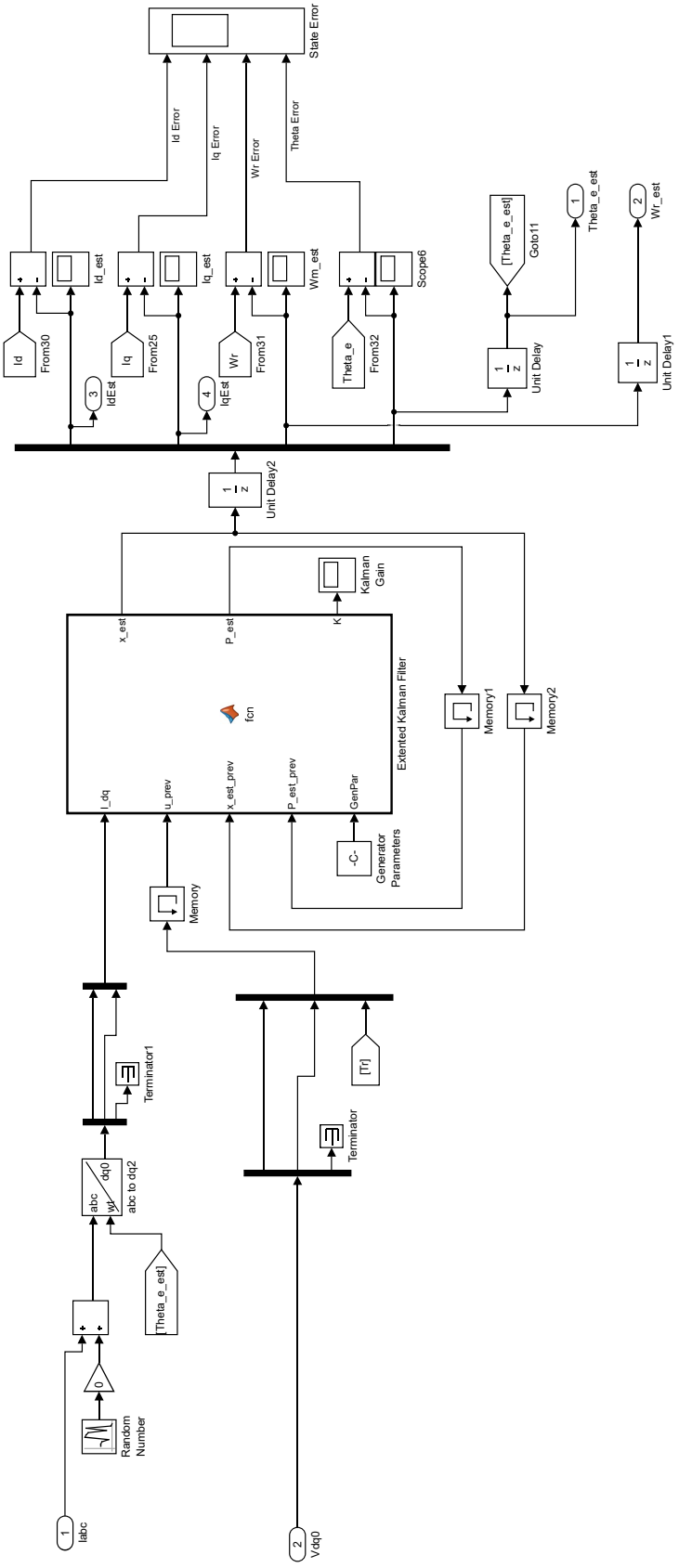

A.12.10 Blade Pitch Control Simulink Model

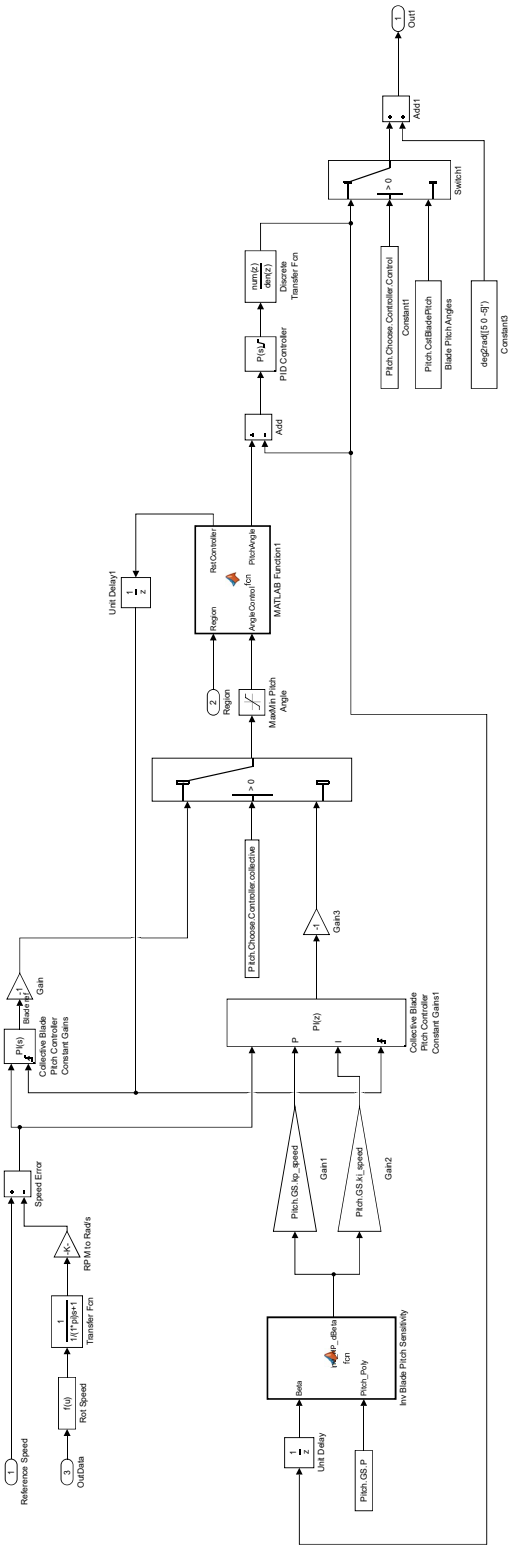

A.12.11 FAST Simulink Model

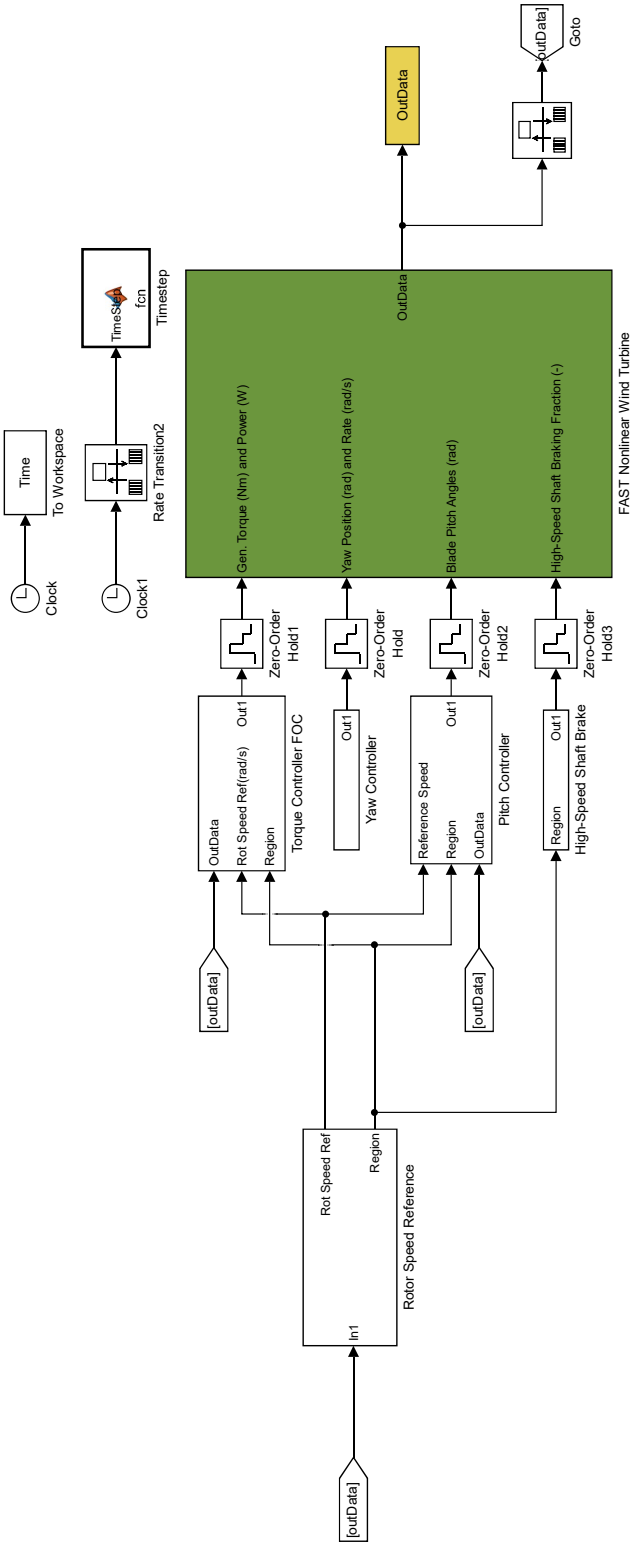

A.13 FAST Input files

A.13.1 AAUE-TLP

```
C:\Users\-Jesper K Jensen\Aalborg Universitet\OneDrive - Aalborg Universitet\EN1-B305\P9_10\Projekt\Matlab\FAST\CertTest\AAUETLP.fst                                                
```

A.13.2 AAUE-TLP ElastoDyn Input File

... Jensen\Aalborg Universitet\OneDrive - Aalborg Universitet\EN1-B305\P9_10\Projekt\Matlab\FAST\CertTest\AAUETLP\AAUETLP_ElastoDyn.dat 1

```
1  ---------e ELASTODYN v1.03.* INPUT FILE ------------------------------------------
2  AAUETLP, Edited by Jesper Kirkegaard Jensen, Kasper Laugesen, Kasper Jessen & Signe Mortensen
3  ---------------------- SIMULATION CONTROL --------------------------------------
4  False         Echo        - Echo input data to "<RootName>.ech" (flag)
5        3       Method      - Integration method: {1: RK4, 2: AB4, or 3: ABM4} (-) 3
6    0.001       DT          - Integration time step (s) "default" E-4 1.25E-03 hydro-elasto:0.020
7  ---------------------- ENVIRONMENTAL CONDITION ----------------------------------
8      9.81584   Gravity     - Gravitational acceleration (m/s^2)
9  ---------------------- DEGREES OF FREEDOM ---------------------------------------
10 False         FlapDOF1    - First flapwise blade mode DOF (flag) True
11 False         FlapDOF2    - Second flapwise blade mode DOF (flag) True
12 False         EdgeDOF     - First edgewise blade mode DOF (flag) True
13 False         TeetDOF     - Rotor-teeter DOF (flag) [unused for 3 blades]
14 False         DrTrDOF     - Drivetrain rotational-flexibility DOF (flag)
15 True          GenDOF      - Generator DOF (flag)
16 False         YawDOF      - Yaw DOF (flag)
17 True          TwFADOF1    - First fore-aft tower bending-mode DOF (flag)
18 True          TwFADOF2    - Second fore-aft tower bending-mode DOF (flag)
19 True          TwSSDOF1    - First side-to-side tower bending-mode DOF (flag)
20 True          TwSSDOF2    - Second side-to-side tower bending-mode DOF (flag)
21 True          PtfmSgDOF   - Platform horizontal surge translation DOF (flag)
22 True          PtfmSwDOF   - Platform horizontal sway translation DOF (flag)
23 True          PtfmHvDOF   - Platform vertical heave translation DOF (flag)
24 True          PtfmRDOF    - Platform roll tilt rotation DOF (flag)
25 True          PtfmPDOF    - Platform pitch tilt rotation DOF (flag)
26 True          PtfmYDOF    - Platform yaw rotation DOF (flag)
27 ---------------------- INITIAL CONDITIONS ---------------------------------------
28       0   OoPDefl     - Initial out-of-plane blade-tip displacement (meters)
29       0   IPDefl      - Initial in-plane blade-tip deflection (meters)
30       0   BlPitch(1)  - Blade 1 initial pitch (degrees)
31       0   BlPitch(2)  - Blade 2 initial pitch (degrees)
32       0   BlPitch(3)  - Blade 3 initial pitch (degrees) [unused for 2 blades]
33       0   TeetDefl    - Initial or fixed teeter angle (degrees) [unused for 3 blades]
34       0   Azimuth     - Initial azimuth angle for blade 1 (degrees)
35      71   RotSpeed    - Initial or fixed rotor speed (rpm)
36       0   NacYaw      - Initial or fixed nacelle-yaw angle (degrees)
37    0.00   TTDspFA     - Initial fore-aft tower-top displacement (meters)
38       0   TTDspSS     - Initial side-to-side tower-top displacement (meters)
39     0.0   PtfmSurge   - Initial or fixed horizontal surge translational displacement of platform  (meters)
40    0.00   PtfmSway    - Initial or fixed horizontal sway translational displacement of platform  (meters)
41  -0.002   PtfmHeave   - Initial or fixed vertical heave translational displacement of platform ( meters)
42       0   PtfmRoll    - Initial or fixed roll tilt rotational displacement of platform (degrees)
43     0.0   PtfmPitch   - Initial or fixed pitch tilt rotational displacement of platform (degrees)
44     0.0   PtfmYaw     - Initial or fixed yaw rotational displacement of platform (degrees)
45 ---------------------- TURBINE CONFIGURATION ------------------------------------
46       3   NumBl       - Number of blades (-) AAUETLP
47  1.0671   TipRad      - The distance from the rotor apex to the blade tip (meters)
48  0.0771   HubRad      - The distance from the rotor apex to the blade root (meters)
49       0   PreCone(1)  - Blade 1 cone angle (degrees)
50       0   PreCone(2)  - Blade 2 cone angle (degrees)
51       0   PreCone(3)  - Blade 3 cone angle (degrees) [unused for 2 blades]
52       0   HubCM       - Distance from rotor apex to hub mass [positive downwind] (meters)
53       0   UndSling    - Undersling length [distance from teeter pin to the rotor apex] (meters)  [unused for 3 blades]
```

A.13.3 AAUE-TLP ElastoDyn Input File


```
          0   Delta3      - Delta-3 angle for teetering rotors (degrees) [unused for 3 blades]
          0   AzimB1Up    - Azimuth value to use for I/O when blade 1 points up (degrees) 0.22
      -0.05   OverHang    - Distance from yaw axis to rotor apex [3 blades] or teeter pin [2 blades]  (meters) (AAUETLP: -0.258)
       0.10   ShftGagL    - Distance from rotor apex [3 blades] or teeter pin [2 blades] to shaft strain gages [positive for upwind rotors] (meters)
        0.0   ShftTilt    - Rotor shaft tilt angle (degrees)
     0.0146   NacCMxn     - Downwind distance from the tower-top to the nacelle CM (meters)
          0   NacCMyn     - Lateral  distance from the tower-top to the nacelle CM (meters)
     0.1176   NacCMzn     - Vertical distance from the tower-top to the nacelle CM (meters)
          0   NcIMUxn     - Downwind distance from the tower-top to the nacelle IMU (meters)
          0   NcIMUyn     - Lateral  distance from the tower-top to the nacelle IMU (meters)
        0.0   NcIMUzn     - Vertical distance from the tower-top to the nacelle IMU (meters)
     0.0520   Twr2Shft    - Vertical distance from the tower-top to the rotor shaft (meters)
       2.11   TowerHt     - Height of tower above ground level [onshore] or MSL [offshore] (meters)
        0.3   TowerBsHt   - Height of tower base above ground level [onshore] or MSL [offshore] (meters)
          0   PtfmCMxt    - Downwind distance from the ground level [onshore] or MSL [offshore] to the platform CM (meters)
          0   PtfmCMyt    - Lateral distance from the ground level [onshore] or MSL [offshore] to the platform CM (meters)
      -0.06   PtfmCMzt    - Vertical distance from the ground level [onshore] or MSL [offshore] to the platform CM (meters)
       0.00   PtfmRefzt   - Vertical distance from the ground level [onshore] or MSL [offshore] to the platform reference point (meters)
---------------------- MASS AND INERTIA ----------------------------------------
          0   TipMass(1)  - Tip-brake mass, blade 1 (kg)
          0   TipMass(2)  - Tip-brake mass, blade 2 (kg)
          0   TipMass(3)  - Tip-brake mass, blade 3 (kg) [unused for 2 blades]
      2.023   HubMass     - Hub mass (kg) 56780
     4.1E-3   HubIner     - Hub inertia about rotor axis [3 blades] or teeter axis [2 blades] (kg m^2)
      1E-05   GenIner     - Generator inertia about HSS (kg m^2)
      7.406   NacMass     - Nacelle mass (kg) 7.406
0.878296922   NacYIner    - Nacelle inertia about yaw axis (kg m^2)
          0   YawBrMass   - Yaw bearing mass (kg)
    114.000   PtfmMass    - Platform mass (kg)
14.25419862   PtfmRIner   - Platform inertia for roll tilt rotation about the platform CM (kg m^2)
14.25419862   PtfmPIner   - Platform inertia for pitch tilt rotation about the platform CM (kg m^2)
9.352674144   PtfmYIner   - Platform inertia for yaw rotation about the platform CM (kg m^2)
---------------------- BLADE ---------------------------------------------------
         20   BldNodes    - Number of blade nodes (per blade) used for analysis (-)
"AAUETLP_Blade.dat"    BldFile(1)  - Name of file containing properties for blade 1 (quoted string)
"AAUETLP_Blade.dat"    BldFile(2)  - Name of file containing properties for blade 2 (quoted string)
"AAUETLP_Blade.dat"    BldFile(3)  - Name of file containing properties for blade 3 (quoted string) [unused for 2 blades]
---------------------- ROTOR-TEETER --------------------------------------------
          0   TeetMod     - Rotor-teeter spring/damper model {0: none, 1: standard, 2: user-defined from routine UserTeet} (switch) [unused for 3 blades] Not used for AAUE-TLP
          0   TeetDmpP    - Rotor-teeter damper position (degrees) [used only for 2 blades and when  TeetMod=1]
          0   TeetDmp     - Rotor-teeter damping constant (N-m/(rad/s)) [used only for 2 blades and  when TeetMod=1]
          0   TeetCDmp    - Rotor-teeter rate-independent Coulomb-damping moment (N-m) [used only for 2 blades and when TeetMod=1]
          0   TeetSStP    - Rotor-teeter soft-stop position (degrees) [used only for 2 blades and when TeetMod=1]
          0   TeetHStP    - Rotor-teeter hard-stop position (degrees) [used only for 2 blades and when TeetMod=1]
          0   TeetSSSp    - Rotor-teeter soft-stop linear-spring constant (N-m/rad) [used only for 2 blades and when TeetMod=1]
          0   TeetHSSp    - Rotor-teeter hard-stop linear-spring constant (N-m/rad) [used only for 2 blades and when TeetMod=1]
---------------------- DRIVETRAIN ----------------------------------------------
        100   GBoxEff     - Gearbox efficiency (%)
          1   GBRatio     - Gearbox ratio (-)
8.67637E+08   DTTorSpr    - Drivetrain torsional spring (N-m/rad)
  6.215E+06   DTTorDmp    - Drivetrain torsional damper (N-m/(rad/s))
---------------------- FURLING -------------------------------------------------
False         Furling     - Read in additional model properties for furling turbine (flag) [must currently be FALSE)  Not used for AAU-ETLP
```

A.13.4 AAUE-TLP ElastoDyn Input File

```
... Jensen\Aalborg Universitet\OneDrive - Aalborg Universitet\EN1-B305\P9_10\Projekt\Matlab\FAST\CertTest\AAUETLP\AAUETLP_ElastoDyn.dat                3
"unused"     FurlFile   - Name of file containing furling properties (quoted string) [unused when  Furling=False]
---------------------- TOWER -----------------------------------------------
          20  TwrNodes   - Number of tower nodes used for analysis (-)
"AAUETLP_ElastoDyn_Tower.dat"    TwrFile    - Name of file containing tower properties (quoted string)
---------------------- OUTPUT ----------------------------------------------
False        SumPrint   - Print summary data to "<RootName>.sum" (flag)
           1 OutFile    - Switch to determine where output will be placed: {1: in module output file only; 2: in glue code output file only; 3: both} (currently unused)
True         TabDelim   - Use tab delimiters in text tabular output file? (flag) (currently unused)
"ES10.3E2"   OutFmt     - Format used for text tabular output (except time).  Resulting field should be 10 characters. (quoted string) (currently unused)
          30 TStart     - Time to begin tabular output (s) (currently unused)
           1 DecFact    - Decimation factor for tabular output {1: output every time step} (-) (currently unused)
           1 NTwGages   - Number of tower nodes that have strain gages for output [0 to 9] (-)
          15 TwrGagNd   - List of tower nodes that have strain gages [1 to TwrNodes] (-) [unused if NTwGages=0]
           0 NBlGages   - Number of blade nodes that have strain gages for output [0 to 9] (-)
           9 BldGagNd   - List of blade nodes that have strain gages [1 to BldNodes] (-) [unused if NBlGages=0]
             OutList    - The next line(s) contains a list of output parameters.  See OutListParameters.xlsx for a listing of available output channels, (-)
"RotSpeed"              - Low-speed shaft and high-speed shaft speeds (rpm)
"GenSpeed"              - Low-speed shaft and high-speed shaft speeds (rpm)
"NacYaw"                - Nacelle yaw angle and nacelle yaw error estimate
"TTDspFA"               - Tower fore-aft and side-to-side displacements and top twist
"PtfmSurge"             - Platform translational surge, sway, and heave displacements
"PtfmSway"              - Platform translational surge, sway, and heave displacements
"PtfmHeave"             - Platform translational surge, sway, and heave displacements
"PtfmRoll"              - Platform rotational roll, pitch and yaw displacements
"PtfmPitch"             - Platform rotational roll, pitch and yaw displacements
"PtfmYaw"               - Platform rotational roll, pitch and yaw displacements
"PtchPMzc1"               - Blade 1 pitch angle (position) (deg)
"PtchPMzc2"               - Blade 2 pitch angle (position) (deg)
"PtchPMzc3"               - Blade 3 pitch angle (position) (deg)
"RotPwr"                - The mechanical output power of the rotor
"RotTorq"               - Rotortorque (kNm)
END of input file (the word "END" must appear in the first 3 columns of this last OutList line)
---------------------------------------------------------------------
```

A.13.5 AAUE-TLP ElastoDyn Blade Input File

...er K Jensen\Aalborg Universitet\OneDrive - Aalborg Universitet\EN1-B305\P9_10\Projekt\Matlab\FAST\CertTest\AAUETLP\AAUETLP_Blade.dat 1

```
------- ELASTODYN V1.00.* INDIVIDUAL BLADE INPUT FILE --------------------------
AAUE-TLP blade input properties.
---------------------- BLADE PARAMETERS --------------------------------------
          20   NB1InpSt    - Number of blade input stations (-)
         3.0   B1dF1Dmp(1) - Blade flap mode #1 structural damping in percent of critical (%)
         3.0   B1dF1Dmp(2) - Blade flap mode #2 structural damping in percent of critical (%)
         3.0   B1dEdDmp(1) - Blade edge mode #1 structural damping in percent of critical (%)
---------------------- BLADE ADJUSTMENT FACTORS -------------------------------
           1   F1StTunr(1) - Blade flapwise modal stiffness tuner, 1st mode (-)
           1   F1StTunr(2) - Blade flapwise modal stiffness tuner, 2nd mode (-)
       0.664   AdjB1Ms     - Factor to adjust blade mass density (-)
           1   AdjF1St     - Factor to adjust blade flap stiffness (-)
           1   AdjEdSt     - Factor to adjust blade edge stiffness (-)
---------------------- DISTRIBUTED BLADE PROPERTIES ---------------------------
BlFract   PitchAxis   StrcTwst   BMassDen    FlpStff    EdgStff
   (-)        (-)       (deg)     (kg/m)     (Nm^2)     (Nm^2)
   0.000      0.250     59.648    5.03E-01   1.80E+02   1.55E+03
   0.030      0.250     58.661    5.90E-01   2.48E+02   2.13E+03
   0.084      0.250     58.422    1.13E+00   9.11E+02   7.84E+03
   0.138      0.250     59.101    1.79E+00   2.39E+02   2.33E+04
   0.192      0.250     57.541    1.79E+00   2.39E+02   2.33E+04
   0.245      0.250     55.796    1.79E+00   2.39E+02   2.33E+04
   0.300      0.250     53.709    1.76E+00   2.32E+02   2.26E+04
   0.354      0.250     51.540    1.71E+00   2.17E+02   2.12E+04
   0.407      0.250     49.311    1.65E+00   2.03E+02   1.98E+04
   0.461      0.250     47.076    1.59E+00   1.88E+02   1.83E+04
   0.515      0.250     44.871    1.52E+00   1.72E+02   1.68E+04
   0.569      0.250     42.721    1.44E+00   1.55E+02   1.51E+04
   0.622      0.250     40.633    1.36E+00   1.37E+02   1.33E+04
   0.677      0.250     38.611    1.26E+00   1.17E+02   1.15E+04
   0.730      0.250     36.651    1.14E+00   9.75E+01   9.51E+03
   0.784      0.250     34.731    1.01E+00   7.60E+01   7.41E+03
   0.838      0.250     32.848    8.63E-01   5.55E+01   5.42E+03
   0.892      0.250     30.914    6.85E-01   3.50E+01   3.41E+03
   0.945      0.250     28.598    4.86E-01   1.76E+01   1.71E+03
   1.000      0.250     26.808    3.09E-01   7.09E+00   6.92E+02
---------------------- BLADE MODE SHAPES --------------------------------------
    0.0201   B1dF11Sh(2) - Flap mode 1, coeff of x^2
    4.9078   B1dF11Sh(3) -            , coeff of x^3
   -7.9478   B1dF11Sh(4) -            , coeff of x^4
    5.5222   B1dF11Sh(5) -            , coeff of x^5
   -1.5024   B1dF11Sh(6) -            , coeff of x^6
    2.0706   B1dF12Sh(2) - Flap mode 2, coeff of x^2
  -25.4296   B1dF12Sh(3) -            , coeff of x^3
   47.1767   B1dF12Sh(4) -            , coeff of x^4
  -19.9877   B1dF12Sh(5) -            , coeff of x^5
   -2.8300   B1dF12Sh(6) -            , coeff of x^6
   -7.5409   B1dEdgSh(2) - Edge mode 1, coeff of x^2
   17.4908   B1dEdgSh(3) -            , coeff of x^3
  -12.6717   B1dEdgSh(4) -            , coeff of x^4
    5.1622   B1dEdgSh(5) -            , coeff of x^5
   -1.4405   B1dEdgSh(6) -            , coeff of x^6
```

A.13.6 AAUE-TLP ElastoDyn Tower Input File

```
...n\Aalborg Universitet\OneDrive - Aalborg Universitet\EN1-B305\P9_10\Projekt\Matlab\FAST\CertTest\AAUETLP\AAUETLP_ElastoDyn_Tower.dat                1
------- ELASTODYN V1.00.* TOWER INPUT FILE ------------------------------------
Tower input properties for the AAUE-TLP.
---------------------- TOWER PARAMETERS ----------------------------------------
          1   NTwInpSt    - Number of input stations to specify tower geometry
        4.9   TwrFADmp(1) - Tower 1st fore-aft mode structural damping ratio (%)
       12.0   TwrFADmp(2) - Tower 2nd fore-aft mode structural damping ratio (%)
        4.9   TwrSSDmp(1) - Tower 1st side-to-side mode structural damping ratio (%)
       12.0   TwrSSDmp(2) - Tower 2nd side-to-side mode structural damping ratio (%)
---------------------- TOWER ADJUSTMUNT FACTORS --------------------------------
          1   FAStTunr(1) - Tower fore-aft modal stiffness tuner, 1st mode (-)
          1   FAStTunr(2) - Tower fore-aft modal stiffness tuner, 2nd mode (-)
          1   SSStTunr(1) - Tower side-to-side stiffness tuner, 1st mode (-)
          1   SSStTunr(2) - Tower side-to-side stiffness tuner, 2nd mode (-)
        1.0   AdjTwMa     - Factor to adjust tower mass density (-)
        0.9   AdjFASt     - Factor to adjust tower fore-aft stiffness (-)
          1   AdjSSSt     - Factor to adjust tower side-to-side stiffness (-)
---------------------- DISTRIBUTED TOWER PROPERTIES ----------------------------
  HtFract       TMassDen         TwFAStif       TwSSStif
   (-)           (kg/m)           (Nm^2)         (Nm^2)
   0             2.633          4.8215e+03      4.8215e+03
---------------------- TOWER FORE-AFT MODE SHAPES ------------------------------
     2.296    TwFAM1Sh(2) - Mode 1, coefficient of x^2 term
    -4.233    TwFAM1Sh(3) -       , coefficient of x^3 term
     6.955    TwFAM1Sh(4) -       , coefficient of x^4 term
    -5.926    TwFAM1Sh(5) -       , coefficient of x^5 term
     1.909    TwFAM1Sh(6) -       , coefficient of x^6 term
     3.6390   TwFAM2Sh(2) - Mode 2, coefficient of x^2 term
    -2.6704   TwFAM2Sh(3) -       , coefficient of x^3 term
    -0.0903   TwFAM2Sh(4) -       , coefficient of x^4 term
     0.1308   TwFAM2Sh(5) -       , coefficient of x^5 term
    -0.0092   TwFAM2Sh(6) -       , coefficient of x^6 term
---------------------- TOWER SIDE-TO-SIDE MODE SHAPES --------------------------
     1.1567   TwSSM1Sh(2) - Mode 1, coefficient of x^2 term
    -0.1582   TwSSM1Sh(3) -       , coefficient of x^3 term
   -0.00030   TwSSM1Sh(4) -       , coefficient of x^4 term
     0.0005   TwSSM1Sh(5) -       , coefficient of x^5 term
     0.0014   TwSSM1Sh(6) -       , coefficient of x^6 term
     3.6390   TwSSM2Sh(2) - Mode 2, coefficient of x^2 term
    -2.6704   TwSSM2Sh(3) -       , coefficient of x^3 term
    -0.0903   TwSSM2Sh(4) -       , coefficient of x^4 term
     0.1308   TwSSM2Sh(5) -       , coefficient of x^5 term
    -0.0092   TwSSM2Sh(6) -       , coefficient of x^6 term
```

A.13.7 AAUE-TLP Inflow Wind Input File

...org Universitet\OneDrive - Aalborg Universitet\EN1-B305\P9_10\Projekt\Matlab\FAST\CertTest\AAUETLP\AAUETLP_InflowWind_Steady8mps.dat 1

```
------- InflowWind v3.01.* INPUT FILE ------------------------------------------------------------
Steady 8 m/s winds with no shear for FAST CertTests #20 and #25
---------------------------------------------------------------------------------------------------
False         Echo                - Echo input data to <RootName>.ech (flag)
         3    WindType            - switch for wind file type (1=steady; 2=uniform; 3=binary TurbSim FF; 4=binary Bladed-style FF; 5=HAWC format; 6=User defined)
         0    PropagationDir      - Direction of wind propagation (meteorological rotation from aligned with X (positive rotates towards -Y) -- degrees)
         1    NWindVel            - Number of points to output the wind velocity    (0 to 9)
         0    WindVxiList         - List of coordinates in the inertial X direction (m)
         0    WindVyiList         - List of coordinates in the inertial Y direction (m)
      2.41    WindVziList         - List of coordinates in the inertial Z direction (m) 90
================== Parameters for Steady Wind Conditions [used only for WindType = 1] ========== ==========
      7.00    HWindSpeed          - Horizontal windspeed                            (m/s)
      2.41    RefHt               - Reference height for horizontal wind speed      (m) 90
         0    PLexp               - Power law exponent                              (-)
================== Parameters for Uniform wind file   [used only for WindType = 2] ========== ==========
"Wind/Wind_Slope.wnd"    Filename       - Filename of time series data for uniform wind field.     (-)
      2.41  RefHt                - Reference height for horizontal wind speed                (m)
        10  RefLength           - Reference length for linear horizontal and vertical sheer (-)
================== Parameters for Binary TurbSim Full-Field files  [used only for WindType = 3] ==========
"Wind/10min/10min8_59ms.bts"   Filename       - Name of the Full field wind file to use (.bts)
================== Parameters for Binary Bladed-style Full-Field files  [used only for WindType = 4] =========
"unused"       FilenameRoot    - Rootname of the full-field wind file to use (.wnd, .sum)
False          TowerFile       - Have tower file (.twr) (flag)
================== Parameters for HAWC-format binary files  [Only used with WindType = 5] ========== ==========
"wasp\Output\basic_5u.bin"   FileName_u      - name of the file containing the u-component fluctuating wind (.bin)
"wasp\Output\basic_5v.bin"   FileName_v      - name of the file containing the v-component fluctuating wind (.bin)
"wasp\Output\basic_5w.bin"   FileName_w      - name of the file containing the w-component fluctuating wind (.bin)
        64   nx              - number of grids in the x direction (in the 3 files above) (-)
        32   ny              - number of grids in the y direction (in the 3 files above) (-)
        32   nz              - number of grids in the z direction (in the 3 files above) (-)
        16   dx              - distance (in meters) between points in the x direction    (m)
         3   dy              - distance (in meters) between points in the y direction    (m)
         3   dz              - distance (in meters) between points in the z direction    (m)
        90   RefHt           - reference height; the height (in meters) of the vertical center of the grid (m)
------------   Scaling parameters for turbulence   ---------------------------------------------------
         2   ScaleMethod     - Turbulence scaling method   [0 = none, 1 = direct scaling, 2 = calculate scaling factor based on a desired standard deviation]
         1   SFx             - Turbulence scaling factor for the x direction (-)   [ScaleMethod=1]
         1   SFy             - Turbulence scaling factor for the y direction (-)   [ScaleMethod=1]
         1   SFz             - Turbulence scaling factor for the z direction (-)   [ScaleMethod=1]
        12   SigmaFx         -   standard deviation to calculate scaling from in x direction (m/s)    [ScaleMethod=2]
         8   SigmaFy         - Turbulence standard deviation to calculate scaling from in y direction (m/s)    [ScaleMethod=2]
         2   SigmaFz         - Turbulence standard deviation to calculate scaling from in z direction (m/s)    [ScaleMethod=2]
------------   Mean wind profile parameters (added to HAWC-format files)   ------------------------------
         5   URef            - Mean u-component wind speed at the reference height (m/s)
         2   WindProfile     - Wind profile type (0=constant;1=logarithmic,2=power law)
         0   PLExp           - Power law exponent (-) (used for PL wind profile type only)
      0.03   Z0              - Surface roughness length (m) (used for LG wind profile type only)
================== OUTPUT ========== ==========
True           SumPrint      - Print summary data to <RootName>.IfW.sum (flag)
               OutList       - The next line(s) contains a list of output parameters.  See OutListParameters.xlsx for a listing of available output channels, (-)
"WindlVelX"                    X-direction wind velocity at point WindList(1)
END of input file (the word "END" must appear in the first 3 columns of this last OutList line)
---------------------------------------------------------------------------------------------------
```

A.13.8 AAUE-TLP AeroDyn Input File

```
... Jensen\Aalborg Universitet\OneDrive - Aalborg Universitet\EN1-B305\P9_10\Projekt\Matlab\FAST\CertTest\AAUETLP\AAUETLP_AeroDyn15.dat                                                
```

A.13.9 AAUE-TLP AeroDyn Input File


```
    1.4002    0.0900    1.0000
    1.5835    0.0900    1.0000
    1.7669    0.0900    1.0000
    1.9503    0.0900    1.0000
    2.1000    0.0900    1.0000
    2.1100    0.0900    1.0000
======  Outputs  ================================================================================ =
True          SumPrint            - Generate a summary file listing input options and interpolated p roperties to "<rootname>.AD.sum"?  (flag)
          0   NBlOuts             - Number of blade node outputs [0 - 9] (-)
          1,          9,         19    BlOutNd             - Blade nodes whose values will be output  (-)
          0   NTwOuts             - Number of tower node outputs [0 - 9]  (-)
          1,          2,          6    TwOutNd             - Tower nodes whose values will be output  (-)
                   OutList             - The next line(s) contains a list of output parameters.  See OutListParameters.xlsx for a listing of available output channels, (-)
RtAeroFyh       Total rotor aerodynamic load (force in y direction)
RtAeroFzh       Total rotor aerodynamic load (force in z direction)
RtAeroFxh       Total rotor aerodynamic load (force in x direction)
RtAeroMxh       Total rotor aerodynamic load (Shaft torque)
END of input file (the word "END" must appear in the first 3 columns of this last OutList line)
--------------------------------------------------------------------------------------------
```

A.13.10 AAUE-TLP Airfoil AH93W300 Input File

```
... Jensen\Aalborg Universitet\OneDrive - Aalborg Universitet\EN1-B305\P9_10\Projekt\Matlab\FAST\CertTest\AAUETLP\Airfoils\AH93W300.dat                                                
```

A.13.11 AAUE-TLP Airfoil AH93W300 Input File


```
           0   k3                ! Constant in the \hat(x)_cp curve best-fit.  [ignored if UAMod<>1]
           0   k1_hat            ! Constant in the expression of Cc due to leading edge vortex effects.  [ignored if UAMod<>1]
         0.2   x_cp_bar          ! Constant in the expression of \hat(x)_cp^v. [ignored if UAMod<>1,  default = 0.2]
         180   UACutout          ! Angle of attack above which unsteady aerodynamics are disabled (deg). [Specifying the string "Default" sets UACutout to 45 degrees] "DEFAULT"
"DEFAULT"     filtCutOff        ! Cut-off frequency (-3 dB corner frequency) for low-pass filtering the AoA input to UA, as well as the 1st and 2nd derivatives (Hz) [default = 20]
!.......................................
! Table of aerodynamics coefficients
      1359   NumAlf            ! Number of data lines in the following table
!    Alpha      Cl      Cd        Cm
!    (deg)      (-)     (-)       (-)
    -180.00     0.000       0.0198     0.0000
    -80.30      -0.25       0.25       0.20
    -80.20      -0.25       0.25       0.20
    -80.10      -0.25       0.25       0.20
    -80.00      -0.25       0.25       0.20
    -79.90      -0.26       0.25       0.20
    -79.80      -0.26       0.25       0.20
    -79.70      -0.26       0.25       0.20
    -79.60      -0.26       0.25       0.20
    -79.50      -0.26       0.25       0.20
    -79.40      -0.26       0.25       0.20
    -79.30      -0.26       0.25       0.20
    -79.20      -0.26       0.25       0.20
    -79.10      -0.27       0.25       0.20
    -79.00      -0.27       0.26       0.20
    -78.40      -0.27       0.26       0.20
    -78.30      -0.28       0.26       0.20
    -78.20      -0.28       0.26       0.20
    -78.10      -0.28       0.26       0.20
    -78.00      -0.28       0.26       0.20
    -77.90      -0.28       0.26       0.20
    -77.80      -0.28       0.26       0.20
    -77.70      -0.28       0.27       0.20
    -77.60      -0.28       0.27       0.20
    -77.50      -0.29       0.27       0.20
    -77.40      -0.29       0.27       0.20
    -77.30      -0.29       0.27       0.20
    -77.20      -0.29       0.27       0.20
    -77.10      -0.29       0.27       0.20
    -77.00      -0.29       0.27       0.20
    -76.40      -0.30       0.27       0.19
    -76.30      -0.30       0.28       0.19
    -76.20      -0.30       0.28       0.19
    -76.10      -0.30       0.28       0.19
    -76.00      -0.30       0.28       0.19
    -75.90      -0.30       0.28       0.19
    -75.80      -0.31       0.28       0.19
    -75.70      -0.31       0.28       0.19
    -75.60      -0.31       0.28       0.19
    -75.50      -0.31       0.28       0.19
    -75.40      -0.31       0.28       0.19
    -75.30      -0.31       0.28       0.19
    -75.20      -0.31       0.28       0.19
```

A.13.12 AAUE-TLP Airfoil SD7003 File

```
... K Jensen\Aalborg Universitet\OneDrive - Aalborg Universitet\EN1-B305\P9_10\Projekt\Matlab\FAST\CertTest\AAUETLP\Airfoils\SD7003.dat                1
  1 ! ------------ AirfoilInfo v1.01.x Input File ----------------------------------
  2 ! Airfoil informaiton for SD7003
  3 ! Made by Jesper Kirkegaard Jensen, Kasper Laugesen, Signe Møller Mortensen
  4 ! note that this file uses Marshall Buhl's new input file processing; start all comment lines with !
  5 ! ------------------------------------------------------------------------
  6 "DEFAULT"     InterpOrd       ! Interpolation order to use for quasi-steady table lookup {1=linear; 3=cubic spline; "default"} [default=3]
  7               1   NonDimArea  ! The non-dimensional area of the airfoil (area/chord^2) (set to 1.0 if unsure or unneeded)
  8               0   NumCoords   ! The number of coordinates in the airfoil shape file.  Set to zero if coordinates not included. @"SD7003_coords.txt"
  9               1   NumTabs     ! Number of airfoil tables in this file.  Each table must have lines  for Re and Ctrl.
 10 ! ------------------------------------------------------------------------
 11 ! data for table 1
 12 ! ------------------------------------------------------------------------
 13               0.1 Re          ! Reynolds number in millions
 14               0   Ctrl        ! Control setting (must be 0 for current AirfoilInfo)
 15 True          InclUAData      ! Is unsteady aerodynamics data included in this table? If TRUE, the n include 30 UA coefficients below this line
 16 !.....................................................
 17               -0.5   alpha0   ! 0-lift angle of attack, depends on airfoil.
 18               10.0   alpha1   ! Angle of attack at f=0.7, (approximately the stall angle) for AOA> alpha0. (deg)
 19               6.5    alpha2   ! Angle of attack at f=0.7, (approximately the stall angle) for AOA< alpha0. (deg)
 20               0      eta_e    ! Recovery factor in the range [0.85 - 0.95] used only for UAMOD=1, it is set to 1 in the code when flookup=True. (-)
 21               7.12499 C_nalpha ! Slope of the 2D normal force coefficient curve. (1/rad)
 22               3      T_f0     ! Initial value of the time constant associated with Df in the expression of Df and f''. [default = 3]
 23               6      T_V0     ! Initial value of the time constant associated with the vortex lift decay process; it is used in the expression of Cvn. It depends on Re,M, and airfoil class. [default = 6] ↵
 24               1.7    T_p      ! Boundary-layer,leading edge pressure gradient time constant in the expression of Dp. It should be tuned based on airfoil experimental data. [default = 1.7] ↵
 25               11     T_VL     ! Initial value of the time constant associated with the vortex advection process; it represents the non-dimensional time in semi-chords, needed for a vortex to travel from LE to trailing edge (TE); it is used in the expression of Cvn. It depends on Re, M (weakly), and airfoil. [valid range = 6 - 13, default = 11] ↵
 26               0.14   b1       ! Constant in the expression of phi_alpha^c and phi_q^c.  This value is relatively insensitive for thin airfoils, but may be different for turbine airfoils. [from experimental results, defaults to 0.14] ↵
 27               0.53   b2       ! Constant in the expression of phi_alpha^c and phi_q^c.  This value is relatively insensitive for thin airfoils, but may be different for turbine airfoils. [from experimental results, defaults to 0.53] ↵
 28               5      b5       ! Constant in the expression of K'''_q,Cm_q^nc, and k_m,q.  [from experimental results, defaults to 5]
 29               0.3    A1       ! Constant in the expression of phi_alpha^c and phi_q^c.  This value is relatively insensitive for thin airfoils, but may be different for turbine airfoils. [from experimental results, defaults to 0.3] ↵
 30               0.7    A2       ! Constant in the expression of phi_alpha^c and phi_q^c.  This value is relatively insensitive for thin airfoils, but may be different for turbine airfoils. [from experimental results, defaults to 0.7] ↵
 31               1      A5       ! Constant in the expression of K'''_q,Cm_q^nc, and k_m,q. [from experimental results, defaults to 1]
 32               0      S1       ! Constant in the f curve best-fit for alpha0<=AOA<=alpha1; by definition it depends on the airfoil. [ignored if UAMod<>1]
 33               0      S2       ! Constant in the f curve best-fit for          AOA> alpha1; by definition it depends on the airfoil. [ignored if UAMod<>1]
 34               0      S3       ! Constant in the f curve best-fit for alpha2<=AOA< alpha0; by definition it depends on the airfoil. [ignored if UAMod<>1]
 35               0      S4       ! Constant in the f curve best-fit for          AOA< alpha2; by definition it depends on the airfoil. [ignored if UAMod<>1]
 36               0      Cn1      ! Critical value of C0n at leading edge separation. It should be extracted from airfoil data at a given Mach and Reynolds number. It can be calculated from the static value of Cn at either the break in the pitching moment or the loss of chord force at the onset of stall. It is close to the condition of maximum lift of the airfoil at low Mach numbers. ↵
 37               0      Cn2      ! As Cn1 for negative AOAs.
 38               0.19   St_sh    ! Strouhal's shedding frequency constant.  [default = 0.19]
 39               0.0119 Cd0      ! 2D drag coefficient value at 0-lift.
 40               -0.0173 Cm0     ! 2D pitching moment coefficient about 1/4-chord location, at 0-lift, positive if nose up. [If the aerodynamics coefficients table does not include a column for Cm, this needs to be set to 0.0] ↵
 41               0      k0       ! Constant in the \hat(x)_cp curve best-fit; = (\hat(x)_AC-0.25).  [ignored if UAMod<>1]
 42               0      k1       ! Constant in the \hat(x)_cp curve best-fit.  [ignored if UAMod<>1]
 43               0      k2       ! Constant in the \hat(x)_cp curve best-fit.  [ignored if UAMod<>1]
```

A.13.13 AAUE-TLP Airfoil SD7003 File

... K Jensen\Aalborg Universitet\OneDrive - Aalborg Universitet\EN1-B305\P9_10\Projekt\Matlab\FAST\CertTest\AAUETLP\Airfoils\SD7003.dat 2

```
          0   k3                ! Constant in the \hat(x)_cp curve best-fit.  [ignored if UAMod<>1]
          0   k1_hat            ! Constant in the expression of Cc due to leading edge vortex effect s.  [ignored if UAMod<>1]
        0.2   x_cp_bar          ! Constant in the expression of \hat(x)_cp^v. [ignored if UAMod<>1,  default = 0.2]
180     UACutout          ! Angle of attack above which unsteady aerodynamics are disabled (deg). [S pecifying the string "Default" sets UACutout to 45 degrees] "DEFAULT"
"DEFAULT"     filtCutOff        ! Cut-off frequency (-3 dB corner frequency) for low-pass filtering the AoA input to UA, as well as the 1st and 2nd derivatives (Hz) [default = 20]
!.......................................
! Table of aerodynamics coefficients
      1228   NumAlf            ! Number of data lines in the following table
!    Alpha      Cl      Cd        Cm
!    (deg)      (-)     (-)       (-)
   -180.00    0.000     0.0198    0.0000
  -82.1000   -0.1841    0.3624    0.2849
  -82.0000   -0.1859    0.3641    0.2851
  -81.9000   -0.1877    0.3656    0.2853
  -81.8000   -0.1895    0.3674    0.2855
  -81.7000   -0.1913    0.3690    0.2857
  -81.6000   -0.1931    0.3707    0.2859
  -81.5000   -0.1949    0.3724    0.2860
  -81.4000   -0.1967    0.3742    0.2862
  -81.3000   -0.1985    0.3758    0.2864
  -81.2000   -0.2004    0.3776    0.2866
  -81.1000   -0.2022    0.3793    0.2868
  -81.0000   -0.2040    0.3810    0.2870
  -80.9000   -0.2058    0.3826    0.2871
  -80.8000   -0.2077    0.3843    0.2873
  -80.7000   -0.2095    0.3861    0.2875
  -80.6000   -0.2114    0.3877    0.2877
  -80.5000   -0.2132    0.3895    0.2878
  -80.4000   -0.2151    0.3912    0.2880
  -80.3000   -0.2170    0.3929    0.2882
  -80.2000   -0.2188    0.3946    0.2883
  -80.1000   -0.2207    0.3964    0.2885
  -78.2000   -0.2569    0.4286    0.2913
  -78.1000   -0.2588    0.4300    0.2914
  -78.0000   -0.2607    0.4317    0.2916
  -77.9000   -0.2627    0.4335    0.2917
  -77.8000   -0.2647    0.4353    0.2918
  -77.7000   -0.2666    0.4369    0.2919
  -77.6000   -0.2685    0.4386    0.2921
  -77.5000   -0.2705    0.4403    0.2922
  -77.4000   -0.2725    0.4420    0.2923
  -77.3000   -0.2744    0.4437    0.2924
  -77.2000   -0.2764    0.4453    0.2925
  -77.1000   -0.2783    0.4470    0.2926
  -77.0000   -0.2803    0.4487    0.2927
  -76.9000   -0.2823    0.4505    0.2928
  -76.8000   -0.2843    0.4521    0.2929
  -76.7000   -0.2863    0.4539    0.2931
  -76.6000   -0.2882    0.4553    0.2931
  -76.5000   -0.2902    0.4571    0.2932
  -76.4000   -0.2922    0.4588    0.2933
  -76.3000   -0.2942    0.4604    0.2934
  -76.2000   -0.2962    0.4621    0.2935
```

A.13.14 AAUE-TLP AeroDyn Blade Input File

...sen\Aalborg Universitet\OneDrive - Aalborg Universitet\EN1-B305\P9_10\Projekt\Matlab\FAST\CertTest\AAUETLP\AAUETLP_AeroDyn_blade.dat 1

```
------- AERODYN v15.00.* BLADE DEFINITION INPUT FILE ----------------------------------
AAUETLP aerodynamic blade input properties; note that we need to add the aerodynamic center to this  file
======  Blade Properties ====================================================
     20   NumBlNds                - Number of blade nodes used in the analysis (-)
BlSpn       BlCrvAC     BlSwpAC     BlCrvAng    BlTwist     BlChord     BlAFID
  (m)         (m)         (deg)       (deg)       (m)         (-)
0.000000    0.000000    0.000000    0.000000   60.000000    0.120000   1
0.030000    0.000000    0.000000    0.000000   59.013000    0.130000   1
0.083330    0.000000    0.000000    0.000000   58.773900    0.180000   1
0.137000    0.000000    0.000000    0.000000   58.940000    0.265000   2
0.190000    0.000000    0.000000    0.000000   57.380000    0.265000   2
0.243000    0.000000    0.000000    0.000000   55.634500    0.265000   2
0.297000    0.000000    0.000000    0.000000   53.547300    0.263000   2
0.350000    0.000000    0.000000    0.000000   51.378800    0.258700   2
0.403000    0.000000    0.000000    0.000000   49.150000    0.254400   2
0.456000    0.000000    0.000000    0.000000   46.914800    0.249500   2
0.510000    0.000000    0.000000    0.000000   44.710000    0.244000   2
0.563000    0.000000    0.000000    0.000000   42.560000    0.237700   2
0.616000    0.000000    0.000000    0.000000   40.472000    0.230500   2
0.670000    0.000000    0.000000    0.000000   38.450000    0.221900   2
0.723000    0.000000    0.000000    0.000000   36.490000    0.211800   2
0.776000    0.000000    0.000000    0.000000   34.570000    0.199000   2
0.830000    0.000000    0.000000    0.000000   32.686200    0.184000   2
0.883000    0.000000    0.000000    0.000000   30.752400    0.163900   2
0.936000    0.000000    0.000000    0.000000   28.436100    0.138000   2
0.989990    0.000000    0.000000    0.000000   26.646100    0.110000   2

!bjj: because of precision in the BD-AD coupling, 61.5m didn't work, so I changed it to 61.4999m
6.150000E+01 -3.2815226E-04 -1.7737470E-01 0.0000000E+00  1.0600000E-01  1.4190000E+00      8
```

A.13.15 AAUE-TLP ServoDyn Input File

```
...K Jensen\Aalborg Universitet\OneDrive - Aalborg Universitet\EN1-B305\P9_10\Projekt\Matlab\FAST\CertTest\AAUETLP\AAUETLP_ServoDyn.dat                1
------- SERVODYN v1.05.* INPUT FILE ------------------------------------------
ServoDyn input file for AAUETLP
---------------------- SIMULATION CONTROL --------------------------------------
False        Echo            - Echo input data to <RootName>.ech (flag)
     2E-4    DT              - Communication interval for controllers (s) (or "default")
---------------------- PITCH CONTROL -------------------------------------------
           4  PCMode          - Pitch control mode {0: none, 3: user-defined from routine PitchCntrl, 4: user-defined from Simulink/Labview, 5: user-defined from Bladed-style DLL} (switch)
           0  TPCOn           - Time to enable active pitch control (s) [unused when PCMode=0]
      9999.9  TPitManS(1)     - Time to start override pitch maneuver for blade 1 and end standard pitch control (s)
      9999.9  TPitManS(2)     - Time to start override pitch maneuver for blade 2 and end standard pitch control (s)
      9999.9  TPitManS(3)     - Time to start override pitch maneuver for blade 3 and end standard pitch control (s) [unused for 2 blades]
           2  PitManRat(1)    - Pitch rate at which override pitch maneuver heads toward final pitch angle for blade 1 (deg/s)
           2  PitManRat(2)    - Pitch rate at which override pitch maneuver heads toward final pitch angle for blade 2 (deg/s)
           2  PitManRat(3)    - Pitch rate at which override pitch maneuver heads toward final pitch angle for blade 3 (deg/s) [unused for 2 blades]
           0  B1PitchF(1)     - Blade 1 final pitch for pitch maneuvers (degrees)
           0  B1PitchF(2)     - Blade 2 final pitch for pitch maneuvers (degrees)
           0  B1PitchF(3)     - Blade 3 final pitch for pitch maneuvers (degrees) [unused for 2 blades]
---------------------- GENERATOR AND TORQUE CONTROL ----------------------------
           4  VSContrl        - Variable-speed control mode {0: none, 1: simple VS, 3: user-defined from routine UserVSCont, 4: user-defined from Simulink/Labview, 5: user-defined from
              Bladed-style DLL} (switch)
           1  GenModel        - Generator model {1: simple, 2: Thevenin, 3: user-defined from routine UserGen} (switch) [used only when VSContrl=0]
        95.0  GenEff          - Generator efficiency [ignored by the Thevenin and user-defined generator models] (%)
           T  GenTiStr        - Method to start the generator {T: timed using TimGenOn, F: generator speed using SpdGenOn} (flag)
           T  GenTiStp        - Method to stop the generator {T: timed using TimGenOf, F: when generator power = 0} (flag)
         500  SpdGenOn        - Generator speed to turn on the generator for a startup (HSS speed) (rpm) [used only when GenTiStr=False]
           0  TimGenOn        - Time to turn on the generator for a startup (s) [used only when GenTiStr=True]
      9999.9  TimGenOf        - Time to turn off the generator (s) [used only when GenTiStp=True]
---------------------- SIMPLE VARIABLE-SPEED TORQUE CONTROL --------------------
 2.0663e+03   VS_RtGnSp       - Rated generator speed for simple variable-speed generator control (HSS side) (rpm) [used only when VSContrl=1]
     0.4325   VS_RtTq         - Rated generator torque/constant generator torque in Region 3 for simple variable-speed generator control (HSS side) (N-m) [used only when VSContrl=1]
       0.39   VS_Rgn2K        - Generator torque constant in Region 2 for simple variable-speed generator control (HSS side) (N-m/rpm^2) [used only when VSContrl=1]
       0.01   VS_SlPc         - Rated generator slip percentage in Region 2 1/2 for simple variable-speed generator control (%) [used only when VSContrl=1]
---------------------- SIMPLE INDUCTION GENERATOR ------------------------------
           5  SIG_SlPc        - Rated generator slip percentage (%) [used only when VSContrl=0 and GenModel=1 ]
          80  SIG_SySp        - Synchronous (zero-torque) generator speed (rpm) [used only when VSContrl=0 and GenModel=1]
          20  SIG_RtTq        - Rated torque (N-m) [used only when VSContrl=0 and GenModel=1]
         1.2  SIG_PORt         - Pull-out ratio (Tpullout/Trated) (-) [used only when VSContrl=0 and GenModel=1]
---------------------- THEVENIN-EQUIVALENT INDUCTION GENERATOR -----------------
      9999.9  TEC_Freq        - Line frequency [50 or 60] (Hz) [used only when VSContrl=0 and GenModel= 2]
        9998  TEC_NPol        - Number of poles [even integer > 0] (-) [used only when VSContrl=0 and GenModel=2]
      9999.9  TEC_SRes        - Stator resistance (ohms) [used only when VSContrl=0 and GenModel=2]
      9999.9  TEC_RRes        - Rotor resistance (ohms) [used only when VSContrl=0 and GenModel=2]
      9999.9  TEC_VLL         - Line-to-line RMS voltage (volts) [used only when VSContrl=0 and GenModel=2]
      9999.9  TEC_SLR         - Stator leakage reactance (ohms) [used only when VSContrl=0 and GenModel=2]
      9999.9  TEC_RLR         - Rotor leakage reactance (ohms) [used only when VSContrl=0 and GenModel= 2]
      9999.9  TEC_MR          - Magnetizing reactance (ohms) [used only when VSContrl=0 and GenModel=2]
---------------------- HIGH-SPEED SHAFT BRAKE ----------------------------------
           4  HSSBrMode       - HSS brake model {0: none, 1: simple, 3: user-defined from routine UserHSSBr, 4: user-defined from Simulink/Labview, 5: user-defined from Bladed-style DLL}
              (switch)
      9999.9  THSSBrDp        - Time to initiate deployment of the HSS brake (s)
         0.6  HSSBrDT         - Time for HSS-brake to reach full deployment once initiated (sec) [used only when HSSBrMode=1]
         100  HSSBrTqF        - Fully deployed HSS-brake torque (N-m)
---------------------- NACELLE-YAW CONTROL --------------------------------------
```

A.13.16 AAUE-TLP ServoDyn Input File

```
...K Jensen\Aalborg Universitet\OneDrive - Aalborg Universitet\EN1-B305\P9_10\Projekt\Matlab\FAST\CertTest\AAUETLP\AAUETLP_ServoDyn.dat                2
         4   YCMode      - Yaw control mode {0: none, 3: user-defined from routine UserYawCont, 4: user-defined from Simulink/Labview, 5: user-defined from Bladed-style DLL} (switch)
      9999.9 TYCOn       - Time to enable active yaw control (s) [unused when YCMode=0]
           0 YawNeut     - Neutral yaw position--yaw spring force is zero at this yaw (degrees)
9.02832E+09  YawSpr      - Nacelle-yaw spring constant (N-m/rad)
 1.916E+07   YawDamp     - Nacelle-yaw damping constant (N-m/(rad/s))
      9999.9 TYawManS    - Time to start override yaw maneuver and end standard yaw control (s)
           2 YawManRat   - Yaw maneuver rate (in absolute value) (deg/s)
           0 NacYawF     - Final yaw angle for override yaw maneuvers (degrees)
---------------------- TUNED MASS DAMPER ---------------------------------------
False          CompNTMD  - Compute nacelle tuned mass damper {true/false} (flag)
"unused"       NTMDfile  - Name of the file for nacelle tuned mass damper (quoted string) [unused when CompNTMD is false]
False          CompTTMD  - Compute tower tuned mass damper {true/false} (flag)
"unused"       TTMDfile  - Name of the file for tower tuned mass damper (quoted string) [unused when CompTTMD is false]
---------------------- BLADED INTERFACE ----------------------------------------- [used only with Bladed Interface]
"ServoData/DISCON_win32.dll"    DLL_FileName - Name/location of the dynamic library {.dll [Windows] or .so [Linux]} in the Bladed-DLL format (-) [used only with Bladed Interface]
"DISCON.IN"    DLL_InFile    - Name of input file sent to the DLL (-) [used only with Bladed Interface]
"DISCON"       DLL_ProcName  - Name of procedure in DLL to be called (-) [case sensitive; used only with DLL Interface]
"default"      DLL_DT        - Communication interval for dynamic library (s) (or "default") [used only with Bladed Interface]
false          DLL_Ramp      - Whether a linear ramp should be used between DLL_DT time steps [introduces time shift when true] (flag) [used only with Bladed Interface]
      9999.9   BPCutoff      - Cuttoff frequency for low-pass filter on blade pitch from DLL (Hz) [used only with Bladed Interface]
           0   NacYaw_North  - Reference yaw angle of the nacelle when the upwind end points due North (deg) [used only with Bladed Interface]
           0   Ptch_Cntrl    - Record 28: Use individual pitch control {0: collective pitch; 1: individual pitch control} (switch) [used only with Bladed Interface]
           0   Ptch_SetPnt   - Record  5: Below-rated pitch angle set-point (deg) [used only with Bladed Interface]
           0   Ptch_Min      - Record  6: Minimum pitch angle (deg) [used only with Bladed Interface]
           0   Ptch_Max      - Record  7: Maximum pitch angle (deg) [used only with Bladed Interface]
           0   PtchRate_Min  - Record  8: Minimum pitch rate (most negative value allowed) (deg/s) [used only with Bladed Interface]
           0   PtchRate_Max  - Record  9: Maximum pitch rate  (deg/s) [used only with Bladed Interface ]
           0   Gain_OM       - Record 16: Optimal mode gain (Nm/(rad/s)^2) [used only with Bladed Interface]
           0   GenSpd_MinOM  - Record 17: Minimum generator speed (rpm) [used only with Bladed Interface]
           0   GenSpd_MaxOM  - Record 18: Optimal mode maximum speed (rpm) [used only with Bladed Interface]
           0   GenSpd_Dem    - Record 19: Demanded generator speed above rated (rpm) [used only with Bladed Interface]
           0   GenTrq_Dem    - Record 22: Demanded generator torque above rated (Nm) [used only with Bladed Interface]
           0   GenPwr_Dem    - Record 13: Demanded power (W) [used only with Bladed Interface]
---------------------- BLADED INTERFACE TORQUE-SPEED LOOK-UP TABLE -------------
           0   DLL_NumTrq    - Record 26: No. of points in torque-speed look-up table {0 = none and use the optimal mode parameters; nonzero = ignore the optimal mode PARAMETERs by setting
                 Record 16 to 0.0} (-) [used only with Bladed Interface]
  GenSpd_TLU   GenTrq_TLU
       (rpm)        (Nm)
---------------------- OUTPUT --------------------------------------------------
True           SumPrint    - Print summary data to <RootName>.sum (flag) (currently unused)
               1 OutFile   - Switch to determine where output will be placed: {1: in module output file only; 2: in glue code output file only; 3: both} (currently unused)
True           TabDelim    - Use tab delimiters in text tabular output file? (flag) (currently unused)
"ES10.3E2"     OutFmt      - Format used for text tabular output (except time).  Resulting field should be 10 characters. (quoted string) (currently unused)
              30 TStart    - Time to begin tabular output (s) (currently unused)
               Outlist     - The next line(s) contains a list of output parameters.  See OutListParameters.xlsx for a listing of available output channels, (-)
"GenPwr"                   - Electrical generator power and torque
"GenTq"                    - Electrical generator power and torque
END of input file (the word "END" must appear in the first 3 columns of this last OutList line)
---------------------------------------------------------------------------------
```

A.13.17 AAUE-TLP HydroDyn Input File

...K Jensen\Aalborg Universitet\OneDrive - Aalborg Universitet\EN1-B305\P9_10\Projekt\Matlab\FAST\CertTest\AAUETLP\AAUETLP_HydroDyn.dat 1

```
1  ------- HydroDyn v2.03.* Input File ------------------------------------------
2  HydroDyn input properties for AAUE-TLP.
3  False          Echo                - Echo the input file data (flag)
4  ---------------------- ENVIRONMENTAL CONDITIONS -------------------------------
5          998    WtrDens             - Water density (kg/m^3)
6         1.92    WtrDpth             - Water depth (meters) 1.92
7            0    MSL2SWL             - Offset between still-water level and mean sea level (meters) [positive upward; unused when WaveMod = 6; must be zero if PotMod=1 or 2]
8  ---------------------- WAVES --------------------------------------------------
9            1    WaveMod             - Incident wave kinematics model {0: none=still water, 1: regular (periodic), 1P#: regular with user-specified phase, 2: JONSWAP/Pierson-Moskowitz spectrum (irregular), 3: White noise spectrum (irregular), 4: user-defined spectrum from routine UserWaveSpctrm (irregular), 5: Externally generated wave-elevation time series, 6: Externally generated full wave-kinematics time series [option 6 is invalid for PotMod/=0]} (switch)
10           0    WaveStMod           - Model for stretching incident wave kinematics to instantaneous free surface {0: none=no stretching, 1: vertical stretching, 2: extrapolation stretching, 3: Wheeler stretching} (switch) [unused when WaveMod=0 or when PotMod/=0]
11        3000    WaveTMax            - Analysis time for incident wave calculations (sec) [unused when WaveMod=0; determines WaveDOmega=2Pi/WaveTMax in the IFFT]
12        0.02    WaveDT              - Time step for incident wave calculations  0.005  (sec) [unused when  WaveMod=0; 0.1<=WaveDT<=1.0 recommended; determines WaveOmegaMax=Pi/WaveDT in the IFFT]
13        0.01    WaveHs              - Significant wave height of incident waves (meters) [used only when WaveMod=1, 2, or 3]
14       1.666    WaveTp              - Peak-spectral period of incident waves      (sec) [used only when  WaveMod=1 or 2] 10
15   "DEFAULT"    WavePkShp           - Peak-shape parameter of incident wave spectrum (-) or DEFAULT (string) [used only when WaveMod=2; use 1.0 for Pierson-Moskowitz]
16           0    WvLowCOff           - Low  cut-off frequency or lower frequency limit of the wave spectrum beyond which the wave spectrum is zeroed (rad/s) [unused when WaveMod=0, 1, or 6]
17          15    WvHiCOff            - High cut-off frequency or upper frequency limit of the wave spectrum beyond which the wave spectrum is zeroed (rad/s) [unused when WaveMod=0, 1, or 6]
18           0    WaveDir             - Incident wave propagation heading direction                (degrees) [unused when WaveMod=0 or 6]
19           0    WaveDirMod          - Directional spreading function {0: none, 1: COS2S}          (-)     [only used when WaveMod=2,3, or 4]
20       0.001    WaveDirSpread       - Wave direction spreading coefficient ( > 0 )                (-)     [only used when WaveMod=2,3, or 4 and WaveDirMod=1]
21           1    WaveNDir            - Number of wave directions 13                                (-)     [only used when WaveMod=2,3, or 4 and WaveDirMod=1; odd number only]
22           0    WaveDirRange        - Range of wave directions (full range: WaveDir +/- 1/2*WaveDirRange) (degrees) [only used when WaveMod=2,3,or 4 and WaveDirMod=1]
23   123456789    WaveSeed(1)         - First  random seed of incident waves [-2147483648 to 2147483647]    (-)     [unused when WaveMod=0, 5, or 6]
24  1011121314    WaveSeed(2)         - Second random seed of incident waves [-2147483648 to 2147483647]    (-)     [unused when WaveMod=0, 5, or 6]
25        TRUE    WaveNDAmp           - Flag for normally distributed amplitudes                    (flag)  [only used when WaveMod=2, 3, or 4]
26  "Wave/JONSWAPSpectrumCoupled/JonswapSpectrumCoupled"  WvKinFile     - Root name of externally generated wave data file(s)     (quoted string)   [used only when WaveMod=5 or 6]
27           1    NWaveElev           - Number of points where the incident wave elevations can be computed (-)     [ma12179.6ximum of 9 output locations]
28           0    WaveElevxi          - List of xi-coordinates for points where the incident wave elevations can be output (meters) [NWaveElev points, separated by commas or white space; ususued if NWaveElev = 0]
29           0    WaveElevyi          - List of yi-coordinates for points where the incident wave elevations can be output (meters) [NWaveElev points, separated by commas or white space; ususued if NWaveElev = 0]
30 ---------------------- 2ND-ORDER WAVES ----------------------------------------- [unused with WaveMod=0 or 6]
31       False    WvDiffQTF           - Full difference-frequency 2nd-order wave kinematics (flag)
32       False    WvSumQTF            - Full summation-frequency  2nd-order wave kinematics (flag)
33           0    WvLowCOffD          - Low  frequency cutoff used in the difference-frequencies (rad/s) [Only used with a difference-frequency method]
34         3.5    WvHiCOffD           - High frequency cutoff used in the difference-frequencies (rad/s) [Only used with a difference-frequency method]
35         0.1    WvLowCOffS          - Low  frequency cutoff used in the summation-frequencies  (rad/s) [Only used with a summation-frequency  method]
36         3.5    WvHiCOffS           - High frequency cutoff used in the summation-frequencies  (rad/s) [Only used with a summation-frequency  method]
37 ---------------------- CURRENT ------------------------------------------------ [unused with WaveMod=6]
38           0    CurrMod             - Current profile model {0: none=no current, 1: standard, 2: user-defined from routine UserCurrent} (switch)
39           0    CurrSSV0            - Sub-surface current velocity at still water level  (m/s) [used only when CurrMod=1]
40   "DEFAULT"    CurrSSDir           - Sub-surface current heading direction (degrees) or DEFAULT (string) [used only when CurrMod=1]
41        0.57    CurrNSRef           - Near-surface current reference depth                (meters) [used only when CurrMod=1]
42           0    CurrNSV0            - Near-surface current velocity at still water level (m/s) [used only when CurrMod=1]
43           0    CurrNSDir           - Near-surface current heading direction              (degrees) [used only when CurrMod=1]
44           0    CurrDIV             - Depth-independent current velocity                  (m/s) [used only when CurrMod=1]
45           0    CurrDIDir           - Depth-independent current heading direction         (degrees) [used only when CurrMod=1]
46 ---------------------- FLOATING PLATFORM --------------------------------------- [unused with WaveMod=6]
47           1    PotMod              - Potential-flow model {0: none=no potential flow, 1: frequency-to-time-domain transforms based on WAMIT output, 2: fluid-impulse theory (FIT)} (switch)
```

```
"HydroData/AAUETLP"    PotFile    - Root name of potential-flow model data; WAMIT output files containing the linear, nondimensionalized, hydrostatic restoring matrix (.hst), frequency-dependent hydrodynamic added mass matrix and damping matrix (.1), and frequency- and direction-dependent wave excitation force vector per unit wave amplitude (.3) (quoted string) [MAKE SURE THE FREQUENCIES INHERENT IN THESE WAMIT FILES SPAN THE PHYSICALLY-SIGNIFICANT RANGE OF FREQUENCIES FOR THE GIVEN PLATFORM; THEY MUST CONTAIN THE ZERO- AND INFINITE-FREQUENCY LIMITS!]
          1.0   WAMITULEN      - Characteristic body length scale used to redimensionalize WAMIT output (meters) [only used when PotMod=1]
       0.1971   PtfmVol0       - Displaced volume of water when the platform is in its undisplaced position (m^3) [only used when PotMod=1; USE THE SAME VALUE COMPUTED BY WAMIT AS OUTPUT IN THE .OUT FILE!]
            0   PtfmCOBxt      - The xt offset of the center of buoyancy (COB) from the platform reference point (meters)  [only used when PotMod=1]
            0   PtfmCOByt      - The yt offset of the center of buoyancy (COB) from the platform reference point (meters)  [only used when PotMod=1]
            1   RdtnMod        - Radiation memory-effect model {0: no memory-effect calculation, 1: convolution, 2: state-space} (switch) [only used when PotMod=1; STATE-SPACE REQUIRES *.ss INPUT FILE]
           10   RdtnTMax       - Analysis time for wave radiation kernel calculations (sec) [only used when PotMod=1; determines RdtnDOmega=Pi/RdtnTMax in the cosine transform; MAKE SURE THIS IS LONG ENOUGH FOR THE RADIATION IMPULSE RESPONSE FUNCTIONS TO DECAY TO NEAR-ZERO FOR THE GIVEN PLATFORM!]
"DEFAULT"        RdtnDT         - Time step for wave radiation kernel calculations (sec) [only used when PotMod=1; DT<=RdtnDT<=0.1 recommended; determines RdtnOmegaMax=Pi/RdtnDT in the cosine transform]
---------------------- 2ND-ORDER FLOATING PLATFORM FORCES ---------------------- [unused with WaveMod=0 or 6, or PotMod=0 or 2]
            0   MnDrift        - Mean-drift 2nd-order forces computed                                       {0: None; [7, 8, 9, 10, 11, or 12]: WAMIT file to use} [Only one of MnDrift, NewmanApp, or DiffQTF can be non-zero]
            0   NewmanApp      - Mean- and slow-drift 2nd-order forces computed with Newman's approximation {0: None; [7, 8, 9, 10, 11, or 12]: WAMIT file to use} [Only one of MnDrift, NewmanApp, or DiffQTF can be non-zero. Used only when WaveDirMod=0]
            0   DiffQTF        - Full difference-frequency 2nd-order forces computed with full QTF          {0: None; [10, 11, or 12]: WAMIT file to use}          [Only one of MnDrift, NewmanApp, or DiffQTF can be non-zero]
            0   SumQTF         - Full summation-frequency 2nd-order forces computed with full QTF           {0: None; [10, 11, or 12]: WAMIT file to use}
---------------------- FLOATING PLATFORM FORCE FLAGS  ------------------------- [unused with WaveMod=6]
True            PtfmSgF        - Platform horizontal surge translation force (flag) or DEFAULT
True            PtfmSwF        - Platform horizontal sway translation force (flag) or DEFAULT
True            PtfmHvF        - Platform vertical heave translation force (flag) or DEFAULT
True            PtfmRF         - Platform roll tilt rotation force (flag) or DEFAULT
True            PtfmPF         - Platform pitch tilt rotation force (flag) or DEFAULT
True            PtfmYF         - Platform yaw rotation force (flag) or DEFAULT
---------------------- PLATFORM ADDITIONAL STIFFNESS AND DAMPING  --------------
            0            0            0            0            0            0   AddF0    - Additional preload (N, N-m)
          130            0            0            0            0            0   AddCLin  - Additional linear stiffness (N/m, N/rad, N-m/m, N-m/rad) surge/sway(uncoupled:110)
            0          130            0            0            0            0
            0            0            0            0            0            0
            0            0            0            0            0            0
            0            0            0            0            0            0
            0            0            0            0            0            0
            0            0            0            0            0            0
            0            0            0            0            0            0   AddBLin  - Additional linear damping(N/(m/s), N/(rad/s), N-m/(m/s), N-m/(rad/s)): (Uncoupled:-47) surge 0 -43.5
            0            0            0            0            0            0
            0            0          500            0            0            0
            0            0            0           50            0            0
            0            0            0            0           50            0
            0            0            0            0            0          100
          950            0            0            0            0            0   AddBQuad - Additional quadratic drag(N/(m/s)^2, N/(rad/s)^2, N-m(m/s)^2, N-m/(rad/s)^2): surge 775 simulink 950
            0          950            0            0            0            0
            0            0          500            0            0            0
            0            0            0          350            0            0
            0            0            0            0          350            0
            0            0            0            0            0          220
---------------------- AXIAL COEFFICIENTS -------------------------------------
```

A.13.19 AAUE-TLP HydroDyn Input File


```
             2   NAxCoef        - Number of axial coefficients (-)
AxCoefID  AxCd     AxCa     AxCp
   (-)    (-)      (-)      (-)
    1     1.00     0.00     0.00
    2     1.00     0.00     0.00
---------------------- MEMBER JOINTS ------------------------------------------
             7    NJoints        - Number of joints (-)   [must be exactly 0 or at least 2]
JointID   Jointxi     Jointyi     Jointzi  JointAxID   JointOvrlp   [JointOvrlp= 0: do nothing at jo int, 1: eliminate overlaps by calculating super member]
   (-)     (m)         (m)         (m)        (-)       (switch)
    1     0.0        0.0          -0.7        1            0
    2     0.0        0.0           0.0        1            0
    3     0.7        0.0          -0.6        2            0
    4    -0.7        0.0          -0.6        2            0
    5     0.0        0.7          -0.6        2            0
    6     0.0       -0.7          -0.6        2            0
    7     0.0        0.0          -0.6        2            0
---------------------- MEMBER CROSS-SECTION PROPERTIES ------------------------
             2   NPropSets      - Number of member property sets (-)
PropSetID    PropD         PropThck
   (-)        (m)            (m)
    1       0.40            0.003
    2       0.20            0.003
---------------------- SIMPLE HYDRODYNAMIC COEFFICIENTS (model 1) --------------
     SimplCd 3.96    SimplCdMG    SimplCa    SimplCaMG    SimplCp    SimplCpMG   SimplAxCa  SimplAxC aMG  SimplAxCp   SimplAxC pMG
       (-)         (-)         (-)         (-)         (-)         (-)         (-)         (-)         (-)         (-)
       1.0        0.00        0.00        0.00        0.00        0.00        0.00        0.00        0.00        0.00
---------------------- DEPTH-BASED HYDRODYNAMIC COEFFICIENTS (model 2) ---------
             0   NCoefDpth       - Number of depth-dependent coefficients (-)
Dpth      DpthCd   DpthCdMG   DpthCa   DpthCaMG       DpthCp   DpthCpMG   DpthAxCa   DpthAxCaMG        DpthAxCp   DpthAxCpMG
(m)       (-)      (-)        (-)      (-)            (-)      (-)          (-)        (-)               (-)         (-)
---------------------- MEMBER-BASED HYDRODYNAMIC COEFFICIENTS (model 3) --------
             0   NCoefMembers       - Number of member-based coefficients (-)
MemberID    MemberCd1     MemberCd2    MemberCdMG1   MemberCdMG2    MemberCa1     MemberCa2    Membe rCaMG1   MemberCaMG2    MemberCp1     MemberCp2    MemberCpMG1   MemberCpMG2
  MemberAxCa1   MemberAxCa2  MemberAxCaMG1 MemberAxCaMG2  MemberAxCp1  MemberAxCp2   MemberAxCpMG1   M emberAxCpMG2
   (-)         (-)           (-)           (-)           (-)           (-)           (-)           (-)           (-)           (-)           (-)           (-)           (-)
                (-)           (-)           (-)           (-)           (-)           (-)           (-)
-------------------- MEMBERS ------------------------------------------------
             5   NMembers       - Number of members (-)
MemberID  MJointID1  MJointID2  MPropSetID1  MPropSetID2  MDivSize   MCoefMod  PropPot   [MCoefMod=1 : use simple coeff table, 2: use depth-based coeff table, 3: use member-based coeff
  table] [ PropPot/=0 if member is modeled with potential-flow theory]
  (-)        (-)        (-)         (-)          (-)        (m)      (switch)   (flag)
   1         1          2           1            1         0.007      1        TRUE
   2         7          3           2            2         0.007      1        TRUE
   3         7          4           2            2         0.007      1        TRUE
   4         7          5           2            2         0.007      1        TRUE
   5         7          6           2            2         0.007      1        TRUE
---------------------- FILLED MEMBERS ------------------------------------------
             0   NFillGroups     - Number of filled member groups (-) [If FillDens = DEFAULT, then FillDens = WtrDens; FillFSLoc is related to MSL2SWL]
FillNumM FillMList             FillFSLoc     FillDens
(-)      (-)                   (m)           (kg/m^3)
---------------------- MARINE GROWTH -------------------------------------------
             0   NMGDepths      - Number of marine-growth depths specified (-)
MGDpth     MGThck       MGDens
```

A.13.20 AAUE-TLP HydroDyn Input File

...K Jensen\Aalborg Universitet\OneDrive - Aalborg Universitet\EN1-B305\P9_10\Projekt\Matlab\FAST\CertTest\AAUETLP\AAUETLP_HydroDyn.dat 4

```
(m)      (m)          (kg/m^3)
---------------------- MEMBER OUTPUT LIST ----------------------------------------
           0  NMOutputs      - Number of member outputs (-) [must be < 10]
MemberID   NOutLoc    NodeLocs [NOutLoc < 10; node locations are normalized distance from the start  of the member, and must be >=0 and <= 1] [unused if NMOutputs=0]
  (-)      (-)          (-)
---------------------- JOINT OUTPUT LIST -----------------------------------------
           0  NJOutputs      - Number of joint outputs [Must be < 10]
   0       JOutLst        - List of JointIDs which are to be output (-)[unused if NJOutputs=0]
---------------------- OUTPUT ----------------------------------------------------
False          HDSum          - Output a summary file [flag]
False          OutAll         - Output all user-specified member and joint loads (only at each member end, not interior locations) [flag]
           3   OutSwtch       - Output requested channels to: [1=Hydrodyn.out, 2=GlueCode.out, 3=both files]
"ES11.4e2"     OutFmt         - Output format for numerical results (quoted string) [not checked for validity!]
"A11"          OutSFmt        - Output format for header strings (quoted string) [not checked for validity!]
---------------------- OUTPUT CHANNELS -------------------------------------------
"WaveElev"                    - Wave elevation at the platform reference point (  0,  0)
END of output channels and end of file. (the word "END" must appear in the first 3 columns of this 1 ine)

```

A.13.21 AAUE-TLP FEAMorring Input File

...Jensen\Aalborg Universitet\OneDrive - Aalborg Universitet\EN1-B305\P9_10\Projekt\Matlab\FAST\CertTest\AAUETLP\AAUETLP_FEAMooring.dat 1

```
1  ---------------------- FAST MOORING FILE -------------------------------------
2  AAUTLP, Edited by Jesper Kirkegaard Jensen, Kasper Laugesen, Kasper Jessen & Signe Mortensen. #rho=9 98; WtrDpth=1.92
3  ---------------------- SIMULATION CONTROL ------------------------------------
4  False          Echo        - Echo input data to <RootName>.ech (flag)
5     1E-04       DT          - Communication interval for module (s) default
6        4        NumLines    - Number of lines
7       10        NumElem     - Total number of elements per line 20
8  default        Gravity     - Gravitational acceleration (m/s^2)
9  default        WtrDens     - Water density (kg/m^3)
10    1000        MaxIter     - Maximum number of static iterations
11    1e-3        Eps         - Static iteration tolerance
12 ---------------------- MOORING LINES 1 ---------------------------------------
13    50E3        LEAStiff    - Axial stiffness: 45E3
14   0.004        LMassDen    - Mass per unit length of the element 116.027
15 7.8383e-04     LDMassDen   - Displaced mass per unit length of the element 12.984
16  0.0016        LineCI      - The inertia force per unit length / unit accel.
17     0.6        LineCD      - The drag force per unit length / unit relative vel squared. 0.5
18    1.22  LStrLen (m) 1.2135    LUnstrLen    - Unstretched length
19    3.0E6       BottmStiff  - Seabed stiffness
20   0.710        LRadAnch    (m) 27.00
21     0.0        LAngAnch    (deg)
22    1.92        LDpthAnch   (m) 200.00
23   0.710        LRadFair    (m) 27.00
24     0.0        LAngFair    (deg)
25    0.70        LDrftFair   (m) 47.89
26   240.0        Tension     - Initial top tension (N) 4.0E6   1.843E+03
27  1.0E8         GSL21       - The linear spring stiffness in x-direction between mooring & platform
28  1.0E8         GSL22       - The linear spring stiffness in y-direction between mooring & platform
29  1.0E8         GSL23       - The linear spring stiffness in z-direction between mooring & platform
30 ---------------------- MOORING LINES 2 ---------------------------------------
31    50E3        LEAStiff    - Axial stiffness: 45E3
32   0.004        LMassDen    - Mass per unit length of the element 116.027
33 7.8383e-04     LDMassDen   - Displaced mass per unit length of the element 12.984
34  0.0016        LineCI      - The inertia force per unit length / unit accel.
35     0.6        LineCD      - The drag force per unit length / unit relative vel squared. 0.5
36    1.22  LStrLen (m) 1.2135    LUnstrLen    - Unstretched length
37    3.0E6       BottmStiff  - Seabed stiffness 1.219
38   0.710        LRadAnch    (m) 27.00
39    90.0        LAngAnch    (deg)
40    1.92        LDpthAnch   (m) 200.00
41   0.710        LRadFair    (m) 27.00
42    90.0        LAngFair    (deg)
43    0.70        LDrftFair   (m) 47.89
44   240.0        Tension     - Initial top tension (N) 4.0E6   1.843E+03
45  1.0E8         GSL21       - The linear spring stiffness in x-direction between mooring & platform
46  1.0E8         GSL22       - The linear spring stiffness in y-direction between mooring & platform
47  1.0E8         GSL23       - The linear spring stiffness in z-direction between mooring & platform
48 ---------------------- MOORING LINES 3 ---------------------------------------
49    50E3        LEAStiff    - Axial stiffness: 45E3
50   0.004        LMassDen    - Mass per unit length of the element 116.027
51 7.8383e-04     LDMassDen   - Displaced mass per unit length of the element 12.984
52  0.0016        LineCI      - The inertia force per unit length / unit accel.
53     0.6        LineCD      - The drag force per unit length / unit relative vel squared. 0.5
```

A.13.22 AAUE-TLP FEAMorring Input File


```
1.22  LStrLen (m) 1.2135      LUnstrLen   - Unstretched length
3.0E6       BottmStiff  - Seabed stiffness
0.710       LRadAnch    (m) 27.00
180.0       LAngAnch    (deg)
1.92        LDpthAnch   (m) 200.00
0.710       LRadFair    (m) 27.00
180.0       LAngFair    (deg)
0.70        LDrftFair   (m) 47.89
240.0       Tension     - Initial top tension (N) 4.0E6   1.843E+03
1.0E8       GSL21       - The linear spring stiffness in x-direction between mooring & platform
1.0E8       GSL22       - The linear spring stiffness in y-direction between mooring & platform
1.0E8       GSL23       - The linear spring stiffness in z-direction between mooring & platform
---------------------- MOORING LINES 4 -----------------------------------------
50E3        LEAStiff    - Axial stiffness: 45E3
0.004       LMassDen    - Mass per unit length of the element 116.027
7.8383e-04  LDMassDen   - Displaced mass per unit length of the element 12.984
0.0016      LineCI      - The inertia force per unit length / unit accel.
0.6         LineCD      - The drag force per unit length / unit relative vel squared. 0.5
1.22  LStrLen (m) 1.2135      LUnstrLen   - Unstretched length
3.0E6       BottmStiff  - Seabed stiffness
0.710       LRadAnch    (m) 27.00
270.0       LAngAnch    (deg)
1.92        LDpthAnch   (m) 200.00
0.710       LRadFair    (m) 27.00
270.0       LAngFair    (deg)
0.70        LDrftFair   (m) 47.89
240.0       Tension     - Initial top tension (N) 4.0E6   1.843E+03
1.0E8       GSL21       - The linear spring stiffness in x-direction between mooring & platform
1.0E8       GSL22       - The linear spring stiffness in y-direction between mooring & platform
1.0E8       GSL23       - The linear spring stiffness in z-direction between mooring & platform
---------------------- OUTPUT --------------------------------------------------
False       SumPrint    - Print summary data to <RootName>.sum (flag) (currently unused)
      1     OutFile     - Switch to determine where output will be placed: {1: in module output file only; 2: in glue code output file only; 3: both} (currently unused)
True        TabDelim    - Use tab delimiters in text tabular output file? (flag) (currently unused)
"ES10.3E2"  OutFmt      - Format used for text tabular output (except time).  Resulting field should be 10 characters. (quoted string) (currently unused)
        5   TStart      - Time to begin tabular output (s) (currently unused)
            OutList     - The next line(s) contains a list of output parameters.  See OutListParameters.xlsx for a listing of available output channels, (-)
"FairT1, AnchT1"
"FairT2, AnchT2"
"FairT3, AnchT3"
"FairT4, AnchT4"
END of input file (the word "END" must appear in the first 3 columns of this last OutList line)
---------------------------------------------------------------------------
```

A.14 Electronics

A.14.1 Electrical Overview

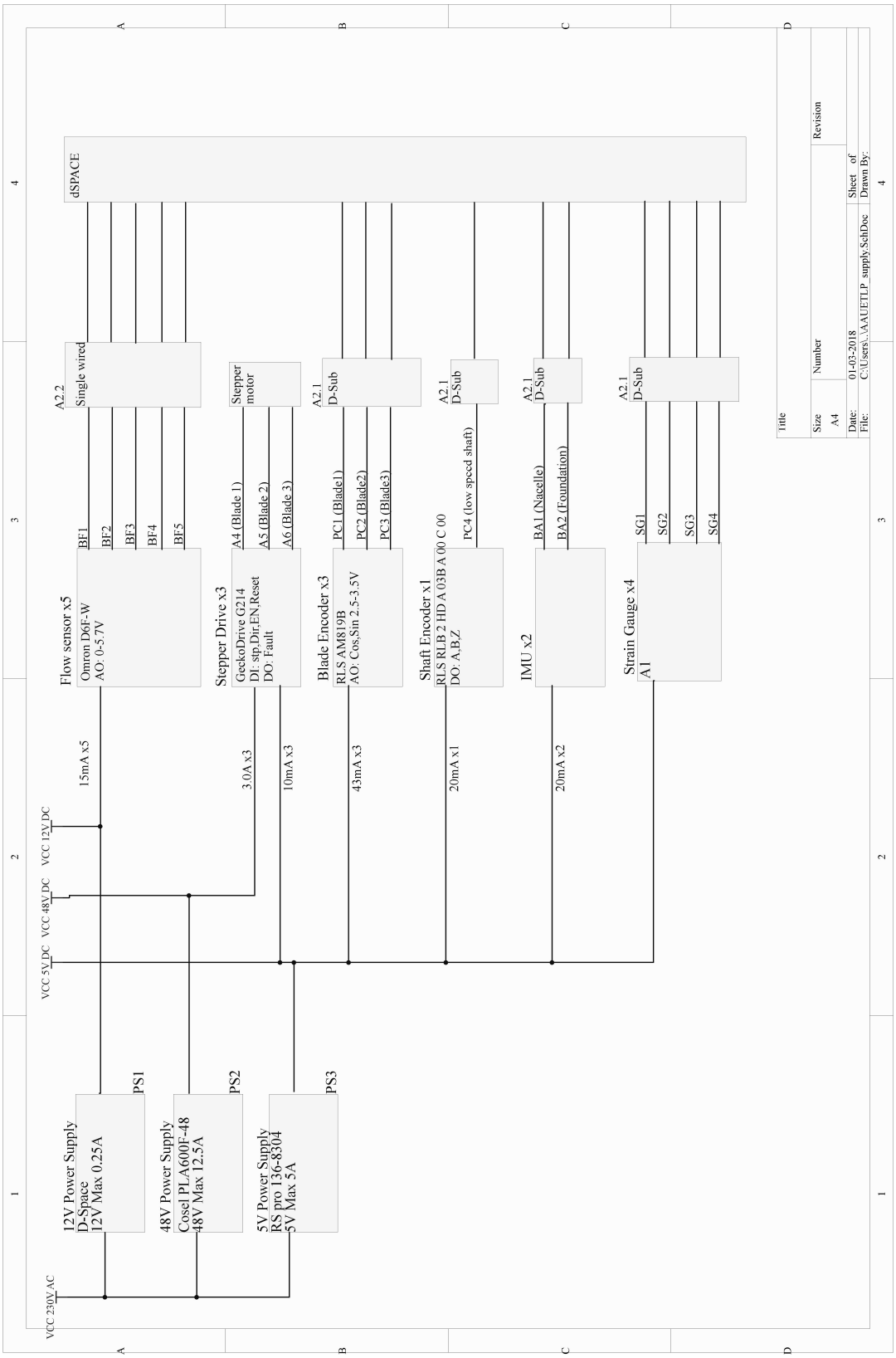

A.14.2 Input / Output List for AAUE-TLP

Table A.1: Signal Input Output List for AAUE-TLP

Wire	Wire no.	A/D	Item	Signal	Desig.	Board	Filter O	d-SPACE
D-sub-1	1	A	Blade Enc (Bl1)	Cos	PC1	A2.1	AO1	AI1-CH1
D-sub-1	2	A	Blade Enc (Bl1)	Sin	PC1	A2.1	AO2	AI1-CH2
D-sub-1	3	A	Blade Enc (Bl1)	Cos	PC2	A2.1	AO3	AI1-CH3
D-sub-1	4	A	Blade Enc (Bl1)	Sin	PC2	A2.1	AO4	AI1-CH4
D-sub-1	5	A	Blade Enc (Bl1)	Cos	PC3	A2.1	AO5	AI1-CH5
D-sub-1	6	A	Blade Enc (Bl1)	Sin	PC3	A2.1	AO6	AI1-CH6
D-sub-1	7	A	Blade Enc (Bl1)	Out	SG1	A2.1	AO7	AI1-CH7
D-sub-1	8	A	Blade Enc (Bl1)	Out	SG2	A2.1	AO8	AI1-CH8
D-sub-1	9	A	Blade Enc (Bl1)	Out	SG3	A2.1	AO9	AI1-CH9
D-sub-1	10	A	Blade Enc (Bl1)	Out	SG4	A2.1	AO10	AI1-CH10
D-sub-1	13	D	Blade Enc (Bl1)	Error	Error	A2.1	P8-1	-
D-sub-1	14	D	Blade Enc (Bl1)	Z(4)	Z	A2.1	P8-2	DIO1.CH35
D-sub-1	15	D	Blade Enc (Bl1)	B(5)	B	A2.1	P8-3	DIO1-CH34
D-sub-1	16	D	Blade Enc (Bl1)	A(6)	A	A2.1	P8-4	DIO1-CH33
		A	Curr sens 1 (Ph u)	Out	A3	A3	AO1	-
		A	Curr sens 2 (Ph v)	Out	A3	A3	AO2	-
		A	Curr sens 3 (Ph w)	Out	A3	A3	AO3	-
		A	Volt sens 1 (Ph u)	Out	A3	A3	AO4	-
		A	Volt sens 2 (Ph v)	Out	A3	A3	AO5	-
		A	Volt sens 3 (Ph w)	Out	A3	A3	AO6	-

Table A.2: Power Input Output List for AAUE-TLP

Wire	Wire no.	A/D	Item	Signal	Desig.	Board	Filter O	d-SPACE
D-sub-2	1	D	Step.Mot. Bl1 ph A	Cos	PC1	A2.1	AO1	AI1-CH1
D-sub-2	2	D	Step.Mot. Bl1 ph $\bar{A}$	Sin	PC1	A2.1	AO2	AI1-CH2
D-sub-2	3	D	Step.Mot. Bl1 ph B	Cos	PC2	A2.1	AO3	AI1-CH3
D-sub-2	4	D	Step.Mot. Bl1 ph $\bar{B}$	Sin	PC2	A2.1	AO4	AI1-CH4
D-sub-2	5	D	Step.Mot. Bl2 ph A	Cos	PC3	A2.1	AO5	AI1-CH5
D-sub-2	6	D	Step.Mot. Bl2 ph $\bar{A}$	Sin	PC3	A2.1	AO6	AI1-CH6
D-sub-2	7	D	Step.Mot. Bl2 ph B	Out	SG1	A2.1	AO7	AI1-CH7
D-sub-2	8	D	Step.Mot. Bl2 ph $\bar{B}$	Out	SG2	A2.1	AO8	AI1-CH8
D-sub-2	9	D	Step.Mot. Bl3 ph A	Out	SG3	A2.1	AO9	AI1-CH9
D-sub-2	10	D	Step.Mot. Bl3 ph $\bar{A}$	Out	SG4	A2.1	AO10	AI1-CH10
D-sub-2	11	D	Step.Mot. Bl3 ph B	Error	Error	A2.1	P8-1	-
D-sub-2	12	D	Step.Mot. Bl3 ph $\bar{B}$	Z(4)	Z	A2.1	P8-2	DIO1.CH35

Table A.3: Optical Input Output List for AAUE-TLP

A/D	Item	VLT (TPC3)	UPC2dSPACE	d-SPACE
Optic	Output PMW	WP	WP1	SIO CH11
Optic	Output PMW	VP	VP1	SIO CH11
Optic	Output PMW	UP	UP1	SIO CH11
Optic	Output PMW	EN	EN1	SIO CH11
Optic	Output PMW	RST	RST1	SIO CH11
Optic	Output PMW	TRIP	TRIP1	SIO CH11
Optic	Output PMW	BR	BR1	SIO CH11

A.14.3 Strain Gauge Amplifier Board for AAUETLP v1.0 A1

Circuit board for strain gauge amplification and completing of half bridge connection. The circuit board complete the half-bridge connection of a wheat-stone half bridge with two resistors together with the strain gauges.

- Completing half bridge
- Amplification of strain gauge signal

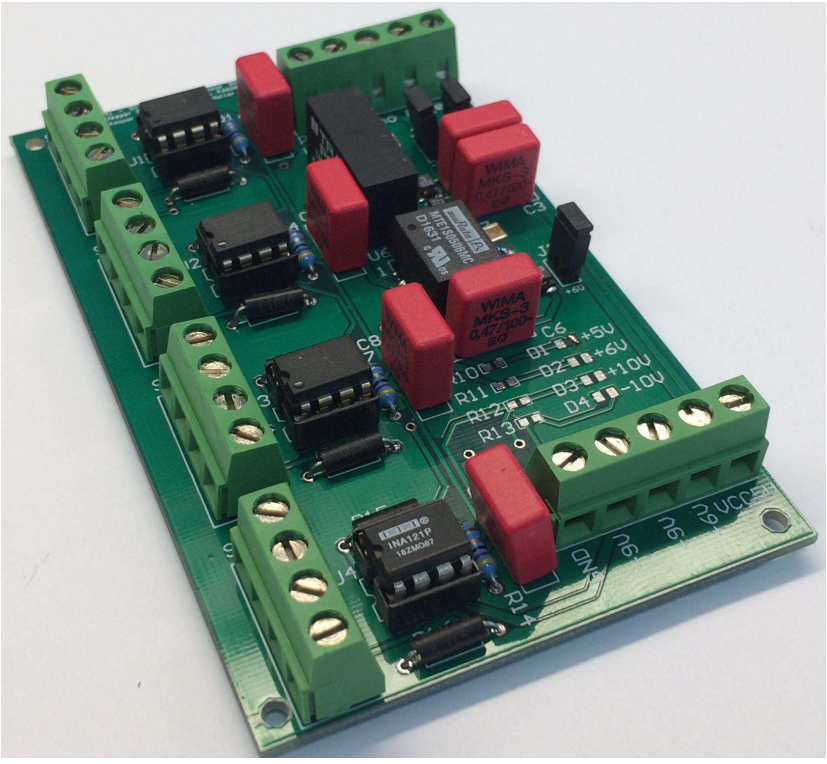

Figure A.17: Strain Gauge Amplifier Board for AAUETLP v1.0 A1

Table A.4: Specifications

	Board Symbol	Typical
Supply Voltage	VCC	5VDC

Table A.5: Connections

Terminal	Connection	Board Symbol
P1-1	Strain Gauge 1-1	SG1
P1-2	Strain Gauge 1-1	SG1
P1-3	Strain Gauge 1-2	SG1
P1-4	Strain Gauge 1-2	SG1
P2-1	Strain Gauge 2-1	SG2
P2-2	Strain Gauge 2-1	SG2
P2-3	Strain Gauge 2-2	SG2
P2-4	Strain Gauge 2-2	SG2
P3-1	Strain Gauge 3-1	SG3
P3-2	Strain Gauge 3-1	SG3
P3-3	Strain Gauge 3-2	SG3
P3-4	Strain Gauge 3-2	SG3
P4-1	Strain Gauge 4-1	SG4
P4-2	Strain Gauge 4-1	SG4
P4-3	Strain Gauge 4-2	SG4
P4-4	Strain Gauge 4-2	SG4
P5-1	Analogue Out SG 1	SG1
P5-2	Analogue Out SG 2	SG2
P5-3	Analogue Out SG 3	SG3
P5-4	Analogue Out SG 4	SG4
P5-5	GND	GND
P6-1	GND	GND
P6-2	-9V	-9V
P6-3	+9V	+9V
P6-4	+6V	+6V
P6-5	5V-Vcc	VCC5V

A.14.3.1 Schematic

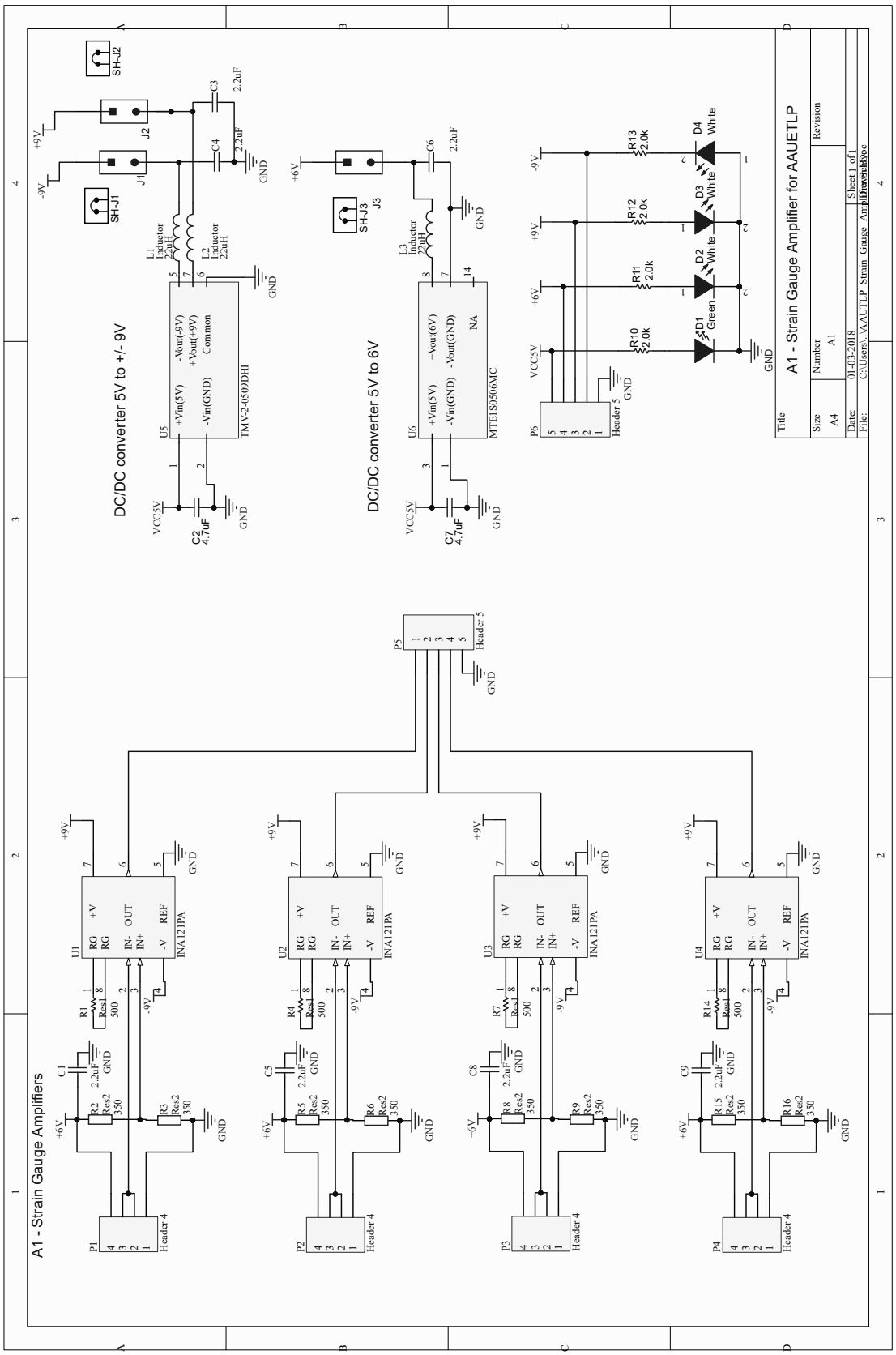

Table A.6: Components (Ordering information)

Part designator	Item	Order No	No of components
P1,P2,P3,P4	Terminal Block 4-pin	282836-4	4
P5,P6	Terminal Block 5-pin	282836-5	2
U1,U2,U3,U4	Instrumentation amplifier	INA 121PA	4
U5	DC/DC converter 5V to ±9V	TMV-2-0509DHI	1
U6	DC/DC converter 5V to 6V	MTE1S0506MC	1
R2,R3,R5,R6,R8,R9,R15,R16	High prepositions resistors	-	8
R1,R4,R7,R14	Hole through resistor	-	4
C1,C5,C8,C9	Hole through capacitor	-	4
C2,C3,C4,C6,C7	Surface mounted capacitors	-	5
D1,...,D4	LED	-	4
R10,R11,R12,R13	Surface mounted resistors	-	6
J1,J2,J3	Jumper 2-pin	M20-9773646	3
	Shunt for jumpers	AKSCT/Z Black	3
L1,L2,L3	Inductors	-	2

A.14.3.2 PCB layout

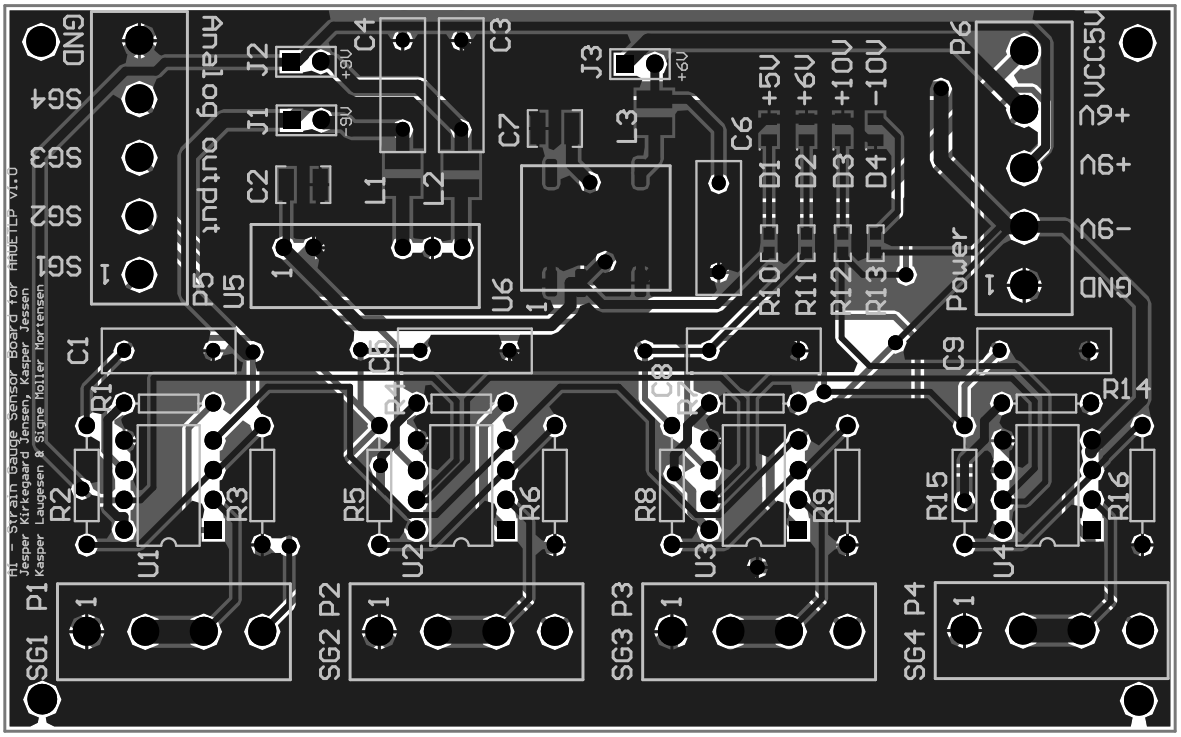

A.14.4 D-sub or terminal to BNC with filter for AAUETLP v1.0 - A2

Circuit board to go from D-sub 25-pin plug or terminals to BNC plugs or terminals with low pass filter on each channel.

- Input D-sub 25-pin and/or terminal
- Output 12 BNC and/or terminal
- Low pass filter on each channel

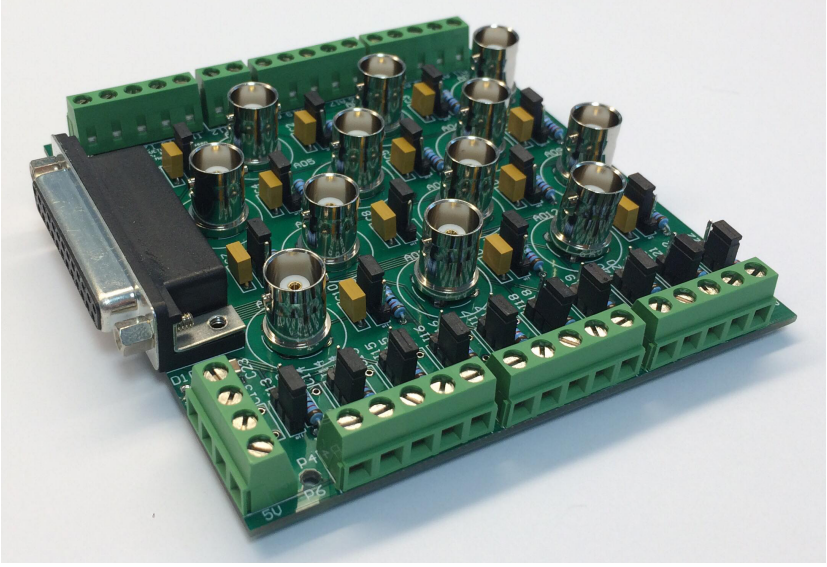

Figure A.18: D-sub or terminal to BNC with filter for AAUETLP v1.0 - A2

Table A.7: Specifications

	Board Symbol	Typical
Supply Voltage	VCC	5VDC

Table A.8: Input Connections

Terminal	D-sub Connections P0	Board Symbol
P1-1	Pin 12	AI12
P1-2	Pin 11	AI11
P2-1	Pin 1	AI1
P2-2	Pin 2	AI2
P2-3	Pin 3	AI3
P2-4	Pin 4	AI4
P2-5	Pin 5	AI5
P3-1	Pin 6	AI6
P3-2	Pin 7	AI7
P3-3	Pin 8	AI8
P3-4	Pin 9	AI9
P3-5	Pin 10	AI10
P4-1	Pin 22	I13
P4-2	Pin 21	I14
P4-3	Pin 20	I15
P4-4	Pin 19	I16
P4-5	Pin 18	I17
P5-1	Pin 17	I18
P5-2	Pin 16	I19
P5-3	Pin 15	I20
P5-4	Pin 14	I21
P5-5	Pin 13	I22
P6-1	Pin 25	GND
P6-2	Pin 26	GND
P6-3	Pin 23	5V
P6-4	Pin 24	5V

Table A.9: Input Connections

Terminal	D-sub Connections P0 (Output from)	Board Symbol
P7-1	Pin 18	O17
P7-2	Pin 19	O16
P7-3	Pin 20	O15
P7-4	Pin 21	O14
P7-5	Pin 22	O13
P8-1	Pin 13	O22
P8-2	Pin 14	O21
P8-3	Pin 15	O20
P8-4	Pin 16	O19
P8-5	Pin 17	O18
AO1	Pin 1	AO1
AO2	Pin 2	AO2
AO3	Pin 3	AO3
AO4	Pin 4	AO4
AO5	Pin 5	AO5
AO6	Pin 6	AO6
AO7	Pin 7	AO7
AO8	Pin 8	AO8
AO9	Pin 9	AO9
AO10	Pin 10	AO10
AO11	Pin 11	AO11
AO12	Pin 12	AO12

A.14.5 Application scheme

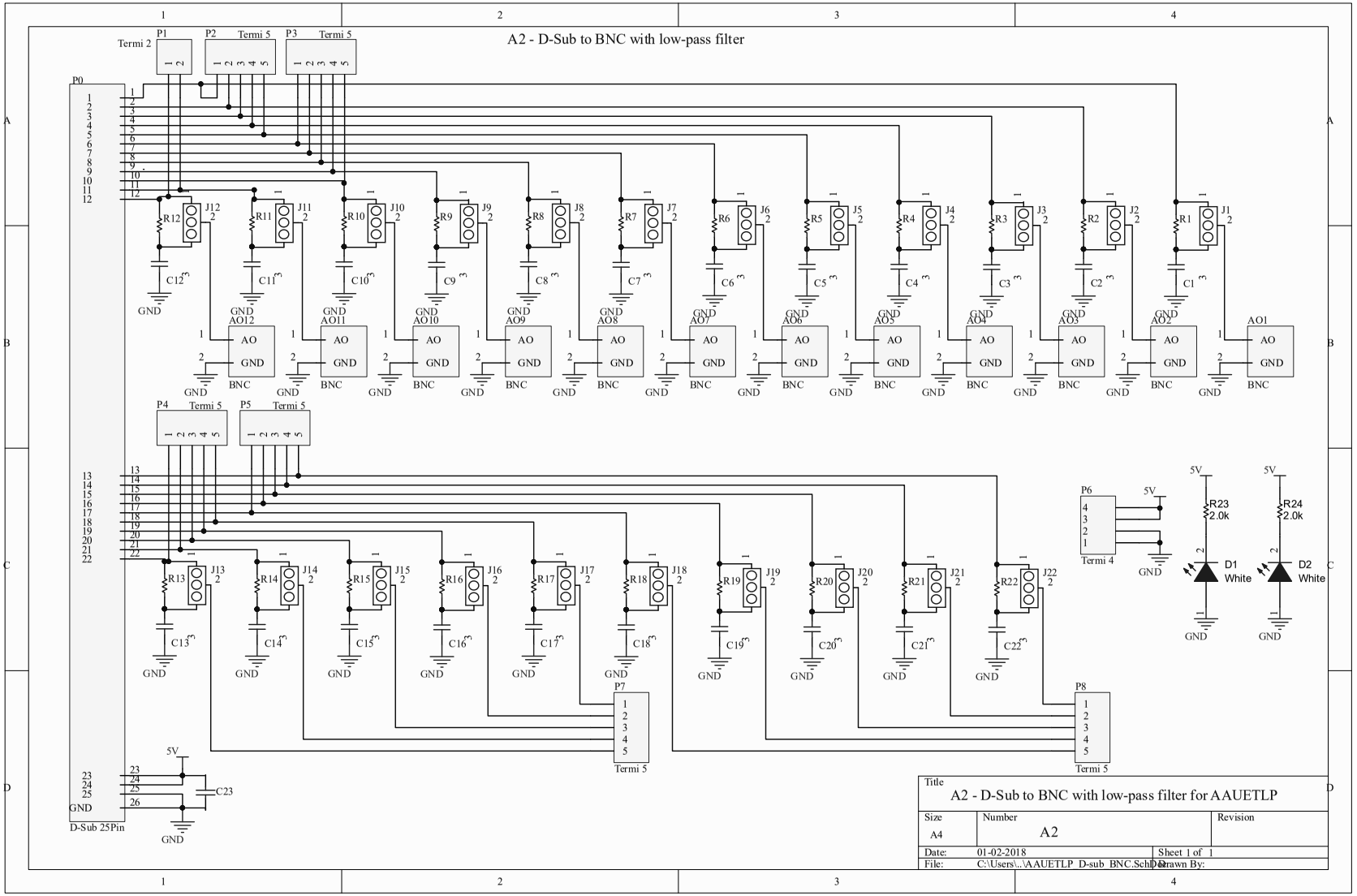
A2 - D-Sub to BNC with low-pass filter
P0
D-Sub 25Pin
P1
Termi 2
P2
Termi 5
P3
Termi 5
P4
Termi 5
P5
Termi 5
P6
Termi 4
P7
Termi 5
P8
Termi 5
R1
R2
R3
R4
R5
R6
R7
R8
R9
R10
R11
R12
R13
R14
R15
R16
R17
R18
R19
R20
R21
R22
R23
2.0k
R24
2.0k
C1
C2
C3
C4
C5
C6
C7
C8
C9
C10
C11
C12
C13
C14
C15
C16
C17
C18
C19
C20
C21
C22
C23
J1
J2
J3
J4
J5
J6
J7
J8
J9
J10
J11
J12
J13
J14
J15
J16
J17
J18
J19
J20
J21
J22
AO1
AO2
AO3
AO4
AO5
AO6
AO7
AO8
AO9
AO10
AO11
AO12
AO
GND
BNC
5V
D1
White
D2
White
Title
A2 - D-Sub to BNC with low-pass filter for AAUETLP
Size
A4
Number
A2
Revision
Date:
01-02-2018
Sheet 1 of 1
File:
C:\Users\...\AAUETLP_D-sub_BNC.SchDoc
Drawn By:

A.14.5.1 Settings

Filter

For each output a low pass filter can be implemented and the cutoff frequency can be adjusted by adjusting the resistor and/or the capacitor.

$$f_{cut} = \frac{1}{2\pi RC} \tag{A.8}$$

The low pass filters can be set on or off by setting a jumper (J1,...,J6)

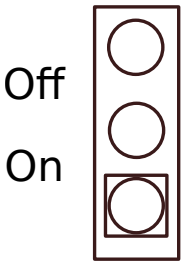

Figure A.19: Filter on/off

Table A.10: Components (Ordering information)

Part designator	Item	Order No	No of components
P0	D-sub 25-pin	1734349-1	1
P1	Terminal block 2-pin	282836-2	1
P1,P2,P3,P5,P7,P8	Terminal block 5-pin	282836-5	6
P6	Terminal block 4-pin	282836-4	1
AO1,...,AO12	BNC - Plug	R13-022-01-002611000	12
C23	Capacitor	133-5646	1
J1,...,J22	Jumper 3-pin	M20-9773646	22
	Shunt for jumper	AKSCT/Z Black	22
R1,...,R22	Hole through resistor	-	22
C1,...,C22	Hole through capacitor	-	22
D1,D2	LED surface mounted	-	2
R23,R24	Surface mounted resistor	-	2

A.14.5.2 PCB layout

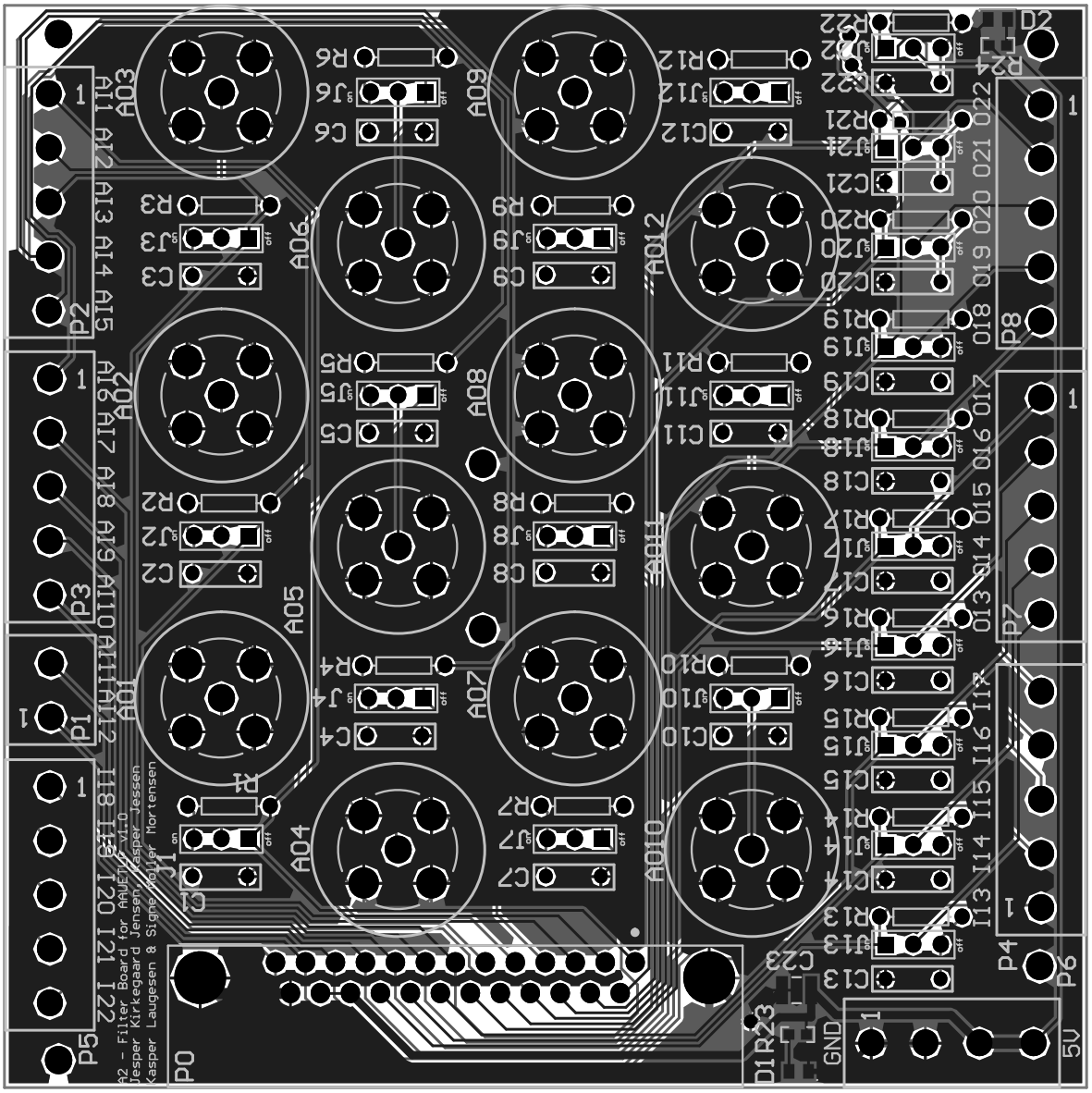

A.14.6 Current and Voltage Sensor Board for AAUETLP v1.0 - A3

The circuit board sense and isolate 3-phase currents by using three LEM LTS 6-NP closed loop current transducers and sense and isolate the 3-phase voltage using three TI INA146 difference amplifiers. An analogue output is provided for each current and voltage sense, filtered by a low pass filter with adjustable cut off frequency.

- Analogue output
- Adjustable current levels
- Adjustable voltage gain
- Adjustable output filter
- BNC plug output

Table A.11: Specifications

	Board Symbol	Typical
Supply Voltage	VCC	5VDC
Current consumption		120mA
Analogue output voltage (Current measurement)	AO1,AO2,AO3	0.5 to 4.5V
Analogue output voltage (Voltage measurement)	AO4,AO5,AO6	-9.0 to 9.0V
Accuracy (Current sense output LTS 6-NP)		± 0.2%
Accuracy (Voltage sense output Ina146)		0.025%
Nominal current measurement level	$\pm I_{PN}$	±2/3/6A

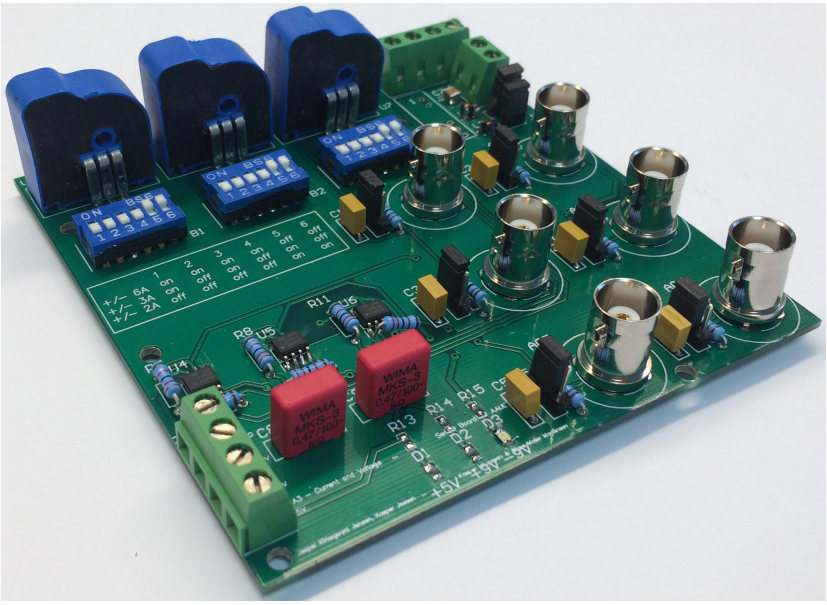

Figure A.20: Current and Voltage Sensor Board for AAUETLP v1.0 - A3

Table A.12: Connections

Terminal	Connection	Board Symbol
P1-1	Ground	GND
P1-2	5VDC supply	5V
P2-1	NC	GND
P2-2	NC	-9V
P2-3	NC	+9V
P2-4	NC	+5V
P3-1	Phase L1	L1
P3-2	Phase L2	L2
P3-3	Phase L3	L3
P3-4	NC	GND
AO1	Analogue out, current of phase 1	I1
AO2	Analogue out, current of phase 2	I2
AO3	Analogue out, current of phase 3	I3
AO4	Analogue out, voltage of phase 1	L1-L2
AO5	Analogue out, voltage of phase 2	L2-L3
AO6	Analogue out, voltage of phase 3	L3-L1

A.14.7 Application scheme Current sense

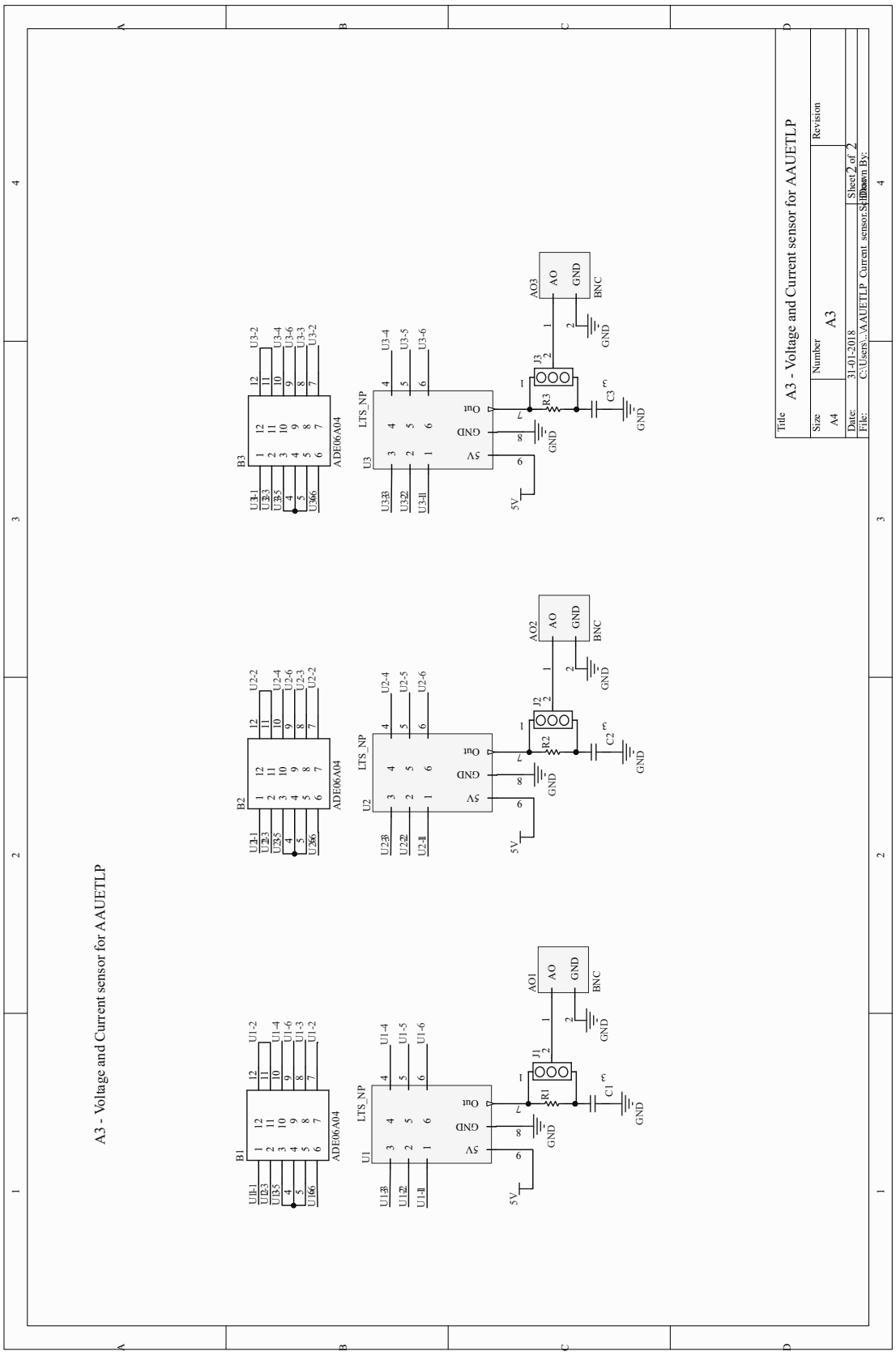

A.14.8 Application scheme Current sense

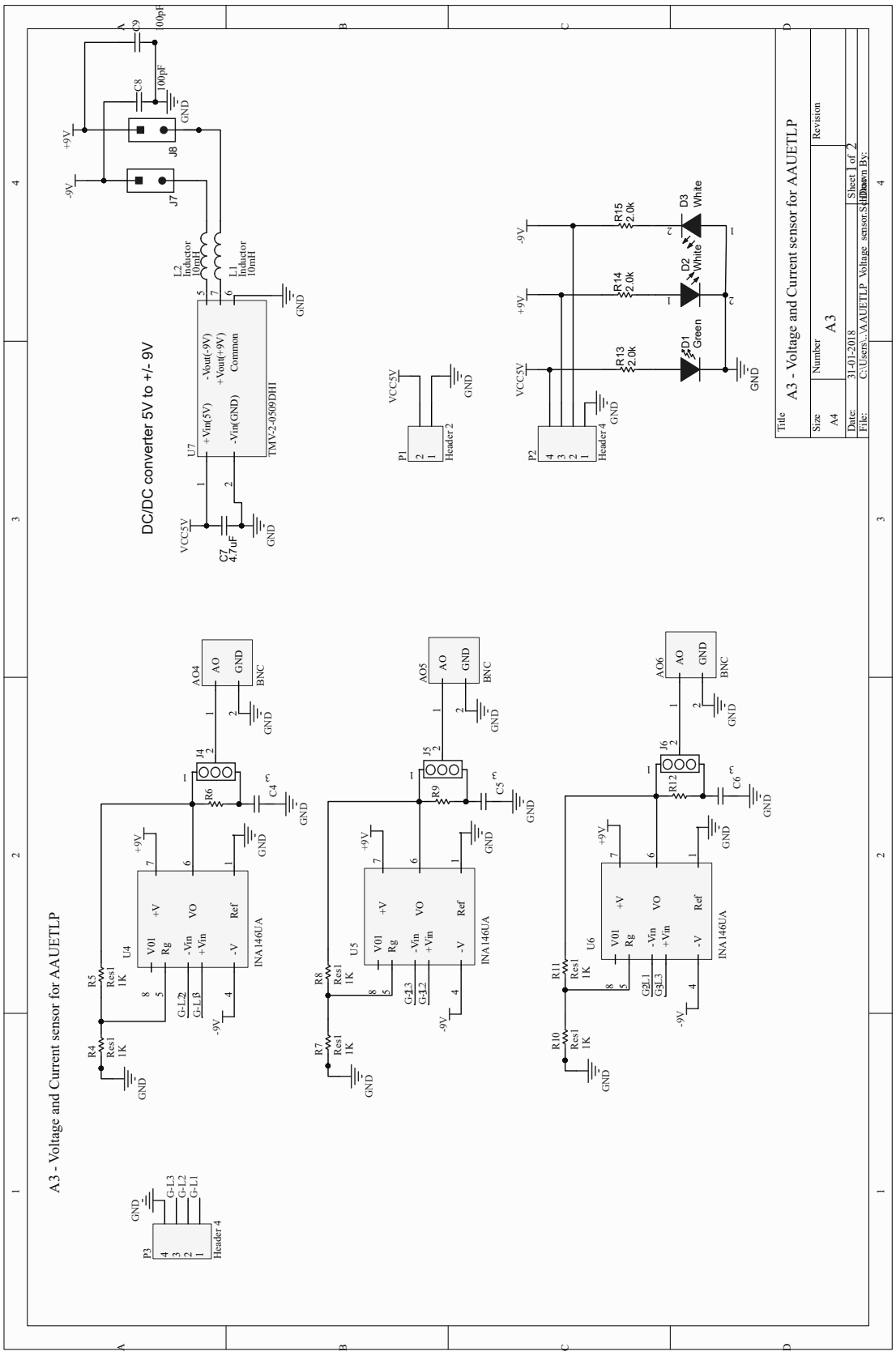

A.14.8.1 Settings

Current Sense

The current measurement can be adjusted to fit different levels of currents (± 2/3/6A) by setting the dip switch for each of the current transducers. The level is set according to the following table

Table A.13: Connections

$\pm I_{PN}$	1	2	3	4	5	6
± 6A	On	On	On	On	Off	Off
± 3A	On	Off	On	Off	On	Off
± 2A	Off	Off	Off	Off	On	On

The output characteristics of AO1, AO2 and AO3 is described by the following

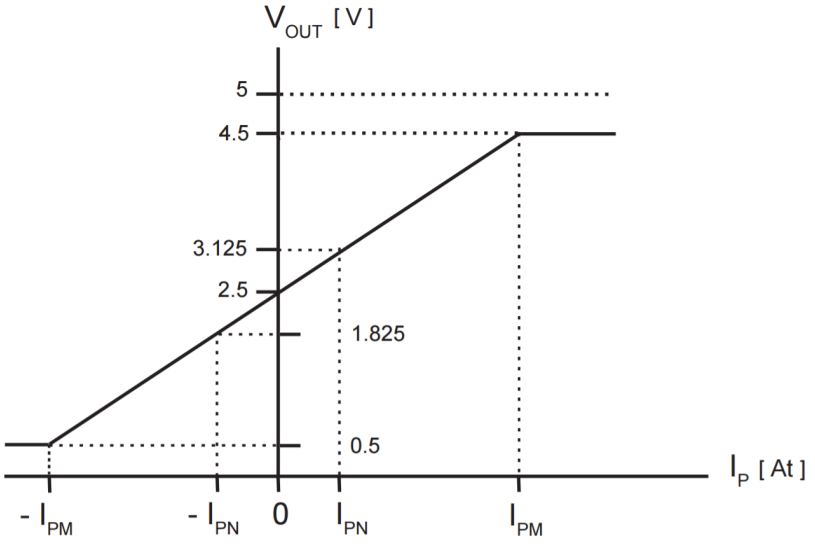

Figure A.21: Output voltage vs measured current LTS 6-NP

The nominel current measurement is set to ±2A

Voltage sense

Each phase voltage is measured through a difference amplifier (INA146) where the gain is set by to resistors.

The ± 9 V converter can be activated by connecting it to the circuit by setting the jumpers J7 and J8

$$Gain = 0.1\left(1 + \frac{R_{G2}}{R_{G1}}\right) \tag{A.9}$$

Where the resistors RG1 and RG2 corresponds to

Table A.14: Connections

	Phase L1	Phase L2	Phase L3
R_{G1}	R4	R7	R10
R_{G2}	R5	R8	R11

The gain is set to 0.2 by 22$k\Omega$ resistors.

Filter
For each output a low pass filter can be implemented and the cutoff frequency can be adjusted by adjusting the resistor and/or the capacitor.

$$f_{cut} = \frac{1}{2\pi RC} \tag{A.10}$$

Resistors of 18$k\Omega$ and capacitors of 33,3 nF is used. The low pass filter can be set on or off by setting a jumper (J1,...,J6)

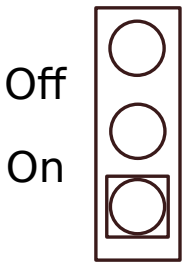

Figure A.22: Filter on/off

Table A.15: Components (Ordering information)

Part designator	Item	Order No	No of components
U1,U2,U3	Current transducer	LTS 6-NP	3
U4,U5,U6	Instrumentation amplifier	INA 146UA	3
U7	DC-Dc Converter 5V to ± 9V	TMV-2-0509DHI	1
B1,B2,B3	Dip switch 6way	ADE06A04	3
P1	Terminal block 2-pin	282836-2	1
P2,P3	Terminal block 4-pin	282836-4	2
AO1,...,AO6	BNC-plug	R13-022-01-002611000	6
J1,...,J6	Jumper 3-pin	AM20-9773646	6
J7,J8	Jumper 2-pin	M20-9773646	1
	Shunt for jumpers	AKSCT/Z Black	8
R1,...,R12	Hole through resistor	-	12
R1,...,C6	Hole through capacitor	-	6
C7	Surface mounted capacitor	-	1
C8,C9	Capacitor	-	2
L1,L2	Inductor	-	2
R13,R14,R15	Surface mounted resistor	-	3
D1,D2,D3	LED, Surface mounted	-	3

A.14.8.2 PCB layout

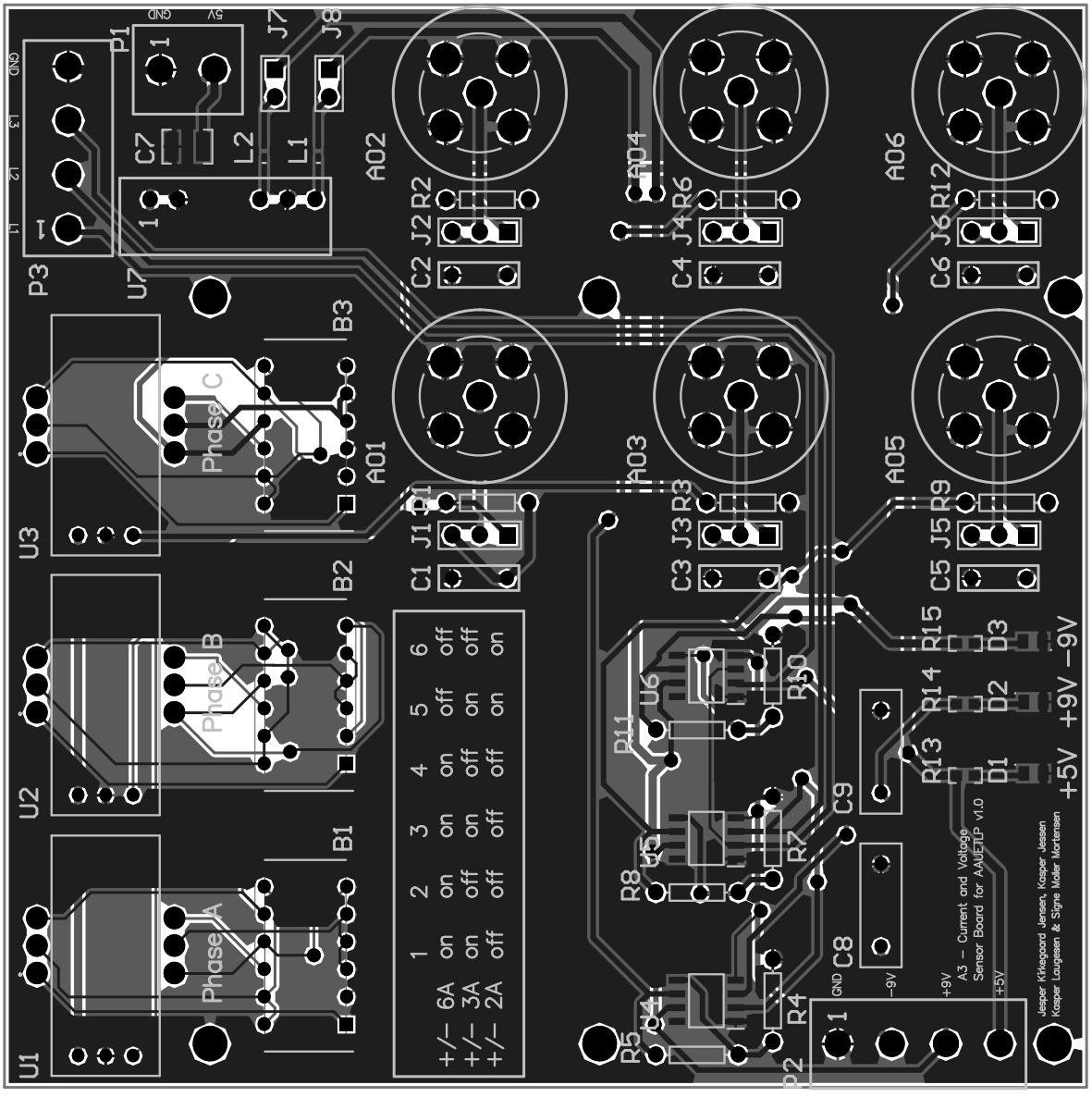

A.14.9 Power converter

The Danfoss VLT AutomationDrive FC 301/FC 302 main supply 200-240V PK75 is modified to be work as an active rectifier by disconnecting the passive rectifier and using the motor output as generator input. The modifications of the VLT is seen in fig A.23

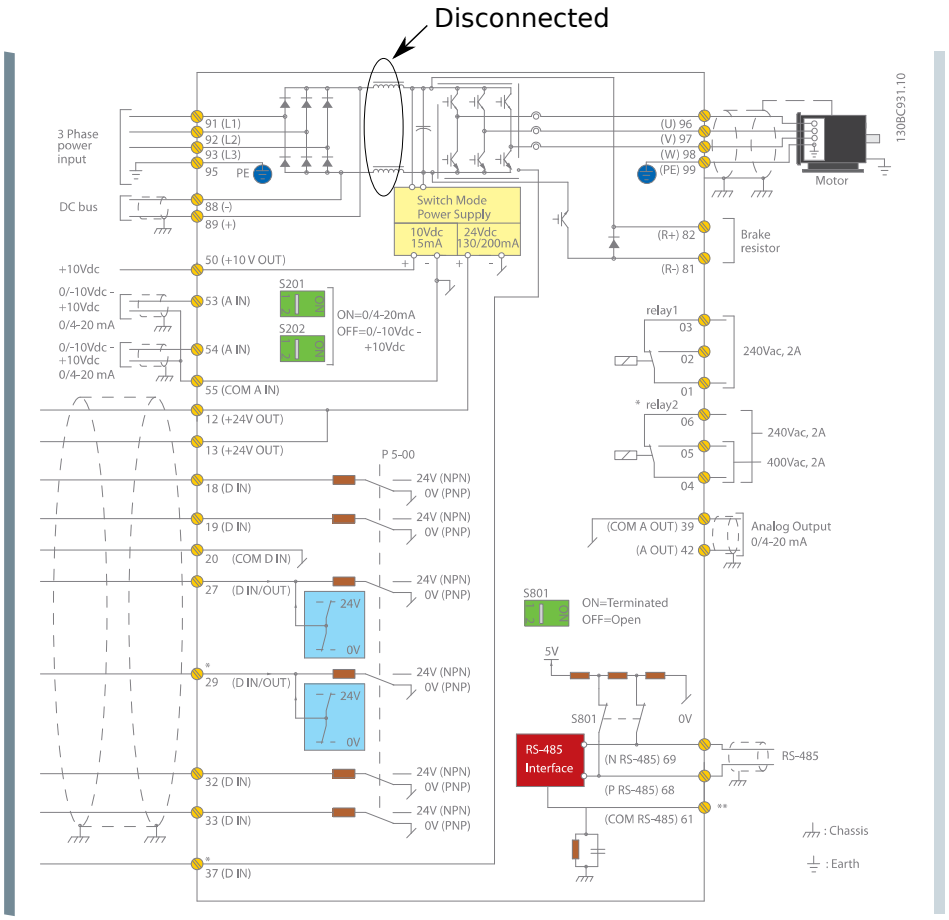

The numbers represent the terminals on the drive

Figure A.23: Modification on Danfoss VLT

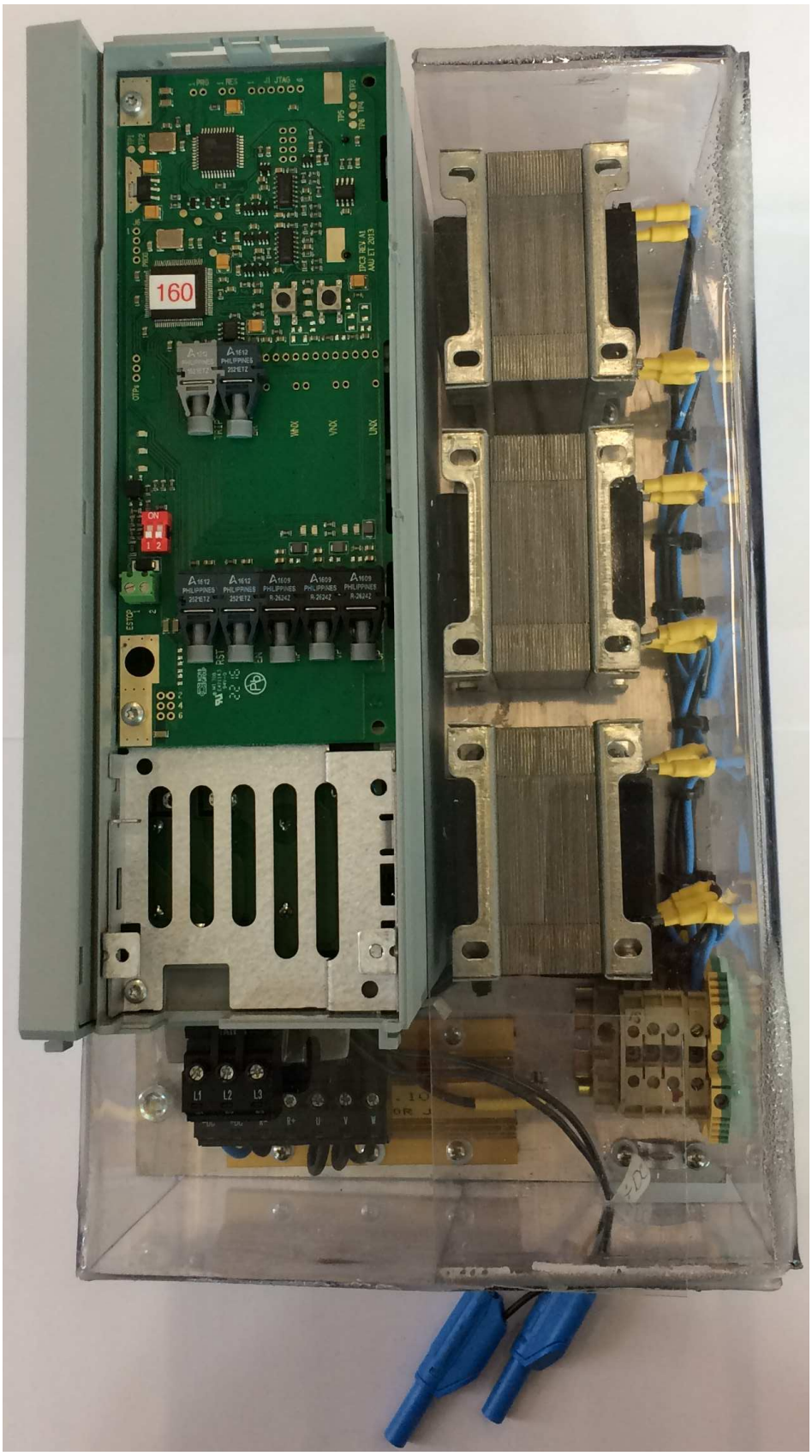

Figure A.24: VLT

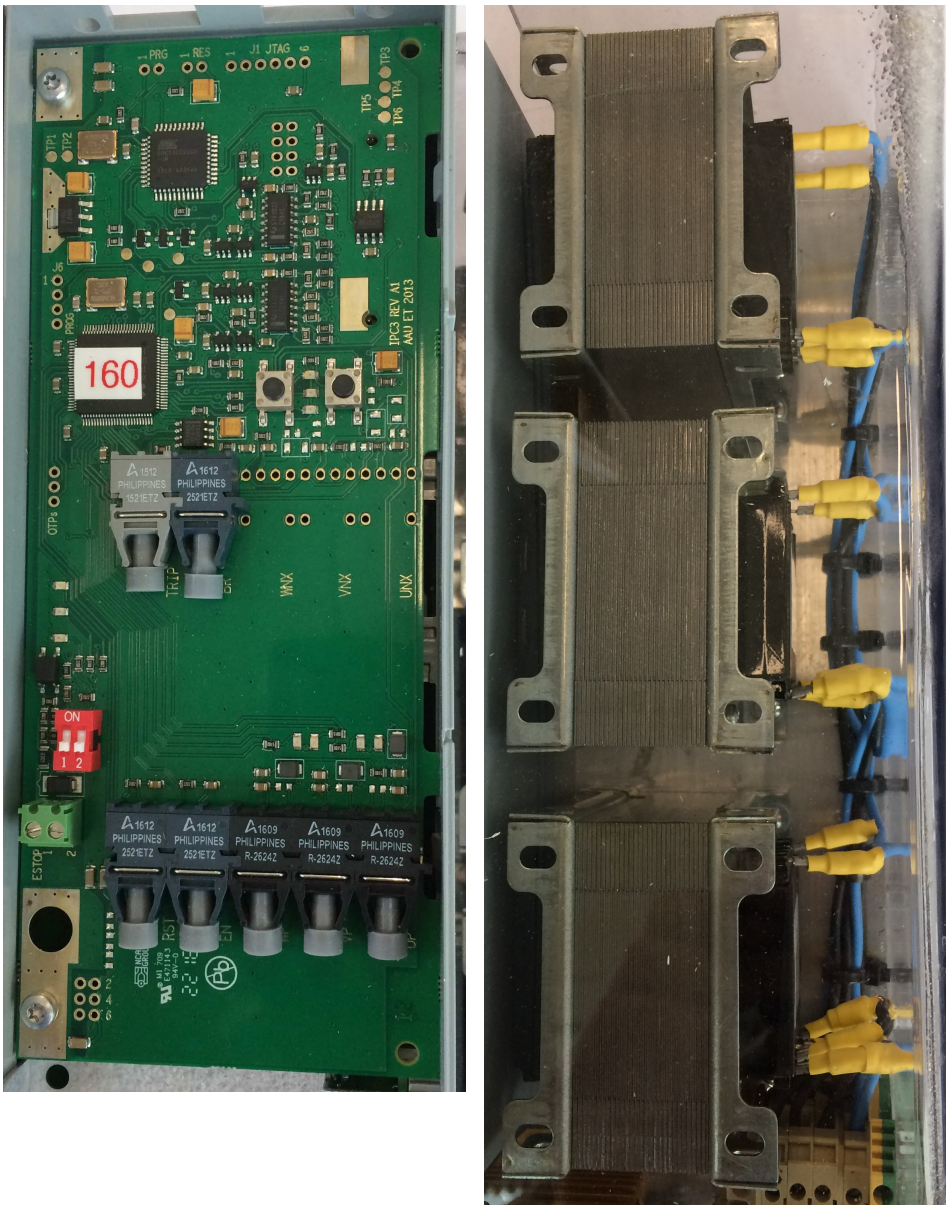

Figure A.25: IPC3 and transformers